

NATIONAL AERONAUTICS AND SPACE ADMINISTRATION

Space Programs Summary 37-42, Vol. IV

Supporting Research and Advanced Development

For the Period October 1 to November 30, 1966

JET PROPULSION LABORATORY
CALIFORNIA INSTITUTE OF TECHNOLOGY
PASADENA, CALIFORNIA

December 31, 1966

Space Programs Summary 37-42, Vol. IV

Copyright © 1967

**Jet Propulsion Laboratory
California Institute of Technology**

**Prepared Under Contract No. NAS 7-100
National Aeronautics & Space Administration**

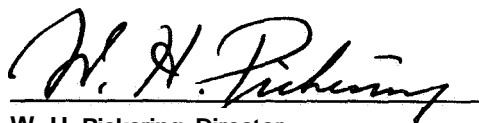
Preface

The Space Programs Summary is a six-volume bimonthly publication designed to report on JPL space exploration programs and related supporting research and advanced development projects. The titles of all volumes of the Space Programs Summary are:

- Vol. I. *The Lunar Program* (Confidential)
- Vol. II. *The Planetary-Interplanetary Program* (Confidential)
- Vol. III. *The Deep Space Network* (Unclassified)
- Vol. IV. *Supporting Research and Advanced Development* (Unclassified)
- Vol. V. *Supporting Research and Advanced Development* (Confidential)
- Vol. VI. *Space Exploration Programs and Space Sciences* (Unclassified)

The Space Programs Summary, Vol. VI, consists of: an unclassified digest of appropriate material from Vols. I, II, and III; an original presentation of the JPL quality assurance and reliability efforts, and the environmental- and dynamic-testing facility-development activities; and a reprint of the space science instrumentation studies of Vols. I and II.

Approved by:



W. H. Pickering, Director

Jet Propulsion Laboratory

Contents

SYSTEMS DIVISION

I. Scientific Programming	1	
A. Dependency of Constraints for Differential Equations	1	✓
NASA Code 129-04-04-01, A. J. Sernfner	1	
B. Corrections to the Lunar Ephemeris	2	✓
NASA Code 129-04-04-02, J. D. Mulholland	2	
C. Combined Radiation-Conduction Heat Transfer in a Finned Cylinder in Space	5	✓
NASA Code 129-04-04-01, W. R. Bunton and E. M. Keberle	5	
D. Electrostatic Charge Densities on an Electro-optical Star Tracker	10	✓
NASA Code 129-04-04-01, N. C. Adorns, E. M. Keberle, and W. Silsby	10	
E. On Geometric Properties of the Estabrook-Wahlquist Function Chain	15	✓
NASA Code 129-04-04-01, E. M. Keberle	15	
References	18	
II. Systems Analysis	19	
A. Relationship Between the Averaging Method of Krylov-Bogoliubov and an Approximate First Integral of Motion	19	✓
NASA Code 129-04-01-01, H. Lass	19	
B. A Note on Stratonovich's Equation for the Conditional Probability Distribution of the State of a Nonlinear System, with Application to Nonlinear Filtering	22	✓
NASA Code 129-04-01-01, S. R. McReynolds	22	
C. On the First Occurrence of Specified Sequences	27	✓
NASA Code 129-04-01-01, C. B. Solloway and H. Lass	27	
D. A Note on Null Geodesics in the General Theory of Relativity	30	✓
NASA Code 129-04-01-01, H. Lass	30	
E. Numerical Integration of Periodic Orbits in the Elliptic Restricted Three-Body Problem	31	✓
NASA Code 129-04-01-02, R. Braucke	31	
References	34	

GUIDANCE AND CONTROL DIVISION

111. Spacecraft Power	35	
A. Sterilizable Battery	35	✓
NASA Code 120-34-01-03, 120-34-01-05, R. Lutwack	35	
IV. Guidance and Control Analysis and Integration	37	
A. Advanced Test Techniques	37	✓
NASA Code 125-23-01-01, T. P. Cerney and R. Lawrence	37	
References	41	

Contents (contd)

V. Spacecraft Control	42	
A. Image Dissector Tube Development	42	✓
NASA Code 186-68-02-19, 186-58-02-02, D. S. Herman		
B. Parametric Analysis for Steady-State Performance of Attitude Control Thrusters	47	✓
NASA Code 186-68-02-26, J. D. Ferrera and P. M. McKown		
C. Approach Guidance Flight Feasibility Demonstration	48	✓
NASA Code 186-68-02-23, F. R. Chamberlain and L. J. Barone		
D. Thin Film Infrared Thermopile Detectors	49	✓
NASA Code 186-68-02-04, D. S. Herman		
References	51	

VI. Guidance and Control Research	52	
A. The Electro-Optic Effect in Barium Titanate	52	✓
NASA Code 129-02-05-01, A. R. Johnston		
B. Space-Charge Distribution in a Neutral Plasma	56	✓
NASA Code 129-02-01-07, K. Shimada		
C. Limitations Imposed by Demagnetizing Fields on Bit Packing Densities Within Mn-Bi Films	59	✓
NASA Code 129-02-05-06, G. Lewicki and D. I. Tchernev		
References	61	

ENGINEERING MECHANICS DIVISION

VII. Materials	63	
A. Ceramic Research	63	✓
NASA Code 129-03-04-01, M. H. Leipold		
B. Thermoelectric Power and the Fermi Surface in Silver-Gold Alloys	64	✓
NASA Code 129-03-15-04, I. Weinberg		
References	66	
VIII. Applied Mechanics	67	
A. Structural Analysis and Matrix Interpretive System Computer Program	67	✓
NASA Code 124-08-01-01, J. R. Chisholm		
References	68	

PROPULSION DIVISION

IX. Liquid Propulsion	69	
A. Gas-Side Boundary Phenomena	69	✓
NASA Code 128-31-06-03, R. W. Rowley		
B. The Reaction Between Oxygen Difluoride and Diborane	73	✓
NASA Code 128-31-06-05, R. A. Rhein		

Contents (contd)

C. Liquid Propulsion Systems	
<i>NASA Code 731-12-03-01, L. R. Toth; 731-12-03-03, R. S. Weiner, O. F. Keller, and H. B. Stanford</i>	80 ✓
D. Resonant Combustion	
<i>NASA Code 128-31-06-01, J. G. Softer and R. M. Clayton</i>	88 ✓
References	103
X. Solid Propellant Engineering	106
A. Polymerization of Acid Chlorides With Epoxides	
<i>NASA Code 128-32-05-10, H. Marsh, Jr. and J. Hutchison</i>	106 ✓
References	109
XI. Polymer Research	110
A. F^{19} NMR of Nitroso Rubbers	
<i>NASA Code 128-32-05-03, J. D. Ingham and D. D. Lawson</i>	110 ✓
B. Reactions of N-Vinylcarbazole With Anionic Initiators	
<i>NASA Code 129-03-11-03, A. Rembaum, A. M. Hermann, and R. Haack</i>	113 ✓
References	118
XII. Research and Advanced Concepts	120
A. Liquid MHD Power Conversion	
<i>NASA Code 129-27-06-03, D. G. Elliott, D. Cerini, and L. Hays</i>	120 ✓
B. Plasma Studies in the Electron Bombardment Ion Engine	
<i>NASA Code 120-26-08-01, T. D. Masek</i>	131 ✓
References	138

SPACE SCIENCES DIVISION

XIII. Space Instrument Systems	139
A. An Algorithm for the Synthesis of Binary Sequence Detectors	
<i>NASA Code 186-68-03-03, M. Perlman</i>	139 ✓
References	146
XIV. Bioscience	147
A. Pyrolysis Fluorescence. I. Detection and Estimation of Organic Matter	
<i>NASA Code 189-55-02-02, P. J. Geiger, J. V. Behar, and J. H. Rho</i>	147 ✓
B. Fluorometric Determination of Nucleic Acids. II. Assay of Purines and Purine Nucleotides of Biological Samples by Chemical Hydrolysis	
<i>NASA Code 189-55-02-02, J. H. Rho</i>	153 ✓
References	156

Contents (contd)

XV. Fluid Physics	158
A. Viscous and Inviscid Amplification Rates of Two- and Three-Dimensional Linear Disturbances in the Laminar Compressible Boundary Layer	
<i>NASA Code 129-01-09-01, L. M. Mack</i>	158 ✓
References	162
XVI. Physics	163
A. Convection and Magnetospheric Turbulence	
<i>NASA Code 129-02-07-02, G. Atkinson</i>	163 ✓
B. Evaluation of Coulomb Integrals of Continuum Functions	
<i>NASA Code 129-02-07-02, M. M. Saffren</i>	165 ✓
C. A Data Reduction Technique for Distribution Analysis	
<i>NASA Code 129-02-03-08, A. B. Whitehead, R. H. Parker, and E. L. Haines</i>	167 ✓
References	170

TELECOMMUNICATIONS DIVISION

XVII. Communications Elements Research	171
A. RF Techniques: Application of DC Potentiometer Insertion Loss Test Set to mm Wavelengths	
<i>NASA Code 125-21-03-04, D. Oltmans and C. T. Stelzried</i>	171 ✓
Reference	173
XVIII. Spacecraft Telemetry and Command	174
A. Linear Bit Packing Density on Standard Instrumentation Magnetic Recording Tapes	
<i>NASA Code 186-68-03-01, W. G. Clement</i>	174 ✓
B. A Magnetic Recording Tape Layer-to-Layer Adhesion Tester	
<i>NASA Code 186-68-03-01, W. G. Clement</i>	176 ✓
References	178
XIX. Spacecraft Radio	180
A. High Impact Antenna Study: Cupped Turnstile Antenna	
<i>NASA Code 186-68-04-06, K. Woo</i>	180 ✓
B. Experimental Results of Multipacting Between Coaxial Electrodes with High b/a Values	
<i>NASA Code 125-22-01-02, R. Woo</i>	182 ✓
C. Mariner S-Band Turnaround Ranging Transponder Improvement Program	
<i>NASA Code 186-68-04-20, L. M. Hershey</i>	183 ✓
References	189
XX. Communications Systems Research	191
A. Block Coding and Synchronization Studies: Rapid Acquisition Sequences	
<i>NASA Code 125-21-02-03, I. J. Stiffler</i>	191 ✓

Contents (contd)

B. Combinatorial Communication: A New Interpretation of a Basic Combinatorial Formula		
NASA Code 125-21-01-01, S. W. Golomb	197	✓
C. Communications Systems Development: Minimizing Range Code Acquisition Time		
NASA Code 150-22-11-08, R. C. Tousworthe	198	✓
D. Communications Systems Development: Cycle Slipping in Phase-Locked Loops		
NASA Code 150-22-11-08, R. C. Tousworthe	200	✓
E. Information Processing: Arithmetic Decoding of Cyclic Codes		
NASA Code 150-22-11-09, G. Solomon	205	✓
F. Data Compression Techniques: Recent Results on Epsilon Entropy		
NASA Code 150-22-17-08, E. C. Posner, E. R. Rodemich and Howard Rumsey, Jr.	208	✓
References	211	

I. Scientific Programming

SYSTEMS DIVISION

N67 18302

A. Dependency of Constraints for Differential Equations, A. J. Semtner

The question sometimes arises as to whether there exists a solution to a system of ordinary differential equations

$$\begin{array}{l} \dot{x}_1 = X_1(x_1, \dots, x_n) \\ o \quad o \\ o \quad o \\ o \quad \bullet \\ \dot{x}_n = X_n(x_1, \dots, x_n) \end{array}$$

which also satisfies a number of constraints

$$\begin{array}{l} \Xi_1(x_1, \dots, x_n) = 0 \\ \bullet \quad o \\ o \quad \bullet \\ o \quad o \\ E_1(x_1, \dots, x_n) = 0 \end{array}$$

A method for answering this question has been proposed.¹ By means of a transformation algorithm, the differential

¹Keberle, E. M., *Partial Stationarity as Compatibility Criterion for Overdetermined Systems of Ordinary Differential Equations Related to Non-differential Constraints*, Interoffice Technical Memorandum No. 314-112, Jet Propulsion Laboratory, Pasadena, California.

equations are transformed successively until a stop condition is satisfied. A necessary and sufficient condition that a solution exist which is compatible with the constraints is that certain functions which arise in the transformation procedure have the value zero when all of their arguments are zero.

A minor variation in the above problem arises when the Ξ 's are allowed to be functions not only of the x 's, but also of certain parameters a_1, \dots, a_m . We then ask *how the constraints must be related (in terms of conditions on the a 's) in order for a compatible solution to exist*. An application of the transformation procedure supplies the answer that such a solution exists if and only if certain functions of the a 's are zero.

For example, consider the equations of motion for a small body subject to the gravitational attraction of a larger body:

$$\left. \begin{array}{l} \dot{r} = \frac{p_r}{m} \\ \dot{\phi} = \frac{p_\phi}{mr^2} \\ \dot{p}_r = \frac{p_\phi^2}{mr^3} - \frac{GmM}{r^2} \\ \dot{p}_\phi = 0 \end{array} \right\} \quad (1)$$

Let us impose the constraints that the potential and kinetic energies have values a , and a_2 , respectively:

$$\left. \begin{aligned} -\frac{GmM}{r} - a &= 0 \\ \frac{1}{2m} \left(p_r^2 + \frac{p_\phi^2}{r^2} \right) - a_2 &= 0 \end{aligned} \right\} \quad (2)$$

We seek one or more relationships between the constants a , and a_2 which will guarantee a solution to Eqs. (1) and (2).

Following the method of the transformation algorithm, we replace the variables r and p_ϕ by

$$\begin{aligned} \xi_1 &= -\frac{GmM}{r} - a_1 \\ \xi_2 &= \frac{1}{2m} \left(p_r^2 + \frac{p_\phi^2}{r^2} \right) - a, \end{aligned}$$

(We assume that solutions are desired for which $p_\phi \neq 0$, so that ξ_1 and ξ_2 are independent.) A new system equivalent to Eq. (1) is given by

$$\left. \begin{aligned} \dot{\xi}_1 &= \frac{p_r(\xi_1 + a_1)^2}{Gm^2M} \\ \dot{\xi}_2 &= \frac{-p_r(\xi_1 + a_1)^2}{Gm^2M} \\ \dot{p}_r &= \frac{\xi_1 + a_1}{Gm^2M} [p_r^2 - m(\xi_1 + a_1) - 2m(\xi_2 + a_2)] \\ \dot{\phi} &= \frac{-(\xi_1 + a_1)}{Gm^2M} [2m(\xi_2 + a_2) - p_r^2]^{\frac{1}{2}} \end{aligned} \right\} \quad (3)$$

We now change ξ_1 and ξ_2 to y_1 and η_1 , respectively, and replace p_r by

$$\xi_3 = \frac{p_r(\xi_1 + a_1)^2}{Gm^2M}$$

A new equivalent system is then given by

$$\left. \begin{aligned} \dot{y}_1 &= \xi_3 \\ \dot{\eta}_1 &= -\xi_3 \\ \dot{\xi}_3 &= \frac{3\xi_3^2}{y_1 + a_1} - \frac{m(y_1}{(Gm^2M)^2} [y_1 + a_1 + 2(\eta_1 + a_2)] \\ \dot{\phi} &= \frac{Gm^2M}{(y_1 + a_1)^3} \xi_3^2 - \frac{2m(y_1 + a_1)(\eta_1 + a_2)}{Gm^2M} \end{aligned} \right\} \quad (4)$$

The *functional dependence* of the right-hand sides of the first two equations above, which formally has been distinguished by the introduction of a variable η_1 instead of y_2 , reflects the law of energy conservation

$$\dot{\xi}_1 + \dot{\xi}_2 = 0.$$

The stop condition is satisfied by Eq. (4); i.e., the expression for $\dot{\xi}_3$ contains none of the original dependent variables. For a solution of Eq. (1) and (2) to exist, the expressions for $\dot{\eta}_1$ and $\dot{\xi}_3$ must be zero when y_1 , η_1 , and ξ_3 are set equal to zero. This requires that $a_1 + 2a_2 = 0$, which is the desired relationship between a , and a_2 .

This particular example tells us that, if the kinetic energy T and potential energy V are constant for a body moving in a central gravitational field, then it must be the case that $V + 2T = 0$. Such motion is well-known to be circular, and circular solutions are indeed obtained by solving Eq. (4) with $y_1 = \eta_1 = \xi_3 = 0$ and transforming back to the original variables.

N67 18303

B. Corrections to the Lunar Ephemeris,
J. D. Mulholland

1. Introduction

Work is currently in progress on improving the adequacy of the lunar ephemeris, as it is now contained in the JPL ephemeris tapes (Ref. 1). This work is part of the continuing effort to provide what may be regarded, at any given time, as the best possible ephemeris that can be obtained at that time. The nature and implications of recent modifications are discussed here. Also, since the phrase "best possible," as used in this context, is somewhat ambiguous and subject to a variety of interpretations, the question of where these changes fit into one such interpretation of this phrase is examined.

2. Corrections

The present lunar ephemeris is essentially the improved lunar ephemeris (Ref. 2), based on the Brown Lunar Theory, to which aberration corrections have been applied to provide a geometric ephemeris, rather than the apparent ephemeris required for most astronomical applications. The modifications being made to this ephemeris can be divided into four categories, each of which is discussed separately in the succeeding paragraphs. These categories may be identified as being due to improvements in: (1) coordinate transformations, (2) basic theory, (3) the treatment of aberration, and (4) astronomical constants.

In the Brown Lunar Theory, the solution was obtained in terms of rectangular coordinates in a rotating reference frame. More than a half-century later, this solution is still as good as the capabilities of modern observational equipment. The solution did, however, have to be transformed into the spherical coordinates commonly used in the lunar problem: longitude, latitude, and sine parallax. The transformations made by Brown and perpetuated in the improved lunar ephemeris (ILE) were much less accurate than the theory itself. This was particularly the case with sine parallax, which is the inverse distance, because astronomers then possessed no means of directly observing the radial distance. Now, of course, this quantity is measurable with high precision. This, plus the requirements for flight operations near the Moon, make it necessary to strive for an ephemeris in which the radial distance is of a precision commensurate with the angular coordinates. Transformation corrections to be added to the ILE coordinates have been derived in Ref. 3. These have the effect of extending the spherical coordinates to include terms as small as 0".0001 in longitude and latitude and 0".000002 in sine parallax, corresponding to linear distances of about 20 cm. The largest terms in each of the three coordinate corrections are

$$\begin{array}{lll} \text{longitude:} & -0''.0090 & \sin(l - l' + 2F + 2D) \\ \text{latitude:} & +0''.0154 & \sin(-l + 3F) \\ \text{sine parallax:} & +0''.005507 & \cos(l - 2F) \end{array}$$

The coefficients correspond to linear distances of about 18, 31, and 617 m, respectively.

Another correction has been suggested, based on a new solution to the lunar problem.² On the basis of this work, it is recommended that the ILE be modified by

$$+0''.072 \sin(2F - 2I)$$

in longitude, corresponding to a maximum value of about 144-m in-track change.

The results of an analytic treatment of the aberration (published in Ref. 4) make it possible to replace the iterative numerical procedure used previously to remove the aberration from the JPL ephemeris by a rigorous set of mathematical expressions. The actual quantitative effect on the ephemeris may be expected to be quite small.

²Eckert, W. J., and Smith, H. F., Jr., *Astronomical Papers of the American Ephemeris*, Vol. XIX, Pt. 2 (In preparation).

The last set of corrections is by far the most significant. The ILE, as well as the above-mentioned modifications to it, are all based on a set of astronomical constants which no longer may be regarded as adequate. Largely because of radar-bounce data and *Mariner II* flight data, the International Astronomical Union (Ref. 5), in 1964, adopted new values for the Earth-Moon mass ratio and the astronomical unit (AU) in meters. These parameters enter strongly into the lunar theory: the former because of its appearance in the perturbing function, and the latter because the lunar ephemeris is given in terms of the equatorial radius of a standard reference geoid. The mass-ratio correction was applied, as with the previous corrections, in the form of Fourier series similar to (but much shorter than) those of the basic theory. The largest terms were

$$\begin{array}{lll} \text{longitude:} & +0''.1683 & \sin D \\ \text{latitude:} & +0''.10136 & \sin D \cos S \\ \text{sine parallax:} & +0''.001315 & \cos D \end{array}$$

The coefficients correspond to linear distances of about 340, 27, and 150 m, respectively. The effect of the new AU was accounted for by merely multiplying the final value of sine parallax by 3422.452/3422.540, the ratio of the new value of the mean parallax to the old. This has the effect of increasing the mean distance of the Moon by about 9856 m, using the adopted equatorial Earth radius of 6,378,160 m.

3. Implications

Obviously, the most important aspect of changing the lunar ephemeris is that the new ephemeris will place the Moon at a different location. We can place very approximate upper bounds on the discordances, translated into linear distances, as follows:

$$\begin{array}{ll} \text{longitude:} & 700 \text{ m} \\ \text{latitude:} & 400 \text{ m} \\ \text{sine parallax:} & 12,000 \text{ m} \end{array}$$

This last figure may be divided into two parts: one due to the scale change, and the other due to all other causes. The latter part has an approximate upper bound of 2000 m. Of course, the real discordances will usually fall much below these figures.

From the standpoint of the trajectory calculations performed at JPL, the largest adjustment, that due to the

revised value of the AU, will ultimately have little discernible effect. The reason is that the orbit-determination programs use an empirical value of the Earth radius in kilometers (REM), a value determined so as to make the available ephemeris fit the flight data to the best degree possible. Thus, a theory based on an inadequate value of the AU is rendered usable by using it in conjunction with a fictitious Earth radius. The introduction of the new AU will require a redetermination of the value of the REM, a value which should more nearly approach the International Astronomical Union's value quoted above. The redetermined value should be quite close to that which would be obtained by multiplying the present value by 3422.452/3422.540. It is, however, very likely that it will not be exactly this value, for the other corrections will very likely exert some effect on the redetermination.

The remainder of the corrections are so small that they will have no significant effect on anything other than flight operations near the Moon. For such missions, however, they will certainly have quite noticeable effects. The use of the new ephemeris, with an appropriate REM, should lead to significant reductions in the residuals for trajectories near the Moon. Preliminary data analysis by W. Sjogren of the JPL Systems Analysis Section tends to verify this statement remarkably well. Further study is under way.

Two problems now remain. First, since the longitude of the Moon is changed, it is conceivable that the adoption of the new ephemeris will have some small effect on the values determined for the deviation of mean solar time from ephemeris time. The present feeling on this matter is that the effect, if any, on the extrapolated values of *AT* will be much smaller than the uncertainty involved in *any* extrapolation of this quantity. Nevertheless, more consideration will have to be given to this question. The second remaining problem relates to the theory on which the calculation of the nutations in longitude and obliquity are based. The lunar theory is part of the input to this calculation, and, while most of the modifications noted here are below the level of significance with respect to the theory of nutation, it is quite possible that the effect of the new values of the astronomical constants will be sensible. This problem is now under study.

4. Value of Corrected Ephemeris

Obviously, we believe that the new ephemeris more accurately represents the real position of the Moon in space. Thus, certain types of orbit residuals may be expected to be reduced.

To ascertain the full value of this work, however, it is really necessary to adopt a somewhat philosophical position as a guide to one's actions. The viewpoint taken here is that accuracy and consistency are of equal importance to our purpose. In traditional astronomical work, it is quite important that a set of ephemerides be internally consistent to the maximum possible extent. Absolute accuracy is secondary, because the basic purpose of the ephemeris is to define a system, not to describe the positions of objects. In space flight operations, positional accuracy is highly important; it cannot be said, however, that internal consistency is secondary. A series of steps in the direction of consistency was previously recommended (SPS 37-29, Vol. IV, pp. 61-65). Some of these steps have already been taken, and others are in progress or planned.

In an ephemeris for space flight purposes, consistency has two primary virtues; both are closely associated with some aspect of accuracy, but with different aspects and in different ways. If an ephemeris of a single body lacks consistency with the ephemerides of other bodies, it is still possible that it may be perfectly adequate for the computation of trajectories which lie entirely within the vicinity of that body, providing all observations are made from the central body or the spacecraft itself. If, however, the trajectory passes near two or more bodies for which the ephemerides are inconsistently based, or if the trajectory lies near one of these bodies and the observations are referenced to another, then a significant amount of empirical adjustment will be necessary to offset the inconsistency of the positional data. Improvement of the internal consistency of the ephemeris reduces the necessary degree of reliance on empiricism.

On the other hand, one of the primary objectives of astronomical research and space flight programs alike is the improvement of the system of astronomical constants. Such improvement has come: and will continue to come, from the observational data obtained from all appropriate sources, including optical and radar observations, as well as spacecraft tracking data. The history of such improvements should prove instructive, however. Every new determination of a fundamental constant is accompanied by some kind of "probable error" estimate. Frequently, the new value of the constant is outside the range of probable values given by the most recent determination. This is merely symptomatic of the fact that, in a situation of this type, the standard deviation given by the statistical analysis is indicative only of the *consistency of the data in terms of the model adopted for the system*. It does not really represent a reliability estimate unless the model

is correct. *An inconsistent model is an incorrect model*, just as an inaccurate model is an incorrect model. If we are to use space vehicle flight data and radar data to obtain better astronomical constants (and certainly no data are better suited to the purpose), then it is absolutely necessary to use as consistent and as accurate an ephemeris as can be found. Every improvement in either of these properties is an improvement in the degree of confidence with which we can improve our basic data.

N67 18304

C. Combined Radiation-Conduction Heat Transfer in a Finned Cylinder in Space, W. R. Buntun and E. M. Keberle

The computation of the equilibrium temperature distributional function of a finned cylinder in the radiation field of the Sun discussed here takes into account the following energy transfers at each infinitesimal surface element:

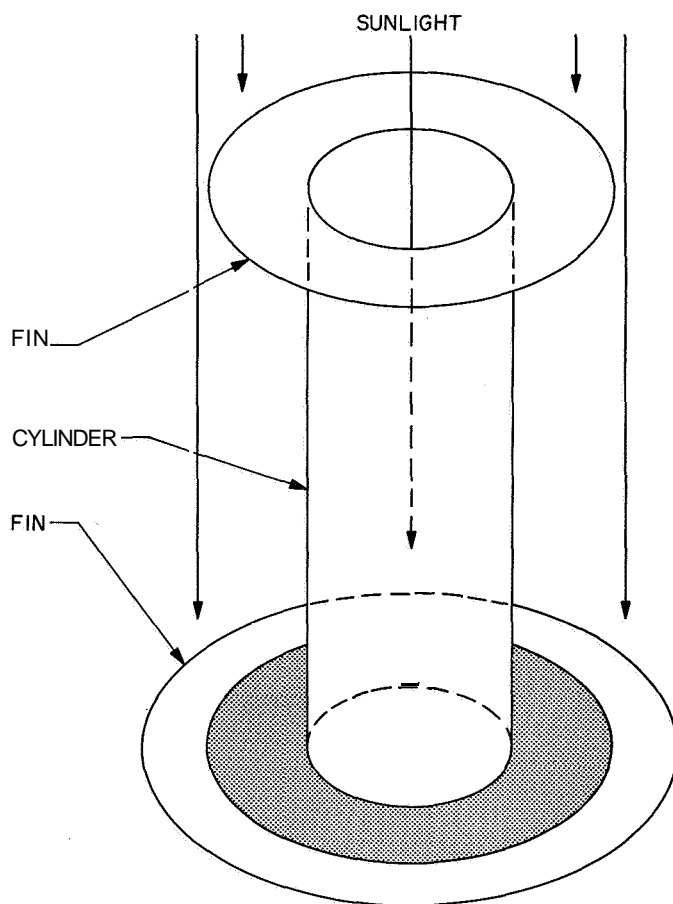


Fig. 1. Finned cylinder model used for computations

- (1) Absorption and reflection of incident radiation from the Sun or other parts of the finned cylinder.
- (2) Emittance of radiation according to the relationship $W = \epsilon \sigma T^4$.
- (3) Conduction of heat inside the surface to neighboring surface elements.

The general derivation of the equilibrium equation to satisfy the energy balance for the above energy transfer mechanisms is given in Ref. 6.

The Thermodynamics Research Group of the JPL Engineering Mechanics Division has supplied the corresponding equations for the special case of the finned cylinder represented in Fig. 1 in the gray-body approximation (emittance and absorption independent of frequency). Fig. 2 shows the model to be symmetric about an axis; thus, the temperature distribution on only one of the two parts of the profile is required, reducing the problem to that of one dimension. Each of the surfaces shown in Fig. 2 has constant, but different, reflectivity and absorptivity coefficients. Surface 3 will be divided into parts 3a and 3b to take formal account of the fact that the radiation from the Sun is direct only in part 3b of this surface. The other part 3a corresponds to the *shaded* area of Fig. 1.

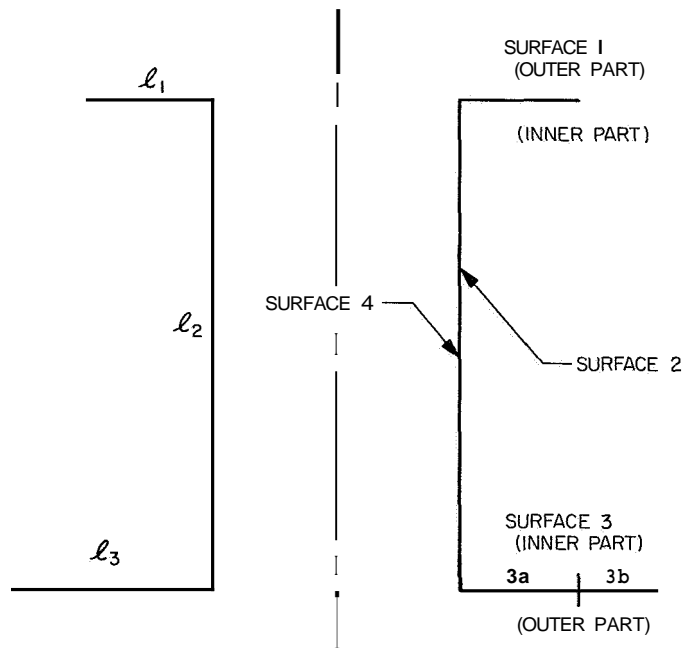


Fig. 2. Side view of finned cylinder model identifying Surfaces 1-4

By definition, the *radiosity* function represents the amount of radiant energy lost per unit surface and per unit time due to $\epsilon\sigma T^4$ emittance, as well as the reflection of incident radiation. Since the outer parts of Surfaces 1 and 3 do **not** radiate to other parts of the cylinder or receive radiation from those parts, two radiosity functions $B(x)$ and $C(x)$ will have to be determined. The first covers the radiosities of the inner parts of Surfaces 1 and 3 and Surface 2; the second covers the radiosity of Surface 4.

After some rearrangement, one obtains a system of three equations (Eqs. 1, 2, and 3) for the three unknown functions: temperature $T(x)$ and radiosities $B(x)$ and $C(x)$.

Equation for temperature $T(x)$: One discontinuous ordinary differential equation of second-order

$$\frac{d^2T}{dx^2} + \frac{\alpha_{1i}}{x} \frac{dT}{dx} + \alpha_{2i} T^4 + \alpha_{3i} B(x) + \alpha_{4i} C(x) + \alpha_{5i} = 0, \\ i = 1, 2, 3a, 3b \quad (1)$$

with coefficients that are constant for each surface i . This differential equation represents the conservation of energy.

Since the constants α_{ki} vary (Table 1), one has actually **four** different ordinary differential equations over four domains, supplemented by initial conditions at the interior vertices. There, each interior initial condition rep-

resents the physical law which is otherwise maintained by the differential equations over their domains. In addition, there exist boundary conditions at each of the two ends of the total domain which take into account the gray-body emittance of radiation due to the thickness of the surface.

The interior initial and exterior boundary conditions are formulated by means of the expression

$$\phi(j) \equiv a_1(j) T'(j) + a_2(j) T^4(j) + a_3(j) B(j) + a_4(j) C(j) + a_5(j)$$

The values for $a_k(j)$ are given in Table 2, and the boundary points are indicated in Fig. 3. Both sides of each vertex are required for the formulation of the interior initial conditions. The interior initial and exterior boundary conditions are as follows:

Interior initial conditions:

$$\phi(1^+) = \phi(2^-), \phi(2^+) = \phi(3a^-), \phi(3a^+) = \phi(3b^-)$$

$$T(1^+) = T(2^-), T(2^+) = T(3a^-), T(3a^+) = T(3b^-)$$

Exterior boundary condition:

$$\phi(1^-) = 0, \quad \phi(3b^+) = 0$$

Table 1. Values of α_{ki}

α_{ki}	Surface			
	1	2	3a	3b
α_{1i}	1	0	1	1
α_{2i}	-0.13712057	-0.326137765	-0.32598998	-0.32598998
α_{3i}	0.11761099	0.00097797862	0.32515979	0.32515979
α_{4i}	0	0.325159787	0	0
α_{5i}	0.019924685	0.00069182933	0	0.0069182933

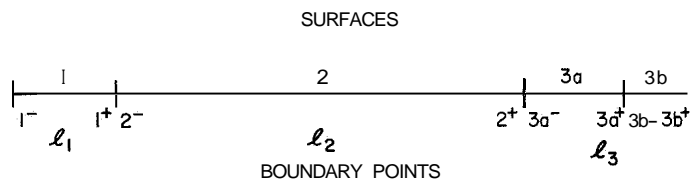


Fig. 3. Exterior and interior boundary points for Surfaces 1-3

Table 2. Values of $a_k(j)$

$a_k(j)$								
	1 ⁻	1 ⁺	2 ⁻	2 ⁺	3a ⁻	3a ⁺	3b ⁻	3b ⁺
$a_1(j)$	1	-1	-1	1	-1	-1	-1	1
$a_2(j)$	0.0078780166	0.0068423440	0.016274338	0.016274338	0.016266964	0	0	0.017302636
$a_3(j)$	-0.0058688113	-0.0058688113	-0.000048801326	-0.000048801326	-0.016225536	0	0	-0.016225536
$a_4(j)$	0	0	-0.016225537	-0.016225537	0	0	0	0
$a_5(j)$	-0.0009942456	-0.00099424569	-0.000034522419	-0.000034522419	0	0	-0.00034522419	-0.00034522419

Equations for radiosities $B(x)$ and $C(x)$: Two integral equations, with piecewise constant coefficients

$$B(x) = \beta_{1i} T^4(x) + \beta_{2i} \int_0^{l_1+l_2+l_3} K_{1,2,3}(x,y) B(y) dy + \beta_{3i},$$

$$i = 1, 2, 3a, 3b \quad (2)$$

$$C(x) = \gamma_1 T^4(x) + \gamma_2 \int_{l_1}^{l_1+l_2} K_4(x,y) C(y) dy + \gamma_3 \quad (3)$$

The values for β_{ki} and γ_k are given in Tables 3 and 4, respectively. The kernels depend on the position and location of the surface elements dx and dy and represent the geometry, with respect to radiation, of the finned cylinder (essentially an integral over $\cos \theta_1$, $\cos \theta_2/r^2$, defined in Fig. 4).

β_{ki}	Surface			
	1	2	3a	3b
β_{1i}	0.85	0.045	0.94	0.94
β_{2i}	0.15	0.955	0.06	0.06
β_{3i}	0	0	0	0.04

γ_k	Surface 4
γ_1	0.94
γ_2	0.06
γ_3	0.004

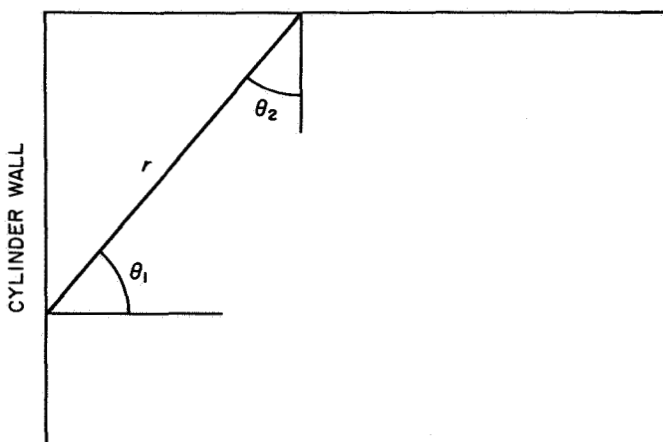
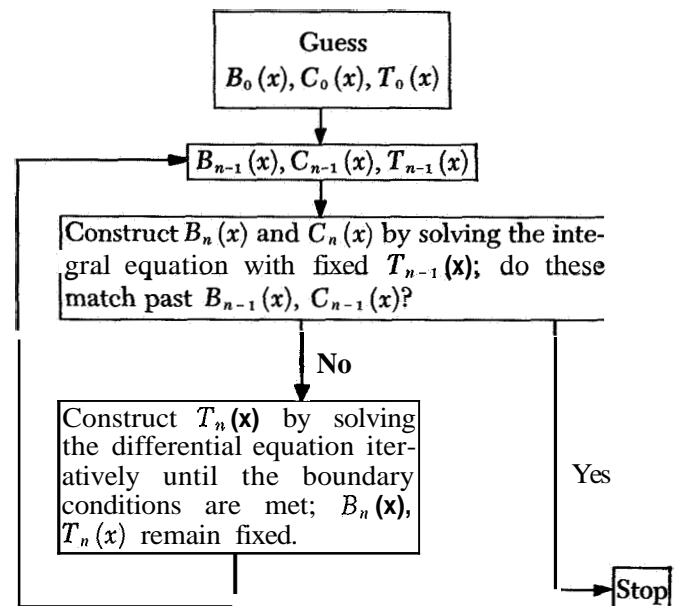


Fig. 4. Definition of geometry for $\cos \theta_1 \cos \theta_2/r^2$

The differential and integral equations are both non-linear. The kernel $K_{1,2,3}(x,y)$, represented in Fig. 5, has discontinuities and point singularities, the latter due to the corners in the profile at the meeting points of Surfaces (1,2) and (2,3). The diagonal squares have a value of zero, since there is no radiation from one element of a surface to another element of the same surface. Kernel $K_4(x,y)$ is represented in Fig. 6. Surface 4 radiates either to the exterior, which does not appear in the kernel, or to itself. Therefore, only one diagonal square appears in Fig. 6, in contradistinction to the case of Fig. 5. In addition to the above complications, the radiosity solution $B(x)$ is discontinuous at the vertex (3a,3b) of Surface 3. This can be seen from the first integral equation, Eq. (2), in which the constant β_{3i} ($i=3a,3b$) suffers a jump due to the fact that part 3a of Surface 3 is in the shadow of Surface 1, whereas part 3b is illuminated directly by sunlight, thereby causing an abrupt change of the reflected radiation.

The results reported here have been obtained by a particular variant of the successive approximation method according to the following flow diagram:



In the integral equation routine, a variable step-size Simpson rule was used; in the differential equation routine, a Runge-Kutta, Adams-Moulton package with automatic error control was used. It was found by experience that convergence was increased time-wise: (1) when the differential equation routine was iterated more often than the integral equation routine, and (2) if the accuracy requirement for the boundary condition (T condition) was not driven to an extreme.

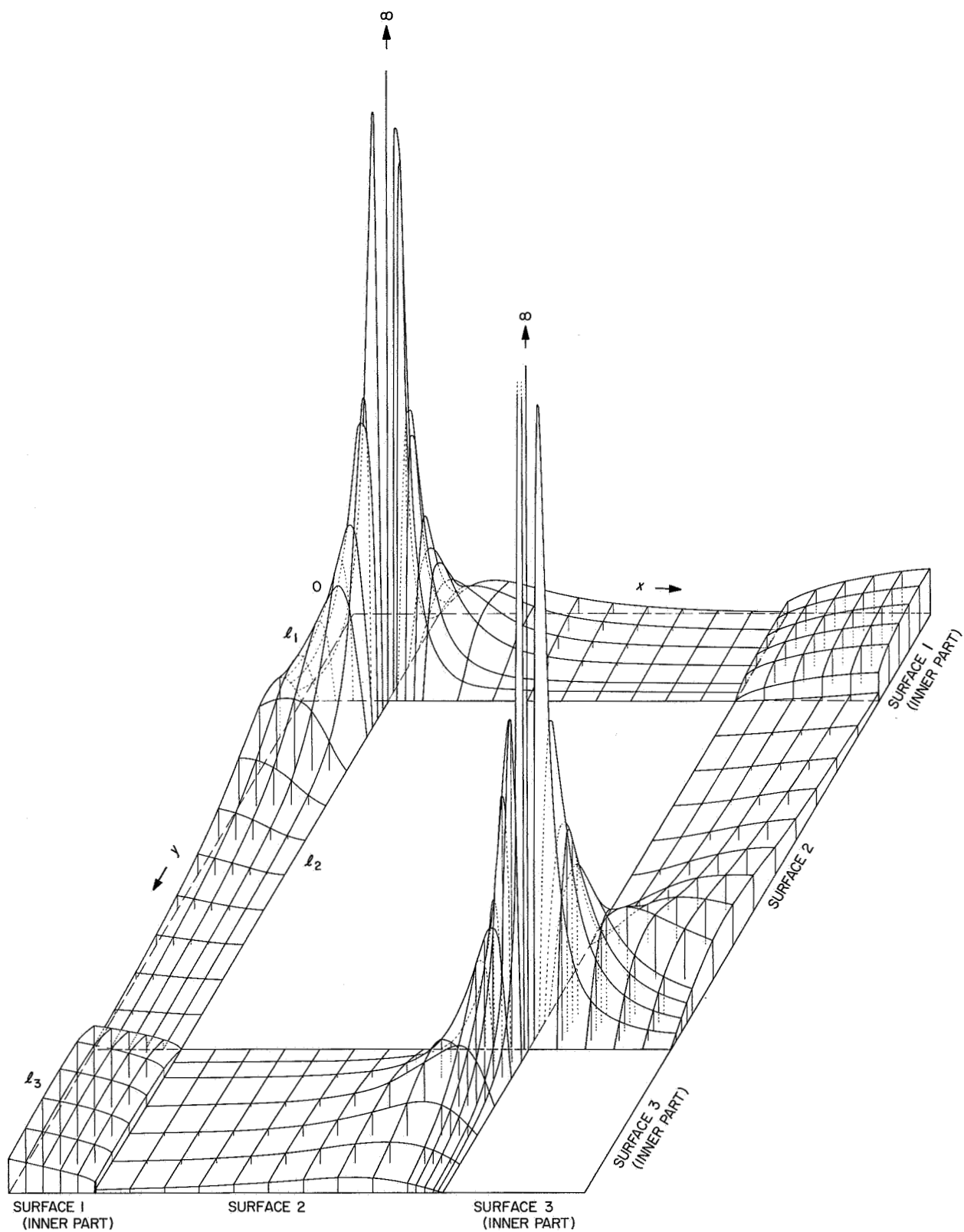


Fig. 5. Kernel $K_{1,2,3}(x,y)$

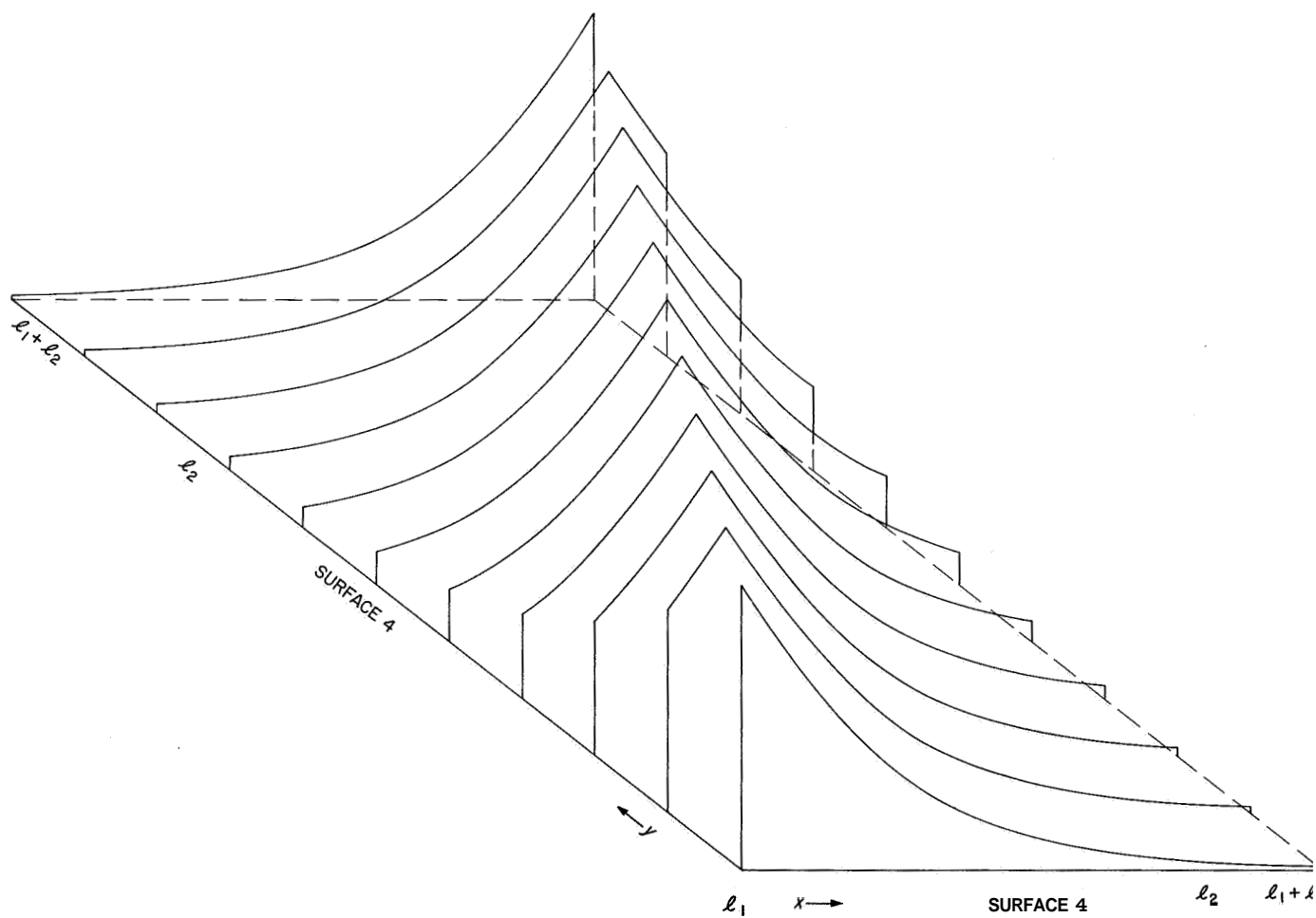


Fig. 6. Kernel $K_4(x, y)$

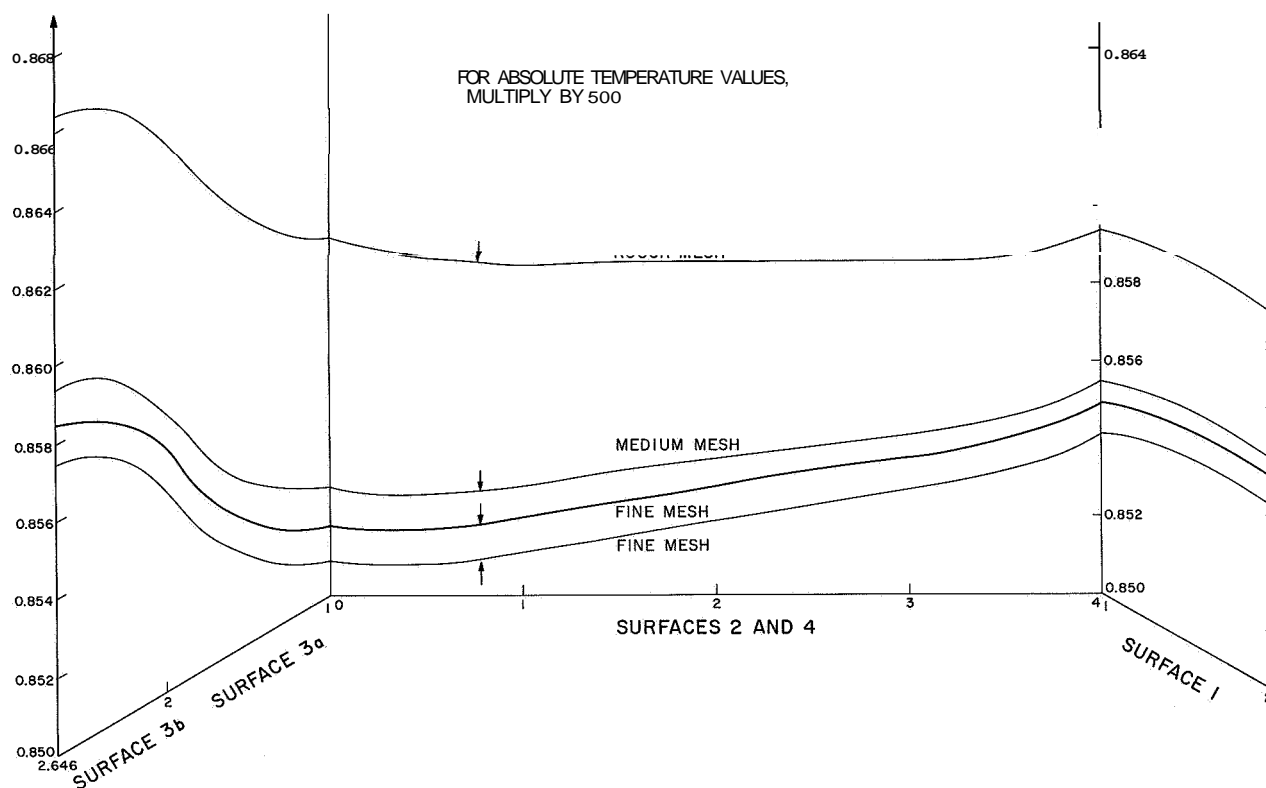


Fig. 7. Computed temperature distribution $T(x)$

In the graphical presentation of the results given in Figs. 7-9, the dependence of the solutions on the mesh size is explicitly exhibited by the different curves according to the runs of Table 5. The solutions were approached with approximate starting functions $T_0(x)$, $B_0(x)$; and $C_0(x)$ with values above the final solution. The stop condition for each run is satisfied if, for each mesh point, at least 5 significant digits of $T_n(x)$, $B_n(x)$, and $C_n(x)$ agree with those of $T_{n-1}(x)$, $B_{n-1}(x)$, and $C_{n-1}(x)$. To check the accuracy of the routine, a fourth run was made. The estimates for Run 4 were from below the expected solutions and with the mesh of Run 3; this result is also presented in Figs. 7-9. Since the difference between the resulting functions of the successive Runs 1, 2, and 3 is diminished by a factor of the order of 10, convergence is exhibited.

Therefore, the true solution lies between the curves of Runs 3 and 4. As can be seen from Figs. 7-9, the error of the resulting curves is of the order of 0.1%.

D. Electrostatic Charge Densities on an Electro-optical Star Tracker, N. C. Adams, E. M. Keberle, and W. Silsby

The electric charge density $\epsilon(x)$ of a system of conducting capacitance surfaces (electrodes) of negligible thickness with prescribed constant potentials $\phi(y)$ satisfies (Ref. 7) the Fredholm integral equation of the first kind (Fig. 10):

$$\iint \epsilon(x) K(x, y) d^2x = \phi(y)$$

with the symmetric kernel

$$K(x, y) = \frac{1}{4\pi} \left(\frac{1}{r} \right)$$

$$r = |x - y|$$

Table 5. Number of meshpoints for each computer run

Run	Mesh	IBM 7094 running time, min	Number of meshpoints for indicated surface			Total number of meshpoints
			1	2	3	
1	Rough	10.5	5	9	11	25
2	Medium	45	11	15	21	47
3	Fine	90	21	31	41	93

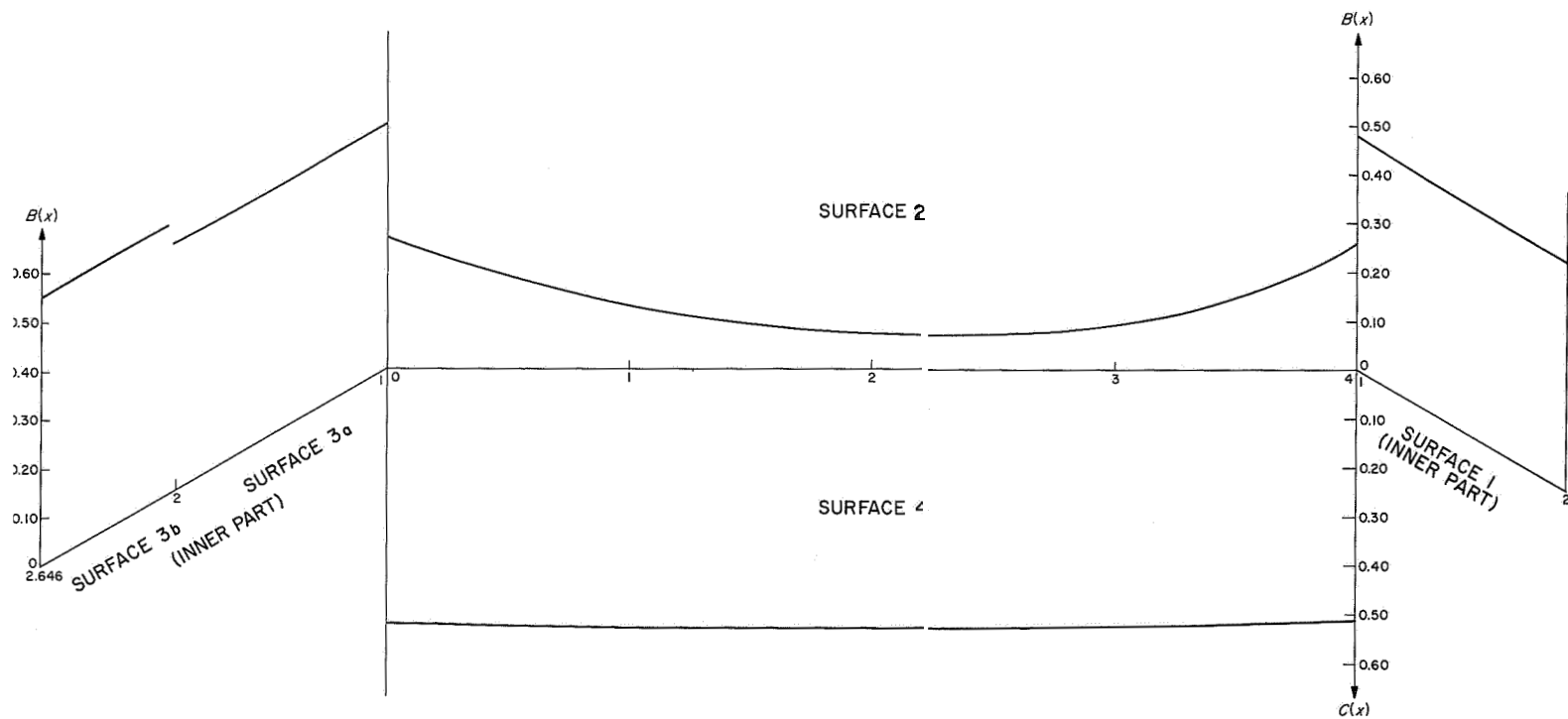


Fig. 8. Computed radiosities $B(x)$, $C(x)$ in a linear scale containing the zero

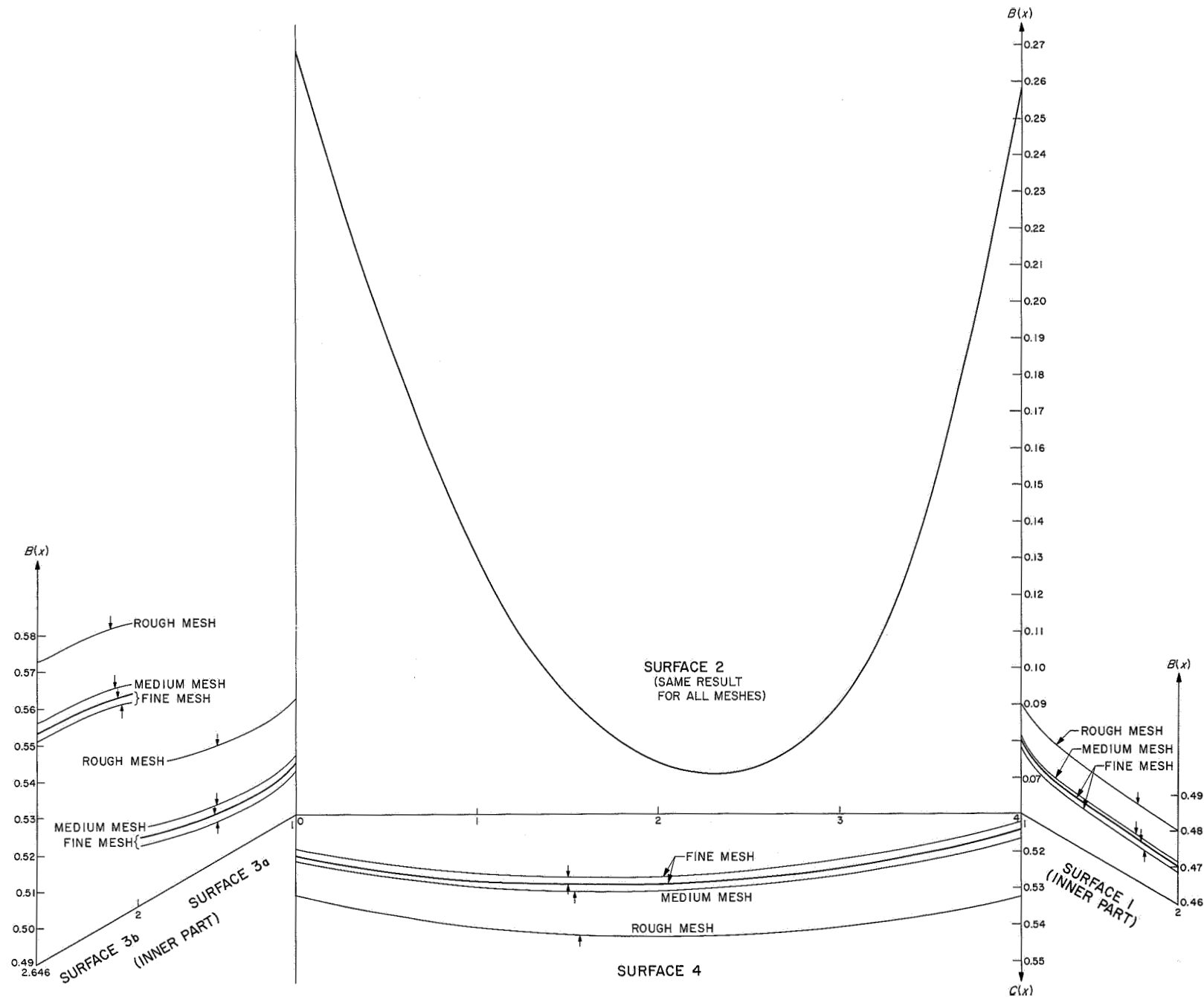


Fig. 9. Computed radiosities $B(x)$, $C(x)$ in magnified scale to show effect of mesh size (bold curves closely approximating theoretical ones)

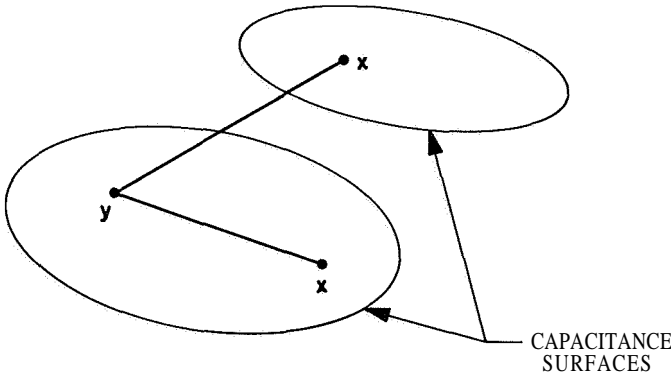


Fig. 10. Geometry of x and y of the capacitance surfaces

For an axial symmetric arrangement of the electrodes, the double integral reduces to a single integral, and the charge density satisfies the one-dimensional Fredholm integral equation with non-symmetric kernel

$$\int_0^{s_0} \varepsilon(s) k(s, t) ds = \phi(t) \quad (1)$$

Results are presented here of machine computations of electric charge densities on axial symmetric electrodes of a star tracker. If the profile $\xi(s), \rho(s)$ of the star tracker is represented, as shown in Fig. 11, by the three curves $\xi_1(s_1), \rho_1(s_1)$; $\xi_2(s_2), \rho_2(s_2)$; and $\xi_3(s_3), \rho_3(s_3)$ in terms of arc length s_1, s_2 , and s_3 with electrode potentials ϕ_1, ϕ_2 , and ϕ_3 (constant, but different, for each surface), the kernel reads explicitly, according to Fig. 12,

$$k(s, t) = \rho(t) \int_0^{2\pi} \frac{d\theta}{\{[\xi(s) - \xi(t)]^2 + [\rho(s) - \rho(t) \cos \theta]^2 + \rho^2(t) \sin^2 \theta\}^{1/2}}$$

The integrand is discontinuous at the intersections (s_1, s_2) and (s_2, s_3) , and the kernel itself is integrable singular for $s = t$. By means of

$$\lambda(s, t) = [\xi(s) - \xi(t)]^2 + \rho^2(s) + \rho^2(t)$$

$$\mu^2(s, t) = 2 \frac{\rho(s) \rho(t)}{\lambda(s, t)}$$

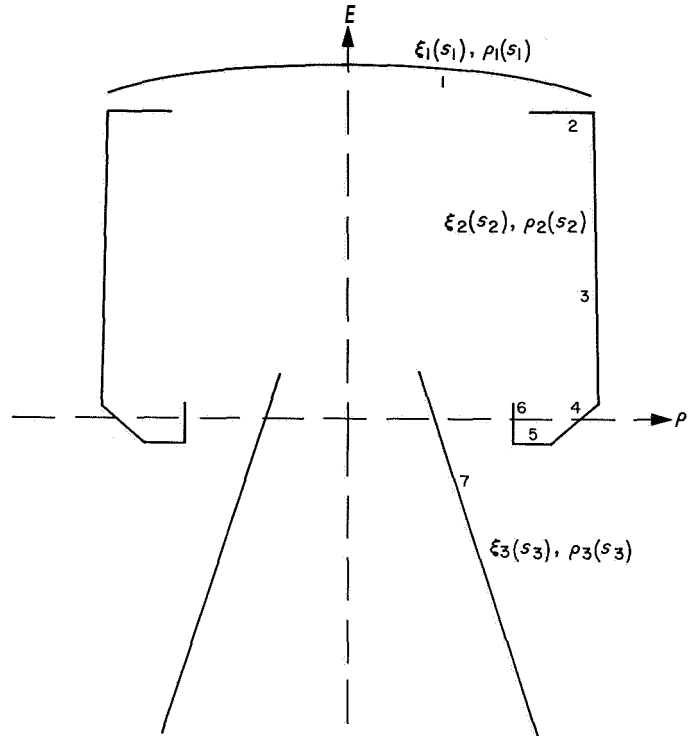


Fig. 11. Profile of the axial symmetric star tracker

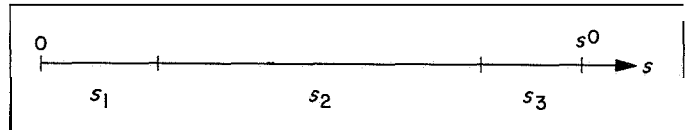


Fig. 12. Three parameter domains of the three capacitance surfaces assembled to one domain with parameter s

one obtains for the kernel

$$k(s, t) = \rho(t) \frac{1}{[\lambda(s, t)]^{1/2}} \int_0^{2\pi} \frac{d\theta}{[1 - \mu^2(s, t) \cos \theta]^{1/2}}$$

with

$$\int_0^{2\pi} \frac{d\theta}{(1 - \mu^2 \cos \theta)^{1/2}} = \frac{4}{(1 + \mu^2)^{1/2}} E \left[\left(\frac{2\mu^2}{1 + \mu^2} \right)^{1/2} \right]$$

where $E[a]$ is the complete elliptic integral of the first kind and is dependent on the electrode functions $\xi(s), \rho(s)$. In the following computations, $E[a]$ is represented by well-known expressions.

For numerical processing, the Fredholm integral equation is approximated by an algebraic linear system of equations

$$\sum_{j=1}^J \varepsilon(s_j) \bar{k}^*(s_j, t_i) = \phi(t_i), \quad i = 1, \dots, J \quad (2)$$

with the algebraic unknowns $\varepsilon(s_1), \dots, \varepsilon(s_J)$ representing the unknown solution $\varepsilon(s)$ of the integral equation. The bar on the kernel indicates integration of the kernel between successive mesh points, and the asterisk denotes

that care was devoted to the fact that $k(s, t)$ is singular for $s = t$. To that extent, $\varepsilon(s)$ is approximated linearly between mesh values $[\varepsilon_j, \varepsilon_{j+1}]$ according to

$$\varepsilon(s) = \varepsilon_j + \frac{\varepsilon_{j+1} - \varepsilon_j}{s_{j+1} - s_j} (s - s_j) \quad (3)$$

and the integration performed between successive mesh points. The approximated integral equation then reads

$$\sum_{j=1}^J \int_{s_j}^{s_{j+1}} \left[\varepsilon_j + \frac{\varepsilon_{j+1} - \varepsilon_j}{s_{j+1} - s_j} (s - s_j) \right] k(s, t_i) ds = \phi(t_i), \quad i = 1, \dots, J \quad (4)$$

or the following, which is of the form given in Eq. (2):

$$\sum_{j=1}^J \left(\varepsilon_j - \frac{\varepsilon_{j+1} - \varepsilon_j}{s_{j+1} - s_j} s_j \right) \int_{s_j}^{s_{j+1}} k(s, t_i) ds + \sum_{j=1}^J \frac{\varepsilon_{j+1} - \varepsilon_j}{s_{j+1} - s_j} \int_{s_j}^{s_{j+1}} s k(s, t_i) ds = \phi(t_i), \quad i = 1, \dots, J$$

Since the kernel $k(s, t)$ depends on the electrode functions $\xi(s), \rho(s)$, the two integrals in the last equation have to be machine-computed in each of the primary intervals $[s_j, s_{j+1}]$. An automatic error control adds points until successive integrals for each primary mesh interval differ by only 10^{-4} . As shown in Fig. 13, for the adjacent subintervals of the kernel singularity, integration is effected by the five-point Gaussian formula; Simpson's rule is applied to all other subintervals.

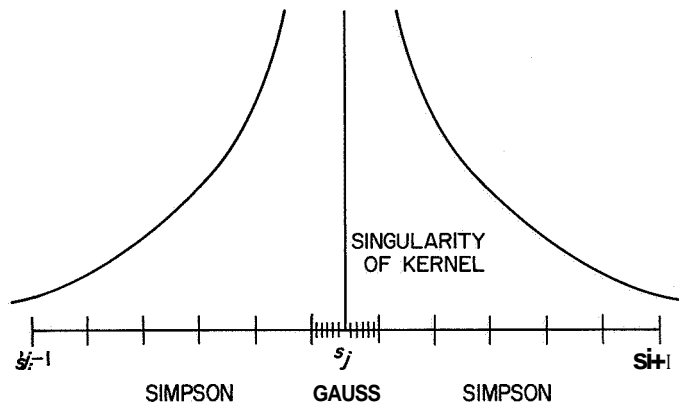


Fig. 13. Subdivision of primary parameter mesh for Simpson and Gauss integration

Thus far, the primary mesh characterized by s_1, \dots, s_J was chosen and improved manually. Allowance had to be made for the integrable charge density to be theoretically infinite at the ends and corners of the electrode profiles by a clustering of primary mesh points at such solution singularities.³ Further improvement of the clustering was halted when the last two intervals had a total charge smaller than a very small constant K.

Three computer runs were made with the diverse meshes listed below:

Run	IBM 7090 running time, min	Number of mesh points for each of seven electrodes	Total number of mesh points
1	3	10	70
2	12	25	175
3	27	36	252

The results are presented in Fig. 14. The Electrode 1 curves show a horizontal tangent at the left-hand side

³The authors gratefully acknowledge the valuable information obtained during a discussion on this subject with Prof. W. R. Smythe of the California Institute of Technology.

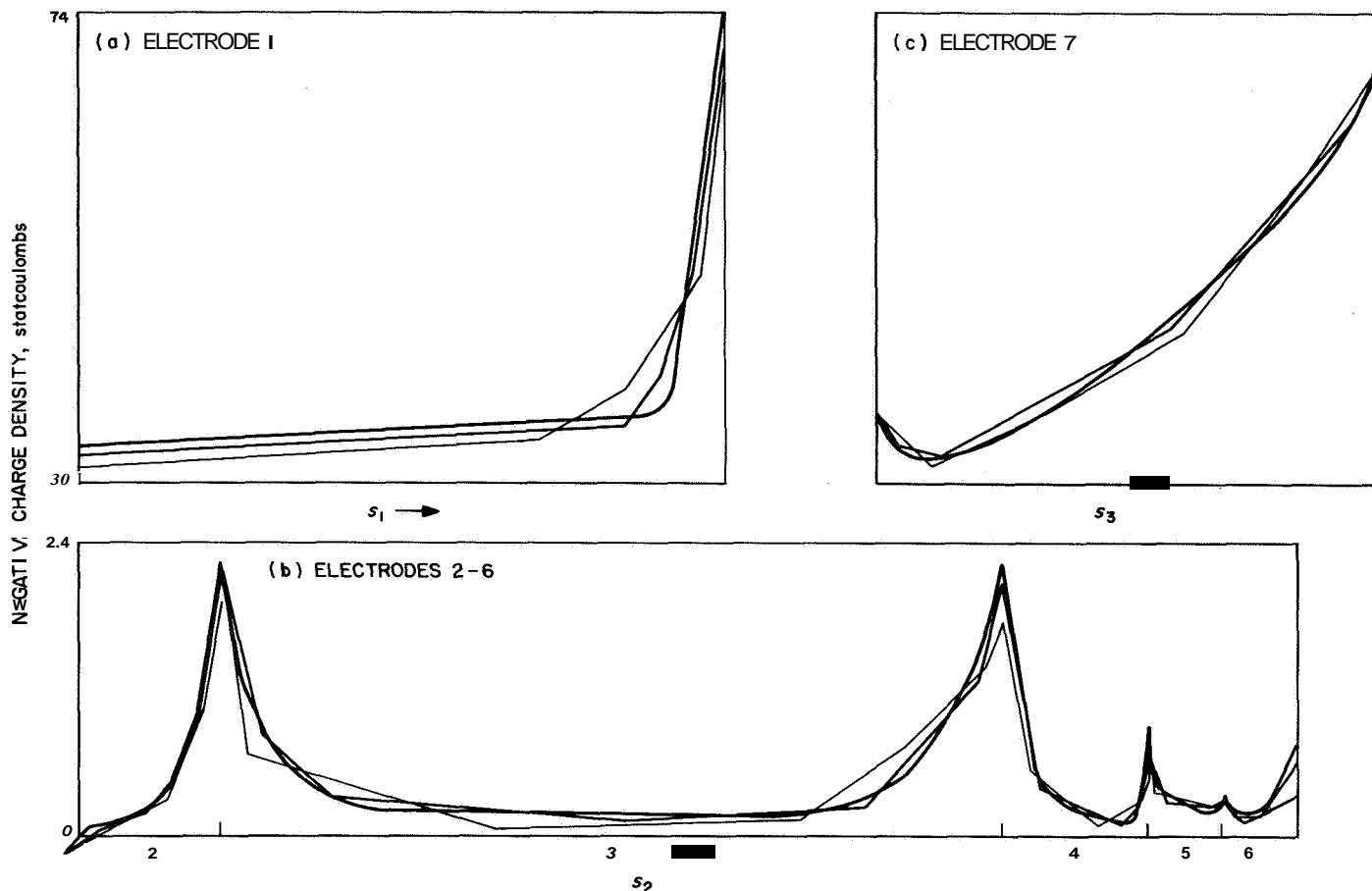


Fig. 14. Negative charge densities for the three capacitance surfaces with constant, but different, potential

which corresponds to its location on the axis. All other electrodes, characterized by corners or openness at their ends, have singularities of the charge densities at these locations. One realizes that an improper account of the singularities (thin mesh) results in an undesirable shift of the flat portions of the curves. The results presented in Fig. 14 exhibit the convergence of the process.

E. On Geometric Properties of the Estabrook-Wahlquist Function Chain, E. M. Keberle

1. Introduction

In their effort to check the relationship of a surface $\Xi(x_1, \dots, x_n)$ to the solutions of a system of ordinary differential equations

$$\begin{aligned} \dot{x}_1 &= X_1(x_1, \dots, x_n) \\ &\circ \quad \circ \\ &\circ \quad \circ \\ &\circ \quad \circ \\ \dot{x}_n &= X_n(x_1, \dots, x_n) \end{aligned} \quad (1)$$

F. Estabrook and H. Wahlquist of the JPL Physics Section have introduced the total derivative

$$\frac{d\Xi(x_1, \dots, x_n)}{dt} = \sum_{i=1}^n \frac{\partial \Xi(x_1, \dots, x_n)}{\partial x_i} \dot{x}_i$$

to obtain a new function, again of the variables x_1, \dots, x_n ,

$$\Xi^{(1)}(x_1, \dots, x_n) = \sum_{i=1}^n \frac{\partial \Xi(x_1, \dots, x_n)}{\partial x_i} X_i(x_1, \dots, x_n)$$

Estabrook, F. B., *Set of First Order Differential Equations With Algebraic Constraints*, Interoffice Memorandum, Jet Propulsion Laboratory, Pasadena, California, October 7, 1966; also acknowledged are various discussions held with Estabrook and Wahlquist during the past 1½ years.

by inserting $X_i(x_1, \dots, x_n)$ for \dot{x}_i into the total derivative. By repeating the same argument each time for the new functions, they obtained inductively the chain of functions

$$\Xi(x_1, \dots, x_n), \quad \Xi^{(1)}(x_1, \dots, x_n), \quad \Xi^{(2)}(x_1, \dots, x_n), \dots \quad (2)$$

The chain stops if, at the l th step, the new function depends on the previous functions

$$\Xi^{(l)}(x_1, \dots, x_n) = H[\Xi^{(k)}(x_1, \dots, x_n), \dots, \Xi^{(l-1)}(x_1, \dots, x_n)] \quad (3)$$

Here the index k indicates the first function to appear in the dependency.

In turn, a necessary and sufficient condition has been formulated⁵ for a solution of the system of ordinary differential equations, System (1), to be compatible with the equation

$$\Xi[x_1(t), \dots, x_n(t)] = 0$$

for all t .

In a forthcoming SPS, Vol. IV, interesting connections between the Estabrook–Wahlquist function chain and the mentioned compatibility condition will be elucidated. Preparatory to this forthcoming article, the function chain is closely examined here.

2. Higher-Order Directional Derivatives

The first total derivative of $\Xi(x)$ can be written as a directional derivative in the form

$$\Xi^{(1)}(x_1, \dots, x_n) = L\Xi(x_1, \dots, x_n)$$

using the operator of directional derivation

$$L \equiv \sum_1^n X_i(x_1, \dots, x_n) \frac{\partial}{\partial x_i}$$

along the direction field $X, (x_1, \dots, x_n), \dots, X_n(x_1, \dots, x_n)$ or, for that matter, along the solutions of System (1). The

⁵Keberle, E. M., *Partial Stationarity as Compatibility Criterion for Overdetermined Systems of Ordinary Differential Equations, Related to Non-differential Constraints*, Interoffice Technical Memorandum 314-112, Jet Propulsion Laboratory, Pasadena, California, February 10, 1966.

notation implies inductively the Estabrook–Wahlquist function chain to be written in the form

$$\Xi(x), \quad L\Xi(x), \quad L^2\Xi(x), \quad L^3\Xi(x) \dots \quad (2a)$$

A normalized directional derivative obtains by the operator

$$\frac{d}{ds} \equiv \mathbf{T} \cdot \nabla$$

introducing the tangent-vector \mathbf{T} according to

$$\frac{\mathbf{X}(x)}{|\mathbf{X}(x)|} = \mathbf{T}(x)$$

such that s is the arc length.

Higher-order normalized directional derivatives appear as products of two tensors, each of order rank m :

$$(\mathbf{T} \cdot \nabla)^m \Xi = \mathbf{T} \cdot \nabla^m \Xi$$

The listed operators satisfy the linearity rule

$$L^m(f + g) = L^m f + L^m g$$

$$L''(af) = aL^m f$$

as well as the Leibnitz rule of ordinary differentiation

$$L(f \cdot g) = gL(f) + fL(g)$$

They also play a role in the theory of harmonic functions since the normalized directional derivatives of higher order applied to the fundamental solution $1/r$ of Laplace's equation lead to the Maxwell–Sylvester representation of the higher-order spherical harmonics (Ref. 8).

3. A Quasilinear Non-elliptic Partial Differential Equation of Higher Order for the Principal Part of the Estabrook-Wahlquist Function Chain

According to Jacobi's theory of dependent functions, a largest index k and a smallest index l will uniquely exist for the function chains (2) and (2a) such that the functional determinant is zero for all points in the n -dimensional domain under consideration; i.e.,

$$\frac{\partial [L^k \Xi, \dots, L^l \Xi]}{\partial [x_1, \dots, x_n]} = 0$$

The $(l - k + 1)$ functions $L^k \Xi, \dots, L^l \Xi$ appearing in the determinant shall be called the **principal part** of the chain. Since the vanishing determinant implies dependency of the form given in Eq. (3), the definition

$$u(x) = L^k \Xi(x)$$

leads to the partial differential equation referred to in the title of this section:

$$L^{l-k} u(x) = H[u(x), Lu(x), \dots, L^{l-k-1} u(x)]$$

with the nonlinear scalar function H of Eq. (3). The highest-order partial derivatives of this equation are of order $l-k$. Since they appear in the linear part on the left-hand side, we call the sum of highest-order partial derivatives the principal part of the nonlinear partial differential equation.

The **characteristic surfaces** of this equation are given by $\Phi(\mathbf{x}) = \text{constant}$, where $\Phi(\mathbf{x})$ satisfies the characteristic linear partial differential equation of first order

$$L\Phi(x) = 0$$

which turns out to be the partial differential equation defining the first integrals of System (1). Accordingly, the characteristic surfaces are real for a real function chain, which implies that the nonlinear partial differential equation is never elliptic.

4. Example

As an example, consider the Kepler problem (see Footnote 4) with the following system of ordinary differential equations

$$\begin{aligned}\dot{x} &= v_x \\ \dot{v}_x &= -x(x^2 + y^2)^{-3/2} \\ \dot{y} &= v_y \\ \dot{v}_y &= -y(x^2 + y^2)^{-3/2}\end{aligned}$$

and the function

$$\Xi(x, v_x, y, v_y) \equiv x^2 + y^2 - C$$

The operator of directional derivation is

$$L = v_x \frac{\partial}{\partial x} - x(x^2 + y^2)^{-3/2} \frac{\partial}{\partial v_x} + v_y \frac{\partial}{\partial y} - y(x^2 + y^2)^{-3/2} \frac{\partial}{\partial v_y}$$

and the Estabrook-Wahlquist function chain becomes

$$\begin{aligned}\Xi &= x^2 + y^2 - C \\ L\Xi &= xv_x + yv_y \\ L^2\Xi &= v_x^2 + v_y^2 - (x^2 + y^2)^{-1/2} \\ L^3\Xi &= -(xv_x + yv_y)\end{aligned}$$

The chain stops with the last expression, since a dependency has been obtained:

$$L^3\Xi = -L\Xi$$

Therefore, the principal part of the chain consists of $L\Xi$, $L^2\Xi$, and $L^3\Xi$. With

$$u(x, v_x, y, v_y) \equiv xv_x + yv_y$$

the nonlinear partial differential equation of Section 3 is of second order and, in this example, is actually linear:

$$L^2 u(x, v_x, y, v_y) = -u(x, v_x, y, v_y)$$

References

1. Peabody, P. R., ~~Scott~~, J. F., and Orozco, E. G., *JPL Ephemeris Tapes E9510, E9511, E9512*, Technical Memorandum **33-167**, Jet Propulsion Laboratory, Pasadena, California, March **2, 1964**.
2. Eckert, W. J., Jones, R., and Clark, H. K., *Improved Lunar Ephemeris 1952-1959*, Nautical Almanac Office, U.S. Naval Observatory, U.S. Government Printing Office, Washington, D. C., **1954**.
3. Eckert, W. J., Walker, M. J., and Eckert, D., *Astronomical Journal*, Vol. **71**, pp. **314-332**, **1966**.
4. Clemence, G. M., Porter, J. G., and Sadler, D. H., *Astronomical Journal*, Vol. **57**, pp. **46, 47**, **1952**.
5. Clemence, G. M., *Annual Review of Astronomy and Astrophysics*, Vol. **3**, pp. **93-112**, L. Goldberg, Ed., Annual Reviews, Inc., Palo Alto, California, **1965**.
6. Sparrow, E. M., and Cess, R. D., *Radiation Heat Transfer*, **1966**.
7. Smythe, W. R., *Static and Dynamic Electricity*, 2nd Ed., McGraw-Hill Book Company, Inc., New York, **1950**.
8. Courant, R., and Hilbert, D., *Methods of Mathematical Physics*, Vol. I, p. **514**, Interscience Publishers, Inc., New York, **1953**.

II. Systems Analysis

SYSTEMS DIVISION

N67 18307

A. Relationship Between the Averaging Method of Krylov-Bogoliubov and an Approximate First Integral of Motion, H. Lass

We consider first the nonlinear equation

$$\frac{dx}{dt} = \mu f(x, t), \quad \mu f < 1 \quad (1)$$

with $f(x, t)$ periodic in t , say of period 2π , and we assume that $f(x, t)$ has a Fourier series development in the argument, t .

If $\Omega(x, t) = \text{constant}$ is a first integral of Eq. (1), then

$$\mu f(x, t) \frac{\partial \Omega}{\partial x} + \frac{\partial \Omega}{\partial t} = 0 \quad (2)$$

Now let (omitting μ^2 and higher order terms)

$$\Omega(x, t) = F(x) + \mu G(x, t) \quad (3)$$

so that Eq. (2) becomes

$$\mu f(x, t) \left[F'(x) + \mu \frac{\partial G}{\partial x} \right] + \mu \frac{\partial G}{\partial t} = 0 \quad (4)$$

Omitting the term containing μ^2 yields

$$f(x, t) F'(x) + \frac{\partial G}{\partial t} = 0$$

$$G(x, t) = -F'(x) \int_0^t f(x, \tau) d\tau \quad (5)$$

and

$$\Omega(x, t) = F(x) - \mu F'(x) \int_0^t f(x, \tau) d\tau = F(x_0) \quad (6)$$

with $F(x)$ arbitrary, $x = x_0$ at $t = 0$. Eq. (6) yields $x = \phi(t, \mu)$, and $F(x)$ will be chosen such that $x = \phi(t, \mu)$ will satisfy Eq. (1) within the order of μ^2 .

Before determining $F(x)$ let us note that if $y = x(t + 2\pi)$ then

$$F(y) - \mu F'(x) \int_0^{t+2\pi} f(x, \tau) d\tau = F(x_0) \quad (7)$$

within the order of μ^2 since x is slowly varying.

From Eqs. (6) and (7) we have

$$F'(x) \left[\Delta x - \mu \int_0^{2\pi} f(x, \tau) d\tau \right] = 0 \quad (8)$$

with $\Delta x = x(t + 2\pi) - x(t)$. Thus

$$\begin{aligned} \frac{\Delta x}{2\pi} &\approx \frac{\mu}{2\pi} \int_0^{2\pi} f(x, \tau) d\tau \\ \frac{dx}{dt} &\approx \frac{\mu}{2\pi} \int_0^{2\pi} f(x, \tau) d\tau \end{aligned} \quad (9)$$

Eq. (9) is the Krylov-Bogoliubov equation for dx/dt which can be obtained from Eq. (1) by replacing $f(x, t)$ by its mean value in time.

Returning to Eq. (6) we obtain

$$F'(x) \left(\frac{dx}{dt} - \mu f(x, t) \right) - \mu \frac{dx}{dt} \left[F''(x) \int_0^t f(x, \tau) d\tau + F'(x) \int_0^t \frac{\partial f}{\partial x} d\tau \right] = 0 \quad (10)$$

by differentiating with respect to t .

The integrals which occur in Eq. (10) may contain secular terms so that we will not omit the $\mu \dot{x} = \mu^2 f$ terms in Eq. (10). Now

$$\begin{aligned} f(x, t) &= a_0(x) + \sum_1^\infty \left[a_n(x) \sin(nt) + b_n(x) \cos(nt) \right] \\ \frac{\partial f}{\partial x} &= a'_0(x) + \sum_1^\infty \left[a'_n(x) \sin(nt) + b'_n(x) \cos(nt) \right] \end{aligned} \quad (11)$$

so that if we choose $F(x)$ such that

$$F''(x) a_0(x) + F'(x) a'_0(x) = 0 \quad (12)$$

it will follow that $x = \phi(t, \mu)$ will satisfy Eq. (1) within the order of μ^2 terms.

Eq. (12) yields

$$F(x) = \int \frac{dx}{a_0(x)} \quad (13)$$

with $a_0(x) = \frac{1}{2\pi} \int_0^{2\pi} f(x, \tau) d\tau$. Once $F(x)$ is determined, Eq. (6) yields $x = \phi(t, \mu)$.

Let us apply this technique to the equation

$$\dot{x} = 2\mu x \sin^2 t \quad (14)$$

We have $a_0(x) = \frac{2x}{2\pi} \int_0^{2\pi} \sin^2 \tau d\tau = x$, $F(x) = \ln x$, and

$$\begin{aligned} \ln x - 2\mu \int_0^t \sin^2 \tau d\tau &= \ln x_0 \\ x &= x_0 e^{\mu \left[t - \frac{\sin 2t}{2} \right]} \end{aligned} \quad (15)$$

which is the exact solution. The K.B. solution is $x = x_0 e^{\mu t}$

The generalization to a system of equations of the form

$$\frac{dx^i}{dt} = \mu f^i(x, t), \quad \mu f^i \ll 1, \quad i = 1, 2, \dots, n \quad (16)$$

is not very difficult. Let

$$\Omega_i = F_i(x) + \mu G_i(x, t) = \text{constant} = c_i \quad (17)$$

for $i = 1, 2, \dots, n$, be a set of first integrals omitting higher order terms in μ .

Then

$$\begin{aligned} f^a(x, t) \frac{\partial F_i}{\partial x^a} + \frac{\partial G_i}{\partial t} &= 0 \\ G_i(x, t) &= - \frac{\partial F_i}{\partial x^a} \int_0^t f^a(x, \tau) d\tau \end{aligned} \quad (18)$$

so that

$$F_i(x) - \mu \frac{\partial F_i}{\partial x^\alpha} \int_0^t f^\alpha(x, \tau) d\tau = F_i(x_0), i = 1, 2, \dots, n \quad (19)$$

is a set of first integrals with $F_i(x)$ arbitrary.

We choose the $F_i(x)$ in such a way that Eq. (19) will yield the set $x_i = x_i(t, \mu)$ satisfying Eq. (16) within the order of μ^2 terms.

Differentiating Eq. (19) with respect to t yields

$$\frac{\partial F_i}{\partial x^\alpha} (\dot{x}^\alpha - \mu f^\alpha) - \mu \dot{x}^\beta \left[\frac{\partial^2 F_i}{\partial x^\beta \partial x^\alpha} \int_0^t f^\alpha(x, \tau) d\tau + \frac{\partial F_i}{\partial x^\alpha} \int_0^t \frac{\partial f^\alpha}{\partial x^\beta} d\tau \right] = 0 \quad (20)$$

Let

$$f^\alpha(x, t) = a^\alpha(x) + \sum_1^\infty \left[a_n^\alpha \sin nt + b_n^\alpha \cos nt \right]$$

If we choose $F_i(x^1, x^2, \dots, x^n)$ such that

$$a^\alpha(x) \frac{\partial^2 F_i}{\partial x^\beta \partial x^\alpha} + \frac{\partial a^\alpha}{\partial x^\beta} \frac{\partial F_i}{\partial x^\alpha} = 0 \quad (21)$$

then $\dot{x}^\alpha = \mu f^\alpha$ neglecting μ^2 terms, since Eq. (21) eliminates the secular terms.

A first integral of Eq. (21) is given by

$$a^\alpha \frac{\partial F_i}{\partial x^\alpha} = k_i = \text{constant}, i = 1, 2, \dots, n \quad (22)$$

It is known that we can obtain the $F_i(x^1, x^2, \dots, x^n)$ which satisfy Eq. (22) if we can solve the system

$$\frac{dx^1}{a^1(x)} = \frac{dx^2}{a^2(x)} = \dots = \frac{dx^n}{a^n(x)} = \frac{dF_i}{k_i} \quad (23)$$

for n first integrals. This is equivalent to solving the system

$$\frac{dx^i}{dt} = a^i(x) = \frac{1}{2\pi} \int_0^{2\pi} f^i(x, \tau) d\tau \quad (24)$$

The solutions obtained from the method outlined above correspond to the Bogoliubov-Mitropolsky first approximate solution.

As a simple example we consider the nonlinear system

$$\begin{aligned} \dot{x} &= \mu y^2 \\ \dot{y} &= \mu x \cos t \end{aligned} \quad (25)$$

with $x = x_0, y = y_0 \neq 0$, at $t = 0$. Eq. (22) becomes

$$y^2 \frac{\partial F_i}{\partial x} = k_i \quad (26)$$

which yields $F_i = y(k_i = 0)$, and $F_i = x/y^2 (k_i = 1)$.

Eq. (19) now yields

$$\begin{aligned} y - \mu x \sin t &= y_0 \\ \frac{x}{y^2} - \mu t + \frac{2\mu x^2}{y^3} \sin t &= \frac{x_0}{y_0^2} \end{aligned} \quad (27)$$

which can be solved for $x = x(t, \mu), y = y(t, \mu)$.

We turn our attention now to the nonlinear equation

$$\frac{d^2 x}{dt^2} + x = \mu f\left(x, \frac{dx}{dt}\right), \mu f \ll 1 \quad (28)$$

or

$$\begin{aligned} \dot{x} &= y \\ \dot{y} &= -x + \mu f(x, y) \end{aligned} \quad (29)$$

If we let

$$\begin{aligned} x &= A(t) \sin t + B(t) \cos t \\ y &= A(t) \cos t - B(t) \sin t \end{aligned} \quad (30)$$

it is a simple matter to show that Eq. (29) yields

$$\begin{aligned}\frac{dA}{dt} &= \mu \cos t f(A \sin t + B \cos t, A \cos t - B \sin t) \\ \frac{dB}{dt} &= -\mu \sin t f(A \sin t + B \cos t, A \cos t - B \sin t)\end{aligned}\quad (31)$$

We are now in a position to solve for $A(t)$, $B(t)$ from the above considerations

N67 18308

B. A Note on Stratonovich's Equation for the Conditional Probability Distribution of the State of a Nonlinear System, with Application to Nonlinear Filtering,
S. R. McReynolds

1. Introduction

A fundamental problem of interest in engineering is as follows. Let $x(t) = (x_1(t), \dots, x_n(t))$ denote the state vector of a system which satisfies the stochastic differential equation:

$$\dot{x}_i = f_i(x, t) + v_i(t) \quad (i = 1, n) \quad (1)$$

$f_i(x, t)$ ($i = 1, n$) are generally nonlinear functions.

$v_i(t)$ ($i = 1, n$) is white noise with the statistical properties

$E(v_i(t)) = 0$; $E(v_i(t) v_j(T)) = Q_{ij}(t) \delta(t - T)$ ($i, j = 1, n$)
 $\delta(t - T)$ is the Dirac delta function. The system is observed by a set of measurements.

$$z_j(t) = h_j(x, t) + w_j(t) \quad (j = 1, p) \quad (2)$$

$h(x, t)$ ($j = 1, p$) are generally nonlinear functions; $w_j(t)$ ($j = 1, p$) is a white noise vector with statistics given by $E(w_j(t)) = 0$; $E(w_i(t) w_j(T)) = R_{ij}(t) \delta(t - T)$ ($i, j = 1, p$)
For the purposes of this paper, it will be assumed that $v_i(t)$ and $w_i(t)$ are statistically independent. An initial probabilities distribution of x is given explicitly

$$P(x_0, t_0) = \text{given} \quad (3)$$

The problem is to find the function $P(x, t/Z_t)$, expressing conditional probability of the state x at time t , given all past measurements $z(t)$ over the interval (t_0, t) and an initial condition (3).

The problem without measurements was originally investigated in the study of Brownian motion. The classical result is the Fokker-Planck equation:

$$0 = \frac{\partial P}{\partial t} + \frac{\partial}{\partial x_i} (P f_i) - \frac{1}{2} \frac{\partial^2}{\partial x_i \partial x_j} (Q_{ij} P) \quad (4)^1$$

This is a second-order, parabolic partial differential equation by which the probability distribution $P(x, t/Z_t)$ may be computed forward in time from the given initial condition.

The problem with measurements was solved recently by Stratonovich (Ref. 2), who obtained the partial differential equation:

$$\begin{aligned}0 &= \frac{\partial P}{\partial t} + \frac{\partial}{\partial x_i} (P f_i) - \frac{1}{2} \frac{\partial^2}{\partial x_i \partial x_j} (Q_{ij} P) \\ &+ P[\hat{H}(z(t), t) - H(x, z(t), t)] = 0\end{aligned} \quad (5)$$

where

$$H(x, z(t), t) = z(t)(R^{-1})_{ij} h_j(x, t) - \frac{1}{2} h_i(x, t)(R^{-1})_{ij} h_j(x, t) \quad (6)$$

$$\hat{H}(z(t), t) = \int_{-\infty}^{+\infty} H(x, z(t)) P(x, t/Z_t) dx \quad (7)$$

Note that Eq. (6), which we shall refer to as Stratonovich's equation, has some additional terms. Kushner (Ref. 3) has contested these terms. Kushner claims the proper equation should be:

$$\begin{aligned}0 &= \frac{\partial P}{\partial t} + \frac{\partial}{\partial x_i} (P f_i) - \frac{1}{2} \frac{\partial^2}{\partial x_i \partial x_j} (Q_{ij} P) \\ &- (z_i - \hat{h}_i)(R^{-1})_{ij} (h_j - \hat{h}_j) P = 0\end{aligned} \quad (8)$$

In this paper we show that Stratonovich's equation, namely, Eq. (5), is the correct equation. Eq. (5) is re-derived. It is then shown that in the case when $f(x, t)$ and $h(x, t)$ are linear in x the solution of Stratonovich's equation yields the Kalman filter, whereas Eq. (8) does not.

A recent paper of Kulman (Ref. 4) also defended Stratonovich's equation. However, Kulman infers, without

¹Summation over repeated subscripts is implied.

proof and incorrectly, that the correct result was arrived at via the discrete version of Kushner's equation.

The importance of Stratonovich's result is illustrated in the paper by showing how it may be used to obtain approximate filters for nonlinear systems. An approximate filter, similar to the Kalman filter, is derived.

2. White Noise

The major source of difficulty in deriving the result lies with conceptual problems connected with continuous white noise. In this section we wish to clearly state the model of white noise by showing how continuous white noise can be defined by applying limiting procedures to a discrete noise. In particular, we wish to clarify the difference between the definitions of white noise appearing in the system equation ("process noise") and measurement noise.

Process white noise originally arose in the mathematical description of Brownian motion. The physical model associated with Brownian motion is a rapid sequence of small, random impulses. These impulses are assumed to be from the same population of possible forces, and members of the sequence are assumed statistically independent.

Over a short time Δt , the state $x(t)$ is subject to a random change in state, Δx , which can be approximated by

$$\Delta x_i = f_i(x, t) \Delta t + \sum v_i(t_j)$$

The discrete impulses $v_i(t_j)$ ($j = 0, 1, \dots$), which occur at the times t_j , ($j = 0, 1, \dots$) in $(t, t + \Delta t)$, are members of a Gaussian population? with the properties $E(v_i) = 0$; $E(v_i v_j) = q_{ij}$.

If N impulses occur per unit time, then assuming that they are independent,

$$\bar{\Delta x}_i = E(\Delta x_i) = f_i(x, t) \Delta t$$

$$E(\Delta x_i - \bar{\Delta x}_i)(\Delta x_j - \bar{\Delta x}_j) = N q_{ij} \Delta t$$

Continuous white noise may now be defined by letting $N \rightarrow \infty$ and $q_{ij} \rightarrow 0$ in such a way that $\lim N q_{ij} = Q_{ij}$

²The law of large numbers may be applied to weaken this hypothesis.

exists. It follows that the probability distribution of Δx can be approximated (with an $(\Delta t)^2$ error) by the Gaussian distribution

$$p(\Delta x, t) = K \exp \left\{ -\frac{1}{2} (\Delta x_i - f_i(x, t) \Delta t) (Q^{-1})_{ij} \right. \\ \left. \times (\Delta x_j - f_j(x, t) \Delta t) / \Delta t \right\} \\ (K = \text{normalizing constant}) \quad (9)$$

Note that $p(\Delta x, t)$ is actually a conditional probability distribution based upon knowledge of the state at time t .

The conceptual approach to white measurement noise is entirely different. Let t_i ($i = 1, \dots$) for a sequence of times at which measurements are taken over the interval $(t, t + \Delta t)$. If Δt is chosen small enough, x may be assumed fixed, and thus the sequence of measurements can be treated as the independent iteration of the same experiment; thus all the information can be expressed simply averaging the measurements. Thus defining

$$\bar{z}_i = \frac{1}{N \Delta t} \sum_{t_j \in (t, t + \Delta t)} z_i(t_j) \\ \bar{w}_i = \frac{1}{N \Delta t} \sum_j w_i(t_j)$$

the information obtained by the measurements over the interval $(t, t + \Delta t)$ can be expressed by

$$\bar{z}_i = h_i(x, t) + \bar{w}_i \quad (10)$$

Now let us assume that $w_i(t_i)$ ($i = 0, \dots$) are independent samples from a Gaussian distribution with the statistical properties

$$E(w_i) = 0$$

$$E(w_i w_j) = r_{ij} \quad (11)$$

Thus

$$E(\bar{w}_i) = 0$$

$$E(\bar{w}_i \bar{w}_j) = \frac{r_{ij}}{N \Delta t} \quad (12)$$

Now as $N \rightarrow \infty$ it is clear that in order that the second moment of w_i remain nonzero but bounded, r_{ij} must approach infinity in such a way that

$$\lim \frac{r_{ij}}{N} = R_{ij} > 0$$

must exist and be bounded. If r_{ij} remains bounded, then $R_{ij} \rightarrow 0$ and perfect knowledge of the measurements would be available. The end result is that \bar{z} is distributed approximately (first order in Δt) by the Gaussian distribution.

$$P(\bar{z}/x) = K \exp \left\{ -\frac{1}{2} (\bar{z}_i - h_i(x, t)) (R)^{-1}_{ij} \times (\bar{z}_j - h_j(x, t)) \Delta t \right\} \quad (13)$$

Now

$$P(x(t + \Delta t), t + \Delta t, \bar{z}/Z_t) = P(\bar{z}/x(t + \Delta t), Z_t) P(x(t + \Delta t), t + \Delta t/Z_t) \quad (15)$$

$$P(\bar{z}/Z_t) = \int P(\bar{z}/x(t + \Delta t), Z_t) P(x(t + \Delta t), t + \Delta t/Z_t) dx(t + \Delta t) \quad (16)$$

Eqs. (14), (15) and (16) are similar to those obtained by Kushner (Ref. 3). Recalling that $P(z/x(t + \Delta t), Z_t)$ is given Eq. (13), the right-hand side of Eq. (14) may be expanded in terms of Δt to yield

$$P(x(t + \Delta t), t + \Delta t/\bar{z}, Z_t) = P(x(t + \Delta t), t + \Delta t/Z_t) \{ (1 + \Delta t(H(\bar{z}, x(t + \Delta t), t + \Delta t) - \hat{H}(\bar{z}, t + \Delta t) + 0(\Delta t^2)) \} \quad (17)$$

The functions $H(z, x, t)$ and $\hat{H}(z, t)$ are given by Eqs. (6) and (7). To obtain a partial differential equation, $p(x(t + \Delta t), t + \Delta t/Z_t)$ must now be expanded around $p(x(t + \Delta t), t/Z_t)$. To do so, one applies Smoluchowski's equation (Doob, Ref. 5, p. 88).

$$P(x(t + \Delta t), t + \Delta t/Z_t) = \int P(x(t + \Delta t) - \Delta x, t/Z_t) P(\Delta x) d(\Delta x) \quad (18)$$

Employing Eq. (9), one may show in a classic calculation (Ref. 6, p. 33) that Eq. (18) may be expanded to obtain

$$P(x(t + \Delta t), t + \Delta t/Z_t) = P(x(t + \Delta t), t/Z_t) + \Delta t \left[\frac{-\partial}{\partial x_i} (P f_i) + \frac{\partial^2}{\partial x_i \partial x_j} (Q_{ij} P) \right]_{x(t + \Delta t), t} + 0(\Delta t^2) \quad (19)$$

Employing Eq. (19) on the right-hand side of Eq. (17) and expanding both sides of the equation around $(x(t + \Delta t), t)$, one obtains

$$0 = \left[\frac{\partial P}{\partial t} + \frac{\partial}{\partial x_i} (P f_i) - \frac{\partial^2}{\partial x_i \partial x_j} (Q_{ij} P) + P(\hat{H}(z, t) - H(x, z, t)) \right]_{t, x-x(t + \Delta t), t} \Delta t + 0(\Delta t^2) \quad (20)$$

This is a conditional distribution, based upon the state at time t is known to be x . Eqs. (9) and (13) are the major results obtained in this section. Both equations are of primary importance in deriving Statonovich's equation.

3. Statonovich's Equation

Let us assume that $P(x, t/Z_t)$, the conditional probability of the state, given all measurement prior to t , has been determined at time t , Z_t designates the measurement over the interval $[t_0, t]$, and \bar{z} designates the average measurement over $[t, t + \Delta t]$. An application of Bayes' rule yields

$$P(x(t + \Delta t), t + \Delta t/\bar{z}, Z_t) = \frac{P(x(t + \Delta t), t + \Delta t, \bar{z}/Z_t)}{P(\bar{z}/Z_t)} \quad (14)$$

Stratonovich's equation is obtained by setting to zero the quantity in the brackets on the right-hand side of Eq. (20).

4. The Kalman Filter

In order to "verify" the correctness of the results we shall show in this section that the solution of Stratonovich's equation for the linear case yields the Kalman (Ref. 7) filter. It should also be shown that Kushner's equation does not yield the Kalman filter.

Let us now examine the case where the system equations are given by

$$\dot{x}_i(t) = F_{ij}(t) x_j(t) + v_i(t) \quad (21)$$

and the measurements are given by:

$$z_i(t) = h_{ij}(t) x_j(t) + w_i(t) \quad (22)$$

The initial probability distribution is Gaussian

$$P(x, t_0) = K \exp \left\{ - (x_i - \bar{x}_i(t_0)) [S(t_0)]_{ij} (x_j - \bar{x}_j(t_0)) \right\} \quad (23)$$

It is generally accepted that the solution to the above problem is given by the continuous Kalman Filter. To see that this is the case, let us look for a solution $P(x, t/Z_t)$ of Stratonovich's equation of the form

$$P(x, t/Z_t) = \frac{|S(t)|^{1/2}}{(2\pi)^{n/2}} e^{-\frac{1}{2}(x_i - \bar{x}_i(t)) S_{ij}(t) (x_j - \bar{x}_j(t))} \quad (24)$$

where $\bar{x}(t)$ is the mean and $S(t)^{-1}$ is the covariance of the multivariate Gaussian distribution $P(x, t/Z_t)$. In the case we are considering Stratonovich's equation can be written as:

$$\begin{aligned} 0 = & \frac{\partial P}{\partial t} + \frac{\partial P}{\partial x_j} F_{ij} x_j + P F_{ii} - \frac{1}{2} \frac{\partial^2 P}{\partial x_i \partial x_j} Q_{ij} \\ & - (z_j - \bar{x}_j H_{ij}) R_{ir}^{-1} H_{rn} (x_n - \bar{x}_n) P \\ & + \frac{1}{2} (x_j - \bar{x}_j) H_{ij} R_{ik}^{-1} H_{kn} (x_n - \bar{x}_n) P \\ & - \frac{1}{2} S_{ij}^{-1} H_{ki} R_{kn}^{-1} H_{nj} P \end{aligned} \quad (25)$$

An application of Kushner's equation (Eq. 8) would result in a similar equation except the last two terms would be omitted. The relevant partial derivatives of $P(x, t)$ are:

$$\begin{aligned} \frac{\partial P}{\partial t} &= \left[\frac{|\dot{S}(t)|}{2|S(t)|} + (x_i - \bar{x}_i) S_{ij}(t) \dot{\bar{x}}_j(t) - \frac{1}{2} (x_i - \bar{x}_i) \dot{S}_{ij}(t) (x_j - \bar{x}_j) \right] P \\ \frac{\partial P}{\partial x_j} &= - (x_i - \bar{x}_i) S_{ij}(t) P \frac{\partial^2 P}{\partial x_i \partial x_j} = (-S_{ij}(t) + (x_k - \bar{x}_k) S_{ki}(t) S_{jn}(t) (x_n - \bar{x}_n)) P(t) \end{aligned}$$

Substituting the above expressions into Eq. (25), cancelling P , and collecting terms results in

$$\begin{aligned} 0 = & \frac{1}{2} \left\{ \frac{|\dot{S}|}{|S|} + 2F_{ii} + \frac{1}{2} S_{ij} Q_{ij} + \frac{1}{2} S_{ir}^{-1} H_{rk} R_{rn}^{-1} H_{nj} + (x_i - \bar{x}_i) \{ S_{ij}(t) \dot{\bar{x}}_j(t) - S_{ij} F_{jk} \bar{x}_k - H_{ji} R_{jk}^{-1} (z_k - H_{kn} \bar{x}_n) \} \right. \\ & \left. + \frac{1}{2} (x_i - \bar{x}_i) [-\dot{S}_{ij} - S_{in} F_{nj} - F_{in} S_{nj} - S_{in} Q_{nm} S_{nj} + H_{in} R_{nm}^{-1} H_{mj}] (x_j - \bar{x}_j) \right\} \end{aligned} \quad (26)$$

This equation can be solved by setting the term between brackets to zero. This results in differential equations for $|S|$, $\bar{x}(t)$, and $S(t)$.

$$|\dot{S}| = |S| (2F_{ii} + S_{ij} Q_{ij} - S_{ij}^{-1} H_{ri} R_{kn}^{-1} H_{nj}) \quad (27)$$

$$\dot{\bar{x}}_i = F_{ij} \bar{x}_j + S_{ij}^{-1}(t) H_{kj} R_{kn}^{-1} (z_n - H_{nm} \bar{x}_n) \quad (28)$$

$$\dot{S}_{ij} = -S_{in}(t) F_{nj} - F_{in} S_{nj} - S_{in} Q_{nm} S_{nj} + H_{ni} R_{nm}^{-1} H_{mj} \quad (29)$$

One should note that Eq. (27) can be obtained from Eq. (29). If $P_{ij}(t) = (S(t))_{ij}^{-1}$ is introduced, Eqs. (28) and (29) became the Kalman filter, namely:

$$\dot{\bar{x}}_i = F_{ij}\bar{x}_j + P_{ij} H_{rj} R_{kn}^{-1} (z_n - H_{nm} \bar{x}_m) \quad (30)$$

$$\dot{P}_{ij} = + P_{in} F_{jn} + F_{in} P_{nj} + Q_{ij} - P_{in} H_{nm} R_{mk}^{-1} H_{rl} P_{lj} \quad (31)$$

If a similar substitution was performed for Kushner's equation the last term in Eq. (31) would be missing.

5. Application of Stratonovich's Equation to Nonlinear Filtering

A current topic of investigation is approximation techniques for nonlinear filtering (Refs. 8, 9, 10). At the present, little numerical experimentation exists to verify the usefulness of the various techniques. In this section, a particular nonlinear stochastic approximation scheme for the continuous case shall be obtained. It shall be seen that the scheme will resemble the Kalman filter, except that various additional terms shall arise from the nonlinearities. The approximate filter is derived by an application of Galerkin's method. One seeks a solution of the form

$$P(x,t) = \sum_{n=0}^{\infty} a_n(t) P_n(x) \quad (32)$$

where $P_n(x)$ are orthogonal polynomials. Substituting this expression into the partial differential equation, one may obtain an infinite series of ordinary differential equations for the coefficients a_n . The approximation, based upon the fact that $a_n \rightarrow 0$ as $n \rightarrow \infty$ for well-behaved solution, is obtained by truncating the expression, i.e., by setting $a_n = 0$ for $n \geq n_0$.

Since the solution of Stratonovich's equation for the linear case is given by a Gaussian distribution, it seems sensible to look for a Gram-Charlier expansion (Cramer, Ref. 11, p. 222).

$$P(x,t) = K(t) e^{-\frac{1}{2}(x_i - \bar{x}_i) P_{ij}^{-1}(t) (x_j - \bar{x}_j)} \times \left[\left(1 + \sum_{n=3}^{\infty} a_n H_n(x - \bar{x}) \right) \right] \quad (33)$$

where $H_n(x)$ is the n th order Hermite polynomial. In this section, the simplest approximation $P_0(x)$ shall be derived by retaining only the first terms in the above expansion.

$$P_0(x,t) = K(t) e^{-\frac{1}{2} (x_i - \bar{x}_i)^{-1} P_{ij}^{-1} (x_j - \bar{x}_j)} \quad (34)$$

As in the derivation of the Kalman filter x_i and P_{ij} shall be chosen to make the linear and quadratic terms in $(x - \bar{x})$ vanish in Stratonovich's equation when expanded around \bar{x} . This results in the differential equations:

$$\dot{\bar{x}}_i = f_i(\bar{x}) + P_{ir} \left[\frac{\partial h_k}{\partial x_r} R_{kn}^{-1} (z_n - h_n(\bar{x})) + \frac{\partial^2 f_k}{\partial x_k \partial x_r} \right] \quad (35)$$

$$\begin{aligned} \dot{P}_{ij} = & P_{in} \frac{\partial f_j}{\partial x_n} + P_{jn} \frac{\partial f_i}{\partial x_n} + Q_{ij} \\ & - P_{in} \left[\frac{\partial h_m}{\partial x_n} R_{mr}^{-1} \frac{\partial h_r}{\partial x_m} + \frac{f_p(\bar{x})}{\partial x_p \partial x_n \partial x_m} \right. \\ & \left. - (z_r - h_r(\bar{x})) R_{rk}^{-1} \frac{\partial^2 h_k}{\partial x_n \partial x_m} \right] P_{mj} \end{aligned} \quad (36)$$

All functions are evaluated at \bar{x} . Comparing Eqs. (30) and (31) with Eqs. (35) and (36), one notes that this approximate filter closely resembles the Kalman filter.

Eqs. (35) and (36) have several important implications. Note that the approximate filter reduces the usual amount of linearization employed around the nominal. What is done is essentially to always choose the mean about which the "linearization" is performed.

Note that several terms are present that would be omitted from the Kalman filter applied to the linearized equations. In the equation for the mean, the additional term $P_{ir} \partial^2 f_k / \partial x_r \partial x_k$ is present. This has the effect of a bias. So that even without measurements, $\dot{\bar{x}} \neq f(\bar{x})$ is generally the case. This term differs from the bias terms obtained by Jazwinski (Ref. 9). Note this term is zero if the equations are linear. For some important nonlinear problems, such as those involving motion in a gravitational field, this term is zero.

The additional term $-P_{in} \partial^3 f_k / \partial x_k \partial x_n \partial x_m (x) P_{mj}$ appears in the equation for the covariance. This term is due to the nonlinearities of the system equation. Note that it may be interpreted as a distortion of the measurement noise. If no measurements are present, it may affect the solution of covariance equations drastically.

Another term which acts like measurement noise is $-P_{in}(z_r - h_r(t))R_{rk}^{-1} \partial^2 h_k / \partial x_n \partial x_m P_{mj}$. This is zero if the measurements are heard or the residue is zero.

6. Summary

In this paper, the Stratonovich equation for the conditional probability distribution of a system, given nonlinear measurements, has been rederived. It has shown to be consistent with the Kalman filter, whereas Kushner's equation does not appear so. Stratonovich's equation was then used to obtain an approximate filter for nonlinear equations. It is seen to resemble the Kalman filter, with the appearance of several additional terms due to the nonlinearities of the functions involved. Recent suggestions have been made by Denham and Pines (Ref. 12) to modify the Kalman filter to correct for nonlinearities. The approximate filter obtained in this paper contains several such terms. It is felt that the effect of these terms should be investigated before higher order approximation schemes are tried.

Then

$$P_n(0,0,0) = q^3 \left[\frac{\lambda_1^{n-1}}{(\lambda_1 - \lambda_2)(\lambda_1 - \lambda_3)} + \frac{\lambda_2^{n-1}}{(\lambda_2 - \lambda_1)(\lambda_2 - \lambda_3)} + \frac{\lambda_3^{n-1}}{(\lambda_3 - \lambda_1)(\lambda_3 - \lambda_2)} \right] \quad (2)$$

and we can obtain the mean number of trials until the first occurrence of "000" by multiplying Eqs. (1) and (2) by n and summing [or alternatively solving the equation $\mu = p(\mu + 1) + pq(\mu + 2) + pq^2(\mu + 3) + 3q^3$].

We obtain

$$\mu(0,0,0) = \frac{1 + q + q^2}{q^3} = \frac{1 - q^3}{pq^3} \quad (3)$$

and the variance is obtained similarly, yielding

$$\sigma^2(0,0,0) = \frac{p(1 + 3q + 6q^2 + 3q^3 + q^4)}{q^6} \quad (4)$$

[This is obtained by solving the equation

$$\sigma^2 = p(\sigma^2 + 1) + pq(\sigma^2 + 4) + pq^2(\sigma^2 + 9) + q^3 \left(\frac{1 + q + q^2}{q^3} - 3 \right)^2 !]$$

C. On the First Occurrence of Specified Sequences, C. B. Solloway and H. Iass

Let a sequence of zeros and ones be transmitted with probabilities p and $q = 1 - p$, respectively, each selection being independent. We are interested in the probability that a specified subsequence, e.g., "101," occur for the first time on the n th transmission, and some of the statistics associated with this probability. We shall solve this problem for the case of all the possible subsequences of length 3.

Let $P_n(0,0,0)$ = probability that the sequence "000" occur for the first time on the n th transmission, $n \geq 3$. It is easily seen that P_n must satisfy the difference equation

$$P_n = p P_{n-1} + pq P_{n-2} + pq^2 P_{n-3} \quad n \geq 4 \quad (1)$$

subject to the initial conditions,

$$P_1 = P_2 = 0, \quad P_3 = q^3$$

Let λ_1 , λ_2 , and λ_3 be the three roots of the characteristic equation $\lambda^3 - p\lambda^2 - pq\lambda - pq^2 = 0$. [There will always be one real and two complex roots of this equation for $0 < p < 1$ and the only rational root occurs for $p = 1/4, q = 3/4$.]

The sequence "111" is treated similarly. Thus, if $P_n(1,1,1)$ = probability that the sequence "111" occurs for the first time on the n th transmission, $n \geq 3$, we have

$$P_n = q P_{n-1} + pq P_{n-2} + p^2 q P_{n-3} \quad n \geq 4 \quad (5)$$

subject to the initial conditions $P_1 = P_2 = 0, P_3 = p^3$.

If λ_1, λ_2 and λ_3 are the three roots of the characteristic equation

$$\lambda^3 - q\lambda^2 - pq\lambda - p^2q = 0$$

then

$$P_n(1,1,1) = p^3 \left[\frac{\lambda_1^{n-1}}{(\lambda_1 - \lambda_2)(\lambda_1 - \lambda_3)} + \frac{\lambda_2^{n-1}}{(\lambda_2 - \lambda_1)(\lambda_2 - \lambda_3)} + \frac{\lambda_3^{n-1}}{(\lambda_3 - \lambda_1)(\lambda_3 - \lambda_2)} \right] \quad (6)$$

The mean and variance are obtained from Eqs. (3) and (4) by interchanging p and q , so that

$$\mu(1,1,1) = \frac{1 + p + p^2}{p^3} = \frac{1 - p^3}{qp^3} \quad (7)$$

and

$$\sigma^2(1,1,1) = \frac{q(1 + 3p + 6p^2 + 3p^3 + p^4)}{p^6} \quad (8)$$

The difference equations associated with the sequences "001" and "110" are, respectively,

$$P_n = p P_{n-1} + pq P_{n-2} + pq^{n-1} \quad n \geq 3 \quad (9)$$

$$P_n = q P_{n-1} + p q P_{n-2} + qp^{n-1} \quad n \geq 3 \quad (10)$$

subject to the initial condition $P_1 = P_2 = 0$ in both cases. If $\lambda_{1,2}$ and $\mu_{1,2}$ are the solutions of the quadratics, $\lambda^2 - p\lambda - pq = 0, \mu^2 - q\mu - pq = 0$, respectively, the solutions are

$$P_n(0,0,1) = \frac{(\lambda_2 - q)pq}{\lambda_1 - \lambda_2} \lambda_1^{n-1} + \frac{(\lambda_1 - q)pq}{\lambda_2 - \lambda_1} \lambda_2^{n-1} + \frac{pq^{n-1}}{1 - 3p} \quad p \neq \frac{1}{3} \quad (11)$$

$$P_n(0,0,1) = -\frac{5}{9} \left(\frac{2}{3} \right)^n - \frac{4}{9} \left(-\frac{1}{3} \right)^n + \frac{n}{9} \left(\frac{2}{3} \right)^n \quad p = \frac{1}{3} \quad (11a)$$

$$P_n(1,1,0) = \frac{(\mu_2 - p)pq \mu_1^{n-1}}{\mu_1 - \mu_2} + \frac{(\mu_1 - p)pq \mu_2^{n-1}}{\mu_2 - \mu_1} + \frac{qp^{n-1}}{1 - 3q} \quad q \neq \frac{1}{3} \quad (12)$$

$$P_n(1,1,0) = -\frac{5}{9} \left(\frac{2}{3} \right)^n - \frac{4}{9} \left(-\frac{1}{3} \right)^n + \frac{n}{9} \left(\frac{2}{3} \right)^n \quad q = \frac{1}{3} \quad (12a)$$

The corresponding means are

$$\mu(0,0,1) = \frac{1}{q^2 p} \quad (13)$$

$$\mu(1,1,0) = \frac{1}{p^2 q} \quad (14)$$

and the variances yield

$$\sigma^2(0,0,1) = \frac{1-5pq^2}{p^2 q^4} \quad (15)$$

$$\sigma^2(1,1,0) = \frac{1-5p^2 q}{q^2 p^4} \quad (16)$$

For the sequences "010" and "101" we obtain, respectively

$$P_n = P_{n-1} - pq P_{n-2} + qp^2 P_{n-3} \quad n \geq 4 \quad (17)$$

and

$$P_n = P_{n-1} - pq P_{n-2} + pq^2 P_{n-3} \quad n \geq 4 \quad (18)$$

subject to the initial conditions $P_1 = P_2 = 0, P_3 = q^2 p$ and $P_1 = P_2 = 0, P_3 = p^2 q$, respectively.

To vary the procedure somewhat and introduce another useful technique, let us define the generating function

$$\phi(Z; 0,1,0) = \sum_{n=3}^{\infty} P_n(0,1,0) Z^n \quad (19)$$

Multiplying Eq. (17) by n and summing on n from 4 to ∞ we obtain

$$\phi(Z; 0,1,0) = \frac{pq^2 Z^3}{1 - Z + pq Z^2 - p^2 q Z^3} \quad (20)$$

Note that

$$\phi(1; 0,1,0) = 1 = \sum_{n=3}^{\infty} P_n,$$

Similarly,

$$\phi(Z; 1,0,1) = \frac{qp^2 Z^3}{1 - Z + pq Z^2 - p^2 q Z^3} \quad (21)$$

Since

$$\phi'(1; 0,1,0) = \mu(0,1,0)$$

and

$$\phi''(1; 0,1,0) - [\phi'(1; 0,1,0)]^2 = \sigma^2(0,1,0) - \mu(0,1,0)$$

where primes denote differentiation with respect to Z , we can obtain immediately (use logarithmic differentiation)

$$\mu(0,1,0) = \frac{1+pq}{pq^2} \quad (22)$$

$$\mu(1,0,1) = \frac{1+pq}{p^2 q} \quad (23)$$

and

$$\sigma^2(0,1,0) = \frac{(1+pq)^2}{p^2 q^4} + \frac{5+pq}{pq^2} \quad (24)$$

$$\sigma^2(1,0,1) = \frac{(1+pq)^2}{p^4 q^2} + \frac{5+pq}{p^2 q} \quad (25)$$

Finally, for the sequences "011" and "100" we have, respectively

$$P_n = P_{n-1} - p^2 q P_{n-3} \quad n \geq 4 \quad (26)$$

$$P_n = P_{n-1} - pq^2 P_{n-3} \quad n \geq 4 \quad (27)$$

with initial conditions $P_1 = P_2 = 0, P_3 = p^2 q$ and $P_1 = P_2 = 0, P_3 = pq^2$, respectively. The generating functions are

$$\phi(Z; 0,1,1) = \frac{p^2 q Z^3}{1 - Z + p^2 q Z^3} \quad (28)$$

$$\phi(Z; 1,0,0) = \frac{pq^2 Z^3}{1 - Z + pq^2 Z^3} \quad (29)$$

so that the means and variances become

$$\mu(0,1,1) = \frac{1}{pq^2} \quad (30)$$

$$\mu(1,0,0) = \frac{1}{p^2 q} \quad (31)$$

and

$$\sigma^2(0,1,1) = \frac{1-5pq^2}{p^2q^4} \quad (32)$$

$$\sigma^2(1,0,0) = \frac{1-5p^2q}{p^4q^2} \quad (33)$$

The question of the first occurrence of such sequences arose from a practical problem associated with the decoding of messages from the Mars *Mariner* spacecraft, but we will not discuss that problem here.

The analysis of other possible sequences can be treated in a similar manner using the techniques illustrated here. An interesting generalization occurs when the transmitted symbols are not independent but are governed by a more general stochastic process. This will be the topic of a future investigation.

D. A Note on Null Geodesics in the General Theory of Relativity, H. Lass

The Schwarzschild line element for a spherically symmetrical mass, M , is given by

$$ds^2 = c^2 \left(1 - \frac{2GM}{c^2 r} \right) dt^2 - \frac{dr^2}{1 - \frac{2GM}{c^2 r}} - r^2(d\theta^2 + \sin^2\theta d\phi^2) \quad (1)$$

for the region external to the mass.

For planar motion, $\theta = \pi/2$, it is known that the geodesics obtained from $\delta \int ds = 0$ yield

$$\frac{d^2u}{d\phi^2} + u = \frac{GM}{h^2} + \frac{3GM}{c^2} u^2 \quad (2)$$

$$r^2 \frac{d\phi}{ds} = h \quad (3)$$

with $u = 1/r$, and h a constant of the motion.

The motion of light is such that $ds = 0$, which yields $h = \infty$ from Eq. (3), so that Eq. (2) becomes

$$\frac{d^2u}{d\phi^2} + u = \frac{3GM}{c^2} u^2 \quad (4)$$

yielding a slight variation from the linear paths in the absence of gravitational masses.

Eq. (4) yields the value of $1.75''$ of arc for the bending of light as it grazes the Sun's surface (angle between the asymptotes), one of the experimental checks for Einstein's theory of relativity.

Since Eqs. (2) and (3) are derived on the premise that $ds \neq 0$, it is difficult to follow how one can justify setting $ds = 0$ to obtain $h = \infty$, and to conclude that the angular momentum of light is infinite.

In this paper we will obtain Eq. (4) by positing that $ds = 0$ and that the coordinate time, t , is extremalized for light paths, namely $\delta \int dt = 0$.

Setting $ds = 0$, $\theta \equiv \pi/2$, in Eq. (1) yields

$$dt^2 = \frac{1}{c^2} \left[\frac{1}{\left(1 - \frac{2GM}{c^2 r} \right)^2} + \frac{r^2 d\phi^2}{1 - \frac{2GM}{c^2 r}} \right] \quad (5)$$

The Euler-Lagrange equation for the coordinate t yields

$$\frac{r^2 \frac{d\phi}{dt}}{1 - \frac{2GM}{c^2 r}} = k = \text{constant} \quad (6)$$

Eliminating dt between Eqs. (5), (6), yields

$$\left(\frac{dr}{d\phi} \right)^2 = \frac{c^2 r^4}{k^2} - \left(1 - \frac{2GM}{c^2 r} \right) r^2 \quad (7)$$

With $r = \frac{1}{u}$, $\frac{dr}{d\phi} = -\frac{1}{u^2} \frac{du}{d\phi}$, we obtain

$$\left(\frac{du}{d\phi} \right)^2 = \frac{c^2}{k^2} - u^2 + \frac{2GM}{c^2} u^3 \quad (8)$$

A simple differentiation with respect to ϕ yields Eq. (4).

This derivation of Eq. (4) seems more satisfactory than the classical approach of setting $h = \infty$. It can be shown also that the light paths are invariant under the set of transformations $t = t, x = x(\bar{x}, \bar{y}, \bar{z}), y = y(\bar{x}, \bar{y}, \bar{z}), z = z(\bar{x}, \bar{y}, \bar{z})$, for any static line element.

N67 18311

E. Numerical Integration of Periodic Orbits in The Elliptic Restricted Three-Body Problem, R. Broucke

The problem of finding periodic orbits in the circular restricted three-body problem has been very extensively studied in celestial mechanics. It is well known that continuous families of periodic orbits exist, for which the period varies in a continuous way. However, all the applications which are found in the solar system correspond to cases with non-zero eccentricities, and the elliptic restricted three-body problem is thus a better approximation than the circular one. For instance, for the motion of a satellite in the Earth-Moon system, as a first approximation, we may assume that the Moon moves around the Earth in circular motion; but as a much better approximation, we can also assume that the Moon moves in an elliptic orbit around the Earth.

We have studied the problem of finding symmetric periodic orbits in the elliptic restricted three-body problem with Earth-Moon mass ratio and Earth-Moon eccentricity. As a matter of fact, the programs which we have prepared are for any eccentricity from 0 to 1 and any mass-ratio from 0 to 1. One of the main difficulties of the elliptic problem is that we have no longer families of periodic orbits with continuously varying period. The satellite has to be synchronized here with the two primaries.

We present here a family of periodic orbits which all have the same period as the Earth and the Moon. They all correspond to the Earth-Moon mass ratio, and they have the eccentricity as the variable parameter. We have computed them for the eccentricities from 0 to 0.5, starting with an orbit with eccentricity zero found previously in the circular problem, and then making differential corrections to increase the eccentricity. All our programs which have been prepared are three-dimensional, although the periodic orbits we present here are two-dimensional.

The numerical integrations have been done with a recurrent power series method. We describe here first the integration method; and at the end of the paper, we comment on the periodic orbits.

We refer the problem to the well-known rotating-pulsating coordinate system, and we use canonical units. In order to avoid the presence of the independent variable (true anomaly) in the right-side members of the differential equations, we add a differential equation for the distance r between the two primaries. The problem is then completely represented by the following system of equations:

$$\ddot{x} - 2\dot{y} = \frac{r}{p} \left[x - \frac{m_1(x + m_2)}{s_1^3} - \frac{m_2(x - m_1)}{s_2^3} \right],$$

$$\ddot{y} + 2\dot{x} = \frac{r}{p} \left[y - \frac{m_1 y}{s_1^3} - \frac{m_2 y}{s_2^3} \right],$$

$$\ddot{z} + z = \frac{r}{p} \left[z - \frac{m_1 z}{s_1^3} - \frac{m_2 z}{s_2^3} \right],$$

$$\dot{t} = \frac{1}{p^{1/2}} r^2,$$

$$\ddot{r} = 2 \frac{\dot{r}^2}{r} + r \left(1 - \frac{r}{p} \right).$$

The parameter $p = 1 - e^2$ is the semi-latus rectum, and m_1 and m_2 are the two masses of the primaries. The distances from the satellite to the primaries are given by:

$$s_1^2 = (x + m_2)^2 + y^2 + z^2,$$

$$s_2^2 = (x - m_1)^2 + y^2 + z^2.$$

We are now transforming the above system to make it suitable for a solution by power series. We shall use 18 dependent variables. For the 13 first variables, we have 13 "first-order-second-degree" differential equations; and for the 5 last variables, we use direct relations to the 13 first ones. The 18 variables and their defining equations are listed in Table 1.

We next write the recurrence relations for a power series solution of the preceding equations (in the true anomaly v). We suppose that every dependent variable P_i is of the form

$$P_i = P_i(1) + P_i(2)v + P_i(3)v^2 + \dots$$

By making the substitution of P_i in the transformed equations of motion, we find a set of recurrence relations for

Table 1. Orbit variables and defining equations

$P_1 = x$	$\frac{dx}{dv} = \dot{x}$	$P_9 = t$	$\frac{dt}{dv} = \frac{1}{p^{1/2}} r^2$
$P_2 = y$	$\frac{dy}{dv} = \dot{y}$	$P_{10} = s_1$	$s_1 \frac{ds_1}{dv} = x\dot{x} + y\dot{y} + z\dot{z} + m_2\dot{x}$
$P_3 = z$	$\frac{dz}{dv} = \dot{z}$	$P_{11} = s_2$	$s_2 \frac{ds_2}{dv} = x\dot{y} + y\dot{z} + z\dot{x} - m_1\dot{x}$
$P_4 = \dot{x}$	$\frac{d\dot{x}}{dv} = +2\dot{y} + \frac{1}{P} r(xA + B)$	$P_{12} = \sigma_1 = s_1^{-3}$	$s_1 \frac{d\sigma_1}{dv} = -3\sigma_1 \frac{ds_1}{dv}$
$P_5 = \dot{y}$	$\frac{d\dot{y}}{dv} = -2\dot{x} + \frac{1}{P} r(yA)$	$P_{13} = \sigma_2 = s_2^{-3}$	$s_2 \frac{d\sigma_2}{dv} = -3\sigma_2 \frac{ds_2}{dv}$
$P_6 = \dot{z}$	$\frac{d\dot{z}}{dv} = -z + \frac{1}{P} r(zA)$	$P_{14} = A = 1 - m_1\sigma_1 - m_2\sigma_2$ $P_{15} = xA + B = xA + m_1m_2(\sigma_2 - \sigma_1)$ $P_{16} = yA = yA$ $P_{17} = zA = zA$ $P_{18} = r^2 = rr$	
$P_7 = r$	$\frac{dr}{dv} = \dot{r}$		
$P_8 = \dot{r}$	$\dot{r} \frac{d\dot{r}}{dv} = 2\dot{r}^2 + r^2 - \frac{1}{p} rr^2$		

the coefficients of the polynomials $P_i(n)$. We obtain the following 18 relations.

$$nP_1(n+1) = P_4(n)$$

$$nP_2(n+1) = P_5(n)$$

$$nP_3(n+1) = P_6(n)$$

$$nP_4(n+1) = +2P_5(n) + \frac{1}{P} \Sigma_1 P_7(p) P_{15}(q)$$

$$nP_5(n+1) = -2P_4(n) + \frac{1}{P} \Sigma_1 P_7(p) P_{16}(q)$$

$$nP_6(n+1) = -P_3(n) + \frac{1}{P} \Sigma_1 P_7(p) P_{17}(q)$$

$$nP_7(n+1) = P_8(n)$$

$$nP_7(1) P_8(n+1) = -\Sigma_2 q P_7(p) P_8(q+1) + P_{18}(n) \\ + \Sigma_1 (2 P_8(p) P_8(q) - \frac{1}{P} P_7(p) P_{18}(q))$$

$$nP_9(n+1) = \frac{1}{Q} P_{18}(n)$$

$$nP_{10}(1) P_{10}(n+1) = -\Sigma_2 q P_{10}(p) P_{10}(q+1) + m_2 P_4(n) \\ + \Sigma_1 (P_1(p) P_4(q) + P_2(p) P_5(q) \\ + P_3(p) P_6(q))$$

$$nP_{11}(1) P_{11}(n+1) = -\Sigma_2 q P_{11}(p) P_{11}(q+1) - m_1 P_4(n) \\ + \Sigma_1 (P_1(p) P_4(q) + P_2(p) P_5(q) \\ + P_3(p) P_6(q))$$

$$nP_{10}(1) P_{12}(n+1) = -\Sigma_2 q P_{10}(p) P_{12}(q+1) \\ - 3\Sigma_1 q P_{12}(p) P_{10}(q+1)$$

$$nP_{11}(1) P_{13}(n+1) = -\Sigma_2 q P_{11}(p) P_{13}(q+1) \\ - 3\Sigma_1 q P_{13}(p) P_{11}(q+1)$$

$$P_{14}(n+1) = -m_1 P_{12}(n+1) - m_2 P_{13}(n+1)$$

$$P_{15}(n+1) = \Sigma_3 P_1(p) P_{14}(q) + m_2 m_1 (P_{13}(n+1) \\ - P_{12}(n+1))$$

$$P_{16}(n+1) = \Sigma_3 P_2(p) P_{14}(q)$$

$$P_{17}(n+1) = \Sigma_3 P_3(p) P_{14}(q)$$

$$P_{18}(n+1) = \Sigma_3 P_7(p) P_7(q)$$

In the above equations, we have used a capital P for the semi-latus rectum, and a capital Q for its square root. We have also used three different kinds of symbols Σ to designate sums with different limits for the indices p and q .

They have the following meaning:

$$\begin{aligned}\Sigma_1 &= \text{sum for } \begin{cases} p = 1, 2, \dots, n \\ q = n, n-1, \dots, 1 \\ p+q = 1+n \end{cases} \\ \Sigma_2 &= \text{sum for } \begin{cases} p = 2, 3, \dots, n \\ q = n-1, n-2, \dots, 1 \\ p+q = n+1 \end{cases} \\ \Sigma_3 &= \text{sum for } \begin{cases} p = 1, 2, \dots, n+1 \\ q = n+1, n, \dots, 1 \\ p+q = n+2 \end{cases}\end{aligned}$$

The above equations are the basis for a computer program which automatically generates lists of periodic orbits with variable eccentricity or mass-ratio. We show in Fig. 1 one particular periodic orbit with mass ratio 0.012155 and with eccentricity 0.50. It belongs to a series of 130 periodic orbits with eccentricities from 0.0 to 0.50.

These orbits are periodic in the inertial coordinate system as well as in the rotating and rotating-pulsating coordinate system, and we represent in the illustration one single orbit in different coordinate systems. (In the pulsating coordinate system, a variable scale factor is used to make the distance between m_1 and m_2 constant and equal to one.) The integration of the orbits has been checked by using the redundancy character of the 18 dependent variables. In Table 2, we give the initial conditions (in pulsating coordinates) of a few of the orbits. These initial conditions correspond to a minimum distance of m_1 and m_2 .

Table 2. Initial conditions of typical orbits

e	x_0	y_0
0.0	0.152132596	3.16061812
0.1	0.127833892	3.32965845
0.2	0.102488812	3.58919746
0.3	0.076226470	3.99558702
0.4	0.049434098	4.68227879
0.49	0.025676646	5.85491003

Georgia Seline has made the computer program (in Fortran 4, for IBM-7094) and all the computer runs.

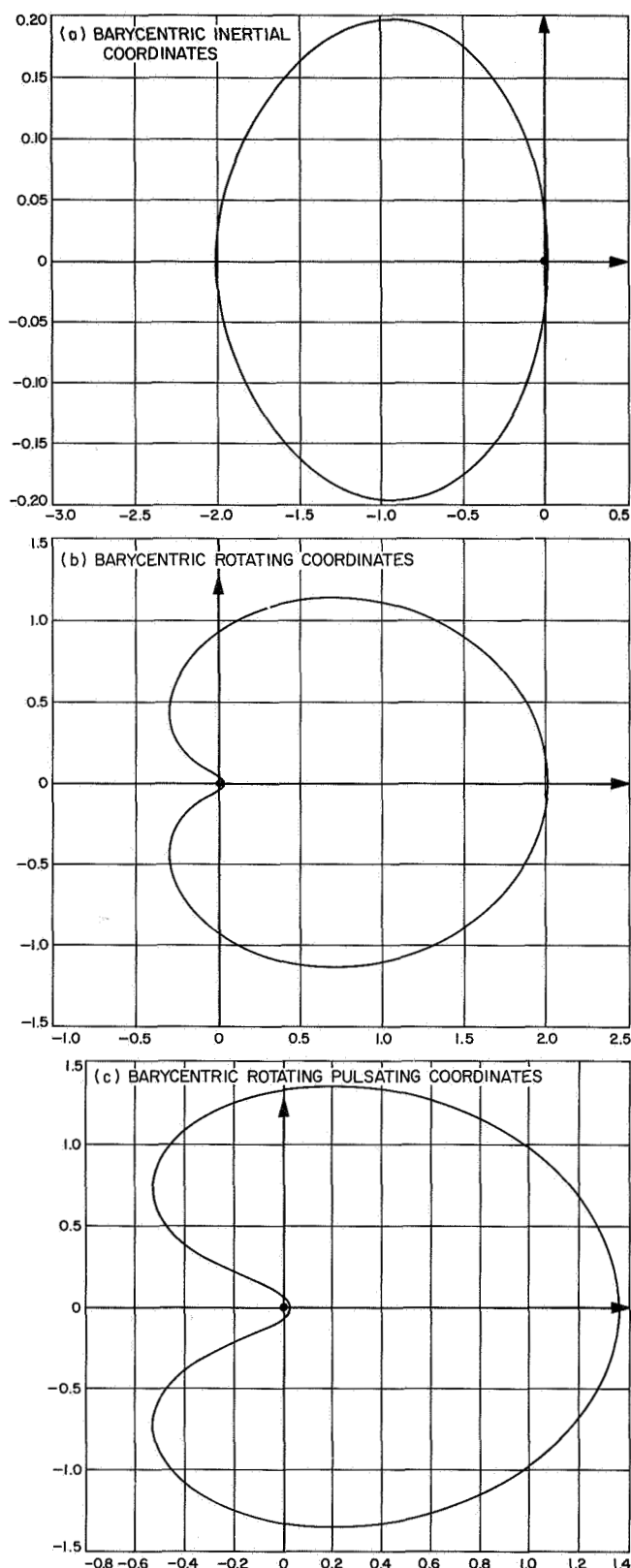


Fig. 1. Elliptic restricted three-body problem

References

1. Bogoliubov, N. N., and Mitropolsky, Y. A., *Asymptotic Methods in the Theory of Nonlinear Oscillations*, Hindustan Publishing Corp., India, 1961.
2. Stratonovich, R. L., "Conditional Markov Processes," *Theory of Probability and Its Applications*, Vol. 5 (No. 2): pp. 156-178, 1960.
3. Kushner, H. J., "On the Differential Equation Satisfied by Conditional Probability Densities of Markov Processes," *SIAM Journal*, Series A: Control, Vol. 2 (1): pp. 106-119, 1964.
4. Kulman, N. K., "A Note on Differential Equations of Conditional Probability Density Functions," *Journal of Mathematical Analysis Applications*, pp. 301-408, 1966.
5. Doob, *Stochastic Processes*, Wiley and Sons, New York, 1953.
6. Chandrasekhar, "Stochastic Problems in Physics and Astronomy," *Selected Paper in Noise and Stochastic*, Ed., Wax, Dover, N.Y., pp. 3-92, 1953.
7. Kalman, R. E., and Bucy, R. S., "New Result in Linear Filtering and Prediction Theory," *J. Basic Engr. Trans. ASME Series D*, Vol. 83, pp. 95-108, March 1961.
8. Aoki, M., *Optimization of Stochastic Systems*, Academic Press, New York, 1967.
9. Jazwinski, A. H., "Nonlinear Filtering With Discrete Observations," AIAA paper No. 66-38, AIAA 3rd Aerospace Science Meeting, New York, New York, Jan. 24-26, 1966.
10. Sorenson, H., "A Nonlinear Perturbation Theory for Estimation and Control of Time Discrete Stochastic Systems." Paper delivered at the *Seminar on Guidance Theory and Control Analysis*, NASA-ERC, May 31-June 1, 1966, MIT, Cambridge, Mass.
11. Cramer, H., *Mathematical Methods of Statistics*, Princeton Univ. Press, Princeton, New Jersey, 1946.
12. Denham, W. F., and Pines, S., "Sequential Estimation When Measurement Function Nonlinearity is Comparable to Measurement Error," AIAA/ION *Guidance and Control Conference*, Minneapolis, Minn., Aug. 1965.

III. Spacecraft Power

GUIDANCE AND CONTROL DIVISION

N67 18312

A. Sterilizable Battery, R. Lutwack

1. Development of Separators for Sterilizable Batteries

The development program for a separator for the Ag-Zn battery comprises research and development contracts with Monsanto Research Corporation, Westinghouse Electric Corporation, and the Southwest Research Institute and a continued evaluation of the modified polyethylene separator material produced by RAI Research Corporation under a JPL contract.

a. JPL Contract 951524 with Monsanto Research Corporation. In evaluation of ligand polymers, it has been shown that 2-vinylpyridine-methacrylic acid and styrene-maleic acid copolymers and **poly-(vinylbenzylcatechol)** are stable under sterilization conditions. The tensile strengths are high for films made from unhydrolyzed 2-vinylpyridine and either methylacrylate or methylmethacrylate. Both types have acceptable electrical resistance after saponification. New ligand polymers, which have been prepared and will be tested, include poly-(4,6-diamino-2-vinyl-s-triazine), a 2-vinylpyridine-diethyl-fumarate copolymer, and a 2-vinylpyridine-maleic anhydride-butylvinyl ether terpolymer.

b. JPL Contract 951525 with Westinghouse Electric Corporation. Composite membranes were prepared and tested in a 40% KOH solution at 135° for 60 hr. A combination of polypropylene and $Zr(OH)_4$ gave a membrane which could be sterilized and had adequate OH- diffusion characteristics. The first series of cast filled-polymer films were brittle and did not meet the OH- diffusion requirement. In a second effort, several amino-substituted 8-hydroxyquinoline derivatives have been incorporated into an epoxy resin matrix. Adequate curing was achieved by using m-phenylenediamine as a hardener. These resins are resistant to sterilization. No films have been made yet.

c. JPL Contract 951718 with Southwest Research Institute. This is a new contract with the purpose of investigating the process of grafting of polyethylene film with acrylic acid using a Co^{60} irradiation source. The main parameters are irradiation dose rate, total irradiation dose, temperature, effect of oxygen, multiple irradiation, and washing methods.

d. Separator material from JPL Contract 951015 with RAI Research Corporation. The RAI-116 and RAI-110 separator materials are being used in the design and

performance evaluation of the sterilizable cells. Sterilized cells made with five layers of -116 perform as well as controls after 40 cycles of 100% depth discharge.

2. Research and Development of the Heat Sterilizable Battery

This contract with the Electric Storage Battery Company is for a research and development program for sealed Ag-Zn and Ag-Cd cells, which provide satisfactory electrical performance after heat sterilization and high impact shocks.

a. Electrochemistry task. Evaluations are continuing of the two RAI separators under conditions of the two sterilization temperatures of 125 and 135°C. These are cells made of packs which were sterilized in nickel cases and then sealed in polystyrene cases. In the investigation of absorbers it has been shown that EM 476 is slightly

improved by sterilization at 135°C and is better than SM 135.

b. Cell case task. The polyphenylene oxides, grades 531-801 and 541-801, are being used in parallel developments as cell case materials. Techniques for molding have been advanced to the stage that moldings of grade 531-801 are uniformly acceptable. Grade 541-801 can be sealed using a hot gas welding process; grade 531-801 **must** be sealed with epoxy resins.

c. Cell fabrication and test task. Cycle data are being obtained on various designs of the Ag-Zn cell. Preliminary data for non-sterilized cells discharged at 80°F have been obtained in a study to determine electrical characteristics in the temperature range of 32 to 150°F; the energy densities for three cell designs vary from 30 to 57 W-hr/lb.

IV. Guidance and Control Analysis and Integration

GUIDANCE AND CONTROL DIVISION

N67 18313

A. Advanced Test Techniques, T. P. Cerney and R. Lawrence

The objective of this study is to devise more comprehensive OSE and spacecraft testing techniques which will result in a more reliably operating spacecraft. Circuit testing techniques which will predict incipient failure of a spacecraft circuit or function are being evaluated. The following techniques are currently being investigated: (1) voltage margin tests, (2) infrared scanning of circuits, and (3) RF noise spectra measurements.

These various testing techniques are being evaluated using a digital system which cycles through a short operational routine. Individual printed circuit cards as well as the complete system are being used in the evaluation study. Also, analog circuit cards and integrated circuit cards are currently being evaluated using these test techniques.

1. Laboratory Test Summary

The circuit cards for the digital test system were cycled through the simulated aging process (temperature cycling) three times during the total program thus far.

To date, the assembled digital test circuit has been subjected to four system voltage margin tests, four infrared scanning tests (card by card while in operation) and three noise-signature system tests. One set of individual card voltage margin tests was also run. The net result of all of these tests shows that there is very little if any detectable drift within the digital test circuit. This result suggests that future work on this project will require drift simulation as a means of evaluating advanced test techniques.

2. Interim Evaluation

A cumulative evaluation of the three test techniques with respect to the measurements on the currently used digital test circuit is presented in this summary. An interim comparative evaluation of the three techniques is shown in chart form in Table 1.

a. Voltage margin techniques. The system voltage margin profile has remained essentially the same after six trials taken over a period of 2 yr (SPS 37-32, Vol. IV, pp. 52-54), in which approximately 1600 hr of operating time were accumulated (Fig. 1). There was no detectable change or trend within the system during that time. This

Table 1. Interim evaluation summary

Requirements for "ideal" failure prediction technique	Power supply voltage margin	Infrared scanning	Noise signature
Measures directly the drift of all component parameters	Indirect; measurement of some component parameters	Indirect as now used; Ref. 4 suggested feasibility of more direct measurement of transistor "recombination currents"	Indirect
Masking and hierarchy effects are a minimum	Masking and hierarchy effects are a problem; the counter cards on the particular system under test dominate the failure indication, and the order of placement of like cards is significant to the results (refer to discussion in Sect. 2a in text)	No problem if both "high-level" and "low-level" scans are made with direct readout; see Notes a and b below	No conclusion
Adaptable to system failure prediction	Readily adaptable to a system type failure prediction	System tests not feasible with present flight hardware configuration; Ref. 6 suggested the use of photo-conductive electroluminescent panels to be used inside of systems	Can be used on a system
Uses non-laboratory type of apparatus and readout	Field type apparatus can be used	Field type equipment can be used	Problem of screening out ambient noise may require cumbersome equipment
Accuracy	Requires further study to determine accuracy. Past tests show a high repeatability of results	With direct readout, accuracy 10% of the temperature range or better (see Note b)	No conclusion
Resolution (measures very small drift in parameter)	Requires further study	Resolution 0.1 °C	No conclusion
Minimum ambient or environmental noise	Environmental noise is low	System noise equivalent to 0.1 °C	Ambient and detector noise problems very serious
Overall feasibility and usefulness in failure prediction	Overall feasibility good	Recommended as feasible especially at circuit and component level	No conclusion as to feasibility
<p>^a On past runs, the hot resistors showed up as bright spots and the low-power transistors appeared as dark spots.</p> <p>^b Present Poloroid print readout is difficult to quantitatively interpret accurately by a human operator/reader; a direct recording of radiometer current will present an unambiguous and accurate data interpretation.</p>			

result parallels the results obtained by the JPL Flight Computers and Sequencers Section on digital flight equipment (the *Ranger* Block III CC&S Life Test Program, in which no change in voltage margins occurred after 10743 hr of operation at room temperature). The voltage margins of the individual circuit cards used in the study described here were correlated with the overall system voltage margin. This correlation was done by superimposing the plots of the individual circuit card voltage margins on the plot of the system voltage margin and noting similarities and points of intersection between the two types of plots. The order of placement of the counter cards of the same type and design but of dif-

ferent intrinsic voltage margins was detected by the system voltage margin tests. This indicates the possibility that drifts in the margins of a circuit card can be detected by measurement of the total system margin. Further testing in component failure and drift simulation should serve to verify this.

The problem of "masking" of incipient failures still remains unsolved. The term "masking" is used here to mean the situation where the parameter drift in one circuit causes the system response to indicate a failure or margin threshold such that the parameter drifts of other circuits within the system remain undetected.

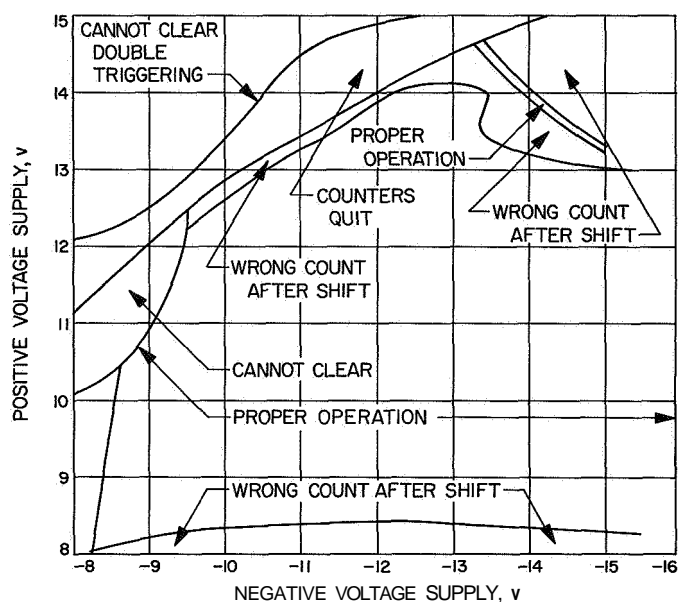


Fig. 1. Digital test system voltage margins

Hierarchy effects are masking effects which are due to the functional order of placement of the circuit cards. A question still to be answered is whether voltage margin tests can detect drifts in piece-part parameters that are known to be good pre-indicators of failure. Some examples of these parameters are leakage current for transistors, capacitors and diodes; forward voltage drop for conventional diodes; and reverse current for Zener diodes. (See also further discussion found in Refs. 1, 2.)

b. Infrared scanning techniques. Laboratory tests and calibrations were made to determine the operating scale factors and threshold sensitivities of the recently repaired Barnes infrared radiometer-camera (Type T-4). This camera (Fig. 2) was placed approximately 36 in. away from the target. Known values of electrical power were applied to a 0.25-watt composition test resistor (target) which was mounted on a target circuit board. The results should apply to typical discrete components, but are very approximate because infrared radiation is dependent upon target size and emissivity. The tests indicated that the radiometer cannot readily detect power changes in the test resistor of less than about 1 mW. Furthermore, the total input power must be above a minimum level in the range 4 to 10 mW to distinguish the test resistor from system noise and background radiation. These restrictions would appear to limit the usefulness of the Barnes T-4 in studying changes in low-power transistor operating characteristics, since these typically operate with dissipations of 10 mW or less.

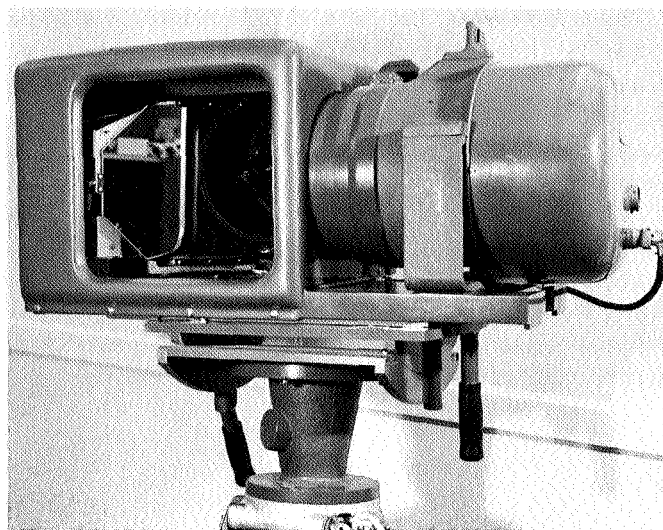


Fig. 2. Barnes infrared radiometer-scanner

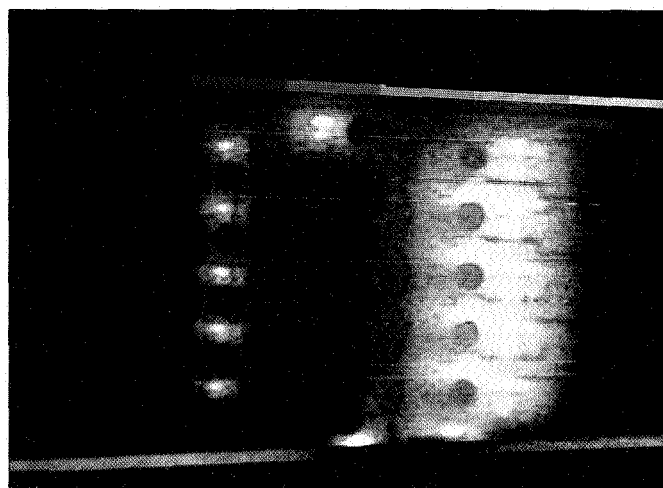


Fig. 3. Infrared scan of circuit card

The temperature of high-level (high-power dissipation) components, as well as low-level components, such as low-power transistors, may be monitored with an infrared radiometer-scanner to a resolution as good as 0.1°C. Achievement of this resolution with both high- and low-level components on the same circuit card requires scanning each card at least twice; once for the high level and once for low level. Control settings of the Barnes T-4 scanner must be changed between scans. Furthermore, to obtain a resolution of 0.1°C, the scanning readout must be recorded directly from the scanner current rather than using the photographic presentation and its accompanying gray scale calibration. The photographic presentation used previously does not give adequate resolution when interpreted by a human operation (Fig. 3).

Preliminary work has been done to develop a direct strip-chart recording of the infrared scanner current. Some results of this work are shown in Fig. 4. A Brush Model 280 recorder was used for this recording. A description of the radiometer scanning raster procedure is necessary for interpretation of Fig. 4. The flat rectangular circuit card, 6 X 5 in., is mounted normal to the optical axis of the radiometer. The card is scanned in a rectangular raster pattern of 180 horizontal lines. Each horizontal sweep requires about 2 sec; the complete pattern requires 6 min. The realization of an approximate "three dimensional" presentation was achieved by the recording technique described here.

In Fig. 4(a, b) are shown two successive horizontal scan sweeps. Distance along the axis of the card is represented as distance in the direction of paper motion, where each inch along the recorder paper corresponds to 1.5 in. along the longitudinal axis of the circuit card. In Fig. 4(c, d), the recorder paper speed was slowed down by a factor of 250. Fig. 4(c) shows the radiometer response for one full scan (180 horizontal sweeps) of the target circuit card. Each of the 180 horizontal sweeps is compressed into a horizontal space of about 0.02 in., and is represented by a vertical line of varying intensity. Fig. 4(c) was obtained for a power supply setting of 10 V; Fig. 4(d) was made at 13 V. A comparison of the two

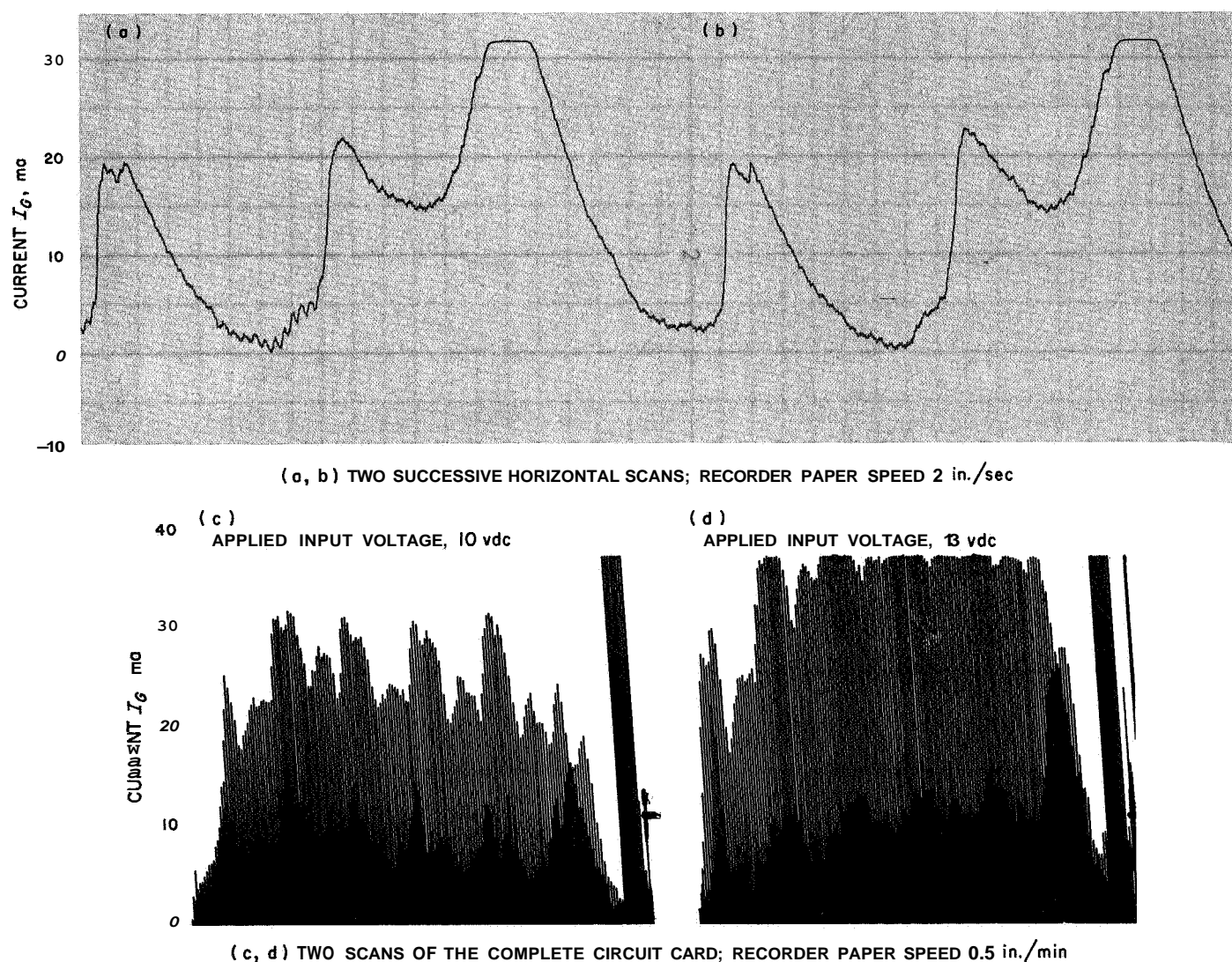


Fig. 4. Thermal profile plots of a circuit card

plots shows that changes in radiated infrared power are easily discernible. The slight slanting of the traces in Fig. 4(c, d) was due to a mechanical misadjustment of the recorder.

A much more striking "three-dimensional" profile plot may be obtained using techniques similar to those discussed in Ref. 3.

With the present limitations of noise, thresholds, and resolution, infrared measurements are considered feasible in detecting degradation of high-level components. However, further studies are required to fully establish the quantitative relationship between infrared radiation changes and circuit or component electrical drifts, especially for low-level components. These studies could well be done in direct correlation with the proposed voltage margin tests using failure simulation. Some of the newer infrared approaches that may be evaluated in the future

are the measurement of recombination currents (Ref. 4) and the measurement of infrared turn-on transients (Ref. 5).

c. Noise signature techniques. For each circuit card, as well as for the system, it was observed that various random non-repeatable noise signature patterns were superimposed upon a characteristic invariant pattern of ambient and detector noise (SPS 37-32, Vol. IV, pp. 54-56). A preliminary conclusion is that a tedious and difficult statistical analysis would be required to obtain significant and meaningful results from the noise tests.

3. Literature Searches

In addition to the laboratory work described above, the activities of this project have included literature searches in the area of infrared testing and in the area of pre-indicators of component failures.

References

1. Klopheke, J. W., et al., *Predictions of Failure in Electronic Components*, RSIC-445, Redstone Scientific Information Center, Redstone Arsenal, Alabama, July 1965.
2. Conrad, G. T., Jr., and Shook, D. C., "A Transistor Screening Procedure Using Leakage Current Measurements," *Journal of Research of National Bureau of Standards—C. Engineering and Instrumentation*, vol. 69C, no. 4, Oct.-Dec., 1965.
3. Webb, G. N., and Rogers, R. E., "The Contourograph," *IEEE Spectrum*, vol. 3, no. 6, pp. 77-87, June 1966.
4. Vanzetti, R., "Infrared—a New Dimension for Electronics Reliability," *Electronics Progress*, vol. VII, no. 6, Raytheon Co., Lexington, Mass., May-June, 1963.
5. Stanfill, D. F., and Yoder, J. R., of Barnes Engineering Co., Stamford, Conn., "Infrared Inspection of Semi-conductors," presented to the *Symposium on Manufacturing In-Process Control and Measuring Techniques for Semi-conductors*, Phoenix, Arizona, March 9-11, 1966.
6. Marks, B. G., et al., "Infrared Testing of Micro-Circuits," *Electro-Technology*, p. 112ff, Philco Corporation, Oct. 1965.

V. Spacecraft Control

GUIDANCE AND CONTROL DIVISION

N67 18314

A. Image Dissector Tube Development, D. S. Herman

Deep-Space Lunar and Planetary Spacecraft utilizing full three-axis attitude control become stable platforms from which photographic and scientific experiments could be performed. The celestial references required for three-axis attitude control on a typical Mars mission are the Sun and the star Canopus. A developmental effort at CBS Laboratories was started in 1962 for an image dissector tube (ID) for a star sensor capable of tracking the star Canopus and meeting the requirements of long life, accuracy, reliability, and high sensitivity.

An accomplishment of this effort was the all electrostatic image dissector vacuum tube. The tube as originally developed was used in the Canopus sensor for the *Mariner Mars 1964* mission. The sensor had no moving parts, consumed little power, could be electronically gimballed to keep Canopus in the field of view over the full variation of the stars position during the mission, and met all other requirements of the 1964 mission. Since the tube was all-electrostatic, it meant that no stray magnetic fields were set up which could affect spacecraft instruments. At last report, the Canopus sensor on *Mariner IV* was maintaining attitude control of the spacecraft after 2 yr of continuous operation in space. Because of mission requirements, the same type of ID tube used on the

1964 *Mariner* will be used in the Canopus sensor for the *Mariner Venus 67* mission.

Fig. 1 is a photograph and Fig. 2 a schematic representation of the latest ID tube configuration. Basically, the tube consists of a photocathode, electrostatic imaging and deflection systems, and a 12-stage electron multiplier. The electrons emitted from the photocathode move through the imaging (or focusing) system under the influence of the electric fields set up by the electrodes. They enter the electrostatic deflection system through a hole in the anode. The electrons emitted from different points of the photocathode can then be deflected through a slit aperture (circular or rectangular, depending upon the application) into the electron multiplier.

Developmental work on the ID tube has been and is a continuing effort because of the changing requirements for a star sensor and for other potential applications. In addition, there are problem areas associated with the tube which create certain constraints on the external optical system as well as prevent the tube from operating at its maximum efficiency. One of the first major activities after the development of an operational tube was ruggedizing it for spacecraft application. This activity was very successful in that a tube is still operating in space and that tubes are contemplated for use in future missions.

A 1-year operational life test was performed on two tubes produced on the ruggedized program. The tubes were operated under simulated loading conditions with

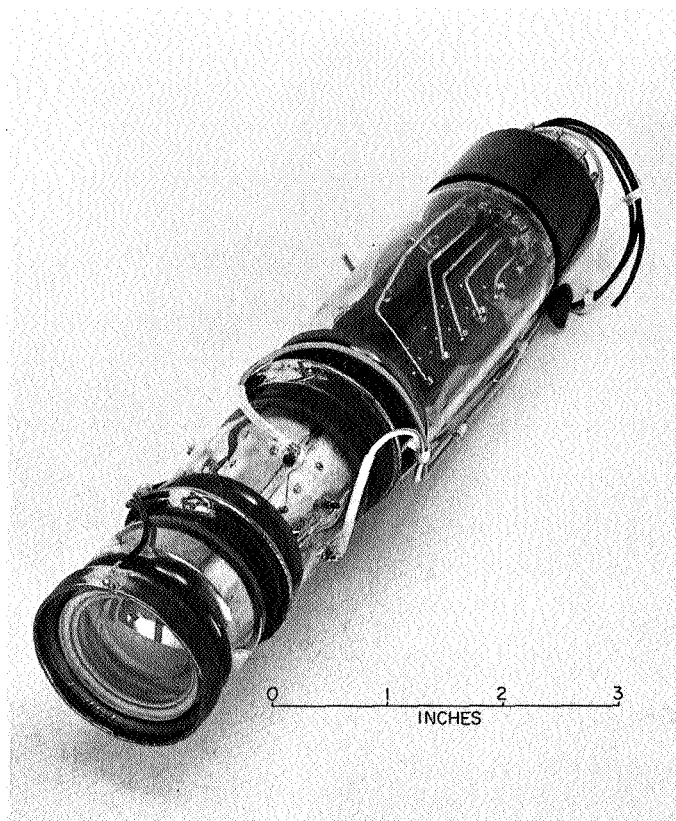


Fig. 1. Image dissector tube for star sensor

specified initial test conditions. The performance was periodically monitored during the test. Fig. 3 shows the changes in the anode signal and dark currents for the two tubes. One tube (M-1089) remained close to the initially set values which indicated random aging processes were occurring, but not enough to adversely affect the tube. However, the other tube (M-1083) showed some type of aging process which was adversely affecting the tube by increasing the anode output currents. Thus, long-term stability is an ever present problem; and as the tubes go through configurational and other changes, it will have to be studied, understood, and overcome.

Another problem area was short-term drift stability of the tube. This work involved the development of an extremely stable drift-free deflection system. Fig. 4 shows the anode-deflection cone assemblies of the previous *Mariner* type tubes and the new integrated assembly type which appears to make the tubes very stable. The deflection elements in the old assemblies were deposited onto an insulating substrate which was located in the same plane as the elements. Photoelectrons landing on the insulation between the deflection elements caused a spurious charging effect which resulted in a deflection instability. In practice, when the tube is used in a star tracker, this instability would be evident by an apparent change in the position of the star. In the new assembly, the deflection elements are formed by a photoetching technique from a hollow metal cone and are supported in free space from the anode assembly by pins, one of which supplies the correct deflection potential. This

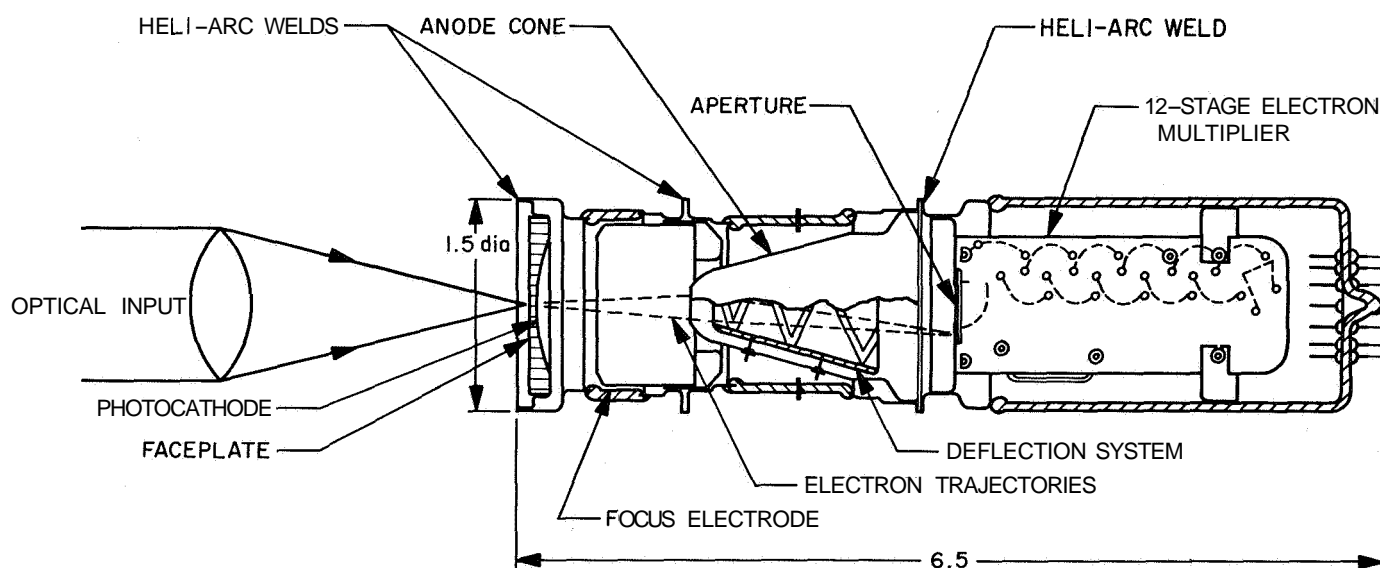


Fig. 2. Electrostatic image dissector tube

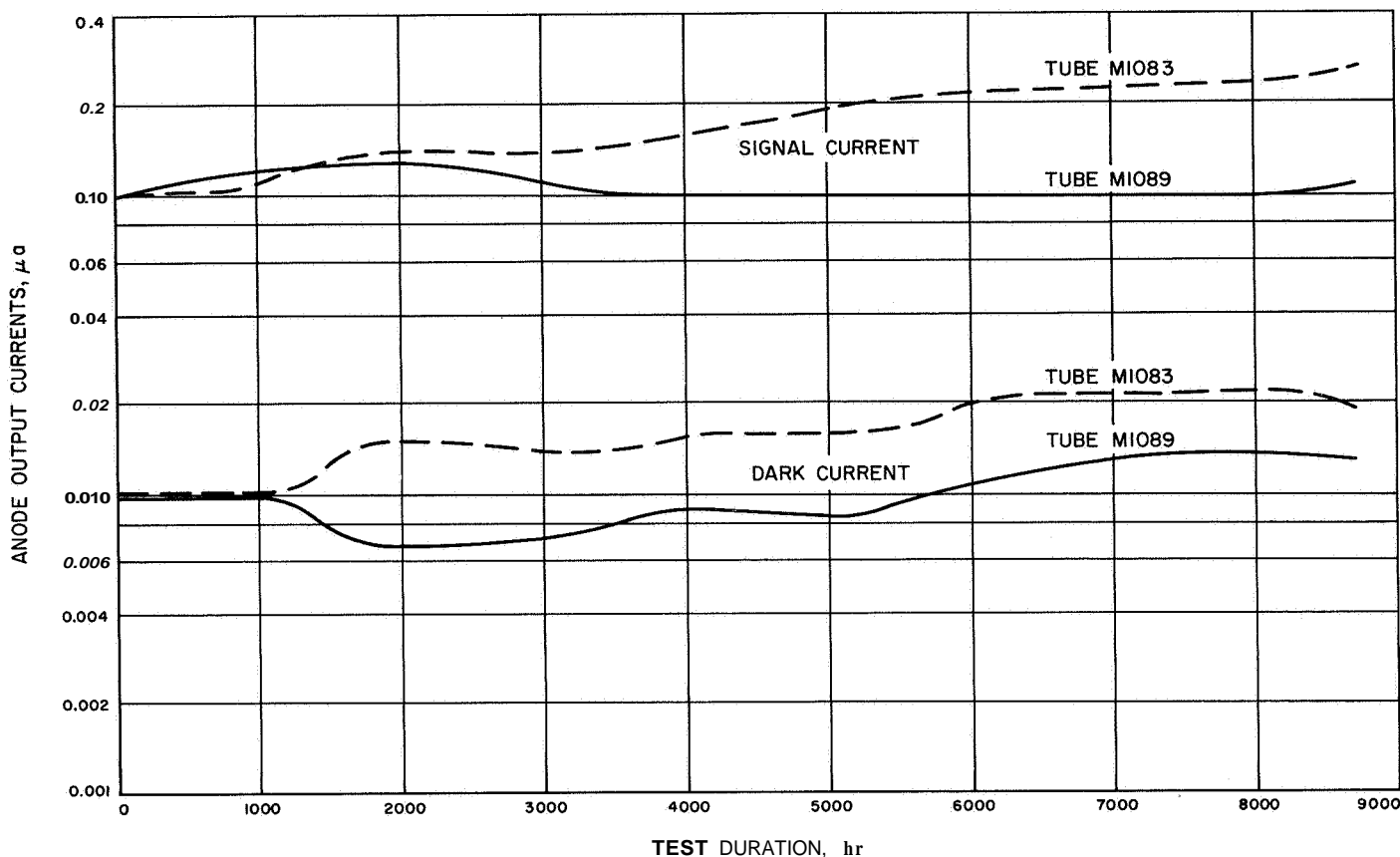


Fig. 3. life-test tube output currents versus time

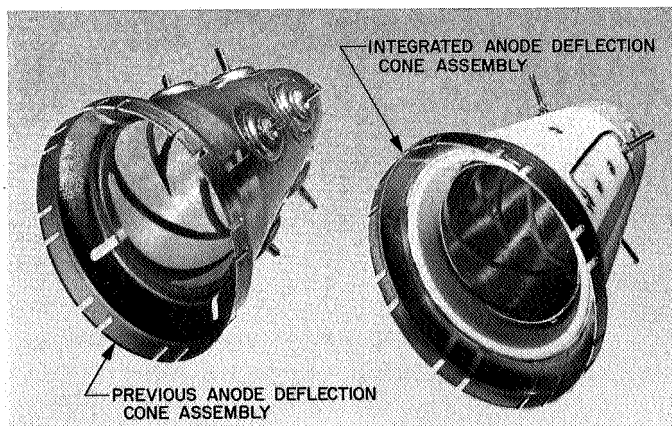


Fig. 4. Anode deflection cones

assembly prevents spurious charging from occurring and makes the tube drift-free.

A large and continuing effort has been expended on the solution of what has been termed the resolution problem. A small optical spot (usually 0.001 in. diameter)

on the photocathode will produce an emission of a group of electrons referred to as electron spot. Using the slit aperture the size of this electron spot can be determined. Fig. 5 shows what happens to the electron spot size as the light spot is moved off the tube axis. The large increase in spot size off-axis has been attributed to poor focusing of the electrostatic imaging system of the ID tube.

Some improvement has been generated with the use of a different type of focus electrode than used on the Mariner-type tubes. Fig. 6 is a photograph of the two types of focus electrodes. In Fig. 5, tubes M-1108 and M-1109 are the Mariner-type tubes having poor off-axis resolution whereas tubes M-1289 through M-1300, using the new type of focus electrode, show good improvement. However, as seen from Fig. 5, even greater improvement is desired. The resolution problem limits the useful area of the photocathode and makes the design of the light optical lenses in front of the ID tube difficult. Continued experimental evidence tends to confirm that the electrostatic imaging system is the cause of the resolution problem.

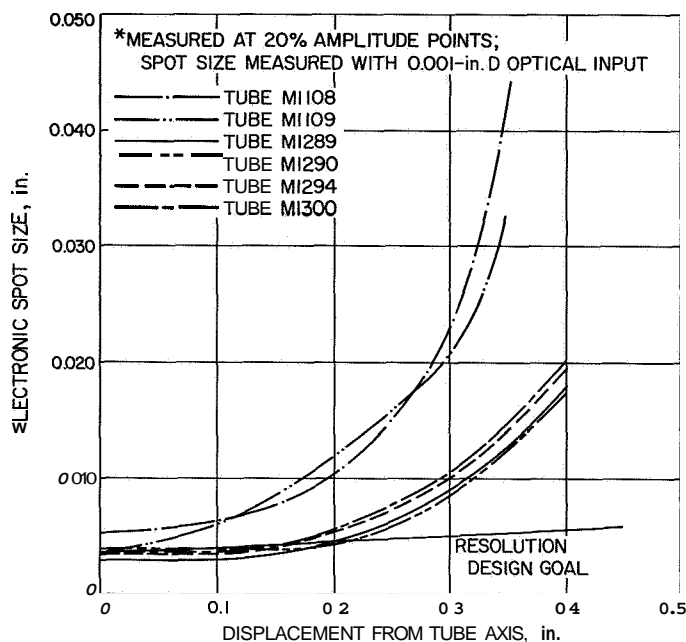


Fig. 5. Electronic spot size versus displacement at photocathode

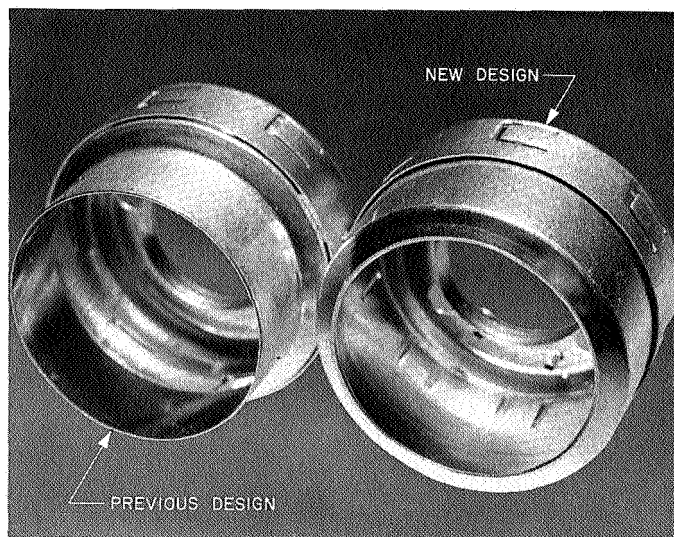


Fig. 6. Focus electrodes

Two different approaches are presently being implemented to solve the resolution problem. The first approach involves a systematic set of changes in the imaging section of the ID tube to determine how they affect resolution. This technique is a rather slow process and involves a good deal of trial and error. The second approach is a computer program for electron-trajectory determination as well as lens design of electrostatic lens systems. In addition to the reasons previously

enumerated, this computer program approach was chosen because of the relatively high cost of producing tubes. The computer program determines the trajectory of electrons from their emission point, through a system of focusing electrodes, and then to an imaging plane, or output electrode. The program is applicable to any rotationally symmetric electrostatic system of which the front end of the ID tube is an example. It is hoped that this trajectory program can form the basis of a design program. Thus, the best lenses for the ID tube can be designed which will overcome the problem of poor off-axis resolution.

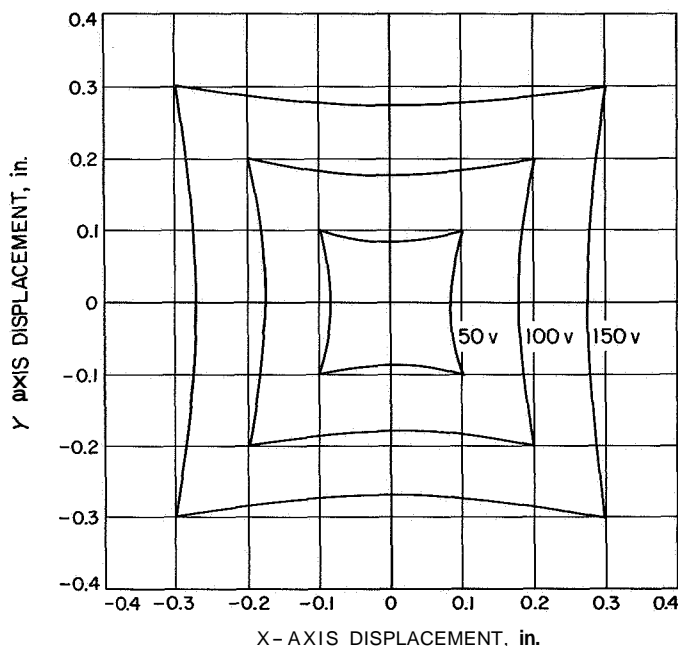


Fig. 7. Image section distortion

Another problem area associated with the electrostatic focusing system is termed "pincushion" distortion of the image. Fig. 7 shows typical equipotential deflection curves indicating the "pincushioning effect. These are plots of the deflection voltage equipotential for spot displacement from the positions shown on the photocathode to the center of the tube. The effect of this aberration, which also occurs in light optic systems, is equivalent to a variation of magnification with radius. The effect should occur in all electrostatic imaging systems unless there is special compensation. Compensation has not been included in the tube whose plot is shown in Fig. 7. Compensation has also not been included in the tube whose equipotential deflection curves is shown in Fig. 8. Here there is very little "pincushion" distortion. The only difference between the two ID tubes is that the one used for

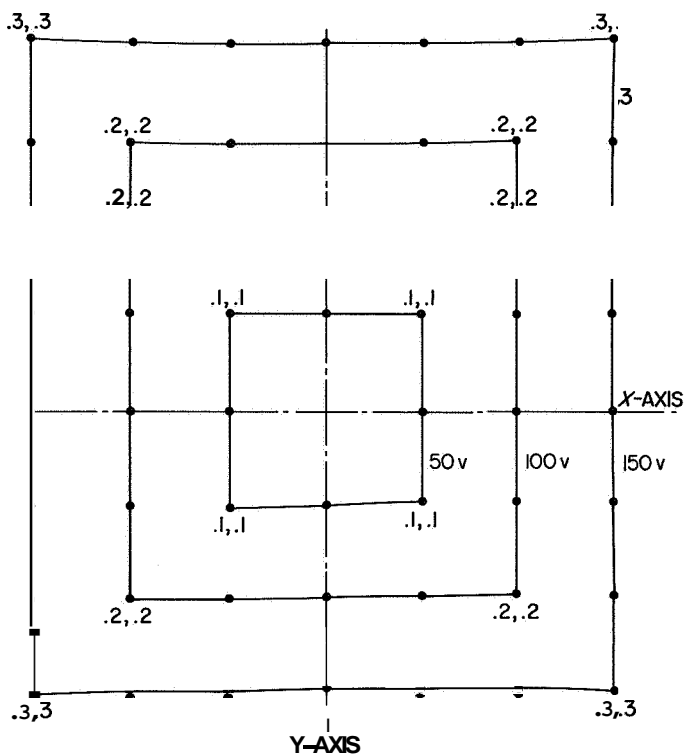


Fig. 8. Equipotential deflection curves for Tube M1383

Fig. 8 has a 0.004 in. circular slit aperture whereas the tube used for Fig. 7 has a 0.030 by 0.166 in. rectangular aperture. Why "pincushion" distortion is found for rectangular aperture tubes, but not for circular aperture tubes, is not understood and is in the process of being examined. Rectangular aperture tubes that contain deflection electrode compensation are being built to determine if the distortion can be removed. Also, since distortion is caused by the electrostatic imaging system, it is hoped that the computer design program can design electrostatic electron lenses with built-in compensation.

Developmental work was begun a few years ago into the area of making ID tubes capable of withstanding sterilization. Lunar and planetary capsule lander missions require that all components, including the ID tube, be sterilized to prevent contamination of the lunar or planetary surface. Since the ID tube is a sealed unit, the tube has no problems in withstanding chemical sterilization. However, the same cannot be said of thermal sterilization. To overcome this problem, a study was instituted to use a photocathode containing a bi-alkali (or S-24 photocathode containing sodium and potassium) antimonide film instead of a cesium (or S-11 photocathode) antimonide film.

The initial program involved development of a processing technique that produced a good photocathode

and then observing how the photocathode withstood thermal sterilization cycling. Measurements of the photocathode parameters of a number of ID tubes were carried out after each thermal cycle. Changes that occurred in the photocathode sensitivity of a number of ID tubes is shown in Fig. 9. This plot is typical of what occurs in other photocathode parameters. Significant decreases occur in most of the photocathode parameters with the major change usually occurring during the first thermal cycle with smaller changes thereafter. However, it should be noted that the sensitivity of one ID tube (M-1319) increased rather than decreased during the first thermal cycle and remained relatively constant thereafter. In addition, its other photocathode parameters had similar results, i.e., small or no changes during the first cycle and very little change thereafter. Tube M-1319 sustained an accident during processing, requiring a change in the processing technique which has apparently permitted the tube to withstand sterilization. Therefore, the effort to achieve a sterilizable photocathode for the ID tube is continuing with emphasis on using the processing technique of tube M-1319 as a starting point. In addition, attempts to understand the nature of the changes occurring in the bi-alkali photocathode film during thermal sterilization have presented other possible answers to the problem of sterilizable photocathodes. This also will be studied in the present effort. They involve the effect of the front faceplate (or substrate) onto which the photocathode film is formed, as well as the nature and amount

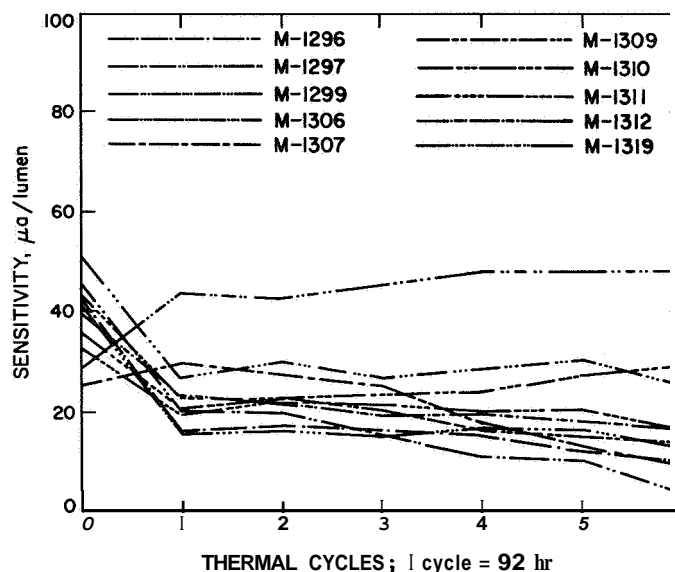


Fig. 9. Effect of 135°C thermal cycling on photocathode sensitivity

of impurities in the film, and its atmosphere, as the film is being formed.

The effort on the ID tubes is continuing to obtain further improvements which can then be incorporated into the tube so that it can be used more efficiently. Image dissector tubes incorporating improvements of the continuing developmental program will be used in two systems on the 1969 *Mariner* to Mars. One tube will be used in the Canopus star sensor while another tube, using a circular aperture rather than a rectangular aperture, will be used as a planet sensor in the Approach Guidance Subsystem. The Approach Guidance Subsystem is an engineering experiment that provides optical tracking of the planet during the 10 days prior to closest approach to the planet Mars. An optical Approach Guidance Subsystem has the advantage of permitting spacecraft orbit determination of greater accuracy than has previously been achieved. In addition, on future spacecraft missions it can be used to control spacecraft in the days prior to encounter.

B. Parametric Analysis for Steady-State Performance of Attitude-Control Thrusters,

J. D. Ferrera and P. M. McKown

As part of the Millipound Attitude Control Actuator Development (MACAD) program, a computerized parametric analysis of reaction jet performance has been initiated. Accurate prediction of this performance, specifically thrust and impulse bit, has become desirable in the design of future thrusters and the determination of thruster requirements. Prior to this study, little effort had been devoted to the prediction of thrust or total impulse for a miniature valve-nozzle system and even less to parametric analyses by the digital computer. Examination of net thrust has been made previously, using simplified nozzle losses and an experimentally determined valve pressure profile. An analytical investigation of the pulse mode operation has also been performed; the model for this examination, however, differs considerably from present flight hardware and losses were only approximated (Ref. 1).

Initially, the examination has been limited exclusively to steady-state operation with consideration of transient phases to be undertaken at a later date. To facilitate this analysis, the model illustrated in Fig. 10 has been used. It is assumed that the flow through the system is isentropic and that any deviation of the annular valve orifice flow from that of a sharp-edged circular orifice of equal

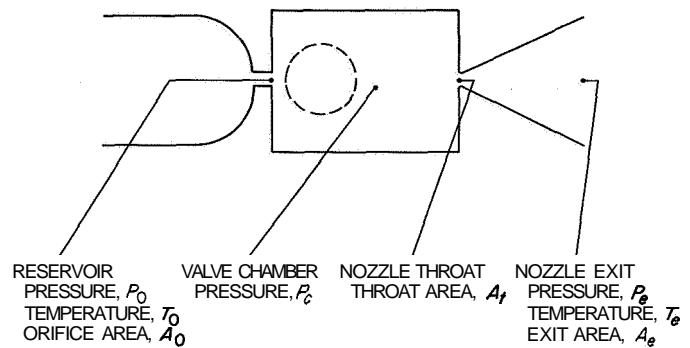


Fig. 10. Analytical model of reaction jet system

area is nullified by an experimentally determined orifice discharge coefficient. In the steady-state operation, the flowrate through the valve orifice is equal to the flowrate through the nozzle throat. By application of this flowrate equality, an algebraic equation in terms of the valve chamber pressure results which is readily solved using computer iteration. The maximum theoretical thrust is directly proportional to this chamber pressure.

Thrust losses have been subtracted from this maximum value to determine the net thrust as detailed by earlier work at JPL on miniature nozzles (Ref. 2). Losses due to the nozzle exit pressure, non-parallel exit flow, and momentum loss in the boundary layer have been considered, the latter representing the major portion of the total loss and the most involved computation. A computer curve-fitting program was used with particular success in determining the ratio of displacement thickness to momentum thickness in the boundary layer as a function of nozzle exit flow Mach number, a process normally requiring extensive computer operations (Ref. 3). Iteration routines were again used in the computer program to determine both nozzle exit flow Mach number and total thrust loss due to the boundary layer.

As a preliminary demonstration of this analysis, a computer program has been generated resulting in a computer plot of net steady-state thrust from the valve-nozzle system as a function of nozzle throat diameter for a range of valve inlet pressures, as shown in Fig. 11. Although the plot program may accommodate a wide range of jet dimensions, the accompanying curve was produced using values associated with *Mariner IV* flight hardware, i.e., nozzle area ratio = 260.5, valve ball travel = 0.010 in., valve orifice discharge coefficient = 0.55, gas inlet temperature = 25°C, assuming cold nitrogen as the propellant and that the system is operating in a vacuum. The analytical values of valve pressure drop and flowrate correlated well with corresponding

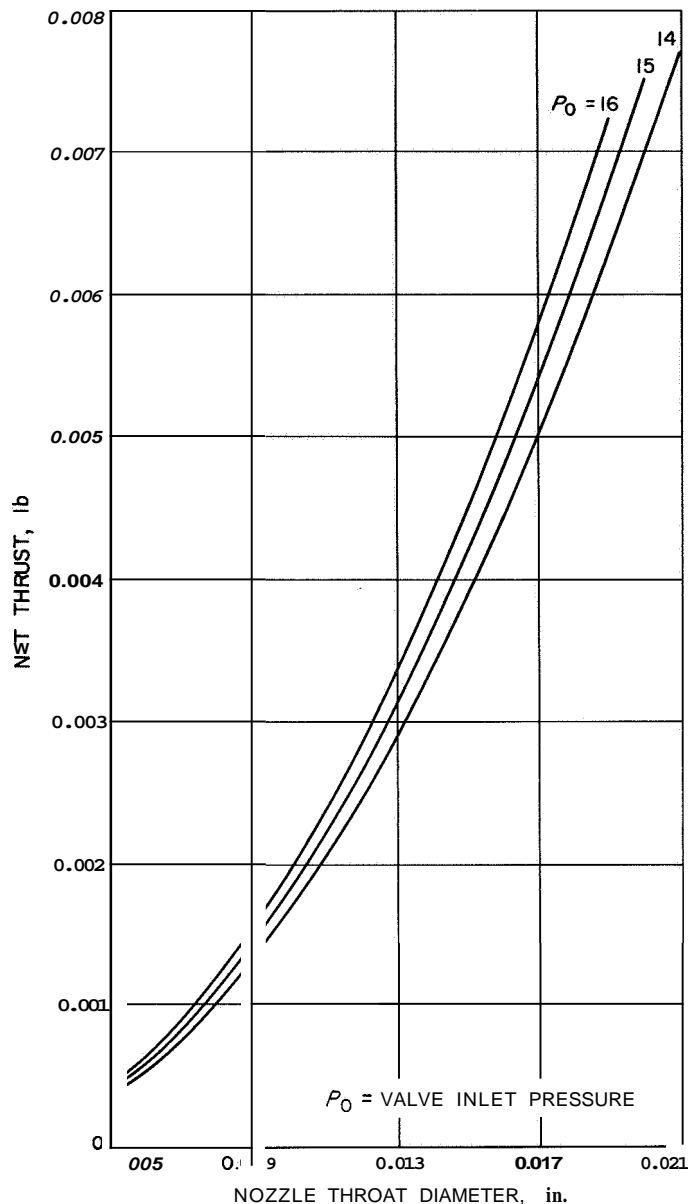


Fig. 11. Net thrust versus nozzle throat diameter

measurements made in the laboratory. Even more significantly, the theoretical values of net steady-state thrust are within 5% of thrust levels from *Mariner IV* flight data.

The steady-state investigation will be summarized in a series of parametric plots detailing reaction jet valve chamber pressure, flowrate, thrust, and total impulse as a function of inlet pressure and jet geometry. Following this analysis, work will be focused on the theoretical prediction of the valve chamber pressure versus time profile to determine pressure accumulation and decay for

transient phases of operation. From this profile, predictions for thrust and total impulse for pulse mode will be made and compared with experimental values.

N67 18316 .

C. Approach Guidance Flight Feasibility

Demonstration, F. R. Chamberlain and L. J. Barone

1. Introduction

Subsystem design, hardware design, and software design have been started for a flight feasibility demonstration of spacecraft-based optical approach guidance aboard the *Mariner Mars* 1969 spacecraft.

Approach guidance is a technique whereby increased accuracy of trajectory prediction is achieved during a period of several days prior to planet encounter (closest approach) and subsequently utilized during this period for guidance purposes in trajectory alteration. Pointing angles to the planet are measured in a spacecraft-fixed coordinate system by an optical tracker; these angular measurements (after correction for attitude control limit-cycle motion) are used to estimate trajectory parameters. Advantages of approach guidance include more exact control of orbit insertion or descent to planetary surface, as well as attainment of a closely controlled trajectory for single or sequenced flyby of one or more planets.

To permit correction for attitude control motion, the Approach Guidance Subsystem (A/G) configuration will include auxiliary Sun sensors for monitoring attitude control motion (pitch and yaw angles) with respect to the Sun. Information from the A/G is supplemented by data from the Canopus sensor of the spacecraft roll attitude control channel to obtain complete data on the orientation of the spacecraft in its limit cycle.

During the flight feasibility demonstration of the approach guidance concept, it is intended that the A/G will track Mars during a 10-day period that ends about 0.5 day before encounter. The measurements of pointing angles to the planet and attitude control information will be telemetered to Earth for processing in the Space Flight Operations Facility (SFOF) on a real-time, operational basis.

2. A/G Software

The approach guidance software used in the SFOF will perform the functions of spacecraft orbit determination (trajectory prediction), dummy maneuver computation, and post-encounter performance evaluation.

The spacecraft orbital parameters will be estimated from the telemetered A/G optical data and Earth-based radio tracking data by the double precision orbit determination program (DPODP) that is also being developed for radio orbit determination. This program employs a weighted least-squares estimation process.

The raw data telemetered from the A/G will be converted into a form acceptable to the DPODP by means of the optical guidance pre-processor program. This program will determine the pointing angles to the target body in a known celestial coordinate system from the telemetered Sun, Canopus star, and planet angular data.

A maneuver, and commands to control execution of this maneuver by the spacecraft, may be computed from the estimated orbital parameters by a maneuver and command computation program. However, for the *Mariner Mars 1969* A/G feasibility demonstration, execution of an approach guidance maneuver is not planned. Data derived from midcourse maneuvers executed earlier in flight can be used to estimate the potential A/G maneuver accuracy, because the A/G would use the same propulsion system if an approach maneuver were to be performed.

Because the spacecraft orbital parameters can be estimated after encounter to a high degree of accuracy from radio data obtained near the point of closest approach, post-encounter comparisons can be made between the target body pointing angles measured during the A/G optical measurement period and the more-accurate estimates of the actual angles derived from the near-encounter radio data. A computer program will be developed to use this comparison data to evaluate both the performance of the A/G and the validity of the preflight error model for the A/G.

3. A/G Hardware

An optical image of a target planet is produced by a 24-in. focal length system, and the optical image is centered on the photocathode of an electrostatic image dissector tube by angular displacements in the field of view which result from counter-rotation of two pairs of prisms. The electronic image produced in the image dissector tube is scanned in such a way that the illuminated planet limb geometry is electronically measured, and orthogonal error signals produced by the scan will control the prism pairs in such a way as to position the center of the planet image at the center of the photocathode.

Digital encoders record the positions of the prism pairs directly and monitor the changes in prism position required for changes in pointing angle to the planet. Ten bits of encoder data for each prism pair define the prism positions to a minimum (center of field) resolution of 55 arc sec per bit, for a field of view which is 10 deg square. A digital converter is used to transform the ten-bit encoder words into a format of seven-bit words compatible with spacecraft telemetry.

Currently, preliminary design of an approach guidance subsystem is in progress, under contract with Electro-Optical Systems, Inc. Prototypes will be delivered early in FY-68, and work under contract for *Mariner-69* flight hardware will commence.

4. Potential Applications

Potential applications include use of a proven approach guidance system to increase the accuracy of either the approach trajectory or an insertion maneuver for a planetary orbiter. An on-board computer may be introduced to eliminate the requirement for telemetry and ground processing as a series part of the guidance process. Such a configuration would be particularly useful on flights where large operational time lags are involved, or where multiple-spacecraft missions result in heavy loading of the DSN.

D. Thin Film Infrared Thermopile Detectors, -

D. S. Herman

Horizon scanners are presently used on orbiting and interplanetary spacecraft to provide information on, and the direction of the geometrical center of a nearby planet. This information is used in the orientation of the spacecraft and to point instruments on the spacecraft at the planet. Also, horizon scanners can be used to provide diameter information. For future spacecraft missions, a horizon scanner is required which has high responsivity, can cover a wide dynamic range in subtended planet diameter, and has an inherently long operating lifetime capability.

In 1963, a contract was let to the Barnes Engineering Company for the development of an infrared Lunar and Planetary Horizon Scanner (LPHS) meeting the above requirements and which has been previously described (*SPS 37-23*, Vol. IV, p. 37). The infrared detectors used in the LPHS are thermopiles each of which consists of 21 vacuum-evaporated bismuth-antimony thermocouples.

The 21 thermocouples are deposited so that the output of each thermocouple and its reference junction are in series. Other thermopile detectors used in horizon scanners can consist of vacuum-evaporated bismuth-tellurium thermocouples in the same or similar configurations.

Greater detector responsivity than that presently realized would be desirable for use on lunar and planetary missions. The effective infrared temperatures of the dark side of the Moon and the polar regions of Mars are much colder (90 to 120°K) than the average temperature of Mars (150°K) or Venus (200°K). It had also been determined that the detectors were probably not operating at their greatest efficiency since bulk metal electrical characteristics were not occurring in the thin films.

In October 1965, a research-type contract was let to the Barnes Engineering Company for the improvement of the thin film infrared thermopile detectors used in the LPHS and other horizon scanners. The aim was to achieve greater responsivity in the detectors through three different approaches. The first approach involved improving the electrical characteristics of the present materials, the second involved the use of new materials, and the third involved a study of the substrate onto which the films were deposited. Another requirement of the contract was that the detectors be capable of meeting thermal sterilization requirements if the LPHS would be used in a lunar or planetary landing application.

Experiments were first performed on individual thin film thermocouples formed from deposition of the two materials desired. When a good technique was developed, thermopile detectors were then fabricated and compared to previously manufactured detectors. Since thin film deposition rate is an important factor, the best rate was determined and maintained through the use of the standard quartz crystal monitoring technique. Individual thermocouples were tested for Seebeck voltage and resistance whereas the thermopile detectors were tested for resistance, responsivity, and time constant. The thermopile responsivity is dependent upon the Seebeck voltage per thermocouple and the number of thermocouples forming the thermopile. It also depends on the heat losses from the hot to the cold junction.

Improvements of the electrical characteristics of the deposited bismuth-antimony and bismuth-tellurium thin film thermocouples were achieved primarily through close control of the deposition rate and to a lesser extent by the substrate temperature during and after the deposition.

These improvements took the form of close to bulk Seebeck voltage and a resistivity value only 1.5 to 2 times the bulk. Fabrication of thermopiles using techniques developed during the studies showed that the elemental thermopile parameters mentioned above could be controlled to far closer tolerances than could be achieved with previously used deposition techniques.

Thermoelectric alloys having high Seebeck voltage and low resistivities were fabricated and films of these materials were deposited and studied. These materials were *n*- and *p*- type Bi₂Te₃ compounds which had previously been reported as giving good results when used as thin film thermopiles (Ref. 4). The deposition rate was controlled in the manner previously described with the materials evaporated from both resistance heated and electron gun sources. The thin film thermocouples had high Seebeck voltages and low resistivities. However, the alloys tend to thermally decompose during evaporation with the components evaporating at different rates. Thus, films having reproducible properties were difficult to obtain with large variations occurring from thermocouple to thermocouple.

The thermopile detector is formed by depositing the films onto 0.25-mil Mylar substrates which are bonded to a grooved aluminum block. The hot junctions are formed over the grooved portions whereas the cold junctions are formed over the metal portions for good heat conduction. In addition the hot junctions are blackened for best infrared absorption. Analysis had indicated that heat losses from the hot junction to the cold junction through the 0.25-mil (—6 p) thick Mylar could cause lowered responsivity. Detectors were fabricated using 2-p thick "Parylene N" as a substrate. This material is manufactured by Union Carbide and has the chemical designation poly-para xylylene. The experimental results indicated that the role played by the substrate in affecting the responsivity is probably small, with a greater influence on heat losses (and therefore responsivity) being caused by the thin film metal interconnections between hot and cold junctions. Therefore, reducing the size of the interconnection would increase the responsivity.

The best results were obtained by evaporating the present materials under very controlled conditions. The ability to obtain highly reproducible thermopile detectors having about the same responsivities as previously gotten was one of the major achievements of this effort. In addition, the ability to produce lower resistance thin film thermopile detectors meant that higher responsivity

detectors could be redesigned for the LPHS without making **it** detector noise limited. It was also found that the detectors would be capable of withstanding thermal sterilization without any major changes if they were given

a pre-sterilization bake of a few hours. The effect of this presterilization bake produces only small changes in the Seebeck voltage and reduces the resistance of the films by a large amount which is a desirable effect.

References

1. Greer, H., and Griep, D. J., *Low Thrust Reaction Jet Performance*, Report No. TDR-469(5230-33)-2, Aerospace Corporation, El Segundo, Calif., August, 1965.
2. Dayman, B., Jr., *Simplified Theoretical Estimates of Thrust Losses in Miniature Nozzles*, Internal Memorandum JPL CP-1, Jet Propulsion Laboratory, Pasadena, Calif., April, 1961.
3. Mack, L. M., *Calculation of the Laminar Boundary Layer on an Insulated Flat Plate by the Klunker-McLean Method*, Progress Report No. 20-352, Jet Propulsion Laboratory, Pasadena, Calif., July 7, 1958.
4. Abowitz, G., et al., "Thin Film Thermoelectrics," *Semiconductor Products and Solid State Technology*, vol. 8, p. 8, Feb. 1965.

N67 18318

VI. Guidance and Control Research

GUIDANCE AND CONTROL DIVISION

A. The Electro-optic Effect in Barium Titanate,

A. R. Johnston

1. Introduction

Study of the electro-optic effect in single-crystal BaTiO₃ is useful because its large polarizability promises a large response, which invites practical consideration in spite of the well-known difficulties, such as unstable domain structure and its associated high dielectric loss. The wide interest shown in it in the past by several laboratories has also produced a great deal of information about its other properties. To date, good experimental values have been obtained at JPL for the electro-optic effect as a function of temperature over a range covering both the polar tetragonal state and the cubic non-polar state.

This work has been reviewed previously (*SPS 37-26*, Vol. IV, p. 52), and the results have been published in the open literature (Refs. 1 and 2). The response was determined first for the low-frequency or undamped condition, and a technique was also developed to measure the transient response, thus obtaining the clamped effect. The experimental methods used are described in Refs. 1 and 2, and also in *SPS 37-36*, Vol. IV, p. 63. An independent determination of the clamped or strain-free response was made by Kaminow (Ref. 3), and the Kerr response was also observed by Geusic, et al. (Ref. 4).

None of these studies dealt with the dispersion of the electro-optic effect, that is, its dependence on the light wavelength. The purpose of this report is to describe the first results, obtained by an extension of our previously described methods, showing the dependence of the electro-optic effect on wavelength. This data is of interest in obtaining a description of the nonlinear interaction which produces the electro-optic effect.

To date, data have been obtained only for the unclamped effect. Both r_{42} and r_c have been measured at room temperature, between 4000 Å and 1.1 μ.

2. Measurement of Birefringence

In order to determine r_{42} , the electro-optic constant for a $\langle 100 \rangle$ field, the birefringence, Δn , of BaTiO₃ crystals must be known, since the constant r_{42} is obtained from the observed rotation of the birefringent axes, a , as follows (Ref. 1):

$$r_{42} = 2 \Delta n \frac{a}{E_a} \cdot \frac{\gamma}{n_{ao}^3} \quad (1)$$

Here, $\Delta n = n_a - n_c$ and, of course, depends on wavelength. γ is a small correction taking into account the

dispersion in n_a and a second-order term in Δn . n_{a0} signifies the index n , at some fixed wavelength, here taken to be 5461 Å.

Meyerhoffer (Ref. 5) determined Δn as a function of temperature on several samples, and found $\Delta n = 0.073$ at room temperature (25°C) and at 5461 Å. Cross, et al. (Ref. 6), determined Δn as a function of λ , but only in relative units. Shumate (SPS 37-35, Vol. IV, p. 52, and Refs. 7 and 8) recently determined n_a and n_c separately for one sample by an interferometric method. His data is restricted to a wavelength interval in which he could observe fringes visually. From his data, Δn was 0.067 at 5461 Å. The difference between this value and Meyerhoffer's is reasonable in view of typical sample-to-sample variations. Fig. 1 shows these values, which lie between 5085 Å and 5892 Å, and also the curve of Cross, et al., which was normalized to fall midway between.

The present measurements were made on two samples, in order to extend the Δn versus λ curve to cover the desired wavelength interval. The samples were thin, flux-

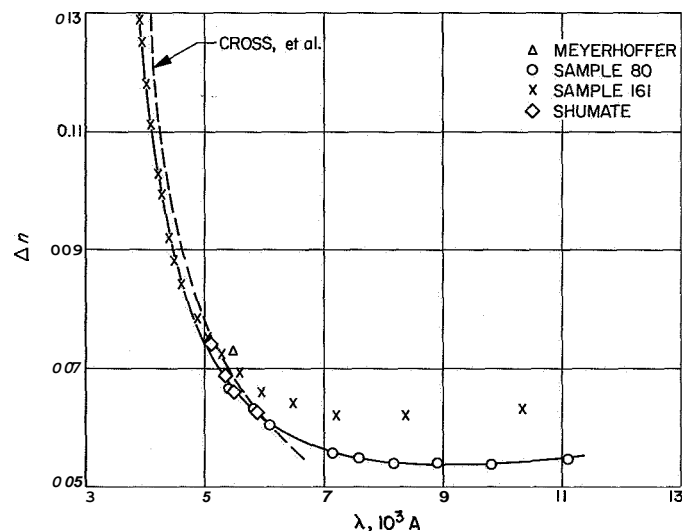


Fig. 1. Birefringence Δn versus λ from several sources

grown plates, each poled in such a way that its c-axis was in the plane of the plate. The crystal was placed in a polarimeter as shown in Fig. 2, normal to the direction of light propagation, with the c-axis rotated 45° from the polarizer orientation. The light source was a Bausch and Lomb high-intensity monochromator. For the detector, a 1P21 photomultiplier was used below about 6500 Å, and one with an S-1 photo surface, a 7102, at longer wavelengths.

With the analyzer oriented 90° from the polarizer, an intensity minimum would be observed as the wavelength is varied, whenever the state of polarization is unaltered by the sample. This occurs whenever the optical retardation by the sample is $2\pi m$, where m is an integer, 0, 1, 2, etc.

The retardation of the crystal is given by δ , where

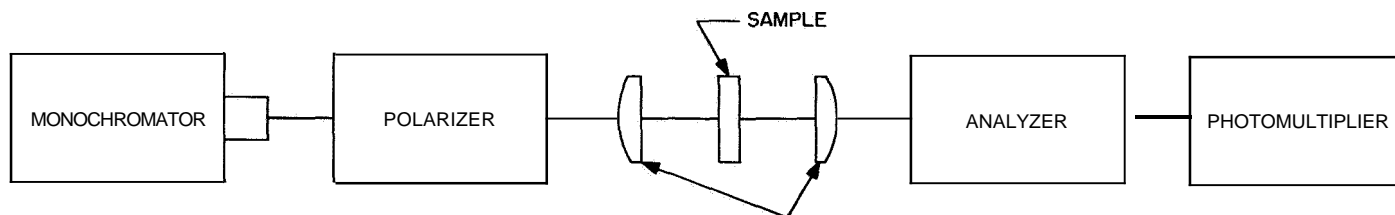
$$\delta = \frac{2\pi \Delta n t}{\lambda} \quad (2)$$

t is the sample thickness. Solving for Δn , one obtains at the intensity minima

$$\Delta n = \frac{m \lambda}{t} \quad (3)$$

Intermediate minima can also be observed by rotating the analyzer 90° so that it is parallel to the polarizer. In this case, intensity minima occur at odd multiples of π retardation; $\pi, 3\pi, 5\pi$, etc., so that the order of interference, m , defined above, takes on the values $1/2, 3/2$, etc.

An unusually thin sample, no. 161, was selected in order to space out the minima, and the wavelengths at which each type of minimum occurred were noted, starting at the limit of the S-1 photo surface and working up to the BaTiO₃ band edge. The actual geometrical thickness was measured as $40.6 \pm 1.5 \mu$, using the vertical fine-focus scale of a microscope. The assignment of the correct



interference order, signified by the value of m , to a particular minimum, must be made independently. The value of m was picked to be 5 at 5510 Å in order to best fit the known value of n_a at 5461 Å. n_a versus λ was then determined from Eq. (3). No correction was made to t in order to match the previous data; the only choice was the assignment $m = 5$ or some other integer. These points are plotted in Fig. 1 as x's.

A similar procedure was followed with another sample, no. 80, from 5461 Å toward longer wavelengths. Sample no. 80 was the sample used by Shumate to obtain n_a and n_r . This sample was much thicker, but its thickness had been determined very carefully by Shumate as $179.1 \pm 0.1 \mu$. The value of m required for best fit (to Shumate's n_a , since this is the same sample), was 21 at 5510 Å. The resulting values for n_a are shown in Fig. 1 as circles.

Both curves flatten out toward longer wavelength, unlike the curve taken from Cross, and even show an indication of rising if the data had been carried to wavelengths longer than 1.1μ . This type of behavior is not easy to accept, especially since the uncertainty in the thickness of no. 161 and the fact that its actual n_a at 5461 is not known make it just possible to select $m = 4$ at 5570 Å, if a rather unlikely combination of uncertainties is accepted. This produces a curve in which n_a decreases toward longer wavelength in a more normal fashion. However, it is not possible to do this for sample no. 80, because these quantities are known, and also because an error of ± 1 in the value picked for m does not change the shape of the curve significantly anyway. In the following, the dependence of n_a on λ given by the solid curve will be used, but further confirmation is desirable.

The values of the indices n_a and n_r themselves are needed as a function of λ for both r_{42} and r_c , although the effect of this dispersion in calculating the electro-optic constants is much smaller. Shumate's data between 5085 Å and 5892 Å was extended by fitting Cauchy's formula to it:

$$n(\lambda) = A + \frac{B}{\lambda^2} \quad (4)$$

This formula is correct if a classical oscillator model is used for n . The values thus determined for A and B are:

	n_a	n_c
A	2.2392	2.2028
B	0.05838	0.04867

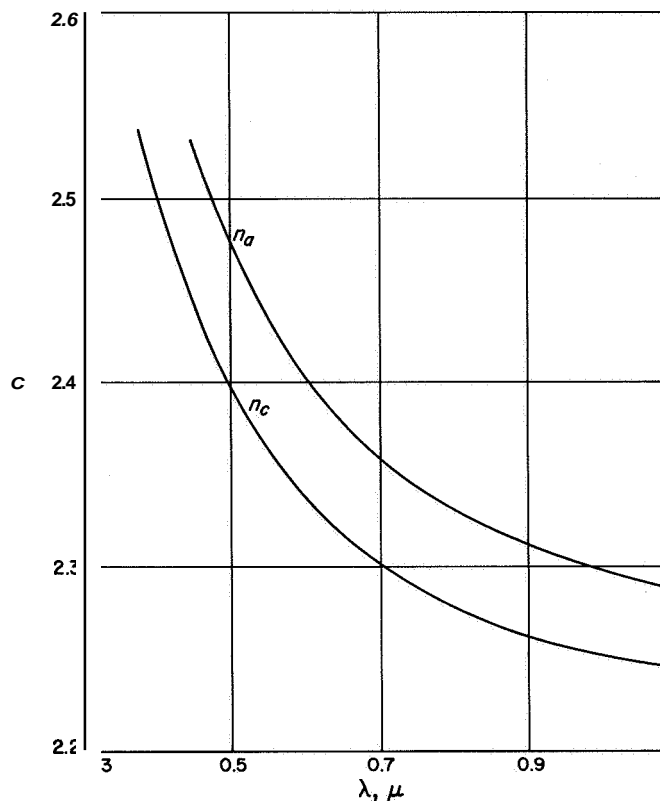


Fig. 3. n_a and n_c versus λ , extrapolated from Shumate's data

The resulting dispersion curves are plotted in Fig. 3. The difference $n_a - n_c$ taken from Fig. 3 decreases somewhat from 6000 Å toward longer wavelengths. Since a large extrapolation is involved, this was disregarded in favor of the measurements described above in plotting n_a versus λ , Fig. 1.

3. Determination of the Electro-Optic Constants

The same apparatus which was used previously (see SPS 37-26, Vol. IV, p. 63) was used for determining r_c , with two exceptions. The high-pressure mercury arc used previously was of course replaced in order to obtain a variable light wavelength. The Bausch and Lomb monochromator with an incandescent source was substituted in its place. The much lower intensity available from this type of source required additional condensing lenses to be placed on either side of the sample. The size of the stop at the sample remained at about 0.75 mm. The decrease in available intensity together with the much lower efficiency of the S-1 photo surface greatly increased the noise level, but a measurement of the low-frequency r_c was still possible with a filtering time constant of a few seconds. A Faraday cell containing benzene was used

in a closed loop to null the rotation produced by the sample plus a properly oriented quarter-wave compensator. Mica quarter-wave plates were used, in a fixture which permitted tipping them in order to trim their retardation to the correct value at each wavelength. The Faraday cell was calibrated as a function of wavelength in order to obtain actual angles.

The results for sample no. 139, calculated with the aid of the index data in Fig. 3, are shown in Fig. 4. From Ref. 1, one obtains

$$r_c = \frac{2\lambda\theta_{fc}\eta}{\pi n_{c0}^3 t E_c} \quad (5)$$

where θ_{fc} is the angular rotation produced by the Faraday cell, and t is the crystal thickness along the light path. η is a small correction taking into account the dispersion in n ; n_{c0} is n , at 5461 Å. The uncertainty in determining each point due to photodetector noise is consistent with the spread of points in the graph, about $\pm 5\%$, except at the extreme end of the wavelength range. There, the lack of useful intensity resulted in greatly increased noise, ultimately preventing any measurement from being accomplished.

A similar measurement of r_{42} was made with a $\langle 100 \rangle$ field, for sample no. 167. The sample was placed between

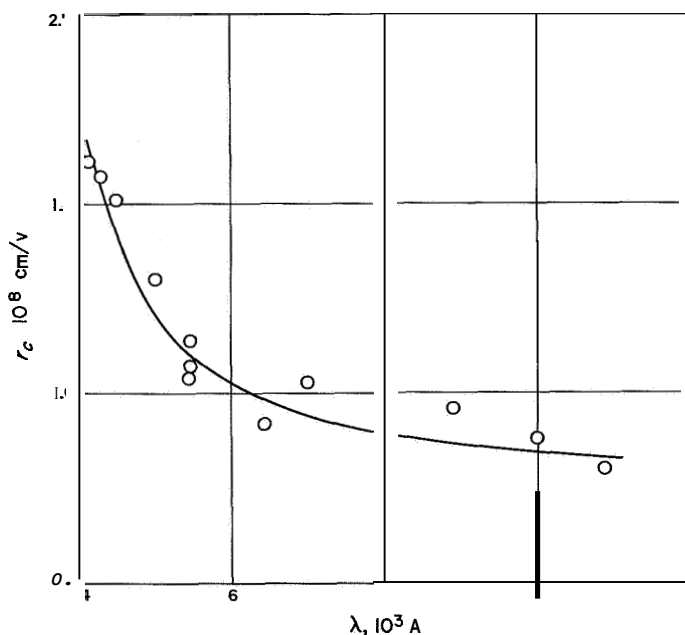


Fig. 4. r_c , the response to a field E_z , determined as a function of λ , undamped

matched Faraday cells, which were used in a nulling loop to measure the angle α in Eq. (1) directly (see SPS 37-26, Vol. IV). Otherwise, the monochromator light source and the condensing lenses near the sample mentioned above remained the only changes made to the apparatus. The angle α was recorded on an x - y plotter as a function of the applied field, E , so that this noise was primarily statistical noise from the photomultiplier. In terms of a $1\text{-}\sigma$ uncertainty in r_{42} , this implies an uncertainty of $\pm 2.5\%$ near 5000 Å up to $\pm 12\%$ at both ends of the wavelength range.

Using the An data shown in Fig. 1, r_{42} was calculated. The result is shown in Fig. 5, adjusted to be consistent with the previous determination at 5461 Å (Ref. 1).

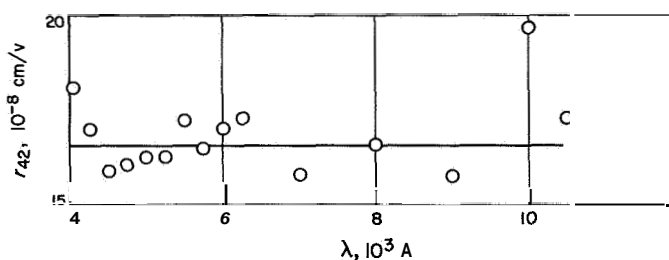


Fig. 5. r_{42} , the response to a field E_z , as a function of λ , undamped

4. Conclusions

The best present conclusion is that there is no significant variation for r_{42} , for wavelengths between 4050 Å and 1.1μ . This is a conclusion that is not altogether unexpected. On the other hand, r_c , which involves both r_{33} and r_{13} ,

$$r_c \simeq r_{33} - r_{13}$$

shows a significant increase toward shorter wavelengths. The increase is greater than 50%, which is far larger than the experimental uncertainty. The shape of the curve of r , as a function of λ , seen in Fig. 4, is quite similar to An versus λ , rising steeply as the absorption edge at 4000 Å is approached.

The results described above should be reinforced by similar determinations on other samples, and by further checking of the value of An . Although strain-free measurements were not possible with the monochromator light source, it appears that by using other lines from the high-pressure mercury arc, and a laser for the longer wavelengths at 6328 Å and possibly 1.15μ , a transient, or

strain-free determination is within reach. The strain-free response would be valuable in explaining the nonlinear interaction because any possible anomaly in the wavelength dependence of the strain contribution could be seen and taken into account.

N67 18319

B. Space-Charge Distribution in a Neutral Plasma, K. Shimada

1. Introduction

The spatial distribution of electrons and ions in a plasma was obtained analytically by assuming that the plasma under consideration was electrically neutral. The results of this analysis were reported in *SPS 37-36*, Vol. IV, p. 68. In this article, this theory is compared with experimental results obtained by Bullis (Ref. 9), using a Langmuir probe. The theoretical characteristic length describing the spatial decay rate of electrons compares favorably with the measured values after probe diffusion limitations are accounted for. Further analysis of the data, in an electron-retarding field, indicates that recombination processes dominate the ionization in the plasma. The time rate of the sink of electric charges, which just equals the divergence of particle fluxes necessary to maintain equilibrium, is found to be 5.15×10^3 /sec per electron.

2. Theory

Based upon the collective motions of charge particles, the following flux equations are obtained (see Table 1 for definitions of symbols):

$$\bar{\Gamma}_+ = \mu_+ \bar{E} n_+ - D_+ \nabla n_+ \quad (1)$$

$$\bar{\Gamma}_+ = -\mu_- \bar{E} n_- - D_- \nabla n_- \quad (2)$$

Here, the temperatures of electrons and ions are assumed to be T_- and T_+ , respectively, throughout the plasma; hence, the temperature gradient terms do not appear in Eqs. (1) and (2). Under steady-state conditions, continuity of convection current must hold throughout the plasma. Thus

$$\nabla \cdot \bar{J} = \nabla \cdot e(\bar{\Gamma}_+ - \bar{\Gamma}_-) = 0 \quad (3)$$

Consistency of electric field with the net charge density requires that

$$\nabla \cdot \bar{D} = \epsilon_0 \nabla \cdot \bar{E} = e(n_+ - n_-) \quad (4)$$

Table 1. Definitions

$\bar{\Gamma}_+$	= vector ion flow density; particles/m ² -sec
$\bar{\Gamma}_-$	= vector electron flow density; particles/m ² -sec
μ_+	= ion mobility; m ² /sec-volt
μ_-	= electron mobility; m ² /sec-volt
\bar{E}	= vector electric field intensity; volt/m
E_x	= x-component of field intensity
i	= unit vector along x-axis
n_+	= ion volume density
n_-	= electron volume density
D_+	= ion diffusion constant; m ² /sec
D_-	= electron diffusion constant; m ² /sec
e	= electron charge 1.6×10^{-19} coulomb
ϵ_0	= dielectric constant of vacuum; 8.85×10^{-12} farad/m
D	= ambipolar diffusion constant; m ² /sec
T_-	= electron temperature; deg Kelvin
T_+	= ion temperature; deg Kelvin
L_a	= characteristic length
τ_a	= time constant defined by Eq. (11)

Solving for the electric field under the constraint of strict charge neutrality ($n_+ = n_-$), we obtain, for the one-dimensional case,

$$\bar{E} = i \bar{E}_x \quad (5)$$

The charge density under the assumption of constant mobilities is given by

$$n_+ = n_- = n_1 \exp(-x/L_a) + n_2 \quad (6)$$

where

$$L_a = (D_- - D_+)/(\mu_+ + \mu_-) E_x \quad (7)$$

The assumption of constant mobilities holds if electron-ion collisions are negligible. Consequently, the current density J_x is given by

$$J_x = e E_x n_2 (\mu_+ + \mu_-) \quad (8)$$

Divergences of $\bar{\Gamma}_+$ and $\bar{\Gamma}_-$ are given by

$$\nabla \cdot \bar{\Gamma}_+ = \nabla \cdot \bar{\Gamma}_- = -\frac{\mu_a E_x}{L_a} n_1 \exp(-x/L_a) \quad (9)$$

where

$$\mu_a = (\mu_+ D_- + \mu_- D_+) / (D_- - D_+) . \quad (10)$$

Using a time constant τ_a , which is defined by

$$\tau_a = L_a / \mu_a E_x , \quad (11)$$

we obtain

$$\nabla \cdot \bar{\Gamma}_+ = \nabla \cdot \bar{\Gamma}_- = -\frac{1}{\tau_a} n_1 \exp(-x/L_a) . \quad (12)$$

By making use of the quantities measured by Bullis, E_x , J_x , and the total electron density n_- , the quantity $n_- - n_2$ can be calculated. This quantity will then be compared with the theoretical value which is expected to have an exponential dependence with distance. A direct comparison between the measured and the calculated charge density was not made since the integration constant n_1 in Eq. (6) was not known because the condition at the boundary between the plasma and the plasma sheath had not been investigated.

3. Experimental Results

The potential distribution in a thermionic energy converter, measured by Bullis, is shown in Fig. 6, which indicates that, in the plasma region, the electric field is directed from the emitter to the collector. Therefore, the relative directions of the current density \bar{J} and the electric field \bar{E} oppose each other as shown. The number density n_2 can be calculated from Eq. (8) using measured values of J_x and E_x . With $J_x = -0.94 \text{ Amp/cm}^2$, $E_x = 0.668 \text{ V/cm}$, and $\mu_+ \ll \mu_-$, the density n_2 may be calculated as $-4.35 \times 10^{13} \text{ electrons/cm}^3$, where the electron mobility is determined from Fick's law and the Einstein relationship under the assumption that the electron-ion collisions are negligible. The mobility thus determined is $20.2 \text{ m}^2/\text{volt-sec}$, and it is nearly equal to an average value of measured mobilities (Ref. 11) which are influenced by electron-ion

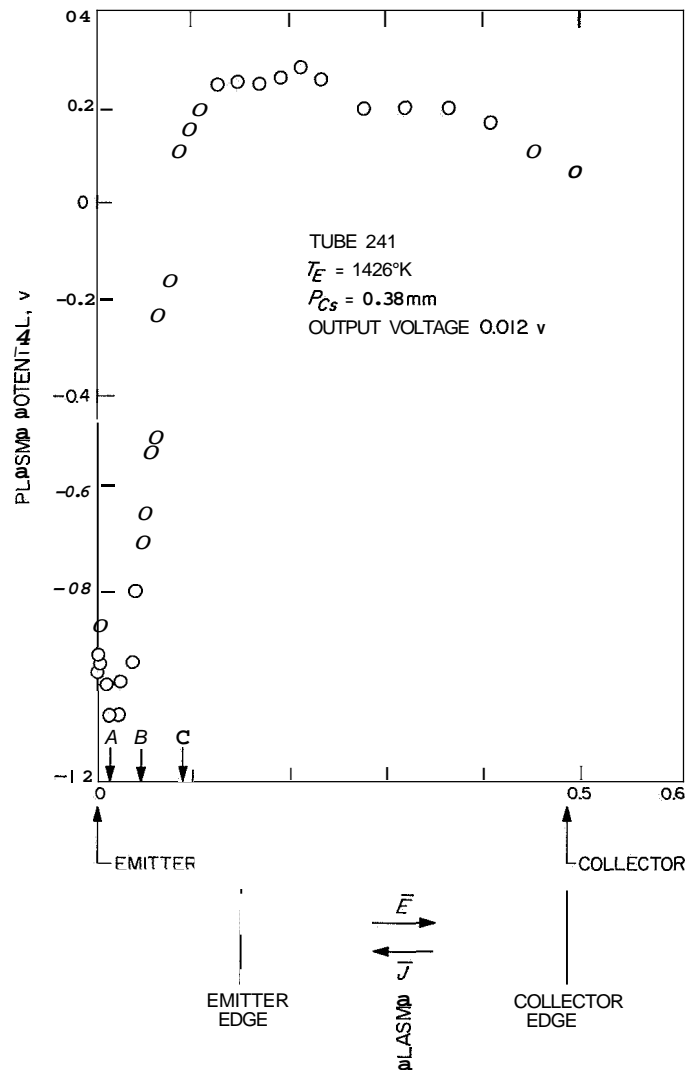


Fig. 6. Plasma potential versus distance

collisions. A negative sign for n_2 means that the particle flow is diffusion-dominated rather than drift-dominated,

Now the quantity $n_- - n_2 = n_- + 4.35 \times 10^{13} \text{ electrons/cm}^3$ can be obtained, since the net electron density n_- is known from the measurements. The results are shown in Fig. 7. The bottom curve represents electron densities which were measured by probes and corrected by a factor of 5. This correction is introduced to compensate for the fact that the number density measured is smaller than the actual density, because of the diffusion limitation of the probe measurements. The top curve represents the resultant charge densities obtained by adding $4.35 \times 10^{13} \text{ electrons/cm}^3$ to the experimental curve. According to Eq. (6), we expect that

$$n_- - n_2 = n_1 \exp(-x/L_a) . \quad (13)$$

If $T_- \gg T_+$, the characteristic length L_a , which was given in Eq. (7), can be approximated by

$$L_a \simeq \frac{D_-}{\mu_- E_x} = \frac{kT_-}{eE_x}. \quad (14)$$

Using measured values of $T_- = 2,550^\circ\text{K}$ and $E_x = 0.668 \text{ V/cm}$, the characteristic decay length L_a is found to be 0.329 cm. In Fig. 7, the quantity $n_1 \exp(-x/0.39)$ is shown as a dashed line. This line yields a value of $n_1 = 1.2 \times 10^{14}$ electrons/cm³ at the emitter edge of the plasma ($x=0$), which is located at a plane 0.15 cm from the emitter. Agreement between theory and measurement, in the spatial dependence of the quantity $n_- - n_2$ and its characteristic length, is reasonably good.

In the steady state, the time rate of change of electron density, n_- , must be zero, hence the following equation must be satisfied:

$$\begin{aligned} \frac{dn_-}{dt} = -\nabla \cdot \bar{\Gamma}_- + \left[\left(\frac{dn_-}{dt} \right)_{\text{ionization}} \right. \\ \left. - \left(\frac{dn_-}{dt} \right)_{\text{recombination}} \right] = 0 \end{aligned} \quad (15)$$

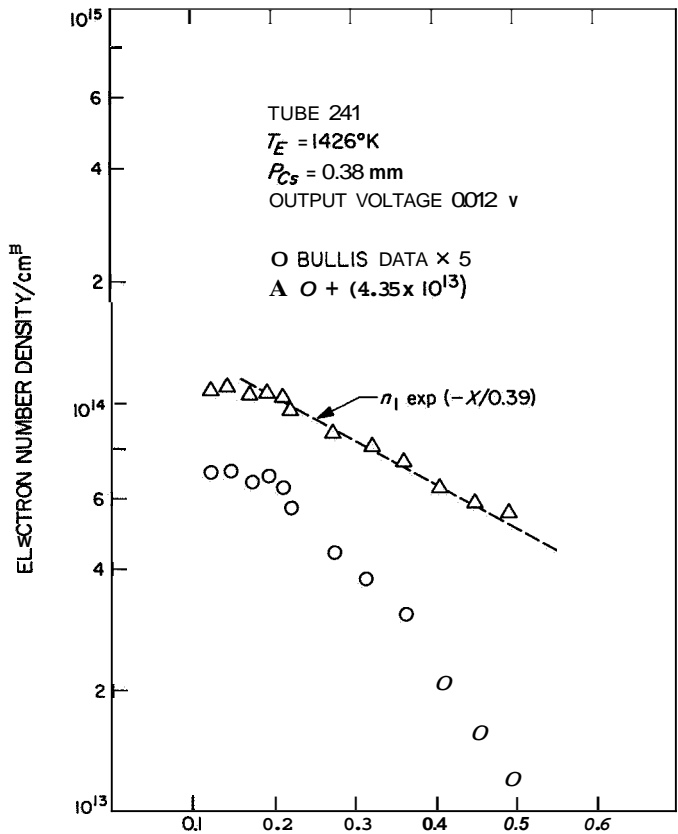
Therefore

$$\left[\left(\frac{dn_-}{dt} \right)_{\text{recombination}} \right] = \nabla \cdot \bar{\Gamma}_- \quad (16)$$

From Eqs. (16) and (12), one obtains

$$\begin{aligned} \left[\left(\frac{dn_-}{dt} \right)_{\text{recombination}} - \left(\frac{dn_-}{dt} \right)_{\text{ionization}} \right] = \\ \frac{1}{\tau_a} n_1 \exp(-x/L_a) \end{aligned} \quad (17)$$

Here the left-hand side of the equation equals the net time rate of the sink of electrons. Since the equivalent mobility, μ_a , is approximately equal to μ_+ if $T_- \gg T_+$, from Eq. (11) we obtain 0.195×10^{-8} sec for τ_a . In other words, the number of recombining collisions exceeds the number of ionizing collisions by 5150 collisions/sec per electron at $x = 0$.



The number of the recombining collisions may be estimated from data published by Wada and Knechtli (Ref. 10). They determined that the recombination coefficient of the order of $10^{-9} \text{ cm}^3/\text{sec}$ at an ion density of $10^{14}/\text{cm}^3$. This gives the number of recombining collisions as $10^5/\text{sec}$ per electron. Consequently, the excess of recombining collisions over ionizing collisions (5150/sec per electron) is only a small fraction of the inelastic collisions in the plasma.

4. Conclusions

Despite simplifications introduced in obtaining the spatial charge distributions in an electrically neutral plasma, the agreement between theory and experiment was reasonably good. Observed charge density can be considered as the sum of an exponential term and a constant term. A characteristic length, which describes the exponential decay rate of the first term in the charge density, shows good agreement between theory and the experiment. The discrepancy may be due to electron-ion collisions which influence the electron mobility (Ref. 11). There is a net

ak for electron-ion pairs when there is an electron-retarding electric field; however, the magnitude of this net sink is so small, compared with the recombination and ionization rates, that the plasma may be considered sinkless and source-less for both electrons and ions. In other words the rate of recombination is approximately equal to the rate of the ionization. The theory described above is currently being improved by including the effect of electron-ion collisions on mobilities. The modified theory gives better agreement with experimental results; this theory will be reported in a subsequent Space Programs Summary.

N67 18320

C. Limitations Imposed by Demagnetizing Field: on Bit Packing Densities Within Mn-Bi Films, G. Lewicki and D. I. Tchernev

1. introduction

This report discusses the limitations imposed by demagnetizing fields on the maximum density of "Curie point writing" on thin ferromagnetic films of manganese bismuthide.

Thin films of manganese bismuthide are potential media for high-density information storage. Bits in the form of "ones" or "zeros" correspond to areas of the film magnetized in one of two possible directions normal to the plane of the film. The state of magnetization of these areas is determined optically with the use of the Faraday effect.

Curie point writing refers to a particular method of reversing the magnetization direction within a selected region of the film (Ref. 12). The region is heated past its Curie temperature and then allowed to cool in a magnetic field having the direction desired for the remnant magnetization and a magnitude sufficient to insure complete switching. This magnetic field is, however, too small to affect portions of the film not having been taken through the temperature cycle. Situations can exist where the demagnetizing field created by the rest of the film at the site of the heated, and thus nonmagnetic, area is opposite in direction to that required for switching. Consequently, the magnitude of the field which is applied in the direction desired for the magnetization has to exceed the value required for switching by the magnitude of this demagnetizing field.

The maximum value of the demagnetizing field has been calculated for two types of bit arrangements. The first arrangement is one where bits correspond to circular

areas on a continuous film; the second arrangement is one where bits correspond to circular areas on a discontinuous film. The film is discontinuous in the sense that individual bits are separated by a nonmagnetic material. These calculations allow the determination of the maximum packing densities achievable on thin ferromagnetic films of manganese bismuthide under the condition that there is a maximum practically realizable field for the purpose of overcoming demagnetizing fields. The results of these calculations are presented below.

2. Worst-case Demagnetizing Field Within a Continuous Film

Consider a continuous film with thickness t and a magnetization M normal to the plane of the film. Within this film there is a circular area, with radius a , which is nonmagnetic.

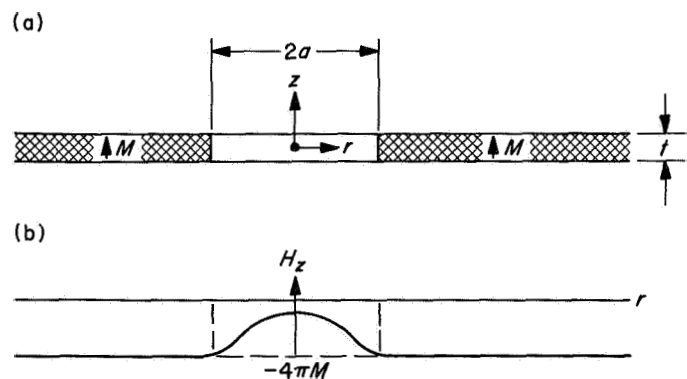


Fig 8. (a) Cross-sectional view of thin film magnetized in a direction normal to plane of film with a circular nonmagnetic region; (b) z -component of demagnetizing field H_z at $z = 0$ as a function of r

This distribution of the magnetization is shown in Fig. 8 and corresponds to a situation where all bits on the films are "ones" with the exception of one bit which, upon having been heated past its Curie temperature, is nonmagnetic. The direction of the demagnetizing field through this heated bit is opposite to that required for switching it to a "one." Inasmuch as this magnetization distribution generates the largest demagnetizing field possible, it can be considered to represent a worst-case situation.

The z -component of the demagnetizing field H_z at $z = 0$ is now calculated to determine the minimum radius of a bit which allows an applied field of magnitude H_a to overcome the worst-case demagnetizing field over

an appreciable portion of the bit. The differential demagnetizing field dH_z , at $z = 0$, at a point a distance r from the center of the non-magnetic bit, resulting from the magnetization within a differential magnetic area dA of the film a distance p from this point, is given by

$$dH_z = -\frac{Mt}{\rho^3} dA \quad (1)$$

if ρ is greater than the film thickness t . If all magnetic regions are taken into account, H_z , for $r - a \gg t/2$, can be expressed as

$$H_z(r) = -\frac{2\pi Mt}{a} \int_0^{2\pi} d\theta \int_1^\infty \frac{s ds}{[q^2 + s^2 - 2qs \cos \theta]^{3/2}} \quad (2)$$

where $q = r/a$. After the integrand in the above equation is replaced by an infinite series, the integral may be evaluated to yield

$$H_z = -\frac{2\pi Mt}{a} \sum_{n=0}^{\infty} \frac{1}{2} [1 + (-1)^n] \frac{(2n+1)! q^n}{n! \left[\left(\frac{n}{2}\right)!\right]^2 2^{2n}}$$

$$+ \sum_{m=0}^{\infty} (-1)^m \frac{n! [2m+2n+1]! q^{2m}}{m! (n+m)! (2n+1)! 2^m (2m+2n+1)!} \quad (3)$$

The first few coefficients of the above power series in q were calculated, and are presented in Eq. (4)

$$H_z = -4\pi M \frac{t}{2a} [1 + 0.75 q^2 + 0.7031 q^4 + 0.6836 q^6 + 0.6729 q^8 + 0.6662 q^{10} + 0.6615 q^{12} + 0.6582 q^{14} + 0.6556 q^{16} + 0.6536 q^{18} + 0.6517 q^{20} \dots]$$

(4)

An applied field with a direction opposite to that of the demagnetizing field and a magnitude equal to $2(4\pi M t/2a)$ will yield a net field in the desired $+z$ direction for $r \leq 0.77 a$, and thus overcome the worst-case demagnetizing field over an appreciable portion of the bit. If the maximum field which can be practically generated for the purpose of overcoming possible demag-

netizing fields is denoted by H_a , the maximum bit packing density D achievable with continuous films is given by

$$D = \frac{1}{(2a)^2} = \left(\frac{H_a}{8\pi M}\right)^2 \frac{1}{t^2}$$

Optimization of the Faraday effect used in reading out the magnetization state of a bit requires the film thickness t to be on the order of 500 Å. The magnetization M , for manganese bismuthide, at room temperature, is equal to 600 G (cgs, emu, Ref. 13). Consequently, a practical value of 10 Oersteds for H_a limits the bit packing density for continuous films to somewhere in the vicinity of 10^4 bits/cm².

3. Worst-case Demagnetizing Field Within a Discontinuous Film

If bits are arranged as circular areas of radius a spaced a distance b apart, with the regions between the circular areas being nonmagnetic, as shown in Fig. 9, the maximum bit packing density for a given practically realizable field, H_a , increases over that for continuous films.

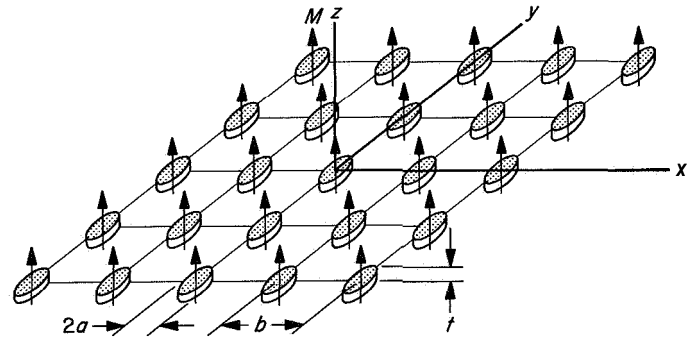


Fig. 9. Bit geometry on a discontinuous film

The x-component of the demagnetizing field generated by a circular bit of radius a with magnetization M in the $+z$ direction in the plane of the bit at a distance r from its center is given by

$$H_x = 4\pi M \frac{t}{a} q^{-3} \sum_{n=0}^{\infty} \frac{1}{2} [1 + (-1)^n] \frac{(2n+1)!}{\left[\left(\frac{n}{2}\right)!\right]^2} 2^n q^{-n}$$

$$+ \sum_{m=0}^{\infty} (-1)^m \frac{(2n+2m+1)! n!}{m! (2m+2n+2)! 2^{2m} (m+n)! (2n+1)!} q^{-2m}$$

(6)

for $r = a \gg t$. In the above expression, q is a normalized parameter equal to r/a . With the use of this result, the z -component of the demagnetizing field at the center of a nonmagnetic bit generated by surrounding bits all magnetized in the $+z$ direction can be determined. Surprisingly, this field is quite accurately represented by the approximation given in Eq. (7).

$$H_z = -4\pi M \frac{t}{2a} \left(\frac{2a}{b} \right)^2 \frac{\pi}{4}. \quad (7)$$

The worst-case demagnetizing field increases slowly for positions away from the center of the nonmagnetic bit. However, an applied field with a direction opposite to that of the demagnetizing field and with a magnitude twice that given in Eq. (7) will overcome the demagnetizing field over most, if not all, of the area of this nonmagnetic bit. Consequently, the maximum bit packing density achievable on a discontinuous Mn-Bi film under the condition that there is a maximum practically realizable field H_a for the purpose of overcoming demagnetizing fields is defined by the equality

$$H_a = 8\pi M \frac{t}{2a} \left(\frac{2a}{b} \right)^2 \frac{\pi}{4}, \quad (8)$$

and thus is given by

$$D = \frac{1}{b^2} = \frac{H_a}{4\pi^2 M} \frac{1}{at}. \quad (9)$$

Optical detection of the state of magnetization of a bit limits a to about 0.5 micron. Using values for M , t , and H_a previously cited, that is: $M = 600$ G (cgs, emu), $t = 500$ Å, and $H_a = 10$ Oersteds, the maximum packing density for discontinuous films becomes something on the order of 10^6 bits/cm².

In conclusion, it should be noted that the packing density in continuous films increases as the square of H_a , while in discontinuous films it increases linearly with H_a . Consequently, higher switching fields will yield higher packing densities for continuous films relative to discontinuous films.

References

1. Johnston, A. R., and Weingart, J. M., *J. Opt. Soc. Am.*, vol. 55, p. 828, 1965.
2. Johnston, A. R., *Appl. Phys. Lett.*, vol. 7, p. 195, 1965.
3. Kaminow, I. P., *Appl. Phys. Lett.*, vol. 8, p. 305, 1966.
4. Geusic, J. E., Kurtz, S. K., Van Uitert, L. C., and Wemple, S. H., *Appl. Phys. Lett.*, vol. 4, p. 141, 1964.
5. Meyerhoffer, D., *Phys. Rev.*, vol. 112, p. 413, 1958.
6. Cross, L. E., Nicolson, M. M., Zlotnicki, B., and Whiddington, R., *Nature*, vol. 165, p. 440, 1950.
7. Shumate, M. S., *AFCRL-64-175*, 13 March 1964.
8. Shumate, M. S., *Appl. Optics*, vol. 5, p. 327, 1966.
9. Bullis, R. H., et al., "Relationship Between the Output Characteristics of an Arc-Mode Thermionic Converter and the Properties of the Neutralization Plasma," presented at the *International Conference on Thermionic Electrical Power Generation*, London, England, September 1965.
10. Wada, J. Y., and Knechtli, R. C., "Measurements of Electron-Ion Recombination in a Thermal Cesium Plasma," *Phys. Rev. Lett.*, vol. 10, no. 12, pp. 513-516, June 1963.

References (contd)

11. Nighan, W. L., "The Determination of an Effective Electron-Cesium Heavy Particle Collision Frequency for Momentum Transfer," *Report on the Thermionic Conversion Specialist Conference*, pp. 84-100, October 1965.
12. Mayer, L., *J. Appl. Phys.*, vol. 29, p. 1454, 1958.
13. Kittel, C., *Rev. Mod. Phys.*, vol. 21, no. 4, p. 541, 1949.

VII. Materials

ENGINEERING MECHANICS DIVISION

N67 18321

A. Ceramic Research, M. H. Leipold

The mechanical testing facility described in SPS 37-34, Vol. IV, pp. 85-87, has been completed with the installation of the last subsystem, the load-measuring equipment. Difficulties with the linearity and capacity of the earlier designs have caused considerable delay. With the installation of the load-measuring equipment, the entire facility is complete, and all subsystems have been tested, evaluated and calibrated, except for the high temperature capability of the furnace units. Actual testing will begin when completely satisfactory alignment procedure for

placing the specimen in the grips is developed. Such development is now under way. Previous procedures were inconsistent; and, although properly aligned specimens have been obtained, it has not been possible to be sure that all specimens placed in the grips were properly aligned.

With the addition of the load-measuring subsystem, it has been possible to make modulus measurements on various specimens. The results obtained are shown in Table 1, and in Fig. 1, a complete stress-strain diagram.

Material	Gauge length mm	Contour	Stress range kg/mm ²	Modulus of elasticity kg/mm ² X 10 ⁴	Remarks
4130 Steel	38.1	No	0-8.8	2.14	Specimen misaligned
4130 Steel	38.1	No	8.8-35.1	2.05	
4130 Steel	38.1	No	35.1-57.9	2.10	
1113 Steel	19.0	Yes	7.0-17.6	1.87	
1113 Steel	19.0	Yes	7.0-17.6	2.03	
1113 Steel	12.7	Yes	0-17.6	2.23	
1113 Steel	12.7	Yes	0-17.6	2.23	
6061-T6 Al	38.1	No	0-3.5	0.78	
6061-T6 Al	38.1	No	3.5-17.6	0.67	Specimen misaligned
6061-T6 Al	38.1	No	17.6-23.7	0.63	
6061-T6 Al	38.1	No	1.7-8.0	0.65	

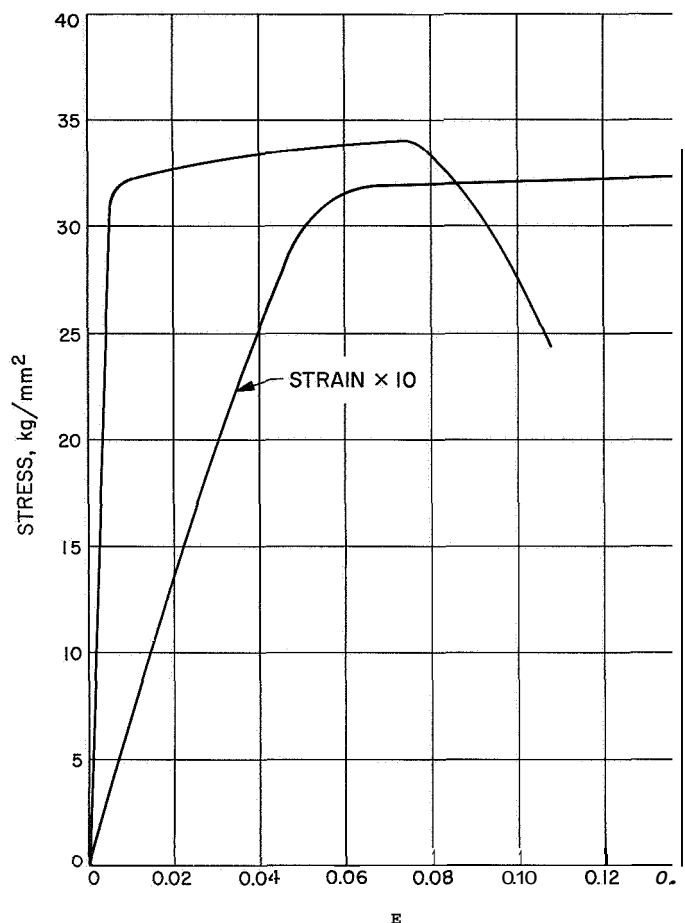


Fig. 1. Stress-strain curve for 6061-T6 aluminum with 38.1 mm gauge length with no contour

These results indicate the capability of the system to measure small stresses and strains accurately. Strains of less than 10^{-4} may be used for meaningful modulus measurements. They also indicate the importance of proper alignment, even with metal specimens where brittleness is not a problem. Note the larger deviations of modulus for specimens not aligned.

Details of the load-measuring subsystem and of the other subsystems in this mechanical testing facility will be published in a formal JPL technical report. A significant amount of this report has been prepared, and it will be completed in the near future.

N67 18322

B. Thermoelectric Power and the Fermi Surface in Silver-Gold Alloys, I. Weinberg

A primary objective in basic materials research is to relate electronic properties to a material suitable for a

given practical application. In this respect, transition elements and transition element alloys are of interest, because of their potential in high temperature applications. A program to determine the essential features in the electronic structure of this type of alloy is now under way. However, with disordered alloys, most of the experimental tools which are useful as Fermi surface probes, such as cyclotron resonance, etc., are inoperative. Thus, one is forced to use, among other things, transport properties, such as thermoelectric power, to probe the electronic structure of disordered alloys.

Thermoelectric power possesses good potential for obtaining information regarding the Fermi surface and other electronic properties in disordered alloys. For this reason, a program, in conjunction with the work on transition metal alloys, has been initiated to study the thermoelectric power in alloys of the noble metals. The primary objective is to determine and extend, using simple alloy systems, the limitations of the thermoelectric power as a Fermi surface probe for ultimate use in the transition metal alloys.

For several reasons, initial work has been directed at the silver-gold alloy system. For example, silver and gold form solid solutions in all proportions with negligible variation in lattice constant from pure silver to pure gold. In addition, silver and gold are monovalent, have the same crystal structure, have nearly the same atomic radii and have the same Fermi energies. Hence, for dilute alloys of gold in silver, one can reasonably expect negligible changes in the Fermi surface with alloying.

With respect to the thermoelectric power, the diffusion component in an alloy is given by the Gorter-Nordheim relation (Refs. 1 and 2)

$$S = S_e^1 + \frac{\rho_0}{\rho} (S_e^0 - S_e^1) \quad (1)$$

where

S = the diffusion thermopower of the alloy

ρ = the electrical resistivity of the alloy

ρ_0 = the resistivity of the pure metal

SQ = the characteristic thermopower of the pure metal

S_e^1 = the characteristic thermopower due to the solute atom

In obtaining Eq. (1) several assumptions are made. The most pertinent assumption, with respect to the present

case, is that which states that the Fermi surface is unaffected by alloying. Close examination of the Gorter-Nordheim relation leads to the conclusion that a plot of S versus $1/\rho$, at constant temperature, should yield a straight line, providing the assumptions are satisfied. As a further check of the validity of Eq. (1), S_e^1 and S_e^0 can be obtained from the aforementioned plot of S versus $1/\rho$.

The thermoelectric power of several dilute Ag-Au alloys is shown in Fig. 2. In Table 2 the resistivities of the alloys, measured at 4.2 and 77.3°K, are shown, together with the pertinent values for silver. To avoid the complicating effects of phonon-drag thermopower, the Gorter-Nordheim plot should be made well above the Debye temperature, in this case 220°K. The required plot, from the data of Fig. 2 and Table 2, is shown in Fig. 3.

From Fig. 3, we obtain the value $S_e^1 = -1.64 \mu\text{V}/^\circ\text{K}$ and $S_e^0 = 1.29 \mu\text{V}/^\circ\text{K}$. The value obtained for S_e^0 is equal, within the experimental error, to the value $1.31 \mu\text{V}/^\circ\text{K}$ obtained for the thermopower of silver at 273°K (Fig. 2).

Table 2. Resistivities of silver and silver-gold alloys at 4.2 and 273°K

Gold concentration, atomic %	Resistivity, $\mu\Omega\text{-cm}$	
	4.2°K	273°K
0.05	0.023	1.48
0.21	0.070	1.52
0.28	0.103	1.54
0.46	0.161	1.62
1.50	0.503	1.99
Pure silver	0.003	1.47

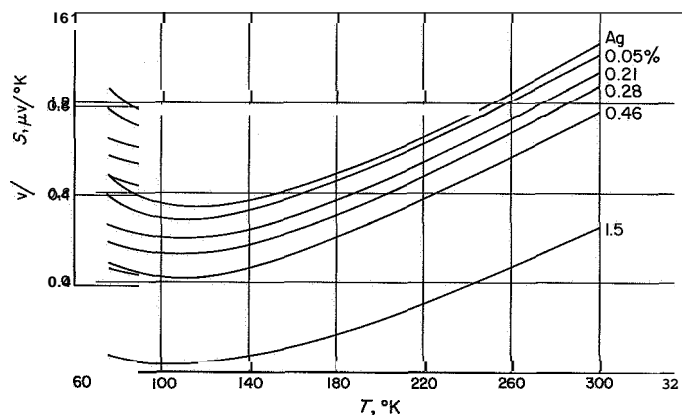


Fig. 2. Thermoelectric power of silver and silver-gold alloys from 77 to 300°K. The percentages listed are in atomic percent gold

At this temperature, S_e^1 can be computed from the Wilson-Mott (Refs. 3 and 4) relation for thermopower and Mott's theory of residual resistivity (Ref. 5), thus

$$S_e^1 = - \frac{\pi^2 k^2 T}{2 |e| E_F} \quad (2)$$

where

k = Boltzmann's constant

T = the absolute temperature

$|e|$ = the absolute value of the electronic charge

E_F = the Fermi energy of silver

Using 5.51 eV for the Fermi energy of silver, the computed result is $S_e^1 = -1.82 \mu\text{V}/^\circ\text{K}$. This latter result is in approximate agreement with the current experimental value.

The good fit of the current data to the Gorter-Nordheim plot confirms the expectation of small, or negligible, Fermi surface changes. These thermopower studies are currently

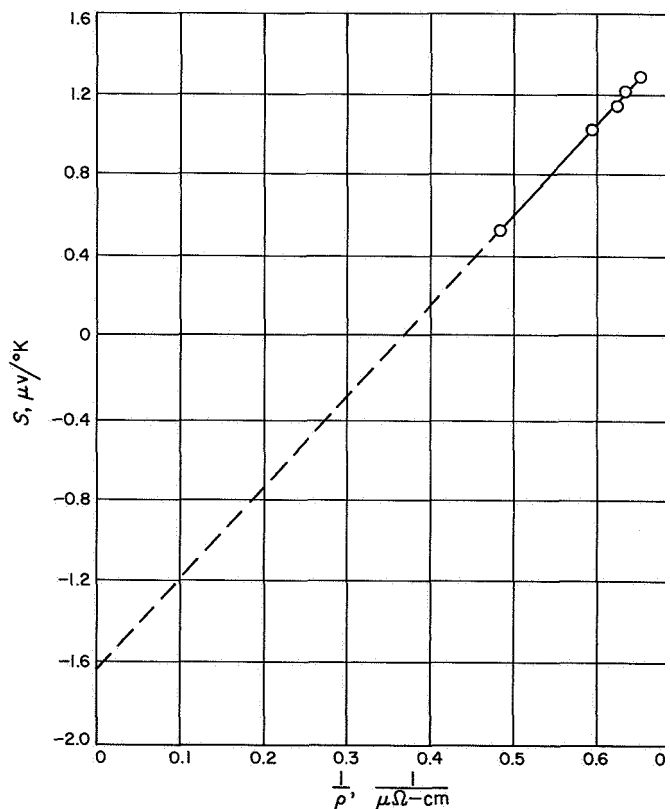


Fig. 3. Gorter-Nordheim plots obtained from the data of Fig. 2 and Table 2

being extended to other temperatures and alloys and significant Fermi surface changes with alloying may be expected. In addition, several experiments designed to probe

the sensitivity of the thermoelectric power to Fermi surface changes are currently under way. The results of these investigations will be reported.

References

1. Nordheim, L., and Gorter, C. J., "Bemerkungen Über Thermokraft Und Widerstand," *Physica*, Vol. 2, p. 383, 1935.
2. Gold, A. V., MacDonald, D. K. C., Pearson, W. B., and Templeton, I. M., "Thermoelectric Power of Pure Copper," *The Philosophical Magazine*, Vol. 5, p. 765, 1960.
3. Wilson, A. H., *Theory of Metals*, Cambridge University Press, 2nd edition, 1953.
4. Mott, N. F., and Jones, H., *Theory of the Properties of Metals and Alloys*, Clarendon Press, Oxford, 1936.
5. Mott, N. F., "The Electrical Resistance of Dilute Solid Solutions," *Proceedings of the Cambridge Philosophical Society*, Vol. 32, p. 281, 1936.

VIII. Applied Mechanics

ENGINEERING MECHANICS DIVISION

N67 18323

A. Structural Analysis and Matrix Interpretive System Computer Program, J. R. Chisholm

The Structural Analysis and Matrix Interpretive System (SAMIS) computer program is a general purpose program to analyze frame and shell type structures. Program development considerations were given to modularization of the program for functionally diverse applications and reduction of errors in program usage. Development of numerical techniques of the finite element method to analyze the more general shell loading cases and non-homogeneous shell constructions is emphasized. Three documents (Refs. 1, 2, and 3) describe, respectively, the programmer aspects, the technical aspects, and the user aspects of the program.

The current version of the SAMIS program includes functional capabilities as follows:

- (1) Capability to generate structural representations composed of bar, beam, plate, and shell elements in any combination. This generation consists of

stiffness; mass; pressure, thermal induced, and inertial loading; and stress matrices. The option of either the potential energy or the classical beam mass matrix representation is provided. Capability to offset element connections to an adjoining structure to represent a layered structure or a stiffened structure and an option to modify the element stiffness matrices to account for displacement discontinuities, such as hinge joints or mono-ball connections, is incorporated in the program.

- (2) Capability to manipulate matrices by the use of any of 16 Fortran II chain links to obtain solutions to static or dynamic structural problems. Capability to solve for frequencies and mode shapes, deflections, reaction forces, stresses or element forces is provided. In addition, nonstructural problems can be solved, such as inverting matrices, determining matrix singularities, etc.
- (3) Capability to efficiently solve matrix problems of 500th order or less. Problems considerably larger

than this have been solved, and the means of obtaining this capability are described in the SAMIS documentation (Refs. 1, 2, and 3). Additionally, band-limited matrices with matrix order less than **10,000** can be inverted; the only size restriction is that the half-bandwidth be less than **200** elements. The half-bandwidth is the number of elements from the diagonal to the last nonzero off-diagonal element in any row of the matrix.

Future modifications and additions to the SAMIS program will provide the capability to solve forced motion problems by the mode superposition method. To effect this change, the appropriate chain **links** will be modified to operate with larger order systems than currently possible, to manipulate matrices with complex arithmetic elements, and to compute damped eigenvectors. In addition, several other detailed program changes will be made that effect program efficiency.

References

1. Melosh, R. J., Diether, P. A., and Brennan, M., *Structural Analysis and Matrix Interpretive System (SAMIS) Program Report*, Technical Memorandum **33-307**, Jet Propulsion Laboratory, Pasadena, October **1966**.
2. Melosh, R. J., Christiansen, H. N., *Structural Analysis and Matrix Interpretive System (SAMIS) Technical Report*, Technical Memorandum **33-311**, Jet Propulsion Laboratory, Pasadena, October **1966**.
3. Lang, T. E., *Structural Analysis and Matrix Interpretive System (SAMIS) User Report*, Technical Memorandum **33-305**, Jet Propulsion Laboratory, Pasadena, October **1966**.

IX. Liquid Propulsion

PROPULSION DIVISION

N67 18324

A. Gas-Side Boundary Phenomena, R. W. Rowley

As a first step in developing an understanding of the relationship between injector design and thrust chamber erosion, an investigation of heat transfer in a spray combustion system has been undertaken. The most recent summary of results of this effort was published in Ref. 1. Presented here is a discussion of some of the physical processes involved in heat transfer between a burning spray and a thrust chamber wall, and a preliminary correlation of some experimental results.

1. Description of Physical Processes

Many liquid rocket engine injectors produce sprays which are not directed entirely parallel to the chamber axis. Depending on the injection method and the propellants used, lateral dispersion of the spray due to jet breakup, jet-on-jet impingement, liquid phase reactions, and the combustion process itself can be expected. In addition, it has become common practice to produce a low mixture ratio "boundary flow" along the chamber wall in order to reduce wall heating and erosion. The dispersion inherent in both main-stream and boundary flows, and the proximity of the boundary flow to the wall,

ensure that some of the propellant strikes the wall while still in the liquid phase. This liquid impingement can be expected to alter the wall temperature from that predicted from purely gas-phase convective heat transfer. If the processes involved in liquid impingement can be controlled and understood, the spray can then be used in a knowing way to reduce the thrust chamber wall temperature. The effects of liquid impingement on the wall may also be of interest in the investigation of combustion-driven waves which produce unstable (i.e., resonant) combustion in liquid rocket engines.

Refs. 2 and 3 presented results of some early studies designed to investigate the effect of injector spray properties on the wall environment. In Ref. 2 the omission of one injector element was shown to produce a notable change in wall heat-transfer rates. In Ref. 3, rearrangement of the elements of a series of ten element injectors was shown to change the erosion patterns of ablative and pyrolytic graphite thrust chambers. Although both studies showed that the environment at the wall was closely related to injector spray properties, in neither case were the mechanisms elucidated. It remains, then, to define the physical processes by which the spray influences wall conditions.

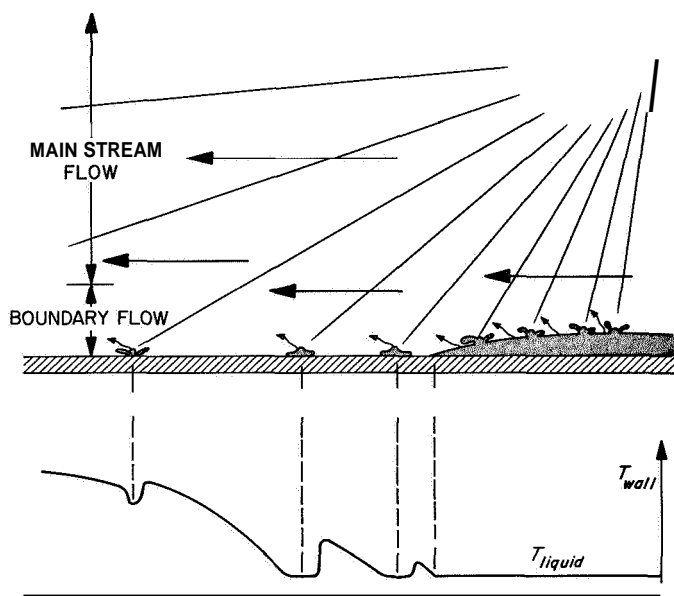


Fig. 1. Schematic of heat transfer from a burning spray

Some effects of impingement of a diverging spray on a thrust chamber wall are sketched (with some artist's license) in Fig. 1. A wide range of wall conditions are possible, depending mainly on the temperature of the wall and on local spray characteristics. As shown at the right of the figure, a liquid film may exist on the wall if droplet impingement rates are high enough, such as very near the injector. This condition is favored by regenerative cooling, which maintains the wall at relatively low temperatures. As the film surface vaporizes under the influence of free-stream heat transfer, the vapors provide a substantial "blocking" or insulating effect at downstream locations. The result is a reduction in heat transferred from combustion products to the wall.

With many of the refractory materials now used for space engine thrust chamber construction, the wall need not be cooled too far below the adiabatic wall temperature in order to remain below the useful temperature limit of the material. In this case, the generation of a continuous liquid film (which always carries the possibility of reducing the engine performance level) would be wasteful of propellant. As shown at the center of Fig. 1, impingement of droplets in numbers insufficient to form a continuous film also results in a cooling effect. If the wall is not too hot, impingement of a drop will temporarily reduce the local wall temperature to the drop temperature. As the small, transient film left by the drop evaporates, the vapors again provide a blocking effect, reducing heat transfer at downstream locations.

At still higher wall temperatures, the droplets vaporize without wetting the wall. This is illustrated at the extreme left of Fig. 1. Various impact phenomena are possible, depending on the wall temperature and the dynamics of droplet impingement. Film boiling, shattering, and rebounding of droplets are possibilities. All are characterized, however, by the generation of vapor at the liquid/wall interface. The blocking effect of this vapor at downstream locations, coupled with the local cooling produced by droplet impingement, result in a reduction in wall temperature from that which would be produced by convective heating alone. Wall temperatures normally encountered in engines using ablative or refractory materials are substantially above the droplet temperatures. Under such conditions, these rapid vaporization phenomena would be expected to be the only ones encountered. However, local areas of lower wall temperature are occasionally observed in engines with nonuniform injector patterns. Thus, droplet impingement over a wide range of wall temperatures must be studied to ensure understanding of wall heat transfer in spray combustion systems.

The cooling effects of droplet impingement may well be observed as far downstream as the nozzle throat. Typical rocket engine injectors produce sprays having a wide distribution of drop sizes. The larger drops, unless shattered, persist far downstream, even in high performance engines. Some of these surviving drops undoubtedly impinge on the converging walls of the nozzle, producing the effects previously described. In addition, the gas phase environment at downstream locations is, in part, determined by reaction products from liquid which strikes the wall at upstream locations. This "boundary flow" mixes very slowly with the freestream, and retains some identity far downstream. Thus, the environment at the wall in the nozzle is related to the wall environment in the combustion chamber, as a result both of flow along the chamber wall and of direct liquid impingement.

A graphic illustration of the effect of liquid impingement on the chamber wall is shown in Fig. 2. This ablative thrust chamber was test-fired for 60 sec with a single-element injector which produced a cone-shaped spray pattern. The uncharred region of the wall, indicating a surface temperature below about 800°F, is aligned with the spray pattern, i.e., with the region of highest spray mass flow rate. This low surface temperature indicates that substantial amounts of liquid impinged on the wall, providing a considerable cooling effect. Adjacent charred areas both upstream and downstream indicate

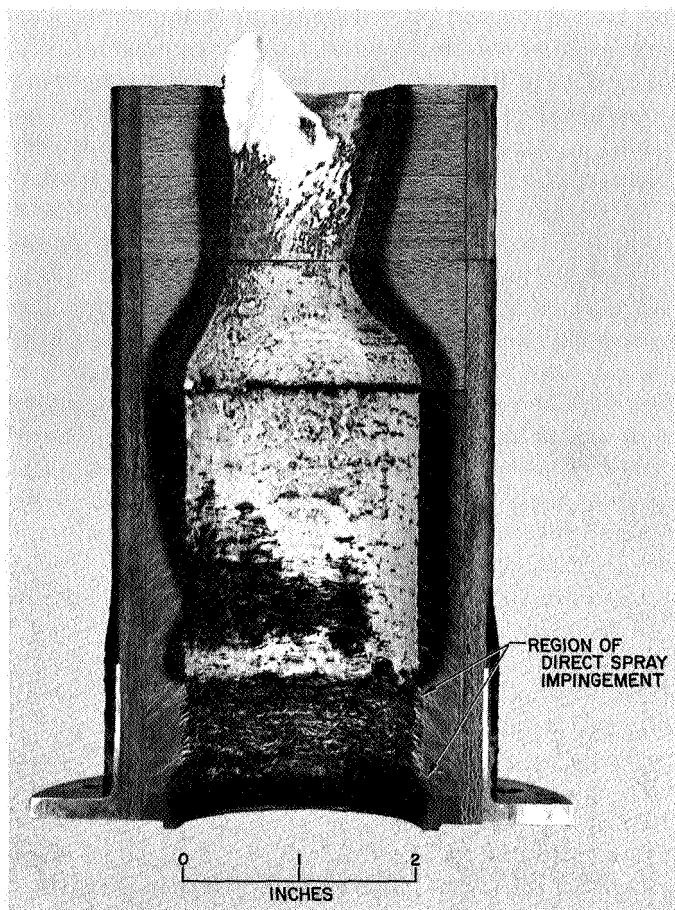


Fig. 2. Sectioned ablative thrust chamber

much higher temperatures; the white coating of melted silica is associated with surface temperatures on the order of 3000 to 4000°F . These high-temperature regions correspond to zones of relatively low spray-impingement rates. The asymmetric erosion of the throat of this thrust chamber also corresponds to a maldistribution of propellant, in this case a circumferential nonuniformity as the result of a structural failure in the injector flow passages during the test. The nonuniform char pattern in the combustion chamber resulted from the same maldistribution. This thrust chamber thus demonstrates two extremes of injector related heat transfer; an area overcooled by impinging too much liquid on the wall, and an area underprotected to the extent that rapid erosion of the wall occurred.

Heat transfer to a rocket engine **thrust** chamber can thus be viewed as a combination of convective (and, in some cases, radiative) heating from freestream combustion products, and heating or cooling as the result of droplet impingement. A complete description of the influ-

ence of the droplets in a burning spray on wall heat transfer must then include at least the following characteristics:

- (1) The properties of the spray at injection, including drop size distribution, drop number density (or local **mass** flow rate), and drop temperature.
- (2) The effect of spray combustion processes on the spray characteristics. The droplets comprising the spray burn (and, in some cases, shatter) at a rate dependent on the combustion chamber environment, including chamber pressure, local gas velocity, and gas temperature. Also, the droplet trajectories are altered as a result of aerodynamic forces.
- (3) Items 1 and 2 above determine the characteristics of the spray as it arrives at the wall, i.e., a new drop-size distribution, new number density or local mass flow rate, new droplet trajectories, and new droplet temperatures.
- (4) Impact phenomena as governed by droplet velocity and angle of impingement, liquid properties such as viscosity and surface tension, and chemical reactivity of the droplet at the wall (particularly important if the droplets are composed of mixed fuel and oxidizer or a monopropellant).
- (5) Properties of the wall, such as wall temperature and thermal diffusivity.

2. Experimental Results

The nature of the processes just described suggests that empirical correlations of spray combustion heat transfer may be more easily obtained than even a relatively simple analytical description. Accordingly, a preliminary correlation of data obtained with the "enclosed spray combustor" (Ref. 1) is presented here. A very simple model for heat transfer is used, in which convective heat transfer from gaseous combustion products and heat transfer from impinging, partially consumed droplets are considered as separate, noninteracting processes. The experimental data are for stagnation heat transfer to a flat plate placed in a burning spray. The spray was formed by impinging jets of methanol and nitric acid. Stagnation flow was achieved by placing the plate perpendicular to the spray resultant momentum line. The spray was burned at atmospheric pressure, the resulting combustion being leisurely enough to allow the insertion of much less sophisticated heat transfer probes than would be required in a spray burning at rocket engine pressure

levels. Heat transfer rates were determined at various distances from the jet impingement point, using a transient temperature measuring technique (Ref. 4).

Shown in Fig. 3 is an experimental curve of heat transfer as a function of distance from the jet impingement point.¹ Also shown are calculated curves based on the assumption outlined above, namely that the total heat transfer rate is the sum of calculated contributions of liquid and gas phase heat transfer. In this case, heat was transferred from the droplets to the heat transfer surface. Heating resulted from the droplets being at temperatures higher than the wall temperature as a consequence of liquid phase reactions between fuel and oxidizer. The contributions of liquid and gas phase heat transfer q were calculated from the following relationships:

$$q_{gas} = K(\dot{m}_{gas})^{1/2}(T_{gas} - T_{wall})$$

$$q_{liquid} = K'(\dot{m}_{liquid})^{1/2}(T_{liquid} - T_{wall})$$

As indicated the film coefficient for gas-phase heat transfer was assumed proportional to the one-dimensional mass

¹As a result of an error in data reduction, similar data presented in Refs. 1 and 4 are incorrect. Fig. 4 of Ref. 1, which indicates a varying film coefficient during each test, is also incorrect. Properly reduced data show a constant film coefficient.

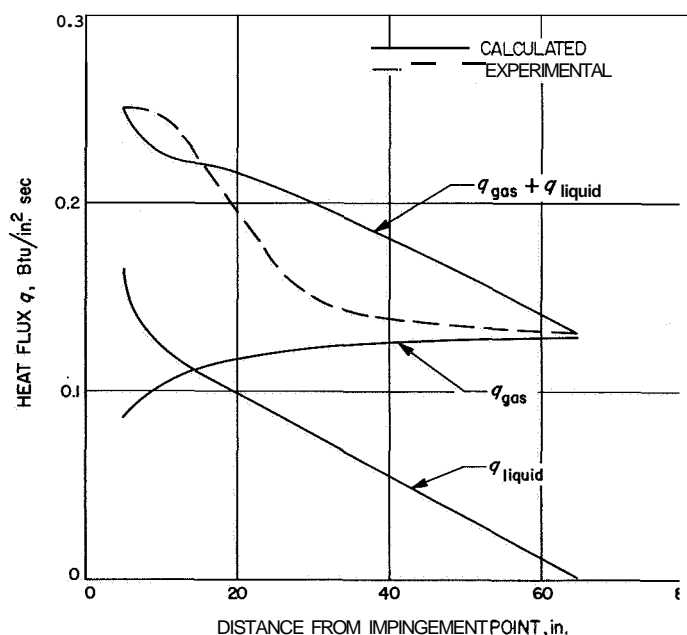


Fig. 3. Stagnation heat transfer in a burning spray

flow rate of burned propellant (\dot{m}_{gas}). The driving temperature used was the equilibrium gas temperature. The film coefficient for liquid phase heat transfer was assumed proportional to the local mass flow rate remaining unburned in a spray which diverges from the impingement point (\dot{m}_{liquid}). The droplet trajectories were assumed to be straight lines. The driving temperature for liquid phase heat transfer was taken as the measured liquid film temperature reported in Ref. 1. This film temperature is assumed identical to the droplet temperature. The exponent of one-half to which both liquid and gas phase flow rates are raised is that predicted for stagnation flow (Ref. 5). The spray mass flow rate near the impingement point was assumed the same as that measured in a spray formed in identical fashion by nonreacting fluids. The constants K and K' used in the expressions for film coefficients were arbitrarily picked to fit the data. All property and dimensional effects are included in these constants and are assumed invariant with distance (and, hence, with the degree of completion of combustion).

One of the biggest uncertainties in any spray combustion analysis is associated with predicting the vaporization rate of the spray. In the present case, a calculated vaporization rate was used to determine the relative proportions of the liquid and gas phases. Vaporization was assumed to be controlled by heat transfer to the droplets; the effect of mass transfer was ignored. The initial drop sizes were taken from a logarithmic-normal distribution with a mass-median drop diameter of 360μ and a standard deviation of 1.67. Nine drop-size groups containing equal mass were used. The droplets were assumed to be mixtures of fuel, oxidizer, and products of liquid phase reactions. However, droplet properties were based on average properties of

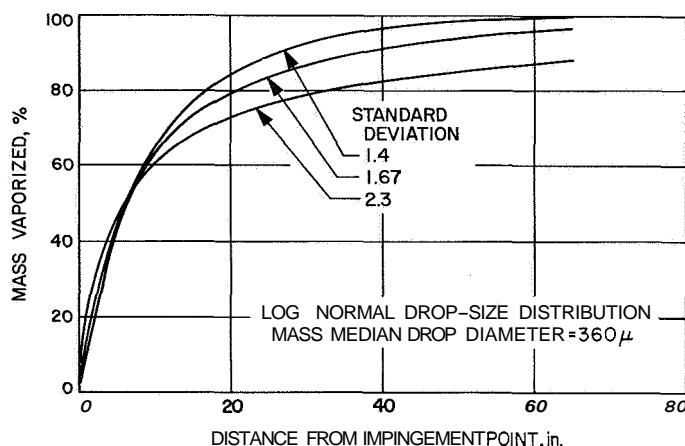


Fig. 4. Effect of drop size distribution on vaporization rate

the mixture, and the drop was treated as if it were a single component. In particular, selective vaporization of low boiling components was ignored. Vaporization and combustion were assumed to occur simultaneously. The conditions chosen resulted in a predicted 97% of the injected mass being vaporized at the last downstream location at which heat-transfer measurements were made (65 in.). However, as shown in Fig. 4, small changes in the initial drop-size distribution assumed can significantly affect the vaporization rate. The three vaporization profiles plotted are for a single mass-median drop size, and demonstrate the effect of relatively small changes in the standard deviation of the spray. (The standard deviation is a measure of the *range* of drop sizes present in a spray.) It follows that heat-transfer predictions, such as those shown in Fig. 3, are heavily dependent on the vaporization rate, and, hence, on the spray drop-size distribution.

3. Future Effort

Extension of this crude correlation to a more useful Nusselt number form is desirable. In the case of droplet heat transfer, such a correlation can be based on a characteristic mean diameter of the spray. For example, in Ref. 6, the area/number mean diameter D_{20} was used as a characteristic dimension. Again, however, any local characteristic diameter chosen is strongly dependent on the vaporization rate of the spray. Accordingly, work is currently under way to predict more accurately the drop size distribution produced by the injector element used in these experiments. Results will be reported in a future SPS. In addition, the computer program used to predict the spray vaporization rate will be modified to account for mass transfer effects. Vaporization of the liquid film which forms on the heat-transfer surface at low surface temperatures will also be included in the analysis.

B. The Reaction Between Oxygen Difluoride and Diborane, R. A. Rhein

1. Preliminary Results

a. Introduction. The reaction between OF₂ and B₂H₆ was selected for study because, when used as spacecraft propellants, this system can provide superior performance over other fuel/oxidizer combinations. Based on the calculated maximum specific impulse (1000 to 14.7 psi) of 368 sec for this system, mission studies (Ref. 7) have indicated that this combination can provide a payload capability exceeding that of F₂/H₂ and O₂/H₂ and, in addition, has decided advantages in handling and space storability. Both OF₂ and B₂H₆ are space storable, have a compatible

liquid range, and are hypergolic, with rather short ignition delay times, at sea level and at high altitudes.

The purpose of this program is to investigate the reaction between OF₂ and B₂H₆ in detail and to describe an appropriate mechanism for this reaction. **This report** discusses the results from some preliminary experiments, designed to provide both a qualitative understanding of the OF₂/B₂H₆ reaction and a guide to further experiments.

In these experiments, the partial pressures of OF₂ or B₂H₆ were 20 torr, or less. The reacting mixture was studied primarily at ambient temperatures, although some experiments were conducted at other temperatures, by the following methods:

- (1) Visual observations of the OF₂/B₂H₆ mixture, contained in pyrex bulbs, while maintaining the bulbs at ambient or lower temperatures.
- (2) Gas composition as a function of time at ambient temperatures was determined from infrared spectra.
- (3) Pressure-temperature relationships of the reacting gas mixtures at low pressures were obtained during a transient heat-up cycle of the mixture contained in a metal "reactor."

b. Experimental methods and results. The initial experiments, conducted in pyrex bulbs that were modified in various ways, were designed to gain only a qualitative, general understanding of the reaction. The next series of experiments were conducted in gas cells so that the gas mixtures could be monitored by infrared spectrometry. The change in composition with time provided the basis for estimates of the change, at ambient temperatures, of the partial pressures of the reactants and the products. In the concluding experiment, the pressure and temperature of an equimolar OF₂/B₂H₆ mixture were simultaneously measured while the mixture was being heated from ambient to 260°C. This experiment was performed to determine if there were any temperature interval in which the total pressure changed rapidly, the inference being that a departure from a linear pressure-temperature relation would indicate the incidence and/or change of a reaction rate.

The B₂H₆² was purified by, first, cooling to -195°C and pumping on it to remove H₂. Then, after warming to -160°C (using an isopentane slush bath), the B₂H₆ was

²B₂H₆ was supplied by Callery Chemical Co.

pumped out and collected in a trap held at -195°C . No impurities could be detected either from vapor pressure measurements, infrared spectroscopy, or mass spectrometry. The OF_2 ³ was purified by distillation in an apparatus described by Dr. F. I. Metz (Ref. 8). Gas density, infrared spectrometry, and vapor pressure indicated negligible impurities in the purified material.

The Pyrex bulbs used for the ambient temperature experiments were made from 100-ml round-bottom flasks, modified as required for the individual experiments. Gas pressure in the bulbs over the range of 0–20 torr were measured by a diaphragm gage,⁴ pressures to 760 torr were measured by a Heise bourdon tube gage.

Visual observations. The results from preliminary investigations of the reaction at OF_2 and B_2H_6 can be summarized as follows:

(1) There was no evidence of rapid reaction when B_2H_6 was added to OF_2 , for partial pressures of 20 torr or less. The initial partial pressures for three different experiments were:

OF_2 , 20 torr	B_2H_6 , 20 torr
OF_2 , 10 torr	B_2H_6 , 19 torr
OF_2 , 7.9 torr	B_2H_6 , 7.4 torr

(2) There was no explosive pressure change, or other evidence of reaction, when a spark was passed through a mixture of 7.9-torr OF_2 and 7.4-torr B_2H_6 . In this experiment, the flask was equipped with two tungsten leads about 0.5 in. apart at the center, and the spark was produced by a Tesla-coil discharge.

(3) Mixtures of OF_2 and B_2H_6 exploded when a spot about 0.25-in. D on the flask was heated to glowing by a glassblower's torch. In one experiment, when the partial pressures were 7.9-torr OF_2 and 7.9-torr B_2H_6 , the mixture exploded with a "ping," and the pressure jumped to 35 torr. In another experiment a mixture of 20-torr OF_2 and 20-torr B_2H_6 exploded when spot-heated, and a yellowish brown oily residue was noted on the inside surface of the flask after the explosion.

(4) In one experiment, as B_2H_6 was added to 20-torr OF_2 , the mixture ignited and burned as the B_2H_6 was

being added; a greenish flame was observed to stabilize itself at the tip of the lead-in tube (an 8-mm pyrex tube extending to the center of the flask). This was the only example of gas-phase hypergolicity noted in this experimental sequence.

(5) When OF_2 was inadvertently condensed on solid B_2H_6 at -195°C , there was no observable reaction. The mixture exploded, however, when it began to warm up. In order to repeat the above experiment, 5.4-torr OF_2 and 5.4-torr B_2H_6 , in a 100-ml spherical flask, were condensed into the tip of a small cold finger, of about 2 mm ID, which was immersed in liquid nitrogen at -195°C . The solid B_2H_6 was seen to coexist with the liquid OF_2 at -195°C . When the liquid nitrogen was removed, allowing the tip to warm, the tip exploded loudly very soon afterward. This result agrees with a reported (Ref. 9) explosion resulting when liquid B_2H_6 , at -169°C , was dropped upon liquid OF_2 , kept at -195°C .

(6) In a brief experiment to determine whether or not the explosive reactions described in (4) and (5) above were the consequence of a low-temperature reaction forming an unstable compound, the following experiment was conducted: OF_2 and B_2H_6 were condensed together in the tip (i.e., bottom 0.25 in.) of a cold finger cooled to -195°C , where the solid B_2H_6 was in intimate contact with the liquid OF_2 . The tip was then warmed to -183°C (by immersing the tip in liquid oxygen). The pressure rose to 5.5 mm, corresponding to the vapor pressure of OF_2 , and also corresponding to the amount of OF_2 originally present (at -183°C , the vapor pressure of B_2H_6 is negligible, Ref. 10). The OF_2 was pumped out, and the tip was allowed to warm to the ambient temperature. The pressure rose to 5.0 torr, corresponding to the B_2H_6 originally present, indicating that essentially no reaction had occurred.

(7) In contrast to the experiments described above, it was shown that mixtures of OF_2 + B_2H_6 can be cooled to -195°C (LN, temp) without initiating a reaction. This was shown in an experiment using a 100-ml round-bottom flask with its neck sealed off at the bottom to form a tube on the flask approximately 12–14 mm ID and 30–35 mm long. When this flask, containing a mixture with initial partial pressures of 5.0-torr OF_2 and 5.4-torr B_2H_6 , was cooled to -195°C by total immersion in liquid nitrogen, and subsequently allowed to warm to the ambient temperature, there was no evidence of reaction, as the total pressure returned to its initial value. Then the bottom 15–20 mm of the tube on the flask was cooled in liquid nitrogen and the pressure in the flask reduced to somewhat less than 1 torr, corresponding to the vapor pressure

³ OF_2 was supplied by Allied Chemical Co.

⁴Wallace and Tiernan, Inc., Catalog FA 141700, 0–20 torr range.

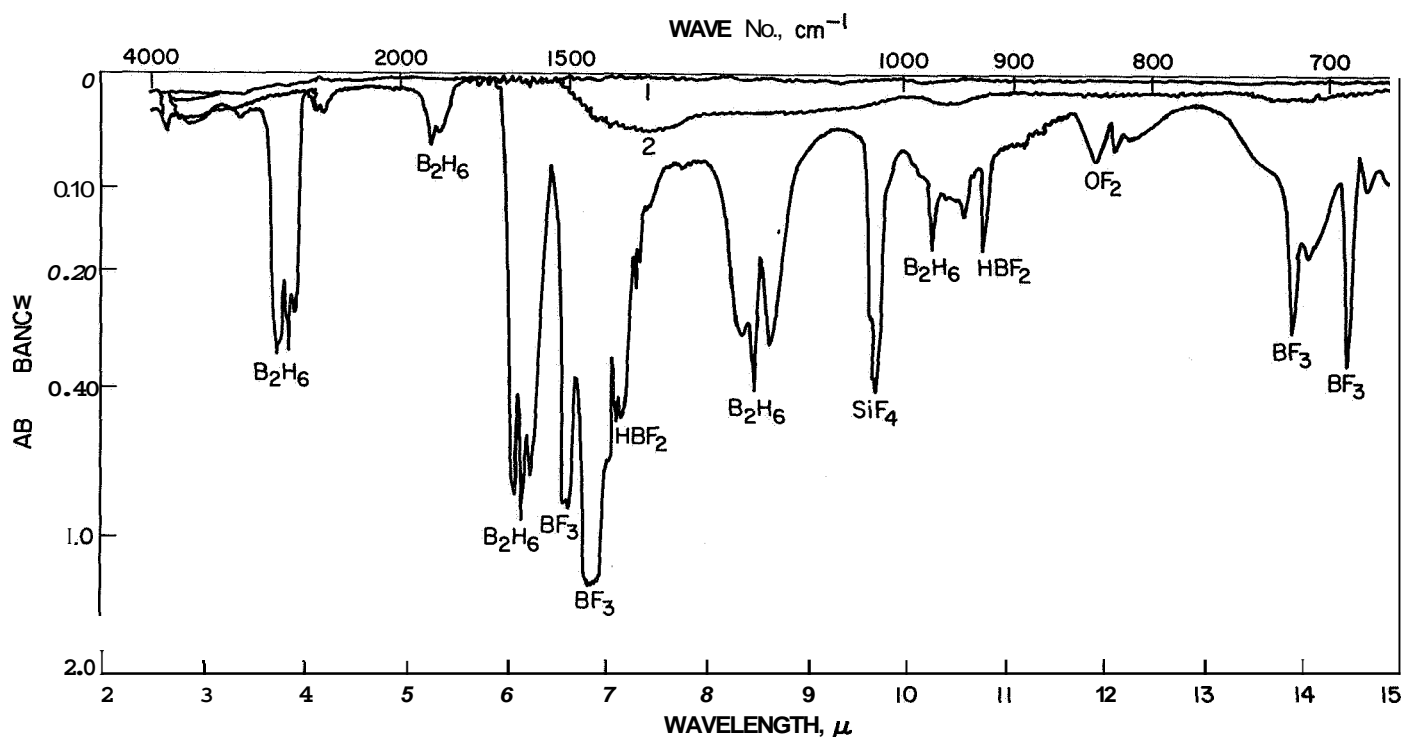


Fig. 5. Infrared spectrum of product composition with 20-torr OF_2 and 20-torr B_2H_6 .

of OF_2 at that temperature. Solid B_2H_6 was seen distributed about the cold portion of the tube. When allowed to warm to ambient, the total pressure returned to its initial value. Therefore, mixtures of OF_2 and B_2H_6 can be cooled to -195°C safely (i.e., without reaction) if sufficient area of the flask is cooled. Presumably this is so because the B_2H_6 is distributed over a relatively large area as it condenses and subsequently freezes; hence, only a very small amount of B_2H_6 and OF_2 are in contact.

Composition measurements with an infrared spectrometer. The product composition for a typical $\text{OF}_2/\text{B}_2\text{H}_6$ reaction was determined from an infrared spectrometer. In this particular experiment, the infrared spectrum was taken 17 hr after the preparation of a mixture consisting of partial pressures of 20-torr OF_2 and 20-torr B_2H_6 . This spectrum is shown in Fig. 5. The compounds responsible for each absorption peak were identified with the help of the information available in the literature as summarized in Table 1 and so designated on the figure.

The identifiable compounds included B_2H_6 , OF_2 , BF_3 , HBF_2 , and SiF_4 . The SiF_4 was presumably formed either by reaction of the OF_2 with the pyrex container during storage prior to the experiment, or between a product of the $\text{OF}_2/\text{B}_2\text{H}_6$ reaction and the wall of the infrared spectrometer cell. The BF_3 was apparently the major

Table 1. Infrared absorption peaks

Compound	Wavelength of absorption peak, μ	Ref.
B_2H_6	3.75, 3.88, 3.92 (s); 5.25, 5.35 (m); 6.10, 6.16, 6.26 (vs); 8.32, 8.50, 8.61 (s); 10.26 (m)	13
BF_3	6.61, 6.67 (s); 6.84, 6.90 (vs); 7.22, 7.33, 7.44 (s); 13.90 (s); 14.46 (s)	14
OF_2	5.70, 5.76 (m); 10.65, 11.10 (m); 11.92, 12.10, 12.26 (s)	15
SiF_4	8.32 (m); 9.70 (vs)	15
HBF_2	6.68, 6.84, 6.87 (s); 7.07, 7.12, 7.19 (vs); 8.33 (m); 10.60 (m); 10.82 (s)	16
B_2F_4	7.07 (s); 7.29 (vs); 8.65, 8.64 (vs)	17
B_2O_3	Broad, 7.5 max (s); broad, 14.0 max (m)	18

A preliminary estimate of the partial pressures of OF_2 , B_2H_6 , and BF_3 as a function of elapsed time from the addition of OF_2 to B_2H_6 is shown on Fig. 6. For this estimate the partial pressures of the constituents were assumed to

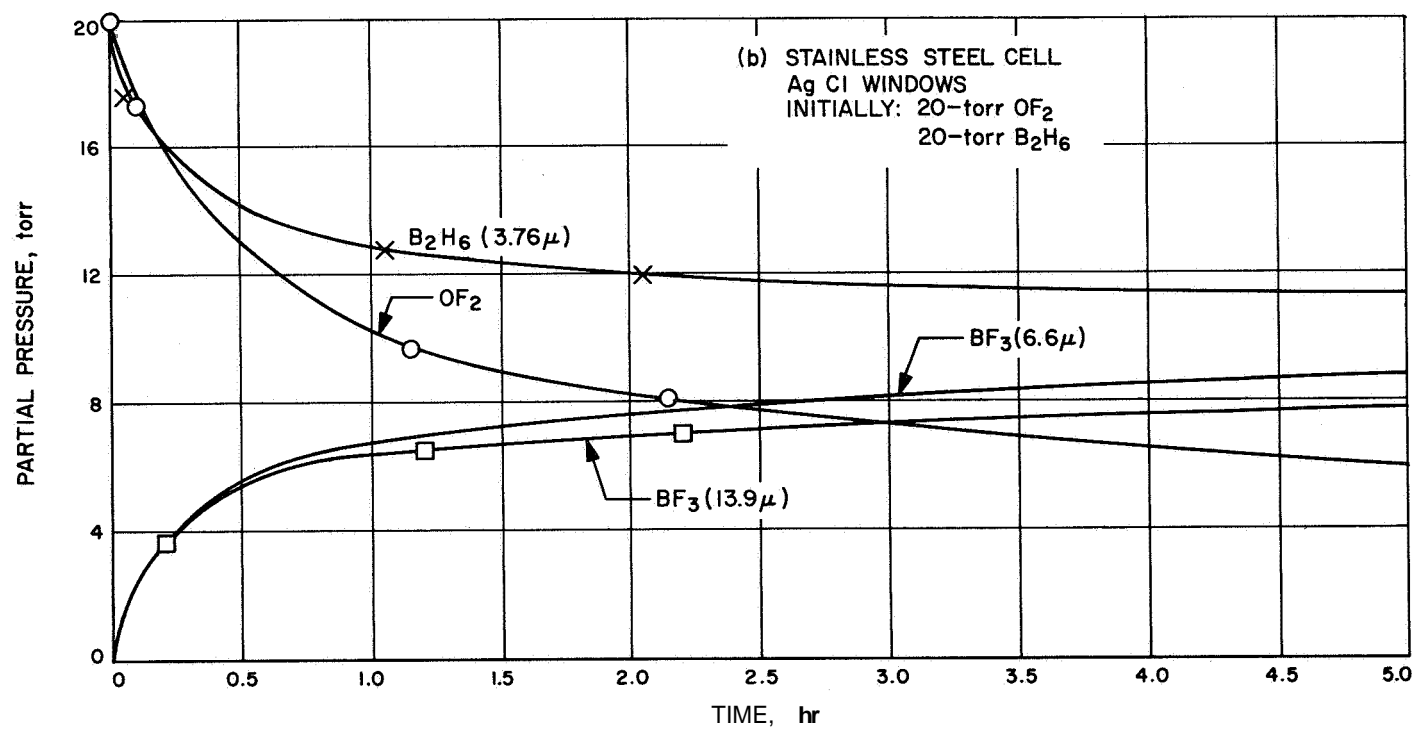
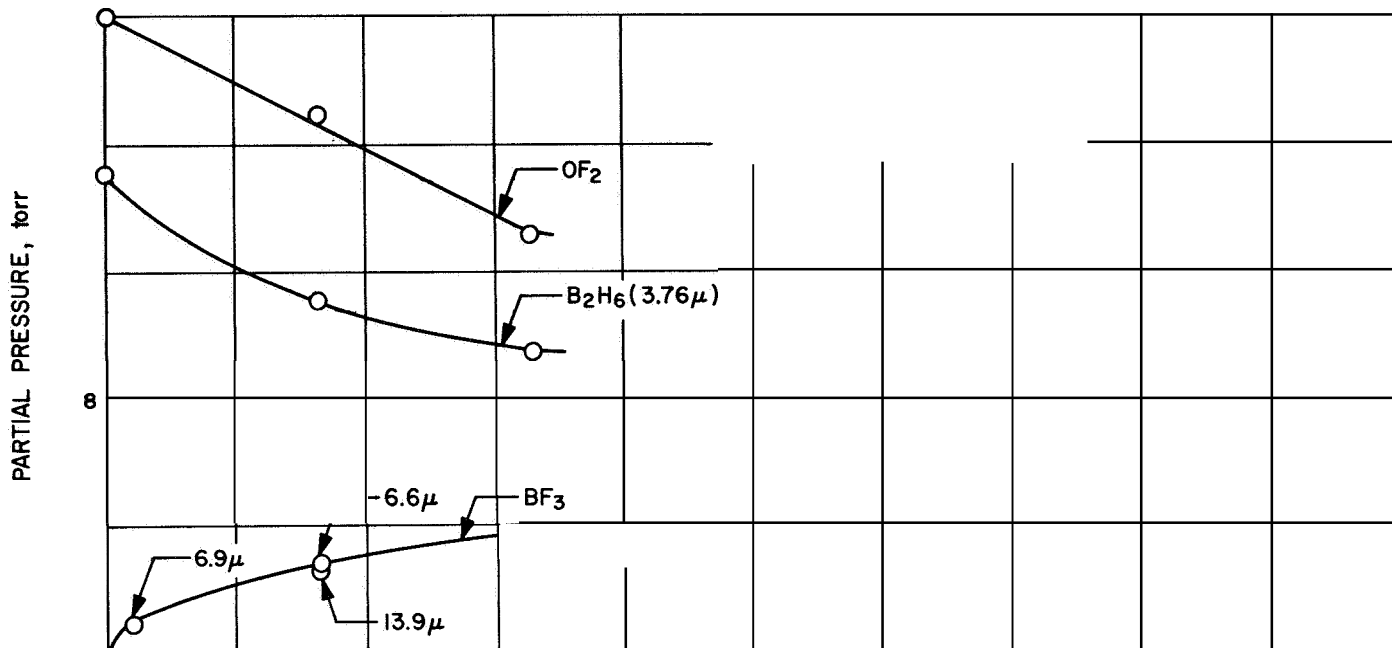


Fig. 6. Calculated concentration versus time for OF_2 , B_2H_6 , and BF_3 resulting from the reaction of OF_2 and B_2H_6 at ambient temperature

be proportional to their infrared absorbance. The estimation of the partial pressures of the constituents would be in error because of light scattering and pressure broadening as indicated in Ref. 11. Although the pressure broadening depends upon the nature of the added gas and its pressure, and for quantitative work should not be regarded as negligible (for pressure broadening of several gases on the infrared spectrum of B_2H_6 , see Ref. 12), it was not accounted for here. Consequently, the estimation of the partial pressures are subject to refinement.

The partial pressures of each constituent were determined from measurements of the absorbance of the unknown mixtures and experimentally determined absorptivities of the pure compounds of BF_3 ⁵ and B_2H_6 . The latter were determined with the aid of the relation $A = abc$, where A is the experimentally measured absorbance, a the absorptivity, b the pathlength, and c the concentration or partial pressure. Absorptivities were determined for these several compounds at several pressures and at different wavelengths, as summarized in Table 2. These values are also subject to refinement, since only a relatively few measurements were made.

The partial pressures (OF_2 , B_2H_6 , and BF_3) were assumed to be proportional to the differential absorbance, D , where $D = A - A_0$; A was the measured absorbance, and A_0 was the absorbance for an evacuated cell ($A_0 > 0$ indicates nonvolatile absorbing species on the windows). In Tables 3 and 4 are presented the results of two experi-

ments at ambient temperatures. In Table 3 the partial pressures were initially 20-torr OF_2 and 5-torr B_2H_6 (pyrex cell, AgCl windows) and in Table 4 the partial pressures were initially 20-torr OF_2 and 20-torr B_2H_6 (stainless steel cell, AgCl windows). Presented in Table 3 and 4 are the values of D , calculated from measured values

OR		B_2H_6		BF_3	
Wave-length, μ	a , cm^{-1} torr $^{-1}$	Wave-length, μ	a , cm^{-1} torr $^{-1}$	Wave-length, μ	a , cm^{-1} torr $^{-1}$
11.9	$1.83 \pm 0.03 \times 10^3$	3.76	$3.1 \pm 0.1 \times 10^3$	6.6	8.1 ± 0.02
				6.9	19.4 ^a
				13.9	3.7 ± 0.6

Table 3. Initial partial pressures — 15-torr B_2H_6 , 20-torr OF_2 ,

lime, hr	OF_2		B_2H_6		BF_3 (product)		
	D^a	c, torr	D^b	c, torr	Wave-length, μ	D	c, torr
0	—	20	—	15	—	—	0
0.04	—	—	—	—	6.9	0.19	0.98
0.33	0.30	16.5	0.36	11.1	6.6	0.21	2.6
0.66	0.24	13.2	0.31	9.6	6.6	0.31	3.8
0.33	—	—	—	—	13.9	0.10	2.7
0.66	—	—	—	—	13.9	0.14	3.8

^a A_0 11.9 μ
^b A_0 3.76 μ

*Produced by The Matheson Company.

Table 4. Initial partial pressures — 20 torr B_2H_6 , 20 torr OF_2 ,

OF_2			B_2H_6			BF_3 (product)			
lime, hr	D^a	c, torr	lime, hr	D^b	c, torr	Time, hr	Wavelength, μ	D	c, torr
0	—	20.0	0	—	20.0	0	—	—	0
0.16	0.305	16.8	0.05	0.57	17.6	0.09	6.6	0.215	2.6
						0.19	13.9	0.137	3.7
1.16	0.177	9.7	1.05	0.415	12.8	1.09	6.6	0.56	6.9
						1.19	13.9	0.24	6.5
2.16	0.147	8.1	2.05	0.39	12.0	2.09	6.6	0.63	7.7
						2.19	13.9	0.26	7.0
5.16	0.110	6.0	5.05	0.37	11.4	5.09	6.6	0.72	8.9
						5.19	13.9	0.29	7.8
17.16	0.062	3.4	17.05	0.323	10.0	17.09	6.6	0.79	9.7
						17.19	13.9	0.27	7.8

of A and A_0 , and the calculated partial pressures for OF_2 , B_2H_6 , and BF_3 . The data from Table 3 and 4 were also plotted in Fig. 6, where it can be seen that the rate of appearance of BF_3 continually decreases with time. It is noted that this experiment clearly indicated that reaction rates are finite but are probably too slow to have been detected in the preliminary experiments.

The OF_2/B_2H_6 reaction at elevated temperatures. The correlation between the temperature and total pressure of the OF_2/B_2H_6 mixture as it was heated from ambient to $260^\circ C$ has been utilized to indicate the reactivity of the mixture. Since a nonreacting mixture (or a mixture where the total number of moles of volatile products were equal to the number of moles of reactants) would exhibit a linear relationship between temperature and pressure (Charles' Law), any noticeable deviation from a linear temperature-pressure relationship would indicate that a reaction occurred. In addition, the pressure measurement would show the total number of moles of gaseous species present.

The temperature-pressure correlation for a typical $OF_2 + B_2H_6$ mixture was obtained by heating a reactor made of nickel 0.125 in. thick, 7.5 in. long, and 4.5 in. in diameter. This can had three thermocouple wells extending radially inward 0.75 in. from the wall and positioned in the axial direction at the center and 0.5 in. from the ends. The top and bottom were each heated by two concentric ring heaters.⁶ The sides were heated by five cylindrical band heaters.⁷ This reactor was placed within a second vessel 9.625 in. D X 11 in. long, and the resulting annular space was filled with insulation.⁸ The voltages to the several heaters were individually varied with auto-transformers to provide controlled heating over the surface of the can. The pressure in the reactor was measured by a transducer,⁹ and its analog displayed, along with the thermocouple output, on an x-y recorder. Preliminary experiments indicated that the three thermocouples indicated very nearly the same temperature over the entire temperature range of operation. Typical full power heating and subsequent cooling curves for the evacuated reactor are shown in Fig. 7. It is assumed for subsequent experiments that small quantities of gas in the reactor will be in thermal equilibrium with the wall.

⁶Chromolox ring heating elements (inner, No. A-00, 120 v, 200 w; outer No. A-40, 120 v, 750 w).

⁷Rama-band heaters, 120 v, 45 w.

⁸Fiberfax Ceramic Blanket, Cat. No. XSWF, The Carborndum Co.

⁹Statham Model 11147, Spec. PA 731TC-2-350, 0-2 psia, 5 v max.

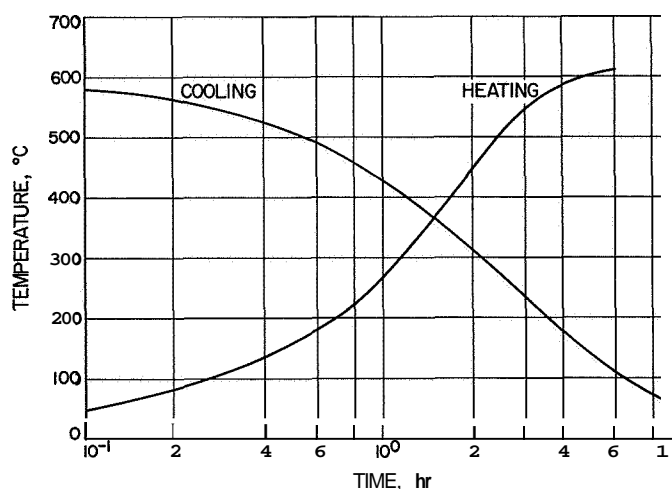


Fig. 7. Temperature versus time for heating at full power and for cooling of a nickel reactor

In order to develop an appropriate interpretation of the state properties produced by the reaction that might occur between OF_2 and B_2H_6 at elevated temperatures, a mixture with 20 torr each of the reactants and mixtures of 20 torr of each of the reactant with 20 torr of inert argon were formed. Each mixture was then subjected to the full-power heating cycle represented by Fig. 7 and the simultaneous change in state properties was recorded. These data are presented in Fig. 8 where they are compared with a calculated curve for a perfect gas.

It was found that the pressure-temperature relationship of the OF_2/Ar mixture followed the calculated curve for the inert gas, indicating that the OF_2 decomposition was negligible. However, similar data for the B_2H_6/Ar mixture indicated appreciable decomposition of the B_2H_6 in the temperature range from 120 to $170^\circ C$. The decline in the B_2H_6 decomposition rate at approximately $173^\circ C$ was probably due to the completion of the B_2H_6 decomposition at that temperature. A qualitative feeling for the complexity of the B_2H_6/OF_2 reaction can be obtained by comparing the temperature-pressure relationship of the B_2H_6/OF_2 mixture with that of the B_2H_6/Ar mixture. During the part of the heating cycle from 25 to $60^\circ C$, the reaction rate of the B_2H_6/OF_2 mixture was somewhat greater than the rate of decomposition of B_2H_6 in the B_2H_6/Ar mixture. From 60 to $80^\circ C$ the OF_2/B_2H_6 reaction was appreciably more rapid than the B_2H_6 decomposition. Above approximately $120^\circ C$ the B_2H_6 decomposition rate was more rapid than the B_2H_6/OF_2 reaction. The OF_2/B_2H_6 mixture followed a complex reaction path for temperatures up to about $220^\circ C$, although above that temperature the reaction appears to have nearly ceased.

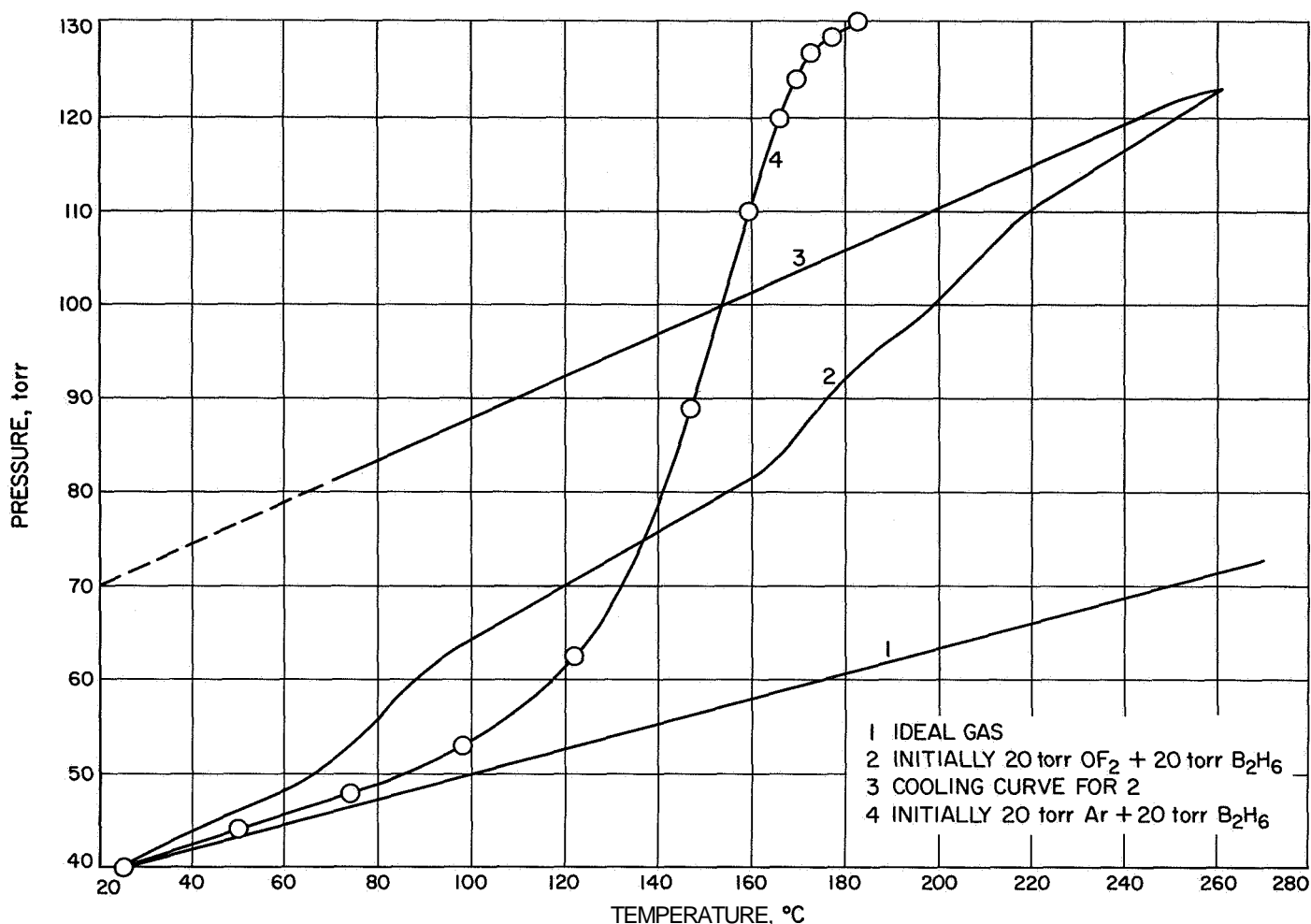
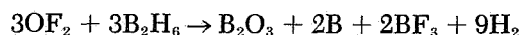


Fig. 8. Pressure-temperature relations for gas heated in nickel reactor

There does not appear to be any simple relation between B₂H₆ decomposition and the B₂H₆/OF₂ reaction. The linear temperature-pressure relationship along the cooling curve indicated that there was no significant reaction during the cooling cycle and permitted an extrapolation from 74°C (where the volatile contents were withdrawn for analysis) to 25°C (where the corresponding pressure for the new equilibrium composition for the reactants is shown to be 71 torr).

In order to determine the composition of these non-condensable reaction products, the reactor containing the products from the OF₂-B₂H₆ reaction was opened to an evacuated bulb through a cold trap held at -195°C. It was found by mass spectral analysis¹⁰ that better than 99% of the material transferred to the bulb was H₂. An infrared spectrum of a sample of the constituents retained

in the cold trap is shown in Fig. 9. Identifiable compounds included BF₃, HBF₄, and SiF₄. A peak at 8.7 μ was attributed to B₂F₄, but that identification was uncertain. BF₃ was definitely the predominant reaction product. If the reaction between OF₂ and B₂H₆ were assumed to be



then the calculated final pressure, for 40-torr initial pressure, would be 73.3 torr, a value very close to the observed 71 torr. The reaction equation assumed that nonvolatile boron and B₂O₃ would have been formed as products of the B₂H₆/OF₂ reaction. This was verified experimentally when 200 mm of F₂ was added to the evacuated reaction heating the reactor to 600°C, and pumping the resulting gases out through a pyrex trap indicated the pressure of BF₃ and SiF₄ (the latter resulting from the reaction of fluorine with the pyrex). The BF₃ must have come from nonvolatile materials in the reactor by such reactions as

¹⁰Performed at JPL by M. Frech.

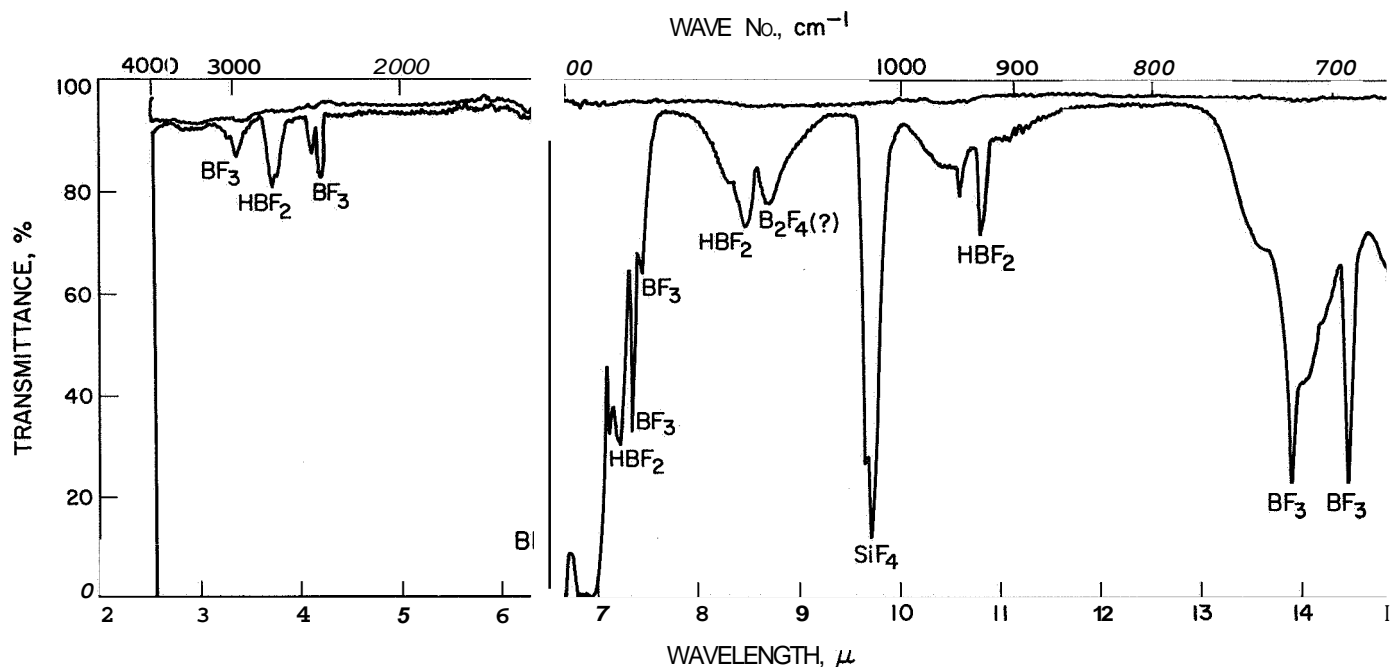
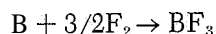
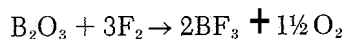


Fig. 9. Infrared spectrum from the product of reaction of OF_2 and B_2H_6 heated in nickel reactor



and its existence serves to substantiate the reaction equation noted above. The composition of the solid materials is likely to be more complex than a mixture of B and B_2O_3 and may well consist of polymeric materials containing boron, hydrogen, and oxygen. Further studies are required to determine their nature.

c. Conclusion. OF_2 and B_2H_6 react slowly at ambient temperatures and low pressures to produce mostly BF_3 and probably H_2 as volatile products. Mixtures of OF_2 and B_2H_6 can coexist at -195°C , but these mixtures can explode while warming to ambient. When these compounds are heated together, nonvolatile boron compounds, along with BF_3 , H_2 and smaller amounts of HBF_2 , and possibly B_2F_4 are produced. The reaction of an equimolar mixture of OF_2 and B_2H_6 may be tentatively represented as



C. Liquid Propulsion Systems

1. Introduction, L. R. Toth

The Advanced Liquid Propulsion Systems program is investigating selected problems generated by spacecraft

operational requirements for propulsion systems capable of high inherent reliability, long-term storage in the space environment, multiple start in free fall (zero gravity), and engine throttling. The solutions proposed to satisfy these requirements are coordinated for practical application in a system.

Periodic reports (starting with SPS 37-8, Vol. IV) describe the progress of work on the various parts of a specific system. Recent accomplishments in bladder and expulsion devices development are outlined below. These include:

- (1) New test fixture for pinhole study.
- (2) Heat sterilization of ethylene-propylene elastomeric material with hydrazine.
- (3) Metal diaphragms.

2. Bladder Development, R. S. Weiner and O. F. Keller

a. Pinhole study test fixture. The test fixture shown in Fig. 10 was designed in continued support of the expulsion bladder investigation. The fixture is required to study fluid leaks from metal foil pinholes, permeation leakages (including diffusivity and solubility) through plastics and elastomers, and various leak mechanisms of composite bladder materials (metal foil and plastic substrates in various combinations).

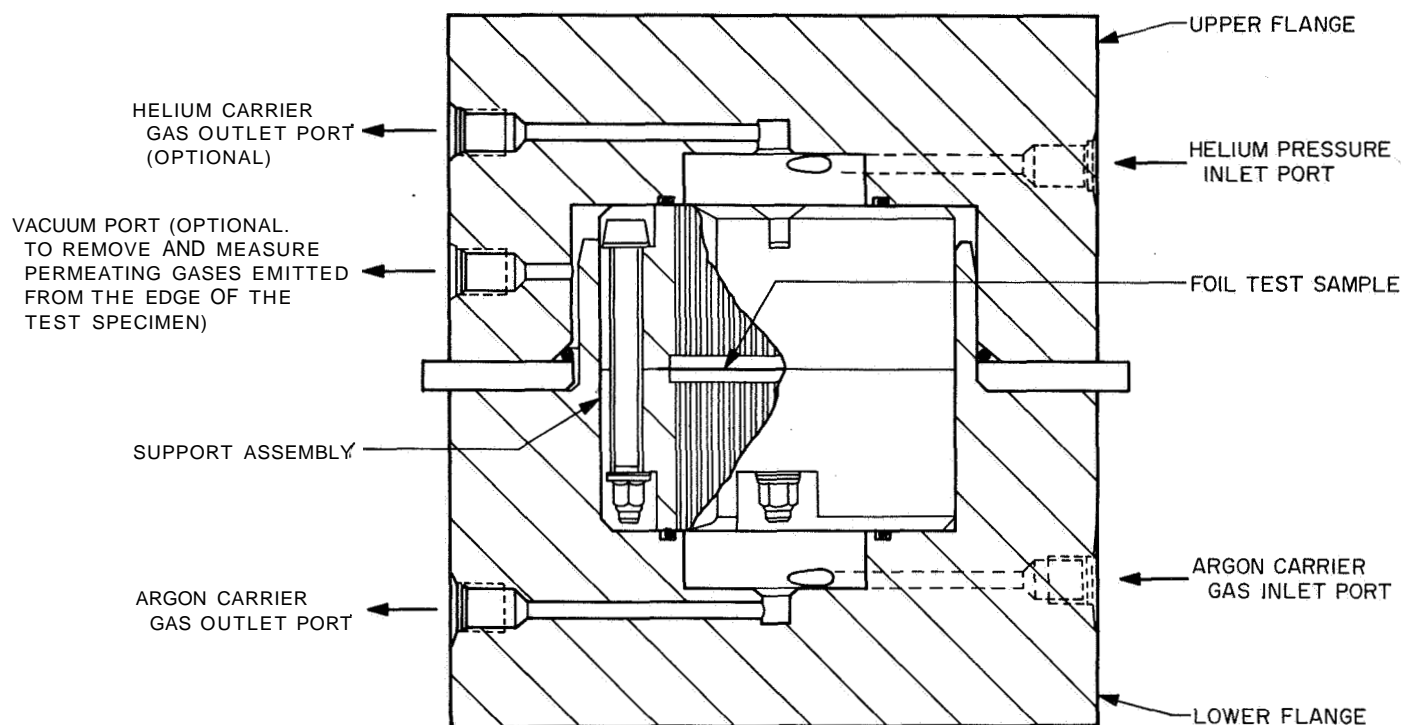


Fig. 10. Permeation leak test fixture assembly

The internal support assembly is the test specimen (membrane) holder and is designed to be small to minimize possible damage to the delicate test specimens during installation. The backup plates have 0.075-in. D flow-straightening holes drilled with a length-to-diameter ratio of 20:1 for studies of the low flow discharge coefficient attributed to metal foil pin holes. Backup plates with 100:1 length-to-diameter ratio holes are being considered. Sintered wire plates in the backup plates protect the test membrane on both sides from damage caused by overpressurization, and keep thin foils from being pressed into the holes. During testing, the assembly is structurally supported by the upper and lower flanges.

The vacuum port serves a variety of uses. The first is to eliminate any air permeating through the outer O-ring seal which could cause misinterpretation of data. The second use is to provide the means for measuring the radial (edgewise) permeation leakage from plastic, elastomeric, or composite structures. The radial leakage is to be drawn out of the fixture through the port and to the analytical instrument. This last measurement is expected to show to what degree leakage through a pinhole in a metal foil substrate will follow flow lines through "equi-potential points" in the plastic substrates. The leakage portion of the bladder investigation, using this new test

fixture, will be performed as a four-phase program to achieve the goals stated above.

Phase I testing will study low flow discharge characteristics (under quasi—steady-state conditions) of gases passing through metal foil pinholes of known geometry at low pressure drops (**0.05psi**, minimum). Helium, nitrogen, and argon will be the test media. Testing will be extended to include propellant vapors at a later time.

Phase II testing will examine the counter diffusion of two concentrated gases through metal foil pinholes of predetermined geometry. The salient test feature will be the maintaining of zero pressure drop across the pinhole, even with system pressures as high as 20 atm. The flow mechanism will be concentration gradient rather than pressure. The empirical data will be correlated with published equations (Ref. 19) for two-component diffusion. The calculated values will be approximations to the experimental data, because the equations are based on system pressures less than 1 mm of mercury; hence, they are also based on low gas concentrations.

Phase III testing will verify the analytical results currently anticipated from **NASA Contract NAS7-505**,

"Permeation Through Teflon and Teflon-Structured Materials." The boundary conditions on the test membrane will be helium on one side and vapor and/or liquid phase propellant on the other side.

Phase IV testing will correlate gas-to-gas and gas-to-vapor permeation leakage. The information will lead to the development of a test technique for predicting an equivalent rate of propellant vapor Permeation through a bladder wall (including test media solubility) as the result of monitoring the permeation of an inert test gas. The test technique will allow the leak testing of an operational bladder without decreasing its useful life because of too early exposure with propellant.

The test fixture shown in Fig. 11 was used in the early bladder permeation studies. It was somewhat simpler than the new assembly in that the test sample was held in position by the heavy main support flanges. This sample installation was cumbersome and produced some damage to certain foil test specimens. The refined fixture will replace this earlier type in the forthcoming tests described.

The first bladder permeation work measured the diffusive flow of helium across a metal foil pinhole in a zero

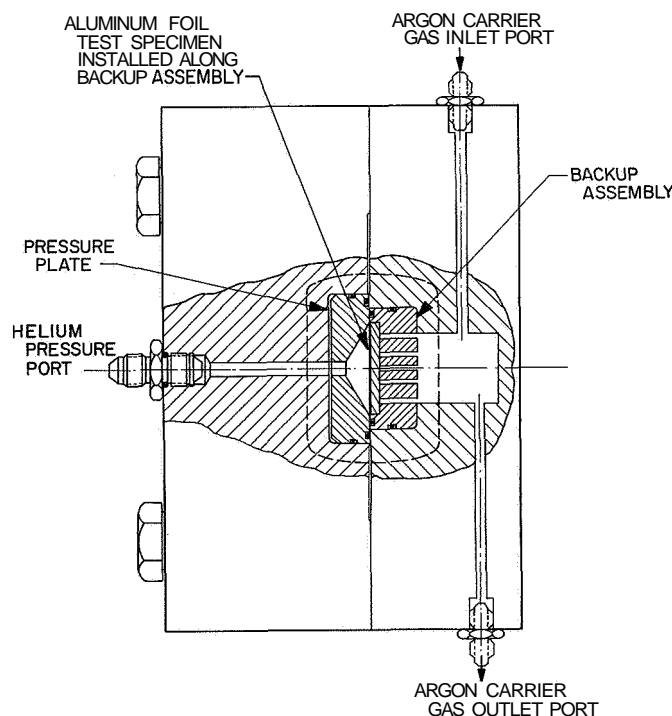


Fig. 11. Former test fixture assembly

differential pressure drop condition. Later testing attempted to obtain the flow discharge coefficients for different hole geometries. All of the earlier work was reported in previous SPS's.

b. Heat sterilization compatibility of EPR in N_2H_4 ; The heat-sterilization test of an ethylene propylene diaphragm-type bladder in a gaseous nitrogen atmosphere is described in Ref. 20. The diaphragm-type cell¹¹ (or bladder) as shown in Fig. 12, was subjected to six consecutive heat cycles of 6 hr/cycle duration in a gaseous nitrogen atmosphere. The actual diaphragm temperature varied from 284 to 301°F during each cycle. There were no apparent adverse effects as a result of this thermal test.

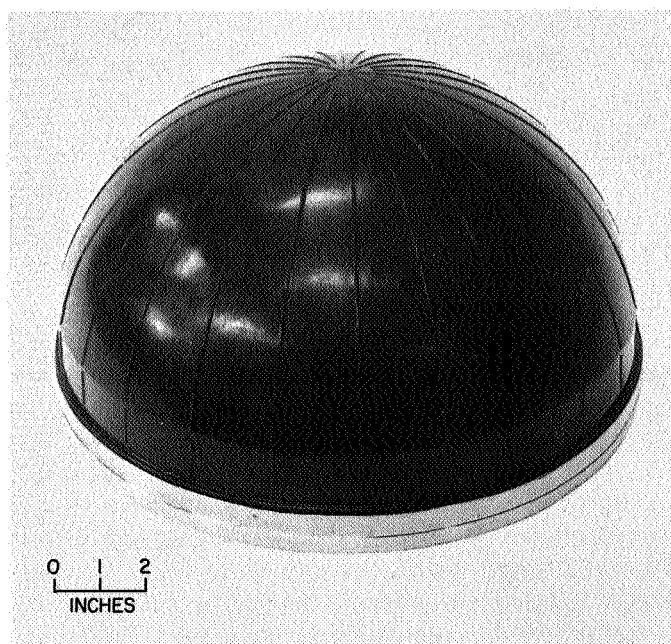


Fig. 12. Diaphragm-type cell (or bladder) used in generant tank

The first phase of heat-sterilization testing with hydrazine has now been started. An ethylene propylene diaphragm-type bladder, as shown in Fig. 12, was used to make 24 individual patch-test samples. Twelve of the samples were 1.5 in. in diameter and 0.040 in. in thickness. The remaining samples were 1.5 × 2 × 0.040 in. thick. Four of these patch-test samples (two of each type) were placed in each of six 2-in. D stainless steel containers, as shown in Fig. 13. The containers are shown mounted in an environmental test chamber used during

¹¹Made of Stillman Compound SR 722-70.

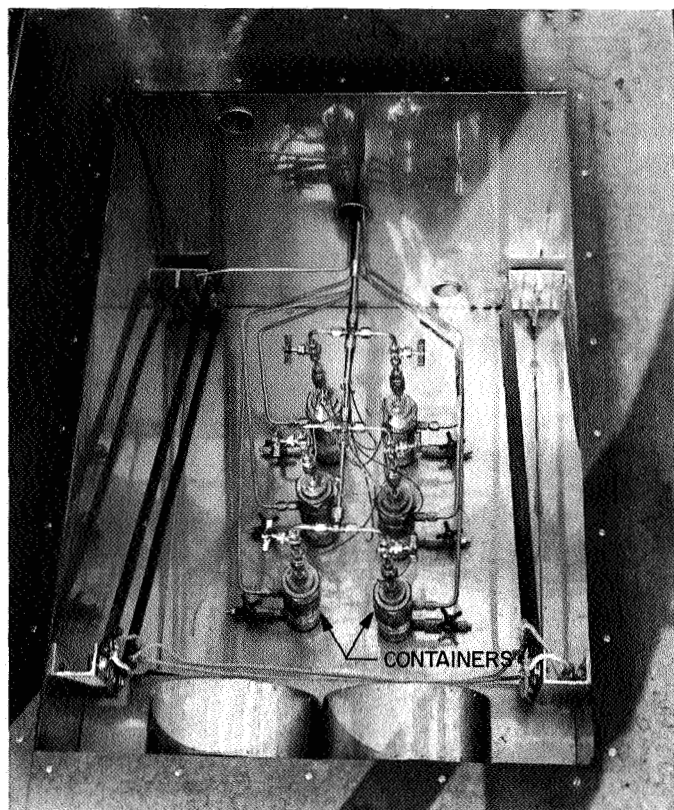


Fig. 13. Stainless steel containers mounted in environmental test chamber for heat-sterilization tests with hydrazine

the hydrazine heat-sterilization test. During the test, the elastomeric patch-test samples were held in place and at the same time separated from each other by a stainless steel wire rack as shown in Fig. 14. All containers were filled with hydrazine through the fill and drain connection at the bottom until the level reached the overflow, or vent, fitting near the top (Fig. 14). The total volume of each container up to the pressure fitting at the top was 370 ml. The total volume of the hydrazine in each container was 220 ml, measured to the bottom of the overflow or vent port. Approximately 4 ft of 0.25-in.-OD tubing was connected to the vent port. During the test, the patch-test samples were completely immersed in hydrazine.

The original test schedule included six cycles each of 60-hr duration at 300°F, and it was planned that one container would be removed after each 60-hr cycle. The actual test schedule followed to date is shown in Table 5.

After 1.5 hr at 300°F, the pressure in the containers had increased from an initial value of 50 to 70 psig. At

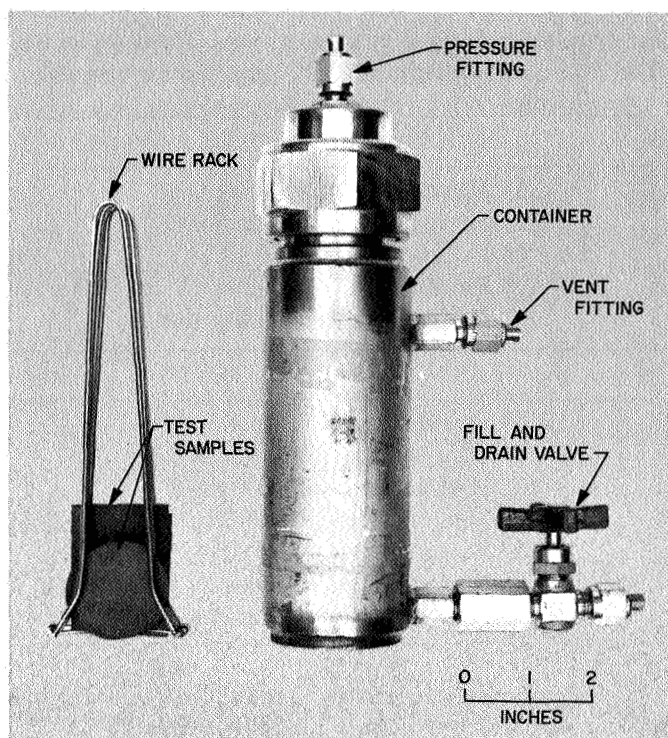


Fig. 14. Stainless steel container and mounting rack for EPR heat-sterilization test

this point, the test temperature was reduced from 300 to 170°F. Container No. 1 was removed from the environmental test chamber after an additional 60 hr at 170°F. The test temperature was then increased to 235°F, and finally to 300°F, as indicated in Table 5.

Table 5. Heat-sterilization compatibility of EPR^a in N₂H₄

Duration of heat soak, hr	Heat-soak temperature, °F	Initial container pressure, psig	Final container pressure, psig	dp/dt, psi/hr
1.5	300	50	70	13.3
60	170	26	31	0.0833
24	235	40	57	0.708
71	235	37	94	0.803
9	300	50	140	10.0
28.5	300	50	300	8.77
88.5	300	55	710	7.41
^b	300	50	^b	^b

^aStillman Compound SR 722-70.
^bTest currently in progress.

The patch-test samples were removed from container No. 1 and were divided into two groups. The samples were then tested according to the following test sequences:

Group I
(1) Reweighing of samples
(2) Shore hardness determination
(3) Vacuum-soak at 100 μ Hg
(4) Reweighing of samples
(5) Hydrazine permeability test
Group II
(1) Reweighing of samples
(2) Shore hardness determination
(3) Hydrazine permeability test
(4) Shore hardness determination
(5) Vacuum-soak at 100 μ Hg
(6) Reweighing of samples
(7) Shore hardness determination

The hydrazine permeability tests will be performed in accordance with procedures outlined in Ref. 21.

After completion of the hydrazine heat-sterilization tests, the patch-test samples will be used to carry out extrusion tests, as described in Ref. 20.

3. Expulsion Devices: Metal Diaphragm, H. B. Stanford

Since 1962 the Aeronautical Division of Honeywell, Inc., Minneapolis, Minnesota has been involved in the development and fabrication of convoluted metal diaphragms for the Jet Propulsion Laboratory's program of advanced development of liquid expulsion devices. During this time significant advancement was made in techniques of fabricating convoluted metal diaphragms from 1100 aluminum (SPS 37-18, 37-21, 37-22, 37-25, 37-27 and 37-32, Vol. IV). Recent effort at Honeywell, Inc., has been directed toward two associated problems of metal diaphragm development, namely: recycling capability and fabrication from metals other than aluminum (Ref. 22).

a. Recycleability. During the initial efforts by Honeywell, Inc., to recycle a convoluted metal diaphragm some success was achieved by cementing fiberglass rings to the nonrolling segments of the diaphragm. Although fiberglass and adhesives are not considered to be acceptable with the candidate propellants hydrazine and nitrogen tetroxide, they were used to prove the feasibility of the reinforced diaphragm concept. In one instance three com-

plete recycles of an 18-in.-D aluminum convoluted diaphragm were obtained by this method. Limited efforts to duplicate these results at JPL by chemically milling the rolling segments of thick-wall 0.040-in. diaphragms to 0.010 in. were unsuccessful.

Also during expulsion testing at Honeywell, Inc., it was observed that most diaphragms during cycling tests move preferentially from one side, rather than rolling smoothly in a level attitude toward the distended position. It was also noted that a greater number of the double folds which result in traveling creases and eventual failure seemed to form in the outer convolution of diaphragms with the most severe tipping.

In a proposal to JPL, Honeywell, Inc., reasoned that if the chemical milling process was adequately controlled to give the requisite thick and thin cross-sections to the nonrolling and rolling segments of a convoluted diaphragm, and if a mechanism to prevent tipping could be applied to the diaphragm, some recycle capability might result. Two different flight-weight, tip-control devices were proposed.

In the torsion ring feedback concept (Fig. 15), a torque results in the torsion ring as the diaphragm rises. If, for instance, side A would tend to rise at a faster rate than side B, tension in the wire attached to the lever pivoting about point A would be greater than tension in its opposite (B) counterpart. The result would be: (1) greater downward component of force on side A, and (2) counterclockwise couple at point A, tending to elevate point B, thus equalizing the two sides. The device also tends to resist any tendency of the diaphragm to shift off center.

In the tension wire concept (Fig. 16), the angle α increases as the diaphragm rises. The downward restoring force increases proportionately. If, for example, side B would tend to rise at a faster rate than side A, the downward restoring force on side B would increase, while side A equalizes.

In theory both of the proposed tip-control concepts provide, by means of their mechanisms, counterforces to the forces which cause the diaphragm to tip during cycling. In operation, as one side of the diaphragm advances ahead of the other side, it meets the opposing force of the restraining mechanism and is slowed down or stopped until the slow side catches up. Geometrical analysis of the torsion ring feedback system indicated that maximum force is applied when the diaphragm nears the extended or hemispherical configuration and is at a

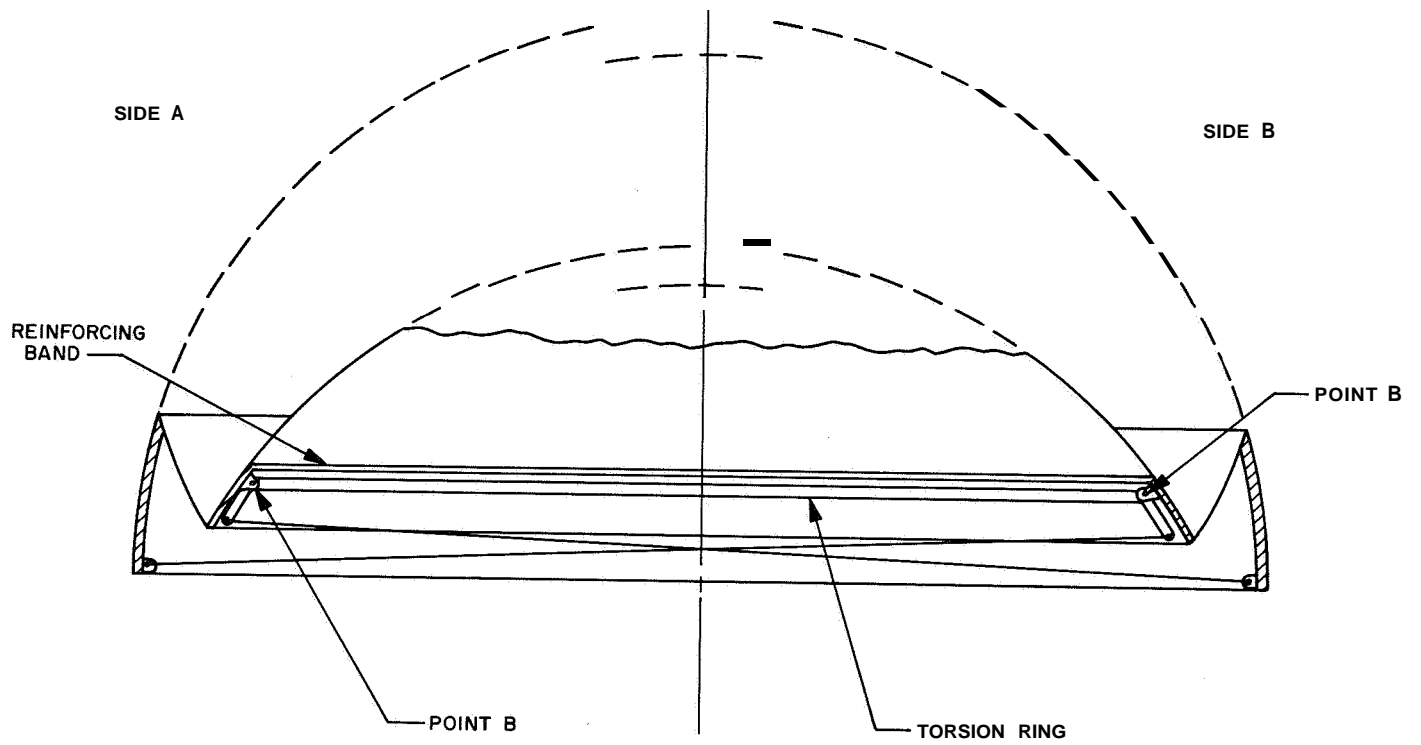


Fig. 15. Torsion ring feedback concept of diaphragm-controlled motion mechanism

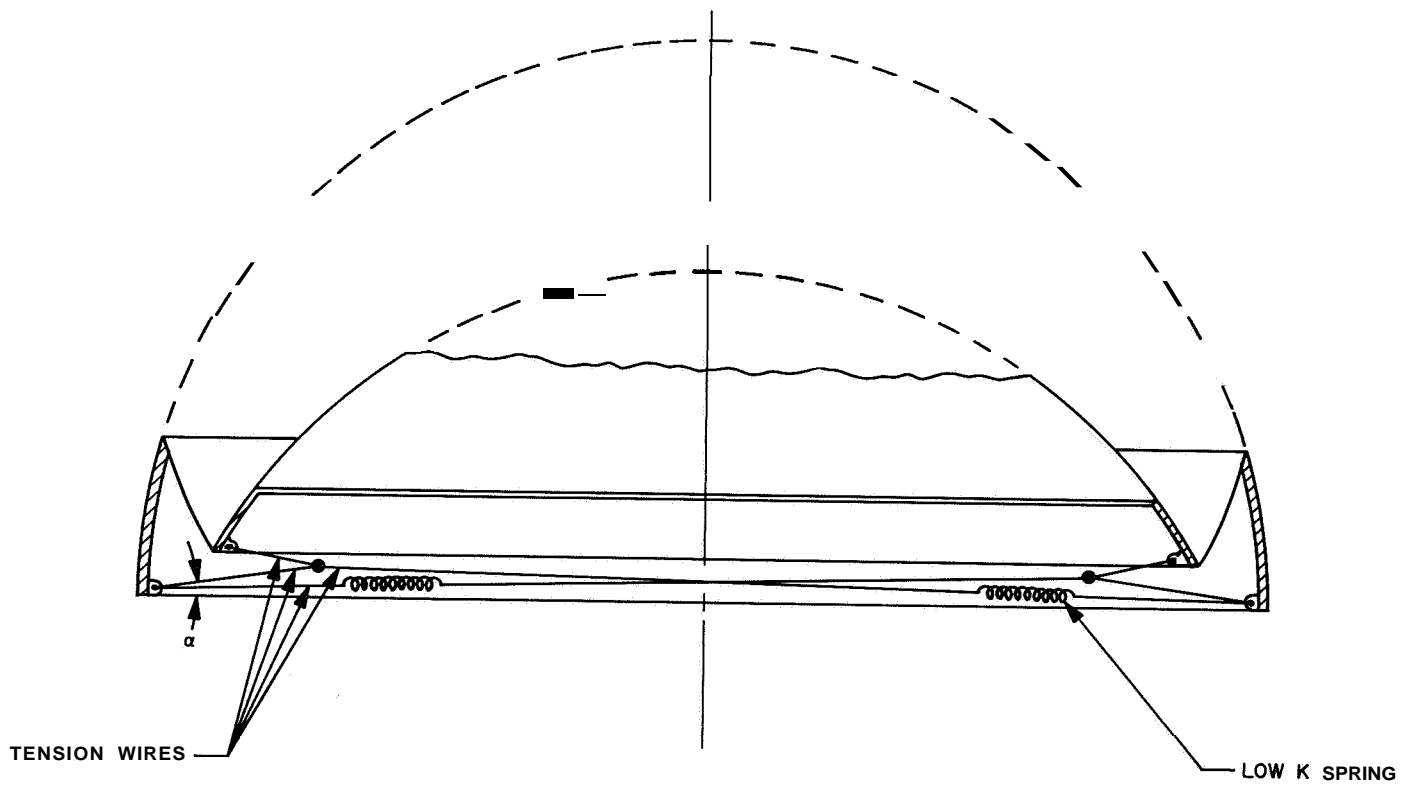


Fig. 16. Spring-wire concept of diaphragm-controlled motion mechanism

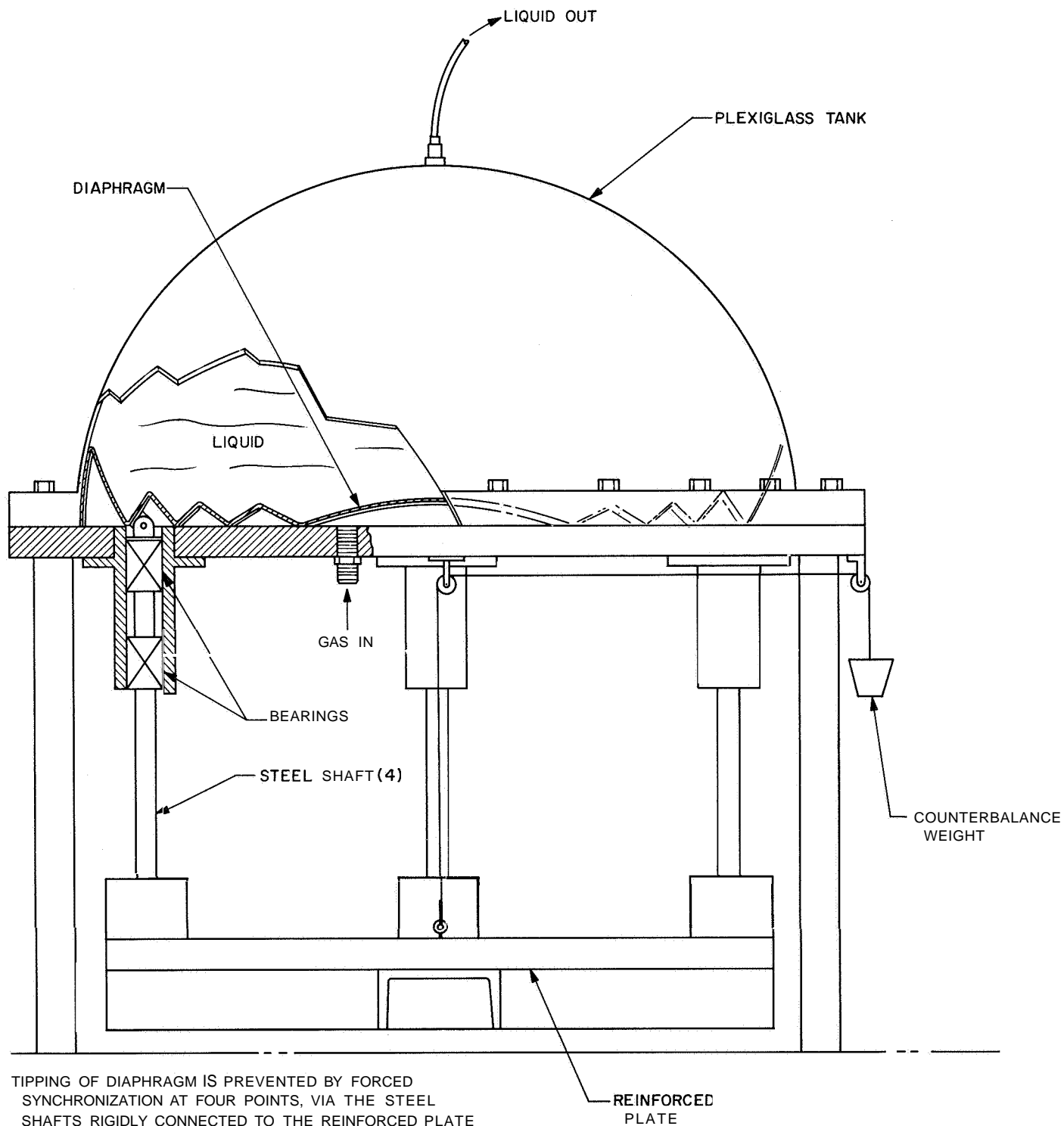


Fig. 17. laboratory model of controlled-motion mechanism

minimum in the initial convoluted position. Although this is not the optimum situation for tip control, the concept was considered worthy of further investigation. As a first step to this end a heavyweight positive tip control mechanism was designed and built at Honeywell, Inc., for the purpose of observing the effect of this type of control on convoluted diaphragms during cycling (Fig. 17). In operation the mechanism worked as planned, and the diaphragms thus controlled did not tip. The fact that the diaphragms were restrained from tipping did not prevent random buckling in the outer convolutions, although inner convolutions appeared free from serious distortions. Five diaphragms were tested in this manner and all buckled severely in the outer convolution. As a result of these failures, tip control testing was discontinued, and attention was focused on the rolling or inner surface of the outer convolution, since this is where the major buckling occurred.

Two methods of hoop reinforcement were proposed to be applied to the rolling surface of the outer convolution, to reduce the tendency of this area to buckle. One method left concentric ribs 0.125 in. wide, spaced at 0.75-in. intervals on the rolling surface of the outer convolution during the chemical milling process (Fig. 18). The other method

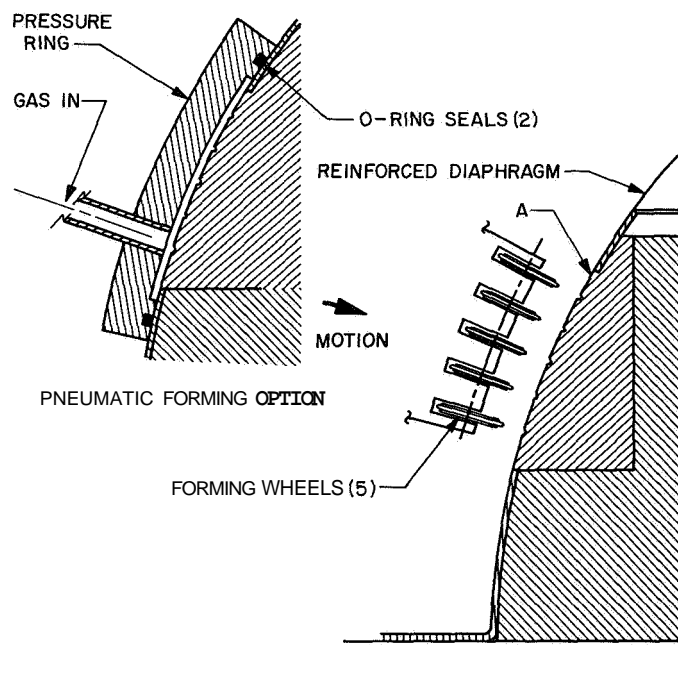


Fig. 18. Concentric groove reinforcement to rolling surface of outer convolution on 18-in.-D chemically milled aluminum diaphragm

involved forming 0.040- wide \times 0.035-in. deep creases or grooves at approximately 0.75-in. spacing in the chemically milled rolling surface (Fig. 19). With both methods the chemical milling and/or groove forming were done to the parts in the hemispherical shape prior to convoluting. Out of ten 18-in.-D aluminum hemispheres with approximately 0.110-in. wall thickness purchased for this effort, five were chemically milled at the rolling surfaces and roll formed to generate the reinforcing grooves in the rolling surface of the outer convolution. Three others were successfully chemical milled (leaving reinforcing ribs in the rolling surface of the outer convolution), and two were ruined in processing. When attempts were made to convolute these hemispheres, both the ribbed and grooved types buckled severely and some cracked along the ribs and grooves. Only one of the ribbed (and none of the grooved) hemispheres was convoluted at all. It appeared that with both ribbed sections and those with grooves there were unpredictable stress concentrations along the ribs and grooves and considerable thickness variation in the chemical milled area. The failures at the reinforcing ribs and grooves during attempts to convolute the chemically milled hemisphere are currently unexplained other than by the fact that abrupt and extreme contrast in cross-section and flexibility exist in the area of fracture. The variation in final metal thickness is due to nonuniform conditions present to some extent in the

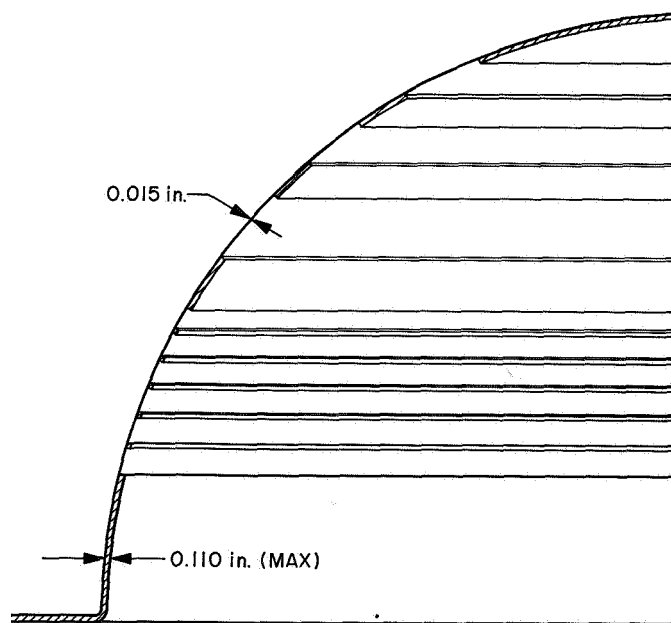


Fig. 19. Reinforcement pattern on 18-in.-D aluminum hemisphere after chemical milling, prior to convoluting

original sheet stock, amplified by the hemisphere-forming process and not corrected by chemical milling.

In conclusion it can be said that reliable recycleability was not achieved by either diaphragm tip control, or the reinforcement obtained through grooves or ribs applied to the rolling segments of a convoluted diaphragm.

b. Fabrication of convoluted diaphragms from stainless steel and titanium. As an extension of the technique developed by Honeywell, Inc., to fabricate convoluted diaphragms from 1100 aluminum, it was decided to investigate the possibility of fabricating convoluted diaphragms from stainless steel and titanium by the same method. Type 321 stainless steel and pure titanium were chosen for candidate materials because of their propellant compatibility and relative qualities of ductility.

As a first step to this effort it was necessary to obtain thin-wall 18-in.-D hemispheres made from the candidate metals. Honeywell, Inc., considered that the method developed by them for forming hemispheres from aluminum would not be adequate for stainless steel or titanium, that to develop a suitable method would be time-consuming and costly, and that the economical approach was to find a subcontractor to supply them. Several vendors were contacted. Aircraft Hydroforming, Gardena, California, was given the subcontract on the basis of guaranteed results and uniformity of wall thickness. Their process, which is proprietary, produces a maximum 0.25-in. flange.

Wall thickness was selected at a nominal 0.010 in. for the stainless steel hemispheres and 0.005 in. for the titanium ones. The stainless steel hemispheres, as delivered, were 0.012 in. in thickness. The titanium was formed at 0.015 in. and chemically milled to a uniform 0.005 in. on one hemisphere and 0.008 to 0.009 in. on the others. Five each of these hemispheres were delivered to Honeywell, Inc., for convoluting. When the first attempt was made to convolute a stainless steel hemisphere with the collapsing punch and die process (SPS 37-25, Vol. IV) the hemisphere buckled severely about 20 deg above the flange, in the area of the outer convolution. It appeared that there was insufficient columnar strength for the thin-walled hemispheres to withstand the pressure that resulted from forming the inner convolutions without additional support. A removable epoxy ring was molded in place to provide this support in the critical area (Fig. 20). In operation, the hemispheres are convoluted down to the support ring, which is removed prior to forming the final convolution. With this modification the four remaining

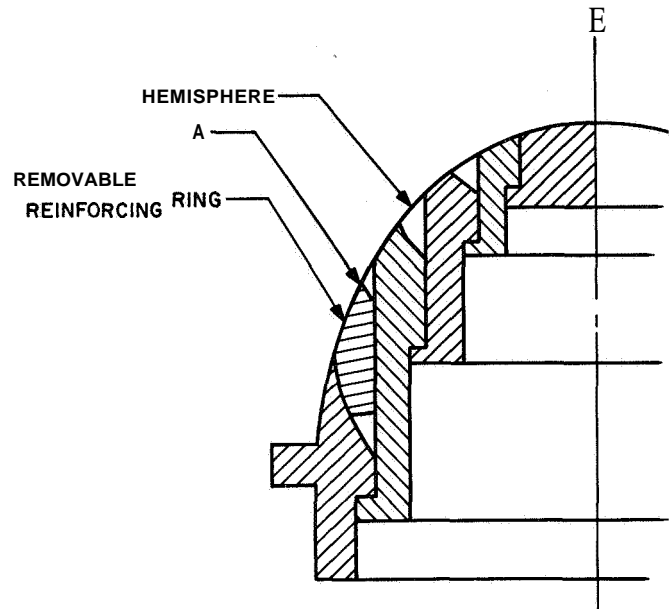


Fig. 20. Telescope punch with removable reinforcing ring

stainless steel hemispheres were successfully convoluted with no serious distortion. Four titanium hemispheres were also successfully convoluted by this method although the rolling or reflected surfaces of the diaphragm were quite wrinkled. The wrinkled surfaces are believed to be due to the fact that some areas of the material yielded while some other areas did not yield during the convoluting process. It is possible that the wrinkling might have been less pronounced had the hemispheres been annealed prior to convoluting.

N67 18327

Q. Resonant Combustion, J. G. Softer and R. M. Clayton

1. Introduction

Early in the Resonant Combustion Program, a series of experiments (Ref. 23) were conducted with an engine using RMIR¹² Injector 5 with *Corporal* fuel and stabilized fuming nitric acid (SFNA) as propellants. This system was characterized by an oscillatory combustion mode exhibiting high-amplitude shock-like waves which ultimately served as a basis for postulating the existence of a detonation-like disturbance. An artist's impression of the wave as reproduced from Ref. 24 is given in Fig. 21.

In continuing these studies, and in particular in attempts to verify this postulate, measurements have been extended to: (1) determine the long-time interaction of

"Rocket Motor Injection Research.

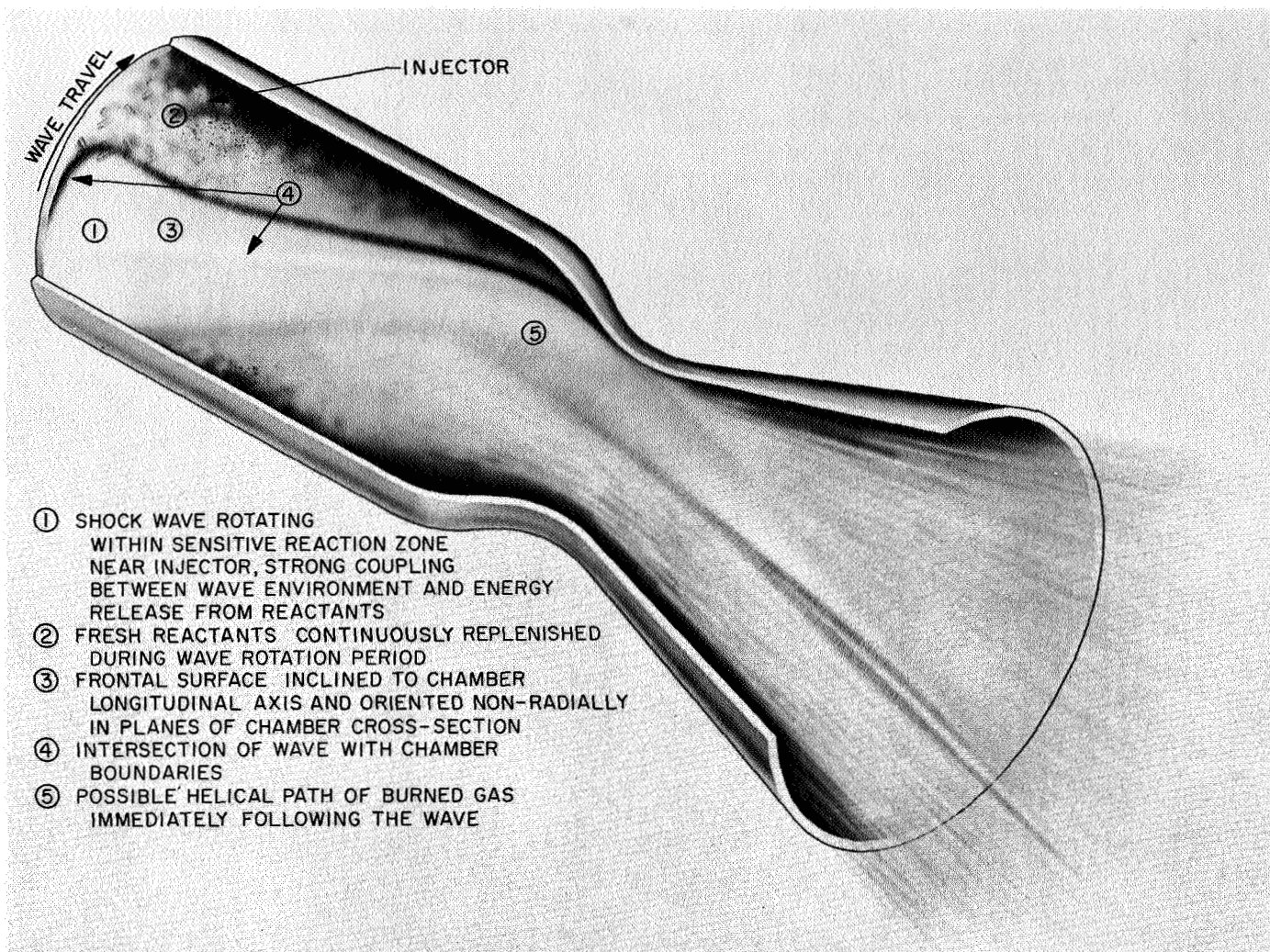


Fig. 21. Artist's conception of rotating detonation-like wave front

the wave on the injection scheme, as described in Sect. 2, (2) attempt to verify certain predictable properties of the steady-state combustion environment through experiment (Sect. 3), (3) present some early results obtained in the process of evaluating some new diagnostic techniques that are still in the developmental stage but are expected to be suitable for the extremely severe environment produced by the wave (Sect. 4), and (4) evaluate the influence of certain geometrical changes in the engine on the properties of the wave (Sect. 5).

2. Injector Response

In a previous report (Ref. 25), a model was developed in which the time-dependent flow of an incompressible liquid through injector orifices was considered as the chamber pressure varied in an arbitrary manner. For the sample calculations, experimental data for a single

cycle of the periodic pressure oscillation were considered typical, and were applied repetitiously to find the long-time behavior of the flow through the orifices. The results of that analysis have now been supplemented by calculations to determine the influence of continuous pressure data for a particular firing, including bomb pulse effects as well as periodic pressure oscillations. In Fig. 22, portions of the pressure history at *two* positions of the face of Injector 7 are shown. The upper curve was obtained from a Kistler measurement at a radius r of 4.35 in.; the lower curve is from the analogous measurement at a radius of 1.45 in. These curves were plotted from readings digitized from the experimental high-response analog records at intervals of 10 psec to a time $t = 25$ msec after the bomb pulse. The last few digitized cycles of oscillation were considered to be typical of the remaining period, and were used repeatedly to extend the time to $t = 50$ msec.

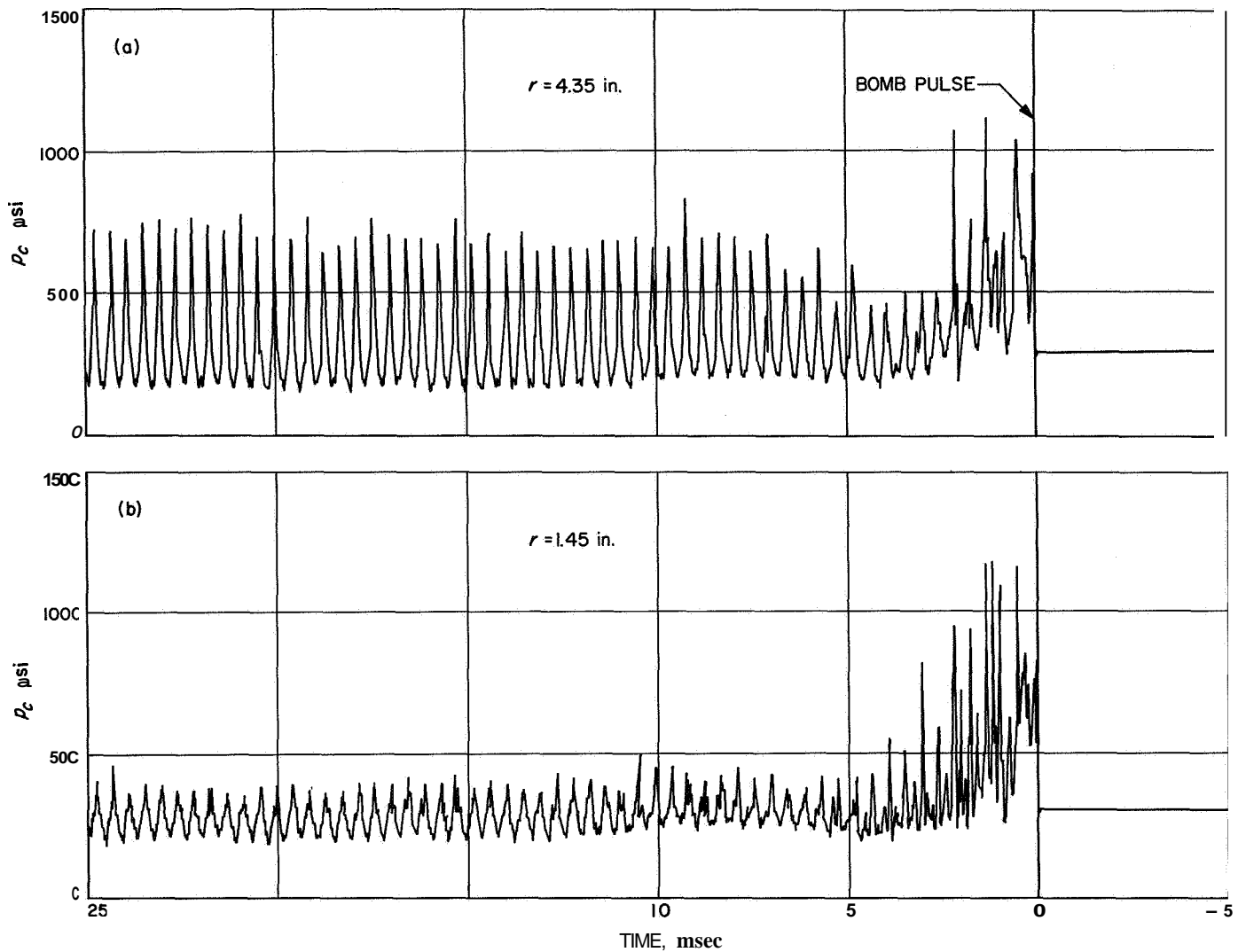


Fig. 22. Measured pressures, Run B1001

Fig. 23 shows the calculated response of the **100 L/D** fuel and oxidizer orifices at both positions on the injector face. Note that at $t = 25$ msec, the flows near the center of the face (Fig. 23b) are about 5% greater than the respective flows near the outer radius (Fig. 23a), although the initial flows (at $t = 0$) for both positions were the same. Later, at $t = 50$ msec (not shown), the mean flow velocities for the outermost location had nearly converged to their initial values, while the flow rates near the center had converged to values nearly 10% greater than the original rates.

The engine steady-state parameters used in these calculations are given in Table 6, and were based on the experimental data for the period just before the bomb

Table 6. Engine steady-state parameters used for injector response calculations

Parameter	N ₂ O ₄	50/50 Fuel (UDMH/N ₂ H ₄)
Viscosity, cp	0.46	1.10
Density, lb/ft ³	91.3	56.2
Orifice diameter, in.	0.173	0.173
Orifice length, in.	17.3	17.3
Orifice/feed-tube diameter ratio	0.692	0.692
Feed tube length, ft	2.33	2.33
Feed velocity, ft/sec	66.1	83.5
Manifold pressure, psia		
calculated	427.9	449.8
measured	448.0	462.0
Chamber pressure, psia	306.0	
Mixture ratio	1.286	

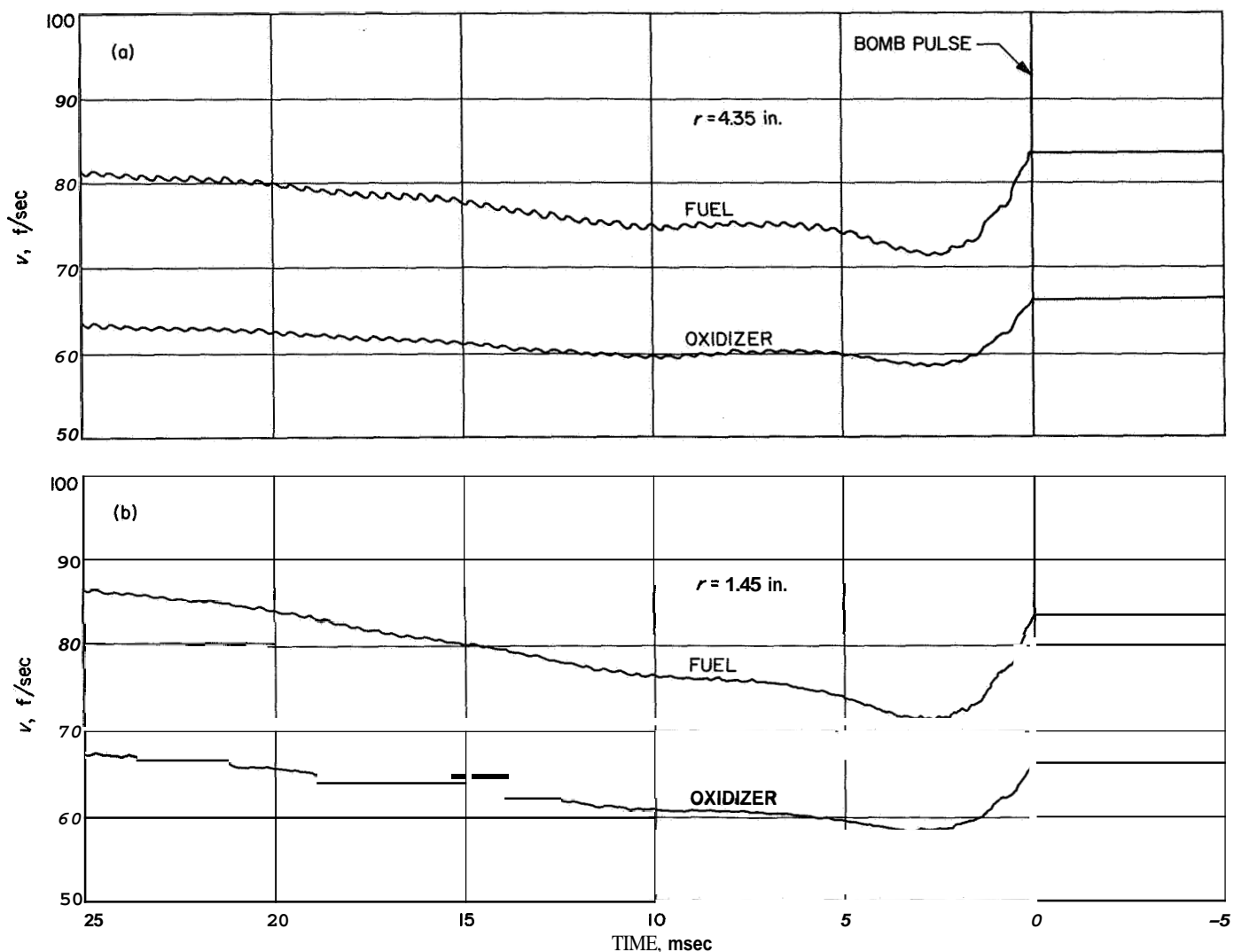


Fig. 23. Calculated flow velocities, Run B1001

pulse. The disagreement indicated between the experimentally measured manifold pressure and the calculated pressure used for the flow calculations is believed largely due to the fact that nonuniformity of the velocity profile was ignored in calculating the total kinetic energy of the flow system (Refs. 25 and 26).

Fig. 24 shows experimental flow measurements for fuel and oxidizer orifices located near the radial positions used for the calculated results just shown. These flows were measured by inserting small turbine flowmeters in four individual orifice flow circuits. This arrangement is shown schematically in Fig. 25 and is possible because of the injector design configuration wherein externally routed flexible hoses are used to connect the orifices to their respective manifolds. While the relatively low-response

capability of these meters does not allow an accurate resolution of the rapid flow transient caused by the bomb pulse, the measured flows for times near the end of the sustained resonant period (near run termination) are believed to be essentially true average flow rates and thus analogous to the converging calculated velocities shown in Fig. 23.

For convenience of comparison, flow rates based on the calculated velocities are shown by the dashed curves in Fig. 24. Note that the time scale of Fig. 24 is considerably compressed relative to Fig. 23, which focuses attention on the relatively large change in flow calculated as a result of the increase in mean chamber pressure, which is precipitated by the bomb pulse. Ignoring for the moment the approximate 10% difference between

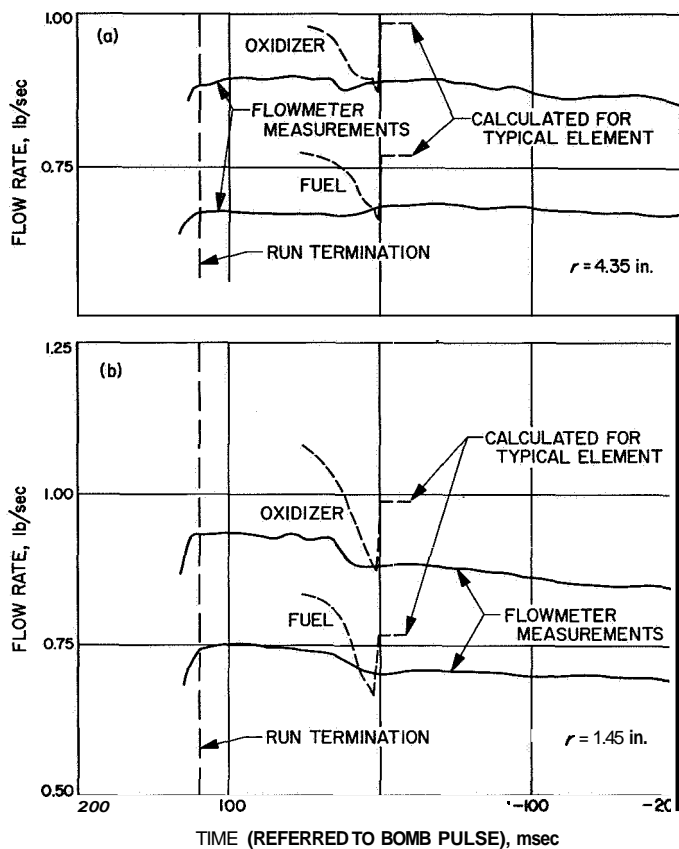


Fig. 24. Measured orifice flow rates, Run B1001

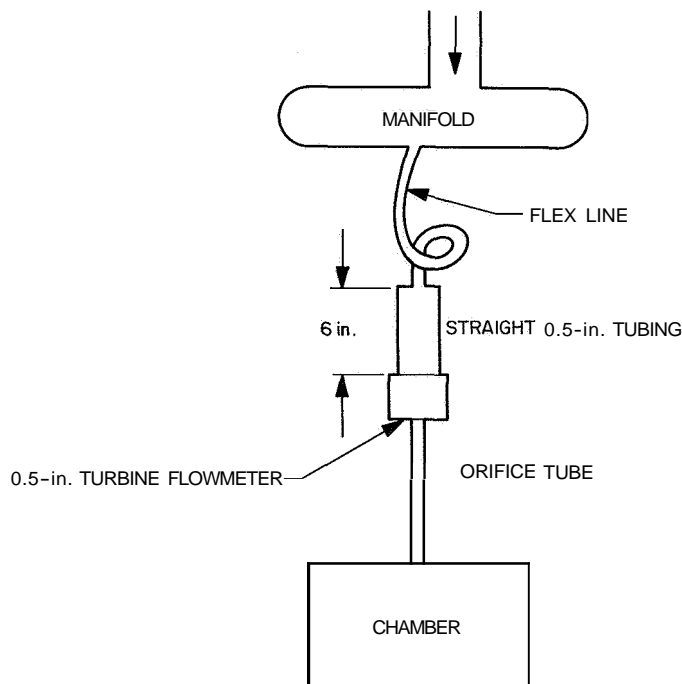


Fig. 25. Flowmeter schematic

calculated and measured steady-state flow rates just before the bomb pulse, note that no appreciable change in the measured mean flow rate occurred for the orifices near the outer radius of the chamber as shown in Fig. 24(a). A clearly increased flow (4-5%) is indicated, however, for the inner orifices as shown in Fig. 24(b). The measurements, therefore, agree qualitatively with the calculations and give some credibility to the simple analytical model—at least for the case of the long orifices used here.

The previously mentioned difference in steady-state flow rates is the result of inserting the flowmeters in the orifices. This restricted the flow somewhat, and thus the measured individual orifice flows were less than the average flows carried by the majority of the orifices (which did not have flowmeters). The calculations were based on these latter orifices.

3. Steady-State Pressure Profile

In order to understand how steady-state combustion can be perturbed into a resonant mode, it is of course desirable to first understand the steady-state process itself. Of particular interest is a knowledge of the spatial distribution of the combustion processes within the chamber volume. One experimental technique from which at least the axial distribution might be deduced is the measurement of the static pressure drop along the length of the engine. This pressure profile is produced mainly by the interrelated effects of local combustion rate (time rate of gas formation), gas acceleration and viscous losses within the gases and at the chamber wall. Assuming that relations between these factors were known to a reasonable

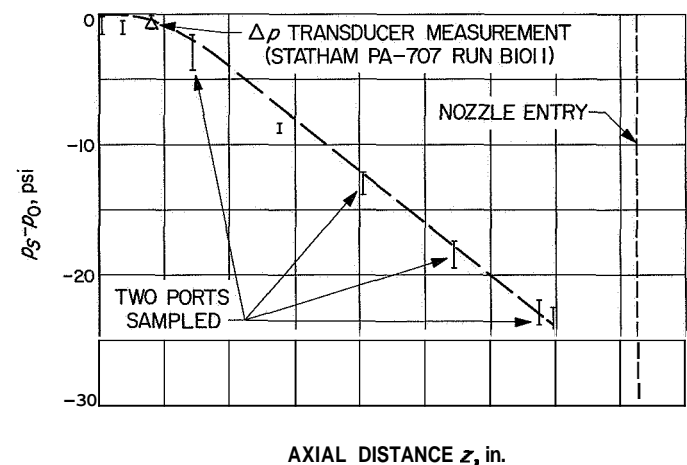


Fig. 26. Experimental pressure drop along engine length, RMIR Injector 5, with standard engine and SFNA plus Corporal fuel

degree of accuracy, a means of estimating local combustion rate and hence verification of a numerical solution for the combustion process might then be provided by static pressure measurements. This presents difficult experimental problems, however, for the axial pressure variations due to combustion are on the order of a few psi. The required accuracy is, therefore, difficult to attain because of the inevitable instrumentation and combustion noise present, even in a very smoothly burning engine.

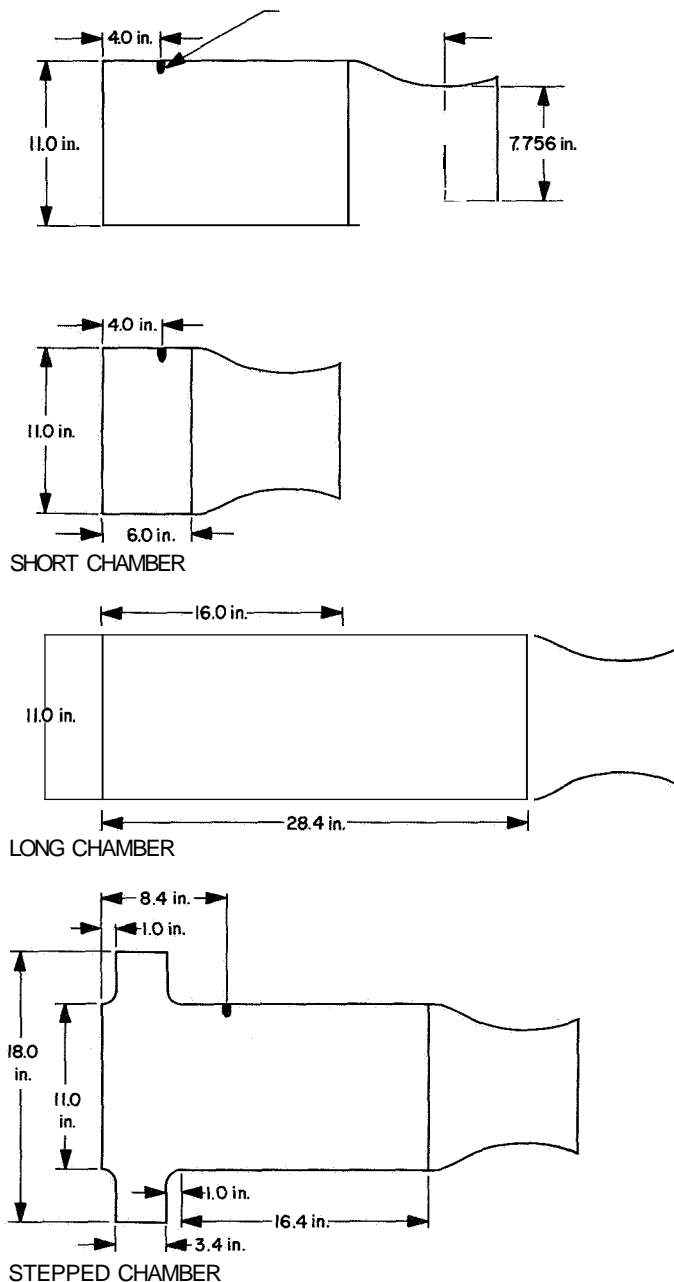


Fig. 27. Engine geometries

Fig. 26 shows the results of such measurements obtained using Injector 5 and the standard chamber configuration shown in Fig. 27. A transducer in the injector face was used to measure injector-end pressure, and this measurement, which, of course, is not completely steady with time, is fixed as the definition of the injector end pressure $p_0(t)$ at time t . Two more transducers were located on the chamber wall 13.9 in. from the injector face. The average of the latter two readings is used for the pressure at that point at time t . The difference between this average and $p_0(t)$ is shown at the 13.9-in. position in Fig. 26. Its variation during a full second of the firing (66 calculated points) is indicated by the spread in the data.

The remainder of the pressure differences shown in Fig. 26 were obtained through the use of a Datex Corporation SP-101A pressure scanner valve (Fig. 28), which scanned a dozen different pressure taps during the 3-sec

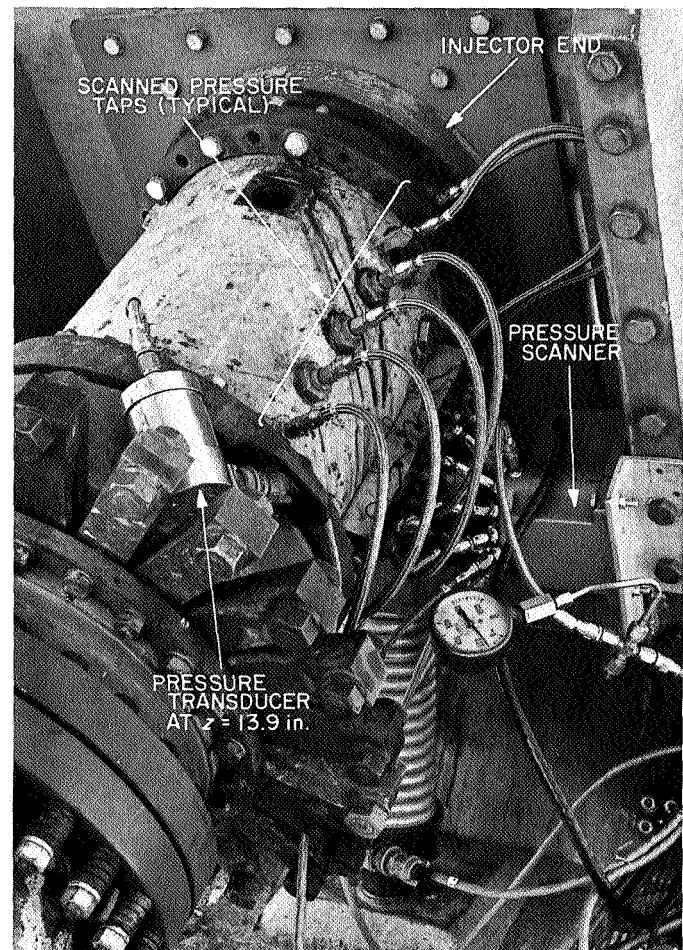


Fig. 28. Pressure scanner installation

run. Thus, a single transducer was used to make all scanner readings. The difference between the scanner reading $p_s(z, t)$ at time t , and $p_o(t)$ at the same instant are shown in the figure. One of the scanned taps was located in the injector face. Note that the scanner reading for this location did not exactly agree with $p_o(t)$, thus $p_s(z, t) - p_o(t)$ is not equal to zero at the face. A small calibration difference between the two transducers is sufficient to account for this discrepancy.

Some of the spread in the plotted data is due to the fact that eight of the taps are located by pairs, both taps in a pair being located the same axial distance from the injector face but separated circumferentially by 135 deg (not shown in Fig. 28). Thus the pressure at these axial stations was measured at two different times, once at each tap. Also, a mishap at the oxidizer manifold in mid-firing caused a slight reduction in oxidizer flow rate, but this seemed to have no noticeable effect on the chamber pressure data.

The dashed curve in the figure is intended to represent the profile of the pressure based on the readings of the scanner transducer. The curve is displaced upward about 1 psi to correct for the previously mentioned discrepancy between the two transducers at $z = 0$. If the plotted curve is an indication of the true profile, it seems to indicate that there is a zone at $0 \leq z \leq 2$ in. where very little combustion is occurring, probably because of incomplete atomization.

More satisfactory data might be obtained by using differential pressure transducers to measure the pressure drop from the injector face to a point z along the chamber. This would eliminate the inaccuracy inherent in taking a small difference between two large numbers which have been obtained experimentally. A single point obtained using a Statham PA-707 differential pressure transducer at the 1.6-in. position, is included in Fig. 26, but interestingly enough shows good agreement with the interpolated data. It is hoped that the use of differential pressure transducers for future measurements will improve the resolution and hence usefulness of such data.

4. Wave Behavior in the Standard Chamber

The wave behavior for RMIR Injector 5 with the standard engine (Fig. 27), as observed along the chamber boundaries, was reported in Ref. 23. The additional results presented here were obtained using: (1) high-speed photography, (2) an ablatively cooled pressure probe, (3) several devices indicating injector-end average pressures, and (4) variations in bomb position.

a. High-speed photography. Photographic results using relatively long exposure times (Fastax camera at up to 16,000 frames/sec) are given in Ref. 25 and 27. Since the sharp-fronted wave moves around the chamber boundary at an average speed of 6160 ft/sec or 0.75 in. per $10 \mu\text{sec}$, it seemed desirable to have as small as possible exposure time in order to stop the motion. A high-speed Beckman-Whitley Dynafax framing camera was used for this purpose.

Fig. 29(a) is a view of the injector face as seen through the nozzle. (The camera-holding device is described in Ref. 25.) Typical photographs of the combustion process taken from this same position are shown in Fig. 29(b). These pictures were taken with an exposure time of 1.3 μsec and a rate of 25,000 frames/sec, but since only every other frame is shown here, the time between frames is 80 μsec . A 50-mm lens ($f/1.5$ aperture) and Kodak Type 2475 recording film (Royal X Pan) were used. The negatives were developed for 15 min at 68°F , using Kodak D-19 developer, with the addition of 1 g of hydrazine dihydrochloride per 1000 cc of developer.

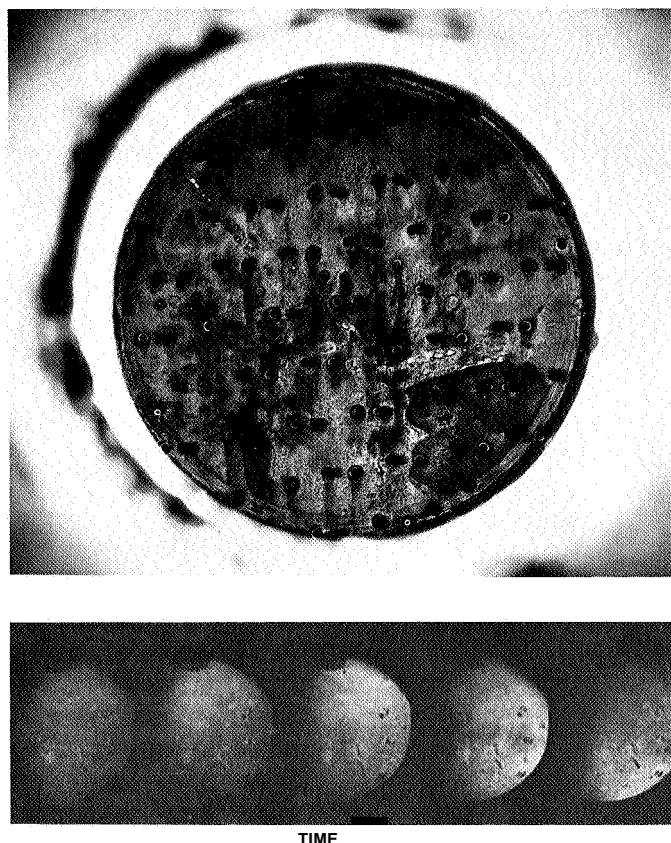


Fig. 29. View from nozzle camera position (a) without combustion (b) during resonant combustion

The bright zone in the pictures is associated with the pressure wave; however, it is not known whether the front of the luminous zone coincides with the front of the pressure rise. The photographs show the luminous front to have a diffuse appearance and is in contrast to the Kistler pressure measurements, which show a very sharp-fronted pressure rise. The difference is not surprising, however, because the gases downstream of the driven portion of the wave also contain large density gradients which tend to diffuse the light; also, experiments with the Fastax camera (Ref. 27) have shown that the field of view of the camera extends only about halfway to the injector face with this particular engine, due to the large amount of carbon smoke produced by the *Corporal* fuel.

b. Downstream shape of the wave. Information on the downstream part of the wave was obtained using the ablatively cooled, high-response pressure probe described in Ref. 25. Portions of pressure-versus-time records for several spatial locations near the nozzle end of the engine are shown in Fig. 30.

These measurements were made during four different resonant firings at about 25 msec, following the initiation of the resonant mode by a bomb pulse, using experimental procedures similar to those described in Ref. 23. The mean operating conditions (including the resonant behavior) were essentially constant for all firings except for Run B1013. The exception for this run was that the wave traveled in a CCW direction about the chamber (as viewed looking upstream). As will be seen later, the travel direction of the sustained wave appeared to depend on the circumferential position (varied for Run B1013) of the bomb relative to the injection scheme. For present purposes, however, the different wave direction for this run is not considered to be important, since previous experiments have indicated that the relative shape of the gross resonant disturbance does not change with wave direction.

The following observations are of particular interest in a study of Fig. 30:

- (1) The same predominant period of pressure oscillation (470 psec) is exhibited by all measurement positions except the centerline location (Trace e) where the oscillations appear to be almost noiselike. It is noted that the 470- μ sec period is the same as previously observed for chamber boundary measurements for this engine (Ref. 23).
- (2) The pressure amplitude of the disturbance just upstream of the nozzle entrance is a maximum at the boundary; decreasing to nearly noisy-combustion

levels at the engine centerline (Traces a, b, and e). This trend is consistent with previous observations for the injector end of the chamber (Ref. 23). Note that for comparisons between probe and wall measurements, the fact that the pressure transducer diaphragms are located in planes normal to each other might itself affect the details of the appearance of one measurement relative to the other, since the gas medium being measured is in rather violent motion relative to both transducers. These effects are presumed to be small, however, for this presentation.

- (3) The phase relationship between the wall measurement (5.52-in. R) and the probe measurement (3.22-in. R) at a common station 13.48 in. from the injector face (Traces a and b, respectively) indicates that the gross wave frontal surface is oriented non-radially with respect to the cylindrical combustion volume. These particular downstream data are shown as crosses on the polar plot on the left hand side of Fig. 33 where they can be seen to be in qualitative agreement with the shape of the wave-to-injector face intersection.
- (4) The disturbance as viewed from the probe at a constant 3.22-in. engine radius propagates beyond the nozzle throat plane but with a much reduced amplitude and a nearly sinusoidal wave form. The phase displacement for the two nozzle positions (Traces c and d) relative to the chamber station (Trace b) suggests a steepening curvature of the disturbance in the direction of rotation as the wave passes through the nozzle (Fig. 21).

c. Changes in injector-end pressure. Several independent measurements indicate that there are substantial changes in local time-average pressure at different radii on the injector face. The time-average pressure p_{av} is defined as:

$$p_{av} = \frac{1}{t_2 - t_1} \int_{t_1}^{t_2} p(t) dt$$

where p is the local value of the pressure, t is time, and $(t_2 - t_1)$ is the time required for n complete revolutions of the wave. Accurate measurements of p_{av} are difficult to obtain in this engine's extremely hostile environment. Though some of the measurements to be discussed below do not merit a great deal of confidence on their own, considerable reassurance is gained from the fact that all three types of measurements seem to indicate that during the high-amplitude tangential resonance, there is an appreciable reduction in p_{av} near the center of the injector.

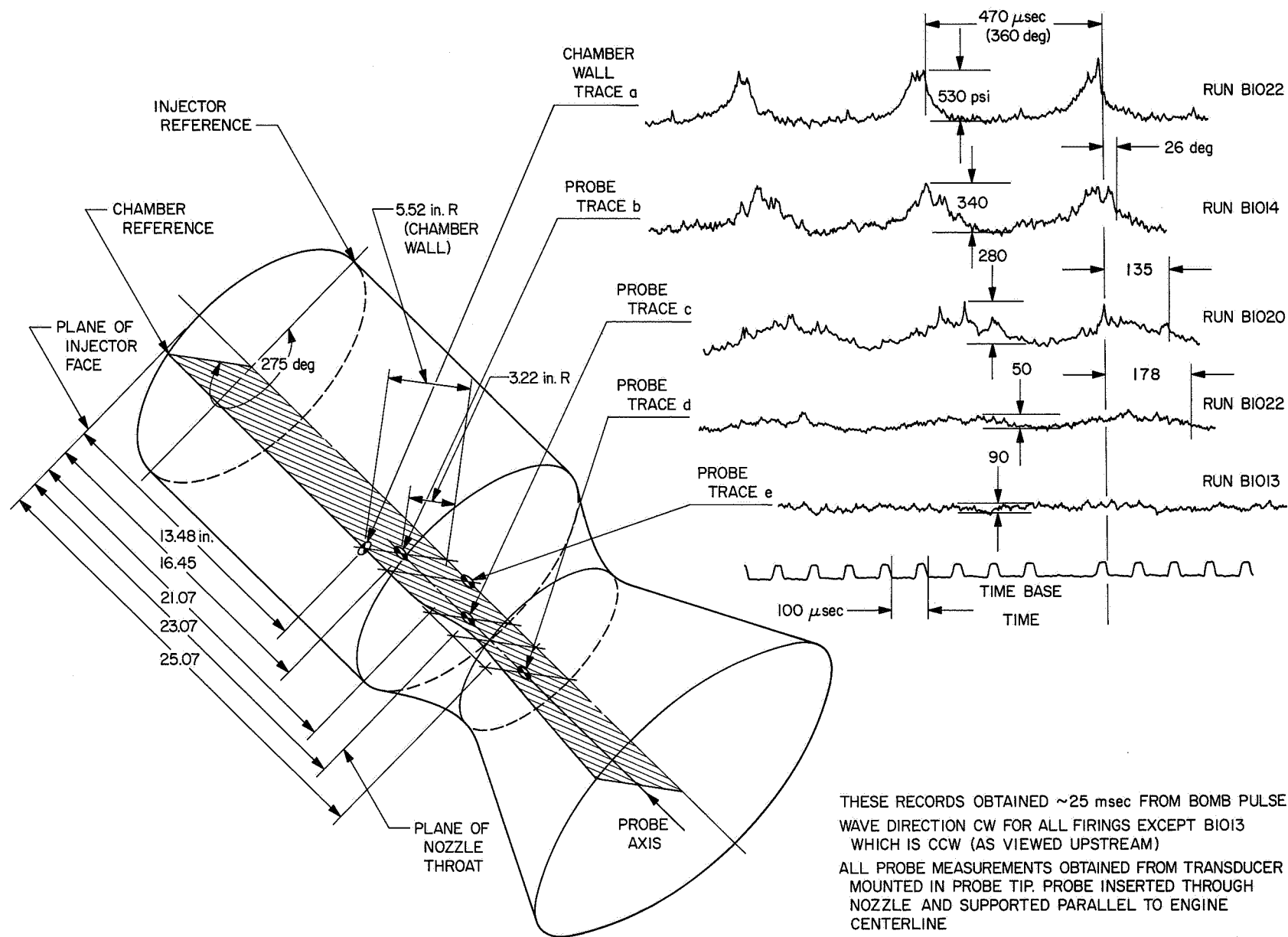


Fig. 30. Typical spatial pressure distribution versus time in the vicinity of the nozzle during resonant combustion; RMIR Injector 5 with standard engine and SFNA plus Corporal fuel

High-frequency pressure measurements. Graphical integration of high-frequency pressure measurements on a single run indicated that p_{av} was on the order of 100 psi lower at $r = 0.8$ in. than at other positions at greater radii. The results for one continuous series of six cycles are shown in Fig. 31. The measurement at $r = 0.8$ in. is considered most reliable because of the low amplitude of the wave there; however, other measurements generally agree in being considerably higher than that at $r = 0.8$ in.

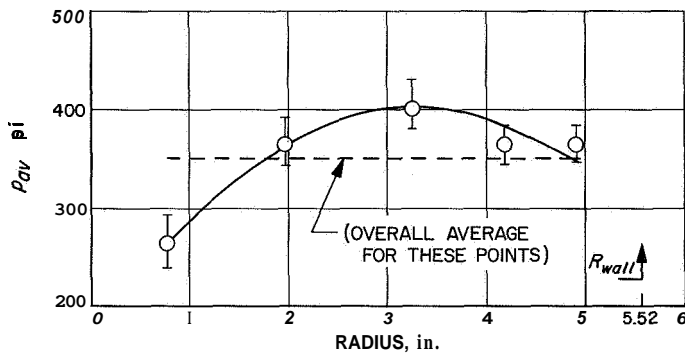


Fig. 31. Average pressures 8 msec after bomb, Run B956

Low-frequency pressure measurements. On all ten resonant firings in this series, a Tabor low-frequency transducer measured a sharp drop in pressure at the center of the injector during the resonant part of the run. The average over the ten runs was 41 psi, or about 14% of the pre-resonant chamber pressure. Again, the data at the center are considered to give a fairly reliable p_{av} . The wave is very low in amplitude at the center of the chamber, and the pressure gauge in question is coupled to the chamber by a long, thin tube, which tends to average the high-frequency pressure changes.

A similar transducer at the outer edge of the injector face recorded a substantial increase in pressure on each run; however, here the transducer is closely coupled to the chamber and the pressure oscillations (being extremely violent) may introduce substantial errors in the averaging characteristics of the transducer coupling cavities. Nonetheless, the indication of increased pressure at the outer periphery of the combustion volume is consistent with the indication from the high response measurements.

Individual orifice flows. Since the propellant tank pressures are maintained constant, a significant change in the time average flow through any particular orifice during resonance is taken as an indication that p_{av} at the orifice exit has changed.

Flows through several different orifices were measured by the method previously discussed for RMIR Injector 7 in Sect. 2. The observed changes in flow rates are listed in Table 7. The radius refers to the location of the particular doublet's impingement point.

Table 7. Changes in flow rates during resonance, RMIR Injector 5

	0	2.5	4.3
Fuel	+ 5%	+4.5%	<1%
Oxidizer	+ 15%	+ 9%	-4%

The results are considered a good indication of a deficit in p_{av} at the center of the chamber, since flow rates increased sharply there. The fact that the oxidizer flows reacted more strongly than the fuel flows is consistent with calculations reported in Ref. 25, in which RMIR Injector 5 parameters were used to investigate the high-frequency response characteristics of the flow system.

d. Variations in bomb position. In a manner apparently analogous to that observed for RMIR Injector 7 (Ref. 24 and 25), the travel direction of the sustained rotating wave for this engine depends upon the circumferential position of the radially oriented bomb relative to the injection scheme. Direction versus bomb position (axial position constant at 4.0 in. from the face) is shown by the arrows in Fig. 32 together with the number of runs performed using each bomb position. The data are superimposed on a representation of the axial mass flux distribution produced by the injector at a cross-section 2.75 in. downstream of the injector face. The mass distribution is based on nonreactive flow and is fully described in Ref. 28. Presumably, the direction of the wave is related to some asymmetry in the mass flux and/or mixture ratio distribution or to some wall-wetting condition; however, the connection is not clear at this time.

5. Variations in Chamber Geometry

The three nonstandard chambers shown in Fig. 27 were employed in order to gain insight into the wave's nature by observing its behavior in the different geometries. The limited number of firings performed (one with each non-standard chamber) showed that essentially the same wave behavior is exhibited by the three various length engines, but that a drastic change resulted with the stepped chamber configuration.

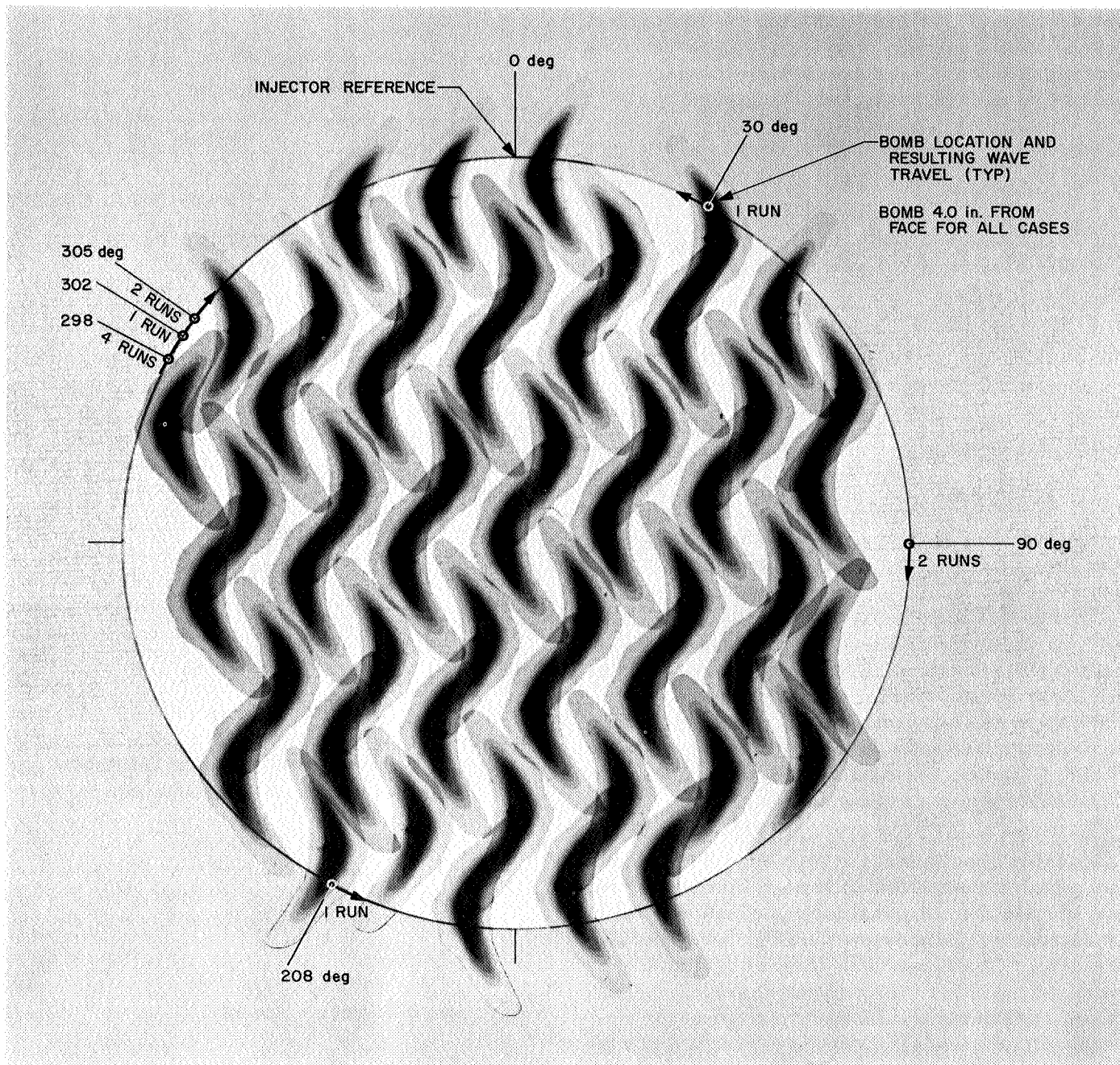


Fig. 32. Wave travel direction versus bomb position relative to injection scheme (RMIR injector 5 with SFNA plus Corporal fuel and standard length chamber)

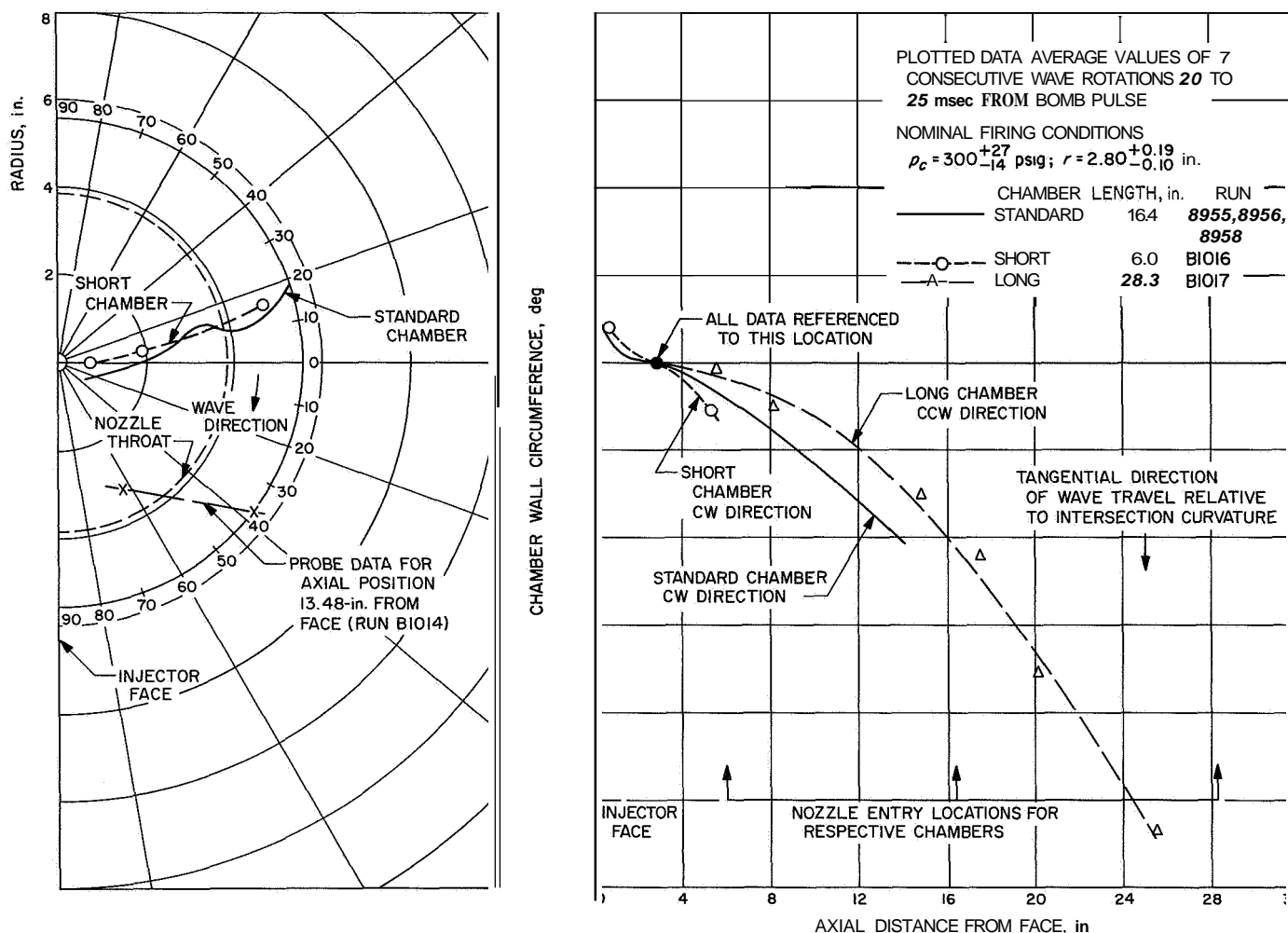


Fig. 33. Intersection of resonant combustion wave with chamber boundary (RMIR injector 5 with SFNA plus Corporal fuel and various length chambers)

When only engine length was varied with the short, standard, and long chambers, the wave had almost exactly the same rotational period in each case: **469,470** and **472** psec, respectively. In addition, the shape of the wave-to-chamber boundary intersection and the trend of the variation in wave amplitude with boundary position, shown in Figs. 33 and 34, respectively, show relatively little dependence on chamber length. These observations seem to be consistent with the concept that the wave's characteristics are mainly determined by processes occurring near the injector face, rather than being connected to some overall chamber behavior analogous to that of the combined tangential-longitudinal modes of classical acoustics.

The behavior of the initial bomb-blast wave for the long-chamber firing is of some interest in itself. The bomb

device was placed an additional 12 in. further from the injector face for this run (total of 15.97 in. downstream); consequently, the initial wave could be observed as it progressed upstream (toward the injector) as well as downstream. This is summarized in Fig. 35, which shows the amplitude and displacement history of the spatially expanding wave. A 30-deg circumferential displacement of the bomb from the longitudinal array of pressure taps along the chamber wall makes it necessary to take into account a transverse component of wave travel; thus, the wave behavior is plotted against straight-line distance from the geometric center of the bomb. The axial distance of each measurement from the injector face is indicated below the abscissa. An apparent wave velocity based on the intervals of straight line distance (Δx) and the time intervals (Δt) between the measurements is also shown

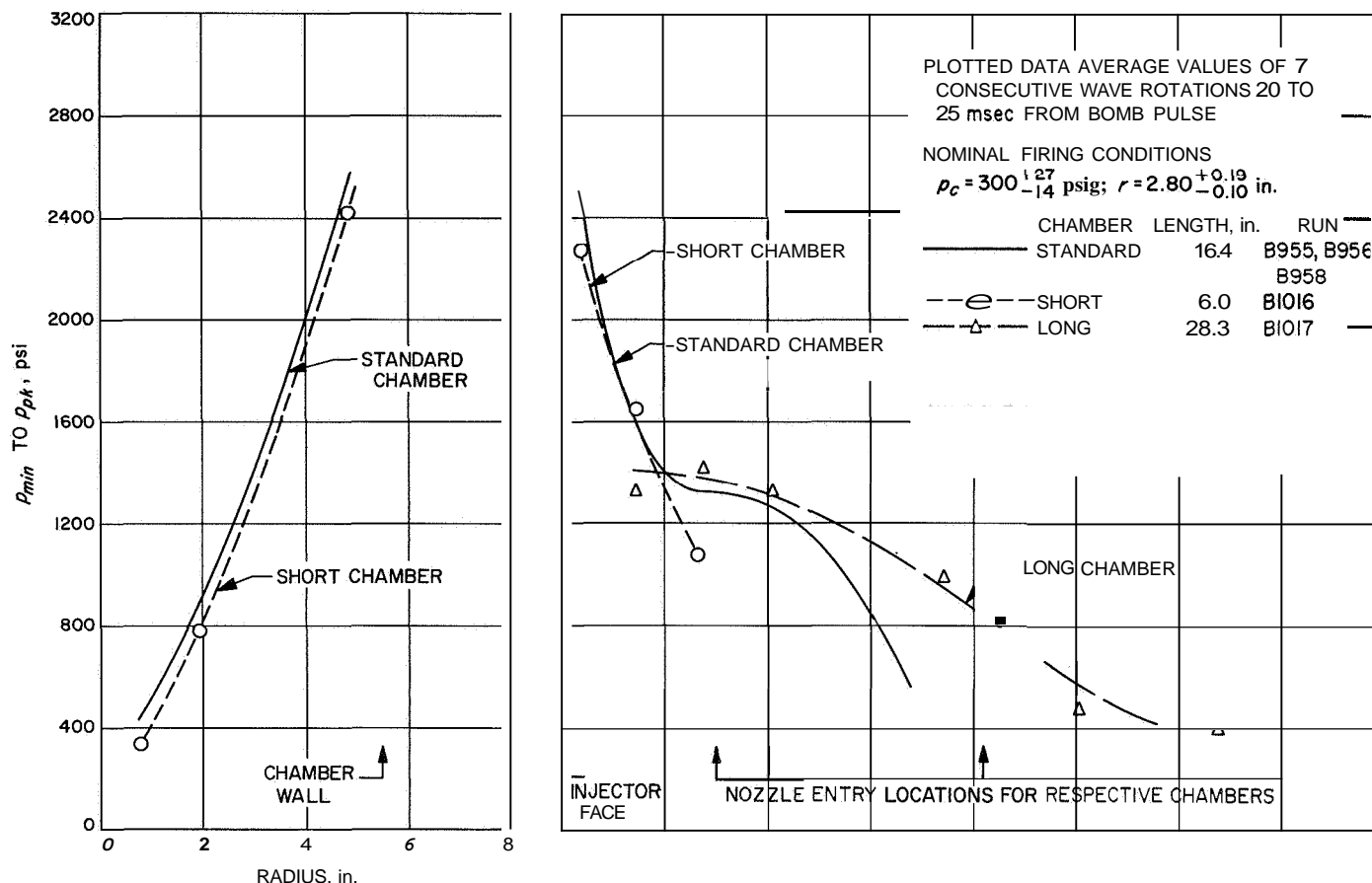


Fig. 34. Resonant combustion pressure amplitude versus chamber boundary position (RMIR Injector 5 with SFNA plus *Corporal* fuel and various length chambers)

for the respective increments of wave travel. It is noted that time $t = 0$ is the time of bomb case rupture, and hence is presumed to be the instant of pressure wave onset.

The significant feature of these data seems to be that the wave is strongly attenuated as it proceeds into the highly reactive zone near the injector face. This is the zone in which the sustained tangential wave—similar in shape (pressure-versus-time) to a blast wave—is very strongly driven, and the difference in behavior between the two is not understood.

The sustained wave—while qualitatively of the same character as for the standard and short engines in all other aspects—rotated in the opposite direction from that expected for the bomb circumferential position of 298 deg. This is believed to be the result of the far-downstream bomb placement and seems to indicate that it is not necessarily the initial blast wave that directly forms the sustained tangentially traveling wave.

For the stepped chamber, a sustained rotating wave was obtained; however, the characteristics of the gross disturbance were substantially different from those observed in the uniform-diameter chambers. These differences are illustrated in Fig. 36, which compares typical pressure-versus-time records for several chamber boundary axial stations for the straight and stepped engines. It is of particular interest to note that:

- (1) The predominant oscillation is almost totally confined to the 18-in.-D portion of the stepped chamber—the 11-in.-D portion exhibiting almost noise-like fluctuations. Also, the period of the disturbance is changed to approximately 700 psec. This compares to the 470-psec period normally observed for the straight 11-in.-D chamber and indicates an approximately constant (within 10%) mean wave velocity for either engine configuration.
- (2) The waveform for the stepped chamber wave (3.0-in. axial position) approaches a sinusoidal form.

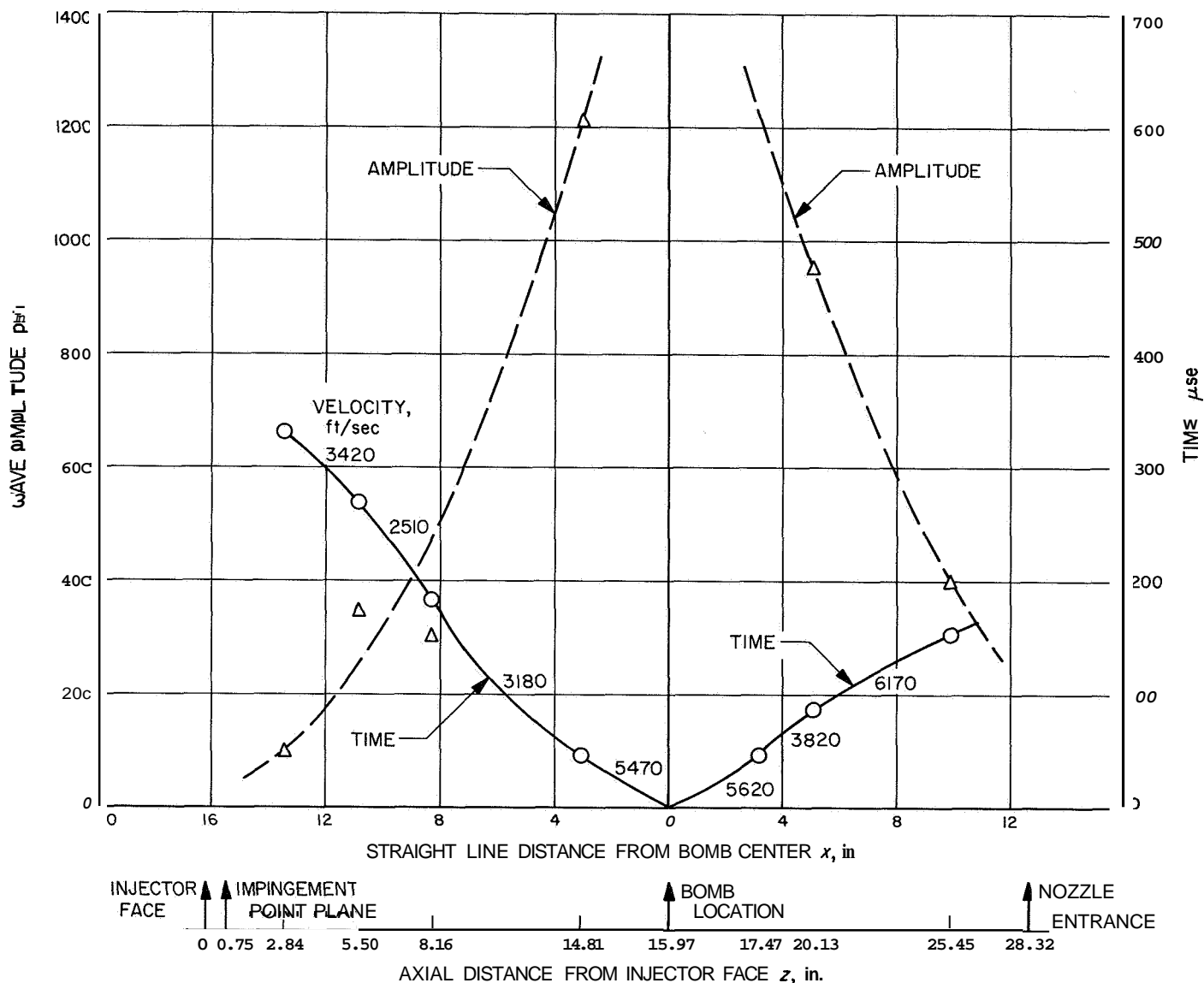


Fig. 35. Bomb wave behavior versus distance from bomb as used in the long chamber, Run B1016

This is converse to the very steep-fronted behavior normally noted at this distance from the injector.

- (3) The amplitude of the stepped chamber disturbance is reduced by at least a factor of three from that normally observed at the boundary in the region 3.0 in. from the injector face. The noiselike fluctuations on the order of 100 psi in the 11-in. section represent even greater reductions in amplitude—if not the complete elimination of the resonance in the downstream chamber.

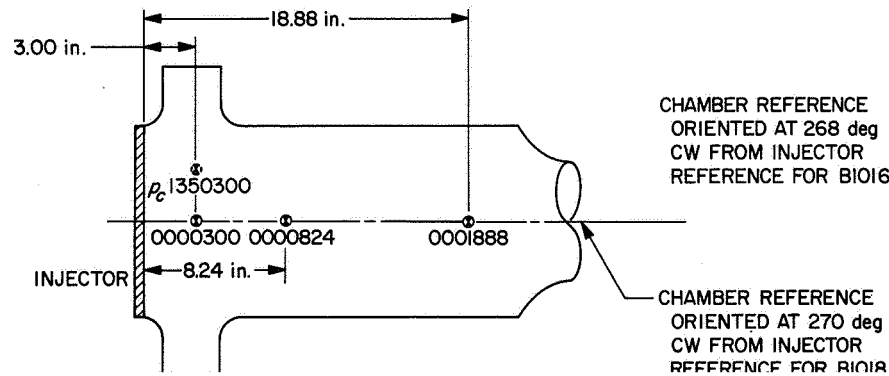
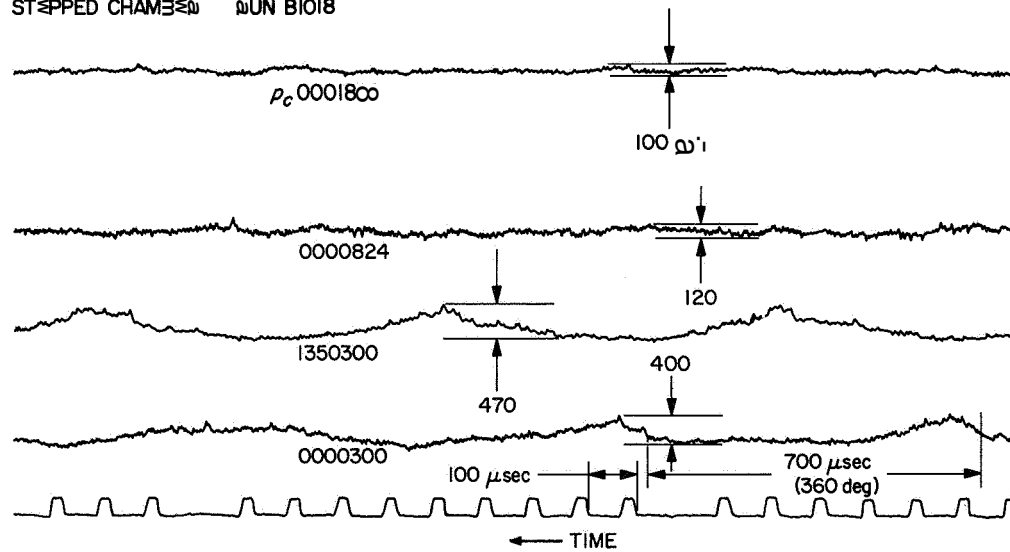
While this experiment was of an exploratory nature and was not refined enough to allow quantizing the changes

made in the actual wave driving mechanisms, it is felt that the essential change was the removal of the chamber wall from the close proximity of the freshly injected propellants. The consequent reduction in the mass and energy source available to the tangentially sweeping pressure wave effectively decoupled the wave and weakened it substantially.

6. Conclusions

- (1) High-frequency, high-amplitude tangential waves in the combustion chamber can produce changes in mass distribution (and mixture ratio) which vary with time and with position on the injector face.

STEPPED CHAMBER RUN B1018



LONG CHAMBER RUN B1016

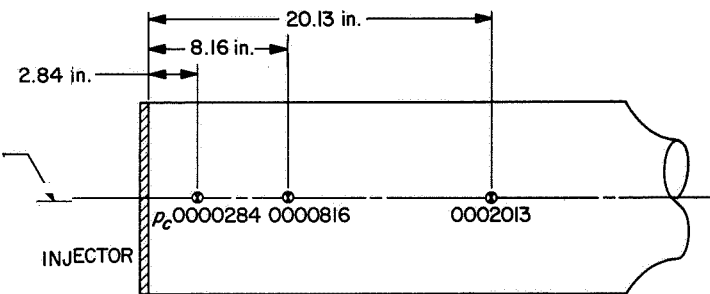
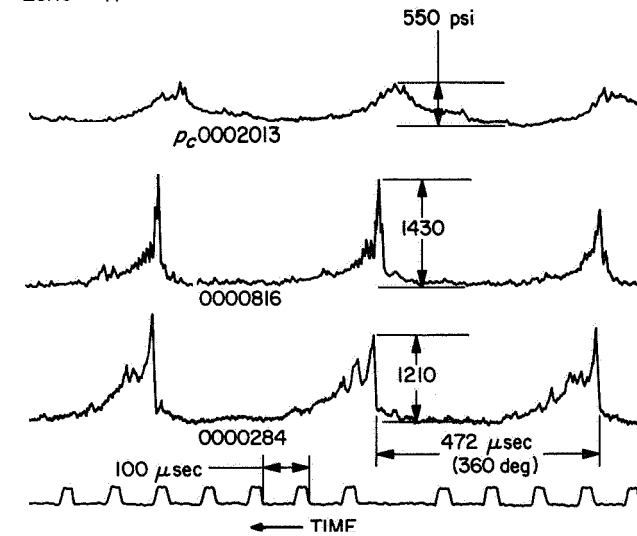


Fig. 36. Resonant wave behavior in stepped chamber, Run B1018

- (2) Reasonably accurate profiles of static pressure versus axial distance can be obtained using the scanner valve technique described; but use of several differential pressure gauges may be preferable.
- (3) High-time-resolution photographs of the steep-fronted wave have been obtained; however, they do not seem to reveal useful additional information on the nature of the wave.
- (4) Limited pressure probe measurements on the resonant disturbance at locations within the chamber volume (away from the boundaries) show a decreasing wave amplitude toward the chamber center and a nonradial spatial orientation, both similar to that observed at the injector face.
- (5) All available evidence seems to indicate that the time-averaged pressure at the center of the chamber is reduced by **40** psi or more during resonant conditions in the standard chamber, using RMIR Injector 5.
- (6) The direction of travel the tangential wave will take in the 11-in. engines utilizing Injectors 5 and 7 can be predicted reliably when certain bomb positions are used.
- (7) The resonant wave behavior for RMIR Injector 5 is not substantially changed by changes in combustion chamber length alone. The stepped-chamber configuration does modify this behavior, however, providing a decoupling effect between the wave and the combustion environment.

References

1. Rowley, R. W., "Gas Side Boundary Phenomena," SPS **37-38**, Vol. IV, Jet Propulsion Laboratory, Pasadena, California, April 30, **1966**, pp. **112-116**.
2. Rupe, J. H., and Jaivin, G. I., *The Effects of Injection Mass Flux Distributions on Local Heat Transfer in a Liquid-Propellant Rocket Engine*, Technical Report No. **32-648**, Jet Propulsion Laboratory, Pasadena, California, October 1, **1964**.
3. Rowley, R. W., and Tyler, W. H., *The Effect of Injector Design on Thrust Chamber Erosion*, Technical Report No. **32-750**, Jet Propulsion Laboratory, Pasadena, California, March 1, **1966**.
4. Rowley, R. W., "Gas Side Boundary Phenomena," SPS **37-32**, Vol. IV, Jet Propulsion Laboratory, Pasadena, California, April 30, **1965**, pp. **162-166**.
5. Schlichting, H., "Boundary Layer Theory," McGraw-Hill Book Co., Inc., New York, N. Y., **1955**.
6. Nurick, W. H., Seader, J. D., and Coultas, T. A., "Transient Heat Transfer from a Liquid Metal Spray Impinging on a Vertical Surface," Seventh National Heat Transfer Conference, American Institute of Chemical Engineers, Cleveland, Ohio, August **9-12**, **1964**.
7. Dawson, B. G., and R. R. Schreib, Jr., "Investigation of Advanced High-Energy Space Storable Propellant System — $\text{OF}_2/\text{B}_2\text{H}_6$," Paper **63-238**, Summer Meeting of the AIAA, Los Angeles, California, June **17-20**, **1963**.

References (contd)

8. Midwest Research Institute, "Structural Studies of Inorganic Oxidizer," Annual Summary Report, Report RPL-TDR-64-98, Contract AF 04(611)-9372, 1964.
9. Dawson, B. E., A. F. Lum, and R. R. Schreib, Jr., "Investigation of Advanced High Energy Space Storable Propellant System," Thiokol Chemical Co., Reaction Motors Division, Report 5507F, Contract NASw-449, June, 1962.
10. Stock, A., "Hydrides of Boron and Silicon," Cornell University Press, 1933.
11. Coggleshall, N. D., and E. L. Saier, "Pressure Broadening in the Infrared and Optical Collision Diameters," *Journal of Chemical Physics*, Vol. 15, No. 1, pp. 65-71, January, 1947.
12. Goldstein, M. S., "The Oxidation of Diborane," Ph.D. Thesis, Rensselaer Polytechnic Institute, Troy, N. Y., 1960.
13. Price, W. C., "The Absorption Spectrum of Diborane," *Journal of Chemical Physics*, Vol. 16, pp. 894-902, 1948.
14. Toy, M. S., W. A. Cannon, and W. D. English, "Solution and Conductivity Studies in Fluorine-Containing Liquid Oxidizers," Douglas Aircraft Co., Astropower Lab., DA-31-124-ARO(D)-115, QPR-5, 1964.
15. Simons, J. H., "Fluorine Chemistry," Vol. II, p. 498, Academic Press, Inc., New York, N. Y., 1954.
16. Coyle T. D., J. J. Ritter, and T. C. Farrar, "Preparation and Properties of Difluoroborane," *Proceedings of the Chemical Society*, p. 25, 1964.
17. Finch, A., I. Hyams, and D. Steele, "Vibrational Spectrum of Diboron Tetrafluoride," *Spectrochimica Acta*, Vol. 21, pp. 1423-1431, 1965.
18. Fisher, H. D., J. Kiehl, and A. Cane, "Infrared Spectra and Thermodynamic Properties of Trifluoroboroxine (FBO)₃," Hughes Tool Co., Report R-HTC-61-90, Contract AF 33(616)-6781, 1961.
19. Dushman, S., and Lafferty, J. M., *Scientific Foundations Of Vacuum Techniques*, John Wiley and Sons, New York, N.Y., 1962.
20. Keller, O. F., and Toth, L. R., *ALPS Generant Tank and Cell Assembly*, Technical Report 32-865, Jet Propulsion Laboratory, Pasadena, California, February 28, 1966.
21. Vango, S. P., *Determination of Permeability of Cast Teflon Sheet to Nitrogen Tetroxide and Hydrazine*, Technical Memorandum No. 33-55, Jet Propulsion Laboratory, Pasadena, California, August 25, 1961.
22. *Eighteen Inch Diameter Expulsion Diaphragm*, Honeywell, Inc., Aeronautical Division, 1383-FR, Final Report, JPL Contract 950569, September 15, 1966.

References (contd)

23. Clayton, R. M., and Rogero, R. S., *Experimental Measurements on a Rotating Detonation-Like Wave Observed During Liquid Rocket Resonant Combustion*, Technical Report No. 32-788, Jet Propulsion Laboratory, Pasadena, California, August 15, 1965.
24. Clayton, R. M., and Sotter, J. G., "Resonant Combustion," SPS 37-36, Vol. IV, pp. 163-173, December 31, 1965.
25. Clayton, R. M., Sotter, J. G., and Woodward, J. W., "Resonant Combustion," SPS 37-41, Vol. IV, pp. 134-151.
26. Bird, R. B., Stewart, W. E., and Lightfoot, E. N., *Transport Phenomena*, John Wiley and Sons, New York, N.Y., 1960.
27. Resonant Combustion Project Film Report No. 3, Jet Propulsion Laboratory Film No. 727.
28. Rupe, J. H., *An Experimental Correlation of the Nonreactive Properties of Injection Schemes and Combustion Effects in a Liquid-Propellant Rocket Engine: Part I, The Application Of Nonreactive-Spray Properties to Rocket Motor Injector Design*, Technical Report 32-255, Jet Propulsion Laboratory, Pasadena, California, July 15, 1965.

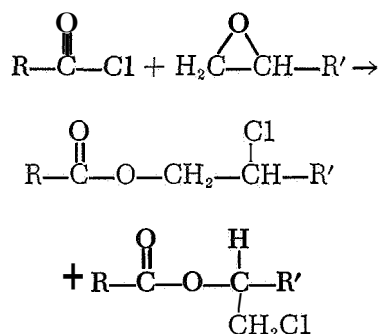
N67 18328

X. Solid Propellant Engineering

PROPULSION DIVISION

A. Polymerization of Acid Chlorides With Epoxides, *H. Marsh, Jr. and J. Hutchison*

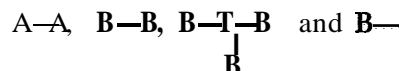
Addition reactions between acid chlorides and epoxides have been reported (Ref. 1-3):



It was thought that this reaction could be used in polymer synthesis. The system was of particular interest because it was a potential model for studies leading to the determination of the functionality of commercial carboxyl-terminated prepolymers. The average functionality of one component in a polymerization mixture can

be determined from modifications (Ref. 4) of fundamental relations derived by Flory (Ref. 5) for cross-linked polymers. This method involves the observation of the effect of a monofunctional component added to a system capable of forming a cross-linked network polymer, i.e., containing difunctional and trifunctional components. Naturally, the greater the functionality of the component being studied (in this case the closer to pure difunctional) the greater the amount of monofunctional species the system can tolerate and still produce a gel.

The requirements for a model system are stringent. It should be a condensation-type polymerization with the species



where the prepolymer under consideration has endgroups **B** (or those which can easily be converted into **B**). The reaction must be capable of reaching a high yield with no significant side reactions. For ease in operation, there should be no elimination products, and the polymerization should take place readily without catalysts or solvent

being required. Once the model system, where $B-B$ is a low molecular weight species of known difunctionality, has been found to operate, mixtures will be prepared where $B-B$ is the prepolymer of unknown functionality. In the case of carboxyl-terminated prepolymers, the carboxyls will be converted to acid chloride.

An added bonus in studying the acid chloride-epoxide polymerization is its possible synthetic value, including solid propellant binders. This system has the apparent advantages of no side reactions or elimination products, possible room temperature cures, and reduced prepolymer viscosities. High viscosity is a serious problem with saturated hydrocarbon prepolymers which are carboxyl terminated, because of endgroup hydrogen bonding. This would be eliminated by conversion to acid chloride.

1. Experiments and Results

The chosen monomers were sebacoyl chloride ($B-B$), trimesoylchloride ($B-T-B$) and ERL 4221 ($A-A$).



The latter is a Union Carbide product: 3,4-epoxycyclohexylmethyl-3,4-epoxycyclohexanecarboxylate.

Using the reagents without purification, a series of homogeneous mixtures was prepared with $R \approx 1$ ($R = \text{epoxide groups/total Cl groups}$) and varying ρ_T from 0.5 to 0 ($\rho_T = \text{Cl in trifunctional molecules/total Cl groups}$). Solid polymers were formed in approximately 2 hr at room temperature. As ρ_T varied from 0.5 to 0, their character changed from hard and brittle to soft and rubbery. These yellowish brown polymers were insoluble in organic solvents and infusible. This is expected with the cross-linked polymers prepared with trimesoylchloride, but is surprising when $\rho_T = 0$ and only difunctional molecules are present. Obviously some side reaction producing cross-links is occurring.

Polymerizations were also carried out in solution with $\rho_T = 0.5$. In benzene, refluxing temperatures were required and solvent removal from the resulting cross-linked polymer was difficult. In tetrahydrofuran no polymerization took place. This was probably a result of the much greater polarity of tetrahydrofuran permitting it to tie up the acid chloride.

In order to remove possible causes of cross-linking, such as water and HCl , the monomers were distilled at reduced pressure before use. Using a vigreux column

and a diffusion pump, the sebacoyl chloride distilled at $135^\circ C$ at 0.040 mm Hg, the ERL 4221 distilled at $140^\circ C$ and 0.003 mm Hg, and the trimesoyl chloride at $100^\circ C$ at 0.005 mm Hg. In the latter case after distillation, recrystallization from hexane under a N_2 atmosphere tent was necessary.

To provide an aliphatic trifunctional acid chloride, tricarballoyl chloride was synthesized using PCl_5 by the method of Emery (Ref. 6). However, repeated distillation at $65-66^\circ C$ and 0.003 mm Hg was unable to remove all traces of PCl_5 contamination. All polymerizations were carried out at room temperature in a N_2 atmosphere dry box with water content less than 3 ppm.

Using only the difunctional components sebacoyl chloride and ERL 4221 ($\rho_T = 0$), it was attempted to produce a linear, noncross-linked polymer (results given in Table 1). This is necessary to demonstrate the absence of interfering side reactions. However, with $R = 0.95, 1.00$, and 1.05 , only insoluble, infusible, rubbery, pale brown products resulted. The only apparent effect of monomer purification was to increase the gel time. Since the probable cause of the cross-linking was small amounts of HCl , from the acid chloride, a tertiary amine was added to remove it. Pyridine was chosen because it is weakly basic and should give the least interaction with the epoxide. The pyridine, purified by distillation from anhydrous barium oxide, clearly increased the rate of polymerization when added in 1-6 mole % of the sebacoyl chloride. The resulting rubbery polymers could be melted but were only swollen by organic solvents except in the case where $R = 0.95$ (i.e., an excess of sebacoyl chloride). Apparently any unreacted epoxide groups can produce cross-linking. They also result in a yellow coloration. Pyridine and ERL 4221 alone, slowly turn yellow. The color is immediately discharged by the addition of an excess of sebacoyl chloride. It was also observed that the order of mixing was critical. If the pyridine was added directly to the sebacoyl chloride, instead of first to the ERL 4221, a yellowish insoluble gum was produced.

The colorless linear polymer mentioned, unlike all previous products, shattered when struck. It also gave a weak, sticky film cast from benzene solution. In summary, to produce a linear colorless polymer with this system there must be an excess of acid chloride and no free HCl .

Polymers were also prepared, using trifunctional acid chlorides, to produce varying degrees of cross-linking

Table 1. Polymerization of sebacoyl chloride and ERL 4221

Run	Composition	Final color	Approximate flow temperature	Solubility	Remarks
9A	$R = 1.0$	Pale brown	Not melt	Insoluble	7 hr \ll gel time < 95 hr
9B	$R = 0.95$	Pale brown	Not melt	Insoluble	7 hr \ll gel time < 95 hr
9c	$R = 1.05$	Pale brown	Not melt	Insoluble	7 hr \ll gel time < 95 hr
13	$R = 1.0$	Pale brown	Not melt	Insoluble	2 hr \ll gel time < 18 hr
16A	$R = 1.0$ Pyridine, 1%, added to ERL	Very light yellow	280°C	Swells	6 hr $<$ gel time \ll 24 hr
16B	$R = 1.0$ Pyridine, 6%, added to ERL	Bright yellow	250°C	Swells	20 min $<$ gel time < 1 hr, heat evolved
18A	$R = 0.95$ Pyridine, 1.5%, added to sebacoyl chloride giving small amount yellow insoluble material	Colorless	260°C		gel time ≈ 7 hr; product shattered when hit. During polymerization it was yellow
18B	$R = 1.05$ Pyridine, 1.5%, added to sebacoyl chloride giving small amount yellow insoluble material	Very light yellow	300°C		gel time > 7 hr. During polymerization it was yellow
18C	$R = 0.95$ Pyridine, 1.5%, added to ERL with good mixing	Colorless	150°C	Soluble benzene, chlorobenzene, CHCl_3	gel time < 5 hr; product shattered when hit. During polymerization it was yellow
18D	$R = 1.05$ Pyridine, 1.5%, added to ERL with good mixing	Bright yellow	250°C	Swells	gel time < 5 hr. During polymerization it was yellow

intentionally (results in Table 2). Tricarballyl chloride immediately gave very dark coloration and with $p_T = 0.5$ a violent exothermic reaction produced a charred brittle mass. It is unlikely that this effect is entirely due to PCL_5 impurities in the tricarballyl chloride. Where $p_T = 0.1$ the product was a very soft rubber which is infusible and swells in benzene and chlorobenzene.

As expected, trimesoyl chloride, being aromatic, was less reactive than the aliphatic tricarballyl chloride. It gave a colorless hard rubber at $p_T = 0.1$ and a brittle, light yellow solid at $p_T = 0.5$. Both melted with decomposition at high temperatures. The former swelled greatly in organic solvents. However, quite surprisingly, the latter was mostly soluble in chlorobenzene. Thus it appears that trifunctional acid chlorides can be used to give a wide variety of properties.

2. Conclusions

The acid chloride-epoxide polymerization is not useful for a model system because of the difficulty in controlling side reactions leading to cross-linking. However, this system shows much promise for synthesis, especially where cross-linking is desired in the product. Of interest for propellant binders is the apparent high-temperature stability, particularly with regard to heat sterilizability.

3. Future Work

It is planned that epoxides will be used for curing acid chloride terminated prepolymers. Aziridines have been found to react violently with sebacoyl chloride and therefore will be investigated for use as curing agents in low concentration and at low temperature. Alternate reactions will be investigated for use in model systems.

Table 2. Polymerization with trifunctional acid chlorides

Composition Composition	Final color	Approximate flow temperature	Solubility	Remarks
Sebacoyl chloride Tricarballoyl chloride ERL 4221 Pyridine 2% $R = 0.95, p_T = 0.5$	Very dark brown	Decomposition and some liquid at 340°C. Bulk was solid	Swells	4 < gel time < 5 hr, some slight warming Soft rubber
Sebacoyl chloride Tricarballoyl chloride ERL 4221 Pyridine 2% $R = 0.95, p_T = 0.5$	Black			Within 10 min got very hot and charred
Sebacoyl chloride Trimesoyl chloride ERL 4221 Pyridine 2% $R = 0.95, p_T = 0.1$	Colorless	290°C	Swells	3 < gel time < 4 hr. Was yellow during polymerization Hard rubber
Sebacoyl chloride Trimesoyl chloride ERL 4221 Pyridine 2% $R = 0.95, p_T = 0.5$	light yellow	330°C	Large fraction soluble in chlorobenzene	Gel time < 3 hr. Was yellow during polymerization Very brittle

References

1. Rider, T. H., *J. Am. Chem. Soc.*, Vol. 54, p. 773, 1932.
2. Ivin, S. Z., *Zhur. Obshchei Khim.*, Vol. 28, p. 180, 1958.
3. Sjöberg, B., *Chem. Zentr.*, Vol. II, p. 25, 1942.
4. Marsh, H. E., Jr., *Ind. and Eng. Chem.*, Vol. 52, p. 768, 1960.
5. Flory, P. J., *Principles of Polymer Chemistry*, Cornell University Press, 1953.
6. Emery, W. O., *Chem. Ber.*, Vol. 22, p. 2920, 1889.

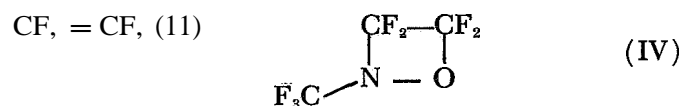
XI. Polymer Research

PROPULSION DIVISION

NOV 18 3 29
FBI - NEW YORK

A. F^{19} NMR of Nitroso Rubbers, J. D. Ingham and D. D. Lawson

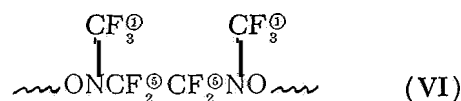
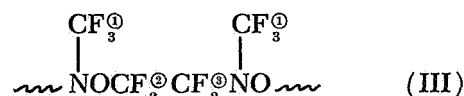
The one-to-one copolymer prepared by the reaction of trifluoronitrosomethane (I) and tetrafluoroethylene (11) is a polymeric material known as nitroso rubber (111) (Ref. 1). This polymer has a relatively low glass transition temperature (-51°C) and shows excellent solvent resistance to hydrogen-containing solvents and other nonfluorinated compounds (Ref. 2).



The reaction of (I) and (11) is most likely a free radical process and is carried out at low temperatures to obtain the polymer. If the reaction of (I) and (11) is carried out at room temperature, the amount of cyclic perfluoro-(2-methyl-1,2-oxazetidine) (IV) is increased. The present NMR study was undertaken to determine the structure of nitroso rubber with respect to the nitrogen-oxygen orientation of trifluoronitrosomethane units. Previous F^{19} NMR spectra indicated a regular orientation as shown for (111) above; however, the spectra were observed at lower resolution than those in this study (Ref. 3).

An F^{19} NMR spectrum of a typical nitroso rubber gum dissolved in hexafluorobenzene is shown in Fig. 1. The

three possible orientations of the adjacent trifluoronitrosomethane units with respect to tetrafluoroethylene are:



On the basis of (111), three lines should be observed with intensities in the ratio 3:2:2. Any contributions of structures (V) and (VI) should result in two additional lines, a fourth one in the vicinity of (III)-②, from (V)-④, and a fifth near (III)-③, from (VI)-④ fluorines. From Fig. 1, it can be seen that five lines are observed, with the structural arrangement of (111) predominating, as shown below. Because of its intensity, the low field signal can be assigned to the fluorine nuclei on the trifluoro methyl groups. On the basis of the analyzed spectrum of perfluoro(2-methyl-1,2-oxazetidine) (IV) according to Lee and Orrell (Ref. 4) and our spectrum of the oxazetidine shown schematically in Fig. 2, the difluoromethylene fluorines attached to oxygen atoms are 4300 and 4135 cps downfield from hexafluorobenzene. The difluoromethylene fluorines attached to nitrogens are assigned to

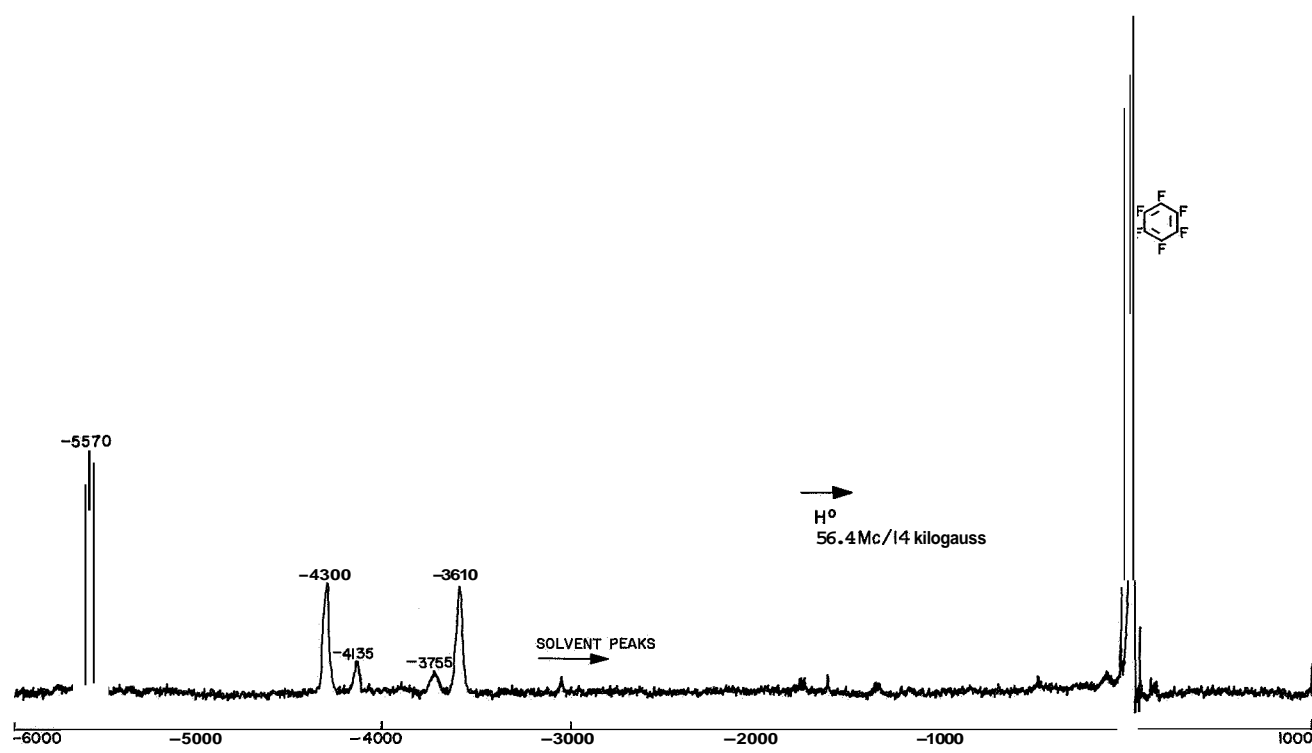


Fig. 1. F^{19} NMR spectrum of $CF_3NO/CF_2=CF_2$ copolymer (~ 10 wt % in hexafluorobenzene)

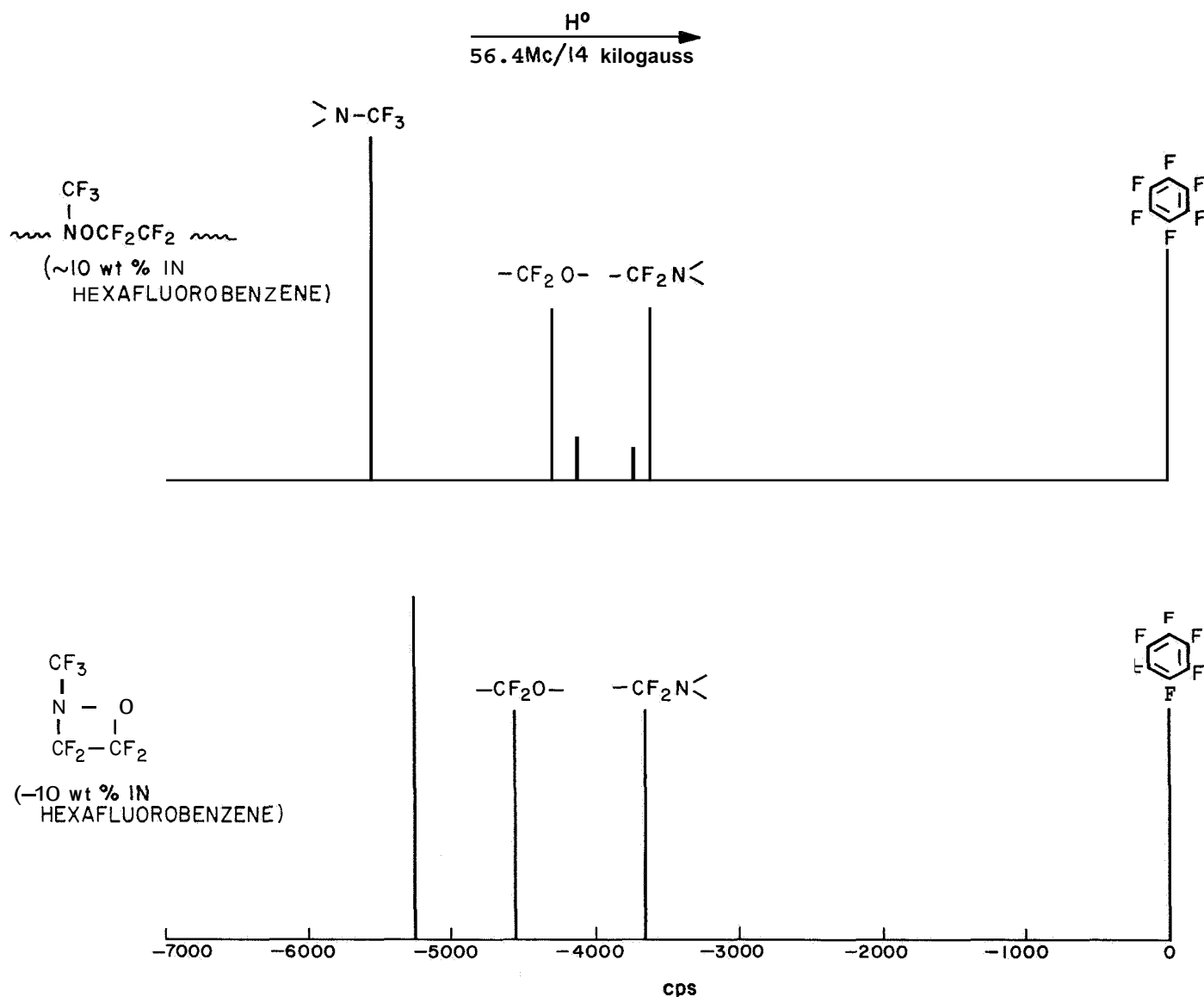


Fig. 2. F^{19} NMR chemical shifts of $CF_3NO/CF_2=CF_2$ copolymer and perfluoro(2-methyl-1,2-oxazetidine)

the signals that appear at 3755 and 3610 cps from hexafluorobenzene. A schematic representation of these spectral assignments is shown in Fig. 2. The two signals at -4135 and -3755 are considered to be (V)-④ and (VI)-@ respectively, because the latter exhibits N^{14} quadrupole broadening and therefore should have nitrogen nuclei as near neighbors. This (VI)-@ assignment reasonably defines the (V)-④ position because it is expected that these two signals would be of equal intensity. Furthermore, earlier work by mass spectrometry of a different nitroso rubber sample (Ref. 5) had indicated the presence of *only* the regular orientation (111). Thus, the more intense signals at -4300 and -3610 cps can be

assigned to the regular structure, from (III)-② and (III)-③ respectively. Since the integrated areas of the NMR signals are proportional to the number of fluorines in each environment, the relative areas of $-CF_3$: $-CF_2O$: $-CF_2N$ should be 3:2:2, irrespective of the nitrogen-oxygen orientation of trifluoronitrosomethane units. Integration of the spectrum in Fig. 1 by weighing gave an over-all ratio of 2.9:2.2:2.0 (or 2.9:1.8:0.4:0.4:1.6 for the five signals). These results further indicate that the assignments are reasonable. It has been determined that the signals that appeared to 3100 cps downfield from hexafluorobenzene were from solvent impurities.

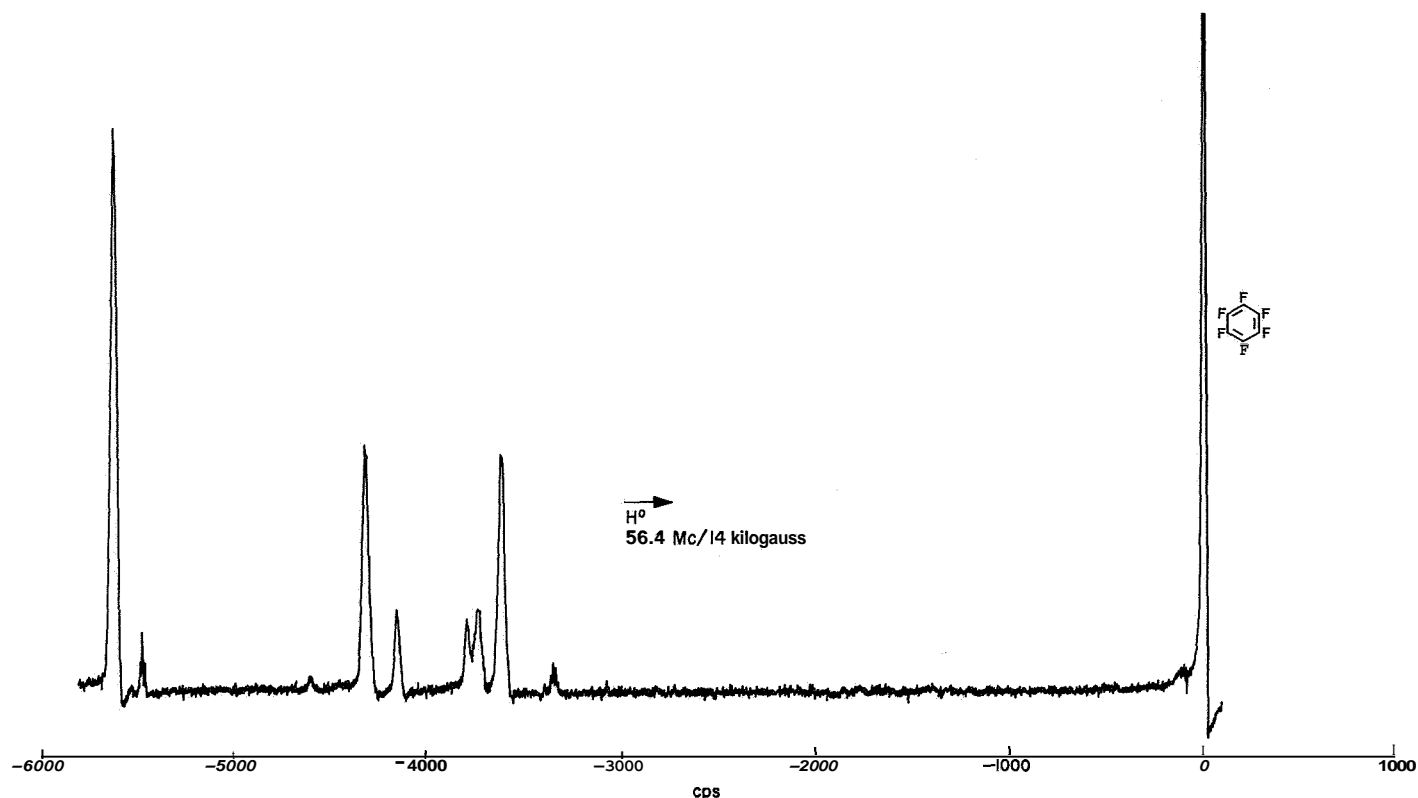
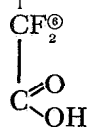
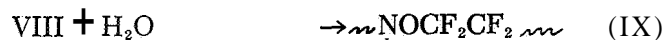
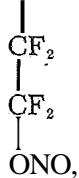
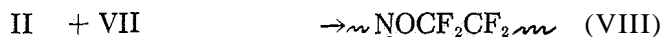
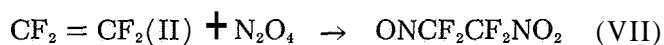


Fig. 3. F^{19} NMR spectrum of $CF_3NO/CF_2=CF_2$ copolymer containing some carboxy difluoromethylene groups (~ 10 wt % in hexafluorobenzene)

When (I) and (11) are reacted in the presence of nitrogen dioxide, a low molecular weight liquid polymer is obtained that contains some isolated carboxy difluoromethylene groups apparently formed by the following reaction steps (Ref. 6):



The F^{19} NMR spectrum of this polymer is shown in Fig. 3. It is identical with the spectrum of ordinary

nitroso rubber except that a new signal appears just downfield from the (VI)-@ fluorines that can be assigned to the (IX)-@ fluorines. This is further evidence that the previous assignments are probably correct in that it appears in the vicinity of the signals believed to arise from these other difluoromethylenes adjacent to nitrogens. A spectrum of polymer believed to contain some nitric ester groups as indicated by (VIII) is shown in Fig. 4. The signal at -4600 cps is apparently from fluorine on the carbon adjacent to $-ONO_2$, since this signal is in the vicinity of other CF_2O fluorines and is decreased, on hydrolysis, to (IX), Fig. 3. The small signals at -2550 and -2460 cps (Fig. 4) have not yet been identified, but are apparently eliminated during hydrolysis and purification.

N67 18330

B. Reactions of N-Vinylcarbazole With Anionic Initiators, A. Rembaum, A. M. Hermann, and R. Haack

1. Introduction

The conversion of N-vinylcarbazole to dimers or low and high molecular weight polymers has aroused a great deal of interest and is the subject of a number of recent

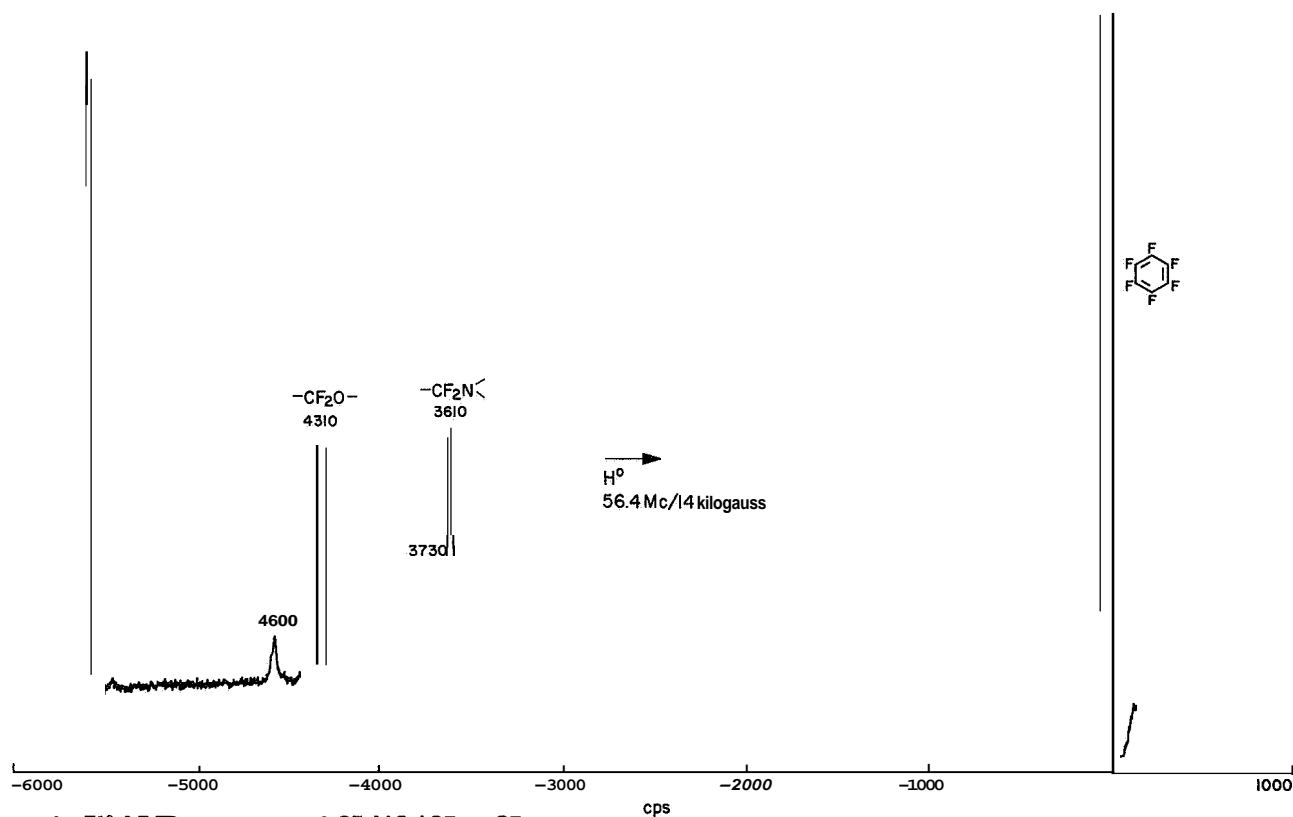


Fig. 4. F^{19} NMR spectrum of $CF_3NO/CF_2=CF_2$ copolymer containing some nitratotetrafluoroethylene groups

investigations (Refs. 7-17). This monomer is easily polymerized by a variety of methods, e.g. by free radical (Ref. 11), cationic (Ref. 7), and Ziegler-type initiators (Ref. 7), as well as by high energy radiation (Ref. 8), and heating (Ref. 10). A considerable effort was made to elucidate the role of charge transfer complexes in the polymerization, which was attributed to an initial formation of positive radical ions (Refs. 15 and 18). In a number of systems the mechanism is still a matter of controversy, e.g. the polymerization of N-vinylcarbazole by means of CCl_4 is not understood unambiguously (Refs. 8, 11, 14, 15, 19, and 20). Similarly, the polymerization mechanism using p.chloranil as initiator was questioned by Meyers (Ref. 21) who demonstrated that p.chloranil acts as a polymerization inhibitor when all reagents are carefully purified.

In this communication we report the results of the reaction of N-vinylcarbazole with anionic initiators such as metallic sodium, "living polystyrene" and butyllithium, since information on this subject is lacking.

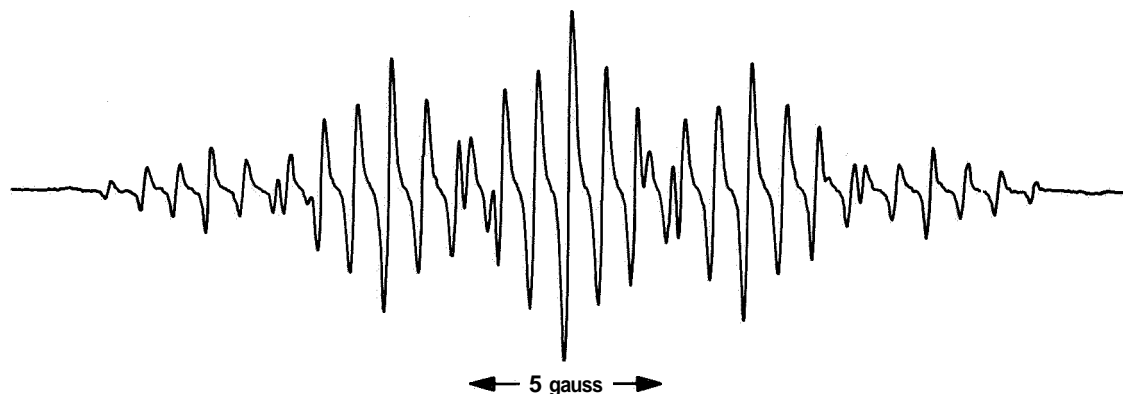
It is demonstrated that (1) the radical anion of N-vinylcarbazole is easily formed at relatively low tem-

perature; (2) it does not undergo dimerization; (3) it does not polymerize but initiates the polymerization of other monomers under well specified conditions; and (4) it is unstable at room temperature because of a C-N bond scission. The failure of this monomer to polymerize by means of anionic initiators may be explained by the high concentration of negative charges around the vinyl group.

2. Experiments

All reactions were carried out in tetrahydrofuran (THF) by means of the well established vacuum technique (Ref. 22). Electron spin resonance (ESR) spectra were recorded on the Varian V-4501 spectrometer at 9500 Mc with high frequency modulation (100 kc). Samples were kept at constant temperature with the aid of a V-4547 variable temperature accessory. Infrared and visible spectra were determined by means of Perkin Elmer 421 and Cary 14 spectrophotometers, respectively. Pressure changes were measured by a mercury manometer sealed to a glass apparatus which was thoroughly degassed prior to reacting N-vinylcarbazole with sodium.

(a) EXPERIMENTAL, REDUCED ON SODIUM IN THF AT -30°C



(b) THEORETICAL, BASED ON SPLITTING CONSTANTS SHOWN IN TEXT, AND A LINE WIDTH OF 240 mgouss

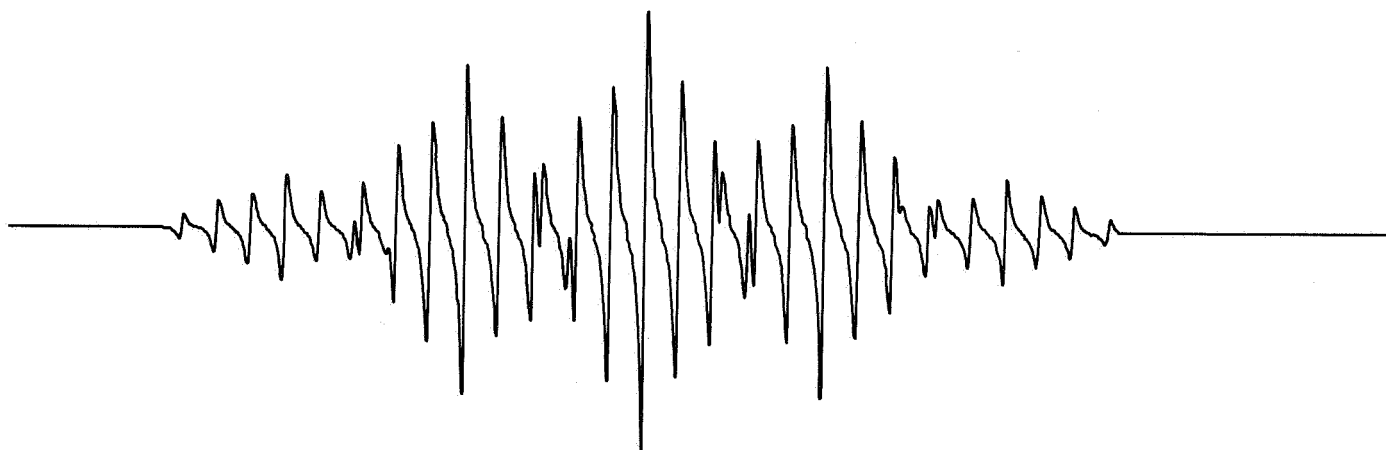


Fig. 5. ESR spectrum of N-vinylcarbazole

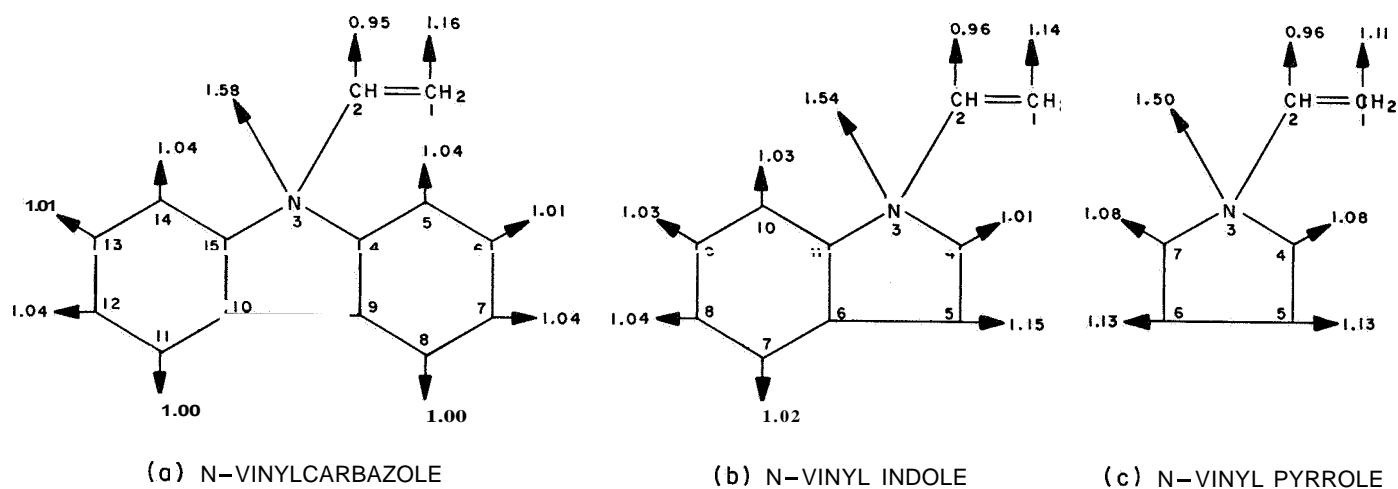


Fig. 6. π -electron density distribution

N-vinylcarbazole was purified by repeated crystallization from methanol (melting point 63°C). THF and styrene were rigorously purified by previously described methods (Ref. 23). Butyllithium in n-hexane (12.5%, Foote Mineral Co.) was used as received.

3. Results

a. ESR measurements. The reaction of N-vinylcarbazole with sodium in THF at -50°C results in a dark blue solution which exhibits an ESR spectrum shown in Fig. 5(a). The hyperfine structure could be reconstructed [Fig. 5(b)] by means of a Jeolco analog computer (RA-1 model) using the following splitting constants:

(For the numbering system, see Fig. 6)

$$a_N = 4.76 \text{ gauss}$$

$$a_{H_1} = 4.76 \text{ gauss}$$

$$a_{H_{7,12}} = 1.80 \text{ gauss}$$

$$a_{H_{5,14}} = 0.93 \text{ gauss}$$

The splitting constants of the remaining protons appear to be too small to be observable since all attempts to improve the resolution by change of temperature, solvent, or concentration were unsuccessful.

HMO calculations of unpaired spin densities failed to give good agreement with the experimental spectrum and the assignment of splitting constants is based on the known chemical reactivity of carbazole and vinylcarbazole towards electrophilic reagents (Ref. 24). An investigation of the overmodulated ESR signal showed an irreversible signal intensity decrease with time at room temperature, and a parallel change in the optical absorption spectrum is shown in Fig. 7.

b. Polymerization. Several attempts to polymerize N-vinylcarbazole with n-butyl lithium at room temperature were not successful and resulted in practically quantitative recovery of the unreacted monomer. The latter produced a change from a red to a yellow color when added to a small amount of low molecular weight "living polystyrene." No poly-N-vinylcarbazole could be isolated and the polystyrene was recovered from the reaction mixture. The N-vinylcarbazole radical anion (0.02 moles/l) when freshly prepared over sodium in THF polymerized styrene (2.1 g) at -80°C to yield a polymer with 99% conversion and an intrinsic viscosity of 0.43. A second

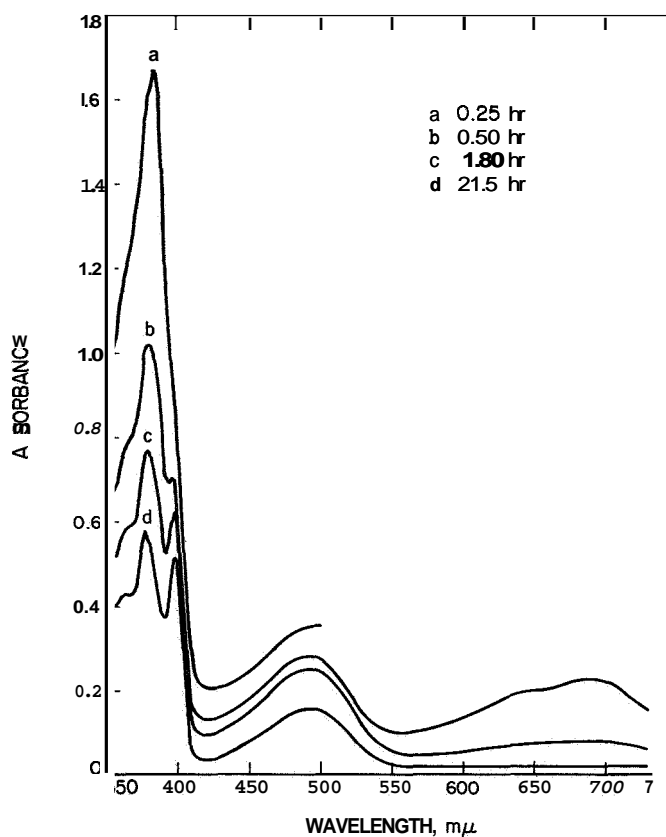


Fig. 7. Absorption spectrum of N-vinylcarbazole as a function of time

portion of the N-vinylcarbazole radical anion solution when kept for 24 hr at room temperature and reacted with styrene under identical experimental conditions resulted in a practically quantitative recovery of unchanged reactants. This fact was attributed to instability of the radical ion.

The ESR as well as the polymerization results indicated a decomposition of the radical ion, the nature and mechanism of which was investigated.

c. Identification of reaction products. The products of the reaction of N-vinylcarbazole with sodium consisted of carbazole and ethylene. The former was identified by its melting point and ultraviolet spectrum and the latter by its infrared spectrum. (The reaction of N-vinylcarbazole with sodium at 20°C for 24 hr yielded approximately 80% by weight of carbazole melting at $241-246^{\circ}\text{C}$. The melting point was unchanged on admixture of pure carbazole.)

The rate of ethylene formation could be followed by measuring the increments of pressure as a function of

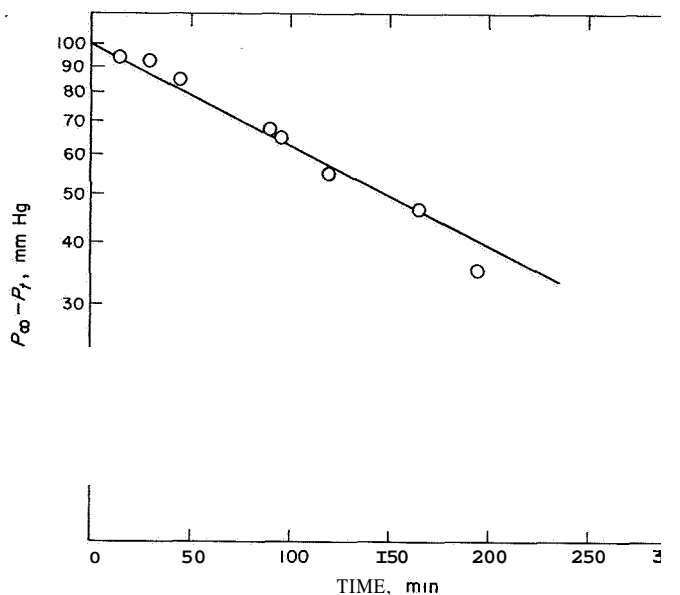


Fig. 8. First-order decomposition of the radical anion of N-vinylcarbazole showing the pressure-time variation of ethylene formed

time. Fig. 8 shows a plot of log of final pressure (P_{∞}), minus pressure at time t (P_t) versus time, and the linear relation obtained indicates that the first-order rate equation is obeyed.

4. Interpretation of Results

The formation of a radical anion of N-vinylcarbazole by means of sodium reduction was previously indicated (Ref. 25). It appeared that the radical anion did not undergo dimerization in contrast to a large number of vinyl monomers and this fact was in agreement with HMO LCAO calculation of π -energy change.

The lack of dimerization reaction is now confirmed by an ESR and chemical study of N-vinylcarbazole reacted with sodium. On the basis of the above results it is possible to represent the reaction path by the following scheme (Fig. 9).

Carbazole is regenerated from its sodium salt by addition of methanol or acid and the ethylene radical is assumed to abstract a hydrogen from the solvent to form ethylene.¹

¹According to recent investigations (Ref. 26) of negative radical ions and their reactions with alkyl halides, one should also consider the possibility that instead of the ethylene radical shown in Fig. 9, an ethylene anion may constitute the intermediate species. An exchange of Na^+ for a proton from the solvent would then yield the ethylene molecule.

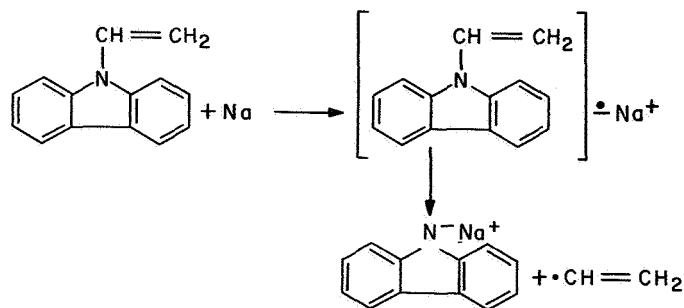


Fig. 9. Reaction mechanism

The examination of π -electron density of N-vinylcarbazole [Fig. 6(a)] calculated by means of the HMO method explains the high reactivity of the vinyl group towards electrophilic reagents and the absence of anionic initiation.

The calculations were performed, using for the coulomb integral of the nitrogen atom: $\alpha_c + p$, and the resonance integrals for the carbon-nitrogen bonds: $\beta_{2,3} = \beta_{3,4} = \beta_{3,15} = 0.9\beta$. Identical parameters used by Pullman (Ref. 27) for the unsubstituted carbazole molecule (similar calculations were also carried out by Longuet-Higgins, Ref. 28) yielded high electron density values for protons 7, 12, 5 and 14, and chemical evidence leaves little doubt that these are the most reactive positions (7 and 12 being preferred) in carbazole towards electrophilic reagents (Ref. 29). A comparison of π -electron density values of carbazole with those of N-vinylcarbazole indicates a slight reduction of the negative charge on the ring carbons in the presence of the double bond, and the high electron density of C, and N atoms makes the vinyl group very reactive toward positively charged species. By the same token, a nucleophilic attack is energetically unfavorable. Thus a close approach to the vinyl group of a negatively charged carbon and consequent formation of a C-C bond is precluded by the high electron density of C_1 as well as of the nitrogen atoms.

The benzene rings of the N-vinylcarbazole molecule must contribute to this high electron density. This statement is substantiated by the HMO calculation of π -electron density of N-vinyl indole and N-vinyl pyrrole [Figs. 6(b) and (c), respectively] which indicate the gradual decrease of negative charge concentration around the vinyl groups of the three structures from (a) through (b) to (c) in Fig. 6. The above theoretical deductions are confirmed by the recent results of Kambara, et al (Ref. 29), who proved the following order of polymerizability by means of electron acceptors: N-vinylcarbazole > N-vinyl indole > N-vinyl pyrrole. If we assume that

the polymerization by means of electron acceptors proceeds by addition of positively charged species to the monomer, then this polymerizability order agrees with the calculated π -electron densities (Fig. 6). An additional conclusion derived from HMO calculations is the

likelihood of anionic polymerization of N-vinyl pyrrole. The decrease of π -electron density around the N and C₁ atoms of this molecule may be sufficient to permit its polymerization by means of anionic reagents, and this possibility is now being investigated.

References

1. Barr, D. A., and Haszeldine, R. N., *Nature*, Vol. 175, p. 991-992, 1955.
2. Morneau, G. A., Roth, P. I., and Shultz, A. R., *J. Polymer Sci.*, Vol. 55, p. 609419, 1961.
3. Crawford, G. H., Rise, D. E., and Montermoso, J. C. Presentation at the 137th National ACS Meeting, April 5-14, 1960.
4. Lee, J., and Orrell, K. G., *Trans. Faraday Soc.*, Vol. 61, p. 2342-2356, 1965.
5. Griffis, C. B., and Henry, M. C., *Rubber Chem. and Tech.*, Vol. 39, p. 481-490, 1965.
6. Diatkin, B. L., Belsker, R. A., and Knunians, I. L., *Doklady Akad. Nauk. SSSR*, Vol. 166, p. 106-109, 1966.
7. Solomon, O. F., Dimonie, M., and Ambrozh, K., *Rev. Chim.* (Bucharest), Vol. 11, p. 520, 1960; Solomon, O. F., Dimonie, M., Ambrozh, K., and Tamescu, M., *J. Polymer Sci.*, Vol. 52, p. 205, 1961.
8. Chapiro, A., and Hardy, G., *J. Chem. Phys.*, Vol. 59, p. 993, 1962.
9. Ishii, T., and Hayashi, M., *J. Soc. Org. Synth.* (Japan), Vol. 7, p. 41, 1949.
10. Scott, H., Miller, G. A., and Labes, M. M., *Tetrahedron Letters*, Vol. 17, p. 1073, 1963.
11. Breitenbach, J. W., and Snra, C., *Polymer Letters*, Vol. 1, p. 263, 1963.
12. Owen, N. L., and Sheppard, N., *Proc. Chem. Soc.* (London), Vol. 264, 1963.
13. Liptay, W., Briegleb, G., and Schindler, K., *Ber. Bunsenges. Phys. Chem.*, Vol. 66, p. 331, 1962.
14. Scott, H., and Labes, M. M., *Polymer Letters*, Vol. 8, p. 413, 1963.
15. Ellinger, L. P., *Polymer Letters*, Vol. 6, p. 549, 1965.
16. Tsui, K., Takakura, K., Nishii, M., Hayashi, K., and Okamura, S., *J. Polymer Sci.*, Vol. A14, p. 2028, 1966.
17. McKinley, S., Crawford, J. N., and Wang, C. H., *J. Am. Chem. Soc.*, Vol. 31, p. 1964, 1966.
18. Pac, J., and Plesch, P. H., Preprints of the International Symposium on Macromolecular Chemistry, Tokyo-Kyoto, Japan, 1966.
19. Breitenbach, J. W., and Olaj, O. F., *Polymer Letters*, Vol. 2, p. 685, 1964.

References (contd)

20. Biswas, M., and Ghosal, S., *Chem. and Znd.*, p. 1717, 1966.
21. Meyers, R. E., paper presented at the Western Regional Meeting of the American Chemical Society, San Francisco, October 1966.
22. Paul, D. E., Lipkin, D., and Weissman, S. I., 3. *Am. Chem. Soc.*, Vol. 78, p. 116, 1956.
23. Morton, M., Rembaum, A., and Hall, J. L., *J. Polymer Sci.*, Vol. 1, p. 461, 1963.
24. Schmid, von H., and Karrer, P., *Helv. Chim. Acta*, Vol. 29, p. 573, 1946.
25. Higasi, K., Baba, H., and Rembaum, A., *Quantum Organic Chemistry*, Interscience, p. 315, 1965.
26. Garst, J. F., Ayers, P. W., Lamb, R. C., 3. *Am. Chem. Soc.*, Vol. 88, p. 4260, 1966.
27. Pullman, B., and Pullman, A., *Quantum Biochemistry*, p. 325, J. Wiley and Sons, New York, 1963.
28. Longuet-Higgins, H. C., and Coulson, C. A., *Trans. Far. Soc.*, Vol. 43, p. 87, 1947.
29. Kambara, S., Hatano, M., and Nomori, H., Preprints of the International Symposium on Macromolecular Chemistry, Tokyo-Kyoto, Japan, 1966.

N67 18331

XII. Research and Advanced Concepts

PROPULSION DIVISION

A. liquid MHD Power Conversion, D. G. Elliott, D. Cerini, and L. Hays

The long lifetimes required of electric-propulsion powerplants make systems without rotating parts attractive. A nonrotating Rankine cycle being investigated is the liquid-metal magnetohydrodynamic system wherein lithium is accelerated by cesium vapor in a two-phase nozzle, separated from the cesium, decelerated in a magnetohydrodynamic generator, and returned through a diffuser and heat source to the nozzle.

Tests of an ac generator with room-temperature NaK were completed. A lithium heater design for high-temperature system tests was evaluated.

1. AC Generator

a. Summary. Forty 2-4-min runs were made. After testing at a current of 15-20 amp/phase (2700-3600 gauss rms field) the current was raised in successive runs until a winding failure occurred at 30 amp and terminated the tests. After disassembly, the generator was found to

be in its original condition except for a melted section of two coil turns and damage to the epoxy in the adjacent slot.

The most significant operating result was that the generator operated self-excited with capacitors supplying the reactive power, as previously achieved elsewhere with the multiple-wavelength generator described in Ref. 1. The self-excited operation was stable, and voltage and output power were smoothly controllable by capacitor and load charges with the frequency adjusting to the required slip.

The most significant performance results were: (1) the compensating poles cancelled the side-plate voltage, eliminating the type of end loss that requires the generator length to be several times the width, and (2) the one-wavelength design was as efficient as a multiple-wavelength design, reducing the limitations on generator length imposed by winding loss. The only significant deviation from theoretical performance was a reduction in power output attributed to field variation between teeth and slots; this loss can be reduced with closed slots.

The highest power attained was 990 w at a NaK velocity of 194 ft/sec, frequency of 710 cps, rms field of 5000 gauss, slip of 0.8, and voltage of 140 v per phase. The powers and efficiencies were:

Net power output	$P_e = 990 \text{ w}$
Winding and core loss	$P_w = 940 \text{ w}$
NaK eddy-current loss under compensating poles	$P_{,,} = 25 \text{ w}$
Power output from the NaK in the traveling- wave region	$P_o = P_e + P_w + P_{ec} = 1955 \text{ w}$
Fluid power input due to electrical retarding force	$P_m = 4300 \text{ w}$
Friction power	$P_f = 6600 \text{ w}$
Gross electrical efficiency	$\eta_o = P_o/P_m = 45\%$

Net electrical efficiency $\eta_e = P_e/P_m = 23\%$

Over-all efficiency $\eta = P_e/(P_m + P_f) = 9\%$

These values and the others to be presented are based on preliminary data reduction and are subject to later correction.

The generator is compared in Table 1 with those previously tested elsewhere (Refs. 1-3). The main differences are the single wavelength and the small length/width aspect ratio of 2.2 compared with the previous values of 9.5-26. Low aspect ratio is essential for high efficiency with the wide flow from a separator and is the reason for employing a single wavelength design (minimum winding loss in a given length) and compensating poles (minimum added length for end-loss suppression). High efficiency was not realized in the experimental generator because of the slot loss and the difficulty in making a low-loss winding of small size. The significance of the experiment was in removing limitations on future designs.

Table 1. Dimensions and performance characteristics of liquid-metal AC generators tested to date

Laboratory	MIT	AI	AEG ^a	JPL
Reference	2	3	1	—
Test date	1963	1965	1966	1966
Total length L_t , in.	72.0	23.7	39.4	3.6
Traveling-wave length L , in.	72.0	23.7	39.4	1.2
Height b , in.	0.38	0.125	0.394	0.095
Width c , in.	2.75	2.50	3.10	1.60
Aspect ratio L_t/c	26	9.5	12.7	2.2
Number of wavelengths N	6	5	3	1
NaK velocity U , ft/sec	10	162	60	194
Frequency f , cps	5	350	50	710
Slip s	1.0	0.3	0.5	0.8
Magnetic field B , gauss (rmr)	100	2500	1400	5000
Net power output P_e , w	— 1500	1840	1000	990
Winding, core, and wall loss P_w , w	1500	2020	—	940
Gross power output P_o , w	0.17	3860	—	1955
Fluid power input due to electric retarding force P_m , w	0.49	5100	—	4300
Friction power, P_f , w	22	45,300	—	6600
Gross efficiency $\eta_o = P_o/P_m$, %	35	76	—	45
Net efficiency $\eta_e = P_e/P_m$, %	—	36	—	23
Over-all efficiency $\eta = P_e/(P_m + P_f)$	—	4	—	9

^aLast seven items not reported.

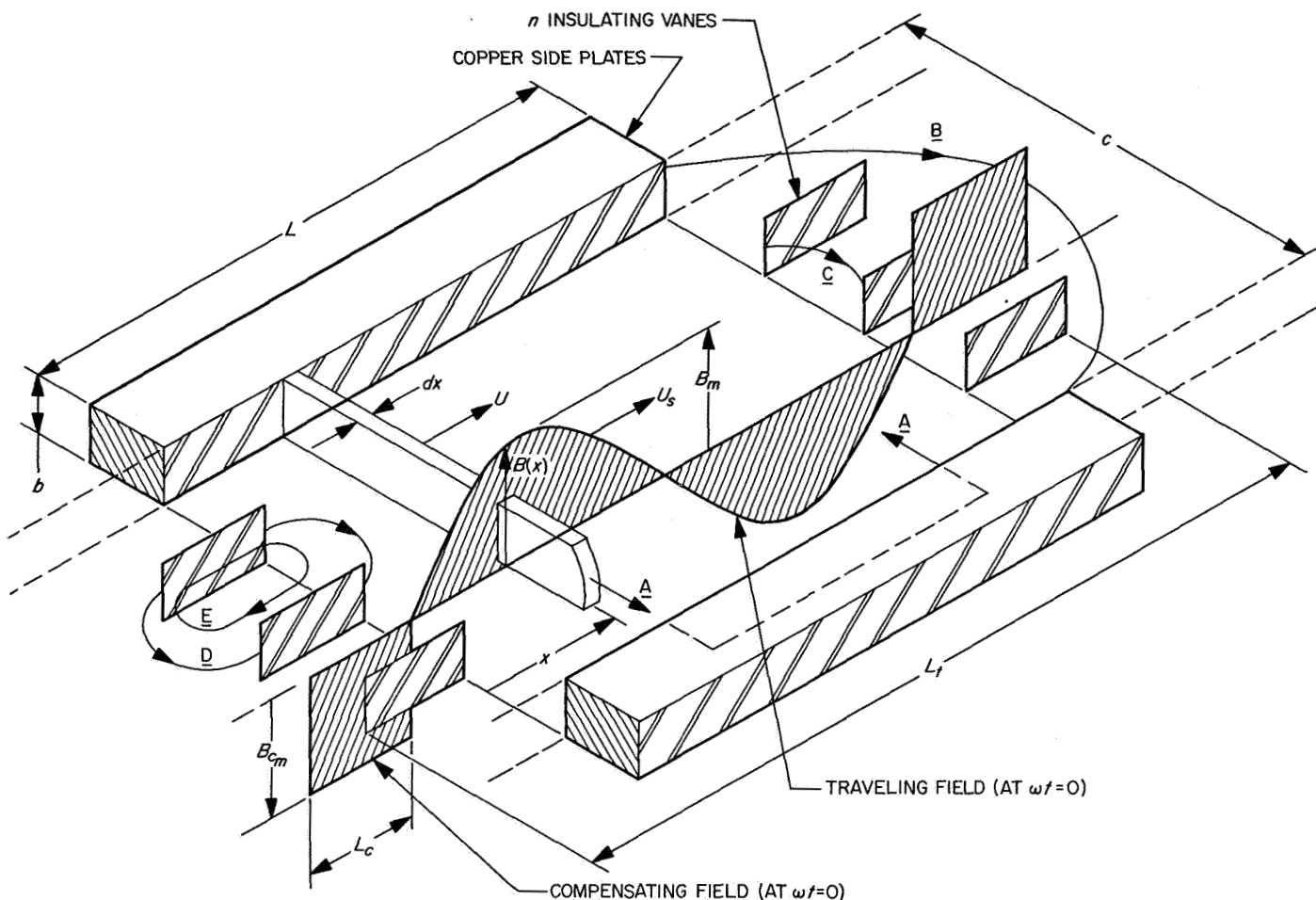


Fig. 1. Processes in an induction MHD generator

b. Theory. The problems studied in the generator experiment are illustrated in Fig. 1. The generator channel has a height b , width c , and length L_t . A sinusoidal magnetic field of amplitude B_m travels downstream at velocity U_s in the traveling-wave region L . Liquid metal of conductivity σ is supplied at velocity $U > U_s$ giving a slip defined as $s = (U - U_s)/U_s$. The slip induces current loops \underline{A} which are completed through the copper side plates. The current loops and the field exert a retarding force on the fluid, and the currents induce voltages in the windings to provide the output power. Capacitors across the output terminals supply the reactive power for the field. Above some value of slip the output power from the liquid metal exceeds the winding and other losses and the generator becomes a self-excited oscillator supplying net power to the load.

The fluid element dx traveling at velocity U has an electromotive force (emf) induced in it by two effects.

First, the fluid velocity relative to the field induces an emf

$$E_1 = c B(x) (U - U_s) \quad (1)$$

Second, the creation of the incoming wave at the entrance continually adds new flux lines around each fluid element, inducing an emf

$$\begin{aligned} E_2 &= c B(o) \omega s \\ &= -c B_m U_s \sin \omega t \end{aligned} \quad (2)$$

The first emf takes opposite directions under the upward and downward poles. No side-plate voltage appears and the emf is short-circuited by the loop \underline{A} .

The second emf, E_2 , has the same direction for all fluid elements and appears as a voltage between the side plates, causing shunt end currents \underline{B} . If the shunt end

resistance is made large, compared with the internal resistance between the side plates, either by adding insulating vanes or making the aspect ratio L/c large enough, there is negligible internal current density due to E , and the side-plate voltage becomes equal to E . Designating the rms field by B , the rms side-plate voltage is

$$V_{sp} = c B U_s \quad (3)$$

The theoretical performance can now be derived in a very simple manner. The generator resistance is

$$R = c/\sigma b L \quad (4)$$

The rms current due to E , is the rms value of E , divided by R

$$I = E_1/R = \sigma b L B U_s s \quad (5)$$

The electrical retarding force is the product of width, rms field, and rms current

$$F = cBI = \sigma b c L B^2 U_s s \quad (6)$$

The power input due to electrical retarding force is the product of fluid velocity and force

$$P_m = UF = \sigma b c L B^2 U_s^2 s(1 + s) \quad (7)$$

The ohmic heating loss is the product of current squared and resistance

$$P_r = I^2 R = \sigma b c L B^2 U_s^2 s^2 \quad (8)$$

The gross output power is the fluid input power minus the ohmic heating loss

$$P_g = P_m - P_r = \sigma b c L B^2 U_s^2 s \quad (9)$$

The gross efficiency for generating is the ratio of electrical output power to fluid input power

$$\eta_g = P_g/P_m = (1 + s)^{-1} \quad (10)$$

The gross efficiency for pumping (negative slip) is the ratio of fluid pumping power ($-P_m$) to electrical input

power ($-P_o$)

$$\eta_p = P_m/P_o = 1 + s \quad (11)$$

The field produced by the current causes the total field B to be less than the empty-channel value by the factor (Ref. 2)

$$B = B_{ec} (1 + s^2 R_m^2)^{-1/2} \quad (12)$$

where R_m is the magnetic Reynolds number based on wavelength

$$R_m = \mu_o \sigma U_s \lambda / 2\pi \quad (13)$$

Eqs. (9)–(13) define the ideal performance of the induction generator.

The shunt end currents \underline{B} due to the side-plate voltage are the main difficulty in system applications where the generator must operate with the wide flow from a separator. Separator exit flows have a width/gap ratio c/b of at least 20, and the generator length/gap ratio L_t/b can be no more than 20 if friction loss is to be limited to, say, 15% of the inlet kinetic energy. These two factors limit the generator aspect ratio L_t/c to 1.0, and for a generator this short, the power dissipated by the end currents is large compared with the generated power.

Shortening the traveling-wave region and adding n insulating vanes at each end breaks the end currents \underline{B} into shorter paths \underline{C} which together have $1/n$ the original loss, but unless the vanes have a length at least equal to c the outlying \underline{B} currents are still excessive. With $L_t/c = 1.0$ it is not possible to accommodate such a vane length.

Compensating poles eliminate this difficulty by canceling out the side-plate voltage. They make the traveling-wave region L the secondary of a transformer and induce an emf equal and opposite to E_s . In Fig. 1, if the rms compensating field amplitude is B_{cm} , the compensating-pole length is L_c , and the field is maximum downward at $\omega t = 0$, then the emf induced in each fluid element by the time rate of change of compensating flux is

$$\begin{aligned} E_3 &= \frac{d}{dt} (-c L_c B_{cm} \cos \omega t) \\ &= c L_c B_{cm} \omega \sin \omega t \\ &= 2\pi c (L_c/\lambda) B_{cm} U_s \sin \omega t \end{aligned} \quad (14)$$

using $\omega = 2\pi U_s/\lambda$. Comparison of Eq. (14) with Eq. (2) shows that E , exactly cancels E_2 , making $V_{sp} = 0$, when

$$B_{cm} = (\lambda/2\pi L_c) B_m \quad (15)$$

If the compensating and traveling fields are equal and the generator is one wavelength long, then the two compensating poles occupy only $(1 + \pi)^{-1} = 24\%$ of the total length L_t .

The compensating poles themselves cause shunt end currents \underline{D} from the motion of the fluid through the compensating field and eddy currents \underline{E} from the time rate of change of the compensating field. Insulating vanes are still needed to reduce losses from these currents, and the utility of the compensating pole scheme depends on reducing such losses with few enough vanes, or with some other current-interrupting method such as gas jets,

to keep added friction losses low. The gain over the uncompensated generator is that the vanes have a length of only $L/2\pi$ instead of c , allowing L_t/c to be 1.0 or less.

c. Experiment. In Fig. 2, an earlier generator is cut away to show the traveling-wave region, compensating poles, windings, copper side plates, and compensating pole vanes. Three vanes were used at each end. Fig. 3 shows the generator installed in the aluminum housing between the inlet and exit pipes. Nitrogen flowed through the housing at **0.3 lb/sec** to cool the windings and exhausted at a pressure 50 psi higher than the channel pressure to minimize NaK leakage into the housing.

The test installation is shown in Fig. 4. Room-temperature NaK was supplied at pressures up to 800 psi from a 250-gal tank in an adjoining cubicle and flowed through an electromagnetic flowmeter, turbine flowmeter,

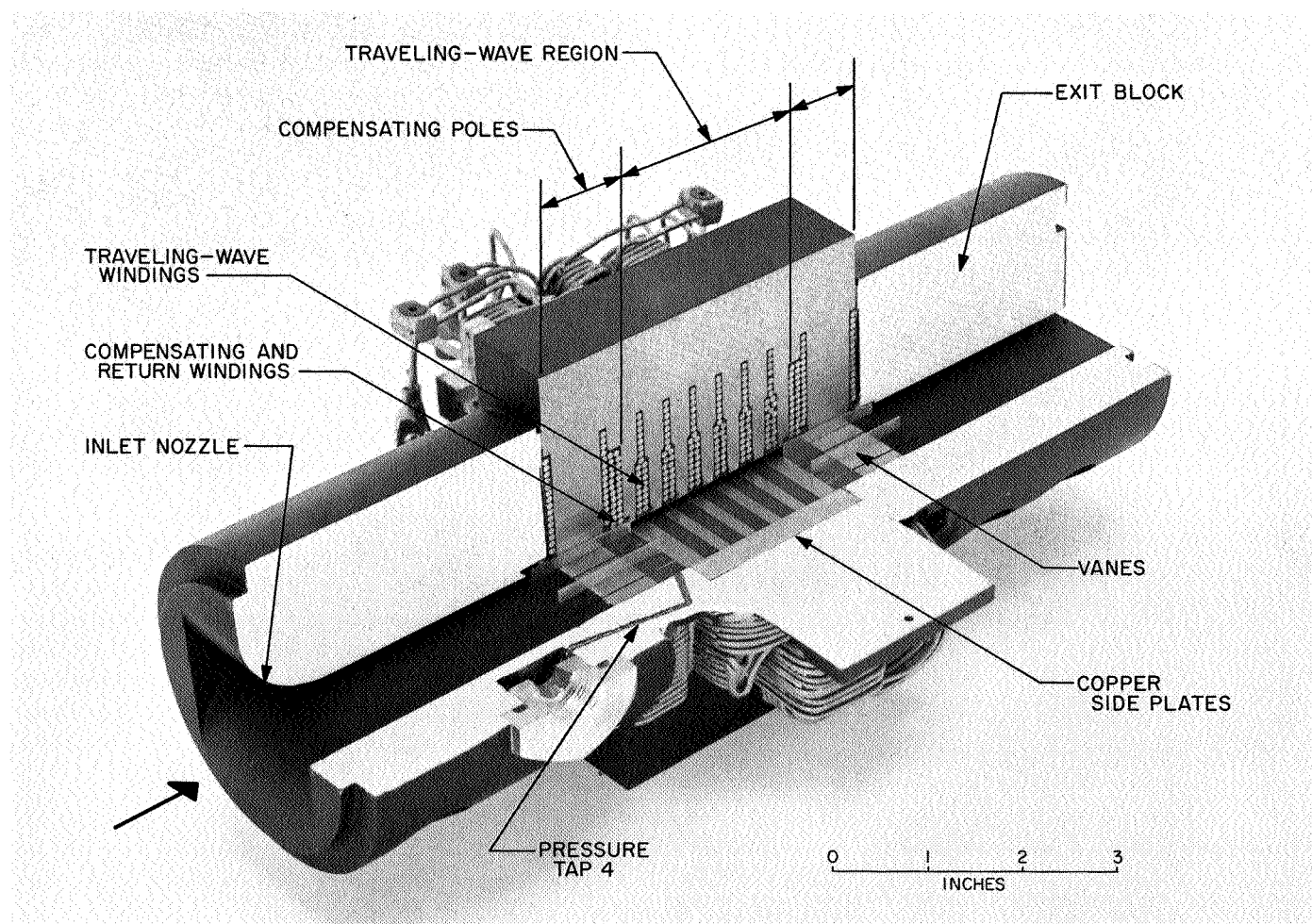


Fig. 2. Experimental generator

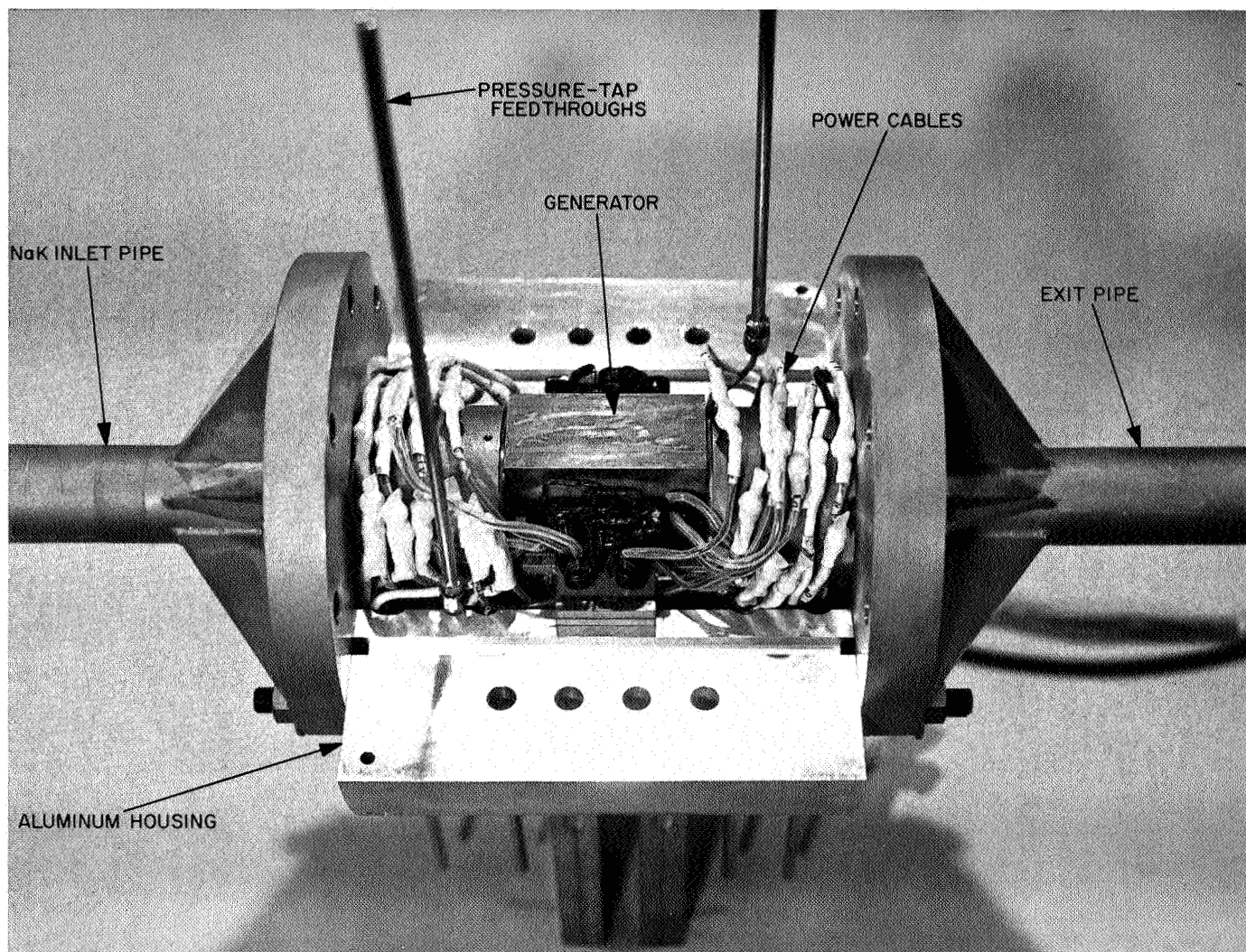


Fig. 3. Experimental generator mated with housing and NaK pipes

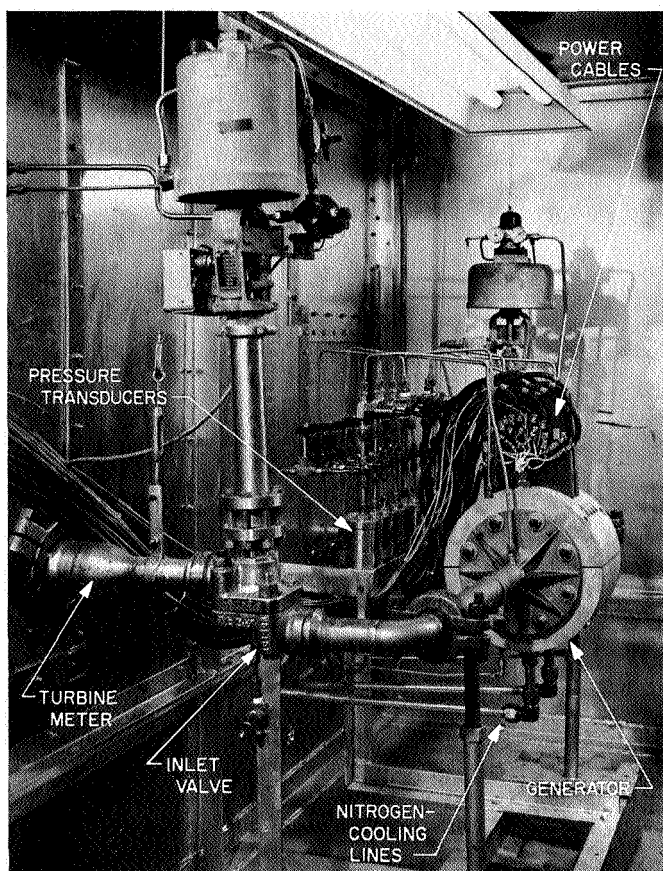


Fig. 4. Generator installed in NaK blow-down facility

and pneumatic valve into the generator. From the generator, the NaK flowed to a receiver tank pressurized at 50 psi. Pressures at eight stations in the channel were measured by strain-gage pressure transducers. Magnetic field was measured by five calibrated search coils embedded in the stator slots. Voltages and current-shunt outputs were measured by thermocouple AC voltmeters. Powers were measured by Hall multipliers scanned by a DC voltmeter. Phase angles were measured by a phase-angle meter with proportional DC output. Instrument outputs were recorded on a digital data system.

For tests in the pumping region (negative slip) and in the generator region up to a slip of 0.4, the generator required power input which was supplied by a three-phase alternator. Capacitors across each phase supplied the reactive magnetizing power. Above a slip of 0.4 the generator was started by bringing up one alternator phase to 70 v and then disconnecting the alternator. Subsequent adjustments were made by changing capacitance and load. Increasing the capacitance increased the current and voltage on the phase adjusted. Increasing the load decreased the frequency. The distribution of load

between phases had little effect on currents or phase angles which were 120 ± 10 deg for most of the runs.

The compensating pole windings were driven from the secondaries of double-primary multiple-tap transformers connected to the desired pair of generator output phases in the ratios required for the desired compensating-pole amplitude and phase angle. The compensating-pole length L_c was 0.6 in. (λ/π) and the required rms compensating field from Eq. (15) was $B/2$.

d. Results. Fig. 5 shows the variation of side-plate voltage with compensating field. Without compensating field, the side-plate voltage was approximately 20% above the theoretical uncompensated value cBU_s (Eq. 3). The side-plate voltage was reduced to 10–30% of the uncompensated value at the theoretically-required compensating field of $B/2$. The excess voltage above theoretical at both conditions could have been due to stray voltage pickup by the side-plate voltage leads, which

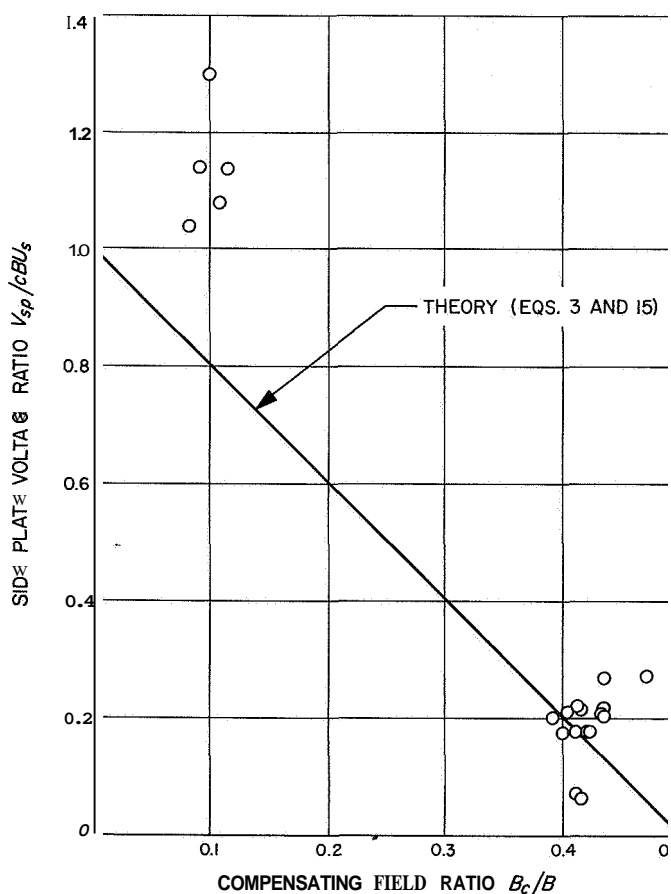
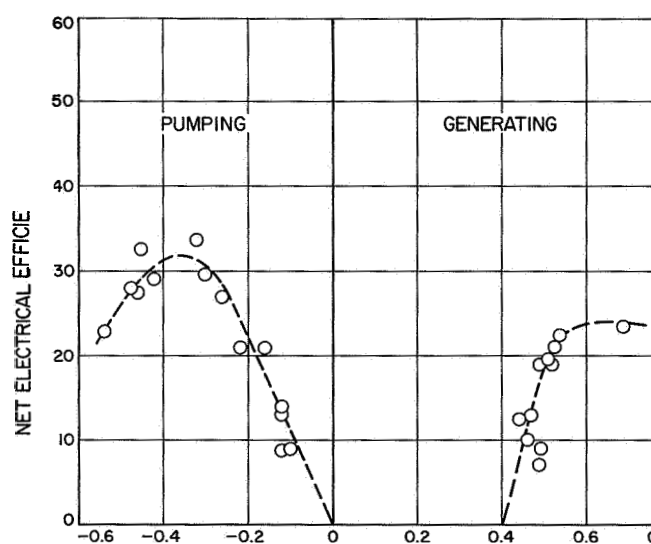
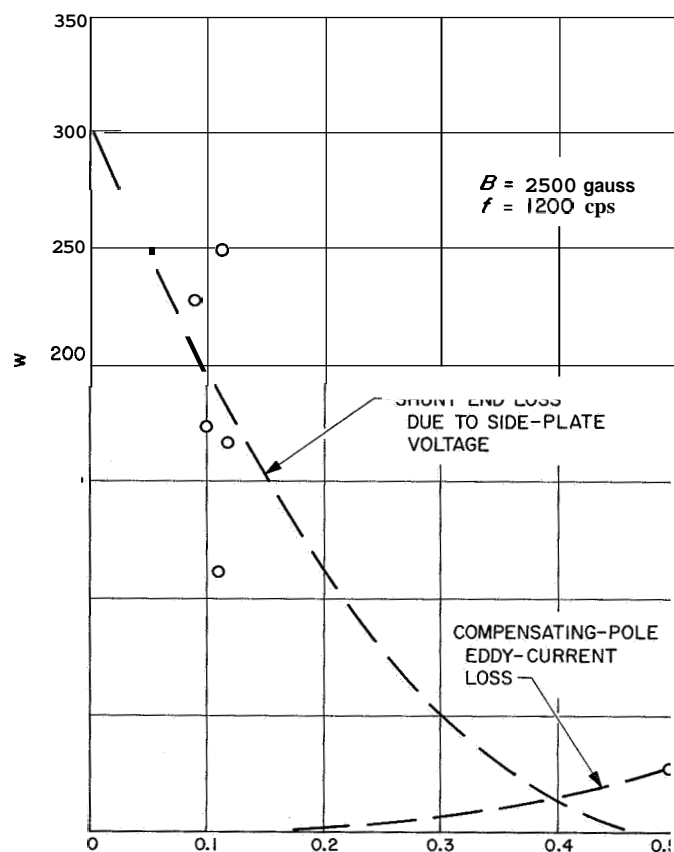


Fig. 5. Variation of side-plate voltage with compensating field

monics in the traveling wave. Reduction of the side-plate voltage to **20%** is adequate for reducing end losses since the losses are proportional to voltage squared.

Fig. 6 shows the reduction in end loss with compensation at 2500-gauss rms traveling-wave field, 1200 cps, and slips from -0.1 to -0.5 . The end loss with compensation is from the \underline{D} and \underline{E} currents in Fig. 1. The \underline{D} loss was found to be negligible in that there was no consistent change in pressure drop across the compensating pole regions when field was applied. The \underline{E} loss was



P_m

(negative for pumping) appeared partly as a pressure drop, which could be measured, and partly as a kinetic energy change from flattening of the velocity profile.

The electrical pressure drop was the difference between the pressure drop across the traveling-wave region (pressure Tap 4 to 5) with power *on* and the pressure drop with power *off* at the same flow rate

$$\Delta p_e = \Delta p_{4-5} (\text{power on}) - \Delta p_{4-5} (\text{power off}) \quad (17)$$

A typical change at low current was from 150 psi with power *off* to 180 psi with power *on*. In the 990-w run, the change was from 163 to 254 psi.

The input power due to Δp_e is $P_m = \dot{v} \Delta p_e$ where \dot{v} is the volume flow rate. This value of P_m proved to be impossibly low for many of the generator runs because it gave gross efficiency values exceeding $(1+s)^{-1}$. To account for the amount of power being generated it was necessary to assume that the velocity profile was completely flattened between Taps 4 and 5, making available the change in kinetic power from the $1/7$ -power profile value $1.045 (\dot{m} U^2/2)$ at Tap 4 to the flat-profile value $\dot{m} U^2/2$ at Tap 5, U being the bulk velocity \dot{v}/bc . Flattening must occur at least to some extent because the boundary layer is pumped while the core is retarded, but the evidence for complete flattening in these runs is only that otherwise η_0 would be greater than $(1+s)^{-1}$ for many of the data points. The assumption is at least conservative and gives the lowest possible efficiencies. The input power for complete flattening is

$$P_m = \dot{v} (\Delta p_e + 0.045 \rho U^2/2) \quad (18)$$

The second term varied from 1.0 Δp_e at low power to 0.1 Δp_e for the 990-w run.

Fig. 8 presents the gross electrical efficiency η_0 , which is

$$\eta_0 = P_o/P_m = (P_e + P_w + P_{ec})/P_m \quad (19)$$

for generating and the inverse for pumping. The eddy-current loss P_{ec} was evaluated from Eq. (16). The winding and core loss P_w was measured as a function of current, field, and frequency in empty-channel calibrations prior to the NaK runs. The gross efficiency η_0 is the efficiency with which power is converted from mechanical to electrical energy, or vice versa, in the NaK in the traveling-wave region and the efficiency which is ideally equal to $(1+s)^{-1}$ for generating and $(1+s)$ for pumping. The

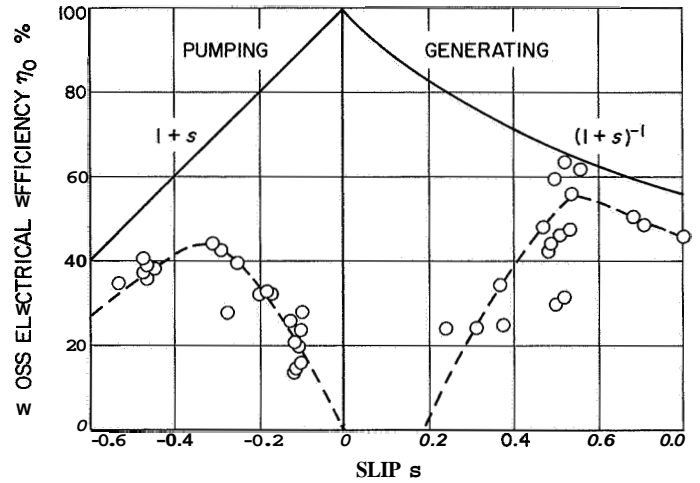


Fig. 8. Measured gross electrical efficiency

measured efficiency closely approached the ideal value for slips greater than 0.5, but dropped rapidly to zero at lower slips. The peak efficiencies were approximately 48% for pumping and 55% for generating.

Zero efficiency must occur at zero slip for pumping and at some low slip for generating because any fixed loss eventually becomes large compared with the power transfer into, or out of, the fluid. The fixed loss evidenced by Fig. 8 is larger than tolerable in an efficient generator, but, as shown below, is explainable as the added ohmic loss due to field variation between slots and teeth, in which case it is remediable with a closed-slot stator design.

The power input and output magnitudes are compared with theory in Figs. 9 and 10. From Eqs. (7) and (9), using $f = U_s/L$, the ideal input and output powers per unit field and frequency, squared, are

$$\frac{P_m}{B^2 f^2} = \sigma b c L^3 s (1+s) \quad (20)$$

and

$$\frac{P_a}{B^2 f^2} = -\sigma b c L^3 s \quad (21)$$

These are the lines plotted in Figs. 9 and 10. The data points are the measured powers divided by $B^2 f^2$ using the field B measured by the search coils.

The normalized input power $P_m/B^2 f^2$, Fig. 9, basing P_m on the flattening assumption (Eq. 18), agrees well

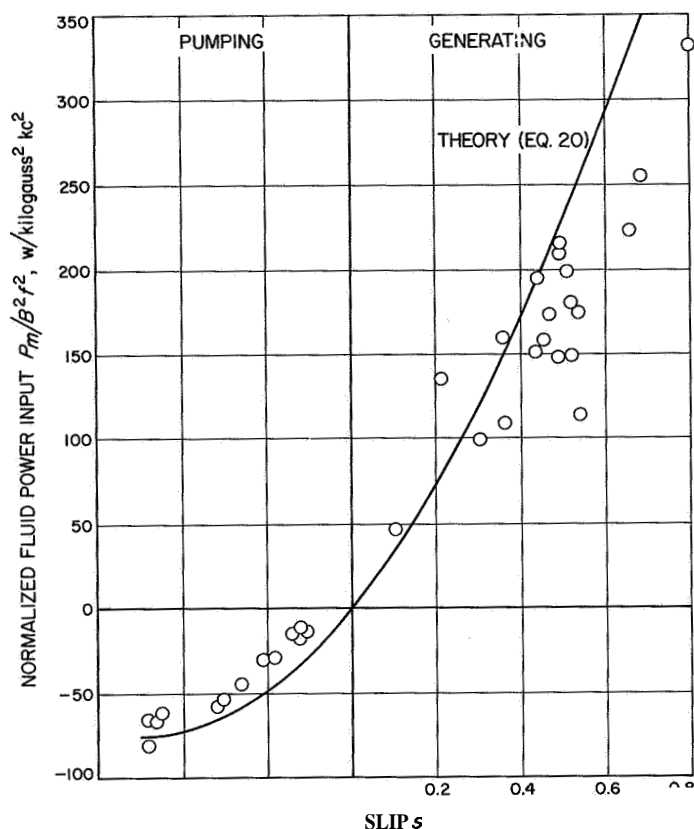


Fig. 9. Comparison of theoretical and experimental fluid input power

with Eq. (20), within the scatter of the pressure-drop measurements, except for a tendency to fall below Eq. (20) with increasing slip. The discrepancy may be more in the field measurements than in the power since the search coils did not indicate as rapid a decrease in field with slip as predicted by Eq. (12).

The normalized gross output power $P_o/B^2 f^2$, Fig. 10, falls below Eq. (21) by an amount which increases with NaK velocity U . The deficiency is attributed to standing currents induced by field variations between the teeth and slots. Fig. 11 is an X-Y plotter record of the rms field about 0.02 in. off the generator center line, which was as close to the wall as the probe could be positioned. The amplitude has six large dips corresponding to the six slots on the near side of the channel and five smaller dips from the slots on the opposite side. The amplitude variation a is approximately 20% and would be expected to increase toward the wall. An a value of 35% might not be an unreasonable mean value averaged across the channel, and this would account for all of the observed loss as shown next.

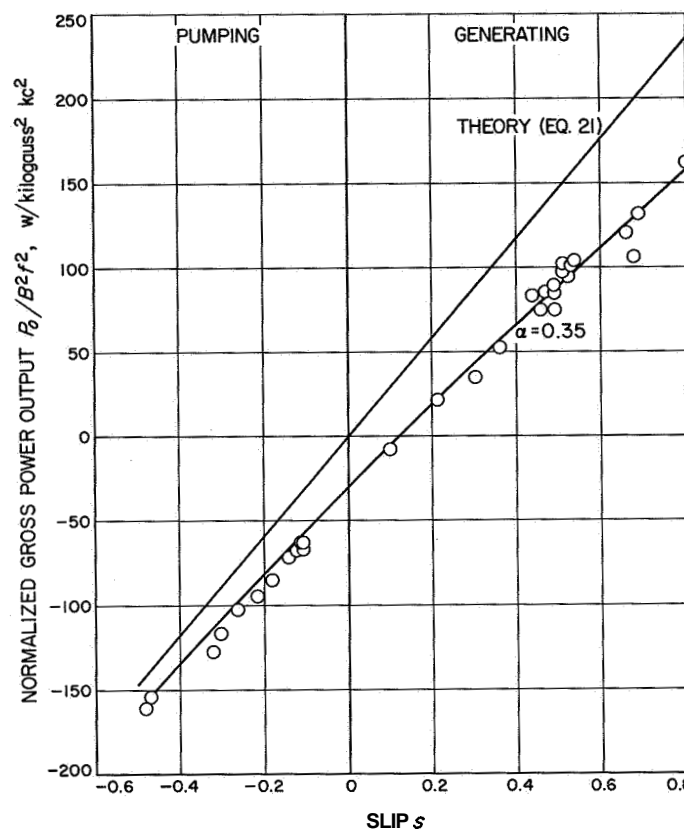


Fig. 10. Comparison of theoretical and experimental gross output power

The mechanism is that the fluid moves at velocity U through the sinusoidal field of rms amplitude variation αB superimposed on the fundamental wave of rms amplitude B . The added power dissipated is then given by Eq. (8) with B replaced by αB and the relative velocity sU_s replaced by U , which is the relative velocity here, and U in turn written as $(1+s)U_s$. Thus,

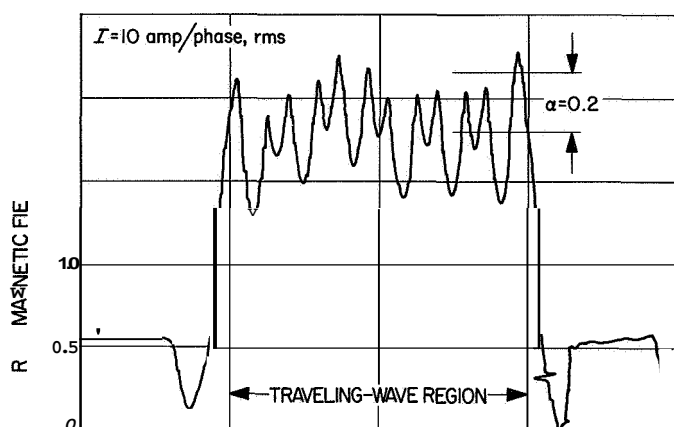
$$\Delta P_r = \sigma b c L \alpha^2 B^2 U_s^2 (1+s)^2 \quad (22)$$

However, the variation αB is decreased from the empty-channel variation by a reaction field so that, from Eq. (12) with sU_s again replaced by $(1+s)U_s$

$$a = a_{ec} [1 + (1+s)^2 R_{m\alpha}^2]^{-1/2} \quad (23)$$

where

$$R_{m\alpha} = \mu_o \sigma U_s \lambda / 2\pi n \quad (24)$$



since the wave length of the amplitude variations is λ divided by the number of dips n . The total I^2R loss, adding Eqs. (8) and (22), and also adding in the calculated side-plate I^2R loss, is then

$$P_r = \sigma b c L B^2 U_s^2 \left[1.047 s^2 + \frac{(1+s)^2 \alpha^2}{1 + (1-s)^2 R_m^2} \right] \quad (25)$$

where a is the empty-channel value. Strictly speaking, if the amplitude variation is sinusoidal, the α in Eq. (25) should be the rms variation rather than the peak variation as labeled in Fig. 11, but near the wall the variation would be more rectangular and a would be the peak value. All that can be accomplished by Eq. (25) in any case, without a detailed knowledge of a across the channel is to show that the observed P_r increase is consistent with a reasonable magnitude of a .

The lower curve in Fig. 10 shows the theoretical gross output power based on $a = 0.35$ (and $R_{ma} = 0.2$, corresponding to the 900 cps frequency of most of the tests). This curve shows that the power loss can be explained by a possible value of a , thus indicating that this mechanism could be the source of the loss.

e. Conclusions:

- (1) Uncompensated generators exhibit a side-plate voltage cBU_s which would cause prohibitive end losses in generators with aspect ratios less than 1.0.
- (2) Compensating poles cancel the side-plate voltage, and the compensating poles have acceptable losses.

- (3) The *gross* electrical efficiency of a one-wavelength generator is the same as for a multiwavelength generator and approaches $(1+s)^{-1}$ to the degree permitted by departure from sinusoidal waveform.
- (4) Even with a single wavelength design and low-loss compensation, the wide gap, low conductivity, and large friction of liquid-metal MHD generators compared with rotating machines will require extreme sophistication in winding and slot design, insulation, and cooling to attain over-all efficiencies greater than 50%.

2. High Temperature Tests

A liquid-metal heater with alumina insulation was tested to complete the initial phase of heater development. Measurements of resistivity of the swaged alumina were made which complement those previously obtained for swaged beryllia (SPS 37-36, Vol. IV). Fig. 12 shows the heater during operation at 2100°F. The results of all tests to date are summarized in Fig. 13, a plot of resistivity versus temperature. The beryllia, in addition to having a higher thermal conductivity, possesses a higher resistivity than alumina over the range tested. For example, at 2200°F the experimental curve for beryllia yields a value of 1×10^5 ohm-cm while the alumina had a resistivity of 0.35×10^5 . The alumina heater suffered

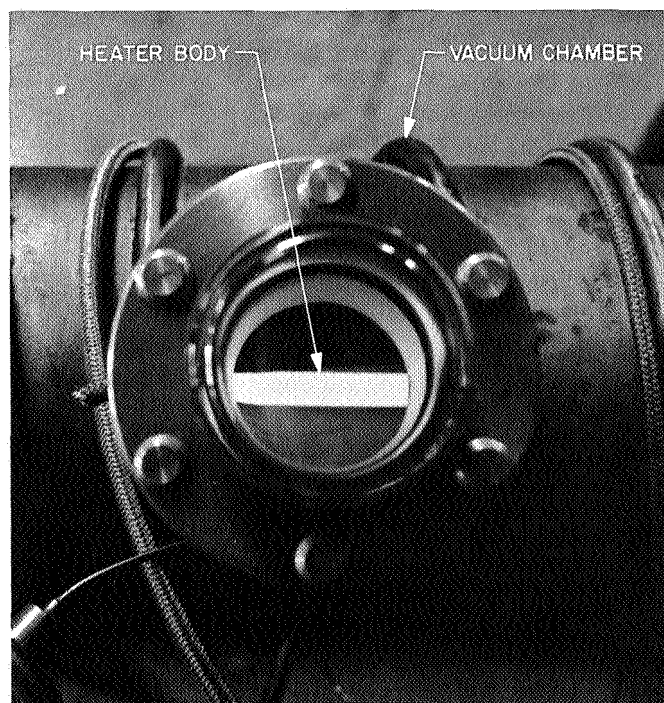


Fig. 12. Experimental heater at 2100°F

eventual breakdown of the ceramic at 2100°F with a field strength of 3.3 v/mil. However, the beryllia was tested up to 4.4 v/mil at 2100°F with no breakdown. Resistivity data for fired beryllia and alumina and for beryllia powder are shown on this plot for comparative purposes. The swaged beryllia data fall between the value for compressed powder and fired ceramic, but are closer to the latter. For example, at 2200°F Bacon's curve for fired BeO (Ref. 4) gives a value of 7.4×10^4 ohm-cm versus approximately 1×10^5 ohm-cm for the experimental curve for swaged beryllia. Ryshkewitch (Ref. 5) gives a value of 3.5×10^6 ohm-cm at this temperature for compressed BeO powder.

The data for the swaged alumina fall somewhat below the values given by Knoll (Ref. 6) for fired alumina. At 2100°F the measured value for swaged alumina was approximately 7×10^4 ohm-cm versus approximately 2×10^5 ohm-cm for the fired material.

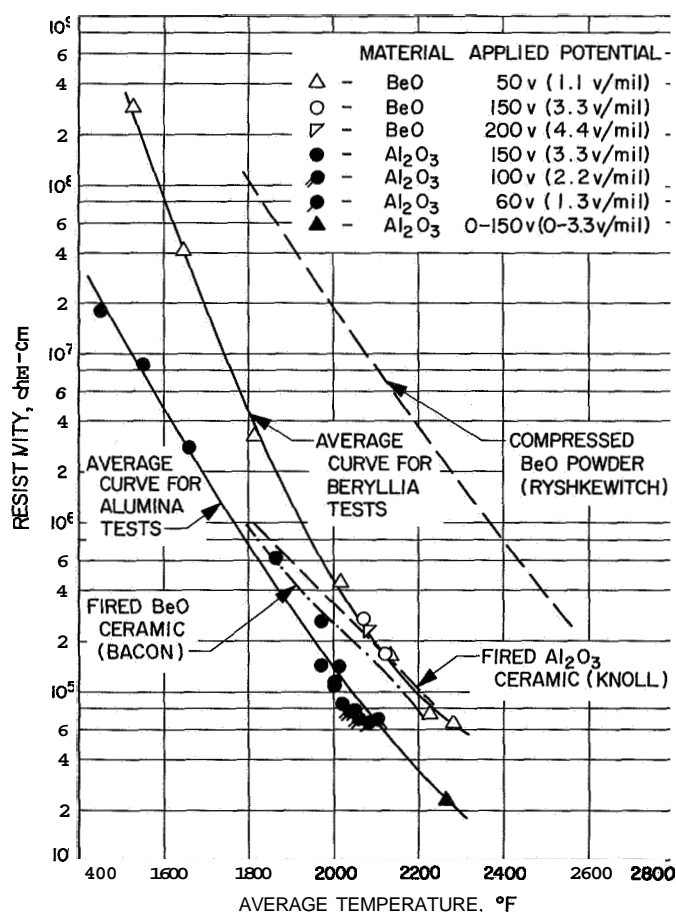


Fig. 13. Electrical resistivity of swaged beryllia and alumina versus temperature

The influence of the time at elevated temperature on resistivity was investigated for the beryllia heater. The temperature during this test varied from 2000 to 2260°F, so the values for resistivity were normalized for temperature to those of Fig. 13. The normalized resistivity underwent an erratic over-all increase until 20 hr at which time it was approximately 40% greater than the initial value. At that time it declined gradually, until at 27 hr a sharp decrease was experienced. At this time the resistivity was approximately 30% below the initial value. The test was discontinued after 31 hr in order to examine the heater to determine the cause of the decrease. A spot on the sheath was discovered where the columbium-1% zirconium had been attacked by impurities in either the vacuum atmosphere or beryllia insulation.

The ruggedness of this type of heater was demonstrated by 20 thermal cycles from ambient to more than 2000°F on the beryllia unit and more than 100 cycles from 350°F to more than 2000°F on the alumina unit. For the latter tests the total time of the heat-cool cycle was 15 min, or greater than 200°F/min.

N67 18332

B. Plasma Studies in the Electron Bombardment Ion Engine, T. D. Masek

1. Introduction

Analytical and experimental investigations of the cesium and mercury electron bombardment ion engine plasmas have been conducted previously to study the basic characteristics of this engine (Refs. 7-9 and SPS 37-32, Vol. IV). These investigations have aided in an empirical formulation of an analytical model of the plasma (Ref. 7) but have shown that further detailed experimental data is required to utilize this model. This report presents results of the first of a series of plasma studies made to obtain the required experimental information.

The most convenient method of measuring plasma characteristics in the electron bombardment engine is with a Langmuir probe. Langmuir probe theory, in general, requires the electron energy distribution in velocity space to be Maxwellian. When the distribution is not Maxwellian, difficulty arises in reducing the probe data and in evaluating the plasma characteristics. It has been found that the mercury engine plasma deviates significantly from a simple Maxwellian electron energy distribution (Ref. 9 and SPS 37-32, Vol. IV). The present report will discuss the electron energy distribution based on recent probe studies to show the non-Maxwellian nature

of the data and to give reasonable explanations for this distribution. The need for a clarification of the energy distribution, considering that previous data from the mercury engine has been published, is due to finding additional features of the distribution which were previously unobserved in this work.

2. Experimental Setup

The engine used in this investigation, shown schematically in Fig. 14, had an anode diameter of approximately 6 in. and a length-to-diameter ratio of 0.71 based on anode diameter and baffle to screen grid length. Both grids were 0.080-in.-thick molybdenum with 0.187-in. diameter apertures. The screen grid to accelerating grid spacing was nominally 0.080 in. A tantalum brush-type cathode (Ref. 10), 0.38 in. in diameter and 2 in. long, coated with radio Mix 3 oxide, was used.

As in previous studies, a single movable Langmuir probe was used to study the plasma. The probe was 0.020-in. diameter tungsten wire sheathed with quartz

except for 0.110 in., which acts as the cylindrical probe. The probe theory and application to the present type of plasma has been discussed previously (Ref. 9).

The probe positions were spaced 0.65 in. apart axially and 0.25 in. radially, starting 0.50 in. off center and 0.18 in. from the screen grid. All data are plotted in normalized coordinates based on anode radius and chamber length with origin at the grid on center. For example, much of the data to be discussed were obtained near the center at the grid so the normalized radial position was 0.167 and the normalized axial position (at the probe tip) was 0.043.

3. Plasma Measurements

A typical set of original data taken with an X-Y-Y plotter is shown in Fig. 15 for several arc currents. The two sets of curves represent different scale factors for probe current. Two curve sets are taken to obtain accurate data at both low and high probe currents. When plotted semilogarithmically, as shown in Fig. 16(a), the

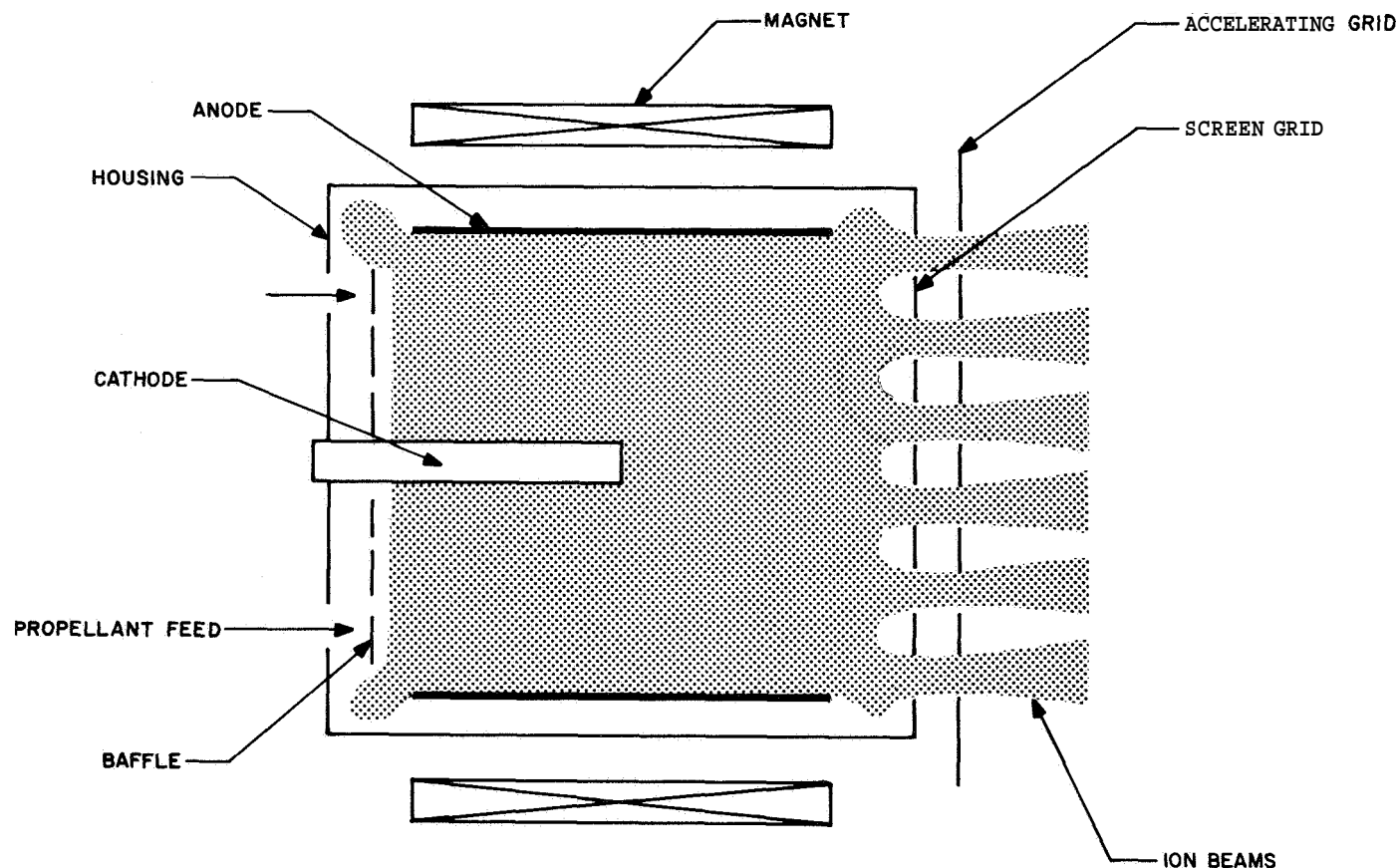


Fig. 14. Conventional electron bombardment ion engine schematic diagram

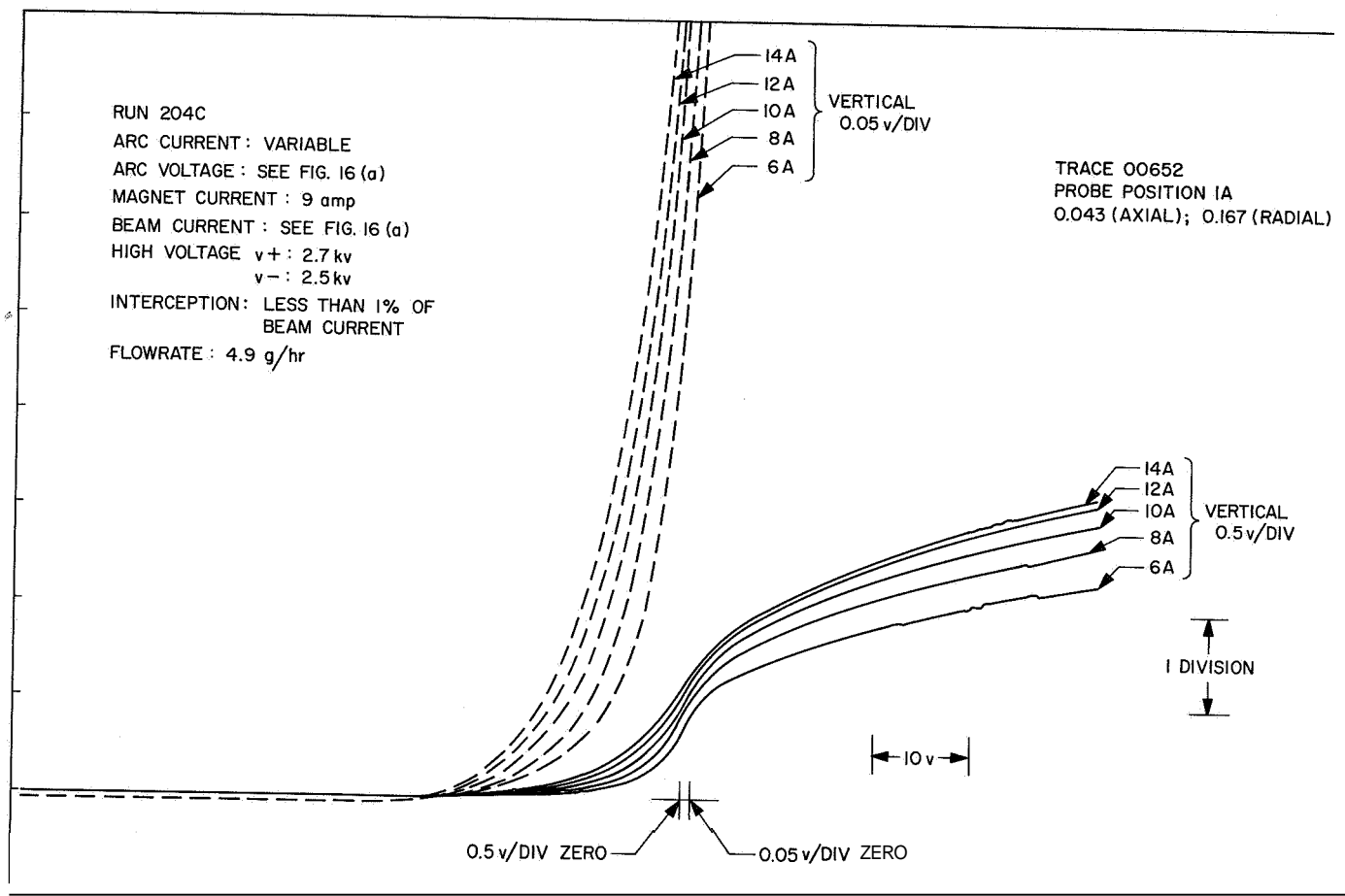


Fig. 15. Langmuir probe trace as taken with X-Y-Y recorder for several arc currents

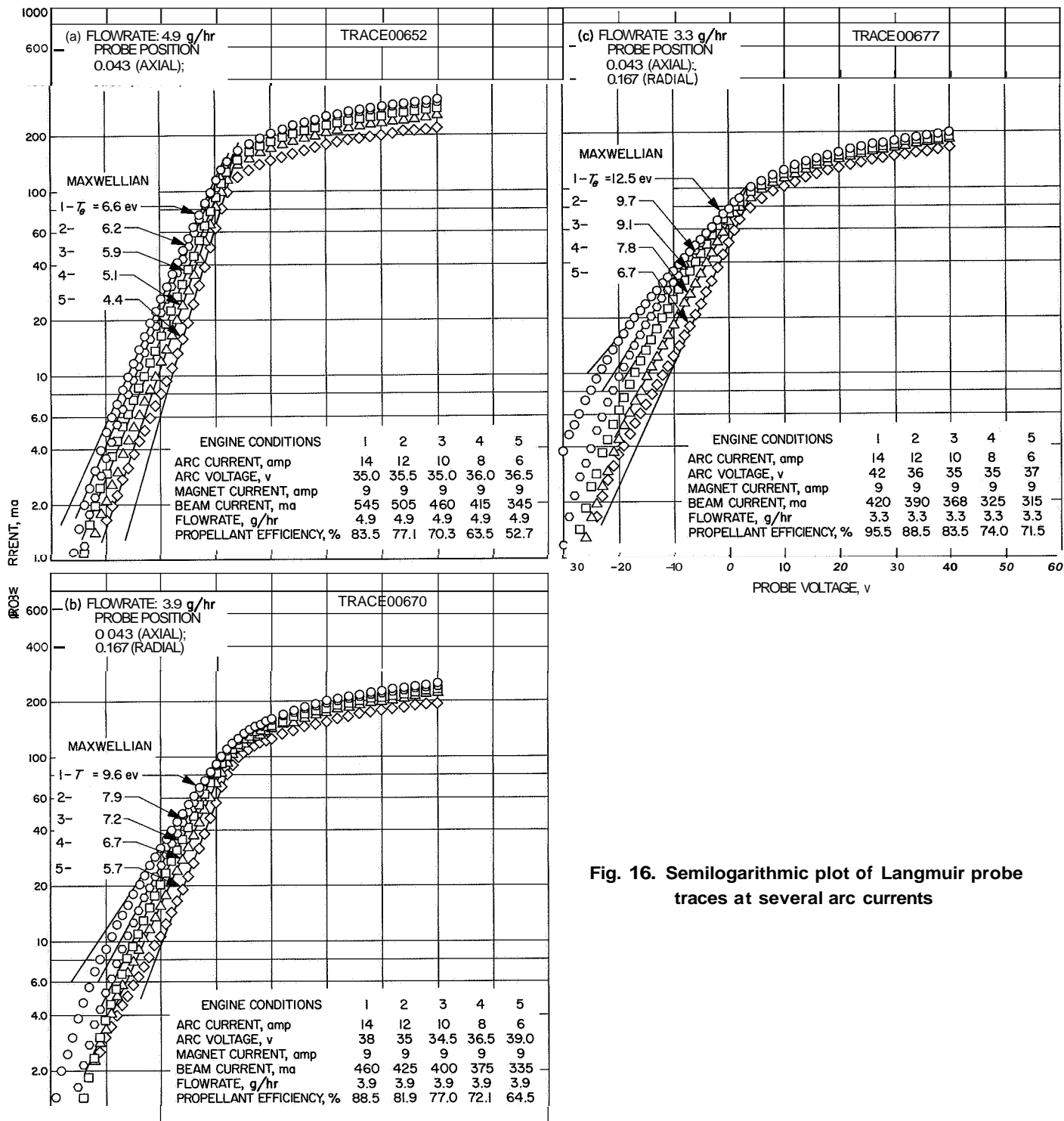


Fig. 16. Semilogarithmic plot of Langmuir probe traces at several arc currents

data to the left of the "knee" should produce a straight line if the electron energy distribution function is Maxwellian. Straight lines have been drawn through the points and it appears that portions of the curves are due to Maxwellian electrons, thus, the local electron energy distribution function can probably be considered to be a Maxwellian distribution perturbed to varying degrees. The causes of the non-Maxwellian distribution will now be considered.

The lower portions of curves in Fig. 16(a), which represent the higher energy electrons, are different from the Maxwellian distribution by varying amounts, depending on the arc current. In the high current conditions, Curves 1 and 2, the data definitely indicate a shortage of high energy electrons relative to a Maxwellian distribution while Curves 4 and 5 indicate a surplus of high energy electrons. Curve 3 is approximately in the middle but appears to be slightly depleted. Curves 4 and 5 are representative of the mercury data of Refs. 7, 9, and *SPS 37-32*, Vol. IV, in which all data were taken with arc currents below approximately 5 amp. Additional sets of data at several arc currents are shown in Figs. 16(b) and (c) for lower propellant flowrates and exhibit characteristics similar to Fig. 16(a). An explanation for the change in the number of high energy electrons with changes in arc current can be attempted by considering the possibilities for a shortage of a surplus of these electrons.

Curves similar to the high arc current cases of Fig. 16 have been reported by Howe (Ref. 11) and Aisenberg (Ref. 12) for mercury arcs with pressures from approximately 2×10^{-3} to 3×10^{-2} torr and arc currents of a few amperes. Howe suggests several reasonable possibilities for a depletion of high energy electrons with one explanation in particular in terms of electron-atom inelastic collisions. Fig 16 data will be discussed in terms of both electron-atom and electron-electron collisions.

At least two mechanisms can be affecting the electron energy distribution in velocity space: one due to particle interactions and one due to electron-container interactions. First, consider only particle interactions. The electron energy distribution, near the cathode at least, is considered to be composed of a primary electron group (those initially emitted from the cathode), and a secondary electron group of lower average energy composed of electrons produced in ionization or in several collisions. The primary electrons are initially accelerated through the cathode sheath and obtain energies approximately equal to the arc voltage. Elastic collisions between primary electrons and secondary electrons distribute pri-

mary energy among the lower energy electrons. This primary energy flux into the electron energy distribution is reflected in Fig. 16 by the change of slope of the curves with arc current changes. The average energy of the distribution is seen to be increased with increasing arc current. In addition, the effect of arc voltage on the electron energy is shown in Fig. 17, where constant arc current data is plotted for several arc voltages. At high arc currents, it is expected that a high percentage of the neutral gas has been ionized. This is indicated by the small change in electron saturation current with arc current change at high currents in Fig. 16.

The primary electron-Maxwellian electron collision frequency for energy exchange should be much higher than the primary electron-ion collision frequency since electrons exchange energy more easily with each other than with ions. Thus, the dominant electron energy exchange mechanism at high ionization percentages is electron-electron collisions. Since the formation of a Maxwellian electron energy distribution depends on electron-electron collisions, it is expected that this distribution would be best achieved at high arc currents.

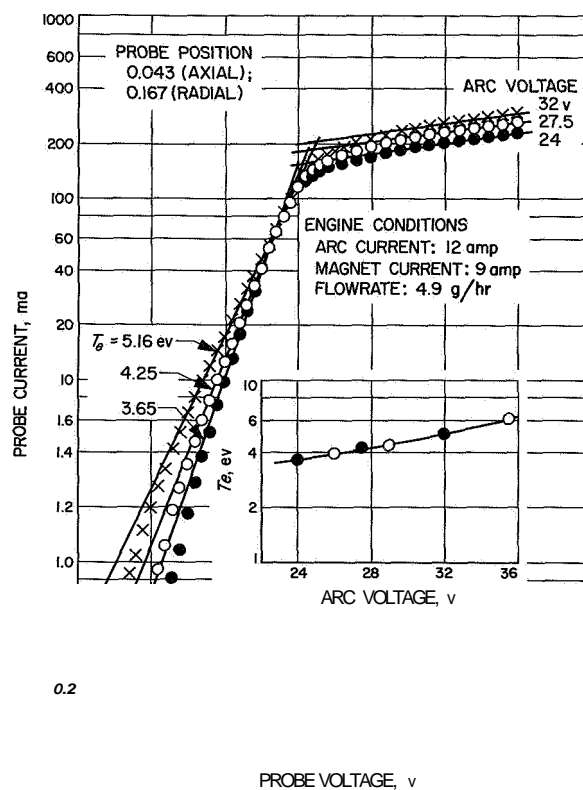


Fig. 17. Semilogarithmic plot of Langmuir probe traces at constant arc voltages (traces for circled data points in insert are omitted for clarity)

The ionization cross section for mercury is a maximum at electron energies of approximately 50 ev. Since the low energy electron distribution near the cathode has fewer electrons of high energy compared to the primary group it is expected that as the arc current is reduced, i.e., the primary electron flux, the fractional ionization would decrease, causing the ion and electron densities to decrease. The electron-electron collision frequency decreases because of the electron density decrease. With more neutrals available, the electron-atom collision frequency is increased but does not return to the high arc current ionization fraction because not all the electron-atom collisions are inelastic. This is shown in Fig. 18 where the mean time between elastic and inelastic collisions is plotted. Note that elastic electron-atom collisions are also ineffective in energy exchange.

Thus, reducing the arc current from the high current cases, in which nearly all primaries have inelastic collisions with atoms or have electron-electron collisions,

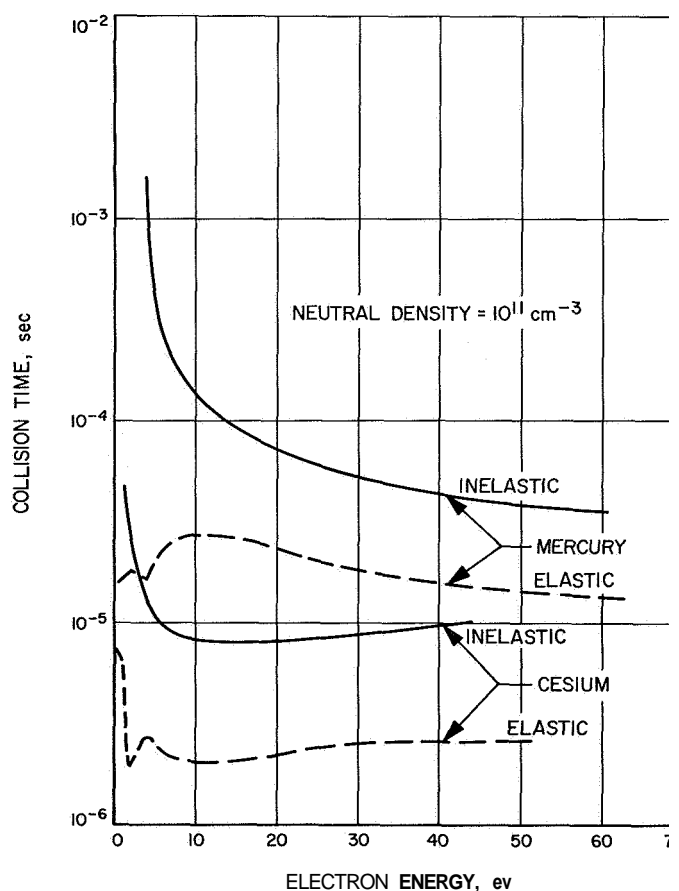


Fig. 18. Elastic and inelastic electron-atom collision times

results in increasing the number of primaries which have neither had inelastic collisions nor have joined the 'lower' energy electron group. This change in collision conditions is illustrated by the shift of high energy electrons from below the Maxwellian lines in Fig. 16 to above the lines for decreasing arc current. The explanation for the shortage of high energy electrons, readily apparent at high arc currents, is yet to be given.

It should be noted that the data of Refs. 11 and 12 do not exhibit the surplus electron property found here even though low arc currents were used (5 amp). This is believed to be due to the static conditions of testing, higher pressures, and a relatively long distance (including a bend in the discharge tube) between the cathode and the probes allowing a more equilibrium plasma to be formed.

A shortage of high energy electrons is expected for all arc currents when the following two points are considered. (Note that the low arc current curves which initially go above the Maxwellian line also turn back down, indicating a general loss mechanism opposing the primary buildup.) First, the electrons, Maxwellian or primaries, lost in inelastic collisions are only those with energies above approximately 5 ev because the inelastic cross section (excitation) is extremely small below this energy (Ref. 13). During the inelastic collision, the electron loses at least 5 ev and thus the high energy electrons (above 5 ev) can be reduced to the low energy group. This energy loss in inelastic collisions disturbs the Maxwellian distribution, formed by electron-electron collisions, by reducing the number of electrons in the high energy portion of the distribution.

The second method for losing high energy electrons is due to collisions with the housing and with the anode. The electrons that reach both the anode and the housing must in general overcome a retarding sheath potential. The retarding potential at the anode is probably only a few volts (i.e., the plasma potential) but the sheath potential at the housing should be of the same order as the cathode sheath. Ions are lost from the plasma to the housing but the electrons flowing to the housing to maintain neutrality must thus be from the high energy part of the electron distribution. This results in a distortion of the distribution function similar to that due to inelastic electron-atom collisions. The data of Figs. 16 and 17 were taken as indicated near the center of the engine at the grid position. Similar data were also obtained throughout the engine but these sets at the other positions are not as complete as Fig. 16. Data taken both near the cathode

and as far as possible from the cathode (near the anode at the grid) are shown in Fig. 19. These curves, at least at high arc currents, appear to be quite similar to those of Fig. 16 and show similar changes with arc current.

Thus, it appears that the nature of the electron energy distribution function does not change spatially throughout the engine for a given set of engine operating conditions.

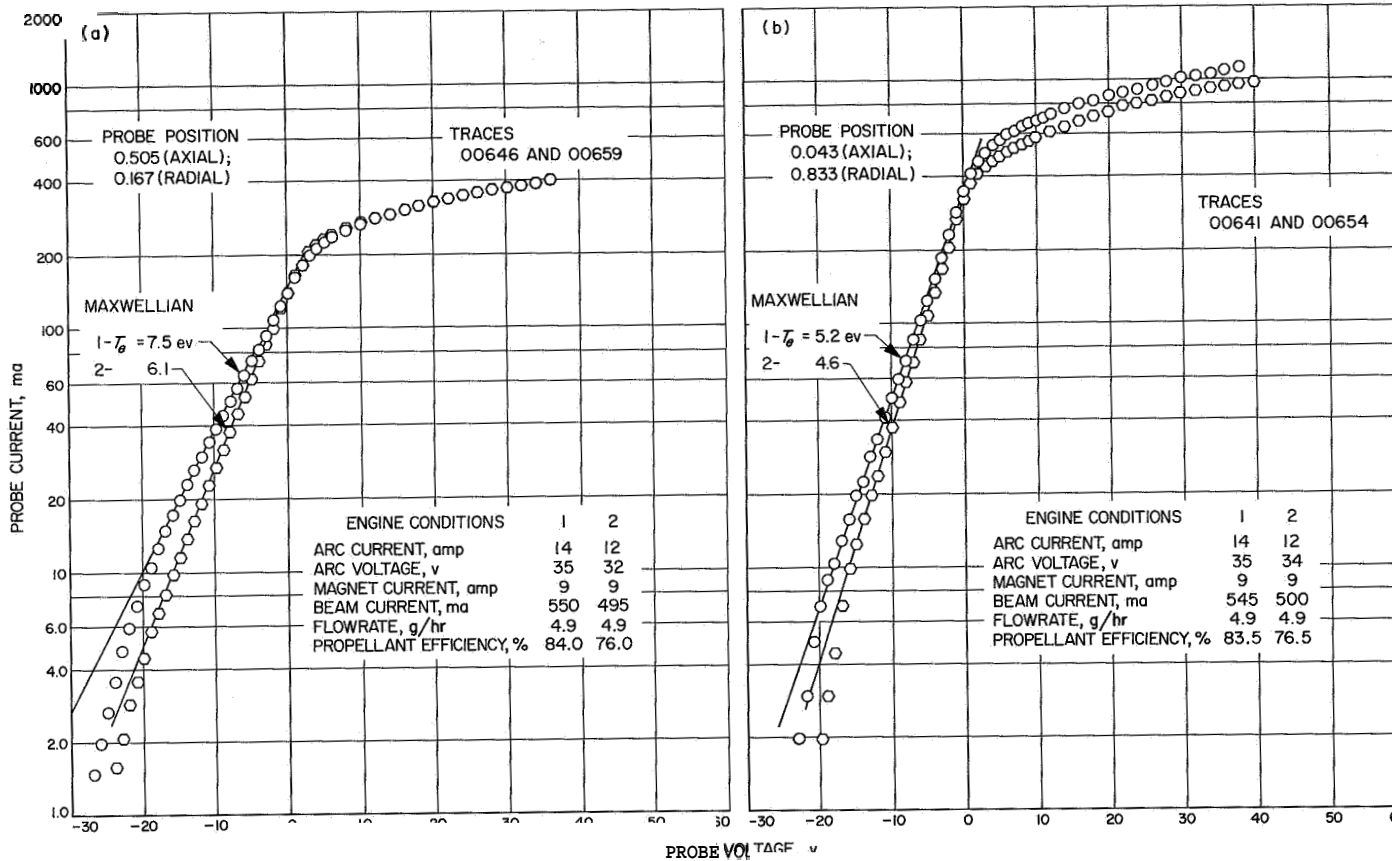


Fig. 19. Semilogarithmic plot of Langmuir probe traces for two arc currents

References

1. Radebold, R., Lang, H., Schulz, T., Weh, H., Klein, E., and Wagner, K. H., (AEG-Forschungsinstitut, Berlin), "Energy Conversion with Liquid Metal Working Fluids in MHD-Staustahlrohr, Status Report '66" Paper No. SM-74/30, International Symposium on Magnetohydrodynamic Electrical Power Generation, Salzburg, Austria, July 4-8, 1966.
2. Jackson, W. D., Pierson, E. S., and Porter, R. P., (Massachusetts Institute of Technology), "Design Considerations of MHD Induction Generators," Paper No. 61, International Symposium on Magnetohydrodynamic Electrical Power Generation, Vol. II, pp. 939-952, Paris, France, July 6-10, 1964. Also, Reid, M. H., "Experimental Investigation of a Liquid Metal Induction Generator," M.S. Thesis, M.I.T., September 1963.
3. Wang, T. C., and Dudzinsky, S. J. (Atoms International), "Theoretical and Experimental Study of a Liquid Metal MHD Induction Generator," Seventh Symposium on Engineering Aspects of Magnetohydrodynamics, pp. 34-42, Princeton, New Jersey, March 30-April 1, 1966.
4. Bacon, J., "The Evaluation of Materials for Application to Magnetohydrodynamic Power Generation," Report No. A-210173-1, Pratt and Whitney Aircraft Division, East Hartford, Connecticut, 1962.
5. Ryshkewitch, E., *Oxide Ceramics*, Academic Press, New York, 1960.
6. Knoll, M., *Materials and Processes of Electron Devices*, Springer-Verlag, Berlin, 1959.
7. Masek, T. D., "Plasma Characteristics of the Electron Bombardment Ion Engine," to be published in Second International Conference on Electron and Ion Beam Science and Technology, R. Bakish (ed), presented April, 1966.
8. Masek, T. D., "Plasma Investigation in a Reversed Current Electron Bombardment Ion Engine," AIAA 5th Elect. Prop. Conf., San Diego, preprint 66-246, March 1966.
9. Strickfaden, W. B., and Geiler, K. L., "Probe Measurements of the Discharge in an Operating Electron Bombardment Ion Engine," *AIAA Journal*, Vol. 1, p. 1815, 1963.
10. Kerslake, W. R., "Preliminary Operation of Oxide-Coated Brush Cathodes in Electron-Bombardment Ion Thrusters," NASA TM X-1105.
11. Howe, R. M., "Probe Studies of Energy Distributions and Radial Potential Variations in a Low Pressure Mercury Arc," *Jour. App. Phys.*, Vol. 24, p. 881-894, 1953.
12. Aisenberg, S., "Modern Probe Techniques for Plasma Diagnosis," 3rd Symposium on Engineering Aspects of Magnetohydrodynamics, Gordon and Breach, Science Publishers, Inc., 1963.
13. Massey, H. S. W., and Burhop, E. H. S., *Electronic and Ionic Impact Phenomena*, Oxford University Press, London, 1952.

N67 18333

XIII. Space Instrument Systems

SPACE SCIENCES DIVISION

A. An Algorithm for the Synthesis of Binary Sequence Detectors, M. Perlman

1. Problem Statement

A detector is required to recognize the arrival of a particular n -place binary sequence within a serialized (bit by bit) data stream. Upon the entry of the n th bit of the sequence into the detector and before the entry of the succeeding bit (i.e., during the n th bit interval), the detector is to furnish an output. The detection of a given 31-bit pseudorandom sequence was treated in SPS 37-31, Vol. IV, pp. 211-214. This has since been extended to the detection of any given n -place binary sequence within a data stream.

2. Application

Binary sequences are inserted at the beginning (or end) of a data frame or subframe emanating from a digital data processor of a spacecraft. Sequence detectors are used in the decoding equipment on the ground to provide "flags" which indicate the beginning (or end) of a data block (e.g., a TV frame).

The sequence detector is, in essence, an electronic combination lock which is opened for one digit period only when the proper sequence of binary digits is entered.

3. Constraint

The probability of n successive data bits being identical to a given n -place sequence should be reasonably low. *A priori* information concerning the data is not generally known. However, if each data bit arrives as a 0 or 1 with equal probability, the probability of n successive data bits being identical to a given n -bit sequence is 2^{-n} if the following constraint is imposed. The sequence of bits must be such that after it has been partially completed, the remaining bits or bit cannot be the beginning of the same sequence.

Example 1. Given the sequence in Fig. 1, where a_i precedes a_{i+1} in time, a_5 through a_{10} and a_9 through a_{11} , correspond to the first six and the first two digits of the sequence, respectively. This is clearly undesirable because

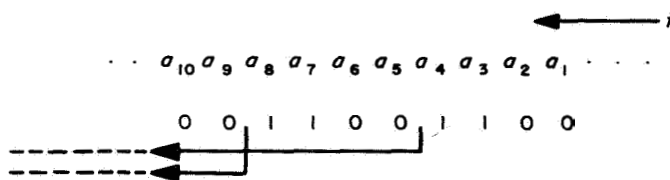


Fig. 1. A 10-bit sequence that does not satisfy the constraint

there is now a higher probability (i.e., $>2^{-10}$) that these partially completed sequences, together with preceding or succeeding data bits, can correspond to the original sequence. The probability that the 10-bit sequence is formed with four data bits followed by a , through a , is 2^{-4} .

The constraint on the sequence to eliminate the preceding possibility may be satisfied in one of two following ways.

a. Cyclic permutation of the original sequence. A sequence where the first and last bit differ, and the longest run of 0's or 1's appears at the beginning of the sequence, satisfies the constraint when the sequence is not a composite of two or more identical sequences. An example is 1101000. Any sequence that is not a composite of two or more identical sequences (such as 1110011100 or 010101), when cyclically permuted such that the longest run of 0's or 1's is at the beginning, will satisfy the constraint. The sequence in Example 1 can be cyclically permuted such that it starts with ... 11 or ... 0000; i.e.,

1100110000

0000110011

Both satisfy the constraint.

b. Prefix coding the original sequence. Prefix coding is employed in two cases:

- (1) The sequence is a composite of two or more identical sequences and cannot be made to satisfy the constraint through a cyclic permutation.
- (2) The sequence contains information which would change under a cyclic permutation. A binary count, e.g., i , may be used to indicate the start of the i th data frame.

The constraint in these two cases can be satisfied by prefixing these sequences with a sufficient number of 0's or 1's. The sequence in Example 1 must be prefixed with 111, resulting in

0011001100111

By prefixing 1110011100 with a single 0, the constraint is satisfied.

4. Two Methods of Detection

a. Shift register and decisional element. A shift register made up of $n - 1$ two-state memory elements together with an n -input decisional element can serve as a detector. The register serially stores $n - 1$ bits. These and the n th bit (just prior to entering the register) are sensed by an n -input decisional element. Thus, by "funneling" a stream of binary digits through the register, one of 2^n possible n -bit sequences can be located wherever it occurs. This method, though straightforward, is uneconomical in terms of the number of memory elements required.

b. Sequential network with a minimum number of memory elements. The minimum number of states the detector must assume is equal to n , the number of bits in the sequence. Thus, the minimum number of memory elements required is $1 + [\log_2 n]$. The bracketed term denotes the nearest integer which is less than $\log_2 n$.

The minimum-state sequential network requires only a fraction of the number of memory elements (for $n > 3$) needed in the shift-register approach. Unfortunately, there is no known algorithm for assigning combinations of state values to each state such that the combinational logic (implemented with decisional elements) is of minimal complexity. In the case of the shift register, the combinational logic will always effectively be a single n -input decisional element.

The algorithm presented in this paper enables a logic designer to:

- (1) Synthesize a detector for an n -bit sequence with r memory elements where $1 + [\log_2 n] \leq r \leq n - 1$. (Sequences for which $r > n - 1$ are not considered.) Make a state assignment that results in combinational logic of reasonable complexity. Compared with that of the shift-register detector, the overall complexity is significantly reduced. The reduction is most pronounced when n approaches 2^i .
- (2) Select an n -bit sequence for any given value of n such that its detector can be synthesized with $1 + [\log_2 n]$ memory elements. Make a state assignment such that the complexity of the combinational logic approaches that of the shift-register detector when implemented with diode gates.

Note that the constraint in Section 3 is implied when referring to an n -bit sequence.

5. An Algorithm for Determining the Number of Memory Elements and an Optimal State Assignment for Detecting a Given Sequence

a. Binary (n, r) ring sequence. A given n -bit sequence (to be detected) may be characterized as a binary (n, r) ring sequence. The number of bits in the sequence is n , and r is a (fixed) number of consecutive bits in each of n distinct subsequences.

Example 2. The sequence 010010111 is a binary $(9, 4)$ ring sequence (illustrated in Fig. 2). Six of the nine 4-bit subsequences are bracketed. The sequence is an ordered cycle such that the last bit is followed by the first as if the sequence were repeated or formed a ring. The nine 4-bit subsequences are:

0111
1011
0101
0010
1001
0100
1010
1101
1110

Note that $2^r \geq n$. The minimum r that yields n distinct r -bit subsequences is of interest. Other values of r where $r_{\min} \leq r \leq n - 1$ will also form n distinct subsequences. The subsequences represent the n states the detector must assume in the detection of the sequence. The length of the subsequences r represents the number of memory elements required.

The synthesis of the detector is illustrated by an example. A state table for the sequential network which is

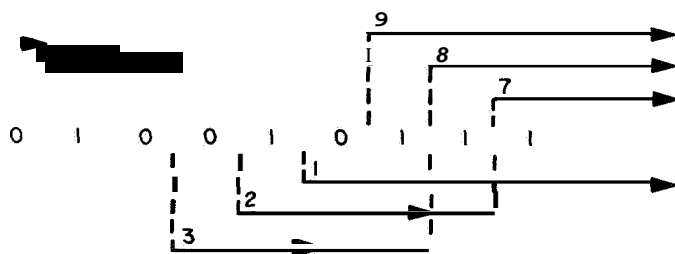


Fig. 2. A binary $(9, 4)$ ring sequence

to serve as a detector is first constructed. This is done as follows for the sequence in Example 2.

0 1 0 0 1 0 1 1 1
9 8 7 6 5 4 3 2 1 bit number

b. State assignment for a sequential network. In Table 1, the states of the sequential network are labeled numerically with an initial state designation of 1. The number of states, 9, corresponds to the number of bits in the sequence. The input to the detector is represented by the Boolean variable x .

Table 1. State table

Present state	Next state		Present output	
	$x = 0$	$x = 1$	$x = 0$	$x = 1$
1	1	②	0	0
2	1	③	0	0
3	1	④	0	0
4	⑤	4	0	0
5	1	⑥	0	0
6	⑦	3	0	0
7	⑧	2	0	0
8	1	⑨	0	0
9	①	3	1	0

The arrival of the first 1 on the x input line (i.e., possible start of the sequence) causes the state transition from 1 (initial present state) to 2 (next state). Should each succeeding bit be part of the sequence to be detected, the sequential network progresses through each state in numerical order. This is indicated by the encircled next states in the state table. During the time the network is in present state 9 and a 0 is on the input line, the detector's (present) output is 1.

If at any time a bit is received that is not in the sequence, though previous bits were identical to the start of the sequence, the network must return to the initial state 1 or to one of the states 2 through 4. Since the sequence begins with a 1, whenever a 0 arrives improperly located in the sequence, the network must return to state 1. However, whenever a 1 arrives improperly located in the sequence, the network must return to either state 2, 3, or 4. For example, assuming the network is in present state 6 (meaning the 5 previous bits correspond to the first 5 bits in the sequence) and the 6th bit is 1 instead of 0, the network should not progress to state 7. Instead, it should

return to state **3**, since bit **5** and bit **6** (now entering) correspond to the first two bits in the sequence. Thus, the 5th bit of the 6-bit block could possibly be the start of the sequence to be detected.

The state assignment for the sequential network is taken from the ordered subsequences in the binary (9, 4) ring sequence. The successive states through which the detector progresses when each bit of the sequence appears in order is made to correspond to successive subsequences. Thus, once an assignment is made for initial state 1, the state assignment is complete. With r memory elements, there are $r - 1$ initial states such that one of the memory elements will track the incoming sequence. In the example, there are three of the nine states, when chosen as an initial state, that will result in one memory element tracking the incoming sequence. Minimization of the combinational logic by means of a computer program (Ref. 1) shows that these initial states result in optimal minimization when state assignments correspond to the n subsequences in the binary (n, r) subsequence. The logic designer, therefore, may reduce the possible number of assignments from $(2' - 1)!/[r!(2' - n)!]$ (see Ref. 2) to $r - 1$. Any of the $r - 1$ assignments yields combinational logic of reasonable complexity. Usually, one or more will be superior to others. In many cases, the feedback shift register (FSR) which is capable of generating the (n, r) sequence provides a clue as to which of the $r - 1$ initial states—hence, state assignments—is the most economical. This will be discussed in a later section.

Four memory elements are required in the example. Let $d_1 d_2 d_3 d_4$ and $D_1 D_2 D_3 D_4$ represent the present and next (combination of) states, respectively. By selecting 1010 as an initial state, $D_i = x$. This is illustrated in Table 2 where all the states of Table 1 have been assigned.

For explanatory purposes, Table 2 is divided into three parts. The top nine entries show how the detector behaves when the sequence is entered. The next nine entries show its behavior when a bit is on the x input line, which is not properly part of the sequence. For example, a total state, $x d_1 d_2 d_3 d_4$ of 10101, indicates that the 5 bits previously entered correspond to the first 5 of the sequence (hence, the network progressed to state 6). However, the present input x equals 1 instead of 0 as in the sequence. The network's next state, $D_1 D_2 D_3 D_4$, is 1110 or state **3**, since the previous input and the present input could be the first two bits in the sequence. The lower portion of Table 3 represents unused total states (i.e., unused internal states combined with the input state). The next states for these entries are treated optionally.

Minimizing $D_1 D_2 D_3 D_4$ and the output Z as functions of x, d_1, d_2, d_3 , and d_4 results in the following:

$$D'_1 = x d'_2 d_4 + x d_2 d'_3 + x' d'_1 d'_3 d_4 \quad (1)$$

$$D_1 = (x' + d_2 + d'_4) (x' + d'_2 + d'_3) (x + d_1 + d_3 + d'_4) \quad (1a)$$

$$D_2 = x \quad (2)$$

$$D_3 = x' d_1 + d, \quad (3)$$

$$D'_4 = x' d_1 + d'_3 \quad (4)$$

$$Z = x' d_2 d'_3 d'_4 \quad (5)$$

where the symbols ' and + denote complementation and logical addition (i.e., OR), respectively. Adjacent Boolean variables, such as $d_1 d_2$, denote logical multiplication (i.e., AND).

The Expression (1a) indicates that D_1 is simpler in the conjunctive form. The complement of the function D'_1 was minimized in disjunctive form as shown in Eq. (1).

By making each entry under x identical to the corresponding entry under d , in the first nine entries, the memory element represented by d , tracks the input (i.e., $D_i = x$, as previously asserted). In the next nine entries, $x = d'_1$. These entries account for all the used total states.

6. Implementation

All functions have been minimized under the criterion of minimum two-level AND-OR gating. Implementation, however, is done with NAND gates acting as decisional elements, since the cost ratio of the RS flip-flop to the NAND gate is apparent. Provision for NAND-AND operation is assumed. The RS flip-flop serves as a memory element. The cost ratio of an RS flip-flop to a diode gate (AND-OR having the same number of inputs as the NAND gate) would be even higher. Thus, the economy realized by reducing the number of memory elements at the expense of adding NAND gates (i.e., fewer equivalent RS flip-flops) is less than that attainable with diode AND-OR gates. When implementing sequence detectors, the RS flip-flop will be used as a delay element to provide memory.

The implementation of the detector in Example 2 is shown in Fig. 3. The cost is 4 RS flip-flops and 12 NAND gates (with 4 or fewer inputs). The RS flip-flop uses a

Table 2. State assignment for detection of 010010111

x	d_1	d_2	d_3	d_4	Present state	D_1	D_2	D_3	D_4	Next state
1	1	0	1	0	1	1	1	0	1	2
1	1	1	0	1	2	1	1	1	0	3
1	1	1	1	0	3	0	1	1	1	4
0	0	1	1	1	4	1	0	1	1	5
1	1	0	1	1	5	0	1	0	1	6
0	0	1	0	1	6	0	0	1	0	7
0	0	0	1	0	7	1	0	0	1	0
1	1	0	0	1	0	0	1	0	0	9
0	0	1	0	0	9	1	0	1	0	1
0	1	0	1	0	1	1	0	1	0	1
0	1	1	0	1	2	1	0	1	0	1
0	1	1	1	0	3	1	0	1	0	1
1	0	1	1	1	4	0	1	1	1	4
0	1	0	1	1	5	1	0	1	0	1
1	0	1	0	1	6	1	1	1	0	3
1	0	0	1	0	7	1	1	0	1	2
0	1	0	0	1	8	1	0	1	0	1
1	0	1	0	0	9	1	1	1	0	3
0	0	0	0	0		ϕ	ϕ	ϕ	ϕ	
0	0	0	0	1		ϕ	ϕ	ϕ	ϕ	
0	0	0	1	1		ϕ	ϕ	ϕ	ϕ	
0	0	1	1	0		ϕ	ϕ	ϕ	ϕ	
0	1	0	0	0		ϕ	ϕ	ϕ	ϕ	
0	1	1	0	0		ϕ	ϕ	ϕ	ϕ	
0	1	1	1	1		ϕ	ϕ	ϕ	ϕ	
1	0	0	0	0		ϕ	ϕ	ϕ	ϕ	
1	0	0	0	1		ϕ	ϕ	ϕ	ϕ	
1	0	0	1	1		ϕ	ϕ	ϕ	ϕ	
1	0	1	1	0		ϕ	ϕ	ϕ	ϕ	
1	1	0	0	0		ϕ	ϕ	ϕ	ϕ	
1	1	1	0	0		ϕ	ϕ	ϕ	ϕ	
1	1	1	1	1		ϕ	ϕ	ϕ	ϕ	

minimum of two transistors whereas the NAND gate has only one. The RS flip-flop may be considered as two cross-coupled NANDs with additional circuitry for the clock input. Thus, a conservative cost ratio of the RS flip-flop to the NAND gate is 3 to 1. Therefore, the cost of the detector in Fig. 3 is equivalent to 24 NAND gates. The shift-register approach would require 8 RS flip-flops and 2 NAND gates. One is used to invert x and the other (with 9 inputs) is used to sense the input and the contents of the register. This is equivalent to 26 NAND gates. The 2 NAND gate reduction represents a modest improvement. However, this example represents the case where

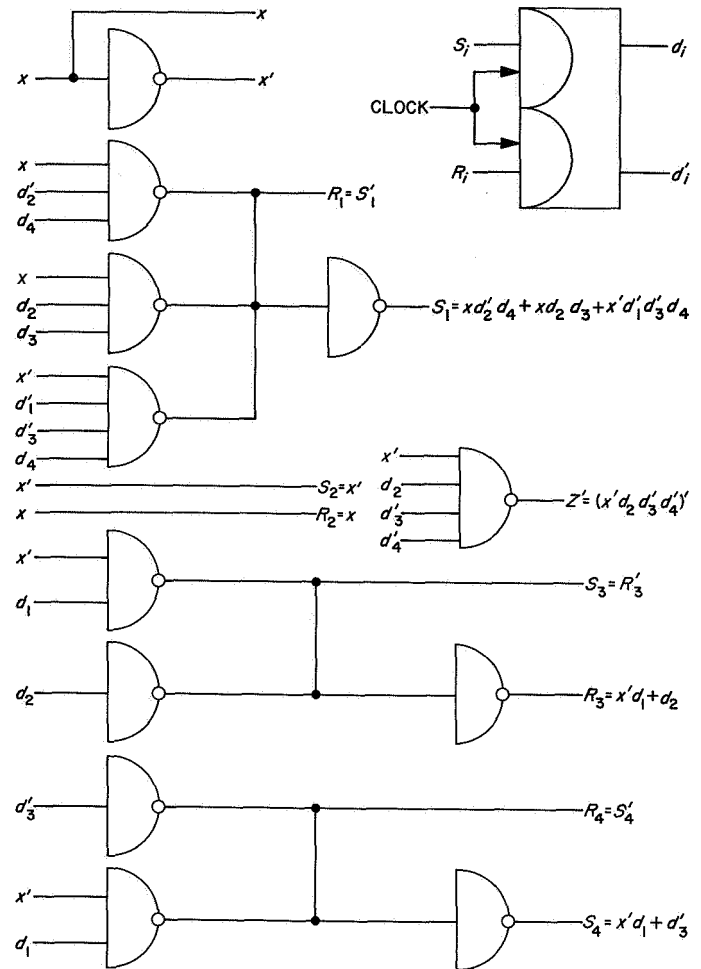


Fig. 3. Implementation of the detector of sequence 010010111

n is small and $n/2^r = 9/16$. As n approaches 2^r for a given r , the improvement increases.

Example 3. The following sequence

10001100101011110000
 21 16 10 5 1

can be characterized as a binary (21,5) ring sequence. Thus, $n/2^r = 21/32$. The state assignment is shown in Table 3. Memory element d_2 tracks the input x , as in Example 2. Note that, in general, there is no assignment such that d_1 tracks x (i.e., D_1 cannot equal x). Thus, the $r - 1$ assignments mentioned previously are those for which either D_2, D_3, \dots, D_r equals x .

Table 3. State assignment for detection of the 21-bit sequence in Example 3

x	d ₁	d ₂	d ₃	d ₄	d ₅	Present state	D ₁	D ₂	D ₃	D ₄	D ₅	x	d ₁	d ₂	d ₃	d ₄	d ₅	D ₁	D ₂	D ₃	D ₄	D ₅	
0	0	1	0	0	0	1	0	0	1	0	0	1	0	1	0	0	0	0	1	0	0	0	0
0	0	0	1	0	0	2	0	0	0	1	0	1	0	0	1	0	0	0	0	1	0	0	0
0	0	0	0	1	0	3	0	0	0	0	1	1	0	0	0	1	0	0	0	1	0	0	0
0	0	0	0	0	1	4	1	0	0	0	0	1	0	0	0	0	1	0	1	0	0	0	0
1	1	0	0	0	0	5	1	1	0	0	0	0	1	0	0	0	0	1	0	0	0	0	0
1	1	1	0	0	0	6	1	1	1	0	0	0	1	1	0	0	0	0	0	1	0	0	0
1	1	1	1	0	0	7	1	1	1	1	0	0	1	1	1	0	0	0	0	1	0	0	0
1	1	1	1	1	0	8	1	1	1	1	1	0	1	1	1	1	0	0	0	1	0	0	0
1	1	1	1	1	1	9	0	1	1	1	1	0	1	1	1	1	1	0	0	1	0	0	0
0	0	1	1	1	1	10	0	1	0	1	1	1	0	1	1	1	1	0	1	0	0	0	0
1	1	0	1	1	1	11	0	1	0	1	1	0	1	0	1	1	1	0	0	0	1	0	0
0	0	1	0	1	1	12	2	1	0	1	0	1	0	1	0	1	1	0	1	0	0	0	0
1	1	0	1	0	1	13	3	0	1	0	1	0	0	1	0	1	1	0	0	0	1	0	0
0	0	1	0	1	0	14	4	0	0	1	0	1	1	0	1	0	1	0	1	0	0	0	0
0	0	0	1	0	1	15	1	0	0	1	0	1	1	0	0	1	0	1	0	1	0	0	0
1	1	0	0	1	0	16	6	1	1	0	0	1	0	1	0	0	1	0	0	0	0	1	0
1	1	1	0	0	1	17	0	1	1	0	0	0	1	1	0	0	1	0	0	1	0	0	0
0	0	1	1	0	0	18	0	1	1	1	1	0	1	0	1	1	0	0	1	0	0	0	0
0	0	0	1	1	0	19	0	0	0	1	1	1	0	0	1	1	0	0	1	0	0	0	0
0	0	0	0	1	1	20	0	1	0	0	0	1	0	0	0	1	1	0	1	0	0	0	0
1	1	0	0	0	1	21	0	1	0	0	0	0	1	0	0	0	1	1	0	0	0	0	0
0	0	0	1	1	1		φ	φ	φ	φ	φ	1	0	0	1	1	1	φ	φ	φ	φ	φ	φ
0	0	1	0	0	1		φ	φ	φ	φ	φ	1	0	1	0	0	1	φ	φ	φ	φ	φ	φ
0	0	1	1	1	0		φ	φ	φ	φ	φ	1	0	1	1	1	0	φ	φ	φ	φ	φ	φ
0	1	0	0	1	1		φ	φ	φ	φ	φ	1	1	0	0	1	1	φ	φ	φ	φ	φ	φ
0	1	0	1	0	0		φ	φ	φ	φ	φ	1	1	0	1	0	0	φ	φ	φ	φ	φ	φ
0	1	1	0	1	0		φ	φ	φ	φ	φ	1	1	1	0	1	0	φ	φ	φ	φ	φ	φ
0	1	1	1	0	1		φ	φ	φ	φ	φ	1	1	1	1	0	1	φ	φ	φ	φ	φ	φ

The minimized expressions for the next state of each memory element are:

$$D_1 = xd_1d'_5 + x'd'_1d_5 + x'd'_2d'_3d'_4 \quad (6)$$

$$D_2 = x \quad (7)$$

$$D'_3 = d'_2 + xd'_1 \quad (8)$$

$$D_4 = xd_1d_3 + x'd'_1d_3 + d_1d'_2d_3 \quad (9)$$

$$D_5 = xd_1d_4 + x'd'_1d_4 + d_1d'_3d_4 \quad (10)$$

$$Z = xd_1d'_2d'_4d'_5 \quad (11)$$

The implementation cost is 5 RS flip-flops and 17 NAND gates (with 5 or fewer inputs). This is equivalent to 32

NAND gates. In the shift-register approach, 20 RS flip-flops and 4 NAND gates are required. The 4 NAND gates are needed to sense the contents of the register and the input. In practice, the input expansion to a NAND gate is limited to 12. Therefore, two levels of NAND gates are required.

The shift-register detector is equivalent to 64 NAND gates. Therefore, a reduction of 2 to 1 is realized with the sequential network.

7. Selection of the initial State

The configuration of the simplest feedback shift register capable of generating the sequence often provides information as to which of the $r - 1$ possible initial states (i.e., which of the memory elements d_2, d_3, \dots , or d_r ,

should track x) yields the best state assignment. Every binary (n, r) ring sequence can be generated by an r -stage shift register where a Boolean function of its contents is fed back. This is termed a feedback shift register or FSR (Fig. 4).

The bit being fed back during the n th clock time interval is

$$a_n = f(a_{n-1}, a_{n-2}, \dots, a_n) \quad (12)$$

Successive subsequences provide a state table for determining $f(a_{n-1}, a_{n-2}, \dots, a_n)$ in minimized form. The columns under $d_1 d_2 d_3 d_4 d_5$ and D_1 in the left half of Table 3 provide the information necessary to determine Eq. (12). D_1 corresponds to a_n , whereas d_1, d_2, \dots, d_5 correspond to $a_{n-1}, a_{n-2}, \dots, a_{n-5}$, respectively. Thus,

$$a_n = a'_{n-2} \oplus a_{n-4} \oplus a_{n-5}$$

where \oplus denotes sum modulo 2 or the EXCLUSIVE-OR operation. The contents of the i th stage at clock time interval n (i.e., a_{n-1}) become the contents of the $(i+1)$ th at clock time interval $n+1$. That is

$$a_{(n+1)-(i+1)} = a_{n-i}$$

It is assumed that the initial loading $a_{-1}, a_{-2}, \dots, a_{-r}$ where $n=0$ is any one of the subsequences. The state assignment is such that an $(i+1)$ th stage of the detector tracks

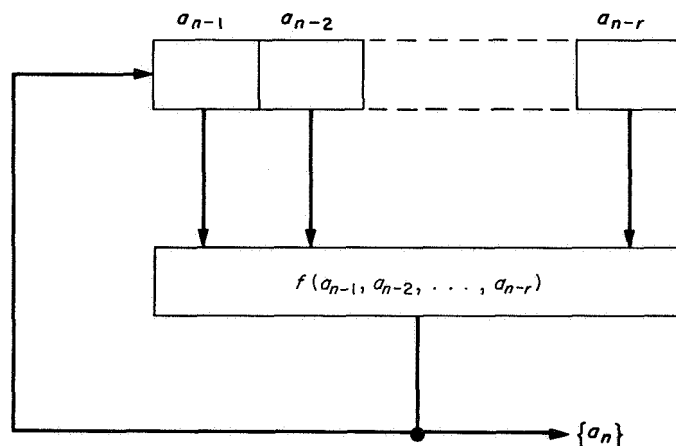


Fig. 4. Generalized feedback shift register for binary (n, r) ring sequence generation

x when the i th stage of the generator is in the feedback path. In the previous example, an initial state was chosen such that $D_3 = X$, since a_{n-2} is in the feedback. The case where $D_5 = X$ gives results that are equivalent in terms of complexity (i.e., minimum AND-OR diode count). As indicated previously, there is no assignment that results in $D_1 = X$.

8. Selection of a Sequence When Only n Is Specified

In Ref. 3, it is proved that a binary (n, r) ring sequence exists for every n and r where $2^r \geq n$. Therefore, a sequence with a specified n can be found such that r is minimum; this means a detector can be synthesized with a minimum number of memory elements.

For every $r > 1$, there are $\phi(2^r - 1)/r$ FSRs with linear logic feedback capable of generating a maximal-length sequence whose length n equals $2^r - 1$; $\phi(n)$ is the Euler +function which denotes the number of positive integers equal to or less than n . The detector for a maximal-length sequence is one of the most efficient in terms of hardware. In SPS 37-31, Vol. IV, the detector for a 31-bit maximal-length sequence was synthesized. The next-state functions were minimized simultaneously for each possible initial state by means of a general-purpose computer program (Ref. 1). The results were optimum for the case where a memory element (in accordance with Example 3) tracked the input.

The feedback function for a maximal-length sequence generator can be determined from tables of irreducible polynomials (Ref. 4). In turn, the sequence $\{a_n\}$ and all the subsequences $a_{n-1} a_{n-2} \dots a_{n-r}$ can be found. (The subscript n denotes clock-time interval and is not to be confused with sequence length n .) Furthermore, there is an algorithm for modifying the feedback function such that any sequence length from 1 to $2^r - 1$ can be obtained (Ref. 5). Of interest are sequence lengths from 2^{r-1} to $2^r - 1$, though a length of 2^{r-1} could be obtained with $r - 1$ memory elements.

The 31-bit sequence previously mentioned is

1	0	0	1	0	1	1	0	0	1	1	1	0	0	0	1	1	0	1	0	1	0	0	0	0	0	0	0	
31	25	20	15	10	5	1																						

The feedback function for the generator is

$$a_n = a_{n-2} \oplus a_{n-5}$$

The next-state functions for the detector are

$$D_1 = x'd_2d_5 + xd_1d_5' + x'd_3d_4d_5 \quad (13)$$

$$D_2 = (x'd_2' + xd_2) d_4 + x'd_3d_4d_5' \quad (14)$$

$$D_3 = x \quad (15)$$

$$D_4 = (x' + d_2) d_3 \quad (16)$$

$$D_5 = (x'd_2' + xd_2) d_4 + x'd_3d_4 \quad (17)$$

$$Z = xd_1d_2d_3d_5d_6 \quad (18)$$

Note that bits 2 through 14 in the original 31-bit sequence have been omitted.

The next-state functions for the detector are

$$D_1 = x'd_2d_5 + xd_2d_5' + x'd_3d_4' \quad (19)$$

D_2 through D_5 are the same as Eqs. (14) through (17); also, Z can be the same as Eq. (18).

For $n = 27$,

$$W = a_{n-1} a_{n-2} a_{n-3}' a_{n-4} a_{n-5}'$$

The sequence is the same as the 31-bit sequence with bits 7 through 10 deleted.

As in the case for $n = 27$, only D_1 differs:

$$D_1 = xd_2d_3'(d_1d_3'd_4d_5')' + x'd_2d_3 + xd_3'd_4d_5' \quad (20)$$

Thus, the 18- and 27-bit sequence detectors require one more NAND gate than the parent 31-bit sequence (whose cost is 5 RS flip-flops and 17 NAND gates). Detectors for sequences of length $n = 16$ through $n = 30$ are also of the same complexity as that for the 31-bit sequences. These, of course, are derived from the same 31-bit sequence.

By modifying the feedback function where

$$a_n = a_{n-2} \oplus a_{n-5} \oplus W$$

a specified number of successive bits within the 31-bit sequence are omitted. W is 1 for a particular nonzero combination of states in the FSR. Two examples follow:

For $n = 18$,

$$W = a_{n-1} a_{n-2}' a_{n-3}' a_{n-4}' a_{n-5}'$$

and the generated sequence is

$$\begin{array}{ccccccccc} 1 & 0 & 0 & 1 & 0 & 1 & 1 & 0 & 0 & 1 & 1 & 1 & 1 & 0 & 0 & 0 & 0 \\ | & | & | & | & | & | & | & | & | & | & | & | & | & | & | & | \\ 18 & 15 & & 10 & & 5 & & & & & & & & & & & 1 \end{array}$$

References

1. Burgess, C. R., *Boolean Algebra Minimizer*, SHARE Program LLBAM 1197, Massachusetts Institute of Technology, Lincoln Laboratory, Lexington, Massachusetts, September 1961.
2. McCluskey, E. J., Jr., and Unger, S. H., "A Note on the Number of Internal Variable Assignments for Sequential Switching Circuits," *IRE Transactions on Electronic Computers*, Vol. EC-8, No. 4, December 1959, pp. 439-440.
3. Yoeli, M., "Binary Ring Sequences," *American Mathematical Monthly*, Vol. 69, November 1962, pp. 852-855.
4. Peterson, W. W., *Error-Correcting Codes*, John Wiley and Sons, Inc., New York, 1961.
5. Baumert, L. D., *Table of Period Generators*, Technical Report 32-564, Jet Propulsion Laboratory, Pasadena, Calif., November 1, 1962.

XIV. Bioscience

SPACE SCIENCES DIVISION

N67 18334

A. Pyrolysis Fluorescence. I. Detection and Estimation of Organic Matter, P. J. Geiger, J. V. Behar¹, and J. H. Rho

1. Introduction

In an experimental program directed toward the detection of extraterrestrial life, it is advantageous to have a simple method to establish first the presence and concentration of organic matter in the alien environment, since life systems with which we are familiar are based upon carbon chemistry (Refs. 1 and 2). The method under development at JPL depends on the fact that all organic materials will form fluorescent products when heated to high temperatures in a closed vessel for a specified period. Pyrolysis forms homo- and hetero-cyclic and polycyclic compounds by cracking the parent molecules. This is followed by such processes as diene synthesis, dehydrogenation and cyclodehydrogenation, depending on the exact conditions of pressure, temperature, and time. The mechanism of formation of aromatic hydrocarbons produced by high temperatures has been clarified particularly by the investigations of Badger and co-workers (Ref. 3), Sweeting and Wilhire (Ref. 4), and others

(Refs. 5-8). Free-radical processes are predominantly involved. Formation of *asphalt* (i.e., a collection of compounds rich in polycyclic forms) has also been demonstrated by the theoretical and experimental investigations of R. V. Eck, et al. in *limited equilibrium* systems (Ref. 9). These recent investigations are particularly pertinent to the development of the method presented here, in which equilibrium conditions are also approached. This method permits synthesis of relatively large molecules which can be detected and quantified in minute amounts by a fluorometric procedure. Other pyrolysis systems involving a flowing stream of hot gases give a greater variety of products, most of which are relatively small molecules not easily detected in minute quantities by simple spectroscopic methods.¹ Fewer molecules that were not only large (molecular weight in the hundreds) but also highly fluorescent have been produced in this laboratory and detected even in nanogram quantities.³

The present paper describes the production and quantitation of fluorescent material from selected pure substances and natural materials, including microorganisms,

¹On leave to complete doctorate in chemistry at University of California, Riverside.

¹Adamcik, J. A., JPL Internal Document, September 1966 (unpublished).

³Geiger, P. J., Unpublished results.

humic acid, and selected soils—without regard to the qualitative nature of the fluorescent materials themselves. The latter will be the subject of a future communication.

2. Experimental Procedure

a. Materials. Aside from materials of natural origin, reagents or substances that were pyrolyzed were analytical reagent grade. The natural soils used (except soil 1-1) were obtained from the collection of R. Cameron and have been fully characterized by the standard techniques of soil science. Soil 1-1 was obtained from the Colorado Desert near Thermal, California. Dried cells of *Micrococcus lysodeikticus* were obtained from Worthington Biochemical Corporation, Freehold, New Jersey. *Escherichia coli* and *Chlorella* cells were grown as previously described (SPS 37-24, Vol. IV, pp. 262-265; SPS 37-25, Vol. IV, pp. 243-248), and *Rhodospirillum rubrum* was grown on a modified Hutner's medium developed by R. Y. Stanier.⁴ These cells were washed and dried before use. Humic acid, practical grade, was obtained from K & K Laboratories, Plainview, New York; its organic carbon was determined to be 95% by the Allison method. Pure (TLC grade) silica was obtained from both the Alleghany Industrial Chemical Company, Butler, New Jersey, and Brinkmann Instruments, Westbury, New York. Fluorometric grade solvents were obtained from the Hartman-Leddon Company, Philadelphia, Pennsylvania. Quartz tubing was obtained from the General Electric Company, Lamp Glass Division, Los Angeles, California.

b. Methods. Pyrolysis was carried out for specified intervals, usually about 30 min, in either a micro-tube furnace or a muffle furnace. Early experiments were done in thick-walled glass tubes of several milliliters capacity, which had been evacuated to 10^{-5} to 10^{-6} torr to remove oxygen. Sample sizes were several hundred milligrams. Later pyrolyses were done with samples of a few milligrams in unevacuated quartz tubes 1-mm ID, 2-mm OD, and 4.5 cm long; these could be easily heated and cooled, and their small size minimized the explosion hazard.

After pyrolysis, most tubes contained gases under high pressure and, accordingly, were opened while being cooled in liquid nitrogen. This was especially necessary for tubes pyrolyzed at 600 to 700°C, as an estimate made with a Topley pump system indicated pressures of about 100 to 300 atm. Natural soils were occasionally too damp to be pyrolyzed directly, since the moisture caused the

tubes to burst at about 300°C. Accordingly, before use, these soils were air-dried overnight in an incubator at 37°C. Opened tubes and their contents were usually dropped immediately into 2 ml of a 2-to-1, volume/volume mixture of chloroform and methanol. The resulting solution was read immediately in the fluorometer or was diluted as necessary before reading. Storage was avoided to minimize product degradation.

Fluorometric measurements were made on a Turner Model 111 fluorometer equipped with a Corning 7-60 excitation filter and a Wratten 2A emission filter. A micro-cell adapter permitted use of 6 X 50 mm pyrex tubes containing a sample of 1 ml or less; quartz tubes were unnecessary. Spectra were observed with a Farrand spectrophotofluorometer modified to permit use of a Moseley Model 2D2 X-Y recorder. Estimates of sensitivity were made from spectral peak heights. A 3-mm quartz microcell, square in cross section, allowed scanning a sample of less than 1 ml. Absorption spectra were taken with a Cary Model 14 spectrophotometer.

Table 1. Production of fluorescence by heating selected organic compounds

Compound	Temperature °C	Time, min	Fluorescence detected
Fructose	250	30	+
Hexamethylenetetramine	265	30	+
Tetracyanoethylene	240	25	—
Dextrose	240	20	+
Glucose phosphate	230	20	+
Nicotinic acid	270	35	+
lysine (DL)	260	25	+
Alanyl alanine	265	20	+
Cyclohexanol (exploded)	300	60	—
n-Hexylamine	300	60	+
Cyclohexanone	300	4	+
Ethylacetoacetate	290	20	+
Cyclohexane	300	40	—
n-Hexane	300	60	±
n-Butylacetate	300	60	±
Hexaldehyde	308	60	+
Hexanoic acid	310	90	+
N,N-Diethylacetamide	280	60	+
2,5-Hexanedione	260	15	+

Compounds were heated at the specified temperatures for the periods indicated. The most reactive compounds were heated at lower temperatures for shorter periods. Thick-walled pyrex tubes several cubic centimeters in volume were evacuated to remove oxygen before heating. Sample quantities of several hundred milligrams were used. Fluorescence was examined by eye under both short and long wavelength UV radiation lamps. In some cases, a specially modified spectrofluorometer was used.

⁴Department of Chemistry, University of California, Berkeley.

3. Results and Discussion

a. Fluorescence by pyrolysis. To show that a wide variety of pure organic compounds will fluoresce after pyrolysis at moderate temperatures and periods of time, the representative group illustrated in Table 1 was chosen. Many of these are biologically important compounds, not just the simple hydrocarbons usually studied in controlled air-pollution work. Because of a lack of hydrogen in the molecule, tetracyanoethylene, as expected, produced no cyclic forms and, hence, no fluorescence. Other negative or doubtful results were due to the relative inertness of the individual molecules. Later experiments at higher temperatures consistently produced the expected fluorescent pyrolyzates. Various temperatures and periods of heating are shown in the table. In general, more reactive molecules were heated for a shorter period. Temperatures were kept low since rigorous heating (600 to 700°C) invariably caused excessive formation of tar and graphite and reduced the yield of fluorescent molecules.

Table 2 presents data on the fluorescence of a group of pyrolyzed components containing both pure and natural

organic substances. This table contains two salient points of information. First, as with almost all the combined excitation-fluorescence spectra of pyrolysis products, the observed peaks had essentially similar maxima. A typical example is illustrated in Fig. 1, which represents products of desert soil (1-1) containing about 0.2% organic carbon, exposed to 400°C (the optimum temperature for production of fluorescence). Peaks with similar broad maxima appear in roughly the same portion of the visible and near ultraviolet spectrum for the wide variety of compounds and natural materials illustrated in the table. Exceptions were observed for 600°C pyrolyzates, which often showed at least two sharp fluorescence peaks, and for 700°C products, which always showed extensive fine structure due primarily to pyrene. This was true of pyrolyzed microorganisms and soils as well as pure organic compounds.

Second, although the spectrofluorometer used was inherently less sensitive than the filter instrument, an estimate of sensitivity was made from peak heights (shown in the last column of the table). Such an estimate is important when considering the size of sample that will

Table 2. Fluorescence of pyrolyzed pure and natural organic substances

Sample	Quantity pyrolyzed		Peak wavelengths		Sensitivity	
	mg	Numbers	Excitation	Fluorescence	Numbers	μg
			mμ	mμ		
Succinic acid	11.6	—	350	430	—	7.3
Citric acid	11.0	—	365	450	—	0.01
Inositol	13.2	—	365	450	—	4.1
Galactose	10.7	—	350	440	—	0.27
Adipic acid	10.5	—	365	450	—	13
Pectin	10.8	—	360	440	—	0.13
1-leucine	10.0	—	375	450	—	0.08
Glycine	10.0	—	350	450	—	0.08
D,1-lysine-HCl	10.0	—	375	450	—	0.08
1-Phenylalanine	10.0	—	380	460	—	0.008
Decanol-1	5.0	—	350	440	—	6.2
Dodecane	5.0	—	350	440	—	6.2
<i>E. coli</i>	—	10 ⁶	365	450	1000	—
<i>Chlorella pyrenoidosa</i>	—	10 ⁷	365	450	600	—
<i>Rhodospirillum rubrum</i>	—	10 ⁷	365	450	1000	—
<i>Micrococcus lysodeikticus</i> (dry sample)	0.42	—	350	450	—	2
Soil (1-1)	5.0	—	350	450	—	0.6
Soil (9-5)	3.7	—	350	450	—	30
Soil (9-5) (dry sample)	6.0	—	350	450	—	0.1

Samples were all pyrolyzed at 300°C further diluted to avoid interferences from self-absorption effects when quantitative estimates from spectral peak heights were made.

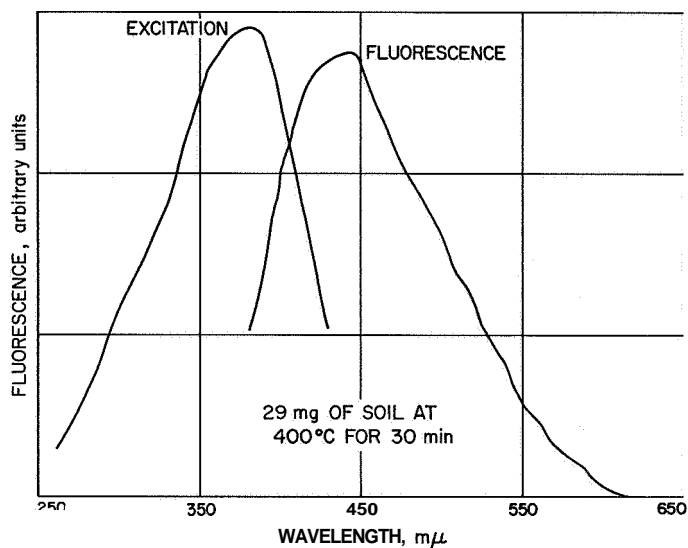


Fig. 1. Excitation and fluorescence spectra of pyrolysis products from desert soil (1-1)

most likely be available for analysis by remote collection on a Mars lander. Sensitivity was estimated from the quantities of starting materials necessary to produce an amount of fluorescence clearly distinguishable above background noise; i.e., a 10-to-1 ratio. The fluorescent products were dissolved in approximately 2.5 μ l of solvent contained in the microcell supplied with the instrument. Clearly, the nanogram range is easily attained. An estimate of the smallest number of organisms that might be observable by such a method is also shown in the table. The notation *dry sample* indicates that fluorescent products in solvent were dried on a small quartz window and then observed at a 30-deg angle of incidence.

b. Temperature optima. In order to quantify the method, it was first necessary to find the temperature optima for various compounds and natural materials. Heating at some arbitrary temperature would not, except fortuitously, be expected to produce the greatest quantity of fluorescent products per milligram of starting material; thus maximal sensitivity would not be achieved. Fig. 2 illustrates results with representative materials. The data in the figure were obtained with a Turner filter fluorometer to achieve maximum sensitivity. Filters were chosen on the basis of many spectra of different pyrolyzates, all similar to those in Fig. 1. Thus, all fluorescent light beyond about 400 $m\mu$ was collected while solutions were excited with a broad band of light that peaked at approximately 360 $m\mu$ and dropped essentially to zero at 400 $m\mu$. Scattering and stray light in the instrument are very low, and the sensitivities attained are shown in the figure. These sensitivities, when estimated in the manner already described,

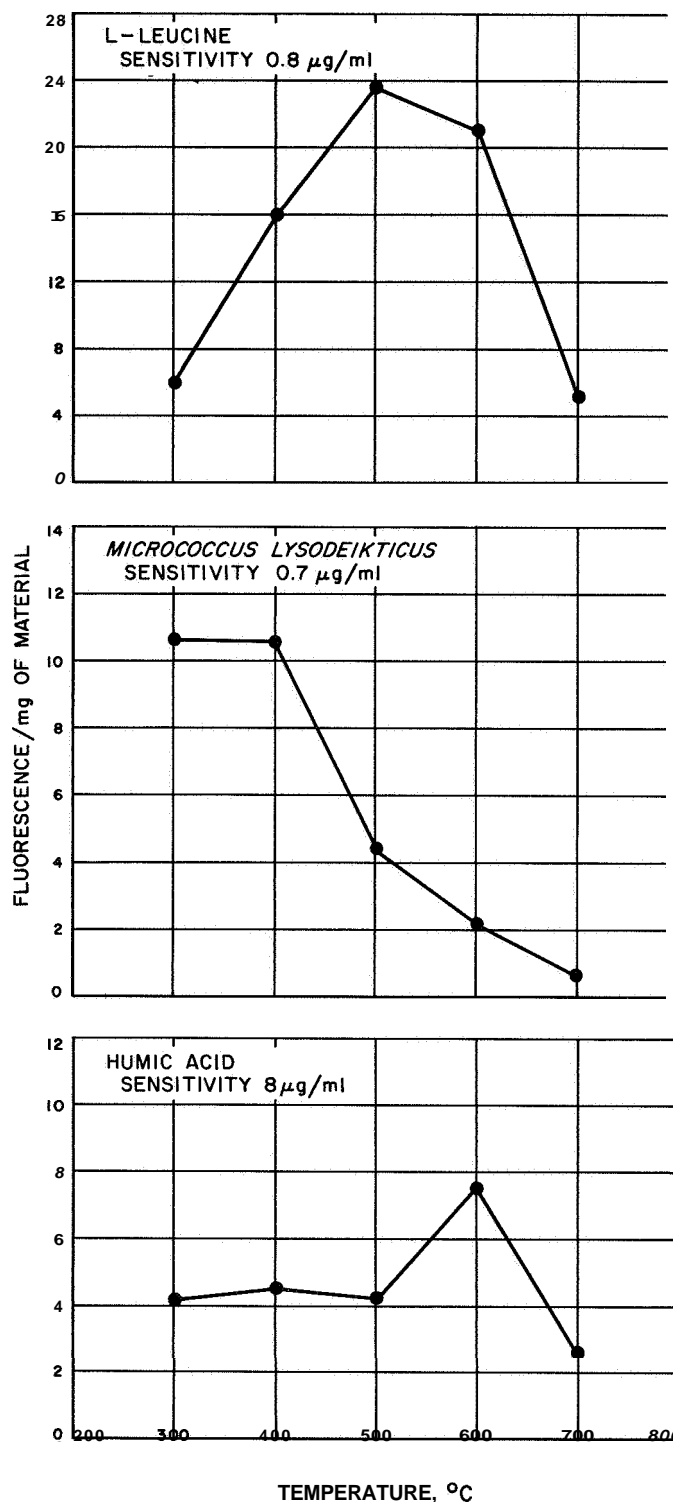


Fig. 2. Fluorescence yield of pyrolyzed substances based on the number of mg of starting material

are well within the nanogram range. It would appear that every compound or natural material, at least within certain generic groups, has its own temperature optimum.

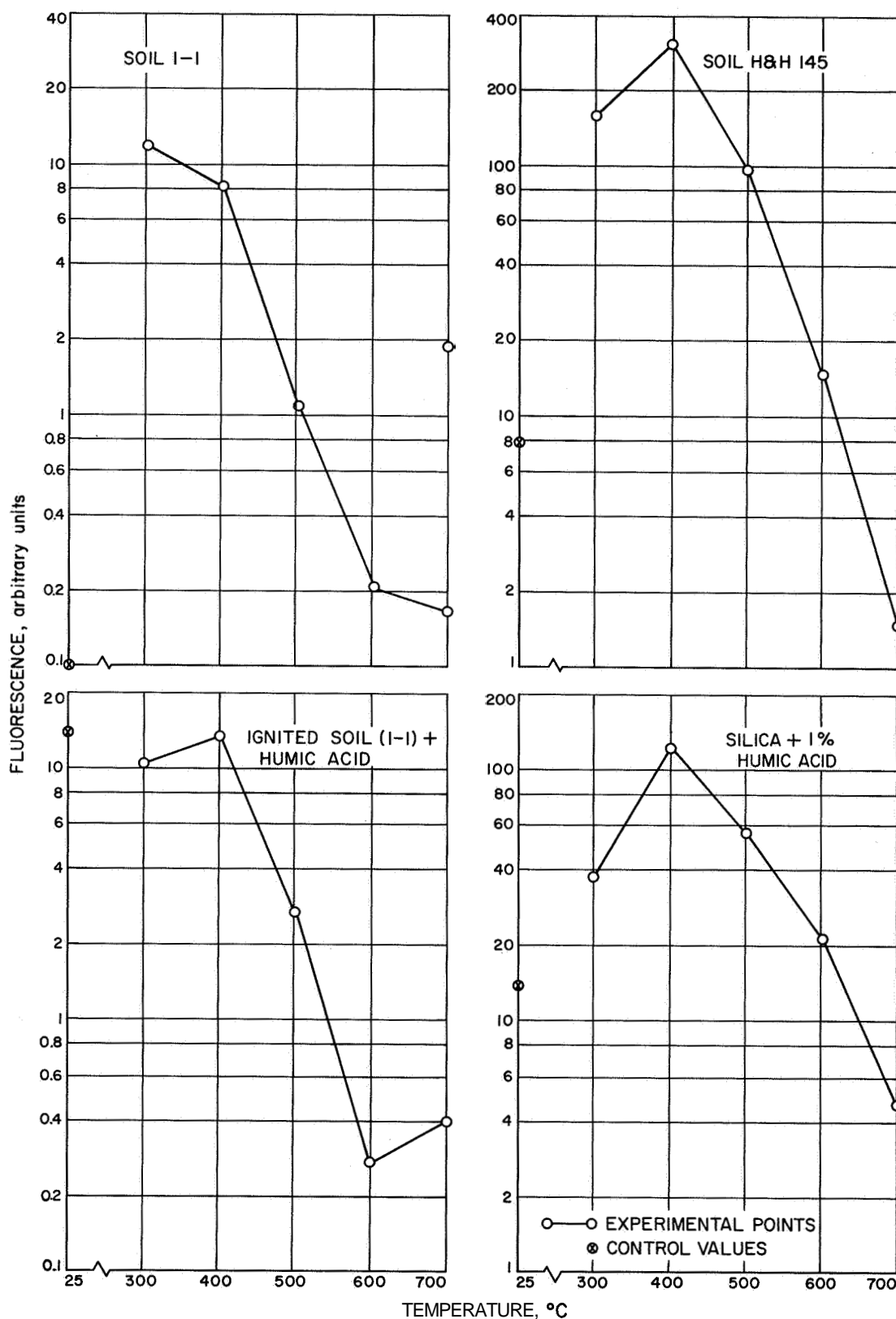


Fig. 3. Variation of fluorescence yield with temperature of pyrolysis for natural and artificial soils

Furthermore, temperatures higher than about 600°C are overly destructive. These results preclude a program of simple heating of an unknown organic sample at some arbitrary temperature in order to obtain a constant amount of fluorescence (within narrow limits) per milligram of starting material.

However, when natural or artificial soils were pyrolyzed, or when several representative materials mixed with pure silica were pyrolyzed, an important result was obtained. The temperature optima were all virtually identical except for the most inert material, paraffin. These results (shown in Figs. 3 and 4) were obtained with the filter fluorometer described earlier. The points labeled on the ordinate in Fig. 3 are fluorescence controls obtained by extracting representative amounts of the materials with solvents; these materials were not treated in any other way. Except for humic acid, these controls emphasize the fact that even if natural fluorescent organic materials are present in a sample, most of the material is likely to be nonfluorescent or poorly fluorescent. Pyrolysis is thus generally necessary to produce fluorescence and to permit detection of nano-gram quantities. In the case of humic acid, although the

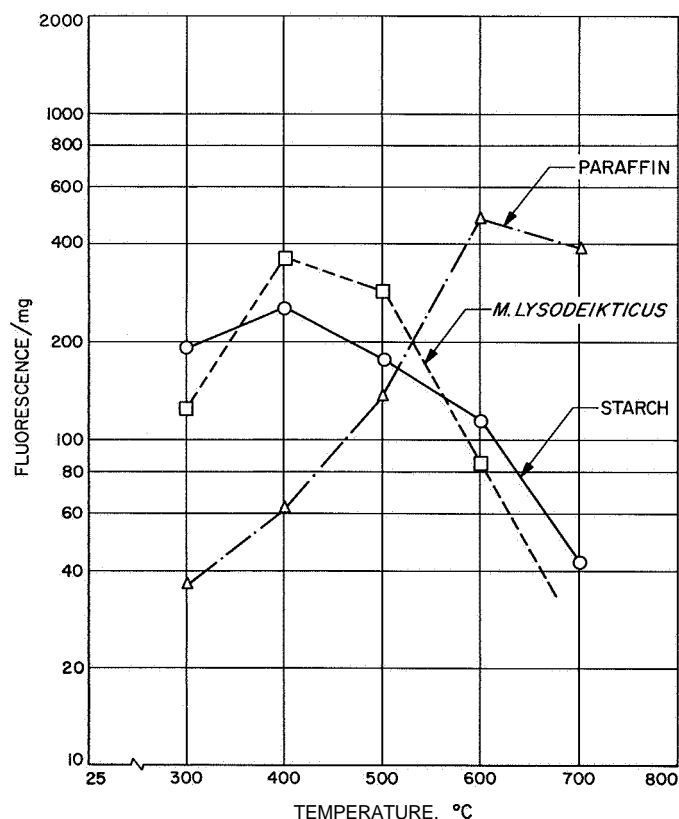


Fig. 4. Variation of fluorescence yield with temperature of pyrolysis for representative materials

control value was high, it was not reduced by pyrolysis. The soils shown vary in the quantity of organic carbon present. Soil 1-1 is a desert soil with 0.2%, while H & H 145 is a relatively rich farm soil containing about 5.2%. Other mixtures shown in Figs. 3 and 4 all contain 1% organic material in pure silica.

With this information on temperature optima, it is possible to provide a quantitative method for determining natural organic matter in an alien soil, assuming that the method of pyrolysis in a sealed tube is valid for a wide range of quantities of pure material or a wide range of concentrations of mixed organic matter in soil.

c. Variation of fluorescence with quantity of pyrolyzed material. Fig. 5 illustrates a typical example of the variation of fluorescence obtained with respect to the quantity of material pyrolyzed. With *M. lysodeikticus*, the curve is

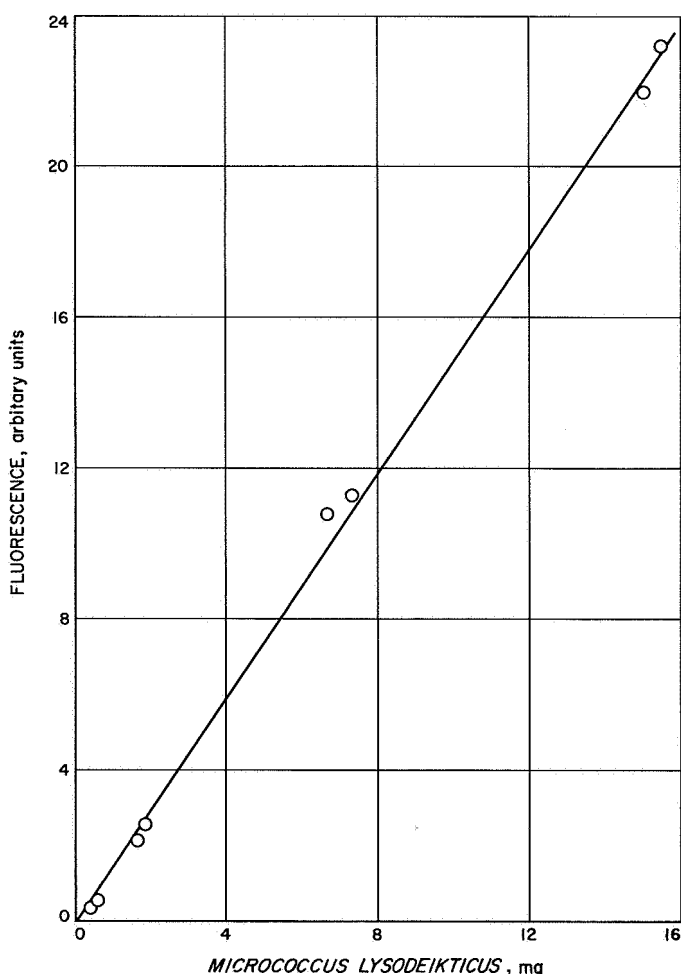


Fig. 5. Variation of fluorescence with quantity of cells pyrolyzed

linear over at least a 30-fold range; the same result has been obtained for **leucine**.⁵ Therefore, it is reasonable to assume from this and previous observations that all organic materials will provide such curves after pyrolysis. This is emphasized by the results shown in Fig. 6; here natural soils with widely varying amounts of organic matter have been pyrolyzed and show the same characteristic linearity. An artificial soil made with pure silica and humic acid is also illustrated. While the number of samples is by no means exhaustive, the results suggest that the organic content of any soil can be determined from a standard curve or family of standard curves. Further work now in progress will demonstrate the importance of the inorganic components of the soil. Preliminary results (with soil 1-1) indicate that soils with a high carbonate content relative to organic carbon may fall on a curve parallel to those shown in the figure but displaced downward. This is also supported by the previously mentioned work of Adamcik. In the event that a curve is displaced downward, an estimate of the carbonate content would be necessary before the fluorescence method could yield more than a rough indication of the quantity of organic matter. Nevertheless, this does not change the inherent linearity of the method. The curves would have the same slopes but be displaced. Oxides of aluminum and iron are important compounds that should also be investigated

Hardy, J. P., Unpublished results.

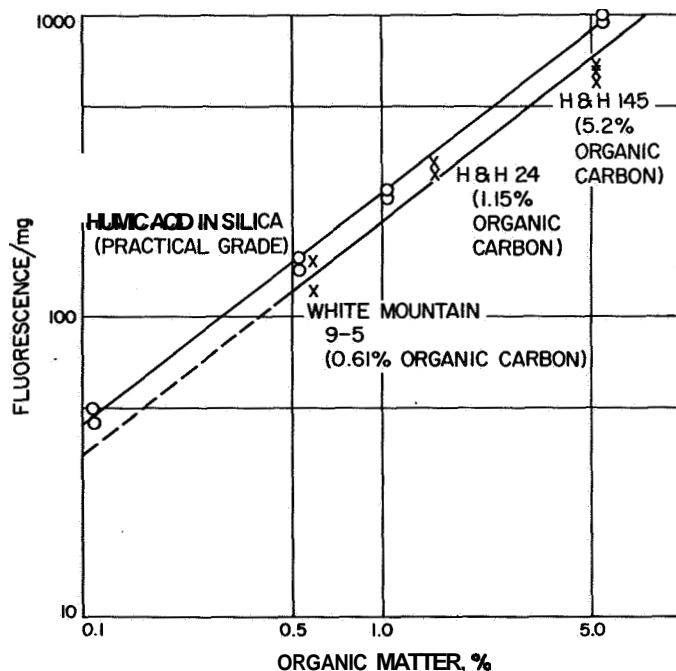


Fig. 6. Variation of fluorescence with quantity of organic matter in pyrolyzed natural soils

in this connection. The carbonates can be investigated in association with calcium and magnesium.

The data in Fig. 6 indicate that the mixture of humic acid and silica provides an excellent model system for soil pyrolysis studies. Work in progress using this system with admixtures of inorganic compounds will also indicate the importance of the variation of pyrolysis time to the production of maximal fluorescence during pyrolysis at a fixed temperature. Results accomplished thus far suggest that a simple quantitative method, which has also proved to be highly sensitive, is now available for determining soil organic matter.

B. Fluorometric Determination of Nucleic Acids, II. Assay of Purines and Purine Nucleotides of Biological Samples by Chemical Hydrolysis, J. H. Rho

1. Introduction

Numerous spectrophotometric methods have been described for the determination of nucleic acids (Ref. 11). In ultraviolet absorption spectrophotometry, spectra of nucleic acid bases are sufficiently characteristic to allow their quantitation in reasonably pure solutions; however, the absorption maxima of **all** the nucleic acid bases are in the range of 250 to 290 mμ. Therefore, this analytical method is not specific for each component in a mixture of these bases. Moreover, many other biological materials absorb at these wavelengths; thus, prior fractionation and purification of the bases are mandatory for their determination.

Differentiation of a number of purine compounds has been accomplished by (1) measuring changes in their ultraviolet absorption after reaction with specific enzymes (Ref. 12), (2) reducing adenine with zinc dust and coupling with N-(1-naphthyl)ethylenediamine (Ref. 13), or (3) formation of a color complex with bases (Ref. 14). These methods are both complicated and time-consuming.

Duggan, et al. (Ref. 15) observed significant fluorescence emission in solutions of many purines, purine nucleosides, and purine nucleotides. On the basis of this observation, a method for the measurement of guanine in nucleic acid hydrolyzates was devised by Udenfriend and Zaltzman (Ref. 16). This paper presents a further modification for the microdetermination of adenine and guanine and its application to the quantitative determination of microbial populations. Also presented is a method for quantitative microdetermination of purine ribonucleotides in ribonucleic acid hydrolyzates and in natural soil samples.

2. Materials

Chlorella pyrenoidosa and *E. coli* cells were grown as previously described (SPS 37-24, Vol. IV, p. 262; SPS 37-25, Vol. IV, p. 243). *Rhodospirillum rubrum* was obtained from R. Y. Stanier,⁶ and was grown in modified Hutner's medium. Natural soil samples were the same as described in SPS 37-41, Vol. IV, p. 170.

The adenine, guanine, 5'-adenosine monophosphate, and 5'-guanosine monophosphate were obtained from the Sigma Chemical Co., St. Louis, Missouri. The deoxyribonucleic acid (DNA, ex herring sperm) was obtained from the California Corporation for Biochemical Research, Los Angeles, California, and the ribonucleic acid (RNA) was obtained from Aldrich Chemical Company, Milwaukee, Wisconsin. Other chemicals were reagent grade.

3. Experimental Procedure

A solution of 0.05 ml containing 5 μg of purine mononucleotides, 1 to 50 μg of RNA and DNA, 10^7 to 10^8 cells of *R. rubrum*, *C. pyrenoidosa*, and *E. coli*, or 20 mg of the sandy desert soil sample was transferred to centrifuge tubes. An equivalent volume of 0.2 N NaOH solution was added to make a final concentration of 0.1 N. The samples were hydrolyzed in a boiling water bath for 20 min. After cooling, the samples were acidified with 0.1-ml volumes of 1 N HCl and diluted, with water, to exactly 0.5 ml. The precipitates were then removed by centrifugation, and a 2.5- μl aliquot of each supernatant was used for the measurement of fluorescence.

In the case of acid hydrolysis of the biological samples, 0.1-ml solutions containing 0.1 to 10 μg of adenine and guanine, 10 to 100 μg of both RNA and DNA, and 10^6 to 10^7 cells of *Chlorella* or *R. rubrum* were placed in glass-stoppered tubes, and HCl was added to a final concentration of 1 N. The samples were hydrolyzed at 100°C in boiling water for 30 min and cooled. The samples were then made up to 0.5 ml, with either 0.1 N HCl or 1 N NH_4OH , for the measurement of fluorescence in either acid medium or alkaline solution. In either case, the precipitates were carefully removed by centrifugation before reading fluorescence.

A Farrand fluorometer with a 150-w Xenon lamp and an RCA IP 28 photomultiplier detector was used throughout the study. For the determination of fluorescence of

trace amounts, a quartz cell with an inside diameter of 1 mm was used. Fluorescence intensities of acid hydrolyzates were determined at 350 $\text{m}\mu$ with a maximum excitation at 280 $\text{m}\mu$, whereas alkaline hydrolyzates were determined at 390 $\text{m}\mu$ with a maximum excitation at 280 $\text{m}\mu$.

4. Results and Discussion

a. Determination of RNA in biological samples. The hydrolysis of RNA in 0.1 N NaOH at 100°C for 20 min yielded a highly fluorescent product which emits maximally at 390 $\text{m}\mu$ in an acid medium. An equivalent amount of DNA hydrolysis product did not produce fluorescence. These results are shown in Fig. 7.

The two types of nucleic acids show different characteristic behaviors in alkali. RNA is split into mononucleotides by treatment in a weak base at a moderate temperature; in contrast, DNA is only slightly affected by this treatment. Such procedures have been used for the fractionation and estimation of the relative amounts of DNA and RNA in tissues (Refs. 17-19).

The microorganisms and the natural soil sample yielded fluorescent products similar to that of RNA hydrolyzate. These products were identified as adenosine and guanosine

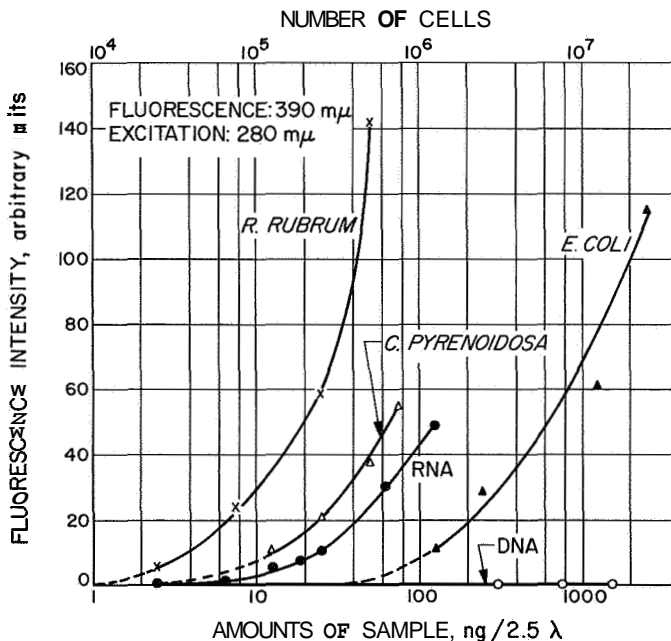


Fig. 7. Fluorescence of alkaline hydrolyzates of RNA and microorganisms

⁶University of California, Berkeley.

mononucleotides by their absorption spectra and by comparing their fluorescence properties with authentic purine mononucleotides. As shown in Fig. 7, the fluorescence intensity is in all cases proportional to either the amounts of RNA hydrolyzed or the number of organisms used. Because of the high sensitivity of the method, even less than 10 ng of RNA could be determined. It is also possible to estimate the amount of RNA per cell of each microorganism. Thus, from Fig. 7, three million cells contain roughly 64 ng of RNA. If we assume that a single cell of *E. coli* weighs approximately 10^{-13} g, three million cells will be equivalent to about 300 ng. The RNA content of the cell is then about 20%. Since the estimate of 10^{-13} g per *E. coli* cell is approximate and a cell may weigh a little more than 10^{-13} g, this estimation seems fairly close; 3.5×10^5 cells of *Chlorella* appear to contain the same amount of RNA as 1.1×10^5 cells of *R. rubrum*. This is again reasonable because of the differences in the sizes of these two types of cells.

When 20 mg of sandy desert soil were hydrolyzed under similar conditions, materials were produced that were similar to the hydrolyzates of microorganisms with respect to their fluorescence properties. Thus, the fluorometric determination of ribonucleotides produced by alkaline hydrolysis of biological samples appears to be a good method for estimating the RNA content of a given population and, hence, the number of microorganisms. This method of measuring ribonucleotides in the hydrolyzates of biological samples does not require any separation from the pyrimidine nucleotides, DNA, or any other biological compounds. It offers a sensitivity at least two orders of magnitude greater than spectrophotometry, and the additional specificity of two spectral requirements instead of one.

b. Determination of total nucleic acids by acid hydrolysis. It is characteristic of both types of nucleic acid that the purine riboside or deoxyriboside linkage is unusually labile to acid hydrolysis, while the pyrimidine riboside or deoxyriboside linkage is relatively resistant (Ref. 11).

The purine bases were liberated from both RNA and DNA and from *R. rubrum* and *C. pyrenoidosa* cells by hydrolysis with 1N HCl at 100°C for 20 min. The guanine base fluoresces strongly in alkaline solution (pH 10.5) at 350 m μ , with excitation at 280 m μ (Ref. 16). The fluorescence intensities with various amounts of biological samples are shown in Fig. 8. A proportionality between the fluorescence intensity and the amounts of guanine, RNA, and DNA can be observed. An increasing number of

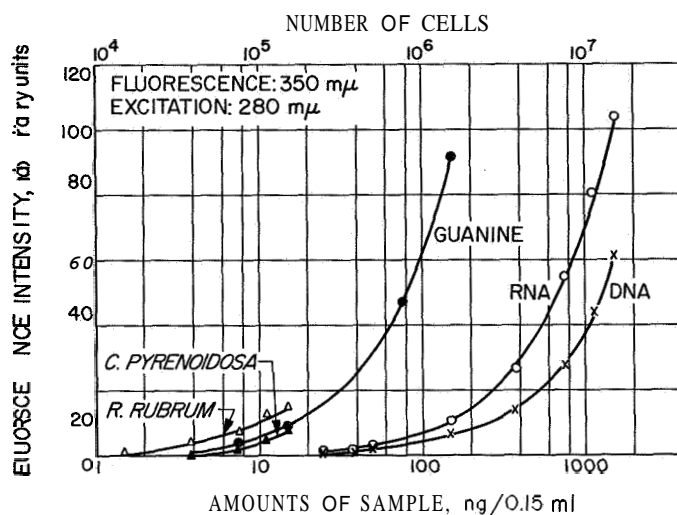


Fig. 8. Fluorescence of acid hydrolyzates of nucleic acids and microorganisms in alkaline solution

microorganisms also yielded proportional increases in the fluorescence intensity. The sensitivity of this method is high—at least two orders of magnitude higher than that of spectrophotometry. The estimation of nucleic acid content of microorganisms by spectrophotometry agrees with that of the fluorescence measurement of purine mononucleotides in alkaline hydrolyzates to within an order of magnitude.

Both adenine and guanine bases fluoresce in acid solution; the fluorescence maximum is 360 m μ and the excitation maximum 280 m μ . The fluorescence intensities from the hydrolyzates of various amounts of samples in acid solution, together with those of authentic guanine and adenine, are presented in Fig. 9. The fluorescence from a microgram of guanine in acid solution (pH 2) was found to be about one-third that of the same concentration of guanine in alkaline solution (pH 10.5). Lower fluorescence yields in the hydrolyzates of nucleic acids in acid medium compared with those in alkaline solution may be noted. Since both adenine and guanine fluoresce in acid, the sum of adenine and guanine can be determined by this method; in alkaline solution, only guanine is determined. This selectivity among purines in different media offers additional specificity in assaying one base in the presence of the other.

5. Summary

A fluorometric method to determine purine ribonucleotides in the alkaline hydrolyzates of RNA has been developed for a quantitative determination of RNA content

of microorganisms. This method does not require any prior separation of purine ribonucleotides from other constituents of the hydrolyzates. A method for the fluorescence

measurement of adenine and guanine has been further modified for microtechnique and applied to estimate the total nucleic acid content of the microorganisms.

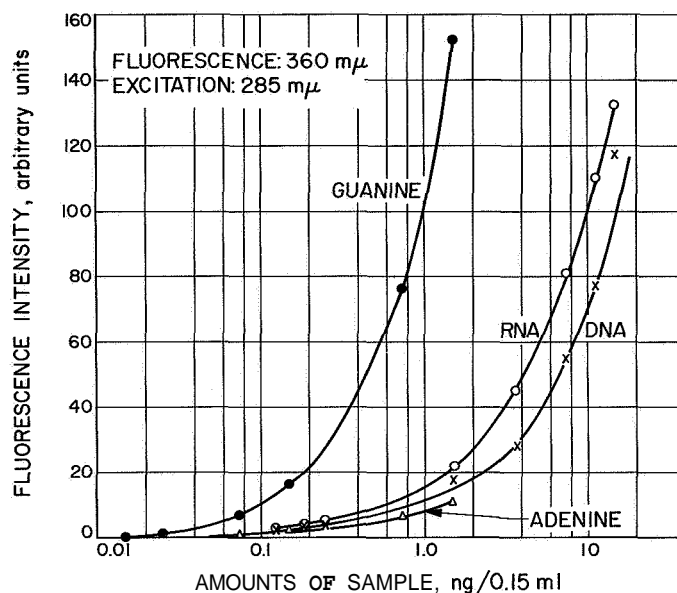


Fig. 9. Fluorescence of acid hydrolyzates of nucleic acids in acid medium

References

1. Wald, G., *Proceedings of the National Academy of Science*, Vol. 52, p. 595, 1964.
2. Horowitz, N. H., and Miller, S. L., *Fortschritte der Chemie Organischer Naturstoffe*, Vol. 20, p. 423, 1962.
3. Badger, G. M., Kimber, R. W. L., and Spotswood, T. M., *Nature*, Vol. 187, p. 663, 1960.
4. Sweeting, J. W., and Wilshire, J. F. K., *Australian Journal of Chemistry*, Vol. 15, p. 89, 1962.
5. Kennaway, E. L., *British Medical Journal*, Vol. 2, p. 1, 1925.
6. Mukai, M., Tebbens, B. D., and Thomas, J. F., *Analytical Chemistry*, Vol. 36, p. 1126, 1964.
7. Mukai, M., Thomas, J. F., and Tebbens, B. D., *Analytical Chemistry*, Vol. 37, p. 398, 1965.
8. Janak, J., *Nature*, Vol. 185, p. 684, 1960.
9. Eck, R. V., Lippincott, E. R., Dayhoff, M. D., and Pratt, Y. T., *Science*, Vol. 153, p. 628, 1966.

References (contd)

10. Schachter, M. M., and Haynie, E. O., Paper presented at **the 11th** Analytical Chemical Conference, Detroit, Mich., October **23, 1963**.
11. Loring, H. S., in *The Nucleic Acids*, Vol. I, p. **191**, Edited by E. Chargaff and J. N. Davidson, Academic Press, New York, **1955**.
12. Kalckar, H. M., *Journal of Biological Chemistry*, Vol. **167**, p. **445**, **1947**.
13. Woodhouse, P. L., *Archives of Biochemistry*, Vol. **25**, p. **347**, **1950**.
14. Davis, J. R., and Morris, R. N., *Analytical Biochemistry*, Vol. **5**, pp. **64-69**, **1963**.
15. Duggan, D. E., Bowman, R. L., Brodie, B. B., and Udenfriend, S., *Archives of Biochemistry and Biophysics*, Vol. **68**, pp. **1-14**, **1957**.
16. Udenfriend, S., and Zaltzman, P., *Analytical Biochemistry*, Vol. **3**, pp. **49-59**, **1962**.
17. Schmidt, G., and Thannhauser, S. J., *Journal of Biological Chemistry*, Vol. **161**, p. **83**, **1945**.
18. Hammarsten, E., *Acta Medica Scandinavica, Supplement*, Vol. **196**, p. **634**, **1947**.
19. Loring, H. S., Bortner, H. W., Levy, L. N., and Hammell, M. L., *Journal of Biological Chemistry*, Vol. **196**, p. **807**, **1952**.

XV. Fluid Physics

SPACE SCIENCES DIVISION

N67 18336

A. Viscous and Inviscid Amplification Rates of Two- and Three-Dimensional linear Disturbances in the laminar Compressible Boundary layer, *L. M. Mack*

In SPS 37-36, Vol. IV, pp. 221-223, the inviscid stability of the laminar boundary layer was computed for three-dimensional disturbances for free-stream Mach numbers M_1 between 4.5 and 10.0. It was found that the most unstable first-mode disturbance is a three-dimensional wave with a wave angle σ (σ is the angle between the wave normal and the free-stream direction) between 50 and 60 deg. The maximum time rate of amplification of the most unstable three-dimensional disturbance in that Mach number range is roughly twice that of the most unstable two-dimensional disturbance. In contrast, the most unstable second and higher-mode disturbances are two dimensional. These predictions were subsequently confirmed in their essential points by the experiments of Kendall at $M_1 = 4.5$ (SPS 37-39, Vol. IV, pp. 147-148).

The experimental results of Laufer-Vrebalovich (Ref. 1) at $M_1 = 2.2$, which have been available for several years, do not agree with the two-dimensional stability theory in either the location of the upper branch of the neutral-stability curve or the maximum rate of amplification.

Experimentally, the latter is about 10 times the theoretical value. The disagreement in the neutral-stability curves led Brown (Ref. 2) to abandon the parallel-flow theory and include in the basic equations all of the terms involving v , the mean vertical velocity in the boundary layer, but without any $\partial/\partial x$ terms. When these equations, in three-dimensional form, were solved for a 55-deg wave, the agreement between the theoretical and experimental neutral-stability curves of frequency was markedly improved.

In spite of this agreement, some fundamental questions still remain. First, it is not known if the eigenvalues, α (the wave number in the x direction) and c_r (the phase velocity), and the amplification rate αc_i of Brown's theory agree with the experimental results. Second, it is not known if the experimental disturbances were or were not three dimensional, or, if they were, whether the component with a 55-deg angle was dominant. The artificial disturbances were intended to be two dimensional, but this point was not checked experimentally. The agreement of the neutral-stability curves and amplification rates for natural and artificial disturbances was used by Laufer and Vrebalovich to conclude that two- and three-dimensional disturbances have the same stability characteristics. However, equally valid interpretations would be that both the natural and artificial disturbances were

either two dimensional or three dimensional. The latter possibility must be regarded as the more probable. Dunn and Lin (Ref. 3) concluded on theoretical grounds that up to about $M_1 = 1.8$, three-dimensional disturbances are no more unstable than two-dimensional disturbances for an insulated-wall boundary layer. This conclusion was based solely on an examination of the critical Reynolds number, which can be a misleading criterion, particularly for disturbances at different wave angles.

In this paper, the parallel-flow theory is used to study the stability characteristics of three-dimensional disturbances at lower Mach numbers than in SPS 37-36, Vol. IV. Since this form of theory gives satisfactory results at $M_1 = 4.5$, it must at least be thoroughly tested at $M_1 = 2.2$ before being abandoned for something more complicated. It might be mentioned that Brown's computation with the mean v equations of a neutral-stability curve at $M_1 = 5.0$ for a 55-deg wave gives an instability region with the upper-branch point at a frequency less than half that measured by Kendall at $M_1 = 4.5$ for the same wave angle.

The inviscid-theory calculations (SPS 37-36, Vol. IV) were extended from $M_1 = 4.5$ down to 1.8, with the results shown in Fig. 1, where the maximum time rate of amplification (for any wave number or any angle) is given as a function of Mach number for both two- and three-dimensional first-mode disturbances. The wave angles of the most unstable disturbances, to the nearest 5 deg, are designated on the figure. The ranges of the experimental measurements at both $M_1 = 2.2$ (Laufer-Vrebalovich) and $M_1 = 4.5$ (Kendall, corrected for boundary-layer thickness) are also shown. R is the square root of the x Reynolds number. It is seen that the ratio of three-dimensional to two-dimensional amplification rates becomes quite large at low Mach numbers. At $M_1 = 1.8$, the maximum amplification rate of the most unstable three-dimensional wave is 130 times that of the two-dimensional wave; at $M_1 = 2.2$, it is 33 times larger than for the two-dimensional wave; and at $M_1 = 3.0$, the ratio of the maximum amplification rates is reduced to 5.8.

The reason for the enhanced instability of three-dimensional disturbances at low Mach numbers is not

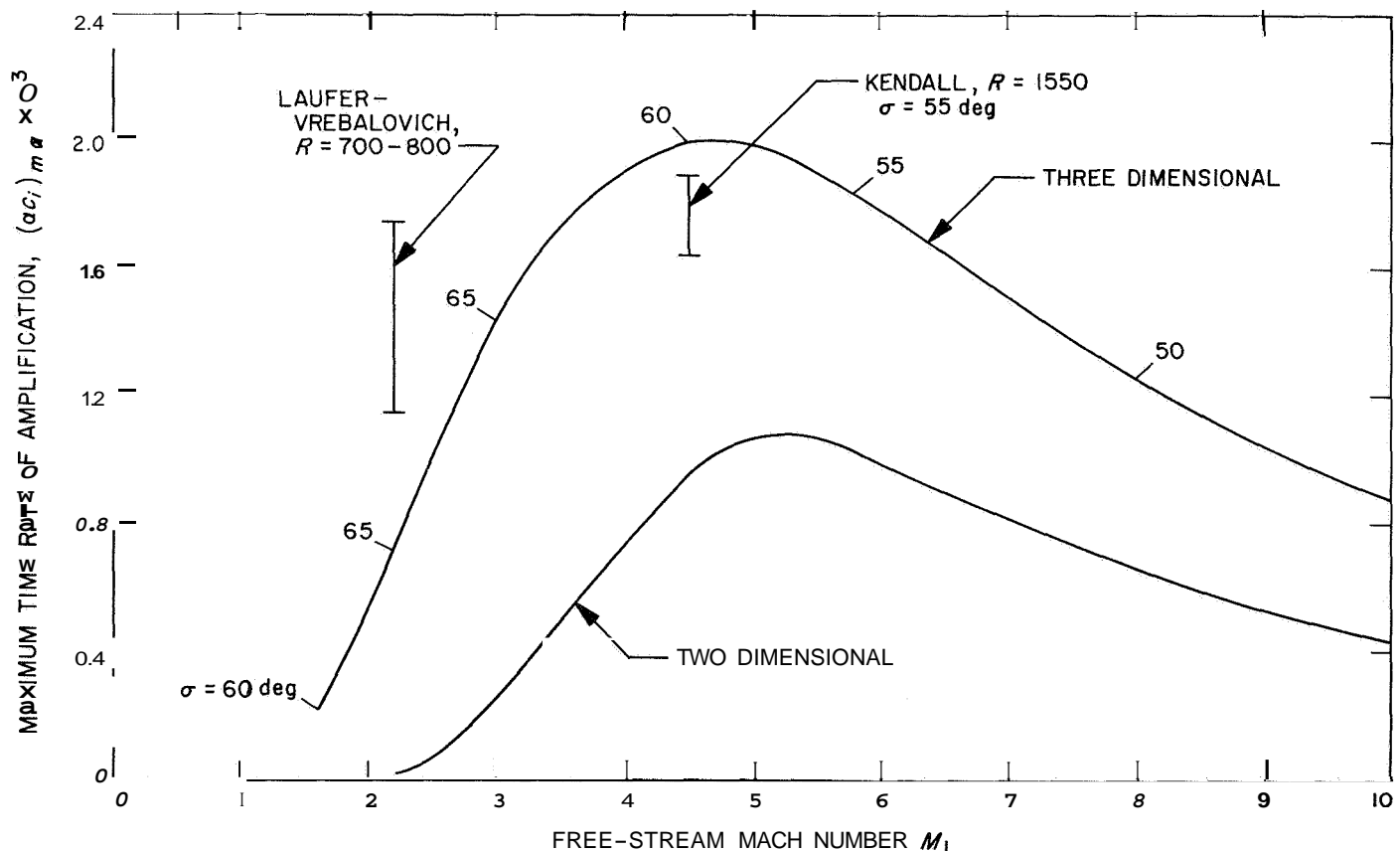


Fig. 1. Inviscid first-mode maximum amplification rates versus Mach number for two- and three-dimensional disturbances

hard to find. The phase velocity of an amplified disturbance is always larger than $c_0 = 1 - (1/M_1)$, the sonic limit, and less than c_s , which is equal to the mean velocity at η_s , the generalized inflection point, where $(u'/T)' = 0$. At the lowest Mach numbers ($M_1 < 1$), c_s is small and the boundary layer is almost stable to inviscid disturbances. Above $M_1 = 1$, c_s increases rapidly, but the instability of a two-dimensional disturbance remains small because c_0 is almost equal to c_s . It is only for $M_1 > 3$, that $c_s - c_0$ becomes sufficiently large for an appreciable two-dimensional instability to develop. For a three-dimensional disturbance, c_0 can always be reduced to zero for a sufficiently large wave angle (small Mach number normal to wave front), and c_s is independent of σ . Consequently, there is no lower bound to c_r other than zero, and the boundary layer can demonstrate what might be called its natural instability.

The inviscid maximum amplification rate at $M_1 = 2.2$ for a three-dimensional wave differs from the experimental values by only a factor of about 2. Whether this improved agreement is further improved or worsened at finite Reynolds numbers depends on the effect of viscosity at this Mach number. For a two-dimensional disturbance, the destabilizing action of viscosity, which is solely responsible for boundary-layer instability at $M_1 = 0$, decreases sharply with increasing Mach number, as shown in Fig. 2, until at $M_1 = 2.6$ the maximum amplification at low Reynolds number is only a local maximum and is equal to the inviscid amplification rate. At Mach numbers above 3, even the local maximum disappears and the action of viscosity is stabilizing over the Reynolds number range of interest; i.e., a decrease of Reynolds number leads to a decrease in the maximum amplification rate. If the action of viscosity is similar for three-dimensional

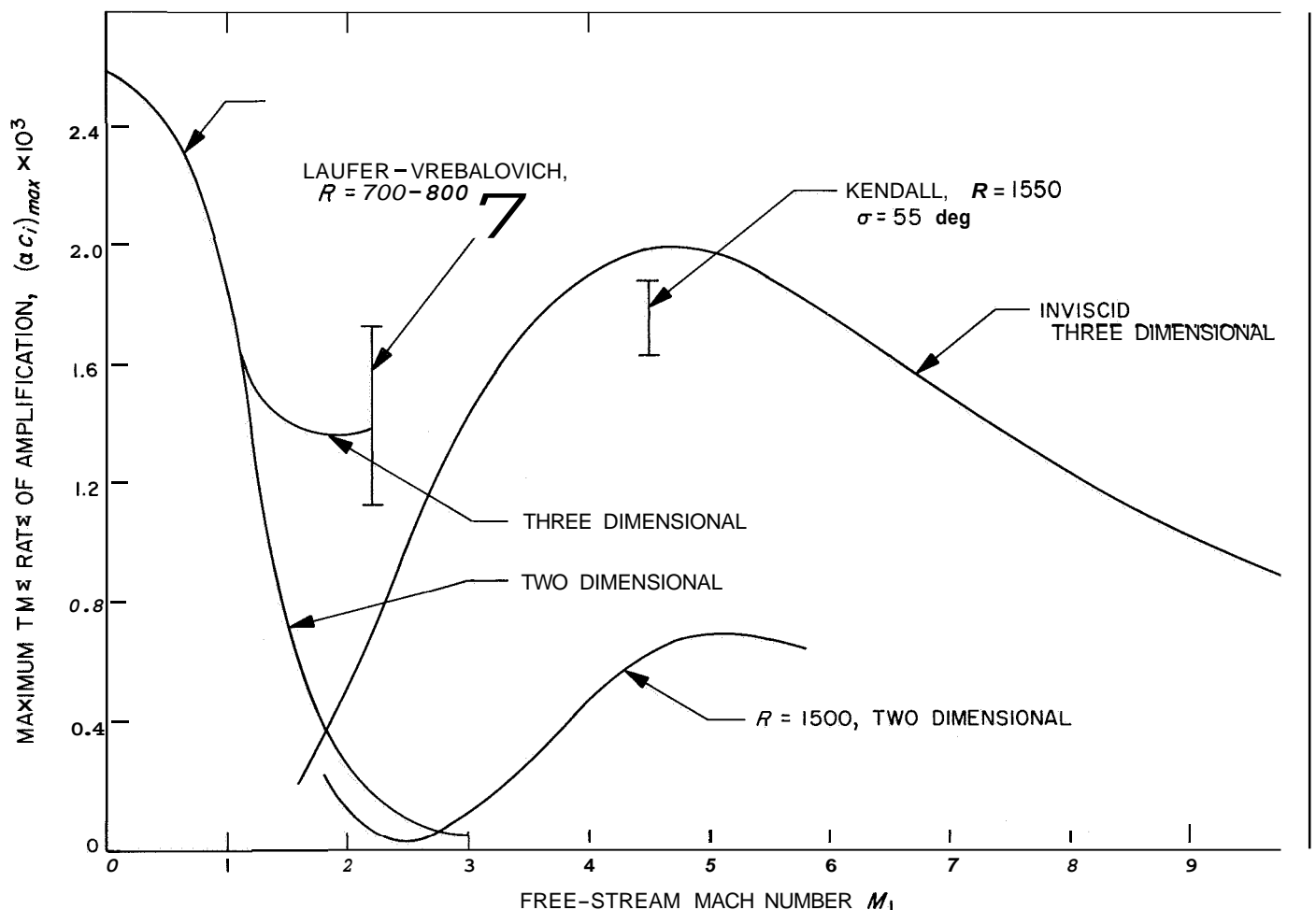


Fig. 2. Viscous first-mode maximum amplification rates versus Mach number for two- and three-dimensional disturbances

disturbances, the amplification rates at finite Reynolds numbers for Mach numbers around 2 will be larger than the inviscid rate, and for $M_1 > 3$ they will be smaller than the inviscid rate. Consequently, the possibility exists that a three-dimensional disturbance has amplification rates in agreement with experiment at both $M_1 = 2.2$ and 4.5.

It is no simple matter to compute the amplification rates of three-dimensional disturbances at finite Reynolds numbers. At $M_1 = 0$, the three-dimensional stability equations are transformed by the Squire transformation into the two-dimensional Orr–Sommerfeld equation for the same boundary-layer profile. The three-dimensional amplification rates can be obtained from the two-dimensional rates already obtained. Further, the two-dimensional disturbance has the largest amplification rate. The generalization of the Squire transformation used by Dunn and Lin, which transforms the three-dimensional inviscid equations (but not the solutions) into two-dimensional equations, does not similarly transform the complete parallel-flow viscous equations. The Dunn–Lin equations, which include only what are supposed to be the leading viscous terms, do transform, as would any set of equations that do not include the dissipation terms in the energy equation. But if all the parallel-flow viscous terms are to be kept, then it is necessary to include an additional momentum equation, as Brown did for the equations with the \mathbf{v} terms. The system of equations is increased to eighth order from the present sixth order, and the computer program must be rewritten.

Within the framework of the sixth-order system, at least three courses of action are possible: First, use the Dunn–Lin equations; second, use a set of equations which are as close as possible to the correct equations; third, use the present complete equations as if all the terms transformed. The second option is perhaps logically superior to the others, but has not yet been done. Both the first and third options have been carried out, with most of the computations performed with the complete equations. Brown has computed a neutral-stability curve at $M_1 = 2.2$ for a wave angle of 55 deg from both the two-dimensional complete equations (including mean \mathbf{v} terms) plus the Squire transformation, and from the eighth-order system. With the \mathbf{v} terms included, there is a considerable increase in the number of terms that do not transform. Even so, the largest error in the Reynolds number of a neutral-stability point at a fixed frequency is about 25%.

Fig. 2 gives the results obtained at finite Reynolds numbers together with the first-mode three-dimensional inviscid curve and experimental results repeated from Fig. 1. Both the two- and three-dimensional results obtained with the complete equations are shown. The two-dimensional disturbance is the most unstable up to about $M_1 = 1$. For higher Mach numbers, the three-dimensional disturbances ($\sigma = 45$ deg at $M_1 = 1.3$, $\sigma = 60$ deg at $M_1 = 2.2$) are the most unstable, with the action of viscosity up to at least $M_1 = 2.2$ plainly destabilizing as for two-dimensional disturbances. Further, the amplification rate at $M_1 = 2.2$ of the most unstable three-dimensional disturbance is within the range of the experimental results.

A few comparisons have been made between amplification rates computed from the Dunn–Lin equations and the complete equations. At $M_1 = 1.3$ the two-dimensional neutral-stability curves computed from the two sets of equations are close together. Table 1 shows that the amplification rates for a 50-deg wave are also in good agreement at a Reynolds number of 1600. At $M_1 = 2.2$, where there is an important difference between the two-dimensional neutral-stability curves, a large percentage difference is evident in the two-dimensional amplification rates. For the 60-deg wave, the arithmetic difference of the two amplification rates is the same as for the two-dimensional wave, but the percentage difference is small. The most important comparison, with the amplification rate computed from the eighth-order system, is not available. However, the good agreement between the results obtained from the Dunn–Lin and complete equations indicates that where the inviscid instability is important, as it is for three-dimensional waves at $M_1 = 2.2$, the leading viscous terms of Dunn’s analysis are truly dominant, and the additional viscous terms, some of which do not transform by the Squire transformation, play only a secondary role in establishing the amplification rate.

Table 1. Comparison of amplification rates computed from the two-dimensional Dunn–Lin and complete viscous equations

M_1	σ , deg	α	R	Dunn–Lin Eqs. $\alpha c_i \times 10^3$	Complete Eqs. $\alpha c_i \times 10^3$
1.3	50	0.060	1600	1.50	1.46
2.2	0	0.045	600	0.30	0.18
	60	0.040	1200	1.49	1.39

References

1. Laufer, J., and Vrebalovich, T., "Stability and Transition of a Supersonic Laminar Boundary Layer on an Insulated Flat Plate," *Journal of Fluid Mechanics*, Vol. 9, Part 2, pp. 257-299, 1960.
2. Brown, W. B., "Stability of Compressible Boundary Layers, Including the Effects of Two-Dimensional Mean Flows and Three-Dimensional Disturbances," *Bulletin of the American Physical Society*, Series II, Vol. 10, No. 6, p. 682, 1965.
3. Dunn, D. W., and Lin, C. C., "On the Stability of the Laminar Boundary Layer in a Compressible Fluid," *Journal of the Aeronautical Sciences*, Vol. 22, pp. 455-477, 1955.

XVI. Physics

SPACE SCIENCES DIVISION

N67 18337

A. Convection and Magnetospheric Turbulence, G. Atkinson

1. Introduction

The convection of flux tubes within the magnetosphere has been discussed by Gold (Ref. 1). Viscous forces are small in such a rarefied plasma, so that convective flow can occur quite freely except for the discharging action of the ionosphere on the flux tubes. Gold used a model in which there was a sharp transition from frozen field conditions to zero conductivity. In the real case, there should be a drag on the moving field lines due to the Pedersen conductivity of the ionosphere (see Fig. 1). This dissipative effect was discussed by Axford and Hines (Ref. 2), Cole (Ref. 3), and Bostrom (Ref. 4). Steady-state convection requires that the electric field be maintained. Therefore, there must be a charge separation current produced in the convecting region to offset the discharging action of the ionosphere. Thus, the plasma convection v requires the electric field $\mathbf{E} = -v \times \mathbf{B}$. This causes a discharge current \mathbf{J}_i in the ionosphere which must be balanced by a charge-separation current \mathbf{j} in the magnetosphere.

2. Turbulence

Consider the possibility of the onset of turbulence driven by the convecting shear flow. This should be a convective type of turbulence, involving the small-scale interchange of flux tubes, and as such would be essentially two dimensional. A two-dimensional model is adopted with magnetic field lines in the z direction with

their feet in plane ionospheres at $z = 0$ and $z = L$. Motion is thus confined to the x and y directions. In an actual flow, the field lines would adopt a parabola-like

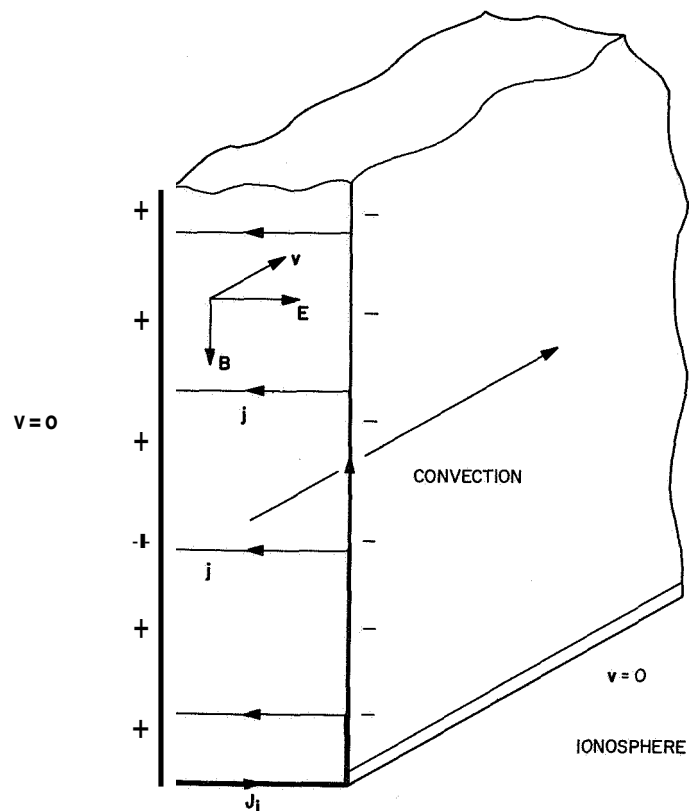


Fig. 1. Cross section of a convecting plasma slab

shape. However, a consideration of the currents indicates that the field lines stay within a few degrees of the z-axis up to foot velocities $\sim 10^4$ m/sec (see the final paragraph of Section 2).

If, in the model, E is assumed to be horizontal and vertically uniform, and B is assumed to be vertical in the ionosphere, then the height-integrated discharge current (in the ionosphere) is $J_i = \sigma_i E$, where σ_i is the height-integrated Pedersen conductivity. Each flux tube feels a dragging force $\iiint (j \times B) dl dA = \iiint j B dA dl$. For a flux tube, $\iiint B dA$ is constant and $E = -v \times B$. Thus, the force on a flux tube at the ionosphere is

$$AB \int j dl = 2BJ_i A = 2\sigma_i v B^2 A \text{ newtons} \quad (1)$$

The factor of 2 is inserted because each flux tube has two feet. Thus the Navier-Stokes equation for the flow, assumed inviscid incompressible, can be integrated along a flux tube of unit area, and takes the following form:

$$\frac{\partial v_i}{\partial t} + v_j \frac{\partial v_i}{\partial x_j} + \frac{1}{\rho} \frac{\partial p}{\partial x_i} = - \frac{2\sigma_i B^2}{L\rho} v_i \quad (2)$$

Because of the convergence of geomagnetic field lines, it is not obvious that the last term in Eq. (2) is a good approximation to the geophysical case. Consider the dissipation in the real case. In a flux tube, $BA = \text{constant}$. Thus, if for high latitude field lines a mapping factor along flux tubes is defined by $g^2 B = B_f$ (the subscript f denotes the value at the feet of flux tubes), then:

$$\begin{aligned} A &= g^2 A_f \\ d &= g d_f \\ v &= g v_f \end{aligned} \quad (3)$$

The dissipation is then

$$\int J \cdot E dV = 2\sigma_i B_f^2 A_f v_{fi} v_{fi}$$

or, using the mapping factors in Eq. (3), for a flux tube with an equatorial cross section of 1 m^2 , the dissipation is

$$\int J \cdot E dV = 2\sigma_i B^2 v_i v_i$$

Hence, there are no mapping factors to be introduced into Eq. (2). The onset of turbulence is determined by the ratio of the second term on the left-hand side of

Eq. (2) and the dissipative term. Thus, a nondimensional number

$$\frac{U\rho L}{2d\sigma_i B^2} \quad (4)$$

replaces the Reynolds number in describing the onset of the turbulence. For the outer magnetosphere (beyond the knee),

$$\begin{aligned} n &\sim 10^6 \text{ m}^{-3} \text{ (Carpenter, Ref. 6)} \\ L &\sim 10^8 \text{ m} \\ B &\sim 10^{-7} \text{ weber m}^{-2} \\ \sigma_i &\sim 10 \text{ mho (Maeda and Matsumoto, Ref. 5)} \end{aligned} \quad (5)$$

and Eq. (4) becomes $U/2d$. This ratio indicates that turbulence resulting from shear flows is unlikely in the magnetosphere, except perhaps in a thin layer at the magnetosphere boundary, as velocity gradients are usually small.

Now consider the possibility of turbulence of the above type being convected into the interior of the magnetosphere from the boundary. Eq. (2) can be treated by the usual turbulence techniques, using ensemble averages and fluctuations from these averages. The resulting equation for the turbulent energy is of the form

$$\frac{\partial \rho v_i v_i}{\partial t} + \dots = - \frac{4\sigma_i B^2}{L\rho} \rho v_i v_i \quad (6)$$

Thus the turbulent energy would be expected to decay with a $1/e$ time of

$$\frac{L\rho}{4\sigma_i B^2}$$

For the values given earlier, this is ~ 0.1 sec.

It was suggested by Axford and Hines (Ref. 2) that turbulence might be convected in from the boundary, with the energy increase due to compression being greater than the energy dissipation. If the turbulence is of the type discussed, it can be shown that the compression rate is insufficient to overcome the dissipation.

Batchelor (Ref. 7) indicated that in the absence of dissipation, the turbulence would be expected to undergo

an adiabatic-like compression; i.e., $pV^\gamma = \text{constant}$, where $p = \rho \bar{v}_i \bar{v}_i$, from which

$$\frac{dp}{dt} = \frac{p\gamma}{V} \frac{dV}{dt} \quad (7)$$

As the field undergoes the same two-dimensional compression, $BV = \text{constant}$ and Eq. (7) becomes

$$\frac{dp}{dt} = p \frac{\gamma}{B} \frac{dB}{dt} = p \frac{\gamma}{B} \frac{dB}{dx} U \quad (8)$$

In the outerregions of the magnetosphere, $U \lesssim 10^5 \text{ m sec}^{-1}$ and $(1/B)/(dB/dx) \sim 10^{-7}$. Thus, a comparison of Eqs. (8) and (6) indicates that energy increase due to compression is three orders of magnitude less than the dissipation.

The assumption that the field is x-aligned for the two-dimensional model can be justified as follows: The greatest deviation is at the feet. At the top of the ionosphere, the Maxwell stress must be equal to the dragging force. The x axis is selected in the flow direction:

$$\frac{B_x B_z}{\mu_0} = \sigma_1 v_f B_z^2$$

$$B_x = \mu_0 \sigma_1 v_f B_z$$

$\sigma_1 \sim 10$ (Maeda and Matsumoto, Ref. 5). Therefore, $B_x \sim 10^{-5} v_f B_z$, and the field lines stay approximately vertical for $v_f < 10^4 \text{ m/sec}$. Thus the approximation of z-aligned field is reasonable.

3. Conclusion

On the basis of the preceding analysis, it seems likely that turbulent-convective motions cannot be driven by shear flows and cannot convect within the magnetosphere, but must, in fact, be the result of a local energy source other than shear flow, such as differences in the properties of the plasma in the flux tubes (Ref. 1) or any externally applied electric field (e.g., ionospheric fields mapped along field lines).

B. Evaluation of Coulomb Integrals of Continuum Functions, M. M. Saffren

Recently it has appeared feasible to calculate the correlation energy of simple atoms by means of perturbation theory rather than configuration interaction (Ref. 8). The basis set used in the perturbation theory consists of

determinants made up of Hartree-Fock orbitals. Because all these orbitals except the n -occupied orbitals are in the continuum, matrix elements of the perturbing energy yield integrals that involve continuum wave functions. The essential matrix element to be computed is that of the interelectronic Coulomb energy. This can be evaluated if we can compute

$$\left(U_{l_1}(r_1) Y_{l_1 m_1}(\theta_1, \phi_1) U_{l_2}(r_1) Y_{l_2 m_2}(\theta_1, \phi_1) \left| \frac{1}{r_{12}} \right| U_{l_3}(r_2) Y_{l_3 m_3}(\theta_2, \phi_2) U_{l_4}(r_2) Y_{l_4 m_4}(\theta_2, \phi_2) \right) \quad (1)$$

In the past, because it was not clear that such integrals converge for continuum wave functions, these integrals have been evaluated by treating the continuum wave functions $U_l(r)$ by the method of "box normalization" (Ref. 8). For free electrons this would be equivalent to replacing the radial part of the free electron continuum wave functions, $j_l(kr)(k \neq 0)$, by the discrete set $j_l[k_n(r/R)]/N_l(R)$ normalized to the "box" of radius R . The box wave functions vanish at $r = R$ [$j_l(k_n R) = 0$; $n = 1, 2, 3, \dots, \infty$] and are appropriate to the problem of the atom at the center of an empty box of radius R having impenetrable walls. We show, however, that this integral is convergent, even in terms of the continuum wave functions themselves. With this assurance, one can go on to evaluate such integrals numerically.

In Eq. (1), the integral over angles can be evaluated in terms of Clebsch-Gordan coefficients. We are then left with an integral of the form

$$\left(1 + \mathcal{J}_{1,3} \mathcal{J}_{2,4} \right) \int_0^\infty \frac{1}{r^{l+1}} P_{l_1}(k_1, r_1) P_{l_2}(k_2, r_2) dr_1 \times \left[\int_0^{r_1} dr_2 r_2^l P_{l_3}(k_3, r_2) P_{l_4}(k_4, r_2) \right] \quad (2)$$

where \mathcal{J}_{mn} interchanges the subscripts m and n ; and $P_l(k, r) = r U_l(k, r)$, and $l_1 + l_2, l_3 + l_4 \leq l$. We now note that the asymptotic form of U_l allows us to write

$$P_l(k, r) = \sin[kr + \delta_l(k)] + \int_{-\infty}^\infty dk' p_l(k, k') e^{ik' r} \quad (3)$$

so that $p_l(k, k')$ is the Fourier transform of $P_l(k, r) - \sin[kr + \delta_l(k)]$, and $\delta_l(k)$ is the phase shift. Now, $\sin[kr + \delta_l(k)] = A e^{ikr} + A^* e^{ik^* r}$ where $A = e^{i\delta(k)}/2i$. Thus, the integral can be written as

$$(1 + \mathcal{J}_{1,3} \mathcal{J}_{2,4}) \int_{-\infty}^\infty \prod_{i=1}^4 dk_i \tilde{p}_{l_i}(k_i, k_i') I_l(k_i, \dots, k_i') \quad (4)$$

where

$$p_{l_i} = \tilde{p}_{l_i} + AS(k'_1 - k_1) + A^*S(k'_1 + k_1) \quad (5)$$

and

$$I_l = \int_0^\infty \frac{dr_1}{r_1^{l+1}} e^{ik_1' r_1} e^{ik_2' r_1} \int_0^{r_1} dr_2 r_2^l e^{ik_3' r_2} e^{ik_4' r_2} \quad (6)$$

We evaluate this integral as an Abelian limit; namely,

$$I_l = \lim_{s \rightarrow 0} \lim_{\rho \rightarrow 0} I_l(p, \beta; s, \alpha) \\ = \int_0^\infty dr e^{-(p+i\beta)r} \frac{1}{r^{l+1}} \int_0^r d\rho \rho^l e^{-(sp+i\alpha)\rho} \quad (7)$$

and we have written $-\beta = k'_1 + k'_2$, $-\alpha = k'_3 + k'_4$. If we now write $a = sp + i\alpha$, we can, after some simple steps, write the integral as

$$\frac{1}{a} \frac{1}{\left(\frac{a}{p}\right)^l} \int_0^\infty dR e^{-R} e^{-i\beta R/p} \frac{1}{R^{l+1}} \int_0^{aR/p} \rho^l e^{-\rho} d\rho \quad (8)$$

If we expand the exponential in the second integral, we can write the second integral as

$$\sum_{n=0}^\infty (-1)^n \left(\frac{a}{p}\right)^{n+l+1} \frac{R^n}{n!(n+l+1)} \quad (9)$$

An elementary integration now shows us that

$$\int_0^\infty dR e^{-R} e^{-i\beta R/p} R^n = \frac{n!}{\left(1 + \frac{i\beta}{p}\right)^{n+1}} \quad (10)$$

so that

$$I_l(p, \beta; s, \alpha) = \sum_{n=0}^\infty (-1)^n \frac{(a/p)^{n+l+1}}{(n+l+1) \left(1 + \frac{i\beta}{p}\right)^{n+1}} \quad (11)$$

If we replace $(a/p)/[1 + (i\beta/p)]$ with x the series is

$$\sum_{n=0}^\infty (-1)^n \frac{x^{n+l+1}}{n+l+1} = \frac{1}{p+i\beta} \frac{1}{x^{l+1}} \sum_{n=0}^\infty (-1)^n \frac{x^{n+l+1}}{n+l+1} \quad (12)$$

This series can be summed as

$$\frac{1}{p+i\beta} \frac{1}{x^{l+1}} \int_0^x \frac{\xi^l}{1+\xi} d\xi \quad (13)$$

With $\xi = xy$, we can write

$$I_l(p, \beta; sp, \alpha) = \int_0^1 \frac{y^l dy}{b+ay}, \quad b = p + i\beta \quad (14)$$

This integral we evaluate by parts

$$\int_0^1 \frac{y^l dy}{b+ay} = \int_0^1 \frac{dz}{b+az} - l \int_0^1 y^{l-1} \int_0^y \frac{dz}{b+az} \quad (15)$$

To complete the evaluation, we need only evaluate

$$\int_0^y \frac{dz}{b+az} \quad (16)$$

as

$$\frac{1}{a} \left[\ln(b+ay) - \ln(b) \right] \quad (17)$$

Now

$$\ln(x + iy) = \ln(|x + iy| e^{i \tan^{-1} y/x}) \\ = \ln|x + iy| + i \tan^{-1} y/x \quad (18)$$

Thus, the integral (Eq. 8) can be written

$$\frac{1}{sp + i\alpha} \left[\ln \frac{(p + psy)^2 + (\beta + \alpha y)^2}{p^2 + \beta^2} \right. \\ \left. + i \tan^{-1} \frac{\beta + \alpha y}{p(1 + sy)} - i \tan^{-1} \frac{\beta}{p} \right] \quad (19)$$

The term multiplying the brackets is $\delta(a) + iP(1/\alpha)$, where δ is the delta function and P denotes principal part. However, because the expression in the brackets vanishes as $\alpha \rightarrow 0$, the δ -function contribution disappears, and the principal part becomes merely $1/\alpha$. Thus, allowing $s \rightarrow 0$, we have

$$\frac{1}{i\alpha} \left[\ln \frac{p^2 + (\beta + \alpha y)^2}{p^2 + \beta^2} + i \tan^{-1} \frac{\beta + \alpha y}{p} - i \tan^{-1} \frac{\beta}{p} \right] \quad (20)$$

If we now allow $p \rightarrow 0$, we obtain

$$J = \frac{1}{i\alpha} \left[\ln \left| \frac{\beta + \alpha y}{\beta} \right| + \frac{i\pi}{2} S(\beta + \alpha y) - \frac{i\pi}{2} S(\beta) \right] \quad (21)$$

where $S(x)$ denotes the step function

$$S(x) = \begin{cases} 1, & x > 0 \\ 0, & x = 0 \\ -1, & x < 0 \end{cases} \quad (22)$$

For well-behaved functions $f(\alpha, \beta)$, integrals of the form

$$\int d\alpha d\beta J(\alpha, \beta) f(\alpha, \beta) \quad (23)$$

should converge. To show this, we write the integral as

$$\frac{1}{i} \int \frac{d\alpha}{\alpha} \int d\beta \ln \left| \frac{\beta + \alpha y}{\beta} \right| f(\alpha, \beta) + \frac{\pi}{2} \int \frac{d\alpha}{\alpha} \int_{-\alpha y}^0 d\beta f(\alpha, \beta) \quad (24)$$

Thus, if

$$f(\alpha, \beta) \xrightarrow{\beta \rightarrow 0} \beta^k$$

where $k > 0$, and

$$f(\alpha, \beta) \xrightarrow{\beta \rightarrow -\alpha y} (\beta + \alpha y)^u, u > 0$$

then the logarithmic singularities do not prevent the first integral from converging. For $\alpha \rightarrow 0$, both integrands are well behaved. Since the singularities that are encountered in

$$\int \int d\alpha d\beta f(\alpha, \beta) \int_0^1 dy y^{l-1} J(\alpha, \beta, y) \quad (25)$$

are even milder, we need not consider the convergence of this integral if Eq. (23) converges. Thus, we have shown that

$$I_l(k'_1, k'_2, k'_3, k'_4) = J(\alpha, \beta, 1) - l \int_0^1 y^{l-1} J(\alpha, \beta, y) dy \quad (26)$$

leads to convergent integrals when substituted in Eq. (4), so that the integral (Eq. 2) can, with confidence, be evaluated numerically. A practical method for the numerical integration will be discussed in SPS 37-43, Vol. IV.

C. A Data Reduction Technique for Distribution

Analysis, A. B. Whitehead, R. H. Parker, and E. L. Haines

Repeated measurements of a physical quantity may be collected in the form of a histogram for subsequent analysis; normally, to include the great number of measurements required for high accuracy, the histogram must be

accumulated in a comparatively large memory. Since memory capacity is limited in many applications, an alternative approach is described here in which the measurements are raised to various powers that are accumulated in a few summing registers—the number of registers required being no greater than the number of independent quantities sought from the experiment. From the summed powers of the measurements, the moments of the analysis of the equivalent histogram may be determined, or the function that describes the statistically meaningful part of this distribution may be generated.

This technique may be useful in (1) spacecraft experiments and (2) multiparameter data analyses.

- (1) The statistically significant part of experimental data from a distant spacecraft must be described concisely for low bit-rate transmission, and the spacecraft has a limited memory capacity for storing distributions. The method of summing the powers of each measurement and transmitting the contents of the summing registers on command is advantageous from both points of view.
- (2) When multiparameter data are sorted in a computer as part of a data analysis routine, memory space often precludes the collection of a full distribution for each combination of values that the other variables may take. The method of summing the powers of each measurement requires that only a few computer words be reserved for each value of the other variables.

A more complete report of this technique, which was developed by the JPL Nuclear Physics Research Group for use in the computer analysis of multiparameter data, will appear in the literature shortly (Ref. 9).

In general, any distribution that can be reasonably described by a few terms of an expansion of orthogonal polynomials may be analyzed in this manner. If we denote the distribution by $f(a)$ and the terms of the orthogonal polynomial series by $P_r(a)$, then

$$f(a) = \sum_r C_r P_r(a) \quad (1)$$

Evaluation of the constants C_r in this expression is straightforward, using the orthogonality properties of the polynomials. If the normalizing coefficients are designated by N_r , then the constants are

$$C_r = \frac{1}{N_r} \sum P_r(a) \quad (2)$$

where the sum is over all of the measurements. Thus, the procedure is to evaluate each term of the polynomial expansion for each measurement and to accumulate these terms as separate sums. For most applications, this would be a rather lengthy process. Therefore, we have concentrated our development on types of analyses in which the constants may be determined from the sums of powers of a .

The data collection procedure is now fairly evident. Each measurement a_i is first digitized, and then converted to a more convenient variable x_i according to the relation

$$x_i = \frac{a_i - a_0}{s} \quad (3)$$

This ensures that the numbers raised to high powers will not overflow or lead to truncation errors. For a single

peaked distribution, a , would be chosen close to the expected mean and s would be chosen to approximate the standard deviation. In the case of analyses where the polynomials are orthogonal over a definite interval, the range of the new variable x would be chosen to coincide with the interval. A set of n sums is accumulated which have the form

$$S_j = \sum_i (x_i)^j \quad (4)$$

where \sum is over all of the measurements. At the end of the data collection period, these sums are retrieved for analysis.

The second step in the technique—extracting the most meaningful information from these sums—presents more problems. If we assume a distorted Gaussian distribution, then the unknowns in the Gauss-Hermite quadrature function

$$f(x) = \frac{C_0}{\sigma(2\pi)^{1/2}} \exp[-(x - \bar{x})^2/2\sigma^2] \left[1 + \sum_{i=3}^n \frac{C_i}{i!} H_i\left(\frac{x - \bar{x}}{\sigma}\right) \right] \quad (5)$$

must be determined. Subject to certain conditions which will be described, the unknowns are determined from the sums in the following manner:

Area or number of measurements	$C_0 = S_0$	}	(6)
Mean	$C_1 = \bar{x} = \frac{S_1}{S_0}$		
Variance	$C_2 = \sigma^2 = \frac{S_2}{S_0} - \bar{x}^2$		
Coefficient of skewness	$C_3 = \frac{1}{\sigma^3} \left(\frac{S_3}{S_0} - 3\bar{x} \frac{S_2}{S_0} + 2\bar{x}^3 \right)$		
Coefficient of kurtosis	$C_4 = \frac{1}{\sigma^4} \left(\frac{S_4}{S_0} - 4\bar{x} \frac{S_3}{S_0} + 6\bar{x}^2 \frac{S_2}{S_0} - 3\bar{x}^4 \right) - 3$		

Further terms may be readily derived.

In the derivation of Eq. (6), it must be assumed that the interval over which the data are collected is sufficiently wide that negligible data fall outside. If this is not the case, errors will be introduced in the sums and in the coefficients of Eq. (5). A second weakness in the method as described is the fact that many distributions cannot be described accurately by a few terms of the function

in Eq. (5). For example, a Gaussian distribution with a background added might require a very large number of terms for an adequate description. The measured mean using this method would differ from the mean of the Gaussian because of the background effect.

Two approaches are suggested to minimize these problems. The first is to choose a different functional form for the distribution. A function which is orthogonal over a

definite interval, such as the cosine expansion,¹ can give nonzero values at the boundaries. However, the coefficients may not bear a simple relationship to the mean, variance, etc., of a distribution. Furthermore, most physical distributions can be described by fewer terms using a Gauss-Hermite expansion.

The second approach to correcting the analysis for the effects of background and the finite boundary is to adjust the parameters of the initially computed function until the function multiplied by the appropriate power of the variable and integrated over the known definite interval equals the corresponding measured sum.

$$\left. \begin{aligned} S_0 - \int_{x_1}^{x_2} f(x; C_0, \bar{x}, \sigma, C_3, C_4, \dots, C_n) dx &= 0 \\ \vdots \\ S_n - \int_{x_1}^{x_2} x^n f(x; C_0, \bar{x}, \sigma, C_3, \dots, C_n) dx &= 0 \end{aligned} \right\} \quad (7)$$

¹Discussed in a more complete account of this work (Ref. 9).

This forms a set of simultaneous integral equations which can be solved numerically with a computer. This method promises the added advantage that the functional form used in Eq. (7) need no longer be the set of orthogonal polynomials. A Gaussian distribution with an additive background could be used provided the total number of unknowns did not exceed the number of equations. To achieve a convergent solution quickly, initial values for the unknowns would be determined from Eq. (6).

Fig. 2 illustrates the technique for a set of real data. The measurements were accumulated into a frequency distribution as shown by the points on the left-hand graph. The measurements were also accumulated as the sums of powers, S_0, \dots, S_4 , and used to compute the function in Eq. (5). This is shown as a solid curve in this graph. Except for small systematic deviations at the edges, the agreement between the points and the curve is quite good. Since distribution is formed from experimental data, there is a small background contribution present and the boundaries chosen were slightly narrow. On the right-hand graph is plotted χ^2/ν , a function which measures the degree to which the statistically significant information has been described. It will approach a limiting value

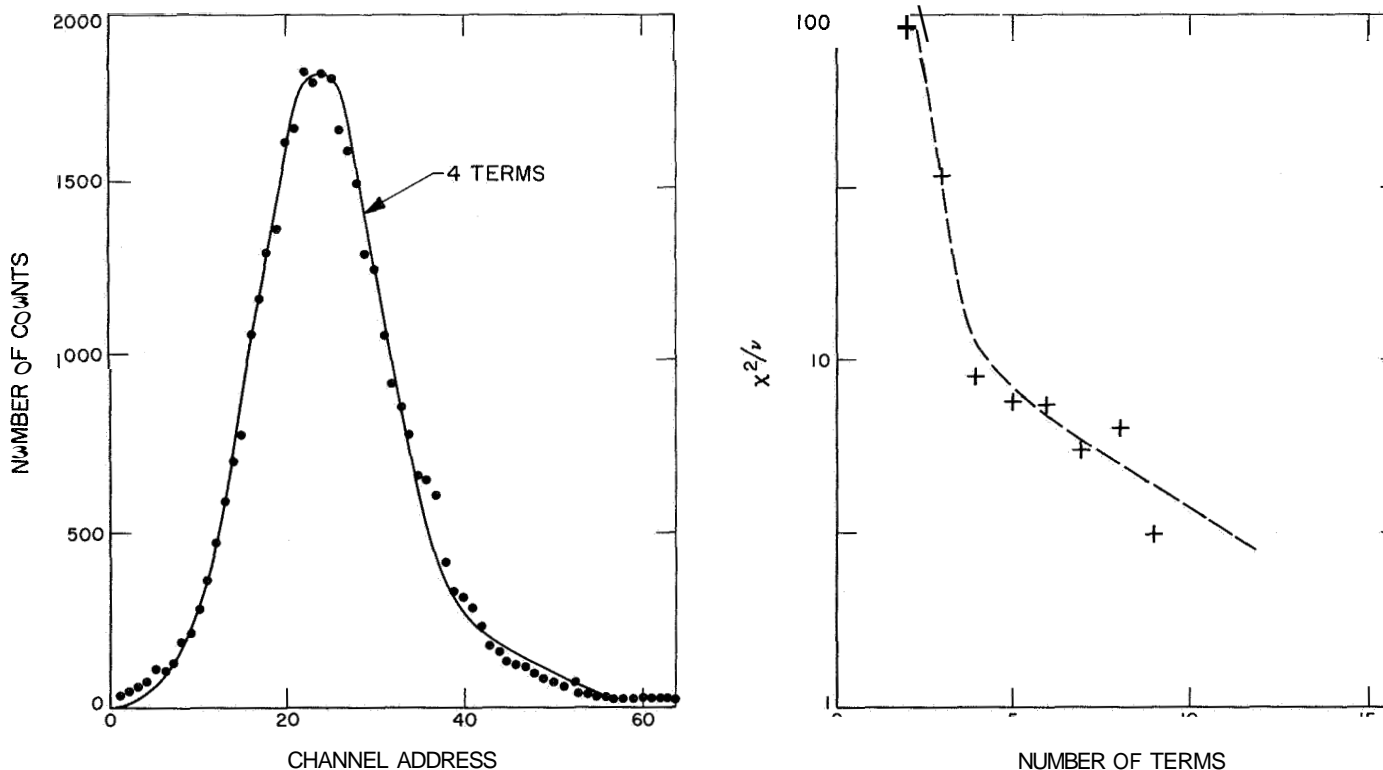


Fig. 2. Real data analyzed using Gauss-Hermite expansion

of unity when the function exactly fits all but the random statistical fluctuations. To obtain the points on this graph, the analysis was repeated, with more terms of the polynomial expansion added each time.

This method of distribution analysis has been used successfully in the treatment of multiparameter data, and may also prove valuable in the handling of scientific data from spacecraft.

References

1. Gold, T., "Motions in the Magnetosphere of the Earth," *Journal of Geophysical Research*, Vol. **64**, No. **9**, p. **1219**, **1959**.
2. Axford, W. I., and Hines, C. O., "A Unifying Theory of High-Latitude Geophysical Phenomena and Geomagnetic Storms," *Canadian Journal of Physics*, Vol. **39**, p. **1433**, **1961**.
3. Cole, K. D., "Damping of Magnetospheric Motions by the Ionosphere," *Journal of Geophysical Research*, Vol. **68**, p. **3231**, **1963**.
4. Bostrom, R., "A Model of the Auroral Electrojets," *Journal of Geophysical Research*, Vol. **69**, pp. **4983-4999**, **1964**.
5. Maeda, K., and Matsumoto, H., "Conductivity of the Ionosphere and Current System," *Report of Ionosphere and Space Research in Japan*, Vol. XVI, No. **1**, p. **1**, **1962**.
6. Carpenter, D. L., "Whistler Studies of the Plasmapause in the Magnetosphere," *Journal of Geophysical Research*, Vol. **71**, No. **3**, p. **693**, **1966**.
7. Batchelor, G. K., "Turbulence and Magnetic Fields," in *Gas Dynamics of Cosmic Clouds* (Proceedings of the Second IAU Symposium, Cambridge, England, July **6-11**, **1953**), pp. **117-120**, Interscience Publishers, New York, **1955**.
8. Kelly, H. P., "Many-Body Perturbation Theory Applied to Atoms," *Physical Review*, Vol. **136**, p. **B896**, **1964**.
9. Whitehead, A. B., Parker, R. H., and Haines, E. L., *Use of Transformations in Multiparameter Data Sorting*, Paper presented at the IEEE **13th** Nuclear Science Symposium, Boston, Mass., October **1966** (to be published in *IEEE Transactions on Nuclear Science*).

XVII. Communications Elements Research

TELECOMMUNICATIONS DIVISION

N67 18340

A. RF Techniques: Application of DC Potentiometer Insertion Loss Test Set to mm Wavelengths, *D. Oltmans, and C. T. Stelzried*

An accurate measurement of the insertion losses of waveguide components is necessary in order to evaluate and use radio telescope receiving systems. A dual-channel insertion loss test set has been constructed (Ref. 1) to make these measurements.

The problems that arise when the insertion loss test set is used at 90 GHz with the present thermistor mounts (Model R486A) are presented in this article, and a new thermistor mount is described that greatly reduces these problems. Also, a method for thermal adjustment of the new mount will be shown. All parts of the test set are commercially available.

The dual-channel insertion loss test set employs two Hewlett Packard Model 431B power meters. Each power meter requires two thermistors, one for RF detection and the other for thermal compensation. The highest frequency, commercially available waveguide thermistor mount is the Hewlett Packard Model R486A, designed for use to 40 GHz.

Waveguide transition sections are required to match the R-band mount to the UG 387/U E-band flange for use at 90 GHz. The mount and transition have some severe restrictions. The VSWR of the transition and mount combination is very poor and exhibits resonance effects. The VSWR can change from less than 1.1:1 to more than 5:1 with only a few megahertz (MHz) change in frequency. Since the actual frequency can only be measured to within ± 200 MHz and resolved to within 50 MHz with our present instrumentation, commercial mounts are unusable for precise measurements, unless refined frequency instrumentation is perfected.

The Model R486A mount also has orientation restrictions (SPS 37-40, Vol. III, p. 30). Rotation of the mount typically produces a change in the zero setting equivalent to $0 \pm 5 \mu\text{W}$, depending on the rotation orientation. For some waveguide configurations this would reduce the accuracy of the measurement of its insertion loss.

A new thermistor mount was assembled using two FXR Model E209A thermistor mounts clamped one on top of the other (Fig. 1). A thin film of silicone heat sink compound was spread between them to give good thermal conduction between the two mounts. A waveguide window was connected to the power detection thermistor

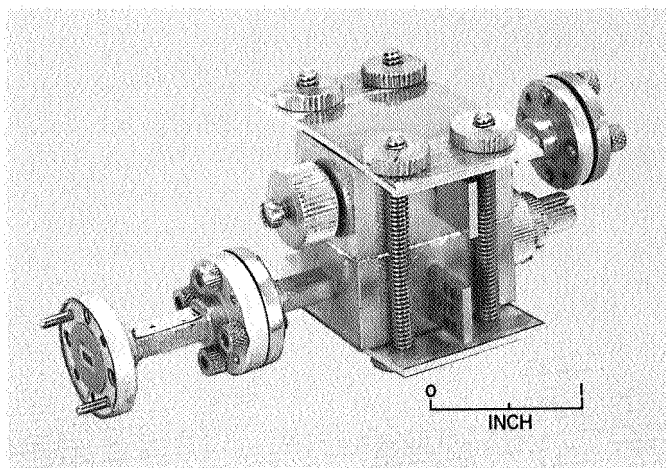


Fig. 1. Photograph of the new mount showing position of the model E209A mounts and associated parts

mount to reduce the effects of convection currents. A termination was connected to the compensation thermistor mount for isolation from the external environment. Elimination of the waveguide transition and addition of the capability to externally adjust the impedance of the new mounts resulted in a greatly improved match between the thermistor mount and the E-band waveguide sections.

One problem with the new mount is the lack of a thermal adjustment for the thermistor, which is necessary for operation with the power meter. A method for thermally adjusting the compensation thermistor was devised using basically the same technique as that used at lower frequencies (SPS 37-40, Vol. III, p. 30). The idea is to add a heat leak to one of the wires connecting the thermistor to the support (Fig. 2). Because of the small size (0.13×0.03 in.) of the rectangular slit in which the thermistor is suspended, a fine paint spray is used instead of epoxy or adjustment screens. The slit is masked with tape with the aid of a microscope to expose only the longest wire to the thermistor. Then paint is sprayed at the masked side of the card from a distance of approximately 2 ft, and a vacuum cleaner pulls the mist through the slit. The amount of spraying required is determined by trial and error, repeatedly testing the card with its pair. If too much paint is applied it can all be removed with acetone, although this will rarely be necessary. A thermistor is shown in Fig. 3 after the thermal adjustment. No ill effects are apparent at present.

Although the mount is compensated it is still sensitive to thermal environment changes, and requires insulation with Eccofoam and a stainless steel waveguide section to



Fig. 2. Photograph showing enlarged thermistor and wires before painting (magnification = 150)

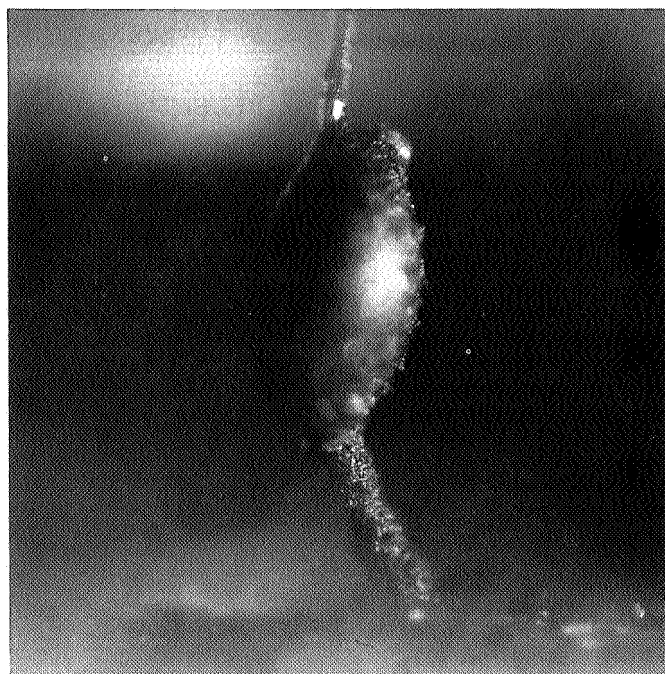


Fig. 3. Photograph showing enlarged thermistor and wires after painting (magnification = 150)

reduce thermal conduction. Improvement in stability can be seen by comparison with the commercial R-band mount. Short term instability (**15** min) of the new thermally compensated mount is about $2 \mu\text{W}$ compared to about **10** μW for the commercial **R486A** mount. The instability is due to the difference in temperature coefficients of the detecting and compensating thermistors, the change in ambient temperature and mount efficiency.

The efficiencies of the new mounts and the Hewlett Packard mount were measured with the Melab **RF**

Calorimeter, Model DE1B (5% accuracy) for frequencies around **90** GHz. The efficiency of the Hewlett Packard mount ranged from 1.7 to 12.5%. The efficiency of the new mounts ranged from **29.4** to **32.32**. Efficiency is defined here as the ratio of power meter reading divided by the power applied to the mount.

The power meter readings, using the new mount, were compared to two Microlab/FXR, Livingston, N.J., rotary vane attenuators, with agreement within 0.12 and 0.15 db over a 5-db range.

Reference

1. Stelzried, C. T., et al., "A Precision DC Potentiometer Microwave Insertion Loss Test Set," *IEEE Transactions on Instrumentation and Measurement*, Vol. IM-15, No. 3, p. 98, September 1966.

XVIII. Spacecraft Telemetry and Command

TELECOMMUNICATIONS DIVISION

N67 18341

A. linear Bit Packing Density on Standard Instrumentation Magnetic Recording Tapes, W. G. Clement

1. introduction

In meeting the limitations of weight, size and power in a tape recording system for spacecraft applications, efficiency of tape utilization is significant. A measure of efficiency for a digital recording system is the linear bit packing density. Many factors including tape characteristics, head design, tape guidance characteristics of the transport, and signal detection and data reconstruction techniques contribute to the system capability in this respect. Tape characteristics are probably the most significant factors. In addition to magnetic characteristics, thickness (Refs. 1-6) and surface smoothness (Refs. 2 and 7) of the tape's oxide coating are directly related to the bit packing efficiency of the recording system in which the tape is used.

A previous article (Ref. 8) reports some of the work done in evaluating magnetic recording tapes for spacecraft data storage applications. Recent availability of new, and presumably better, tapes has stimulated further evaluation effort, one phase of which is covered in this article.

2. Work Accomplished

Output signals from seven different tapes from four different manufacturers were measured at various bit

densities and the values plotted (Fig. 1). For each tape sample the record-current was set at a value which gave the maximum output at a bit density sufficiently low that no reduction in amplitude due to bit crowding occurred. Fig. 2 is a plot of these same data, adjusted to a common level at the low densities. It presents, therefore, a clearer

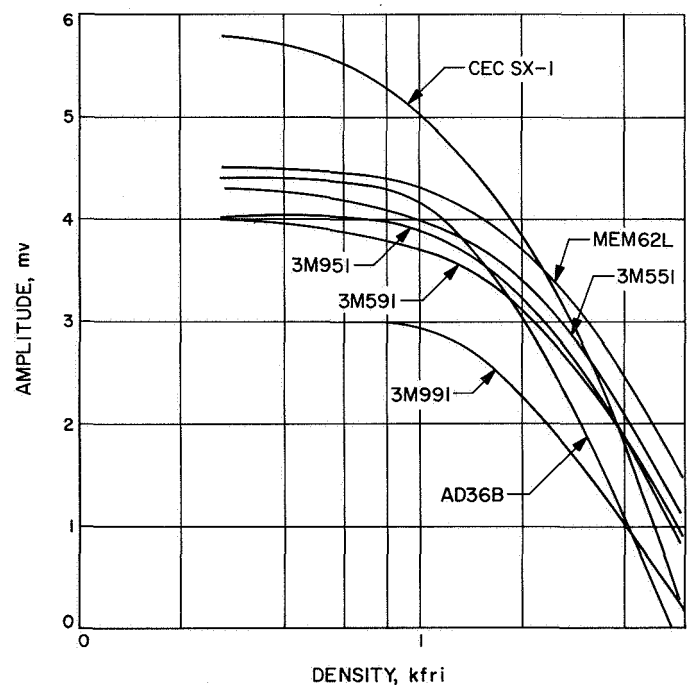


Fig. 1. Record current chosen for maximum output under condition of no-pulse crowding

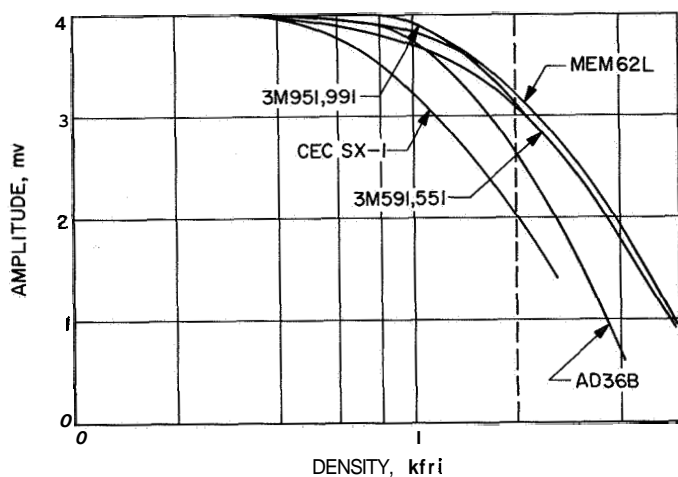


Fig. 2. Record current chosen for maximum output under condition of no-pulse crowding. Normalized to amplitude 4 at 267 fri

basis for comparing bit packing capability of various tapes, since one can choose a specific density somewhere on the slopes of the curves, for example at 2000 flux reversals/in. (fri) and compare tapes, using amplitude as a figure of merit.

This comparison, however, is valid only at the specific record-currents used in obtaining data. In general, at bit packing densities sufficiently high that pulse crowding exists, e.g., amplitude is reduced by virtue of overlapping remanent fields, a reduction in record-current results in less bit crowding and, hence, in correspondingly higher signal amplitudes. It follows that higher bit packing densities can be achieved with lower record-current values. This has been borne out in other studies (Refs. 4, 5, 9-11).

However, one of the outstanding advantages of a nonreturn-to-zero (NRZ) recording format is that no separate erase function is needed, since the record function serves to erase previous recordings. An additional constraint, therefore, is placed on the value of record-current. Not only must it be a value to assure high readout signals, but, also, it must be sufficient to obliterate previous recordings. This additional requirement opposes the attainment of higher packing densities, particularly when a two-frequency NRZ recording format, such as Manchester or Potter code, is used.

Since the advantages of these recording formats are considerable, it was felt that tapes should be evaluated on the basis of their suitability for such two-frequency systems. Therefore, additional tests were run on the same

seven tape samples with record-current values for each tape chosen so that a record frequency of f Hz completely obliterated signals previously recorded at $2f$ Hz and vice-versa. Determination of these current values was an iterative process, and the worst case (highest current requirement) proved to be with the higher frequency signal obliterating a recording made with the lower frequency signal. This result is consistent with the theory relating recording penetration with recorded wavelength (Refs. 12 and 13). The two recording frequencies were chosen so that f Hz produced 1000 fri and $2f$ Hz produced 2000 fri, thus simulating a 1000-bit/in. self-clocking system.

Output signals corresponding to the record-current values determined in accordance with the above procedure were measured at flux reversal densities of 1000, 2000, 4000, and 8000 fri for each tape sample and plotted (Fig. 3). In order to assess more readily the relative merit of each tape sample, a measure of the slope of the amplitude versus density characteristic was obtained and is given in the right hand column of Table 1 as a percent

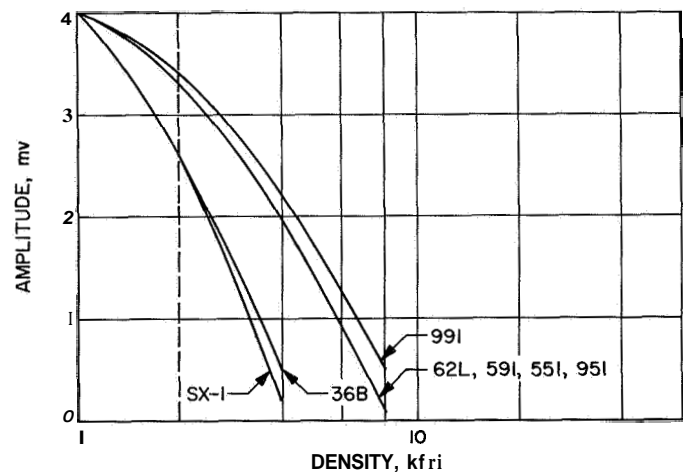


Fig. 3. Record current chosen for suitable erase in two-frequency system. Normalized to amplitude 4 at 1000 fri

Tape	I_R , ma	1 kfri (A), mv	2 kfri (B), mv	$\frac{A-B}{A} \times 100$, %
MEM 62L	32	4.0	3.3	17.5
AD 36B		1.0	2.6	35.0
3M 591		1.0	3.3	17.5
3M 551		1.0	3.3	17.5
3M 951		1.0	3.3	17.5
3M 991		4.0	3.4	15.0
CEC SX-1	84	4.0	2.6	35.0

decrease in amplitude from a normalized 1000 fri level to the 2000 fri level. Table 2 is a similar compilation of data from the first set of tests, wherein record-current was adjusted for maximum no-crowding output amplitude.

Table 2. Normalized data

Tape	I_R, ma	1 kfri (A), mv	2 kfri (B), mv	$\frac{A - B}{A} \times 100, \%$
	25	4.0	3.4	15.0
	36	4.0	2.9	27.5
	26	4.0	3.4	15.0
	30	4.0	3.4	15.0
	30	4.0	3.3	17.5
	30	4.0	3.2	20.0
	35	4.0	2.9	27.5

3. Results and Conclusions

A criterion has been developed for evaluating the bit resolution capability of magnetic tapes for use in digital NFU recording systems. Examination of Table 1 shows 3M991 tape to have slightly higher bit-density capability than the other samples. It is doubtful, however, that the accuracy of the measurements is sufficient to justify this conclusion. It is more reasonable to conclude that five of the seven samples are equally good, and that the other two samples have significantly less capability. It is interesting to note that Table 2 ascribes an order of merit to the tape samples, which is different from that in Table 1. This indicates the importance of establishing test conditions which approximate, as closely as possible, the eventual system conditions when evaluating any single component of a magnetic recording system.

N67 18342

B. A Magnetic Recording Tape Layer-to-layer Adhesion Tester, W. G. Clement

1. Introduction

A potential problem in the use of reel-to-reel magnetic tape recorders for spacecraft data storage is the phenomenon of layer-to-layer adhesion, commonly referred to as "blocking." This phenomenon may be aggravated in space missions because of long-term dormancy of the tape transport, coupled with elevated temperatures (Ref. 14) during cruise modes.

When interlayer adhesion occurs, even in a mild form, tape tension increases, and, in conventional tape transports, the departure of tape from the pack or reel becomes nontangential. This change in the angle of pull not only

changes the length of tape between the reel and the pulling point but also increases the layer-separating action of the pulling mechanism. Both effects combine to produce an unstable, usually oscillatory, rate of unwinding accompanied by tension variations which cause signal nonuniformities during recording and playback (Ref. 15).

If severe interlayer adhesion occurs, and if sufficient transport drive power is available, the oxide layer may be torn away from its backing material. In typical spacecraft tape recorders, where minimal motor drive power is provided, the mechanism would probably be incapable of starting or, if already operating in a normal fashion, would come to a sudden stop upon reaching a blocked portion of the tape.

2. Work Accomplished

In order to evaluate the interlayer adhesion problem and to obtain a measure of the relative susceptibility of various tapes to this phenomenon a test apparatus has been designed and constructed as an in-house project. Fig. 4 is a schematic diagram of the test apparatus, the design of which is based on the idea that as the pack is rotated in a direction to unspool the tape, the free end will break away from the pack at some point between west (tangent, no adhesion) and south (radial, maximum adhesion), depending on the weight used and the degree of adhesion existing. If the weight is insufficient to unstick the tape when hanging from a point due south (radially),

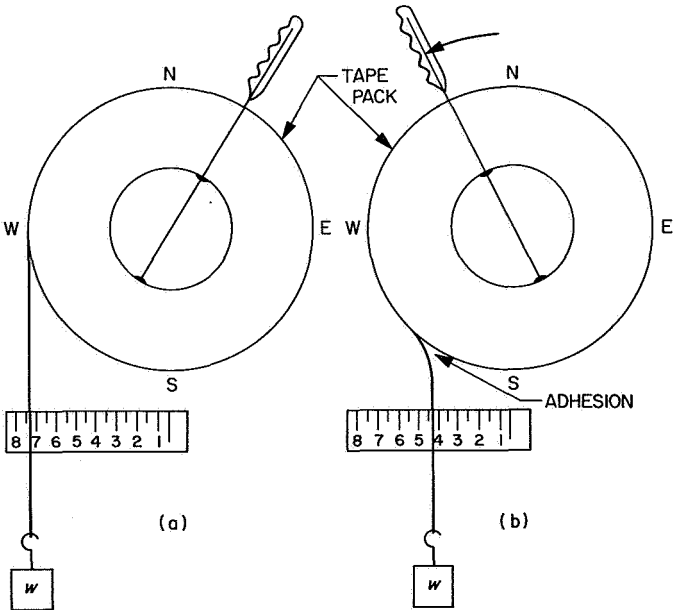


Fig. 4. Test apparatus schematic diagram

a heavier weight is needed, since further rotation of the pack with the same weight will only reduce the force component tending to unstick the tape.

Fig. 5 shows the geometry involved and gives the derivation of the peel force from the measurements made. From a measurement of the tape-pack radius, and the distance x between the breakaway point and the vertical centerline (see scale in Fig. 4) the angle α may be determined. The weight w necessary to overcome adhesion at the measured breakaway point can then be resolved into its tangential and radial components, the latter being the peel force of interest.

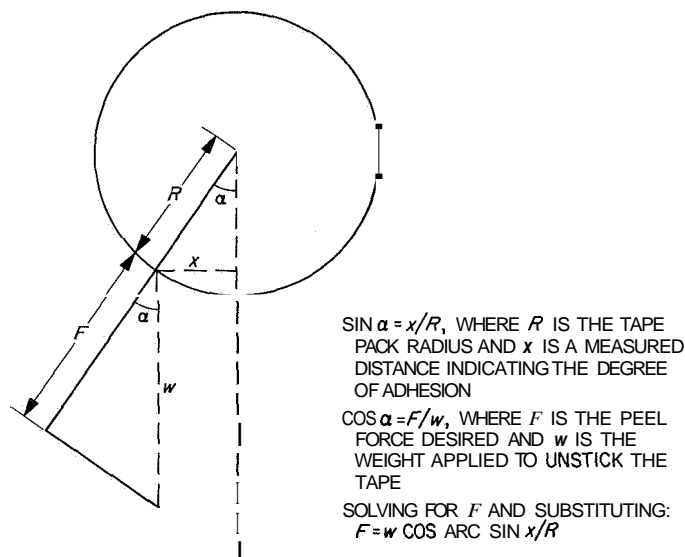


Fig. 5. Test apparatus geometry and peel-force derivation

It was decided to construct the apparatus so that it would conveniently fit in a 1-ft³ oven, since this size is the most readily available for tests. Eight 1/4-in. tape packs could be simultaneously subjected to an environment, after which each in turn could be evaluated for interlayer adhesion. The tape packs, measuring 1 1/4-in. ID and 3 5/32-in. OD, are the size used in the most recent JPL tape transport design. Various size weights can be hung on the tape by means of spring clips, and a suitable scale for measuring x can be moved along from tape pack to tape pack.

Fig. 6 is a photograph of the apparatus ready for load-ing. Fig. 7 is a photograph of the apparatus loaded with tape and undergoing interlayer adhesion testing subsequent to a temperature soak. The weights suspended from the left hand tape packs maintain winding tension during the soak period. Prior to the adhesion evaluation the packs

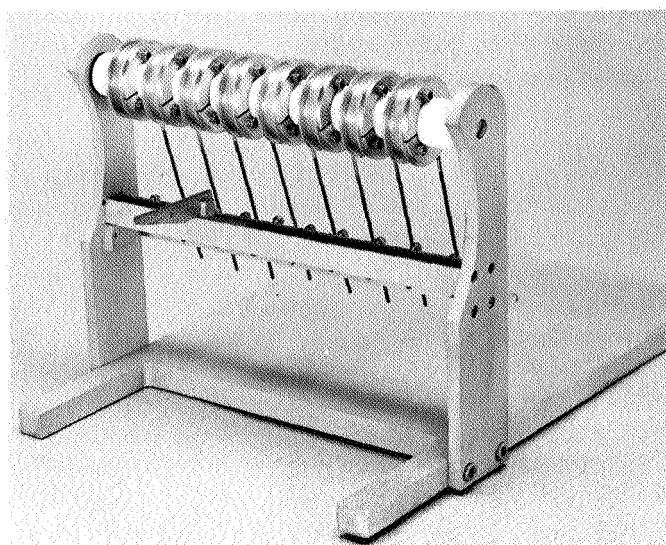


Fig. 6. Test apparatus

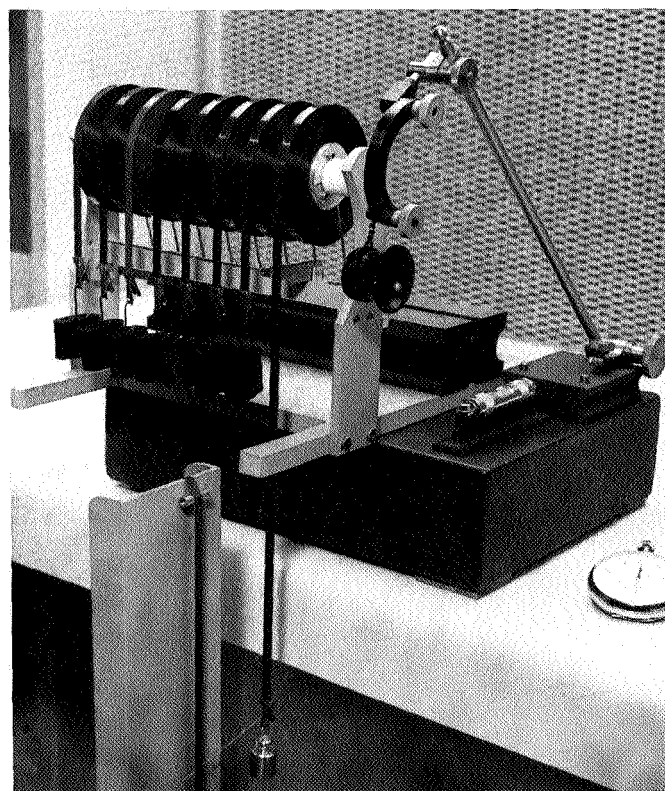


Fig. 7. Apparatus undergoing layer-to-layer adhesion test

are restrained from rotating by mechanical locks on the handles.

It was found that in measuring the interlayer adhesion of certain tapes there was a pronounced tendency for the

free end to twist. This was effectively prevented by attaching a stiff wire to the spring clip and guiding this wire in a vertical slot, as shown in Fig. 7.

In the initial test-runs repeatability of data was poor. Scale measurements of x were made while the tape pack was being rotated, and it appeared that the instantaneous rotational rates significantly affected the readings. It was decided, therefore, to incrementally rotate the tape pack, taking readings during the intervals of no motion. Several increments, with corresponding readings, were taken over a complete revolution of the tape pack and the maxima and minima recorded. At this point, it was discovered that the amount of time which elapsed between termination of rotational motion and the reading of the scale caused varying results. The tape was slowly unsticking itself from the next layer so that the free end (with weight attached) moved from right to left (Fig. 4), changing the scale reading. It was further noted that the amount of this unsticking, in terms of the change in scale reading, diminished very rapidly with time. A procedure was, therefore, adopted of measuring the x distance 10 secs after pack rotation ceased.

Thereafter, repeatability between separate test runs was satisfactory, provided oxide did not actually tear free from its backing. When this occurred peel-force values became highly erratic.

3. Results and Conclusions

Eight different tapes from five different manufacturers have been tested at several time-temperature soak combinations. Peel forces measured on these eight samples ranged from **0.042 to 2.490 oz.** This extreme variation in layer-to-layer adhesion among standard telemetry quality tapes indicates the importance of evaluating this characteristic before committing any given tape to a flight program involving the use of a reel-to-reel transport.

The accuracy of results obtained from the apparatus described herein is indicated by data which repeated within **1.1%** for two different tape samples on two separate test runs. Evaluation of additional tape samples, as well as different time-temperature soak combinations, continues using this interlayer adhesion test apparatus.

References

1. Hoagland, A. S., *Digital Magnetic Recording*, John Wiley & Sons, pp. **67, 103, 104, 1963.**
2. Mee, C. D., *The Physics of Magnetic Recording*, North-Holland Publishing Co., pp. **139-143, 1964.**
3. Eldridge, D. F., "Magnetic Recording and Reproduction of Pulses," *IRE Transactions on Audio*, March-April **1960.**
4. Miyata, J. J., and Hartel, R. R., "Recording and Reproduction of Signals on Magnetic Medium Using Saturation Type Recording," *IRE Transactions on Electronic Computers*, June **1959.**
5. Teer, K., *Investigation of Magnetic Recording Process with Step Functions*, Phillips Research Report No. **16, 1961.**
6. Wallace, R. L., Jr., "The Reproduction of Magnetically Recorded Signals," *Bell System Technical Journal*, pp. **1148, 1149, October 1951.**
7. Brophy, J. J., "High Density Magnetic Recording," *IRE Transactions on Audio*, March-April **1960.**

References (contd)

8. Clement, W. G., "Magnetic Tape Study," SPS 37-22, Vol. IV, Jet Propulsion Laboratory, Pasadena, pp. 226-229.
9. Barkouki, M. F., and Stein, I., "Theoretical and Experimental Evaluation of RZ and NRZ Recording Characteristics," IEEE *Transactions on Electronic Computers*, April 1963.
10. Batsel, C. N., and Ross, W. L., "High Density Digital Magnetic Tape Recording," Wesson paper, 1961.
11. Morrison, J. R., and Speliotis, D. E., "The Optimum Write Current for Digital Recording on Particulate Oxide and Metallic Recording Surfaces," *International Conference on Nonlinear Magnetism* paper, 1964.
12. Begun, S. J., *Magnetic Recording*, Murray Hill Books, p. 81, 1949.
13. Komei, O., "Frequency Response of Magnetic Recording," *Electronics*, p. 124, August 1947.
14. Jack, R. W., "Evaluation of Magnetic Tape," *Instruments and Control Systems*, July 1962.
15. *Magnetic Tape Study*, Final Report, Contract DA 18-119-SC-42, General Kinetics Corp., Arlington, Virginia, January 31, 1960.

XIX. Spacecraft Radio

TELECOMMUNICATIONS DIVISION

N67 18343

A. High Impact Antenna Study: Cupped Turnstile Antenna, K. Woo

1. Introduction

This article describes the progress made in developing another indirect type high impact antenna, a cupped turnstile (Ref. 1). The antenna has successfully sustained a **10,000-g** shock imparted into its mounting structure, and showed a relatively higher gain and lower axial ratio than the high impact antennas previously reported (SPS 37-40, 41, Vol. IV, pp. 201 and 239, respectively).

2. Antenna Design

The antenna (Fig. 1) consists of a pair of turnstiles (aluminum) backed by a cylindrical cup (aluminum, **3.75 in. ID, 1.5 in. deep**). The turnstiles are driven by an open ended quarter-wave length balun (Ref. 2) and are completely recessed in the cup for protection against impact. The outer conductor of the balun is strengthened by gradually increasing its wall thickness toward the cup base to prevent bending from impact. The antenna is fed through its input terminal, a low-loss connector (Ref. 3), at the rear of the cup. When excited the antenna will radiate circularly polarized waves, if the dimensions of the turnstiles, and the size and location of the cup are properly chosen. The primary function of the cup is to improve the circularity of the antenna over a wide beam angle by equalizing the E- and H-plane patterns (Ref. 4).

3. Results

An indirect impact test of the antenna at **10,000-g** level was performed with a horizontal impact tester (Ref. 5). The antenna was mounted in a test fixture, and then the fixture was impacted against a target. Postimpact examination of the antenna revealed no visible damage. Fig. 2 shows the radiation patterns of the right circularly polarized (RCP) and left circularly polarized (LCP) components before and after impact, measured at **2298 MHz**. As can be seen, the electrical performance of the antenna changed very little as the result of the impact. Also, there has been no appreciable difference in input VSWR (**2.7** before impact, **2.6** after impact).

The above results demonstrate that the antenna:

- (1) Can be used as an indirect impact antenna up to **10,000-g** level.
- (2) Has a substantially higher gain and lower axial ratio than the high impact antennas previously reported.

Future work on the antenna includes:

- (1) Careful trimming of the cup base to reduce antenna weight.
- (2) Slight modification of the balun dimensions to lower input VSWR.
- (3) Further improvement of the axial ratio.

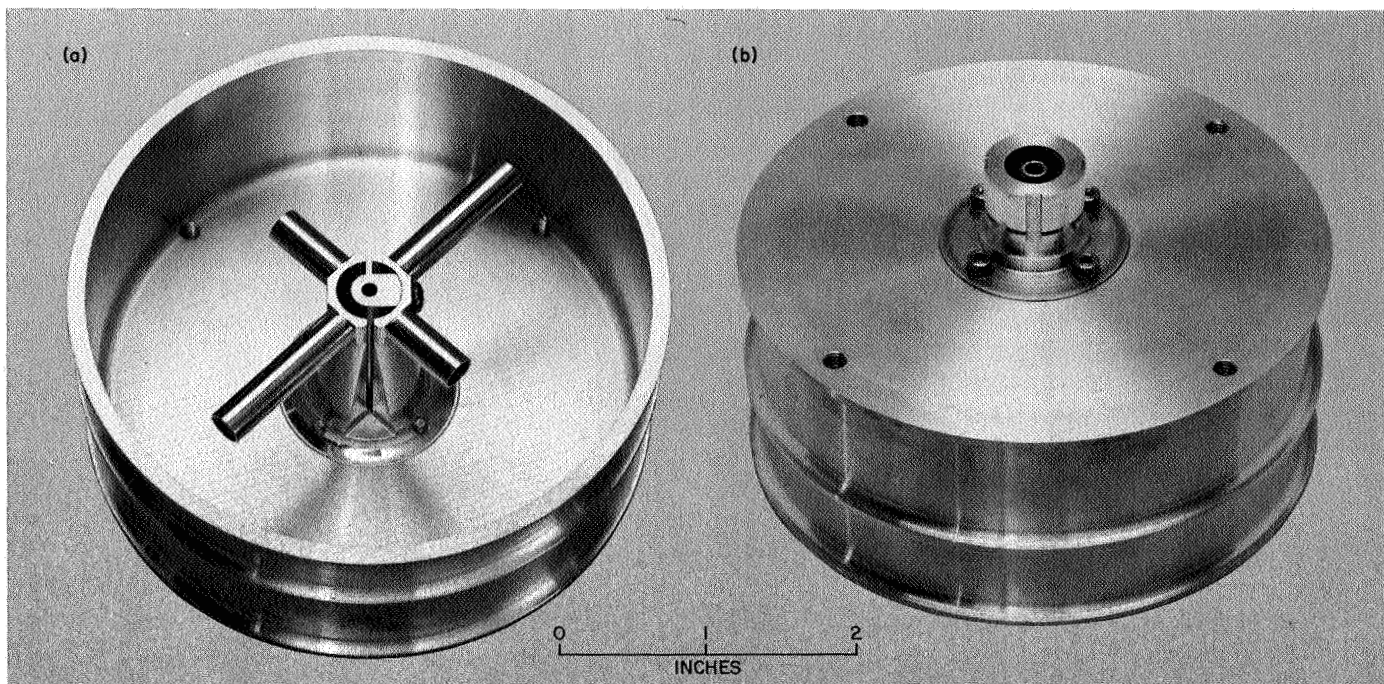


Fig. 1. Cupped turnstile antenna: (a) front, (b) rear

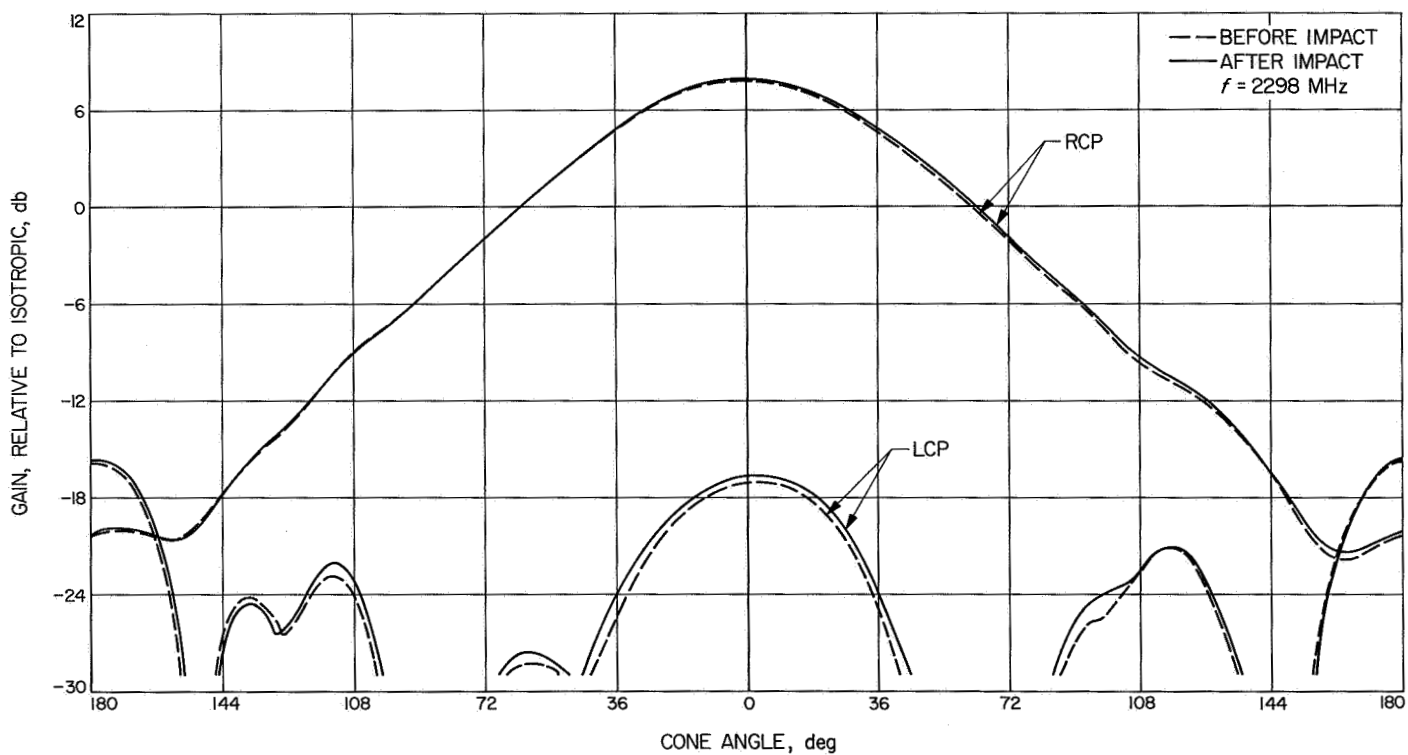


Fig. 2. Radiation patterns before and after impact

N67 18344

B. Experimental Results of Multipacting Between Coaxial Electrodes With High b/a Values, R. Woo

1. Introduction

Experimental results for multipacting between coaxial electrodes, where the ratio of outer to inner radii b/a was 2.3, were presented in SPS 37-41, Vol. IV, p. 242. It was shown that the scaling results predicted by our similarity principle for multipacting were well demonstrated in the experimental data. The scaling laws are put to a more severe test if higher b/a ratio cases are chosen, since the electric fields become more nonuniform.

2. Results

Experiments were conducted with coaxial electrodes where b/a varied up to 18.26. The experimental setup and procedure described in SPS 37-41, Vol. IV were used. Reproducibility of the data was generally within the limits described therein.

Fig. 3 shows the results of three cases where b/a is greater than 2.3. RF breakdown voltage is plotted as a function of fd . The multipacting region is seen to shift to higher values of V_{rf} with increasing b/a , which indicates that an increase in nonuniformity of the electric fields makes it more difficult for multipacting to occur. For both the lower and upper phase-controlled boundaries V_{rf} follows the $(fd)^2$ dependence in accordance with our similarity principle remarkably well.

As can be seen in Fig. 3, the slope of the lower boundary for $b/a = 2.3$ is less than 2, while that of $b/a = 4.56$ is exactly 2. An intermediate case, $b/a = 3.05$, was examined and the lower boundary fell between $b/a = 2.3$ and $b/a = 4.56$. However, this lower boundary was very erratic, especially for values of fd greater than 200 MHz-cm. This, then, represents a transition region.

The observed behavior can be interpreted in the following manner. For $b/a = 2.3$ the electric fields are relatively uniform and higher modes can exist. Consequently, there is an overlap of the $\frac{1}{2}$ -cycle mode and higher order modes in the data for the lower boundary (Ref. 6). If the electrodes are outgassed, there is a reduction in secondary emission yield so that only the M-cycle mode exists, and the lower boundary varies as $(fd)^2$ (SPS 37-41, Vol. IV). As b/a is increased, the fields become more nonuniform and higher order modes cannot exist. As a result, the lower boundary varies as $(fd)^2$, even without outgassing.

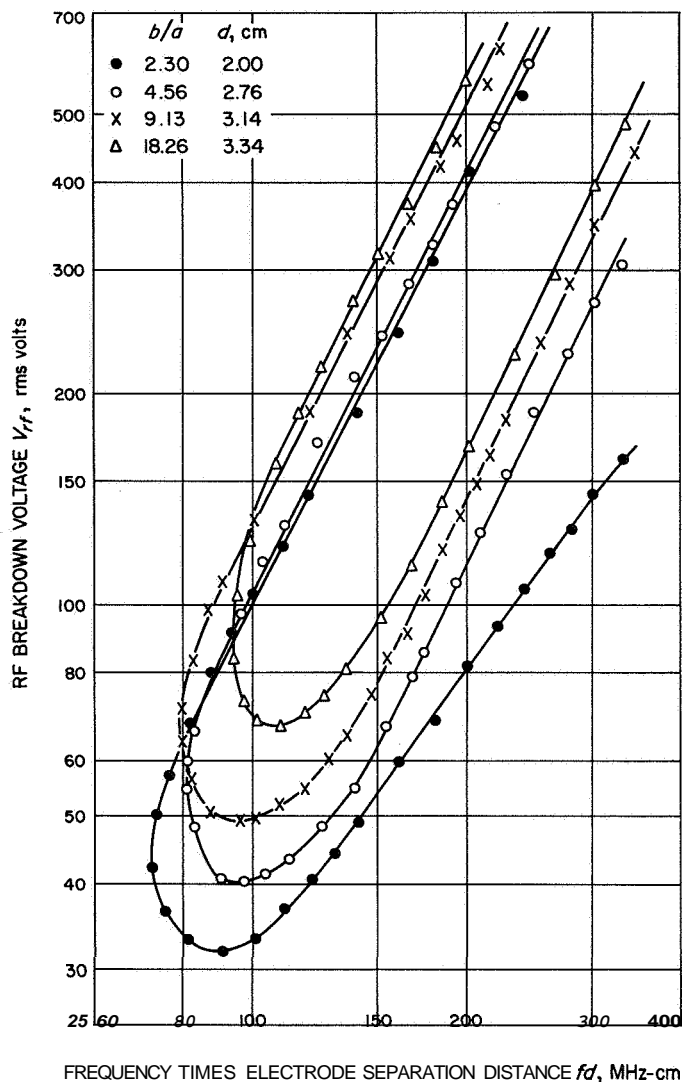


Fig. 3. Multipacting region for coaxial electrodes with varying values of b/a

It should be emphasized that although the multipacting regions for the higher b/a ratios are similar, the multipacting mechanism need not be. For instance, as b/a is increased the phase determined boundaries might represent phase conditions for one-sided multipacting. At any rate, the similarity principle still holds and $V_{rf} \sim (fd)^2$ along these boundaries.

Scaling of electrodes of different sizes, but of equal b/a ratios, was checked for values of b/a up to 18.26. Shown in Fig. 4 are the data for two sets of electrodes of different sizes and $b/a = 9.13$. Note that the dimensions of one set are twice the dimensions of the other set, so that this represents a significant change. As in the case of $b/a = 2.3$, the minimum energy boundary decreases with a decrease

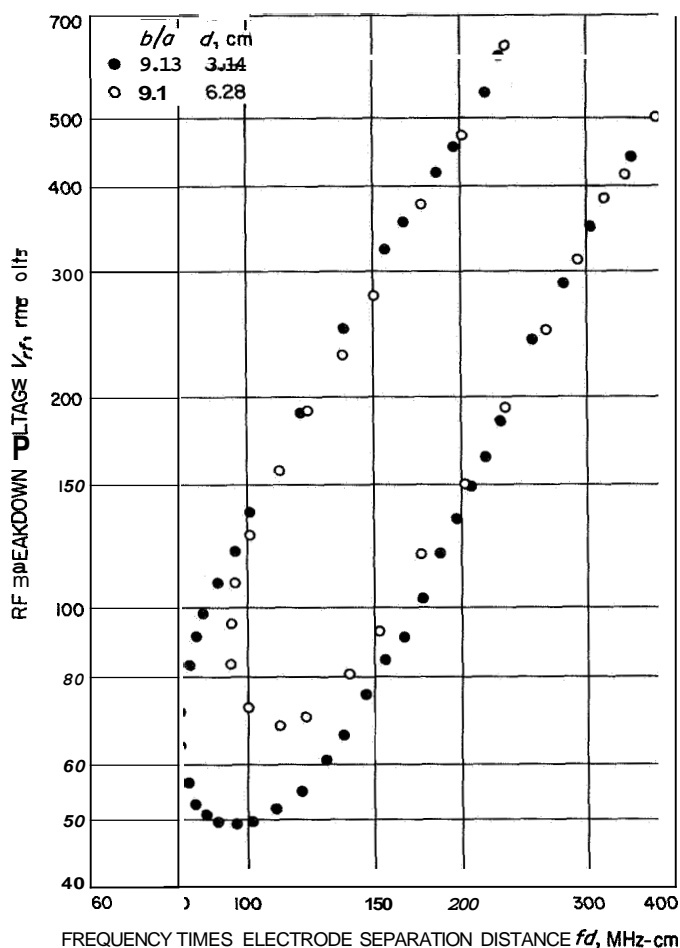


Fig. 4. Multipacting region for coaxial electrodes with $b/a = 9.13$

in size of electrodes (SPS 37-41, Vol. IV). The reason for this behavior cannot be pinpointed, but it must be remembered that reproducibility of the data is only within 15% due to the high sensitivity of the data to the electrode surface conditions. For the phase-controlled boundaries the scaling correspondence is seen to hold within experimental error. Instances other than $b/a = 9.126$ will not be presented, since they exhibited similar scaling correspondence results.

3. Conclusions

Experimental results have been presented to demonstrate the scaling laws of our similarity principle for coaxial electrodes where b/a is high. In general, the correspondence is very good. Further experiments are being conducted with a DC voltage applied to the coaxial electrodes in addition to the RF voltage. Also, isolation of the one-sided multipacting mode from the two-sided mode by the use of mesh electrodes is being studied.

C. Mariner S-Band Turnaround Ranging Transponder Improvement Program, L. M. Hershey

1. Introduction

Improvements are being made on the S-band turn-around ranging transponder used on Mariner Mars 1964 spacecraft so that it can be employed confidently on advanced projects. The existing circuitry is being studied by Philco's Western Development Laboratory (WDL) Division. Selected design improvements will be incorporated in an existing *Mariner* transponder and tested in the final phase of the program.

This article describes the transponder, the problems which have been encountered with the original design, the improvement program instituted to analyze and correct the problems, the results of the study, and the effect of the resulting changes.

2. Description of Transponder

The S-band transponder provides the functions of a double superheterodyne command receiver, a phase-coherent transponder, a turn-around ranging transponder, and a telemetry transmitter. As shown in Fig. 5, it employs three loops: the ranging, automatic gain control (AGC), and automatic phase control (APC) loops. In the absence of a signal received from the DSIF, the spacecraft telemetry information is encoded on a signal whose frequency is controlled by an auxiliary oscillator. When a signal from the DSIF is present in the transponder receiver at a level of about -150 dbm or higher, the APC loop will lock to it, and the AGC voltage will develop in the AGC loop. This voltage, besides controlling the receiver gain for proper operation, also produces a command voltage which turns off the auxiliary oscillator and causes the 19.125 MHz VCO to be switched to the transmitter input in its place. In this manner, closing the APC loop provides an exact ratio of 240 to 221 between the transmitted and received frequencies. In addition, the AGC voltage is telemetered to provide received signal strength information,

The signal received from the DSIF may have either range or command information phase modulated on it. The second mixer provides two outputs, one to the 9.56 MHz narrow-band command and APC channel, and another to the broad-band 9.56 MHz range channel. The range code is demodulated by the phase detector in the range channel, amplified, and remodulated onto the transmitted signal along with the telemetry input. The

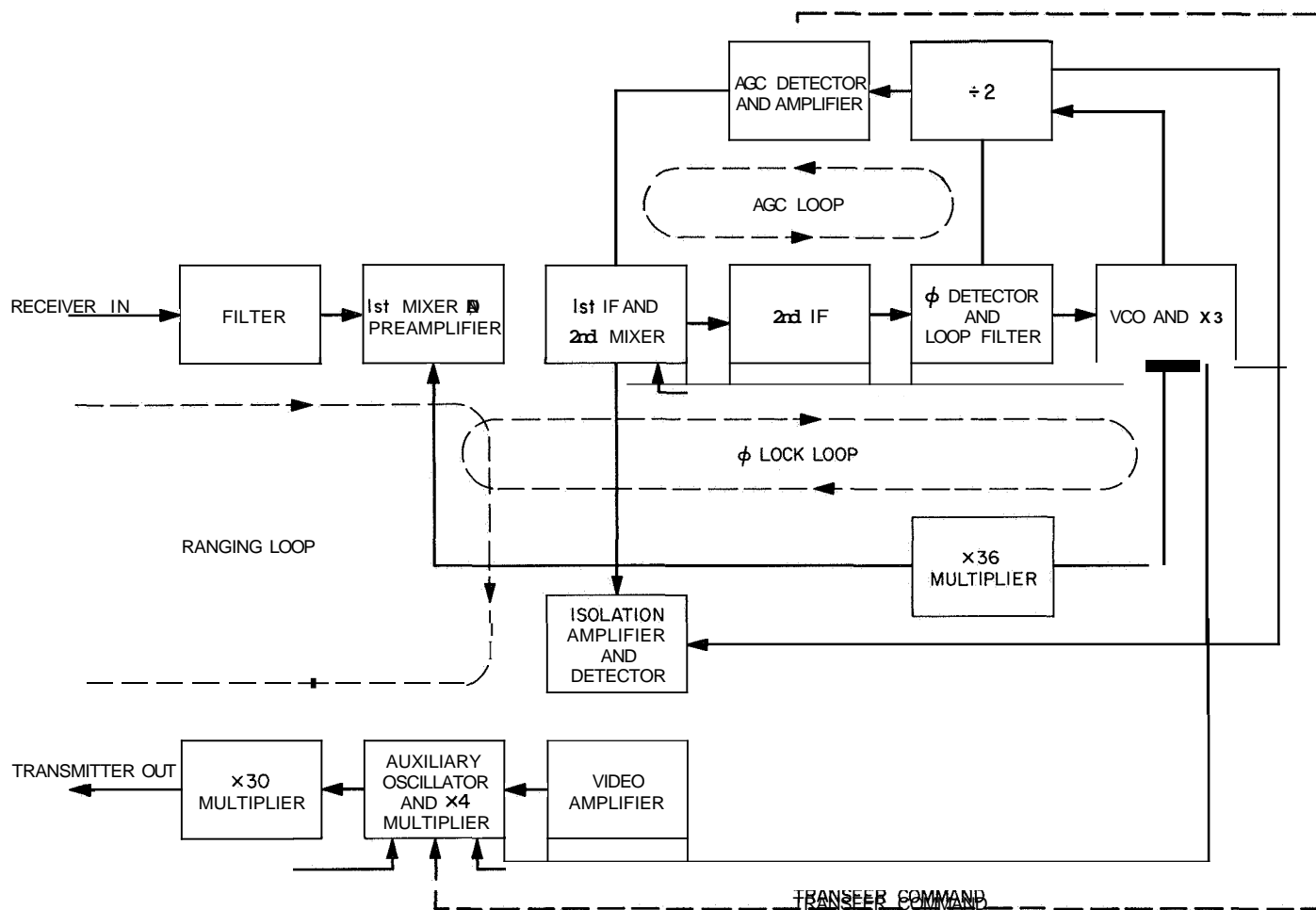


Fig. 5. S-band ranging transponder block diagram

command information is demodulated by the phase detector in the narrow-band channel.

Physically, the transponder consists of 13 types of modules, which correspond to the blocks in Fig. 5. These modules are grouped together in "six-packs," two six-packs for the receiver, and one six-pack for two (redundant) transmitters. A six-pack weighs about 10½ lb.

3. Improvement Program

The improvement study consists of both analysis and experimental work. Improved versions of the first and second IF amplifiers and the X30 multiplier have been completely breadboarded. Partial breadboards have been built of improved versions of the mixer-preamplifier, AGC detector, VCO, and auxiliary oscillator. Ranging and AGC performance and the self-lock phenomenon have been analyzed, and ranging delay variation measurements are being performed. Some recommendations have been

made, but no appreciable work has been done to date on the phase detector, frequency divider, and X36 multiplier.

4. Initial Problems

The problems encountered in the *Mariner* transponder were of two types: system problems, and problems peculiar to individual modules.

Three main system problems were found to exist. Under certain conditions, the transponder APC loop would lock to a transponder-generated signal when the range channel was turned on, and this prevented the reception of the ground station signal. The turnaround delay time for the ranging modulation varied excessively with temperature, which prevented accurate range determination. The transponder AGC voltage versus received signal strength characteristic varied excessively with temperature. This

reduced the accuracy with which received signal strength could be determined.

Module performance parameters were unstable with temperature and voltage fluctuations; the modules were not readily reproducible, and tests and adjustments were long and tedious.

Because of the tight *Mariner* Mars 1964 schedule, some early design problems were allowed to remain. In order to correct them, and to bring the transponder closer to the present state of the art, a transponder improvement program has begun.

a. Self-lock. The self-lock phenomenon became apparent only after a considerable amount of test time, because it occurs only in a few modes of operation out of a great number of possible modes. However, once the condition was found to exist, it was also found that it could be reproduced on almost any given transponder. Two requirements must first be met in order to produce self-lock. A spurious output signal must be generated by the transponder transmitter, and a receiver response must exist near the spurious signal frequency. When these conditions are met and the ranging channel is turned on and modulates the transmitter, the receiver locks onto the spurious signal. A very strong signal at the receiver design frequency is required to produce the desired phase lock on the DSIF signal.

The spurious signal may be generated anywhere in the ranging loop. One source is a spurious oscillation in the X30 multiplier; the multiplier exhibits a considerable amount of feedback from output to input circuits, and spurious oscillations are readily produced by mismatching its output. At certain phase angles, mismatches as low as 1.2 can cause spurious outputs. Whenever a new frequency is generated, nonlinearities in the multiplier chain produce multiples and modulation products of the spurious and desired signals separately and in combination, producing an output frequency spectrum that has many components. Leakage of coherent signals between modules is also a possible cause of self-lock. Interstage and intermodule filtering and shielding were measured and analyzed, and improvements are being made to increase the margin of safe operation against this mode of self-lock.

A breadboard of a redesigned X30 multiplier was built and tested. Modern techniques, such as a transistor amplifier-multiplier (TAM) instead of a varactor, were used. The breadboard was found to be substantially less

subject to the effects of impedance mismatch than the original design, and it showed no spurious output with impedance mismatches as high as 2, at any phase angle.

b. Ranging. The ranging improvements are directed toward reducing the turnaround ranging time delay variations through the transponder and increasing the ranging modulation bandwidth. Increasing the bandwidth will help reduce time delay variations.

The time delay through the *Mariner* transponder varies with temperature by as much as 200 nanosec or 30 m, round trip range. The DSIF specifies a maximum variation of 100 nanosec, but would prefer substantially less. Preliminary calculations have been made of the absolute delay of each module due to bandwidth and transistor transit times (Table 1). Delay measurements will be made with each module individually subjected to temperature testing in order to evaluate and isolate the causes of the variation.

Table 1. Transponder ranging delay

Module	Delay, nanosec
Mixer-preamplifier	108
1st IF amplifier	66
Isolation amplifier	80
Auxiliary oscillator and X 30 multiplier	380
Video amplifier	122
Transit time and miscellaneous	3
Total calculated	659
Measured delay	990

The ranging modulation bandwidth is determined by the bandwidth characteristics of the receiver circuits from the preselector through the video amplifier and the transmitter circuits from the modulator through the X30 multiplier. The presently specified bandwidth, 1.8 MHz, is difficult to achieve in the present transponder. The tendency toward regeneration in the old X30 multiplier caused a higher Q and smaller bandwidth in its circuits, and severely limited the modulation bandwidth.

Breadboard modulator and X30 circuits have been built and tested with a resulting increase in modulation bandwidth from a marginal 1.8 to over 4 MHz and a decrease in the effects of temperature on modulator sensitivity, from ± 10 to $\pm 5\%$. The modulation bandwidth of the old and new designs is compared in Fig. 6.

The X30 multiplier consists of amplifiers, a doubler, a X5 multiplier and a tripler. The total multiplication of

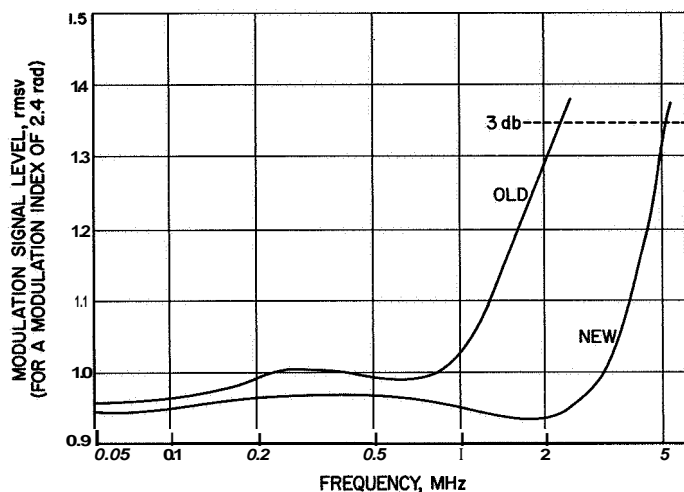


Fig. 6. Ranging modulation sensitivity

the auxiliary oscillator frequency of 120 times is accomplished by the **X30** module and a **X4** multiplier, which precedes the modulator in the auxiliary oscillator module. It was found that tuning the idler circuits in the **X5** multiplier stage affected the high-frequency modulation response of the range channel. Therefore, a different multiplier order is being investigated. The **X5** multiplier stage will be interchanged with the **X4** stage in the auxiliary oscillator. Tests will be made of the modulation performance of improved breadboards incorporating this change.

The video amplifier will be redesigned to broaden its response, improve its rejection of spurious signals, and improve its limiting action so that the ranging modulation index will be more constant with variations in uplink signal.

c. Automatic gain control. The AGC loop includes the **47.8 MHz** IF amplifier, **9.6 MHz** IF amplifier, AGC detector, and AGC amplifier. If accurate indications of received signal strength are to be produced for telemetry, the preselector and mixer preamplifier must also perform in a uniform manner under all conditions.

The AGC system includes a coherent detector, deriving its input from the second IF linear output, and an AGC amplifier, with the AGC voltage applied as forward bias to the bases of three cascode amplifiers in the **47.8 MHz** first IF amplifier. Excessive overall drift of the AGC characteristics occurred due to drifting of the DC amplifier and detector output, and gain variations in the IF amplifier, with temperature and power supply voltage variations. The DC amplifier was extremely sensitive to

temperature variations, particularly at high temperatures where drift of the output reached as much as **3 v**.

A commercial operational amplifier has been suggested as a possible replacement for the original design and is being evaluated. The detector output drift appears to be due to the inherent characteristics of its parts. The drift consists mainly of diode drift, with a minor contribution from phase error. Temperature compensation of the diodes will be investigated.

Temperature variations were found to cause the AGC-controlled **47.8 MHz** IF amplifier to drift over 20 db in gain at **-7v** AGC voltage, as shown in Fig. 7. In addition, the gain characteristic slope varied by a factor of **3.7** over the dynamic range. The amplifier was redesigned to use four grounded emitter single transistor amplifier stages instead of the original three cascode amplifiers. Linearity was improved about **3** to **1**, and temperature drift was reduced to less than **4 db**, as shown in Fig. 7.

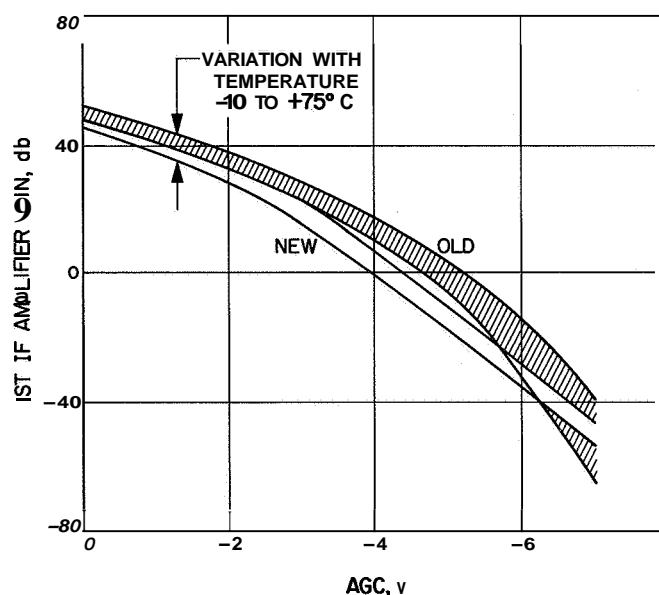


Fig. 7. First IF AGC characteristics

The **9.56 MHz** IF linear amplifier gain drifted **4 db** with temperature. Redesign reduced this to **<1 db**.

Individual instability contributions, due to all causes, are compared in Table 2. These figures are open-loop contributions and are not correlated as to polarity of error. They cannot be directly summed to obtain total error.

d. Modules. Only those modules which have been breadboarded and tested will be discussed here.

Table 2. AGC open loop instability contributions

Input signal	-150 dbm		-70 dbm	
	old, db	new, db	old, db	new, db
Mixer-preamplifier	2	2	2	2
1st IF amplifier	4.5	4	22	5
2nd IF amplifier	4	1	4	1
Detector offset	4.5	4	3.3	2.7
DC amplifier offset	2	0.3	1.5	0.2
ϕ errors (IF, detector, $\div 2$)	2.5	0.3	2.5	0.2

Mixer-preamplifier. The overall noise figure of the transponder has been measuring about 9.5 to 10 db. A 1-db improvement under worst case conditions (high temperature and low drive) has been accomplished by redesigning the first mixer to use hot carrier mixer diodes and changing to a lower noise transistor in the first stage of the intermediate frequency amplifier following the mixer. This will produce approximately a 1-db improvement in the threshold performance of the transponder. In addition to the improved noise figure, the input VSWR of the new unit has been reduced from 1.8 to 1.5, and the output impedance has been stabilized at 50 Ω . The noise figure of the new design at three temperatures and over a range of drive levels is shown in Fig. 8.

47.8 MHz IF amplifier. The principal problem in the 47.8 MHz IF amplifier was the gain versus temperature characteristic. A breadboard of the new design was tested with the results described earlier under AGC performance.

9.56 MHz IF amplifier. The redesigned 9.56 MHz IF amplifier breadboard produced a more constant limited output, varying only 0.5 db over the temperature range compared to 2 db for the original design. Differential phase shift variations between limited and linear outputs with temperature were reduced from 45 to 2.5 deg. Output linearity was improved from a ± 2 to ± 0.5 db departure from a straight line. The number of select-at-test parts was reduced from 14 to 5, and the number of semiconductor components was reduced from 9 to 6.

Auxiliary oscillator. The principal problem in the auxiliary oscillator module was that frequency variations of the crystal with temperature were not good, and were not coordinated with circuit performance. As a result, one crystal would partially compensate circuit drifts, while another would add to them. The solution to this problem was to put closer tolerances on the crystal temperature coefficient and to have a less temperature-sensitive oscillator circuit. The old and new crystal specifications are compared in Fig. 9, and the old and new oscillator circuit

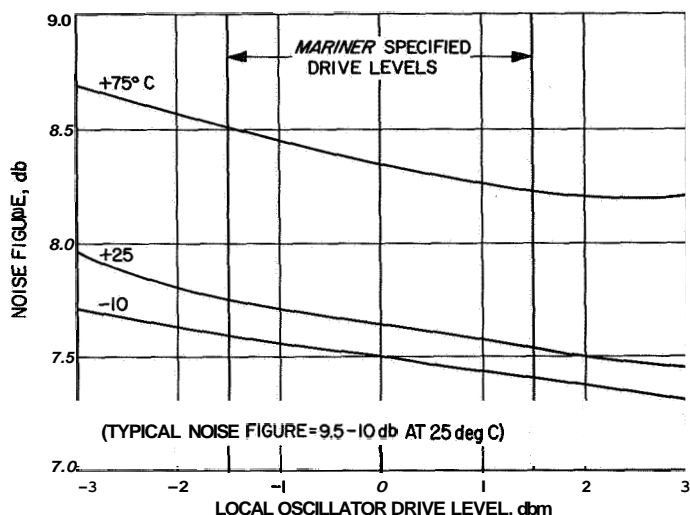


Fig. 8. Noise figures at 3 temperatures for the mixer-preamp with preselector

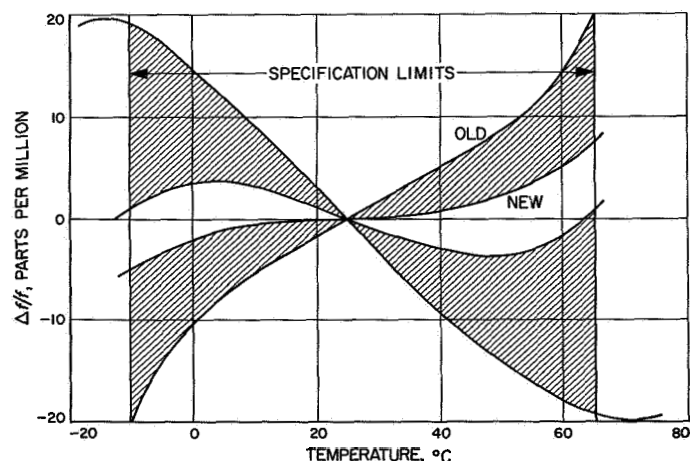


Fig. 9. Crystal specification for temperature stability

drifts are shown in Fig. 10. When the old and new crystals and circuits were compared overall, as shown in Fig. 11, only a small improvement was found. This was because the original crystal characteristic fell, by chance, within that part of the specification range where it compensated circuit drift.

In the old circuit, high crystal current caused crystal heating and resulted in some turn-on drift. Reduced crystal drive in the new circuit reduced this effect from 8 Hz in 30 min to 2 Hz in 30 min.

The new breadboard demonstrated that the crystal could be brought to the tighter specification and used with a substantial reduction in auxiliary oscillator drift.

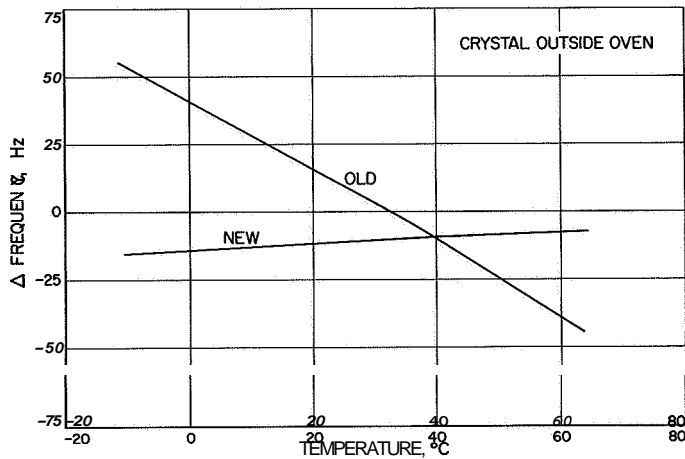


Fig. 10. Auxiliary oscillator circuit stability versus temperature

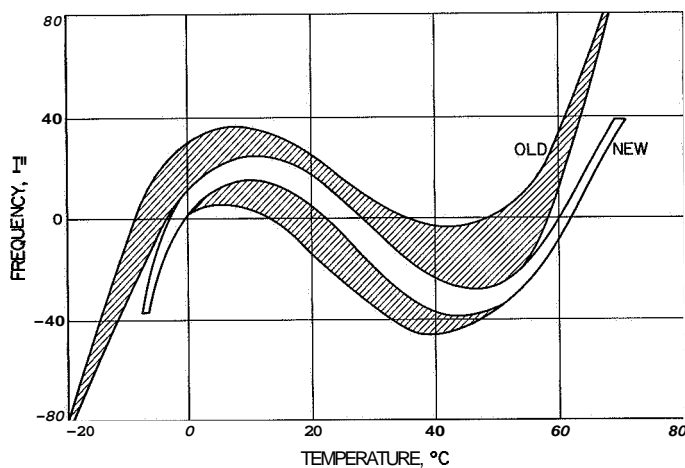


Fig. 11. Auxiliary oscillator frequency versus temperature

Voltage controlled oscillator. The VCO circuit behaved in a manner similar to the auxiliary oscillator. Measurement of its temperature drift (Fig. 12) shows that the crystal and circuit failed to compensate each other in this case and that the resulting drift is large, particularly at the temperature limits. Preliminary tests indicated that the new circuit and crystal produced the improvement shown. Some additional work remains to be done on this module.

X30 multiplier. The X30 multiplier was difficult to tune, inherently regenerative, and its stability left much to be desired. Fig. 13 shows the output level with varying

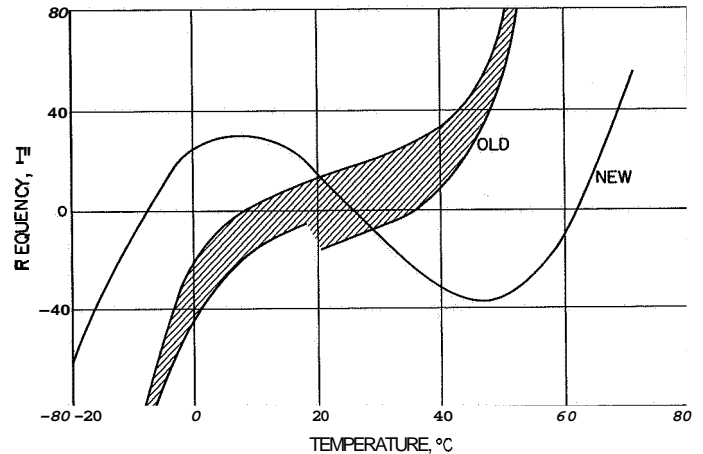


Fig. 12. VCO frequency versus temperature

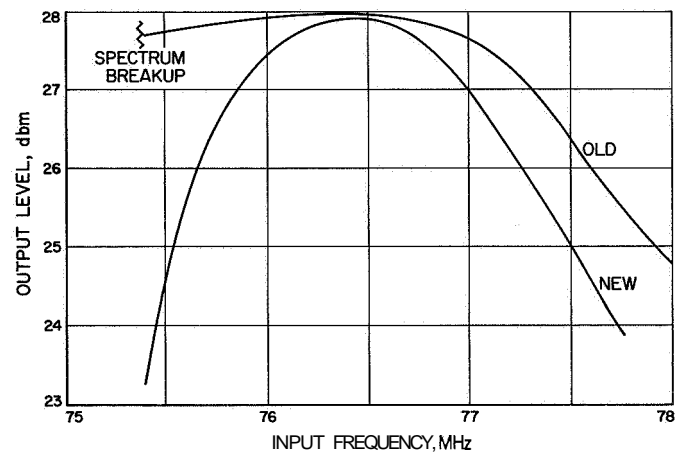


Fig. 13. X30 multiplier output level versus input frequency

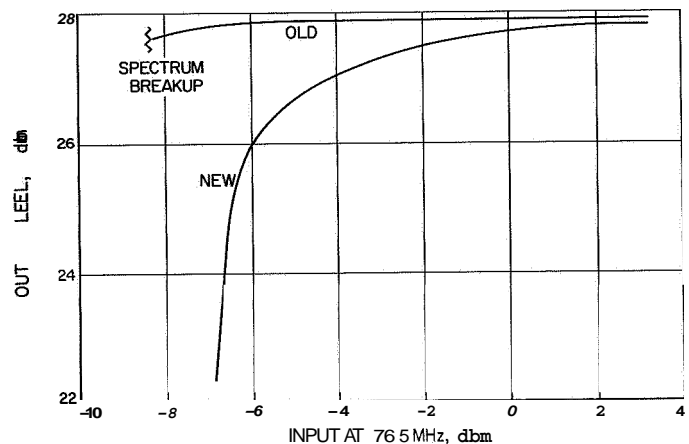


Fig. 14. X30 multiplier limiting characteristics

input frequency. A spectrum breakup, due to oscillation in the multiplier, occurred at low frequencies. While the bandwidth of the new multiplier appears to be narrower in this graph, modulation bandwidth measurements, described earlier under subsection *b.*, **Ranging**, clearly show that the bandwidth of the new multiplier is adequate and an improvement over the old one.

The limiting characteristics of the new and old circuits are compared in Fig. 14. Again, spectrum breakup of the old multiplier's output is shown. The new limiting characteristics, while not as flat as the old, provide adequate range. The new multiplier is inherently stable.

It was noted earlier that a new breadboard of a X24 multiplier is being tested and is expected to replace the present module.

5. Conclusion

The foregoing has been limited to a discussion of some of the highlights of a study contract which will continue for several more months. This program is being coordinated closely with the **Mariner Mars 1969** project's transponder program. Both contracts are in the same part of the Philco WDL organization, and some of the improvements resulting from this study are being incorporated in the Mariner Mars 1969 transponder.

References

1. Boreham, J. F., *Capsule Antenna Study*, Technical Memorandum No. 33-272, Vol. I, Jet Propulsion Laboratory, Pasadena, pp. 215-218, January 31, 1966.
2. Silver, S., *Microwave Antenna Theory and Design*, McGraw-Hill Book Co., New York, p. 246, 1949.
3. Brejcha, A. G., Low-Loss *Spacecraft Coaxial Cable Systems*, Section Report 367-1, Jet Propulsion Laboratory, Pasadena, July 1, 1966.
4. Chlavin, A., 'A New Antenna Feed Having Equal E- and H-Plane Patterns,' IRE *Transactions on Antennas and Propagation*, Vol. AP-2, p. 113, July 1954.
5. Lonborg, J. O., *High Impact Survival*, Technical Report No. 32-647, Jet Propulsion Laboratory, Pasadena, September 30, 1964.
6. Hatch, A. J., and Williams, H. B., "Multipacting Modes of High Frequency Gaseous Breakdown," *Physical Review*, Vol. 112, pp. 681-685, 1958.

PRECEDING PAGE BLANK NOT FILMED.

N67 18346

XX. Communications Systems Research

TELECOMMUNICATIONS DIVISION

A. Block Coding and Synchronization Studies: Rapid Acquisition Sequences, J. J. Stiffler

1. Introduction

Both ranging and synchronization problems are often attacked by repeatedly transmitting a binary sequence and attempting to determine its phase at the receiver. If the transmitted sequence is $x = \{\xi_1, \xi_2, \dots, \xi_N\}$, the desired information is obtained by ascertaining which of the cyclic permutations x^i of x is being received where $x^i = \{\xi_{i+1}, \xi_{i+2}, \dots, \xi_{i+N}\}$, the subscripts interpreted modulo N . We shall assume for the moment that only integer values of i need be considered. In the absence of any equipment constraints, the optimum procedure for determining i is well-known. If the additive noise is white and Gaussian, the optimum receiver would simultaneously perform, for each value of $(k = 0, 1, \dots, N - 1)$, the correlation $I_k = \sum_i \xi_{i+k} y_i$

with

$$y_i = \int_{i \frac{T}{N}}^{(i+1) \frac{T}{N}} y(t) dt$$

where $y(t)$ denotes the received signal and T its period. The subscripts of the ξ_{i+k} terms are again taken modulo

N . As soon as a suitable number of terms y_i are available, the index k_0 is accepted as indicating the phase of the received sequence, where $\max_k \{I_k\} = I_{k_0}$. Typically, however, N is large, and equipment limitations preclude the simultaneous determination of all N of the correlations $\{I_k\}$. Indeed, often only one such correlation can be determined at a time.

It is to this problem of signal acquisition when the search is constrained to be serial in nature that this article is addressed. In particular, it is concerned with the selection of signals which can be used efficiently for this purpose. This signal design problem has been investigated in some detail when parallel or simultaneous search is possible. The optimum sequences in this case are the maximal-length shift-register sequences (and others having the same autocorrelation property). Efforts have been made to design sequences for serial acquisition by combining, in various ways, relatively short shift-register sequences (Refs. 1 and 2). Specifically, if m sequences having relatively prime periods p_1, p_2, \dots, p_m are suitably combined, the resulting sequence has period $N = p_1 p_2 \dots p_m$. Yet, by determining the phase of each of the component sequences separately, only on the order of $L = \sum_{i=1}^m p_i$ different binary decisions need be made. This number L , nevertheless, far exceeds the

theoretically minimum number ($\log_2 N$) of binary decisions needed for a given value of N , primarily because the periods p_i of the component sequences are constrained to be relatively prime.

In this article, a class of binary sequences of lengths $N = 2^n$ (for all integer values of n) is presented. The phase of any of these sequences can be determined in every case after only $n = \log_2 N$ binary decisions. The sequences are described in the next section and shown to be nearly optimum (a degradation by a factor of $2/\pi$ is sustained in requiring the sequences to be binary). The time needed for acquisition is calculated in Section 3 and compared to that required using maximal-length shift-register sequences. In Section 4, a modification is introduced in the rule defining these sequences whereby a "clock" component, heretofore assumed present, can be obtained directly from the sequences themselves. Finally in Section 5, these techniques are extended briefly to include non-binary decisions.

2. The Sequences

The acquisition problem under consideration here is just the problem of identifying which of the N equally-likely (*a priori*) possible phase positions is the "correct" one. One method for accomplishing this with a series of $\log_2 N$ binary decisions is to use $\log_2 N$ separate channels as follows: transmit over the first channel a square wave of period $2T/N$ and correlate the received signal with a locally-generated square wave of the same period. Since the correct phase is initially known to be one of N equally-spaced time displacements, there are only two possibilities for the relationship between the phases of the received and the locally-generated signals. Either they are in phase, and the expected value of the correlation attains its maximum possible value, or they are 180 deg out of phase, and the expected correlation is as small (as large a negative value) as possible. A binary decision is required to distinguish between the two cases. A correct decision reduces the number of contending positions by one-half, leaving $N/2$ equally-spaced possibilities for the correct phase. The second channel can therefore halve once again the number of possible phase positions if it is used to transmit a square wave with period $4T/N$. In general, the number of phase positions remaining under consideration after the $(i - 1)$ st channel decision has been made can be halved by transmitting over the i^{th} channel a square wave with the period $2^i T/N$. This, of course, enables the final decision to be made after only $\log_2 N$ binary decisions, as desired.

Since a correct decision is equally important at each stage of the search, (i.e., since each channel conveys the same amount of information) an equal amount of power, $(1/\log_2 N)$ th of the total power, should be relegated to each channel. When the available power is divided among the $\log_2 N$ channels in this way, it is apparent that no other scheme would permit a more rapid acquisition, subject to the conditions assumed here.¹ Each decision depends upon the ability to distinguish between two situations, which, under the constraints outlined, are maximally distinguishable. Since $n = \log_2 N$ such binary decisions are required, each channel can represent only $(1/n)$ th of the total power. No further improvement is possible.

An apparent disadvantage to this approach is in the requirement of $\log_2 N$ separate channels. This limitation, however, is easily overcome upon recognizing that the signals transmitted over each channel are mutually orthogonal. Consequently, the $\log_2 N$ square waves can be summed and transmitted over one channel without altering the performance of the system whatsoever, so long as the correlation interval is some integer multiple of T , the maximum period of any of the signals. Thus, denoting the shortest-period square wave by the sequence 1, -1, 1, -1, ..., the next shortest period square wave by 1, 1, -1, -1, 1, 1, -1, -1, ..., etc., the transmitted signal has the form, for example, when $N = 8$,

$$\begin{array}{cccccccc} 1 & -1 & 1 & -1 & 1 & -1 & 1 & -1 \\ 1 & 1 & -1 & -1 & 1 & 1 & -1 & -1 \\ 1 & 1 & 1 & 1 & -1 & -1 & -1 & -1 \\ \hline 3 & 1 & 1 & -1 & 1 & -1 & -1 & -3 \end{array}$$

Summing the signals to eliminate the need for separate channels, however, introduces another disadvantage: the composite signal is no longer binary. Frequently, the demands of transmitter efficiency and simplicity restrict the class of permissible signals to be binary. This requirement can also be met using the approach suggested here, but this time not without some degradation in performance. Fortunately, however, the degradation is slight—as will be shown.

The method we propose for obtaining a rapid-acquisition binary sequence $x = \{x_1, x_2, \dots, x_N\}$ is simply

¹This, of course, would not be true if it were possible to alter the transmitted signal in the course of the search; i.e., if a feedback channel were also available.

to replace each term in the summed sequence by its sign. That is, if $s_i = \{\sigma_1^i, \sigma_2^i, \dots, \sigma_N^i\}$ denotes the sequence corresponding to a square wave with period $2^i T/N$, the optimum rapid-acquisition sequence, as discussed above, consists of the terms $\xi_j' = \sum_i \sigma_j^i$. To obtain a binary sequence, we transmit instead the sequence of terms

$$\xi_j = \text{sgn} \left\{ \sum_i \sigma_j^i \right\} \text{ where}$$

$$\text{sgn} x = \begin{cases} 1 & x \geq 0 \\ -1 & x < 0 \end{cases}$$

(Note: Usually $\text{sgn}\{x\}$ is equated to zero when $x = 0$. Here, however, we are restricted to only two levels, so we have altered the definition accordingly.) The correlation ρ_i between the sequence $x = \{\xi_1, \xi_2, \dots, \xi_N\}$ and each

of the sequences s_i is easily determined upon observing that the set of n -tuples $\sigma_j \equiv \{\sigma_j^1, \sigma_j^2, \dots, \sigma_j^n\}$ contains each of the N binary n -tuples once, and only once. Moreover,

$$\rho_k - \rho_i = \frac{1}{N} \sum_{j=1}^N (\sigma_j^k - \sigma_j^i) \xi_j = \frac{2}{N} \left[\sum_{S_1} \xi_j - \sum_{S_2} \xi_j \right]$$

where S_1 is the set of integers j such that $\sigma_j^k = 1$ and $\sigma_j^i = -1$, and S_2 the set such that $\sigma_j^k = -1$ and $\sigma_j^i = 1$. But ξ_j is a symmetric function of σ_j^k and σ_j^i . Hence, for every ξ_j with $j \in S_1$, there is an equal $\xi_{j'}$ with $j' \in S_2$, and conversely. Thus, for all i and k ,

$$\rho_i = \rho_k$$

Accordingly,

$$\begin{aligned} \rho_i \equiv \rho &= \frac{1}{n} \sum_{i=1}^n \rho_i = \frac{1}{Nn} \sum_{j=1}^N \sum_{i=1}^n \sigma_j^i \text{sgn} \sum_{k=1}^n \sigma_j^k \\ &= \frac{1}{Nn} \sum_{j=1}^N \left| \sum_{i=1}^n \sigma_j^i \right| \\ &= \frac{2}{Nn} \sum_{\nu=0}^{\left[\frac{n}{2} \right]} \binom{n}{\nu} (n - 2\nu) = \begin{cases} \frac{1}{2^{n-1}} \binom{n-1}{\frac{n-1}{2}} & n \text{ odd} \\ \frac{1}{2^n} \binom{n}{\frac{n}{2}} & n \text{ even} \end{cases} \end{aligned} \quad (1)$$

When n is large, Sterling's formula can be used to establish that

$$\rho \simeq \sqrt{\frac{2}{\pi}} \frac{1}{(\log N)^{1/2}} \quad (2)$$

This would be the correlation using the separate channel method if the power transmitted over each channel were reduced by a factor of $2/\pi$ (i.e., if the signal amplitude were reduced by the factor $\sqrt{2/\pi}$).

It is easy to show, incidentally, that the sequence $x = \{\xi_1, \xi_2, \dots, \xi_N\}$ is indeed the optimum binary sequence to use, in the sense that no other binary sequence has a larger minimum (average) correlation with the set

of sequences $\{s_i\}$. This follows because

$$\begin{aligned} \min_i \rho_i &\leq \text{avg}_i \rho_i = \frac{1}{Nn} \sum_i \sum_j \sigma_j^i \xi_j \\ &= \frac{1}{Nn} \sum_j \xi_j \left(\sum_i \sigma_j^i \right) \leq \frac{1}{Nn} \sum_j \left| \sum_i \sigma_j^i \right| \end{aligned} \quad (3)$$

the equality holding if, and only if,²

$$\xi_j = \text{sgn} \left\{ \sum_i \sigma_j^i \right\} \quad (4)$$

²The definition of ξ_j is arbitrary, of course, so far as the average is concerned when $\sum_i \sigma_j^i = 0$.

And since, here,

$$\min_i \rho_i = \text{avc } \rho_i = \frac{1}{Nn} \sum_j \left| \sum_i \sigma_j^i \right| \quad (5)$$

both the minimum and average of the correlation coefficients ρ_i have been maximized by the sequence x as defined above.

3. On the time needed for a decision

If, at the i th stage of the search, the locally-generated sequence s_i and the received sequence are in-phase (modulo 2^i), the correlator output, after τ seconds of integration, has the expected value $\rho A \tau$, where ρ is as determined in the previous section, and A is the amplitude of the received binary signal.³ If the two signals are 180 deg out-of-phase, the expected correlator output is $-\rho A \tau$. If the noise is white and Gaussian with the single-sided noise spectral density N_0 , the correlator output is Gaussianly distributed with a variance $\sigma^2 = N_0/2 \tau$.

Perhaps the most straightforward decision procedure is to determine τ in advance and to observe the sign of the correlator output at the end of this interval. It is concluded that the locally-generated signal is in phase with the received signal if the output is positive and is out of phase if it is negative. Thus, the probability of a correct decision at the i th stage of the search is

$$\begin{aligned} P_c(i) \equiv P_0 &= \frac{1}{\sqrt{2\pi}\sigma} \int_0^\infty e^{-\frac{(x-\mu)^2}{2\sigma^2}} dx \\ &= \frac{1}{2} \left[1 + \text{erf} \left(\frac{\mu}{\sqrt{2}\sigma} \right) \right] \end{aligned} \quad (6)$$

where $\mu = \rho A \tau$ and $\sigma^2 = N_0/2 \tau$. Since $n = \log_2 N$ decisions are required, the probability of a current acquisition is

$$P_c = \prod_i P_c(i) = P_0^n \quad (7)$$

³The integration period τ is assumed to be some integral multiple of T , the sequence period.

as $P_c(i)$ is independent of i . Using a well-known approximation to the error function, we have

$$P_c \approx \left(1 - \frac{1}{\sqrt{2\pi}} \frac{e^{-\frac{\mu^2}{2\sigma^2}}}{\frac{\mu}{\sigma}} \right)^n \approx 1 - \frac{n}{\sqrt{2\pi}} \frac{e^{-\frac{\mu^2}{2\sigma^2}}}{\frac{\mu}{\sigma}} \quad (8)$$

$$= 1 - \frac{1}{2 \left(\frac{2A^2\tau}{N_0} \right)^{1/2}} \exp \left[-\frac{2}{\pi} \frac{A^2\tau}{N_0 n} - \frac{3}{2} \ln n \right]$$

Accordingly, if the probability of an error is to be small, τ must be on the order of $\frac{N_0}{A^2} n \ln n = \frac{N_0}{A^2} \log_2 N \ln(\log_2 N)$. The total search time required T , is just $\log_2 N$ (the number of successive decisions needed) times τ :

$$T_s \approx \frac{N_0}{A^2} (\log_2 N)^2 \ln(\log_2 N) \quad (9)$$

In contrast, consider the amount of time needed in searching serially for the correct phase of a maximum-length shift-register sequence of length N . If the received and locally-generated sequences are in-phase, the expected correlator output is $A \tau$; if they are not in-phase, it is $-\frac{A}{N} \tau$. Thus, using the value $\frac{N-1}{2N} A \tau$ as a threshold, (an output is interpreted as an in-phase reading if this threshold is exceeded, and an out-of-phase reading otherwise), the probability P_0 of a correct decision at any step is again given by Eq. (6), but now with $\mu = \frac{N+1}{2N} A \tau$. The probability of a correct decision P'_c is approximately⁴

$$\begin{aligned} P'_c &= \sum_{v=1}^N \Pr(\text{correct decision} \mid v \text{ phases observed}) \\ &\quad \times \Pr(v \text{ phases observed}) \\ &= \frac{1}{N} \sum_{v=1}^N P_0^v = \frac{P_0}{N} \frac{(1 - P_0^N)}{1 - P_0} \approx 1 - \frac{N+1}{2} (1 - P_0) \end{aligned} \quad (10)$$

⁴This formulation ignores the possibility of missing the correct phase on the first attempt and finding it on a subsequent try. The probability of this event will generally be small.

where P_0 is assumed to be nearly unity. Thus

$$P'_c \approx 1 - \frac{N+1}{2\sqrt{\pi}} \frac{e^{-\left(\frac{N+1}{2N}\right)^2 \left(\frac{A^2\tau}{N_0}\right)}}{\left(\frac{N+1}{N}\right) \left(\frac{A^2\tau}{N_0}\right)^{1/2}} \\ \approx 1 - \frac{1}{2\sqrt{\pi}} \frac{e^{-\left(\frac{A^2\tau}{4N_0} - \ln N\right)}}{\left(\frac{A^2\tau}{N_0}\right)^{1/2}} \quad (11)$$

and τ must be on the order of $\frac{N_0}{A^2} \ln N$. The expected number of correlations needed for an acquisition is approximately $N/2$, yielding for the total search time

$$T'_s \approx \frac{N_0}{A^2} \frac{N}{2} \ln N \quad (12)$$

When N is large, T'_s can well be orders of magnitude greater than the T_s of Eq. (9).

Of course, more sophisticated search procedures, including those involving sequential decisions, could be used with either class of sequences. In the latter situation, in fact, in which all but one of the phases being observed yield identical correlation, a substantial saving in search time can be realized by always investigating the phase currently most likely to be the correct one (Ref. 3). Unfortunately, this involves making many very rapid decisions concerning each possible phase, and, since here it is the correlation over the complete sequence that is constrained rather than short-term correlations, rapid decisions are generally not meaningful. In practice, while the search time with either class of sequences can be decreased by these more sophisticated techniques, it remains on the same order of magnitude in either case, and, consequently, does not affect the relative advantage of the rapid-acquisition sequences.

This problem of the short-term, or "local" correlation properties of these sequences, incidentally, is often significant even when the sequential decision techniques of the previous paragraph are not being used. The times needed for the individual decisions were derived under the assumption that the expected Correlation between the received and locally-generated signals is as stated. But this is true only if the correlation proceeds for an integer

number of periods of the sequence. **If** the decision time is, in fact, less than one period of the sequence, the decision made may be unreliable because the actual expected correlation is not as assumed. Some efforts have been made to characterize the local correlation properties of maximal-length sequences. They seem to indicate that the decision time can indeed be considerably less than the sequence length without causing any significant bias in the decision. The rapid-acquisition sequences seem to be less favorably endowed in this regard. On the other hand, the time needed for each decision is greater with these sequences by a factor of $\log_2 N$ relative to the shift-register sequences, so the local correlation problem is much less significant in this case.

Another property of the rapid-acquisition sequences may be useful in increasing the reliability of the search; viz., if an erroneous decision is made at the $(i-1)$ st stage, the expected correlation at the i th stage of the search will be essentially zero. Thus, if, at any stage of the search, the correlation obtained is not sufficiently different from zero, the decision of the previous stage might be re-investigated. To verify this property of the rapid-acquisition sequences, observe, first of all, that the product of two coherent square waves, one with period T_s and the other with period $2T_s$, is a square wave with period $2T_s$ shifted 90 deg relative to the original square wave of that period. That is, if $s_1 = 1, -1, 1, -1, 1, -1$, and $s_2 = 1, 1, -1, -1, 1, 1, \dots$ represent two square waves, then $s_1 \cdot s_2 = 1, -1, -1, 1, 1, -1, \dots$ and has the same period as the sequence s_2 , but is shifted 90 deg relative to it. If an erroneous decision is made at the $(i-1)$ st stage, the correlation performed at the i th stage is not with the sequence s_i , but rather with s_i shifted by ± 90 deg, that is, with the sequence $\pm s_{i-1} s_i$. But the correlation between x and $\pm s_{i-1} s_i$ is just $\rho = \pm(2A-N)/N$ where A is the number of times the i th term of x is positive and $\sigma_{i-1}^i = \sigma_i^i$ plus the number of times the i th term of x is negative and $\sigma_{i-1}^i = -\sigma_i^i$. Therefore,

$$A = \sum_{i=0}^{\left[\frac{n}{2}\right]} \binom{n-2}{i} + 2 \sum_{i=0}^{\left[\frac{n-3}{2}\right]} \binom{n-2}{i} \\ + \sum_{i=0}^{\left[\frac{n-4}{2}\right]} \binom{n-2}{i} \quad (13) \\ = \begin{cases} 2^{n-1} & n \text{ odd} \\ 2^{n-1} + \binom{n-2}{\frac{n}{2}} - \binom{n-2}{\frac{n}{2}-1} & n \text{ even} \end{cases}$$

Thus,

$$\rho = \begin{cases} 0 & n \text{ odd} \\ \pm \frac{1}{2^{n-1}} \frac{1}{\left(\frac{n}{2}-1\right)} \left(\frac{n-2}{2}\right) & n \text{ even} \end{cases} \quad (14)$$

4. Enhancing the Clock

In the discussion up to this point, a "clock" has been assumed to be available. The clock provides the basic timing whereby the periods of the received sequence and the locally-generated sequences can be kept equal. Moreover, because of the clock, only a finite number rather than a continuum of phases needs to be considered. Typically, the clock is transmitted in the form of a sinusoid or a square wave and "tracked" at the receiver with a phase-locked loop or similar device. Actually, the clock component, if it too is a square wave, can be transmitted over the same channel as the other sequences, as discussed in the previous sections; i.e., the square wave with the shortest period is used as the clock. Now, however, it is necessary to be able to distinguish the actual phase of the received clock component to within some tolerable error. It is no longer sufficient to determine whether the local clock is in phase or 180° out of phase with the transmitted clock. For this reason, it may be necessary to allocate more power to this clock component than before. That is, since the clock is conveying more information than the other components, it generally should represent more power.

A simple method for enhancing the clock component in the transmitted sequence, while still retaining its binary character, is as follows: the clock is represented as the sequence $a, -a, a, -a, a, \dots$ while all the other component sequences are represented by $+1$'s and -1 's, as before. The composite sequence terms are again determined by taking the sign of the sum of the corresponding terms in each of the component sequences. (If the sum is zero, the sign is again taken to be positive.) Thus, suppose $N = 16$ and $a = 2$. Then the composite sequence is defined as follows:

$$\begin{array}{cccccccccccccccc} 2 & -2 & 2 & -2 & 2 & -2 & 2 & -2 & 2 & -2 & 2 & -2 & 2 & -2 & 2 & -2 \\ 1 & 1 & -1 & -1 & 1 & 1 & -1 & -1 & 1 & 1 & -1 & -1 & 1 & 1 & -1 & -1 \\ 1 & 1 & 1 & 1 & -1 & -1 & -1 & -1 & 1 & 1 & 1 & 1 & -1 & -1 & -1 & -1 \\ 1 & 1 & 1 & 1 & 1 & 1 & 1 & 1 & -1 & -1 & -1 & -1 & -1 & -1 & -1 & -1 \\ \hline 1 & 1 & 1 & -1 & 1 & -1 & 1 & -1 & 1 & -1 & 1 & -1 & 1 & -1 & -1 & -1 \end{array}$$

The (normalized) correlation between the transmitted sequence and the clock is, in this case, $3/4$, while that between it and any of the other component sequences is $1/4$.

Obviously, increasing the value of a increases the correlation between the composite sequence and the clock at the expense of its correlation with the other component sequences. This effect is readily determined quantitatively by a straightforward extension of the arguments of section 2. The correlation between the composite sequence and the clock sequence for an arbitrary integer a

is found to be $\frac{P}{P} c\ell = \frac{2A-N}{N}$ where

$$A = 2 \left[\sum_{i=0}^{\left\lfloor \frac{n-1+a}{2} \right\rfloor} \binom{n-1}{i} \right] - \left(\frac{n-1}{\frac{n-1+a}{2}} \right)$$

where the binomial coefficient $\binom{n-1}{\frac{n-1+a}{2}}$ is taken to zero if $\frac{n-1+a}{2}$ is not an integer, and where $[x]$ denotes the integer part of x . Similarly, the correlation between the composite sequence and any one of the component sequences is $\rho_{com} = \frac{2B-N}{N}$, where

$$B = 2 \left[\sum_{i=0}^{\left\lfloor \frac{n-1+a}{2} \right\rfloor} \binom{n-2}{i} \right] - \left(\frac{n-2}{\frac{n-1+a}{2}} \right) + 2 \left[\sum_{i=0}^{\left\lfloor \frac{n-1-a}{2} \right\rfloor} \binom{n-2}{i} \right] - \left(\frac{n-2}{\frac{n-1-a}{2}} \right)$$

Clearly, if $a > n-1$, $\rho_{cl} = 1$ while $\rho_{com} = 0$. At the other extreme, when $a = 1$, the situation discussed in section 2 obtains, with $\rho_{cl} = \rho_{com}$. By choosing the proper value of a , almost any desired clock correlation can be obtained, particularly when the sequence length is large. Other clock correlations can be obtained by using the sequence $a, -b, a, -b, \dots$ rather than the $a, -a, a, -a, \dots$ in

determining the composite sequence. Still other results occur when other sequences are used, although, in general, the correlations between the composite and component sequences will no longer be identical for all of the component sequences.

5. Conclusions

A class of binary sequences which lend themselves to rapid acquisition when serial binary decisions are prescribed has been presented. It was shown that these sequences suffer a degradation of only a factor of $2/\pi$ (in power) relative to the optimum (non-binary) acquirable sequences under these constraints. The ratio of the time needed to acquire one of these sequences of length N to that needed using a shift-register sequence of the same length was found to be approximately $2(\log_2 N)\log_2(\log_2 N)/N$. This ratio obviously decreases very rapidly as N increases and is already only **3/16** when $N = 256$. Finally, several techniques for increasing the "strength of the clock component in the composite sequence were explored.

It is interesting to note that the requirement of *binary* decisions at each step is not really a significant limitation. Returning to the separate channel method, suppose that $\log_2 N$ channels are used, each channel designed to reduce the ambiguity by a factor of m . Then each channel can represent $\left(\frac{1}{\log_m N}\right)^{th}$ of the total power, and the integration time must be sufficient to resolve the correlation between the received and locally-generated signals to one of m levels. Thus, paralleling the arguments of section 3, we find the time needed for each decision is proportional to $\frac{m^2}{4} \frac{N_0}{A^2} \log_2 N \ln(\log_m N)$, and the total search time is proportional to

$$T_s'' \approx \frac{m^2}{4} \frac{N_0}{A^2} (\log_m N)^2 \ln(\log_m N)$$

Treating m as a continuous variable and differentiating, we find T_s'' attains a minimum when

$$\log_e m = 1 + \frac{1}{2 \ln \left(\frac{\ln N}{\ln m} \right)} \approx 1$$

or when $m \approx e$. Consequently, the optimum situation occurs when $m = 2$ or $m = 3$, and little is lost by requiring the decisions to be binary.

B. Combinatorial Communication: A New Interpretation of a Basic Combinatorial Formula,⁵ S. W. Golomb

A basic problem of elementary enumeration is the number of samples of size r from a population of size k , with or without replacement, and with or without regard to order. The four answers are well known to be:

- 1) With replacement and regarding order: k^r .
- 2) Without replacement and regarding order: $(k)_r$.
- 3) With replacement and disregarding: $\binom{k+r-1}{r}$.
- 4) Without replacement and disregarding order: $\binom{k}{r}$.

All of these formulas are immediate except the third, which is customarily proved by the artifice of including $k - 1$ "partitions" along with the r samples, and then selecting a subset of r objects from this mixed assortment of $k - 1 + r$ objects (Ref. 4).

Another proof of the third formula can be given, based on a different interpretation of the underlying situation, as follows:

Let the k elements of the population be regarded as cards numbered from 1 to k . We are interested in the number of r -card hands which can be formed from the k -card deck, allowing repetition. To the k -card deck, we adjoin $r - 1$ extra "wild" cards, numbered from $k + 1$ to $k + r - 1$, and bearing the respective instructions:

- $k + 1$: "repeat lowest-numbered card"
 $k + 2$: "repeat 2nd lowest-numbered card"

•	•	•	•	•
•	•	•	•	•
•	•	•	•	•
•	•	•	•	•

- $k + r - 1$: "repeat $(r - 1)$ th lowest numbered-card."

Then the r -card hands *without* repetition from this enlarged $k + r - 1$ card deck are in natural one-to-one

⁵Prepared under JPL contract 951076 with the University of Southern California, Electrical Engineering Dept., Los Angeles.

correspondence with the r-card hands *allowing* repetition from the original k-card deck. The reader can supply the correspondence.

N67 18348

C. Communication Systems Development: Minimizing Range Code Acquisition Time,

R. C. Tausworthe

1. Introduction

The application of composite coding to ranging schemes (Refs. 1, 5 and 6) has produced systems capable of very accurate, relatively quick distance measurements, with large unambiguous range intervals. Optimization of these codes (Ref. 2) without constraint leads to a set of requirements on the component sequences not physically consistent, but does indicate what the important features are. For example, an unconstrained optimum would require all the components to be short PN sequences of the same period; but short codes combine to make longer ones only when their periods are different, and pseudonoise sequences only exist for periods of the form $p = 4N + 3$.

Still, the optimization shows that the components should be short, relatively prime in length, and have distinguishable correlation functions.

Based on the supposition that all periods are equal, optimum choice of the encoding logic leads to a code having equal cross-correlation characteristics with each component sequence. Since the periods cannot be actually the same, there may sometimes be a better encoding logic than the one producing equal component correlations. This article investigates coding to minimize acquisition time under the constraint that all periods be different.

2. Probability of Correct Acquisition

The probability that a particular component having two-level autocorrelation with period is correctly acquired by maximum-likelihood techniques is given by

$$P = \frac{1}{\sqrt{\pi}} \int_{-\infty}^{+\infty} e^{-x^2} \left\{ \frac{1}{2} [1 + \operatorname{erf}(x + \beta)] \right\}^{p-1} dx$$

in which $\operatorname{erf}(\)$ is the error function (Ref. 7) and β is defined by

$$\beta = C_{\max}(1 - C_{\min}/C_{\max}) \sqrt{\frac{ST}{N_0}}$$

The parameters appearing in β are

$\frac{S}{N_0}$ = The signal-power-to-noise-spectral-density ratio

T = The integration time-per-phase

C_{\min}, C_{\max} = The minimum and maximum normalized cross-correlation values between the composite code and the component sequence

The total time required to correlate each phase sequentially is

$$T' = pT = \frac{(N_0/S) p \beta^2}{C_{\max}^2 (1 - C_{\min}/C_{\max})^2}$$

which for an n-component code, yields a total acquisition time of

$$T_{\text{acq}} = \sum_{i=1}^n T'_i = (N_0/S) \sum_{i=1}^n \frac{p_i \beta_i^2}{C_{\max(i)}^2 [1 - C_{\min(i)}/C_{\max(i)}]^2}$$

The probability of correct acquisition is

$$P_{\text{acq}} = \prod_{i=1}^n P_i$$

Under the assumption that it is desirable to acquire each component with equal likelihood, we set $P_i = P_j$ and have

$$P_i = P_{\text{acq}}^{1/n}$$

3. Minimization of the Acquisition Time

Suppose we are given a desired P_{acq} ; to achieve this, we compute each P_i , and translate this into a value of β_i . Suppose also that we elect to use PN sequences, for these maximize $(1 - C_{\min}/C_{\max})$ and thus tend to minimize T_{acq} . Under this latter assumption,

$$1 - C_{\min}/C_{\max} = (1 + p)/p$$

Since T_{acq} decreases monotonically with each C_{\max} , we must find a set of $C_{\max(i)}$, subject to realizability, that are mutually as large as possible. It is known (Ref. 2) that the $C_{\max(i)}$ are constrained by the relation

$$\sum_{i=1}^n C_{\max(i)} \approx 2^{-n} \sum_{\mathbf{x}} f(\mathbf{x}) [n - 2 || \mathbf{x} ||]$$

where $f(\mathbf{x})$ is the encoding logic function, $f(\mathbf{x}) = \pm 1$, \mathbf{x} is a binary (0,1) vector truth-table variable, and $\|\mathbf{x}\|$ denotes the number of *ones* in \mathbf{x} . (The approximation is due only to an imbalance of ± 1 's in the component sequences.) Note for example that $\sum C_{\max}$ is greatest when $f(\mathbf{x})$ is a majority-vote logic, i.e. when $f(\mathbf{x}) = 1$ if $\|\mathbf{x}\| < n/2$ and $f(\mathbf{x}) = -1$ if $\|\mathbf{x}\| > n/2$. Tie votes when n is even are immaterial to the sum, but change individual values of $C_{\max(i)}$.

We shall fix the sum $\sum C_{\max(i)} = \alpha$ to find how each $C_{\max(i)}$ should be related to the period p_i . Using standard Lagrange multiplier techniques, we define $\Phi = T_{\text{acq}} + \lambda (\sum C_{\max(i)} - \alpha)$. Then optimum $C_{\max(i)}$ values satisfy

$$\frac{\partial \Phi}{\partial C_{\max(i)}} = -2 \left(\frac{N_0}{S} \right) \left[\frac{p_i^3}{(1+p_i)^2} \right] \frac{\beta_i^2}{C_{\max(i)}^3} + \lambda = 0$$

Hence we see that each $C_{\max(i)}$ is related to the period p_i of its component sequence by

$$C_{\max(i)} = K \beta_i^{2/3} \frac{p_i}{(1+p_i)^{2/3}}$$

For some constant K , evaluated to be

$$K = \alpha \left[\sum_i \beta_i^{2/3} \frac{p_i}{(1+p_i)^{2/3}} \right]^{-1}$$

The optimum value of T_{acq} can now be computed:

$$\begin{aligned} T_{\text{acq}}^{(\text{opt})} &= \frac{1}{\alpha^2} \left(\frac{N_0}{S} \right) \left\{ \sum_{i=1}^n \left[\beta_i^{2/3} \frac{p_i}{(1+p_i)^{2/3}} \right] \right\}^3 \\ &= \alpha (N_0/S) / K^3 \end{aligned}$$

Example: Assume we are given the following:

$$\begin{aligned} n &= 6 & p_3 &= 11 \\ N_0/S &= -9.6\text{db} = .11 & p_4 &= 15 \\ P_i &= 0.99, i=1, \dots, 6 & p_5 &= 19 \\ p_1 &= 2 & p_6 &= 23 \\ p_2 &= 7 \end{aligned}$$

The β_i^2 compute to be

$$\begin{aligned} \beta_1^2 &= 5.41 & \beta_4^2 &= 9.73 \\ \beta_2^2 &= 8.35 & \beta_5^2 &= 10.14 \\ \beta_3^2 &= 9.18 & \beta_6^2 &= 10.47 \end{aligned}$$

In the usual case, and we shall assume it here, the first component having length $p_1 = 2$ is acquired differently than the rest; we shall further suppose that for practical reasons it is necessary to maintain 25% correlation with this component. With α set equal to its maximum value of 1.875, we can modify the previous theory to include optimization over the remaining five correlation values.

First we compute

$$\begin{aligned} K &= \frac{1.625}{\sum_{i=2}^6 \beta_i^{2/3} p_i / (1+p_i)^{2/3}} \\ &= \frac{1.625}{24.62} = 0.066 \end{aligned}$$

and then the desired values of correlation:

$$\begin{aligned} C_{\max(1)} &= 0.250 & C_{\max(4)} &= 0.333 \\ C_{\max(2)} &= 0.234 & C_{\max(5)} &= 0.368 \\ C_{\max(3)} &= 0.290 & C_{\max(6)} &= 0.399 \end{aligned}$$

These are the values we would like to have if the encoding logic were capable of giving a continuous range of values. Being discrete, however, the set of correlation values most nearly equal to those above is obtained from the encoding logic whose truth-table appears in Table 1, which has

$$\begin{aligned} C_{\max(1)} &= 0.2616 & \Delta_1 &= 0.0116 \\ C_{\max(2)} &= 0.2498 & \Delta_2 &= 0.0158 \\ C_{\max(3)} &= 0.3104 & \Delta_3 &= 0.0204 \\ C_{\max(4)} &= 0.3143 & \Delta_4 &= -0.0187 \\ C_{\max(5)} &= 0.3694 & \Delta_5 &= 0.0014 \\ C_{\max(6)} &= 0.3918 & \Delta_6 &= -0.0072 \end{aligned}$$

—an outstanding fit. In fact, the C_{\max} values above are better than the desired ones listed previously; this is due to the fact that the constraint $\sum C_{\max} = \alpha$ is only approximate, being affected by the imbalance of ± 1 's in the

Table 1. An optimum ranging encoding logic

x ₁	x ₂	x ₃	x ₄	x ₅	x ₆	f(x)	x ₁	x ₂	x ₃	x ₄	x ₅	x ₆	f(x)
0	0	0	0	0	0	0	1	0	0	0	0	0	0
0	0	0	0	0	1	0	1	0	0	0	0	1	0
0	0	0	0	1	0	0	1	0	0	0	1	0	0
0	0	0	0	1	1	0	1	0	0	0	1	1	0
0	0	0	1	0	0	0	1	0	0	1	0	0	0
0	0	0	1	0	1	0	1	0	0	1	0	1	0
0	0	0	1	1	0	0	1	0	0	1	1	0	1
0	0	0	1	1	1	1	1	0	0	1	1	1	1
0	0	1	0	0	0	0	1	0	1	0	0	0	0
0	0	1	0	0	1	0	1	0	1	0	0	1	0
0	0	1	0	1	0	0	1	0	1	0	1	0	1
0	0	1	0	1	1	1	1	0	1	0	1	1	1
0	0	1	1	0	0	0	1	0	1	1	0	0	0
0	0	1	1	0	1	1	1	0	1	1	0	1	1
0	0	1	1	1	0	1	1	0	1	1	1	1	1
0	1	0	0	0	0	0	1	1	0	0	0	0	0
0	1	0	0	0	1	0	1	1	0	0	0	1	1
0	1	0	0	1	0	0	1	1	0	0	1	0	0
0	1	0	0	1	1	1	1	1	0	0	1	1	1
0	1	0	1	0	0	0	1	1	0	1	0	0	0
0	1	0	1	0	1	1	1	1	0	1	0	1	1
0	1	0	1	1	0	0	1	1	0	1	1	0	1
0	1	0	1	1	1	1	1	1	0	1	1	1	1
0	1	1	0	0	0	0	1	1	1	0	0	0	1
0	1	1	0	0	1	0	1	1	1	0	0	1	1
0	1	1	0	1	0	0	1	1	1	0	1	0	1
0	1	1	0	1	1	1	1	1	1	0	1	1	1
0	1	1	1	0	0	0	1	1	1	1	0	0	1
0	1	1	1	0	1	1	1	1	1	1	0	1	1
0	1	1	1	1	0	1	1	1	1	1	1	0	1
0	1	1	1	1	1	1	1	1	1	1	1	1	1

component sequences. The values listed were obtained with each PN sequence having an excess -1.

Acquisition time of the latter five components is about 617 sec; the "ideal" values would require 621 sec; and a symmetric majority logic would require 735 seconds! The modified majority logic, in this case, affords a saving of almost two minutes over a symmetric majority.

D. Communication Systems Development: Cycle Slipping in Phase-locked loops, R. C. Tausworthe

1. Introduction

Cycle slipping in phase-locked receivers is an observed phenomenon that is unpredictable and not accounted for by linear theories of loop operation. Viterbi (Ref. 8) was able to solve a Fokker-Planck equation to arrive at the expected time from lock to a slipped cycle for a first-order loop; however, extensions to higher-order loops by these methods have not, as yet, been forthcoming.

This article shows that the expected first-slip time of a loop of arbitrary order satisfies a linear differential equation reducible to one of the first order, to which formal solutions, at least, are easily given. The derivation follows directly from a random-walk model not restricted to processes of the Markov type. computation of an exact solution involves being able to evaluate a certain conditional expectation, which ordinarily requires a prior solution for the probability function of the phase-error process. For the first-order loop, however, the expectation can be evaluated directly without computing $p(\phi, \dot{\phi})$, so the method yields the exact result. Rather than attempting to compute $p(\phi, \dot{\phi})$, for higher-order loops (which is still an unsolved problem), this article presents an approximate evaluation of the expectation valid for loops of any order. Specific behavior of second-order loop cycle-slipping is evaluated.

2. The Random-Walk Model

Let $\{x(t)\}$ be a stochastic process, and let t_0 be any observed time such that for a particular sample function $x(t)$ we have $|x(t_0)| < \lambda$, where λ is a given constant. Let $\tau(x_0)$ be the time required for the sample function starting from x_0 at t_0 to reach or pass the limits $\pm \lambda$ for the first time; that is, $\tau(x_0)$ is the random variable defined by

$$\tau(x_0) = \sup \{ \tau; |x(t_0 + \delta)| < \lambda \text{ for all } 0 \leq \delta < \tau \} \quad (1)$$

Given t_0 and x_0 , the mean value of $\tau(x_0)$ will be denoted

$$T(x_0) = E \{ \tau(x_0) | t_0, x_0 \} \quad (2)$$

Now let $\Delta t > 0$ be given, and define $\Delta x_0 = x(t_0 + \Delta t) - x(t_0)$; naturally Δx_0 is a random variable depending on

x_0 . For a particular sample function, let us suppose Δx_0 is observed. Then it follows (Fig. 1) that

$$\tau(x_0) = \Delta t + \tau(x_0 + \Delta x_0) \quad (3)$$

That is, the time required to reach a limit from x_0 is Δt seconds longer than the time from a point $x_0 + \Delta x_0$ observed Δt seconds later. Then when we average, given x_0 ,

$$T(x_0) = \Delta t + E \{ \tau(x_0 + \Delta x_0) | x_0 \} \quad (4)$$

The latter expectation can be accomplished in two steps: first by averaging with Δx_0 fixed, and then averaging with respect to Δx_0 .

$$\begin{aligned} T(x_0) &= \Delta t + E_{\Delta x_0} E \{ \tau(x_0 + \Delta x_0) | x_0, \Delta x_0 \} \\ &= \Delta t + E_{\Delta x_0} T(x_0 + \Delta x_0) \end{aligned} \quad (5)$$

Now let us suppose $T(x_0)$ admits of a Taylor series:

$$T(x_0 + \Delta x_0) = T(x_0) + \Delta x_0 T'(x_0) + \frac{1}{2} (\Delta x_0)^2 T''(x_0) + \dots \quad (6)$$

Inserted into the equation immediately preceding it, this last equation provides the result

$$\begin{aligned} \Delta t + E [\Delta x_0 | x_0] T'(x_0) + \\ + \frac{1}{2} E [(\Delta x_0)^2 | x_0] T''(x_0) + \dots = 0 \end{aligned} \quad (7)$$

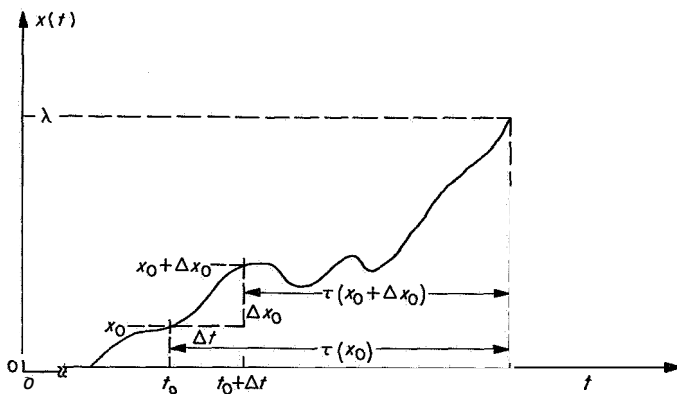


Fig. 1. The time required for a particular sample function to reach $\pm \lambda$ from an observed x_0 at t_0 is Δt longer than the time required from the point $x_0 + \Delta x_0$ observed Δt later

In the limit as $\Delta t \rightarrow 0$, presuming that higher-order terms become negligible, we find that $T(x_0)$ satisfies the linear differential equation

$$T''(x_0) + g(x_0)T'(x_0) + h(x_0) = 0 \quad (8)$$

where $g(x_0)$ and $h(x_0)$ are the functions

$$\begin{aligned} g(x_0) &= 2 \lim_{\Delta t \rightarrow 0} \frac{E[\Delta x_0 | x_0]}{\Delta t} \cdot \frac{\Delta t}{E[(\Delta x_0)^2 | x_0]} \\ h(x_0) &= 2 \lim_{\Delta t \rightarrow 0} \frac{\Delta t}{E[(\Delta x_0)^2 | x_0]} \end{aligned} \quad (9)$$

The solution $T(x_0)$ is subject to the boundary condition

$$T(\lambda) = T(-\lambda) = 0 \quad (10)$$

The absence of a $T(x)$ term in Eq. (8) allows reduction of the differential equation to a standard form of substituting $y = T'$:

$$y' + gy + h = 0 \quad (11)$$

The solution to Eq. (11) is known (Ref. 9) to be

$$y = \exp \left(- \int^x g dz \right) \left[k - \int^x h \exp \left(\int^w g dz \right) dw \right] \quad (12)$$

and the value of $T(x_0)$ is then merely the integral of this y . By setting the upper limits of integration equal to λ , one of the boundary constraints in the solution to $T(x_0)$ is satisfied.

$$\begin{aligned} T(x_0) &= \int_{x_0}^{\lambda} \exp \left(\int_x^{\lambda} g(z) dz \right) \\ &\times \left[k - \int_x^{\lambda} h(w) \exp \left(- \int_w^{\lambda} g(z) dz \right) dw \right] dx \end{aligned} \quad (13)$$

At $x_0 = -\lambda$, the remaining boundary condition gives

$$k = \frac{\int_{-\lambda}^{\lambda} \int_x^{\lambda} h(w) \exp \left(\int_x^w g(z) dz \right) dw dx}{\int_{-\lambda}^{\lambda} \exp \left(\int_x^{\lambda} g(z) dz \right) dx} \quad (14)$$

It is clear from Eq. (12) that k is related to the point at which $T(x_0)$ takes a zero derivative; specifically, if x_{\max} denotes the value of x_0 such that $T'(x_{\max}) = 0$, then

$$k = \int_{x_{\max}}^{\lambda} h(w) \exp \left(- \int_w^{\lambda} g(z) dz \right) dw \quad (15)$$

This latter expression, when x_{\max} is known from other considerations, permits a simplification of Eq. (13); with k eliminated,

$$T(x_0) = \int_{x_0}^{\lambda} \int_{x_{\max}}^x h(w) \exp\left(\int_x^w g(z) dz\right) dw dx \quad (16)$$

3. Relating g and h to loop Parameters

Let $\phi(t)$ be the phase-error process of a phase-locked loop subjected to a constant frequency offset; it is described by the equation (Ref. 10)

$$\dot{\phi} = \Omega_0 - AKF(p) \left[\sin \phi + \frac{n(t)}{A} \right] \quad (17)$$

where, in the usual model, A is the rms input signal voltage, K is the open-loop gain, $F(s)$ is the loop filter, Ω_0 is the VCO frequency offset, $p = d/dt$ is the Heaviside operator, and $n(t)$ is a stationary white noise with spectral density N_0 . Purely for convenience, we shall treat only the case $\Omega_0 = 0$; then by symmetry, $T'(0) = 0$, so Eq. (16) supplies the equation to be evaluated, with x_{\max} set to zero. One of the quantities in Eq. (9) to be determined is

$$\begin{aligned} E[\Delta\phi_0 | \phi_0] &= E\left[\int_{t_0}^{t_0+\Delta t} \dot{\phi} dt | \phi_0\right] \\ &= - \int_{t_0}^{t_0+\Delta t} AKF(p) \left\{ E\left[\sin \phi | \phi_0\right] \right. \\ &\quad \left. + E\left[\frac{n(t)}{A} | \phi_0\right] \right\} dt \end{aligned} \quad (18)$$

The random portion of $\Delta\phi_0$, designated ν , is then

$$\begin{aligned} \nu &= \Delta\phi_0 - E[\Delta\phi_0 | \phi_0] \\ &= \int_{t_0}^{t_0+\Delta t} AKF(p) \left\{ \sin \phi - E\left[\sin \phi | \phi_0\right] \right. \\ &\quad \left. - E\left[\frac{n(t)}{A} | \phi_0\right] + \frac{n(t)}{A} \right\} dt \end{aligned} \quad (19)$$

Let us denote the loop filter impulse response by $f(t)$. Computationally, the operator notation we have used indicates

$$F(p) y(t) = \int_0^\infty f(\tau) y(t - \tau) d\tau \quad (20)$$

We shall assume that $f(t)$ is of the form

$$f(t) = F\delta(t) + c(t) \quad (21)$$

where $c(t)$ is continuous on $(0, \infty)$, and the constant F is merely $F(\infty)$. The variance of ν , here designated σ_ν^2 , is readily calculated to the terms of the order $(\Delta t)^2$:

$$\sigma_\nu^2 = K^2 F^2 N_0 \Delta t + 0(\Delta t^2) \quad (22)$$

All higher-order moments of ν are at least $0(\Delta t^2)$, and as a result

$$\lim_{\Delta t \rightarrow 0} \frac{E[(\Delta\phi_0)^N | \phi_0]}{\Delta t} = 0 \quad (23)$$

for all $N > 2$.

The conclusion at this point is that *differential Eq. (8) holds exactly for all order loops*, and solutions depend only upon being able to compute g and h . But from Eq. (22) we have

$$\lim_{\Delta t \rightarrow 0} \frac{E[(\Delta\phi_0)^2 | \phi_0]}{\Delta t} = K^2 F^2 N_0 \quad (24)$$

and from Eq. (18) we have

$$E(\dot{\phi}_0 | \phi_0) = \lim_{\Delta t \rightarrow 0} \frac{E[\Delta\phi_0 | \phi_0]}{\Delta t} \quad (25)$$

from which g and h are determined. If we denote $E(\dot{\phi}_0 | \phi_0)$ by μ ,

$$\begin{aligned} h &= \frac{2}{K^2 F^2 N_0} \\ g &= \frac{2\mu}{K^2 F^2 N_0} = p h \end{aligned} \quad (26)$$

As a further note of interest, we see that whenever $F = 0$, differential Eq. (8) reduces to one of the first order

$$T'(\phi_0) + \frac{1}{\mu} = 0 \quad (27)$$

from which $T(\phi_0)$ is immediately obtainable whenever μ can be calculated.

4. First-Order loop

With $F(s) = 1$, **Eq. (17)** describes the first-order loop. Trivially, **Eq. (25)** gives

$$h = \frac{2}{K^2 N_0} = \frac{\rho}{2w_L}$$

$$g = \frac{-2AK \sin \phi_0}{K^2 N_0} = -\rho \sin \phi_0 \quad (28)$$

where $p = A^2/N_0 w_L$ (i.e., the SNR in the loop bandwidth w_L as in Ref. 10).

By setting $\lambda = 2\pi$, **Eq. (16)** gives the mean time to a skipped cycle. Then Viterbi's result (which he obtained a different way) follows.

$$T = T(0) = \frac{\rho}{2w_L} \int_0^{2\pi} \exp(-\rho \cos x) \int_0^x \exp(\rho \cos w) dw$$

$$= \pi^2 p I_0^2(\rho)/w_L \quad (29)$$

in which $I_0(\rho)$ is the zero-order modified Bessel function of the first kind. Asymptotically, for large p ,

$$T = \frac{\pi e^{2\rho}}{2w_L} \quad (30)$$

5. Approximations to Higher-Order loops

We have defined $\mu = E[\dot{\phi}_0 | \phi_0]$, a quantity not strictly computable for higher-order loops because $p(\phi, \dot{\phi})$ is unknown. From **Eq. (18)**, however, we find that the form of μ is

$$\mu = -AKF \sin \phi_0 - AKF \int_0^{t_0} c(t_0 - x) \left\{ E \left[\sin \phi(x) \right]_{\phi_0} + E \left[\frac{n(x)}{A} \right]_{\phi_0} \right\} dx$$

$$= -AKF \sin \phi_0 + B(\phi_0) \quad (31)$$

in which $B(\phi_0)$ is an odd function in ϕ_0 , hence of the form

$$B(\phi_0) = b_1 \phi_0 + b_3 \phi_0^3 + \dots \quad (32)$$

We now note that

$$E(\dot{\phi}_0 \phi_0) = E_{\phi_0} [\phi_0 E(\dot{\phi}_0 | \phi_0)] = E_{\phi_0} [\phi_0 \mu]$$

$$= -AKF E[\phi_0 \sin \phi_0] + E[\phi_0 B(\phi_0)] \quad (33)$$

The first coefficient b_1 of $B(\phi_0)$ may be evaluated by resorting to linear loop theory. During those times of loop operation when ϕ is small, there is a linear operator relationship between ϕ and the loop noise. Specifically,

$$\phi = -L(p) \left[\frac{n(t)}{A} \right] \quad (34)$$

where $L(s)$ is the well-known loop transfer function

$$L(s) = \frac{AKF(s)}{s + AKF(s)} \quad (35)$$

By fairly straightforward means, it is possible to show that

$$E(\dot{\phi} \phi) = \frac{-N_0}{2A^2} \ell^2(0)$$

$$= -\ell^2(0)/2w_L \rho \quad (36)$$

in which $\ell(\tau)$ is the unit impulse response of $L(s)$, and, in particular,

$$\ell(0) = \lim_{s \rightarrow \infty} sL(s) \quad (37)$$

It then follows that

$$-\frac{\ell^2(0)}{2w_L \rho} = (-AKF + b_1) \sigma_\phi^2 + O(\sigma_\phi^4)$$

$$= (-AKF + b_1)/\rho + O\left(\frac{1}{\rho^2}\right) \quad (38)$$

which leads, in the limit as $p \rightarrow \infty$, to the conclusion that

$$b_1 = AKF - \ell^2(0)/2w_L \quad (39)$$

Thus we have

$$\mu = -AKF \sin \phi_0 + (AKF - l^2(0)/2w_L)\phi_0 + \dots \quad (40)$$

The remaining coefficients b_i , if needed, must be evaluated by other means. Fortunately, for the second-order loop, and perhaps for those of higher order as well, this does not seem to be necessary to provide excellent approximations to actual behavior.

6. Applications to the Second-Order loop

As a specific example of the approximation in the previous section, let us assume that $F(s)$ takes the form

$$F(s) = \frac{1 + \tau_2 s}{\tau_1 s} \quad (41)$$

We then have $F = \tau_2/\tau_1$; furthermore, AK and τ_2 are related to the loop damping and bandwidth parameters r ,

and w_L by (Ref. 10)

$$r = \frac{AK\tau_2^2}{\tau_1} = 4\xi^2$$

$$w_L = \frac{r+1}{2\tau_2} \quad (42)$$

In terms of these and the loop SNR, $\rho = A^2/N_0 w_L$, the parameters h and $l(0)$ are

$$h = \frac{2}{K^2 F^2 N_0} = \frac{1}{2} \left(\frac{r+1}{r} \right)^2 \frac{\rho}{w_L}$$

$$l(0) = AKF = \frac{2rw_L}{r+1} \quad (43)$$

Digital computer (Ref. 12) implementations of loop Eq. (17) for the second-order loop of which Fig. 2 is

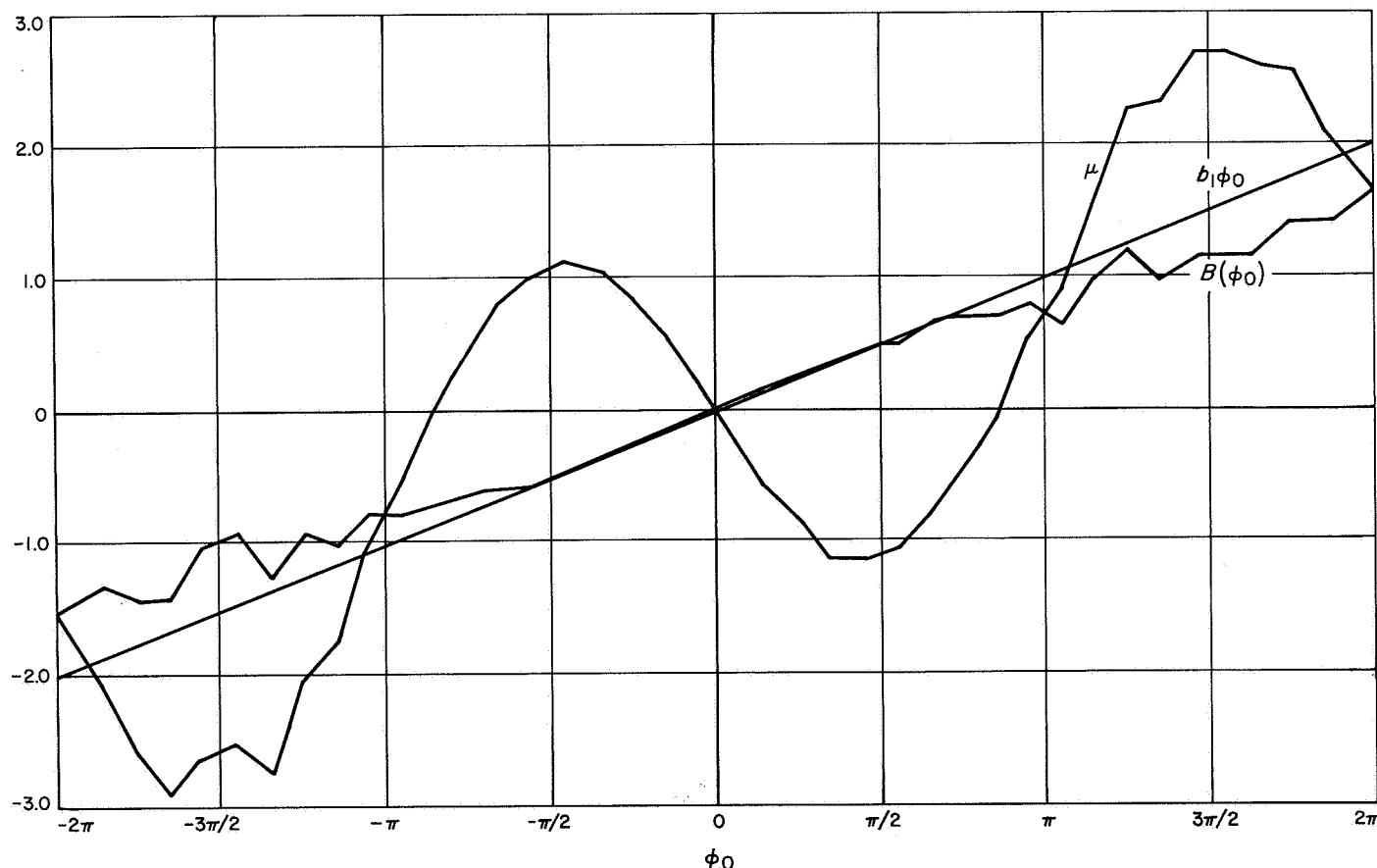


Fig. 2. Normalized first-slip time

typical, indicate that over the range $(0, 2\pi)$, the approximation

$$B(\phi_0) = b_1 \phi_0$$

is an extremely valid one. We thus have

$$g(\phi_0) = -\left(\frac{r+1}{r}\right) \rho \sin \phi_0 + \left(\frac{\rho}{r}\right) \phi_0 \quad (44)$$

A closed-form integration of $T = T(0)$ with the $g(\phi_0)$ given in Eq. (44) is not known; however, numerical methods are easily applied. Viterbi was able to show in his article (Ref. 8) that the first-order case result also holds for second-order loops whenever r is very large; the model we have developed verifies this behavior, for as the reader will note, as $r \rightarrow \infty$, the parameters in Eqs. (43) and (44) approach those in Eqs. (28) and (29). A comparison of mean time to cycle-slip appears in Fig. 3, along with a few experimentally-determined points (Ref. 12). Both the theoretical approximation and the experimental results show that the mean slip-time is degraded at lower values of r , i.e., for loops with little damping. This is unfortunate, since most tracking loops are designed with $1 < r < 7$ for acquisition or minimal noise reasons.

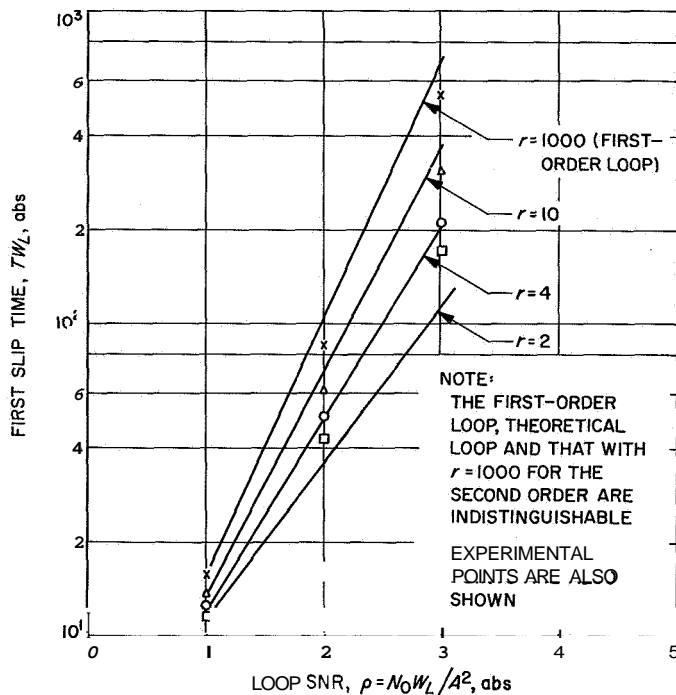


Fig. 3. Experimental plot of $\mu = E[\phi_0 | \phi_0]$ and $B[\phi_0]$ as a function of ϕ_0 for $r = 4$, $W_L = 1$, $p = 3$

7. Conclusions

The model developed here is applicable to the determination of the mean first-slip times for a loop of arbitrary degree. The only questionable approximation we have made is the representation of $B(\phi)$ by the first term in its Taylor expansion, which does not seem to be serious for the second-order loop, and is probably valid for higher-order loops as well. The experimental work in Ref. 12 seems to indicate that the probability distribution on the slipped cycles is perhaps best fit by a Gamma density

$$p(x) = \frac{(\mu/\sigma^2)^{(\mu/\sigma^2)^2} x^{(\mu/\sigma^2)^2} - 1}{\Gamma[(\mu/\sigma^2)^2]} e^{-\mu x/\sigma^2} \quad (45)$$

where μ is the average slip-time (we have used $\mu = T$ here), and σ is the standard deviation of slip-times. Experiments further show that the ratio (μ/σ) ranges from about 1.3 at $p = 0.5$ down to about 1.04 at $p = 2$; inserted in the above, one sees that $p(\alpha)$ then is very nearly a Poisson (the case with $\mu/\sigma = 1$) density. Data published in other works (Refs. 13-15) tend to bear this out further. Hence, with the average first slip-times given in this article, the entire distribution on first slip-times becomes known.

N67 18350

E. Information Processing Arithmetic Decoding of Cyclic Codes, G. Solomon

1. Summary

We present a simplified arithmetic decoding procedure for the $(2^k - 1, k)$ maximal-length shift register codes, and for the cyclic versions of the second-order Reed-Muller $(2^k - 1, 1 + k + (k/2))$ codes. The procedure is arithmetic in nature, requiring only a fixed permutation, vector addition, and weight counting. It takes k steps in the maximal-length case and m steps in the Reed-Muller case, where m is the number of information bits. The algorithm is independent of the number of errors. For low rate codes with high error-correction ability, this is an improvement in the state of the art.

2. Maximal Length Shift Register Codes

a. The $(2^k - 1, k)$ code. Step 1. Let $\bar{a} = (a_0, a_1, a_2, \dots, a_{2^k-2})$ be the received word. Perform the prescribed permutation \dagger (see below) on the coordinates to obtain the vector $\bar{b} = (b_0, b_1, b_2, \dots, b_{2^k-2})$. Form the vector sum $\bar{a} + \bar{b}$, and compute the weight $w(\bar{a} + \bar{b})$ (the number of ones in the vector $\bar{a} + \bar{b}$).

If $w(\bar{a} + \bar{b}) < 2^{k-1} - 1$, decode \mathbf{a} , = 0

$w(\mathbf{a} + \mathbf{b}) > 2^{k-1} + 1$, decode \mathbf{a} , = 1

Step 2. Cyclically shift the vector \bar{a} one position to the right to obtain $T\bar{a} = (a_1, a_2, a_3, \dots, a_k)$. Perform step 1 on the vector $T\bar{a}$ to obtain the decoded a_1 .

Step 3. Shift $T\bar{a}$ one position to the right to obtain $T^2\bar{a}$ and decode a_2 using step 1. Continue shifting until a_3, \dots, a_{k-1} are decoded. These are the corrected information bits.

Check Procedure. Feed the decoded k information bits into the encoding shift register to obtain the code word \bar{a}^* . Compute $w(\bar{a} + \bar{a}^*)$. If $w < 2^{k-2}$, we have decoded correctly. If $w > 2^{k-2}$, we have detected an uncorrectable error.

b. The $(2^k - 1, k + 1)$ code. This is the maximal-length shift register code and its complement. The procedure is almost identical to the steps in (a) with two modifications.

step 1. If $\bar{a} = (a_0, a_1, \dots, a_{2^k-2})$ is the received vector, the permuted $\phi(\bar{a}) = \mathbf{b}$ is $(c_0, b_1, b_2, \dots, b_{2^k-2})$ with c_0 unknown. The weight $w(\bar{a} + \bar{b})$ is computed over all the positions save the first. The decoding of a_1 is as before.

Step 4. Take the decoded k information bits a_1, a_2, \dots, a_{k-1} and feed into the encoding shift register to obtain a^* . Compute $w(a + a^*)$. If $w(a + a^*) < 2^{k-2}$, a^* is the decoded word. If $w(a + a^*) > 2^k - 1 - 2^{k-2}$, the decoded word is $(a^*)^c = (a + 1, a + 1, a + 1, \dots)$. If $2^{k-2} < w < 2^k - 1 - 2^{k-2}$, then we have detected an uncorrectable error.

To prove that the above procedure works, we follow Mattson-Solomon (Ref. 16). Every code word \bar{a} in the $(2^k - 1, k + 1)$ cyclic code is given by $\mathbf{a} = (a_i) = g_a(\beta^i) \mathbf{i} = 0, 1, 2, \dots, 2^k - 2$ where

$$g_a(x) = c_0 + \text{Tr } cx,$$

$$c_0 \in GF(2), c \in GF(2^k);$$

$$\text{Tr } x = x + x^2 + \dots + x^{2^{k-2}};$$

$$\beta \text{ a primitive } (2^k - 1)^{\text{st}} \text{ root of unity}$$

The map $x \rightarrow x + 1$ (Ref. 17) is a permutation of the elements of $GF(2^k)$ which takes $1 \rightarrow 0, 0 \rightarrow 1, \beta \rightarrow \beta + 1$, etc. The code word \bar{a} is permuted under this transformation into $\phi\bar{a} = \{c_0 + \text{Tr } c(x + 1)\} = \{c_0 + \text{Tr } c + \text{Tr } cx\} = (c_0 + \text{Tr } c, c_0 + \text{Tr } c + \text{Tr } c\beta, c_0 + \text{Tr } c + \text{Tr } c\beta^2, \dots)$. The permuted word $\phi(\bar{a})$ is again a code word of the $(2^k - 1, k + 1)$ code. The vector sum $\bar{a} + \phi(\bar{a})$ is the constant vector $\{\text{Tr } c\} = \{a_0 + c\}$ which yields \mathbf{a} , for the $(2^k - 1, k)$ code if $c_0 = 0$. Let us suppose that $e < 2^{k-2}$ errors have been made in the received word \bar{a} ; then the permuted vector $\phi(\bar{a})$ has at most 2^{k-2} errors, too. Therefore, $\bar{a} + \phi(\bar{a})$ has at most $2e$ errors, and therefore if $a_0 + c_0 = 0$, then $w(\bar{a} + \phi(\bar{a})) < 2e < 2^{k-1} - 1$. If $a_0 + c_0 = 1$, $w(\bar{a} + \phi(\bar{a})) > 2^k - 1 - 2e > 2^{k-1} + 1$. We need only compute the weight on the $(2^k - 2)$ coordinates, excluding the 0th coordinate. Thus $\mathbf{a} + c_0$ is clearly the majority value in the vector $\mathbf{a} + \phi(\mathbf{a})$.

The same operations on the cyclic shifts of \bar{a} will yield values for $a_i + c_i, i = 1, 2, \dots, k - 1$. The correct value of c_0 is determined by a comparison of the generated code word using the $a_i + c_i$ as information bits with the received word \bar{a} . There are k steps in the procedure plus a final comparison in the $(2^k - 1, k + 1)$ code. There are $(k + 1)$ basic steps, all of the same nature (a permutation, a vector sum, and a counting of ones.)

For large k , this method is simpler and faster than the methods in existence today.

Example. Let $k = 4$, $\mathbf{A} = (15, 5)$ code generated by $f(x) = (x^4 + x + 1)(x + 1)$. The code \mathbf{A} is generated by the recursion

$$a_{n+5} = a_{n+4} + a_{n+2} + a_{n+0} \quad n = 0, 1, 2, \dots$$

Let $\bar{a} = (1, 0, 1, 1, 1, 0, 1, 1, 1, 0, 1, 0, 1, 1, 1)$ be the received word.

$$= (\text{Tr } cx + c_0), a_i = \text{Tr } c\beta^i + c_0, \\ \text{p a root of } x^4 + x + 1$$

The map $x \rightarrow x + 1$ takes:

$$\begin{array}{ll} 1 \rightarrow 0 & \\ 0 \rightarrow 1 & \beta^5 \rightarrow \beta^{10} \\ \beta \rightarrow \beta + 1 = \beta^4 & \beta^6 \rightarrow \beta^{13} \\ \beta^2 \rightarrow \beta^8 & \beta^7 \rightarrow \beta^9 \\ \beta^3 \rightarrow \beta^{14} & \beta^{11} \rightarrow \beta^{12} \end{array}$$

yielding the permuted vector

$$\begin{aligned}\phi(\bar{a}) &= (x, 1, 1, 1, 0, 1, 1, 0, 1, 0, 1, 1, 1) \\ a + \phi(\bar{a}) &= (x + 1, 1, 0, 0, 1, 1, 0, 1, 0, 1, 1, 1, 0, 0), \\ w(\bar{a} + \phi(\bar{a})) &= 8\end{aligned}$$

We conclude that $a_0 + c_0 = 1$.

Continuing the procedure, we obtain **1,0,0,0**, as the correct information bits with $c_0 = 0$.

The method here is simpler than that of Ref. 18, p. 88, which is a majority decoding procedure for maximal-length codes, but requires an orthogonalization procedure first.

3. More General Cyclic Codes

For purposes of using our decoding techniques for other cyclic codes, it becomes advantageous to identify certain classes of cyclic codes with respect to our permutation ϕ .

Definition. Let (M_0, k) be the $(2^k - 1, 1)$ code containing the all-one vector. Let (M_1, k) be the maximal length shift register code $(2^k - 1, k + 1)$. The code (M_2, k) is the largest cyclic code A of length $2^k - 1$ such that if $\bar{a} \in A$, and ϕ is the permutation $x \rightarrow x + 1$ of $GF(2^k)$, $a + \phi(a) \in (M_1, k)$. We define, inductively (M_j, k) also such that $\bar{a} + \phi(\bar{a}) \in (M_{j-1}, k)$. Clearly, if (M_1, k) corrects e errors with $e < 2^{k-2}$, then (M_2, k) will surely correct e errors with $e < 2^{k-3}$, and so on. These codes are essentially cyclic versions of the shortened Reed-Muller codes.

One need not restrict oneself to $\phi: x \rightarrow x + 1$. Clearly, $\phi: x \rightarrow x + \gamma$, $\gamma \in GF(2^k)$, will lead to the same (M_j, k) .

Theorem 1: The (M_2, k) code is generated via recursion by $f = \prod_{i \in T} f_i(x)$, where $f_i(x)$ is the irreducible polynomial over $GF(2)$ with β^i as a root; β is a primitive $(2^k - 1)$ st root of unity; $\deg f(x) = k(k + 1)/2 + 1$ and $T = \{0, 1, 2^r + 1, r \geq 1\}$.

Example. $(M_2, 5)$ is the **(31, 16)** code generated by $f(x) + (x + 1) f_1 f_3 f_5$ where $f_1(x) = x^5 + x^2 + 1$.

Proof of Theorem 1. The $g_a(x)$ for an (M_2, k) code must contain some $\text{Tr } c x^r$, r odd. The permutation $x \rightarrow x + 1$ transforms $\text{Tr } c x^r$ into $\text{Tr } c (x + 1)^r = \text{Tr } \sum c x^j \binom{r}{j}$. If $r = \sum b_j 2^j$ is the binary expression of r , we have $\binom{r}{2^j} \equiv$

b_j . Therefore, if $b_j = 1$, $\binom{r}{2^j} = 1$ and so is $\binom{r}{r - 2^j}$ giving rise to an x^{r-2^j} term. In order for $\bar{a} + \phi(\bar{a})$ to belong to (M_1, k) , $g_{a+\phi(a)}$ cannot contain terms of the form x^{r-2^j} where $r - 2^j \neq 2^e$. But r is odd; thus, $r = 2^j + 1$, and is of form stated.

We have shown that

$$g_a(x) = \sum_{i \geq 1}^k c_i x^{2^{i-1}+1}$$

Now, there are k admissible numbers of form $2^{i-1} + 1$, $i = 1, \dots, k$.

For k odd, $2^{k-r} + 1$ is the same conjugate class as $2^r + 1$ since

$$2^r(2^{k-r} + 1) = 2^k + 2^r = 1 + 2^r \pmod{2^k - 1}$$

Thus, 1 has one conjugate class, and the $k - 1$ other possible integers are in $k - 1/2$ classes. Since k is odd, these are k distinct conjugates to each class (no periodicity is possible since there are only two ones). We thus have $\deg f = k + k(k - 1)/2 + 1 = k(k + 1/2) + 1$. For k errors, we have as before

$$2^{k-r} + 1 = 2^r + 1 \pmod{2^k + 1}$$

But $r = k/2$ gives only one element so we have k elements in the class of $2^0 + 1$, $k/2$ elements in $2^{k/2} + 1$, and k in the $k - 2/2$ classes above, giving rise to

$$\begin{aligned}\deg f &= k + \frac{k}{2} + \frac{(k-2)k}{2} + 1 \\ &= \frac{k}{2}(k+1) + 1\end{aligned}$$

Thus, the (M_2, k) codes are of dimension $k(k + 1)/2 + 1$ and will correct $e < 2^{k-2} - 1/2$ errors. These are the cyclic versions of the Reed-Muller codes.

Examples of Some Codes of this Type:

$k = 4$	(15,11)	$e = 1$
$k = 5$	(31,16)	$e = 3$
$k = 6$	(63,22)	$e = 7$
$k = 7$	(127,29)	$e = 15$ etc.

b. Theorem 2: (M_3, k) is the $\left(2^k - 1, 1 + k + \binom{k}{2} + \binom{k}{3}\right)$ cyclic code generated by

$$f(x) = \prod_{i \in T} f_i(x)$$

$$T = [0, 1, 2^r + 1, (r \geq 1), 2^r + 2^r + 1, r \neq s \geq 1]$$

β a primitive root, f_i an irreducible polynomial with (β^i) as a root. Also, (M_3, k) corrects errors $e < 2^{k-4}$. The proof is omitted.

c. Theorem 3: (M_j, k) is the j th order Reed-Muller code (without the parity check on all the elements) generated by the appropriate $f(x)$, $e < 2^{k-j-1}$. The proof is also omitted.

4. Decoding Procedures

One possible decoding procedure of the (M_2, k) lending itself to mechanization is basically $\binom{k}{2}$ times as long as that for the $(2^k - 1, k + 1)$ code. Let A be a code generated by $f(x)$ described above. Then for $a \in A$, $\bar{a} = (a_i) = \{g_a(\beta^i)\}$ where

$$g_a(x) = c_0 + \text{Tr } c_1 x + \text{Tr } (c_2 x^3 + c_3 x^5 + c_4 x^9 + \dots)$$

The permutation $x \rightarrow x + 1$ takes \bar{a} into the permuted vector $+(a) = (c_0 + \text{Tr } (c_1 + c_3 + c_5 + \dots), \dots)$. One notes that $\text{Tr } cx^{2^{k+1}}$ goes into $\text{Tr } c(x + 1)^{2^{k+1}}$, and

$$\begin{aligned} \text{Tr } (cx^{2^{k+1}} + cx^{2^k} + cx + c) &= \text{Tr } cx^{2^{k+1}} \\ &+ \text{Tr } c + \text{Tr } x(c^{2^{-k}} + c) \end{aligned}$$

Therefore, $\bar{a} + (a)$ is a code word in the $(2^k - 1, k + 1)$ code and is given by

$$\{\text{Tr } (c_1 + c_3 + c_5 + \dots) + \text{Tr } (x \sum (c_i^{2^{-(i-1)}} + c_i))\}$$

Clearly, if e errors occur in \bar{a} , $\bar{a} + \phi(\bar{a})$ has at most $2e$ errors. If $2e < 2^{k-2}$, we can decode $\bar{a} + \phi(\bar{a})$ in $(k + 1)$ steps to obtain the value of $\text{Tr } \sum c_i$. Repeating this technique for the m shifts of \bar{a} and finally checking for the value of c_0 , we obtain a correctly decoded word.

Example: The $(127, 29)$ code generated by $f_0 f_1 f_3 f_5 f_9$ corrects 15 errors in 297 steps, repeatedly using the permutation ϕ , $x \rightarrow x + 1$, adding the vectors and summing the number of ones. In each step, we permute a vector of

length $2^k - 1$ and perform $(2^k - 1) \bmod 2$ additions to obtain a vector whose ones we count. The computation of the vector $a + (a)$ takes fewer operations than the computation of a symmetric power sum: $k < 2^{k-2}$, which is the number of symmetric power sums to be computed before beginning the algebra of root finding. So for large e , this method is more efficient. But for small e and high information rates, the standard BCH decoding procedures are preferred.

N67 18351

F. Data compression Techniques: Recent Results on Epsilon Entropy, E. C. Posner, E. R. Rodemich, and Howard Romsey, Jr.

1. Summary

This note summarizes a paper submitted to the Annals of Mathematical Statistics, entitled "Epsilon Entropy of Stochastic Processes." We introduce the concept of *epsilon-delta entropy* for objects called probabilistic metric spaces. A *probabilistic metric space* is a probability space and also a metric space in which every open set is measurable. The epsilon-delta entropy of a probabilistic metric space is defined for arbitrary positive epsilon and non-negative delta as the infimum of the entropies of all *epsilon-delta partitions* of the space. An epsilon-delta partition of a probabilistic metric space is a partition of all of the space except at most delta in probability by measurable sets of diameters at most epsilon; the entropy of such a partition is the entropy of the conditional discrete distribution induced by the partition. The concept arises in the study of efficient data transmission, in other words, in *data compression*.

We are here concerned with the class of examples of probabilistic metric spaces obtained from mean-continuous stochastic processes on the unit interval. Thus, consider the space of real-valued square-integrable functions on the unit interval with distance between two functions given by the L_2 -norm of the difference of the two functions. The probability measure is to be the one induced on the function space via the Kolmogorov Consistency Theorem. Now for any epsilon and delta both greater than zero, the epsilon-delta entropy of any probabilistic metric space is finite. However, when delta is zero, the resulting entropy, called simply the *epsilon entropy* of the space, can be infinite. We give a condition on the eigenvalues of the process such that any process satisfying that condition has finite epsilon entropy for any epsilon greater than zero. And, for any set of eigenvalues not satisfying the given condition, we produce a

mean-continuous process on the unit interval having infinite epsilon entropy for every epsilon greater than zero.

2. Introduction

This subject is motivated by the following considerations relating to efficient data transmission, a subject that has come to be known as *data compression*. Suppose one has an experimental source on board a spacecraft. This source is given by some probability law which is assumed known. One wishes to transmit the outcomes to Earth using as few bits of information as possible. There is assumed to be a certain *fidelity criterion* such that the actual outcome occurring is to be known to the recipient of the message within a given fidelity after he receives the message. One is also allowed to ignore a certain fraction of the outcomes, that is, one does not attempt to transmit them. What is the minimum number of bits that one can get away with under these constraints? That is, what is the best way to *compress* the data? Recent issues of this publication have considered aspects of this problem.

We idealize this situation by defining the concept of *probabilistic metric space* and its ϵ, δ entropy $H_{\epsilon, \delta}(X)$. Thus, define a probabilistic metric space $X = (X, d, \mu)$ as follows:

1. (X, d) is to be a complete separable metric space, of points of the set X under the metric d .

2. (X, μ) is to be a probability space, where the Borel field of sets on which μ is defined is to be the class of Borel sets in (X, d) , that is, the Borel field generated by the open sets of X .

The probability space (X, μ) represents the space of experimental outcomes. The metric d represents the fidelity criterion, stating how close one outcome is to another.

Now any transmission system, it is reasonable to assume, works as follows. Given the received message, there is a certain Borel set of outcomes of X that could have arisen and still yielded the same message. The requirement that outcomes be known within ϵ can be translated as the requirement that the Borel sets occurring in this way have diameters at most ϵ . Thus, we are led to consider partitions of X by Borel sets of diameters at most ϵ (called briefly ϵ -sets). However, since we are allowed to ignore a certain fraction, say δ at most, of X in designing our data compression system, we need only

require that the union of the sets in the ϵ -partition of X have probability at least $1 - \delta$. Such a partition we call an ϵ, δ partition, which is defined for $\epsilon > 0, \delta \geq 0$. (When $\delta = 0$, we call such partitions briefly *E-partitions of X* .) We consider only partitions by a finite or denumerably infinite number of sets; or equivalently, partitions in which all but a denumerable number of the sets lie in a set of probability 0.

Now when we have an ϵ, δ partition of X , the number of bits necessary to describe into which set of the partition the outcome actually falls is given by a well-known formula of Shannon (Ref. 19). Namely, let p_i denote the probability of the i th set U_i of the partition U which has positive probability. Let $\{q_i\}$ denote the discrete distribution $\{p_i / \sum p_i\}$. This distribution has an entropy given in terms of base e logarithms; we call this entropy $H(U)$, the *entropy of the partition U* :

$$H(U) = \sum q_i \log \frac{1}{q_i}$$

Thus, $H(U)$ is the minimum number of bits necessary to describe into which sets of U the outcome falls, given that it falls into the part of X covered by some set of the ϵ, δ partition. However, our ϵ, δ partition may not have been especially well chosen. Thus, it is natural to consider, for the class $\mathcal{U}_{\epsilon, \delta}$ of ϵ, δ partitions of the probabilistic metric space X , the quantity $H_{\epsilon, \delta}(X)$ defined by

$$H_{\epsilon, \delta}(X) = \inf_{U \in \mathcal{U}_{\epsilon, \delta}} H(U)$$

This quantity $H_{\epsilon, \delta}(X)$ is called the ϵ, δ entropy of X . (When $\delta = 0$, we write $H_\epsilon(X)$ and call it the ϵ entropy of X). The ϵ, δ entropy of X then measures the smallest number of bits necessary to describe at least $1 - \delta$ of X by sets of diameter at most ϵ .

The way $H_{\epsilon, \delta}(X)$ is defined leaves open the possibility that $H_{\epsilon, \delta}(X)$ be infinite. That is, no ϵ, δ partition might have finite entropy. However, when $\delta > 0$, we can prove that $H_{\epsilon, \delta}(X)$ is finite. This is proved by producing a finite ϵ, δ partition, which of course has finite entropy. This proof, as well as all others in this note, is omitted.

It turns out that $H_\epsilon(X)$ can be infinite. It is, in fact, of special interest in this subject to give conditions on certain classes of probabilistic metric spaces which makes the ϵ -entropy finite. In this note, we shall describe results for the class of probabilistic metric spaces given by

$L_2[0,1]$ under the measure induced by a mean-continuous stochastic process. Before we do this, however, we shall give some results on the continuity of $H_{\epsilon;\delta}(X)$ in ϵ and δ .

3. Continuity in δ and in ϵ

It is the purpose of this section to give the following continuity results about the function $H_{\epsilon;\delta}(X)$.

Theorem 1: For fixed positive ϵ , $H_{\epsilon;\delta}(X)$ is a function of δ continuous from above. Furthermore, if either X is non-atomic, or $H_\epsilon(X)$ is infinite, then for $\delta > 0$, $H_{\epsilon;\delta}(X)$ is continuous in δ from below.

Remark: When X has atoms, $H_{\epsilon;\delta}(X)$ need not be continuous in δ from below. Just consider a two-point space X in which each point is at distance 1 from the other and has probability 1/2. Then

$$H_{1/2;1/2}(X) = 0, \text{ whereas } \lim_{\delta \rightarrow 1^-} H_{1/2;\delta}(X) = \log 2$$

We now state that for δ fixed, $H_{\epsilon;\delta}(X)$ is continuous in ϵ from above. Even in the non-atomic case, there is no hope of proving that $H_{\epsilon;\delta}(X)$ is continuous from below in ϵ . For let X be the unit circle with probability measure given by normalized angular probability measure, and metric given by the Euclidean metric in the plane. Then $H_2(X) = 0$, whereas $\lim_{\epsilon \rightarrow 2^-} H_\epsilon(X) = \log 2$. The latter is true because no set in an ϵ -partition of X can contain a pair of antipodal points for $\epsilon < 2$.

Theorem 2: Let X be a probabilistic metric space, and let $\delta \geq 0$ be given. Then $H_{\epsilon;\delta}(X)$ as a function of ϵ is continuous in ϵ from above.

Remark: Since $H_{\epsilon;\delta}(X)$ is monotone non-decreasing in, both ϵ and δ , it now follows that $H_{\epsilon;\delta}(X)$ is jointly continuous from above in ϵ and δ .

Remark: Let us define $H_{\epsilon;\delta}(X)$ (and $H_\epsilon(X)$) for $\epsilon = 0$ as follows: $H_{0;\delta}$ is infinite if there is no partition of at least $1 - \delta$ of X by sets of diameter 0 (atoms); if there is such a partition, the definition is the same as before. With this definition, $H_{0;\delta}(X)$ is continuous in δ from above. And $H_{\epsilon;\delta}(X)$ is continuous from above in ϵ as $\epsilon \rightarrow 0$, δ fixed. The following result is also true:

Theorem 3: If $H_{0;\delta}(X)$ is finite for $\delta > \delta_0$, infinite for $\delta < \delta_0$, then $X = Y \cup Z$, Z the set of atoms of X and Y its complement, with $\mu(Z) = 1 - \delta_0$, $H(Z) = H_{0;\delta_0}(X)$.

($H(Z)$ is the possibly infinite entropy of the distribution of atoms.)

The following corollary is of interest, but is to be expected: one should expect to need arbitrarily many bits to prescribe a non-atomic probabilistic metric space with arbitrary precision.

Corollary: If X is non-atomic, $H_{0;\delta}(X)$ is infinite for every $\delta < 1$. Thus, $H_{\epsilon;\delta}(X) \rightarrow \infty$ as $\epsilon \rightarrow 0$, for $\delta < 1$. If X is not purely atomic, $H_\epsilon(X) \rightarrow \infty$ as $\epsilon \rightarrow 0$.

4. Finite-Dimensional Euclidean Spaces

As preparation for the final section, this section considers the ϵ -entropy of distributions in Euclidean n -space with ordinary sum-of-squares metric. This certainly yields a probabilistic metric space. We assume that $E(\|x\|^2) < \infty$, where E denotes expectation. We can prove:

Theorem 4: Let X be Euclidean n -space with a probability distribution such that $\|x\|^2$ has finite expectation. Then $H_\epsilon(X)$ is finite, for every $\epsilon > 0$. In fact,

$$H_\epsilon(X) \leq n \log \frac{1}{\epsilon} + C + o(1)$$

as $\epsilon \rightarrow 0$, where the constant C and the function o depend only on n and $\{E(x_i^2)\}$, x_i the i th coordinate function.

5. Mean-Continuous Stochastic Processes

The first theorem of this final section can be regarded as a generalization of Theorem 4 to countable-dimensional Euclidean spaces, in particular, to $L_2[0,1]$. Let $Y(t,\omega)$, $\omega \in \Omega$, be a separable mean-continuous stochastic process on the closed unit interval (see Ref. 20, Chap. X for definitions). Let $R(s,t) = E(Y(s,\omega)Y(t,\omega))$, a continuous positive definite function. Let $\sigma_1^2 \geq \sigma_2^2 \geq \dots \geq 0$ be the eigenvalues of the integral equation $\int R(s,t)\phi(t)dt = \sigma^2\phi(s)$, with associated normalized continuous eigenfunctions $\phi_n(t)$.

(It is known that $R(s,t) = \sum \sigma_n^2 \phi_n(s)\phi_n(t)$ uniformly on the unit square; also, $\sum_{n=1}^{\infty} \phi_n^2$ is finite and equal to $E(\int_0^1 Y^2(t,\omega) dt)$. Then there exist uncorrelated random variables $\xi_n(\omega)$, $E(\xi_n^2) = 1$, such that with probability 1 on Ω

$$\sum_{n=1}^N \sigma_n \xi_n(\omega) \phi_n(t) \rightarrow Y(t,\omega) \text{ in } L_2[0,1]$$

as $N \rightarrow \infty$.

Using the techniques of Ref. 21, what we really have is a probability distribution μ on an abstract separable Hilbert space with orthonormal basis $\{\phi_n\}$ (the form of $\{\phi_n\}$ has nothing to do with the L_2 -structure of the process). The measure μ is uniquely determined from the finite-dimensional distributions of $(\xi_1, \xi_2, \dots, \xi_n)$, all n . The distribution in this n -space is that of $\sum_{j=1}^n \sigma_j \xi_j \phi_j$. All other facts about the process can be ignored in what follows.

It might be reasoned, by analogy with Theorem 4, that, since $\sum \sigma_n^2 < \infty$, the E-entropy of the probabilistic metric space X consisting of $L_2[0,1]$ under L_2 -norm with measure μ might be finite for every positive ϵ . Such, however, is not the case. (Don't try to find an example of a mean-continuous process which is Gaussian with infinite E-entropy for some ϵ , though. We can prove that the ϵ -entropy of $L_2[0,1]$ for Gaussian processes is always finite.) We call the ϵ -entropy of $L_2[0,1]$ the E-entropy of the process, for convenience.

Theorem 5: If $\sum n\sigma_n^2 < \infty$, any mean-continuous stochastic process on $[0,1]$ with eigenvalues $\{\sigma_n^2\}$ has finite ϵ -entropy H_ϵ . Specifically,

$$H_\epsilon = o\left(\frac{1}{\epsilon^2}\right), \quad \text{as } \epsilon \rightarrow 0,$$

where the function o depends only on the eigenvalues σ_n^2 of the process.

The following theorem shows that Theorem 5 is the best possible, in the sense that if $\sum n\sigma_n^2 = \infty$, there is a process under which $L_2[0,1]$ has infinite ϵ -entropy. The construction has the property that with probability 1, only finitely many ξ_n are non-zero. Thus, the sample

functions can be made say entire functions with probability 1.

Theorem 6: If $\sum n\sigma_n^2 = \infty$, there is a mean-continuous stochastic process on $[0,1]$ with eigenvalues $\{\sigma_n^2\}$ which has infinite ϵ -entropy for every $\epsilon > 0$.

Theorem 6 can be used to show that $\sum n\sigma_n^2 < \infty$ for processes on $[0,1]$ whose covariance function $R(s,t)$ satisfies $|2R(s,t) - R(s,s) - R(t,t)| = O(|s - t|^{1-\delta})$ as $|s - t| \rightarrow 0, \delta > 0$.

Remark: It can be shown that there exist mean-continuous stochastic processes on the unit interval (Gaussian in fact) with finite ϵ -entropy for every positive ϵ , but such that H_ϵ is an arbitrarily rapidly increasing function as $\epsilon \rightarrow 0$. Of course, for these processes, $\sum n\sigma_n^2$ diverges. Examples can also be given of processes with finite ϵ -entropy for some ϵ but not others (these can be taken to have the support of μ be a bounded set in L_2). We note that the Wiener process in $[0,1]$ has ϵ -entropy H_ϵ with $1/2\epsilon^2 \lesssim H_\epsilon \lesssim 1/\epsilon^2$. For this process,

$$\sigma_n^2 = \frac{1}{\pi^2 \left(n - \frac{1}{2}\right)^2}, \quad n \geq 1,$$

and so $\sum n\sigma_n^2$ diverges, as it must by Theorem 5. By Theorem 6, however, there exists a (non-Gaussian) process with the very same eigenvalues whose ϵ -entropy is infinite for every $\epsilon > 0$. As we have remarked previously, for any eigenvalues σ_n^2 with $\sum \sigma_n^2$ finite, no matter how slowly decreasing, there exists a process with finite E-entropy for every positive ϵ . Namely, any Gaussian process with those eigenvalues will do. In other words, no given slow rate of decay of the eigenvalues guarantees infinite ϵ -entropy.

References

1. Golomb, S., "Deep Space Range Measurement" Research Summary 36-1, pp. 3942, Jet Propulsion Laboratory, Pasadena, California, February 15, 1960.
2. Titsworth, R. C., "Optimal Ranging Codes" Technical Report 32-411, Jet Propulsion Laboratory, Pasadena, California, April 15, 1963.

References (contd)

3. Posner, E. C., and Rumsey, H., "Continuous Sequential Decision in the Presence of a Finite Number of Hypotheses," *IEEE Trans. on Information Theory*, Vol. IT-12, no. 2, pp. 248-255, April 1966.
4. Feller, W., *An Introduction to Probability Theory and Its Applications*, Vol. I, Section 11.5, Wiley, 1950.
5. Easterling, M. F., "Acquisition Ranging Codes and Noise" Research Summary 36-2, pp. 3136, Jet Propulsion Laboratory, Pasadena, California, April 15, 1960.
6. Easterling, M. F., "Long-Range Precision Ranging System" Technical Report 32-80, Jet Propulsion Laboratory, Pasadena, California, July 10, 1961.
7. *Handbook of Mathematical Functions*, National Bureau of Standards AMS-55, pp. 297-308, 1964.
8. Viterbi, A. J., "Phase-Locked Loop Dynamics in the Presence of Noise by Fokker-Planck Techniques," *Proc. IEEE*, vol. 51, no. 12, pp. 1737-1753, December 1963.
9. Ford, L. R., *Differential Equations*, pp. 33-36, McGraw-Hill, New York, 1955.
10. Tausworthe, R. C., "Theory and Practical Design of Phase-Locked Receivers," Technical Report 32-819, Chapter 4, Jet Propulsion Laboratory, Pasadena, California, February 1966.
11. *Handbook of Mathematical Functions*, National Bureau of Standards AMS-55, June 1964.
12. Sanger, D., and Tausworthe, R. C., "An Experimental Study of the First-Slip Statistics of the Second-Order Phase-Locked Loop," Jet Propulsion Laboratory SPS 37-43, vol. IV, February 1967 (to be published).
13. Charles, F. J., and Lindsey, W. C., "Some Analytical and Experimental Phase-Locked Loop Results for Low Signal-to-Noise Ratios" *Proc. IEEE*, vol. 54, no. 9, pp. 1152-1166, September 1966.
14. Smith, B. M., "The Phase-Lock Loop with Filter: Frequency of Skipping Cycles" *Proc. IEEE*, vol. 54, no. 2, pp. 296-297, 1966.
15. Sanneman, R. W., and Rowbrotham, J. R., "Unlock Characteristics of the Optimum Type II Phase-Locked Loop," *IEEE Trans. on Aerospace and Nav. Elec.*, vol. ANE-11, pp. 15-24, March 1964.
16. Mattson, H. F., and Solomon, G., "A New Treatment of Bose-Chaudhuri Codes," *J. Soc. Ind. Appl. Math.*, vol. 9, pp. 654-669, 1961.
17. Peterson, W. W., *Error Correcting Codes*, MIT Press-Wiley, New York, 1961.
18. Massey, J. L., *Threshold Decoding*, M.I.T. Press, 1963.
19. Shannon, Claude S., "A Mathematical Theory of Communication," *Bell Syst. Tech. Jour.*, vol. 27, pp. 379-423, 1948.

References (contd)

20. Loève, Michel, *Probability Theory—Foundations. Random Sequences*, Van Nostrand, New York, 1955.
21. Prokhorov, Yu. V., “Convergence of Random Processes and Limit Theorems in Probability Theory,” translated, *Theory of Prob. and Appl.*, vol. I, pp. 157–214, 1956.